

# **Cell-Free Artificial Photosynthesis System**

A Thesis

Submitted to the Faculty

of

Drexel University

by

Xiang Ren

in partial fulfillment of the  
requirements for the degree

of

Doctor of Philosophy

January 2016



© Copyright 2016  
Xiang Ren. All Rights Reserved.



DREXEL UNIVERSITY

Graduate College

# DISSERTATION/THESIS APPROVAL FORM

This form is for use by all doctoral and master's students with a dissertation/thesis requirement. Please print clearly as the library will bind a copy of this form with each copy of the dissertation/thesis. All doctoral dissertations must conform to university format requirements, which is the responsibility of the student and supervising professor. Students should obtain a copy of the Thesis Manual located on the Graduate College or library website.

Dissertation/Thesis Title: Cell-Free Artificial Photosynthesis System

Author: Xiang Ren

**This dissertation/thesis is hereby accepted and approved.**

**Signatures:**

**Examining Committee**

Chair

Jack G. Zhou

Members

Moses Noh

Parkson Lee-Gau Chong

E. Caglan Kumbur

Baris Taskin

Wenqiao Yuan

Academic Advisor

Department Head

*J. Zhou*

*M. Noh*

*P. Lee-Gau Chong*

*E. Caglan Kumbur*

*B. Taskin*

*W. Yuan*

*J. Zhou* 1/20/2016

*[Signature]* 2016 Feb 02

## ACKNOWLEDGEMENTS

My research of "artificial photosynthesis system" was supported by National Science Foundation (NSF) CMMI-1141815 (and CMMI-1239138) "EAGER/Collaborate Research: Solid Freeform Fabrication of a Conceptual Artificial Photosynthesis Device", CMMI-1300792 (and CMMI-1266338, CMMI-1266306) "GOALI/Collaborative Research: Additive Manufacturing for a Highly Efficient Artificial Photosynthesis Device with Multi-Layer Interconnected Channels and Micro-Porous Structures", CBET-1437798 (and CBET-1437930) "Collaborative Research: Artificial Photosynthesis Based on Archaeal Lipids and Proteins for Biofuels" and some other funding source for partial projects CMMI-1266306 and CBET-1437930, for a total of \$380,053.00 (\$832,668.00 in total with other collaborators). I would like to thank Dr. Jack G. Zhou (Mechanical Engineering and Mechanics) for helping me get admitted to the Ph.D program at Drexel University, supporting me with salary and giving me the opportunity to teach Department of Mechanical Engineering and Mechanics (MEM) core courses MEM437/438 and MEM687/688. It was an honor and pleasure to be able to teach and develop course materials as a college educator and to be able to pass knowledge to students.

I would like to thank the collaborators and consultants for this project, as well as those who participated in labs during my research and experiments. I probably would have never finished my Ph.D research without them. Specifically, I would like to thank my co-advisor Dr. Hongseok (Moses) Noh (Mechanical Engineering and Mechanics) and Dr. Parkson Lee-Gau Chong (Temple University, School of Medicine, Biochemistry) for helping me getting on to the right path to Ph.D research and providing emotional, academic and financial support throughout my research process. My co-advisor Dr. Moses Noh led me to his research lab with all the facilities and equipment supporting, and provided me academic advices. He was pivotal in helping me prevent



making mistakes in my research, so that I would not be wasting too much time during my research. Dr. Moses Noh had also kindly provided financial support for me to attend Hilton Head conference and MicroTAS conference. Dr. Parkson Chong provided me with research materials and chemicals, as well as assisted me in finding research projects that were promising and reasonable. Specifically, Dr. Parkson Chong taught me how to choose specific research plan, write manuscript, and prepare data or figure results for better publications.

I also would like to sincerely thank other faculty members and organizations for allowing me to use their equipments, labs and resources, includes Dr. E.Caglan Kumbur (Mechanical Engineering and Mechanics), Dr. Wenqiao Yuan (North Carolina State University, Biological and Agricultural Engineering), Dr. Baris Taskin (Electrical and Computer Engineering), Dr. Ying Sun (Mechanical Engineering and Mechanics), Dolores Conover (Biomedical Engineering), and Centralized Research Facilities. I must also thank Dr. Andreas Andreou and Dr. Ralph Entienne-Cummings for opening the door to the scientific world of MEMS and microelectronics, and these experiences had greatly benefited my Ph.D research on specific projects and tasks.

I would also like to thank my colleagues for helping me with my collaborative research and partial research tasks, sharing their experiences and thoughts in the research work, including Dr. Qingwei Zhang, Kewei Liu, Miao Yu, Yoontae Kim, Youngbok Kang, Xin Yang, Hao Lu, and Steven Leist.

Last but not least, I would like to thank Huijie Zhang, whom I owe this opportunity, my life and happiness to.

## PREFACE

### Overview of research work

My Ph.D research project involves multiple disciplines in scientific fields, such as mechanical engineering, electrical engineering, mathematics, physics, chemistry, and biology. Specifically, this dissertation “Cell-free Artificial Photosynthesis System” includes micro-electro-mechanical system (MEMS), microfluidic devices and systems, microfabrication, digital logic circuit, mixed-mode VLSI, mathematical modeling, additive manufacturing, botany, natural phosphor lipid membranes, copolymer membranes, electrochemical impedance spectroscopy, physics in vibration, and chemical sensing, etc.

Ph.D study provides a good opportunity for students to become masters. The experiences of research, training, lecturing, and collaboration enhance the skills and abilities helpful in both industry and academic fields. Doctoral degree in philosophy means the students should have their own ideas, hypothesis, and theories, with proper physics and mathematics support.

When starting a Ph.D research topic, it is critical to have a good background survey and estimation of potential research work and results. Projects supported by National Science Foundation (NSF) are less likely to fail, because a proposal reviewing board formed by professional experts and university professors review and evaluate the research tasks and proposed plans. However, the plans issued in a funding proposal do not guarantee successful results. The objectives and introduction background in a funding proposal are established by sufficient literature study. The literature search source is limited to reliable resource, such as scientific journals. The scientific quality of public news and conference publications are not guaranteed. The scientific journal articles have to pass two or more reviewers’ examination and evaluation. Many reviewers are experts and willing to give rejection to those unqualified manuscript.

Funding proposal is the second step in establishing a scientific research. The funding proposal includes a list of possible research tasks, even though without experiments supporting. However, basic mathematical, physical, and theoretical principles have to be reasonable. A good funding proposal can be a guide to the future graduate research for three to five years. Personally, my research of “cell-free artificial photosynthesis system” got approved by NSF funding both in “EARly-concept Grants for Exploratory Research (EAGER)” and “Grant Opportunities for Academic Liaison with Industry (GOALI)” program from the NSF Division of Civil, Mechanical and Manufacturing Innovation (CMMI).

Mistakes are allowed for research students during their Ph.D research and study, especially on the experiments of exploring new methods. However, not all kinds of mistakes are beneficial in research work. Mistakes happened because of new factors or unknown theories are good things, which make people learn, and make technologies improve. On another hand, mistakes made because of lacking of knowledge or careless are not good things, which will be a waste of time and money, or even the quality of research work. Geniuses exist in the science world, but not many. Everyone have a dream starting from childhood, to become a great scientist, as Isaac Newton, Albert Einstein, or Steven Hawking. However, this kind of great scientist exists only one for every 100 years. If someone brings the dream from childhood to Ph.D study, this dream will become naïve behaviors, or even lead to ambiguous and unrealistic behaviors. Putting the hope of succeed on miracle will have higher chance to failure than the chance of winning a lottery or the chance of getting lightening shot for seven times.

The experiments are one of the major works during a Ph.D research. Planning ahead is helpful for the successful chance of experiments. Some students spend hours and hours on some experiments without thinking about why and what they can get. Unfortunately, I also wasted two and half years before I realize this. Luckily, I met my co-advisors and academic consultants, who finally lead me onto the correct way on Ph.D research. The Ph.D research is focused on what we can do and what we can improve or create. During Ph.D research, we are doing experiment, not advertisement.

Data management is important in research work. All research theory requires a statistical results and a large amount of data base to support mathematical models and physical equations. The data is got from experiments, not from imagination. Without realizing the physics and mathematics in an experiment, data will not show its means by itself. Researchers are responsible to analysis and extract the useful theory from data, which requires a solid background knowledge of mathematics, includes statistics, probability theory, and proper data analysis, etc., and the ability to use scientific data analysis software.

### **Contents in this dissertation**

The chapters were arranged based on the full story of completion of my Ph.D research project: cell-free artificial photosynthesis system.

Chapter 1: the introduction of photosynthesis and current status in artificial photosynthesis approaches.

Chapter 2: the membrane embedded on PCB, and the mathematical modeling of membrane vibration based on physics principles.

Chapter 3: the membrane in microfluidic chips, including stability study and ion transfer study.

Chapter 4: carbon dioxide absorption study in gas-liquid interface.

Chapter 5: glucose synthesis using microfluidic device with gas-liquid interface mechanism.

Chapter 6: the porous platform for glucose synthesis/storage using additive manufacturing.

Chapter 7: the integration and interconnection of multiple units.

Chapter 8: a summary of completed research projects.

X. Ren

A handwritten signature in black ink that reads "Xiang Ren". The signature is written in a cursive style with a horizontal line underneath the name.

Philadelphia, Pennsylvania

January, 2016

## TABLE OF CONTENTS

LIST OF FIGURES .....	xiii
LIST OF TABLES .....	xxv
ABSTRACT.....	xxvi
Chapter 1. INTRODUCTION .....	1
1.1 Background of natural photosynthesis .....	1
1.2 Photosynthesis to bio-fuel.....	5
1.3 Research in artificial photosynthesis.....	7
1.4 Existing technologies on artificial photosynthesis.....	8
1.4.1 Type I artificial photosynthesis (light reaction only).....	9
1.4.2 Type II artificial photosynthesis (dark reaction only).....	13
1.4.3 Type III artificial photosynthesis (light & dark reactions with living cells) .....	15
1.4.4 Type IV: cell-free artificial photosynthesis (light & dark reactions).....	17
1.4.5 Summary of existing artificial photosynthesis.....	26
1.5 Artificial photosynthesis blueprint.....	27
1.5.1 Motivations and principles .....	27
1.5.2 Artificial photosynthesis reactions assay .....	29
1.6 The proposed artificial photosynthesis system .....	32
1.6.1 Aim 1: Light reaction unit .....	33
1.6.2 Aim 2: Dark reaction unit .....	34
1.6.3 Aim 3: Organic compound storage platform .....	35
1.6.4 Aim 4: Simulation of integrated system .....	35
1.7 Arrangement of chapters.....	36
Chapter 2. LIGHT REACTION UNIT: MEMBRANE IN FLUIDIC PCB .....	38
2.1 Introduction on membrane materials .....	40
2.1.1 PMOXA-PDMS-PMOXA, PEtOz-PDMS-PEtOz, POPC, POPC/POPS (1:1) .....	40
2.1.2 Non-symmetrical lipid: PLFE .....	41
2.2 Electrochemical impedance experiment on planar biomembranes .....	42
2.2.1 Selection of PDMS .....	42
2.2.2 Fabrication of PDMS thin film.....	43
2.2.3 Fabrication of PDMS fluidic devices .....	45
2.2.4 PCB board and electrodes.....	46
2.2.5 Formation of planar membranes.....	49
2.2.6 Impedance measurements.....	49

2.3	EIS result analysis.....	51
2.3.1	Results .....	51
2.3.2	Discussion .....	55
2.4	Mathematical modeling on planar membrane's physical stability.....	58
2.4.1	Planar membrane stability factors .....	58
2.4.2	Membrane vibration .....	59
2.4.3	Round membrane vibration .....	64
2.5	Contributions.....	79
2.5.1	Fluidic PCB for Basic EIS properties of planar membranes .....	79
2.5.2	Extended modeling of round planar thin membranes .....	80
Chapter 3.	LIGHT REACTION UNIT: MEMBRANE IN MICROFLUIDICS.....	81
3.1	Microchip EIS principle.....	81
3.1.1	Existing microchip technologies in EIS .....	81
3.1.2	EIS principle in microchip.....	83
3.2	Microchip Fabrication.....	86
3.2.1	Bottom silicon fabrication .....	87
3.2.2	Top glass fabrication .....	90
3.2.3	Microchip dicing and wiring .....	92
3.2.4	Middle layer PDMS: double-sided mold replica .....	94
3.2.5	Middle layer PDMS: laser drilling .....	99
3.2.6	Membrane formation .....	100
3.2.7	Temperature control .....	101
3.3	Electrochemical impedance measurement results.....	102
3.3.1	Experimental setup .....	103
3.3.2	Single membrane EIS results.....	103
3.3.3	SPICE simulation results .....	105
3.3.4	Control groups for microchip EIS .....	106
3.3.5	Dual-membrane EIS results.....	108
3.4	Membrane stability EIS results .....	111
3.4.1	Definition of stability .....	111
3.4.2	EIS results for long term.....	111
3.4.3	Difference materials .....	113
3.4.4	Difference of temperatures .....	116
3.4.5	Difference in membrane dimension (hole size) .....	117
3.5	Proteins in planar membrane .....	122
3.5.1	Ion channel protein alamethicin .....	122

3.5.2	Experimental procedure.....	123
3.5.3	Experimental results .....	124
3.5.4	Further experimental device .....	126
3.6	Contributions.....	127
3.6.1	Planar membrane stability .....	127
3.6.2	Microfabrication method improvement .....	127
3.6.3	Planar membrane on microchip with ion channels .....	128
Chapter 4.	DARK REACTION UNIT: CO <sub>2</sub> ABSORPTION.....	129
4.1	Gas permeability and diffusivity in gas-liquid interface.....	131
4.2	Porous PDMS and sugar leaching.....	131
4.2.1	Porous PDMS cubes fabrication.....	131
4.2.2	Porous PDMS film fabrication .....	132
4.3	pH indicator .....	137
4.3.1	pH sensitive pigment .....	137
4.3.2	Color analysis by Matlab.....	138
4.3.3	Carbon absorption amount by pH value .....	139
4.3.4	Channel pH color identification .....	141
4.3.5	Comparison pH color bar .....	143
4.4	PDMS molding replica and stereolithography.....	145
4.4.1	Mold 3D stereolithography.....	145
4.4.2	Fluidic device fabrication .....	146
4.4.3	Fluidic agitation simulation.....	148
4.5	Porous PDMS disc between gas channel and flow channel.....	149
4.5.1	Experimental .....	149
4.5.2	Results .....	151
4.6	CO <sub>2</sub> absorption with porous PDMS cube.....	153
4.6.1	Experimental .....	154
4.6.2	Static fluidic status .....	154
4.6.3	Dynamic flow status .....	155
4.6.4	Parylene-C coated porous PDMS cubes .....	157
4.7	CO <sub>2</sub> absorption with porous PDMS film .....	159
4.7.1	Experimental .....	159
4.7.2	Results .....	160
4.8	Discussion and conclusion.....	162
4.9	Contributions.....	165
4.9.1	Real-time pH monitoring by cell-phone with Matlab.....	165

4.9.2	Gas-liquid interface by porous PDMS.....	166
Chapter 5.	<b>DARK REACTION UNIT: GLUCOSE SYNTHESIS.....</b>	<b>167</b>
5.1	ATP synthesis materials.....	167
5.1.1	Buffer solution.....	168
5.1.2	Vesicle preparation.....	169
5.1.3	ATP synthesis assay.....	170
5.2	Glucose synthesis materials.....	170
5.2.1	Buffer solution.....	170
5.2.2	Enzymes mixing.....	171
5.2.3	Glucose synthesis assay.....	172
5.3	Experimental.....	173
5.4	Results.....	175
5.5	Discussion and conclusion.....	177
5.6	Contributions.....	179
Chapter 6.	<b>ORGANIC COMPOUND STORAGE PLATFORM.....</b>	<b>180</b>
6.1	Physics and chemistry properties of chitosan.....	182
6.2	Rapid prototyping technology.....	185
6.3	Additive manufacturing: 3D printing.....	186
6.4	Preliminary research on heterogeneous printing.....	190
6.4.1	Preliminary printing study.....	190
6.4.2	Existing problems.....	190
6.5	Theories: 3D printing by pneumatic valve dispenser.....	192
6.5.1	Fluid mechanics analysis inside dispenser.....	192
6.5.2	Mathematical modeling.....	194
6.5.3	Scaffold printing modeling.....	196
6.5.4	Modeling of EFD 741 MD valve extrusion behavior.....	199
6.6	Other materials used in printing.....	203
6.6.1	Sucrose printing results by height increment and line distance model.....	204
6.6.2	PCL printing by pneumatic valve dispenser extrusion model.....	206
6.7	Conclusions in 3D printing viscous materials.....	209
6.8	Chitosan structure fabrication: casting.....	209
6.8.1	ABS Mold Printing.....	210
6.8.2	PDMS Molding.....	210
6.8.3	Chitosan Casting and Lyophilization.....	211
6.8.4	Casting Results.....	211



6.9	Chitosan structure fabrication: rapid prototyping .....	212
6.9.1	Chitosan Printing without Support Material .....	212
6.9.2	Chitosan Printing with Sodium Bicarbonate as Support Material .....	213
6.10	Assembling onto artificial photosynthesis board .....	214
6.11	Contributions.....	215
6.11.1	Technical improvement on 3D printing .....	215
6.11.2	Chitosan printing with powder support material .....	215
Chapter 7.	SIMULATION OF INTEGRATED SYSTEM.....	216
7.1	Motivation of integrated system .....	216
7.2	Integrate light reaction units .....	216
7.3	Principle: increase SNR .....	218
7.3.1	Mathematical analysis and proof of increasing SNR.....	219
7.3.2	Increasing SNR by increasing repeat times .....	221
7.4	Capacitive sensor .....	222
7.4.1	Current mirror and amplification.....	222
7.4.2	Basic logic units .....	227
7.5	Ion channel monitoring .....	250
7.5.1	ADC .....	250
7.5.2	OTA.....	252
7.5.3	ADC schematic simulation .....	263
7.5.4	ADC Layout .....	267
7.6	Future work: microchip fabrication and test .....	268
7.7	PCB demonstration board .....	269
7.7.1	Light reaction units integration.....	269
7.7.2	Dark reaction units integration .....	270
7.7.3	PCB layout and fabrication.....	270
7.8	Contributions.....	272
Chapter 8.	SUMMARY .....	273
8.1	Project summary .....	273
8.2	Future prospect.....	274
REFERENCES	.....	276
Appendix I: Technical terms and abbreviations	.....	292
Appendix II: Matlab codes.....	.....	297
Appendix III: Significance threshold of the correlation coefficient	.....	305

Appendix IV: Copyright clearance and reuse permission..... 306  
Vita..... 308

## LIST OF FIGURES

- Figure 1-1. Dicotyledons (or dicots) leaf structure: a typical C3 plant leaf cross-section view [5].  
Reused with permission from MacMillan..... 1
- Figure 1-2. Plant cell structure: a photosynthesis higher plant cell. Reused with permission from  
Wikipedia..... 2
- Figure 1-3. Chloroplast ultrastructure: 1. outer membrane; 2. intermembrane space; 3. inner  
membrane; 4. stroma; 5. thylakoid lumen; 6. thylakoid membrane; 7. granum; 8.  
thylakoid; 9. Starch; 10. Ribosome; 11. plastidial DNA; 12. plastoglobuli [8].  
Reused with permission from Wikipedia..... 4
- Figure 1-4. (a) Normal boiling points of representative C6-hydrocarbons formed by removal of  
oxygen atoms from hexose, compared to the normal boiling point of ethanol; (b)  
Schematic diagram of the process for conversion of fructose to DMF. [24]  
Reproduced with permission from Nature Publishing Group..... 6
- Figure 1-5. The quantity of publication (by Web of Science publications) with artificial  
photosynthesis topic in three decades. .... 7
- Figure 1-6. Schematic representation of the photosynthetic chain in the oxygenic  
photosynthesis.[40] Reused with permission from the American Society of  
Photobiology..... 9
- Figure 1-7. Schematic diagrams of a photo-electrochemical biofuel cell (a) and an artificial  
photosynthetic water splitting cell (b). Both cells use light to generate hydrogen.[34]  
Reproduced with permission from American Chemical Society..... 10
- Figure 1-8. (a)  $\text{Ru}^{\text{II}}\text{-Ru}_2^{\text{II,II}}$  complex attached to a  $\text{TiO}_2$  nanoparticle being photo-oxidized to the  
 $\text{Ru}^{\text{II}}\text{-Ru}_2^{\text{II,III}}$  state. [48] Reuse permission by John Wiley and Sons. (b)  
 $\text{Mn}_2^{\text{II,II}}\text{-Ru-ND}^{\text{I2}}$  triad showing long-lived charge separation. [49] Reproduced with  
permission from American Chemical Society. .... 11
- Figure 1-9. Schematic drawing of the photoelectron-chemical cell used in [FeFe]-hydrogenase-  
catalyzed  $\text{H}_2$  production. [50] Reused with permission from American Chemical  
Society..... 11
- Figure 1-10. Structural diagrams of artificial photosynthesis reactions [38, 53]. Reused with  
permission from Nature Publishing Group and John Wiley and Sons..... 12
- Figure 1-11. Graphene-based photocatalyst catalyzed artificial photosynthesis of formic acid from  
 $\text{CO}_2$  under visible light. [54] Reused with permission from American Chemical  
Society..... 12

- Figure 1-12. Depiction of flow-through photocatalytic membrane for CO<sub>2</sub> conversion; [11, 56] Reproduced with permission from American Chemical Society. .... 13
- Figure 1-13. (a) Field emission scanning electron microscope (FESEM) top images of a mechanically fractured TiO<sub>2</sub> nanotube array sample; (b) Field emission scanning electron microscope (FESEM) cross-sectional images of a mechanically fractured TiO<sub>2</sub> nanotube array sample. [11] Reproduced with permission from American Chemical Society. .... 14
- Figure 1-14. Transmission electron microscope (TEM) image of nanowire and Schematic of the photoreduction processes of CO<sub>2</sub> on Rh/Cr<sub>2</sub>O<sub>3</sub> and Pt-decorated GaN nanowires. [57] Reproduced with permission from American Chemical Society. .... 14
- Figure 1-15. Operating principles of a MFC (not to scale). [21] Reused with permission from American Chemical Society. .... 15
- Figure 1-16. Design of a rectangular air-lift photo bioreactor. [63] Reused with permission from John Wiley and Sons. .... 15
- Figure 1-17. Arrangement of redox factors in PSII. The aqueous phases at the acceptor side (stroma) and donor side (lumen) are separated by a lipid bilayer (thylakoid membrane). [64] Reused with permission from American Chemical Society. .... 16
- Figure 1-18. Oxygenic photosynthesis takes place in the vegetative cells (yellow, left), separated from the micro-oxic, nitrogen-fixing heterocysts. Heterocyst-specific transcriptional regulation was studied using the green fluorescent protein (bright green). [47] Reused with permission from American Chemical Society. .... 16
- Figure 1-19. Schematic illustrations for (A) natural photosynthesis system and (B) microfluidic artificial photosynthesis system. [29] Reused with permission from Royal Society of Chemistry. .... 17
- Figure 1-20. An illustration of the BR/FoF1 ATP synthase vesicle solar conversion system coupled to the RuBisCO CBB cycle and trapped within the foam channels. [28] Reused with permission from American Chemical Society. .... 19
- Figure 1-21. (i) Schematic representations of BR-ATP synthase–proteopolymersomes prepared (a) from PM (method A) and from BR monomer (method B), (b) from PM (method B); (ii) Schematic representation of the procedures: (a) the previous method using ethanol (method A); (b) the new method without using ethanol (method B).[69] Reused with permission from IOP Publishing Ltd. .... 21
- Figure 1-22. TEM of PEtOz–PDMS–PEtOz vesicles in DI water: (a) low magnification, (b) high magnification. [71] Reused with permission from IOP Publishing Ltd. .... 22

Figure 1-23. Nyquist plots ( $\text{Re}(Z')$ versus $\text{Im}(Z'')$ ) of a free-standing PEtOz–PDMS–PEtOz triblock copolymer membrane. [71] Reused with permission from IOP Publishing Ltd. ....	22
Figure 1-24. Schematics of triblock copolymer membrane in planar membrane (a) and vesicle structure (b) with ~4 nm thick wall. [71] Reproduced with permission from IOP Publishing Ltd. ....	22
Figure 1-25. Illustration of ATP production. [28] Reused with permission from American Chemical Society. ....	24
Figure 1-26. G3P production in foam structure. [28] Reused with permission from American Chemical Society. ....	25
Figure 1-27. Calvin Cycle reactions with molecular quantities. [5] Nelson and Cox, Lehninger principles of Biochemistry, 5th Ed., 2008, page 775; Reused with permission from WH Freeman/Worth Publishers. ....	28
Figure 1-28. Molecular mechanism of proton ( $\text{H}^+$ ) pumping in bacteriorhodopsin. Retinal is bound in the space between the seven membrane-spanning helices (A to G) by a lysine in helix G [78]. Reused with permission from Nature Publishing Group. ....	30
Figure 1-29. An illustration of the FoF1 ATP synthase showing the major component of the structure the rotary part (Fo) which is embedded in the cell membrane and the stator part (F1) which is located in the cytoplasm [79]. Reproduced with permission from Annual Reviews. ....	30
Figure 1-30. (a) Method 1: Artificial light reaction with BR-ATPase vesicles. (b) Method 2: Artificial light reaction with BR-ATPase planar membrane. ....	32
Figure 1-31. Illustration of cell-free artificial photosynthesis system. ....	33
Figure 2-1. Chemical structures of PMOXA-PDMS-PMOXA triblock copolymer, POPC, and POPS. ....	40
Figure 2-2. Illustrations of the molecular structures of the bipolar tetraether lipids in PLFE isolated from <i>S. acidocaldarius</i> . PLFE contains (a) GDGT (or caldarchaeol, ~10%) and (b) GDNT (or calditolglycerocaldarchaeol, ~90%). The number of cyclopentane rings in each biphytanyl chain can vary from 0 to 4. $\text{R}_1$ = myo-inositol, GDGT $\text{R}_2$ = $\beta$ -D-galactosyl-D-glucose, and GDNT $\text{R}_2$ = $\beta$ -D-glucose linked to calditol. GDG(N)T-0 and GDG(N)T-4 contain 0 and 4 cyclopentane rings per molecule, respectively. [98] Reprinted with permission from American Chemical Society. ....	41
Figure 2-3. PDMS thin film fabrication procedures. ....	45
Figure 2-4. 3D lithography of the PDMS chamber mold made by a photopolymer Photosilver...	46

Figure 2-5. Procedures for assembling the fluidics device. ....	47
Figure 2-6. Image of the assembled PCB-based fluidic device. ....	48
Figure 2-7. Conceptual illustration of the EIS setup for a planar membrane on a PDMS thin film sitting on the PCB board within a PDMS chamber. Impedance ( $Z$ ) is the ratio of voltage ( $U$ ) and current ( $I$ ) at a given frequency ( $f$ ). ....	50
Figure 2-8. (A) Re-vs-Im Nyquist plot of various planar membranes. (B) Frequency ( $f$ ) vs. impedance magnitude ( $ z $ ) in various planar membranes. (C) Frequency ( $f$ ) vs. phase angle ( $\angle\phi$ ) in various planar membranes. ....	52
Figure 2-9. (a) Equivalent circuit of triblock copolymer, POPC or POPC/POPS planar membranes: $R1+C2//R2$ ; (b) equivalent circuit of PLFE planar membranes: $R1+C2//R2//(L3+R3)$ . $R1$ is the resistance of the electrolyte. ....	53
Figure 2-10. Forces on a rectangular membrane element. (Modified from [152] Page 66, Reproduced with permission from Springer-Verlag New York) ....	60
Figure 2-11. Bessel function $J_0\sim J_5$ , the solution used in free-standing round membrane function. ....	64
Figure 2-12. Force analysis on a small area of a round membrane element. This model is similar to our situation to analyze the lipid or copolymer membrane on the small hole. ....	66
Figure 3-1. Illustration of EIS principles for planar membrane imbedded in a microchip. ....	83
Figure 3-2. The equivalent circuit for single-membrane, dual-membrane, and empty group in microchip. ....	85
Figure 3-3. Silicon wafer in KOH etching. ....	88
Figure 3-4. KOH etched silicon focus planes, (a) top edge (b) bottom edge. ....	88
Figure 3-5. Mask alignment by alignment mark during secondary photolithography. ....	89
Figure 3-6. BOE etched glass slide focus planes, (a) top edge (b) bottom edge. ....	91
Figure 3-7. Fabrication process flow of microchip. ....	92
Figure 3-8. (a) Diced silicon microchip (9*9mm) by dicing saw. (b) Diced glass slide (9*9mm) by dicing saw. ....	93
Figure 3-9. Aluminum wires are soldered on (a) bottom layer silicon electrode; and (b) top layer glass electrode. ....	93
Figure 3-10. PDMS replica molding by clamping molding to avoid the cliff on edge. ....	94
Figure 3-11. Fabrication process flow of double-sided PDMS replica molding by SU-8 molds. ....	95
Figure 3-12. SU-8 pillar on wafer used for double-sided replica molding. ....	99

Figure 3-13. (a) The cross-section view of a non-through hole drilled by laser; (b) One laser shot compared to the 200 $\mu\text{m}$ through hole mark; (c) Through hole by laser drilling on PDMS thin film.....	99
Figure 3-14. Free-standing membrane formation procedure. Step a1~a2: single membrane; step b1~b2: dual-membrane. ....	101
Figure 3-15. Temperature of cooling plate water bath determined by power (current and voltage). ....	102
Figure 3-16. Nyquist plot of four different materials single membrane. ....	103
Figure 3-17. Amplitude impedance in Bode plot of the four different materials single membrane. ....	104
Figure 3-18. Phase frequency response in Bode plot of four different materials single membrane. ....	104
Figure 3-19. LTspice simulation circuit (schematic). ....	105
Figure 3-20. Planar membrane Bode plot simulation by LTspice: (a) PMOXA-PDMS-PMOXA triblock copolymer; (b) POPC; (c) POPC/POPS (1:1).....	106
Figure 3-21. Frequency response of empty microchip (a) impedance amplitude; (b) phase angle. ....	107
Figure 3-22. Schematic of equivalent circuit of control group. ....	107
Figure 3-23. SPICE simulation of Bode plot of control group. ....	108
Figure 3-24. Schematic of membrane systems embedded in microchip based on SOI wafer fabrication (SOIMUMP) technique.....	109
Figure 3-25. Equivalent circuit of two time constants model with Voigt's structure [R/C R/C] (a) and its graphical impedance presentation: complex plane impedance diagram (b); Bode plots (c) [206]. Reuse permission by Springer Science & Business Media...	109
Figure 3-26. Nyquist plot of dual-membrane of two time constants model with Voigt's structure [R/C+R/C].....	109
Figure 3-27. (a) Amplitude impedance's frequency response of Bode plot of dual-membrane structure; (b) Phase angle's frequency response of Bode plot of dual-membrane structure.....	110
Figure 3-28. Impedance of triblock copolymer at (a) room temperature ( $\sim 23^\circ\text{C}$ ); (b) $51^\circ\text{C}$ .....	112
Figure 3-29. Impedance of PLFE at (a) room temperature ( $\sim 23^\circ\text{C}$ ); (b) $39^\circ\text{C}$ .....	112
Figure 3-30. Impedance of POPC at (a) room temperature ( $\sim 23^\circ\text{C}$ ); (b) $50^\circ\text{C}$ . ....	112
Figure 3-31. Impedance data of different materials at room temperature ( $\sim 23^\circ\text{C}$ ).....	114
Figure 3-32. Impedance data of different materials at $\sim 40^\circ\text{C}$ .....	114

Figure 3-33. (a) Impedance of PLFE at 39°C in long term stability study; (b) Impedance of PLFE and triblock copolymer at 39°C in long term stability study; (c) Impedance of PLFE and triblock copolymer at 11~13°C in long term stability study. ....	115
Figure 3-34. (a) Impedance of triblock copolymer at different temperatures; (b) Defined stability of triblock copolymer at different temperatures.....	116
Figure 3-35. (a) Impedance of PLFE at different temperatures; (b) Defined stability of PLFE at different temperatures. ....	116
Figure 3-36. (a) Impedance of POPC at different temperatures; (b) Defined stability of POPC at different temperatures. ....	117
Figure 3-37. Impedance of triblock copolymer with different membrane diameters. ....	118
Figure 3-38. Impedance of triblock copolymer with equivalent membrane diameter of 100 $\mu\text{m}$ . ....	118
Figure 3-39. Defined stability of triblock copolymer with different membrane diameters. ....	119
Figure 3-40. Impedance of PLFE with different membrane diameters.....	119
Figure 3-41. Impedance of PLFE with equivalent membrane diameter of 100 $\mu\text{m}$ . ....	120
Figure 3-42. Defined stability of PLFE with different membrane diameters. ....	120
Figure 3-43. Impedance of POPC with different membrane diameters. ....	121
Figure 3-44. Impedance of POPC with equivalent membrane diameter of 100 $\mu\text{m}$ . ....	121
Figure 3-45. Defined stability of POPC with different membrane diameters.....	121
Figure 3-46. (a) CV input signal; (b) CA input signal. ....	123
Figure 3-47. Current-voltage curve of alamethicin on planar membrane in microchip in CV experiment.....	124
Figure 3-48. Current trace of alamethicin ion channel on planar membrane in microchip in CA experiment: (a) 0~2 s; (b) 0.2~0.55 s. ....	125
Figure 3-49. Corresponding current amplitude histogram within 2 s in CA experiment.....	126
Figure 3-50. Photo of PCB fluidic testing board for ion channels on planar membrane. ....	126
Figure 4-1. Dicotyledons (or dicots) leaf structure: a typical C3 plant leaf cross-section view [5]. Reproduced with permission from MacMillan. ....	129
Figure 4-2. Illustration of facilitating capillary rise of PDMS in sugar cube and rice paper. (a) Hydrophobic surface of porous PDMS cube; (b) Optical microscope image of porous PDMS cube; (c) Hydrophobic surface of porous PDMS film; (d) Optical microscope image of porous PDMS thin film.....	133
Figure 4-3. Capillary effect of uncured PDMS on porous rice paper at room temperature (24°C) and freezer (-18°C). ....	134



Figure 4-4. BTB structure; BTB structure is changed in different pH environment. Reused with permission from Wikipedia.....	137
Figure 4-5. Algorithm of the fluid's pH identification by Matlab. ....	138
Figure 4-6. Theoretical carbon concentration with standard pH value by Henderson-Hasselbach equation.....	141
Figure 4-7. Illustration of calculation CO <sub>2</sub> absorbed by channel pH color.....	142
Figure 4-8. Standard pH color bar for image processing; (a) yellow: pH=4, green: pH=7, blue: pH=10; (b) yellow: pH=6, green: pH=7, blue: pH=7.6. ....	143
Figure 4-9. Standard pH to color bar for image analysis calibration with gray image color.....	144
Figure 4-10. Theoretical carbon concentration with standard pH value by Henderson-Hasselbach equation.....	145
Figure 4-11. (a) 3D stereolithography product of dragon, gray photosilver (left) and coated with gold paint (right); (b) 3D wax printed dragon by Solidscape®. ....	146
Figure 4-12. Fabrication process flow of fluidic channels with porous PDMS cubes and film. .	147
Figure 4-13. (a) Mesh analysis of the fluid in microfluidic channels with pillar bars; (b) Flow velocity profile in microchannel with pillar bar.....	149
Figure 4-14. Experiment setup of gas-liquid interface using dry ice as CO <sub>2</sub> source. ....	150
Figure 4-15. BTB color alteration before and after introducing CO <sub>2</sub> . ....	151
Figure 4-16. RGB color intensity comparison results.....	151
Figure 4-17. pH value change over time in static and dynamic conditions. ....	152
Figure 4-18. Carbon concentration in the liquid chamber. ....	153
Figure 4-19. Experimental setup for CO <sub>2</sub> absorption in a flow channel with porous PDMS cubes. ....	154
Figure 4-20. pH value and carbon concentration change with time in static flow in PDMS microchannel.....	155
Figure 4-21. Fluid pH value at stable status of different flow rates.....	156
Figure 4-22. pH value and carbon concentration change with time in dynamic flow at 20 μL/min in parylene-C coated fluidic channel with porous PDMS cubes.....	157
Figure 4-23. pH value and carbon concentration change with time in dynamic flow at 40 μL/min in parylene-C coated fluidic channel with porous PDMS cubes.....	158
Figure 4-24. pH value and carbon concentration change with time in dynamic flow at 80 μL/min in parylene-C coated fluidic channel with porous PDMS cubes.....	158
Figure 4-25. Fluid pH value at stable status of different flow rates in parylene-C coated fluidic channel with porous PDMS cubes. ....	159

Figure 4-26. Schematic comparison of CO <sub>2</sub> absorption in a microchannel through (a) porous PDMS cube, and (b) porous PDMS thin film. ....	160
Figure 4-27. CO <sub>2</sub> absorption result for porous PDMS cubes and porous PDMS film. ....	161
Figure 5-1. Illustration of BR-ATPase triblock copolymer vesicle structure. ....	167
Figure 5-2. pH difference between inside and outside of the vesicles. ....	168
Figure 5-3. ATP synthesis amount by BR-ATPase triblock copolymer vesicles under 5W green LED. ....	168
Figure 5-4. Three phase reactions in Calvin Cycle of 3PG synthesis for glucose/fructose synthesis. Reproduced from [5] Nelson and Cox, Lehninger principles of Biochemistry, 5th Ed., 2008; Reproduced with permission from WH Freeman/Worth Publishers. ....	171
Figure 5-5. Glucose assay principle using o-dianisidine as redox indicator. Reused with permission from Sigma Aldrich. ....	172
Figure 5-6. Experimental setup for glucose synthesis analysis. ....	173
Figure 5-7. Optical density value change at different glucose concentration with an emission at 540 nm. ....	175
Figure 5-8. Glucose assay of static flow and dynamic flow at 50 μL/min using oxidized o-dianisidine color change by adding sulfuric acid. ....	176
Figure 6-1. Illustration graph of a leaf-like device from the principle of photosynthesis. ([5] Reused with permission from MacMillan.) (a) artificial tree with photosynthetic leaves; (b) artificial tree branch; (c) artificial leaves with filtration channels; (d) product collection container; (e) layers' structure of artificial leaves; (f) triblock membrane; (g) porous structure with "dark reaction" solutions. ....	180
Figure 6-2. Image of plant (a) sieve tube; and (b) vascular bundle [5]. Reused with permission from MacMillan. ....	181
Figure 6-3. Molecular structure of chitosan [285]. Reused with permission from Wikipedia. ....	183
Figure 6-4. Morphology of micro-porous chitosan produced by liquid nitrogen lyophilization process: (a) Cross-section view; (b) Perpendicular section view. ....	184
Figure 6-5. Rapid prototyping: (a) subtractive manufacturing; (b) additive manufacturing. ....	186
Figure 6-6. Preliminary printing examples, (a) PEG; (b) PCL in 40% acetic acid; (c) two kinds of colored PCL in 42% acetic acid. ....	190
Figure 6-7. (a) EFD valve printing system setup; (b) EFD valve with material reservoir. ....	193
Figure 6-8. The printing path: actual tool path and the printed material boundary. ....	196
Figure 6-9. Model for maximum line distance without support material. ....	197
Figure 6-10. Model for height increment in Z direction. ....	198

Figure 6-11. Model of viscous fluid flow in 741MD pneumatic valve. Reproduced with permission from EFD®.....	200
Figure 6-12. Additional pressure's relationship to material viscosity and controller step time. ..	203
Figure 6-13. The deposition of a meander scaffold using dispensing valve [336]. Reused with permission from Springer.....	203
Figure 6-14. Sucrose printing results (a: cylinder; b: meander mesh). .....	205
Figure 6-15. Optical microscope view of PCL sample with different G-code federate, layer thickness, PCL concentration, needle tip inner diameter, reservoir back pressure, and EFD controller step time. ....	207
Figure 6-16. Chitosan printing and casting in leaf-shape results: (a) chitosan gel; (b) chitosan with internal channels; (c) chitosan after lyophilization; (d) PDMS mold and casted chitosan after lyophilization. ....	211
Figure 6-17. Front view and side views of 5 layers chitosan scaffold with 7% (wt%) medium molecular weight chitosan. ....	212
Figure 6-18. Chitosan printing results using sodium bicarbonate as a support material: (a) second layer printing after adding sodium bicarbonate on the first layer; (b) interconnection between printed first layer and second layer; (c) two layers chitosan with support material; (d) side view of four layers of chitosan scaffold with support material; (e) back view of four layers of chitosan scaffold with support material. ....	213
Figure 7-1. Demonstration of tree falling and plant cells interconnection. Reused with permission from Wikipedia. ....	216
Figure 7-2. Illustration of single unit's X and Y coordinate identification. Blue and red wires represent different metal layers. ....	218
Figure 7-3. Schematic simulation of NMOS with $W = 2.4 \mu\text{m}$ and $L = 4.8 \mu\text{m}$ . ....	223
Figure 7-4. Schematic simulation of current mirror. ....	224
Figure 7-5. Schematic simulation result of $V_b$ in current mirror. ....	225
Figure 7-6. Schematic simulation result of $V_b$ in current mirror with a step of $V_b$ of 0.05 V.....	225
Figure 7-7. Schematic simulation result of $V_b$ in current mirror with a step of $V_b$ of 0.5 V. ....	226
Figure 7-8. Schematic simulation of current mirror gain.....	226
Figure 7-9. DC response of current mirror using VCCS of 10 nA. ....	227
Figure 7-10. Unit sized inverter: (a) schematic; (b) symbol. ....	228
Figure 7-11. Testing schematic for unit-sized inverter. ....	228
Figure 7-12. Simulation results of a unit-sized inverter with dc 0~5 V input.....	229
Figure 7-13. Simulation results of a unit-sized inverter with pulse voltage input. ....	229

Figure 7-14. Layout of a unit-sized inverter. ....	230
Figure 7-15. A switch with clear function: (a) schematic; (b) symbol. ....	231
Figure 7-16. Schematic simulation of a buffer. ....	231
Figure 7-17. Structure of transmission switch: (a) schematic; (b) symbol; (c) layout. ....	232
Figure 7-18. Schematic simulation of AND gate with 2 inputs: (a) schematic; (b) test circuit; (c) simulation results. ....	233
Figure 7-19. Structure of dynamic AND gate: (a) schematic; (b) symbol; (c) layout. ....	234
Figure 7-20. Schematic simulation of AND gate with 3 inputs: (a) schematic; (b) test circuit; (c) simulation results. ....	235
Figure 7-21. Layout of dynamic AND gate with 3 inputs. ....	236
Figure 7-22. Schematic simulation of OR gate with 2 input. (a) schematic; (b) test circuit; (c) simulation results. ....	236
Figure 7-23. Layout of dynamic OR gate with 2 inputs. ....	237
Figure 7-24. Schematic simulation of NAND gate with 2 input. (a) schematic; (b) test circuit; (c) simulation results. ....	237
Figure 7-25. Schematic structure of static NAND gate in Cadence. (a) Schematic; (b) symbol. ....	238
Figure 7-26. Schematic simulation structure of static NAND gate. ....	238
Figure 7-27. Test results of transient response of a static NAND gate. ....	239
Figure 7-28. Schematic simulation of NOR gate with 2 input. (a) schematic; (b) test circuit; (c) simulation results. ....	240
Figure 7-29. Schematic structure of static NOR gate in Cadence. (a) Schematic; (b) symbol. ....	240
Figure 7-30. Schematic simulation structure of static NOR gate. ....	241
Figure 7-31. Test results of transient response of a static NOR gate. ....	241
Figure 7-32. Schematic simulation of XOR gate with 2 input. (a) schematic; (b) test circuit; (c) simulation results. ....	242
Figure 7-33. Layout of dynamic 2-input XOR gate. ....	242
Figure 7-34. 3-input dynamic XOR gate: (a) schematic; (b) layout. ....	243
Figure 7-35. Schematic simulation of XNOR gate with 2 input. (a) schematic; (b) test circuit; (c) simulation results. ....	244
Figure 7-36. Schematic design of positive edge triggered master-slave register [365]. ....	244
Figure 7-37. Schematic design of positive edge triggered master-slave register with reset function. ....	245
Figure 7-38. Schematic simulation structure of positive edge triggered DQ register. ....	245
Figure 7-39. Test results of transient response of DQ register. ....	246

Figure 7-40. Schematic simulation circuit of DQ register with reset function “clr” .....	246
Figure 7-41. Schematic simulation of DQ register with reset function. ....	246
Figure 7-42. Schematic designs of DQ register for creating symbols in LTspice. ....	247
Figure 7-43. Schematic simulation results of the created DQ register in LTspice. ....	247
Figure 7-44. Schematic simulation results of edge-triggered DQ register symbol in LTspice.....	248
Figure 7-45. Schematic simulation results of rising-edge-triggered DQ register symbol in LTspice. .....	248
Figure 7-46. Schematic simulation of 2-4 binary decoder. (a) schematic; (b) simulation results. .....	249
Figure 7-47. Schematic simulation of 3-8 binary decoder. (a) schematic; (b) simulation results. .....	250
Figure 7-48. Block diagram of Delta-Sigma ADC. ....	251
Figure 7-49. Circuit diagram of ADC.....	251
Figure 7-50. (a) A wide-range low noise full differential OTA; (b) Bode plot of full differential OTA. ....	253
Figure 7-51. Schematic design of 5-transistor OTA. ....	253
Figure 7-52. Schematic simulation results of 5-transistor OTA. ....	254
Figure 7-53. Schematic simulation of comparator formed by 5-transistor OTA. ....	254
Figure 7-54. Schematic simulation DC response results of comparator formed by 5-transistor OTA. ....	255
Figure 7-55. Schematic simulation results of integrator formed by 5-transistor OTA. ....	255
Figure 7-56. Schematic simulation of one bit ADC formed by 5-transistor OTA with input of 3 V. .....	256
Figure 7-57. Schematic simulation results transient response of one bit ADC formed by 5- transistor OTA; the input voltage was 3 V.....	256
Figure 7-58. Schematic simulation of one bit ADC formed by 5-transistor OTA with input of 2.6 V. (The figure only demonstrated the input voltage).....	257
Figure 7-59. Schematic simulation results transient response of one bit ADC formed by 5- transistor OTA; the input voltage was 2.6 V.....	257
Figure 7-60. Diagram of balanced CMOS OTA.....	258
Figure 7-61. Schematic design of 9-transistor OTA (configuration 1).....	258
Figure 7-62. Schematic simulation results of 9-transistor OTA (configuration 1). ....	259
Figure 7-63. Schematic simulation of 9-transistor OTA (configuration 2). ....	259
Figure 7-64. Schematic simulation results of 9-transistor OTA (configuration 2). ....	260

Figure 7-65. Schematic simulation of 9-transistor OTA (configuration 3). .....	260
Figure 7-66. Schematic simulation results of 9-transistor OTA (configuration 3). .....	261
Figure 7-67. Schematic simulation of integrator. ....	261
Figure 7-68. Schematic simulation results of integrator formed by 9-transistor OTA. ....	262
Figure 7-69. Schematic design of comparator constructed based on 9-transistor OTA. ....	262
Figure 7-70. Schematic simulation results of comparator constructed based on 9-transistor OTA. .....	263
Figure 7-71. Schematic simulation design of ADC. ....	263
Figure 7-72. Schematic simulation results of ADC with testing input voltage from 2.0 V to 3.0 V. .....	267
Figure 7-73. Schematic symbol design of comparator and OTA.....	267
Figure 7-74. Layout design of comparator and OTA.....	268
Figure 7-75. Schematic of Hilbert curve with 64 (8×8) units. ....	269
Figure 7-76. Schematic of low current amplifier for inspecting ion channels.....	270
Figure 7-77. Image of the integrated PCB with both light reaction units and dark reaction units. .....	271
Figure 7-78. Integrated light reaction units identification. ....	271
Figure 8-1. Illustration of cell-free artificial photosynthesis system. ....	273

## LIST OF TABLES

Table 1-1. Comparison of different types of artificial photosynthesis.....	26
Table 1-2. Comparison between cell-free artificial photosynthesis system with other type IV artificial photosynthesis. ....	27
Table 2-1. Comparison of electric properties of different planar membranes. ....	55
Table 3-1. Dielectric properties of four different membrane materials* .....	102
Table 4-1. Thickness measurement of porous PDMS film. ....	135
Table 4-2. PDMS (Sylgard 184 silicone elastomer to PDMS curing agent weight ratio 10:1) curing time with temperature. ....	136
Table 4-3. Absorbed $\text{CO}_2$ , $\text{H}_2\text{CO}_3$ , $\text{HCO}_3^-$ , and $\text{CO}_3^{2-}$ concentration (unit: mol/L) with the change of pH. ....	141
Table 5-1. Microplate optical density (OD) value reading with emission at 540 nm .....	176
Table 6-1. Chitosan porosity after lyophilization. ....	185
Table 7-1. Relationship between current and W/L in NMOS.....	224

## ABSTRACT

### Cell-free Artificial Photosynthesis System

Xiang Ren

The objective of this research is to create a cell-free artificial platform for harvesting light energy and transforming the energy to organic compounds. In order to achieve this objective, we took the approach of mimicking the photosynthetic processes of a plant leaf and integrating them into a compact system using microfabrication technology.

Photosynthesis consists of two parts: light reaction and dark reaction. During the light reaction, light energy is transformed to chemical energy in ATP that is a biological energy source, while during the dark reaction. Carbon dioxide is absorbed and used to synthesize organic compounds such as glucose and fructose. Many scientists had tried to realize artificial photosynthesis for energy harvesting for decades. However, most of the previous systems were simply based on light reaction and produced less desirable energy sources, such as explosive hydrogen gas and unstable electricity. Other works had been reported that combined both light and dark reactions to produce useful organic compounds, but they were all based on utilizing living cells that were difficult to maintain and were not reusable.

We developed a cell-free artificial platform conducting both light and dark reactions. To the best of our knowledge, such a device had not been reported so far. This device was able to harvest light energy and transform the energy to organic compounds, mimicking a plant leaf. We envision integrating the “artificial leaves” to create a compact energy harvesting system with a promising



efficiency. In order to create an artificial photosynthesis device, we had come up with four specific parts as follows.

**Part 1:** Light reaction was realized in a microfluidic platform that consists of two fluid chambers separated by a planar membrane with embedded proteins that convert light energy into ATP. Four different materials were investigated as potential membrane materials and the optimal (most stable) material was identified through impedance spectroscopy. Since these membrane materials were very soft, it was challenging to integrate them in a microfluidic platform. Diverse support materials and fabrication techniques were investigated to identify the optimal fabrication process. Once the best membrane material was identified and a microfluidic platform was constructed, we would have light-converting proteins embedded in the membrane followed by the evaluation its light reaction performance.

**Part 2:** Dark reaction was realized in another microfluidic platform porous PDMS cubes as gas-liquid interface media. We used porous PDMS as a gas-liquid interface between microfluidic channels to create a “one-way” diffusion path for carbon dioxide. The CO<sub>2</sub> transport was evaluated based on pH change and successful CO<sub>2</sub> transport would produce precursors (C3 compounds) for glucose production.

**Part 3:** Glucose synthesis and storage unit was developed by mimicking sponge mesophyll found in a leaf (dicotyledons leaf). Chitosan porous structures with interconnected pores were used for this purpose and they were fabricated by lyophilization after casting or 3D printing.

**Part 4:** The circuits for an integrated light reaction platform was designed and simulated. The digital encode/decode of microchip array was simulated. A high-resolution, low-speed analog-to-digital converter was also designed and simulated for ion channel monitoring purpose.

While carrying out this research, the following scientific contributions were also made. *First*, electrochemical property database of planar membranes made of different biomaterials were established. *Second*, a novel gas-liquid interface was developed for microfluidic platforms using porous PDMS and its performance was thoroughly investigated by on-chip pH measurement.

*Third*, during the study on 3D printing of chitosan porous structure, a mathematical model was established for identifying optimal operational parameters for printing non-Newtonian fluids with a pneumatic printer.

This research brought together expertise in advanced manufacturing (MEMS and additive manufacturing), biochemistry and biomaterials, and system control and integration. We envisioned integrating the “artificial leaves” to create a compact energy harvesting system with high efficiency.



## Chapter 1. INTRODUCTION

### 1.1 Background of natural photosynthesis

Sunlight provides energy for all the life forms on the Earth for over 4 billion years. Eventually, almost all the energy of the energy resources on the Earth are coming directly and indirectly from the sun energy, including the fossil fuels and living creatures. After millions of years' evolution, photosynthesis is the major way to utilize the sunlight energy to produce organic compounds. Different from other living creatures, the metabolism of green plant is auto-tropism. Green plants perform photosynthesis, which is “the most important chemical reaction on earth”, according to the comments of Nobel Prize Foundation committee. Scientists started to consider using the principles of photosynthesis to generate sustainable energy [1, 2]. Most green plants have two major steps in photosynthesis: light reactions and dark reactions. In light reaction, chlorophyll absorbs light energy and photolyzes water molecule and release oxygen. As for the further organic product, there are several kinds of dark reactions in nature; however, people didn't find the principles of dark reactions until 1940s, when long term carbon-14 ( $^{14}\text{C}$ ) isotope experiments were applied in this field [3, 4].

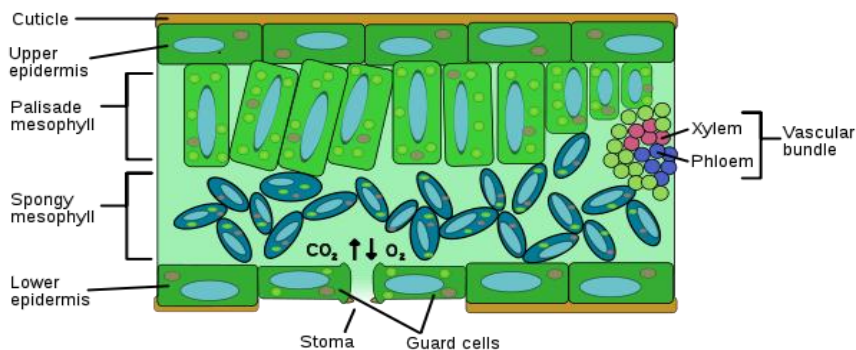


Figure 1-1. Dicotyledons (or dicots) leaf structure: a typical C<sub>3</sub> plant leaf cross-section view [5]. Reused with permission from MacMillan.

Besides botany, many other scientific research fields were established, such as plant physiology, plant functional genomics, and plant molecular physiology, etc. For instance, green

plant following Calvin Cycle in dark reaction, produces 3-phosphoglycerate (3-PGA) as first stable compound, and further reactions produce glucose or fructose as the final output of glyceraldehydes-3-phosphate (G3P) which is produced from the oxidation of nicotinamide adenine dinucleotide phosphate (NADPH). This kind of plants are also known as C3 plant [6]. In dark reactions of C3 plant, the carbon dioxide is fixed by enzyme ribulose-1,5-bisphosphate carboxylase/oxygenase (RuBisCO) and reacted into ribulose-1,5-bisphosphate (RuBP), and forms three carbon phosphate compounds, and in further Calvin Cycle reactions. It forms glucose and fructose to create cellulose [6, 7]. Carbon fixation rate is one of the critical factors that determine the photosynthesis rate and efficiency.

The structure of dicotyledons leaf is demonstrated in Figure 1-1. Vascular bundle provides support and transportation of photosynthesis related chemicals. Each pair of guard cells forms a stoma for CO<sub>2</sub> and O<sub>2</sub> exchange. Each palisade mesophyll and sponge mesophyll contains 10~100 chloroplasts, which contains thylakoid that carries light reaction [8].

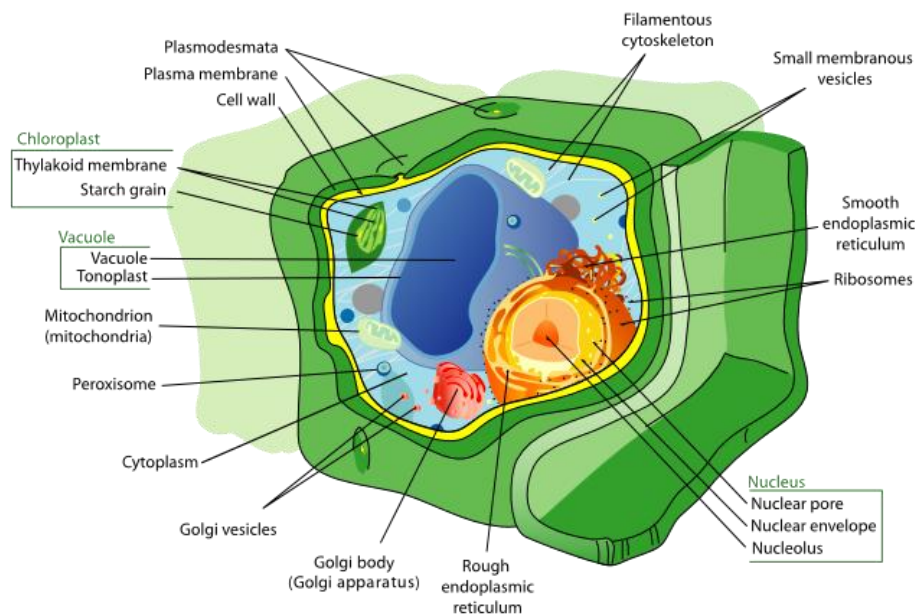


Figure 1-2. Plant cell structure: a photosynthesis higher plant cell. Reused with permission from Wikipedia.

The membrane system in higher plant leaf cells is critical in the evolution history, as shown by the green plant cell structure in Figure 1-2. The membrane with pumping proteins forms the

basic structures for transferring energy flow in cells, including proton  $H^+$ , NADPH, and adenosine triphosphate (ATP), etc. The proton is a little different with membrane potential's definition. The unit for electrochemical potential difference is proton motive force (mpf). The plasma membrane (includes outer membrane and inner membrane) provides a platform for the interface of the cell content exchange, which has higher resistance around  $10^9 \sim 10^{11} \Omega \cdot \text{cm}$ . Many kinds of ion channels and ion carriers, such as functional membrane proteins, are also capable to alternate the membrane resistance. The endoplasmic reticulum (ER) system inside a true nucleus cell, including smooth ER and rough ER, created a place to synthesize proteins and lipids for cell functioning or structuring. The Golgi apparatus or Golgi complex formed by stacks can sort and process the proteins and transfer the proteins to a determined position. The central vacuole is surrounded by a large membrane, providing for exchanging of ions, amino acid, hydrolysis enzymes, etc. In some true nucleus plant cells, microbody is formed by single layer membrane, including peroxisome and glyoxysome. The peroxisome is a catalyst for the reaction with intermediate of hydrogen peroxide ( $H_2O_2$ ). The peroxisome is used to consume the hydrogen elements in organic compound by consuming oxygen molecules. In the mesophyll cells, peroxisome usually participate the photorespiration with chloroplast and mitochondria. The nucleus in cells includes inner and outer nucleus membrane, where the genetic information carried by deoxyribonucleic acid (DNA) is stored. Nucleus membrane forms multiple nucleus pores (35~60 holes per micron square, hole diameter 40~100 nm) in double-layer membrane system, for the ribonucleic acid (RNA) exchange and transport. The small molecules and large proteins or RNA transportations are carried out by the complex membrane systems or microfilaments inside the true nucleus plant cells.

Chloroplast is ellipsoid shape in most of the higher plant cells with average diameter of 4~6  $\mu\text{m}$ , and thickness of 2~3  $\mu\text{m}$  (Figure 1-3). Most higher plant cells contain 50~200 chloroplasts taking around 40% of the volume in a cell. All the photosynthesis pigments (including chlorophyll-a chlorophyll-b,  $\beta$ -carotenoids, and phycobilin or phycoerythrin) or accessory

pigments functioned in light reaction are located on the membrane of thylakoid, while the carbon fixation is performed in the stroma with water soluble enzymes. Thylakoid is aligned along the longer axis of a chloroplast and stacked into granum or grana, with diameter of 0.25~0.8  $\mu\text{m}$ . The chloroplast has its own DNA, RNA and ribosome as its own genetic information. However, most of the constructing proteins are coded, translated by the plant cell, and transferred into the chloroplast. In the chloroplast, majority of the plastidial DNA is used to translate the carbon dioxide fixation enzyme RuBisCO, which is continuously consumed during the dark reactions. If the generated RuBisCO does not involve the reactions by capturing  $\text{CO}_2$  and ATP for carbon fixation reactions, the RuBisCO will be hydrolyzed and reconstructed. Typically, enzymes have high chemical catalyst reaction rate. An enzyme can process up to over 1000 target molecules within 1 s. However, RuBisCO can only fix 3 molecules of  $\text{CO}_2$  within 1 s.

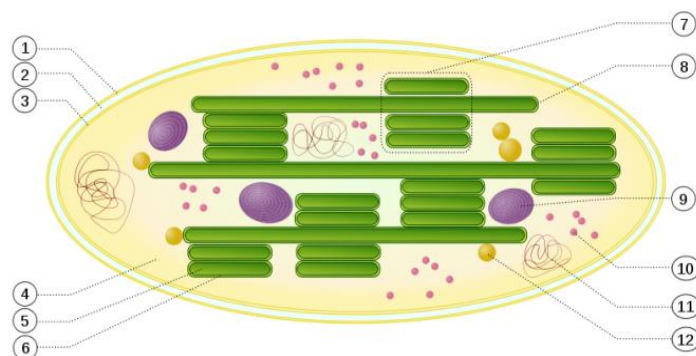


Figure 1-3. Chloroplast ultrastructure: 1. outer membrane; 2. intermembrane space; 3. inner membrane; 4. stroma; 5. thylakoid lumen; 6. thylakoid membrane; 7. granum; 8. thylakoid; 9. Starch; 10. Ribosome; 11. plastidial DNA; 12. plastoglobuli [8]. Reused with permission from Wikipedia.

My research on artificial photosynthesis was based on natural photosynthesis and artificial construction of vascular bundle, stoma, and thylakoid. Specifically, I needed to find an artificial way to achieve the functions of membrane systems at cell and system level. The second step for a cell-free artificial photosynthesis system will be to realize the pigment function on the artificial membrane systems, which has a functional cell behavior but without any living cells implanted.

## 1.2 Photosynthesis to bio-fuel

After scientists realized the importance and the necessity of reusable energy, they tried to find ways to produce biofuel. Biofuel is a general concept of the fuel produced from biomass [9, 10]. The main reason is that the green house gas production increased significantly after 20th century, mainly from coal-fired power plants [10, 11], and people therefore tried to find a way to recycle the CO<sub>2</sub> from combustion product and produce hydrocarbon fuel. Hydrocarbon fuel has higher energy density (J/m<sup>3</sup>) compared to fossil fuel, and people already have made bio-ethanol from sugar or starchy crops such as sugar cane and from plant cellulose using fermentation processes [12]. Biodiesel is long-chain alkyl (methyl, ethyl or propyl) esters, which can be produced from oil crops such as corn, soybean, jatropha, canola, coconut, oil palm, etc. or using micro algae [13-15]. Methanol can be converted from CO<sub>2</sub> by using solar energy, and a photo-catalyst is needed [11].

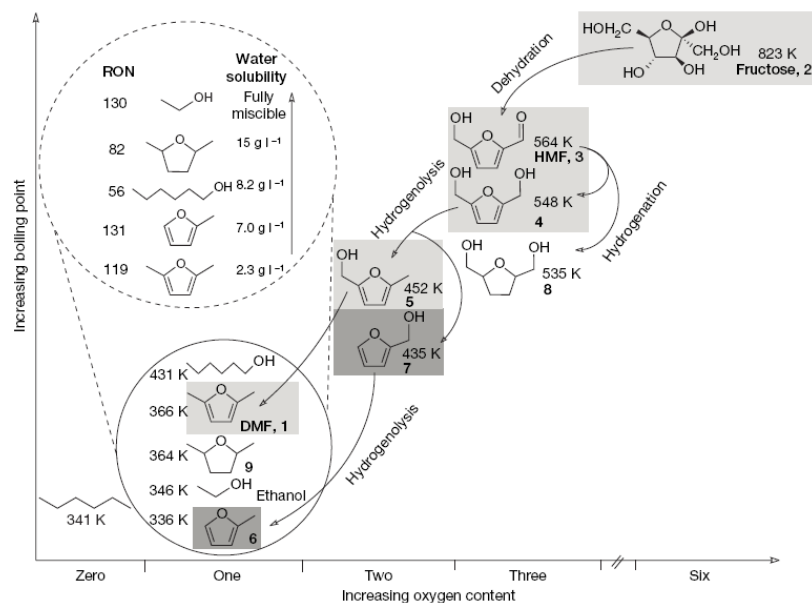
As for producing biofuel from biomass, the basic process is via photosynthesis. For the past years, scientists have tried different ways to use reusable energy such as sunlight to catalyze certain chemical reactions to produce fuels [16-19]. After 1985, scientists tested some microbial fuel cells (MFC) which can be integrated with photosynthesis, namely photoMFC [20-23]. These approaches unfortunately still contain live organic cells and the biocatalyst, but most importantly, the energy generated from light energy is not easily stored.

In recent years, artificial photosynthesis and artificial leaf became popular ideas to produce biofuel, not only because the photosynthesis and leaf are the nature's way to produce organic compound, but also because of the high sun light energy (85000 TW/year) available.

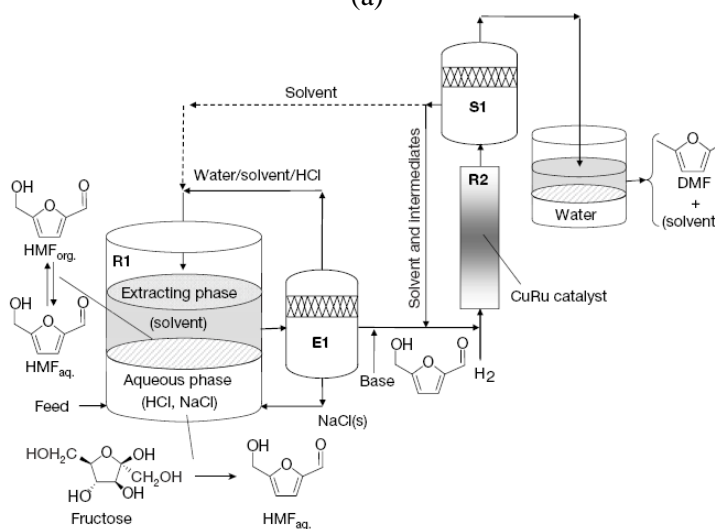
Scientists developed a series of experiments to perform light reactions and dark reactions based on principles of photosynthesis. The most important part is the dark reactions which produce organic compound like glucose and fructose. Specifically, the fructose-based 2,5-



dimethylfuran (DMF) can be produced from fructose by existing chemical reactions (Figure 1-4) [24, 25].



(a)



(b)

Figure 1-4. (a) Normal boiling points of representative C6-hydrocarbons formed by removal of oxygen atoms from hexose, compared to the normal boiling point of ethanol; (b) Schematic diagram of the process for conversion of fructose to DMF. [24] Reproduced with permission from Nature Publishing Group.

DMF is better than ethanol: 1) 40% higher energy density, which makes the combustion performance similar to gasoline; and 2) a slightly higher boiling point at 92~94°C, which makes

DMF less volatile than ethanol [26]. Thus, DMF has the potential to be used in engine to replace the regular gasoline. Scientists have done experiments to test the combustion properties of DMF in a direct-injection spark-ignition engine and compared it to ethanol and gasoline [27]. The conclusion shows the emissions of DMF are similar to gasoline, and the energy density is better than ethanol [26].

The natural photosynthesis has intermediate energy product ATP in Calvin Cycle reactions, which is also a type of bio-energy product that can be used in lab-on-chip or bio-experimental applications, such as further synthesis of organic compound glucose, fructose [28] or other amino acids [29]. This artificial photosynthesis approach will be an ideal mimicking of the natural photosynthesis reactions that capturing sunlight and transfer the sunlight energy into ATP.

### 1.3 Research in artificial photosynthesis

Artificial photosynthesis is studied in multiple research areas and subjects. From the publication about artificial photosynthesis over these years, the research of photosynthesis is focused on the replicating of photosynthesis reactions methods and technologies (Figure 1-5). Most researches are in chemistry, physics, and materials science which involve reproducing partial reactions from natural photosynthesis.

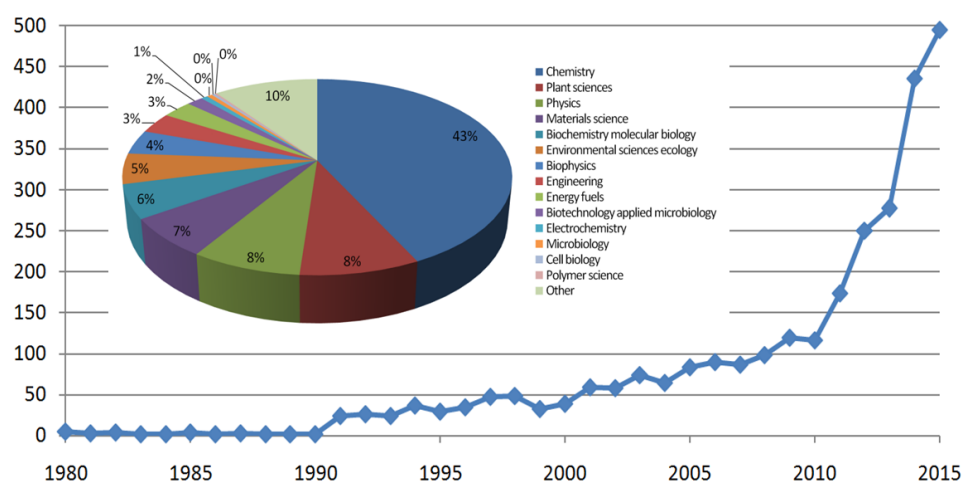


Figure 1-5. The quantity of publication (by Web of Science publications) with artificial photosynthesis topic in three decades.

Artificial photosynthesis topic publication increased dramatically after the 21st century, mainly because the artificial photosynthesis brought a new way to harvest energy. This may be a good way to solve the increased energy need after people began to realize the limited fossil fuel resource on this planet [30, 31].

For decades, scientists have devoted much time to the research on mimicking the natural process of photosynthesis to convert solar energy into stored chemical energy [2, 32]. Artificial photosynthesis utilizes the fundamental scientific principles of the natural process to design solar energy conversion systems [33], and the artificial process can potentially produce similar end products as those under the natural process: sugars (hexose like glucose or fructose), cellulose and O<sub>2</sub>. It is one of the promising technologies to produce liquid fuels in a sustainable manner and to replicate the natural process of photosynthesis, converting sunlight, water, and CO<sub>2</sub> into carbohydrates and/or hydrogen with oxygen as byproduct. Majority of plants and some photosynthetic bacteria have photosystem I (PSI) and photosystem II (PSII) to conduct light reactions in oxygenic photosynthesis [34]. PSI involves nicotinamide adenine dinucleotide phosphate (NADP<sup>+</sup>) photo-reduction, forming reductant NADPH for Calvin Cycle reactions. Photosystem II (PSII) involves photo-oxidation of water, releases electrons for PSI and forms O<sub>2</sub> as byproduct. At the same time, during electron transfer, the proton gradient can generate ATP with help of ATP synthase (ATPase) [35]. As for the further organic product, there are several kinds produced in the dark reactions in nature [36]. For instance, in green plant that follows Calvin Cycle as dark reaction, it produces G3P as first stable compound, and further reactions can produce D-glucose [3].

#### **1.4 Existing technologies on artificial photosynthesis**

The definition of artificial photosynthesis is widely used in all photosynthesis related topics and experiments. The energy production experiment that is related to either light reaction or dark reaction or partial chemical reactions is named artificial photosynthesis. Therefore, the new

definition of artificial photosynthesis can be categorized into four types based on the photosynthetic principles involved. Since we do not have a naming system for artificial photosynthesis processes so far, we would use type I, II, III and IV to refer to each kind of synthetic approach. Type I was using light reaction principles only; type II is using dark reaction principles only; type III is using living plant cells or photosynthetic organism cells; type IV is artificial photosynthesis with both light and dark reactions without living cells. Our artificial photosynthesis system belongs to type IV artificial photosynthesis.

### 1.4.1 Type I artificial photosynthesis (light reaction only)

The first type of artificial photosynthesis was the reaction involving light reactions only. Light energy is used to generate energy product on artificial fabricated or manufactured structures or devices to enhance the light energy conversion [37]. Visible light has a broad spectrum with wavelengths from 390 nm to 780 nm. After millions of years of evolution, the remaining plants were capable to utilize the visible light provided by the sun. In type I artificial photosynthesis, light energy collected were mainly used for water oxidation [22, 38, 39].

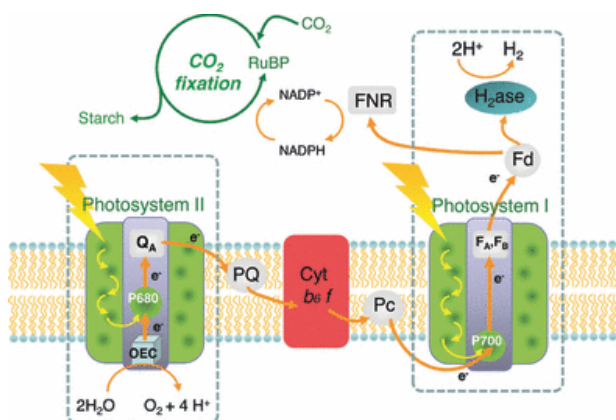


Figure 1-6. Schematic representation of the photosynthetic chain in the oxygenic photosynthesis.[40] Reused with permission from the American Society of Photobiology.

The schematic in Figure 1-6 represented a photosynthetic plan using photosystem I (PSI) and photosystem II (PSII) [40]. Light absorption was happened in PSII, and then activated the photosynthesis procedure. The water oxidation happened with the presence of oxygen evolving

complex (OEC). The whole system was built to realize the light reaction procedure and hydrolysis of water into oxygen and hydrogen. The possible application would be using the byproduct hydrogen ions from light reaction to catalyze the subsequent dark reactions and starch synthesis. However, there was no artificial way to synthesis starch by Calvin Cycle reactions, because some key enzymes require the living chloroplast structure and the stroma environment to be present.

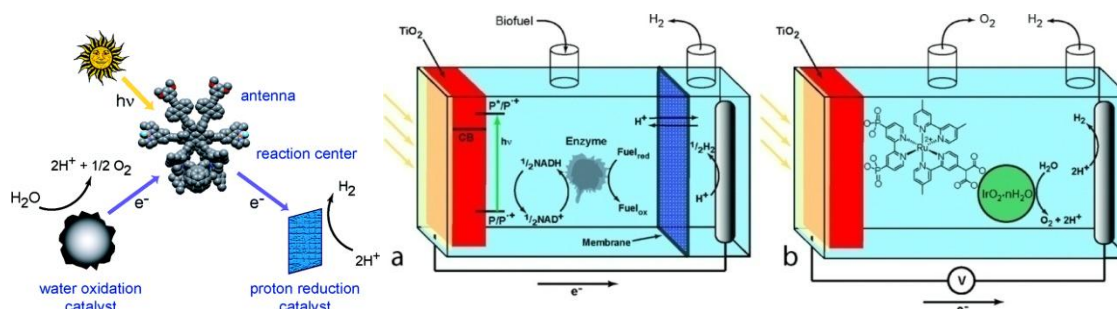


Figure 1-7. Schematic diagrams of a photo-electrochemical biofuel cell (a) and an artificial photosynthetic water splitting cell (b). Both cells use light to generate hydrogen.[34] Reproduced with permission from American Chemical Society.

The diagrams of photo-electrochemical biofuel cells, shown in Figure 1-7, also used the photosynthetic light reaction to hydrolyze water into oxygen and hydrogen [34, 41, 42]. One example is using “antenna” (i.e. carotenoid-porphyrin-fullerene artificial reaction center) [33, 43] to absorb sunlight and convert solar energy into electrochemical energy [44]. The electrochemical energy can further be used to produce hydrogen gas utilizing additional enzymes and reductant NAD(P)H [45]. However, this system cannot produce biofuel and is not ideal for practical solar energy conversion [33]. These solar water splitting systems provide an experimental approach to generate hydrogen, but are not stable to be practical to produce solar fuels [33, 46]. Moreover, these artificial photosynthesis approaches are not quite the same as natural photosynthesis because they do not form a stable chemical architecture to store the energy from sunlight [47]. The major problem of type I artificial photosynthesis reaction was that the  $\text{O}_2$  and  $\text{H}_2$  created were in gas status, with an amount of substance ratio of 1:2, respectively, which was a perfect

ratio for explosion. The storage, transportation, and the utilization of these gas energies would be extremely difficult and dangerous.

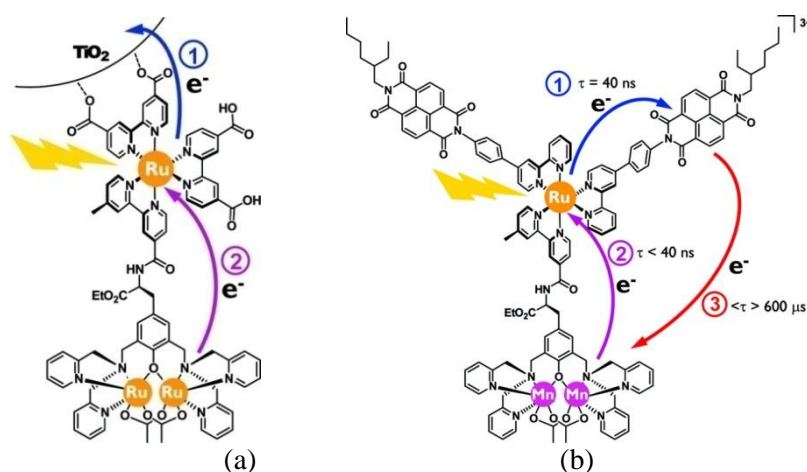


Figure 1-8. (a) Ru<sup>II</sup>-Ru<sub>2</sub><sup>II,II</sup> complex attached to a TiO<sub>2</sub> nanoparticle being photo-oxidized to the Ru<sup>II</sup>-Ru<sub>2</sub><sup>II,III</sup> state. [48] Reuse permission by John Wiley and Sons. (b) Mn<sub>2</sub><sup>II,II</sup>-Ru-ND<sup>12</sup> triad showing long-lived charge separation. [49] Reproduced with permission from American Chemical Society.

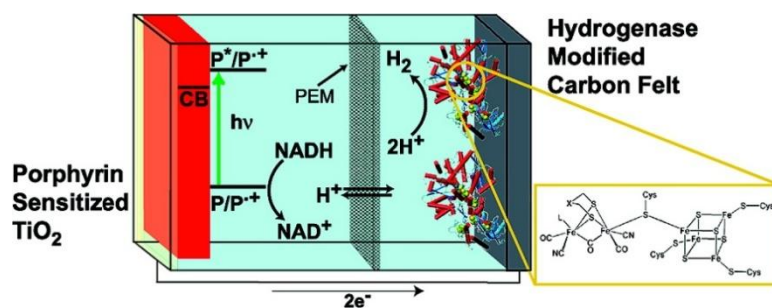


Figure 1-9. Schematic drawing of the photoelectron-chemical cell used in [FeFe]-hydrogenase-catalyzed H<sub>2</sub> production. [50] Reused with permission from American Chemical Society.

Utilizing TiO<sub>2</sub> as electrode during light reaction helps facilitate the energy from hydrolysis of water, while the byproduct H<sup>+</sup> can be set into multiple applications involving NADH or NADP<sup>+</sup> (Figure 1-9) [34, 48-51]. Different catalysts in H<sub>2</sub> production and O<sub>2</sub> release would result in different energy conversion efficiency. H<sup>+</sup> was used as charge carrier and this application allowed collection of electrical energy from the light reaction. Whether using electricity or hydrogen gas, the product or energy created as a result of this type of artificial photosynthesis was hard to collect or utilize.

As shown in Figure 1-10, the structure of the carotenoid-porphyrin-fullerene molecular dyad system was constructed by the porphyrin photocatalyst with C60 fullerene [38]. Figure 1-10b illustrated a single-step semiconductor particle with attached hydrogen- and oxygen-evolving co-catalysts. Figure 1-10c demonstrated a two-step system: mixture of semiconductor particles with attached hydrogen- or oxygen-evolving co-catalyst and redox electrolyte couples. Figure 1-10d and e indicated the single-excitation-step water-splitting cell, containing a semiconductor electrode with water oxidation co-catalysts and a counter-electrode to reduce water, which was split into hydrogen and oxygen by the generation of electrons flow [52].

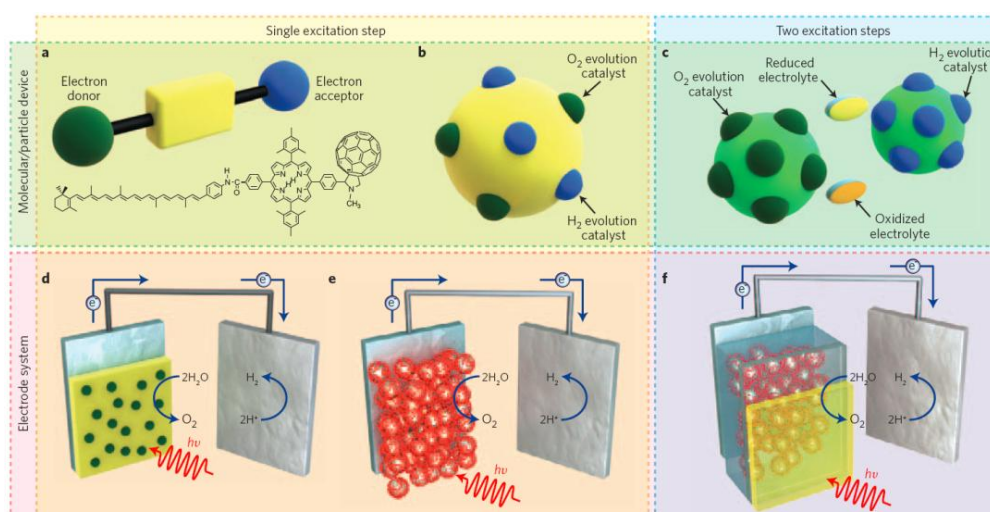


Figure 1-10. Structural diagrams of artificial photosynthesis reactions [38, 53]. Reused with permission from Nature Publishing Group and John Wiley and Sons.

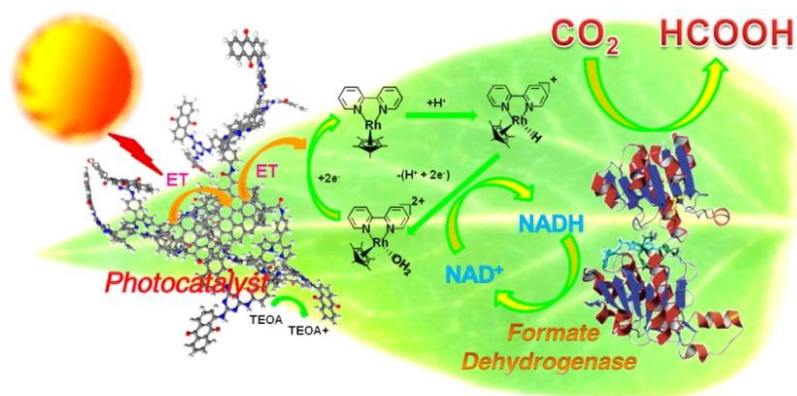


Figure 1-11. Graphene-based photocatalyst catalyzed artificial photosynthesis of formic acid from CO<sub>2</sub> under visible light. [54] Reused with permission from American Chemical Society.



Some type I artificial photosynthesis research focused on studying photo-catalyst similar to proton reduction catalyst [34] or porphyrin with ruthenium (Ru) or manganese (Mn) [48, 49], and using the created energy for some organic compound synthesis using chemical methods. Since the chemical method to synthesize organic compound from  $\text{CO}_2$  was an example of the applications for sunlight energy, we still categorized these researches in type I artificial photosynthesis photo-catalyst study for water splitting.

The photo-catalyst was studied to collect sunlight energy for NADH regeneration, and using the chemical energy to trigger formic acid ( $\text{HCOOH}$ ) synthesis from  $\text{CO}_2$  (Figure 1-11) [54]. As the photocatalyst were broadly used in other applications of type I artificial photosynthesis [34, 48, 49], the graphene-based photocatalyst was a material which covalently bonded the chromophore (as an electron donor), such as anthraquinone substituted porphyrin with the chemically converted graphene (as an electron acceptor).

#### 1.4.2 Type II artificial photosynthesis (dark reaction only)

The second type of artificial photosynthesis is where the reactions absorb gas and generate further energy product. The energy source come from either the transmitted light energy or external energy applied to the system, mostly by chemical or electrochemical reduction [55].

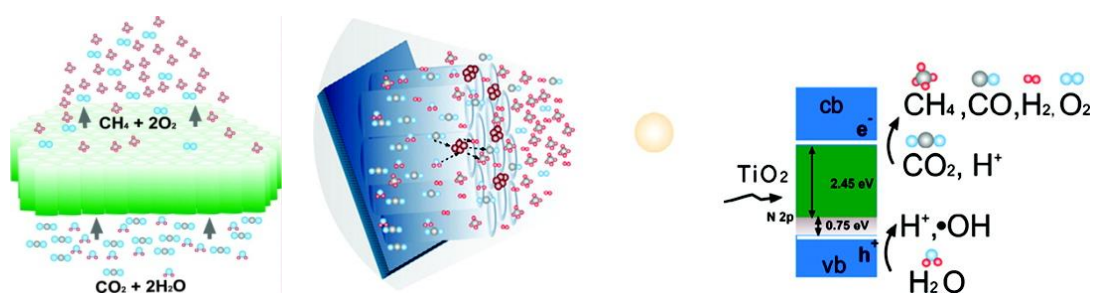


Figure 1-12. Depiction of flow-through photocatalytic membrane for  $\text{CO}_2$  conversion; [11, 56] Reproduced with permission from American Chemical Society.



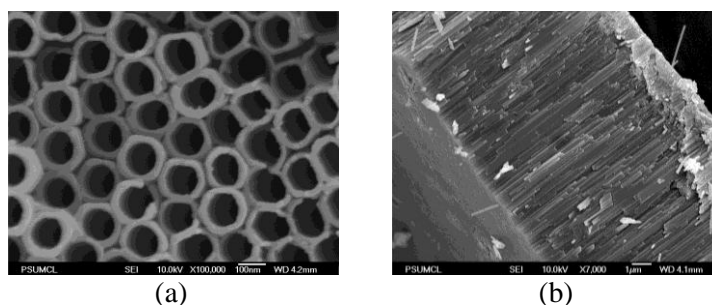


Figure 1-13. (a) Field emission scanning electron microscope (FESEM) top images of a mechanically fractured  $\text{TiO}_2$  nanotube array sample; (b) Field emission scanning electron microscope (FESEM) cross-sectional images of a mechanically fractured  $\text{TiO}_2$  nanotube array sample. [11] Reproduced with permission from American Chemical Society.

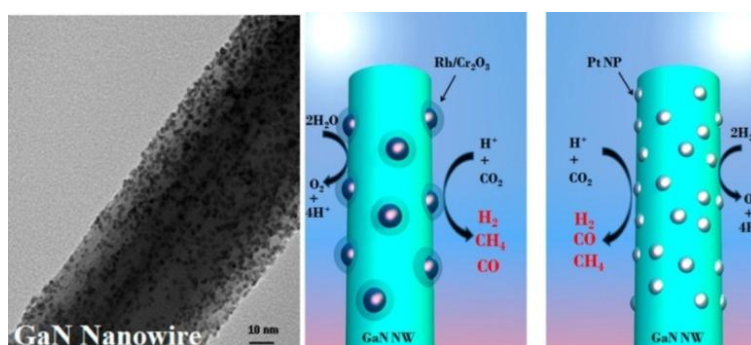


Figure 1-14. Transmission electron microscope (TEM) image of nanowire and Schematic of the photoreduction processes of  $\text{CO}_2$  on  $\text{Rh}/\text{Cr}_2\text{O}_3$  and Pt-decorated GaN nanowires. [57] Reproduced with permission from American Chemical Society.

$\text{Rh}/\text{Cr}_2\text{O}_3$  core/shell decorated with gallium nitride (GaN) nanowire and Pt nanoparticles deposited on GaN nanowire worked as platforms to synthesize  $\text{CO}_2$  into carbon monoxide (CO) and methane ( $\text{CH}_4$ ) with the help of  $\text{H}^+$  generated from the hydrolysis of water (Figure 1-13 and Figure 1-14). Unlike the type I artificial photosynthesis, type II used metal-nitride nanowire arrays as a highly efficient catalyst for the direct photoreduction of  $\text{CO}_2$  into chemical fuels, achieving the same results as photosynthesis dark reaction [58]. However, the  $\text{CO}_2$  absorption and fixation were different with the natural photosynthesis dark reaction C3 path (Calvin Cycle) or C4 path. The microfluidic technologies would benefit the fuel cells to create hydrogen or other energy types [59].

### 1.4.3 Type III artificial photosynthesis (light & dark reactions with living cells)

The third type of artificial photosynthesis is the system that utilizes living cells, especially photosynthetic cells or organisms [60, 61]. Functional photosynthetic living cells could perform photosynthesis by themselves with regular cell metabolism. The customized system, however, provides a better environment in enhancing the cells' reactions ratio or collecting of the product in a more efficient way, including byproduct extraction and energy product purification [62].

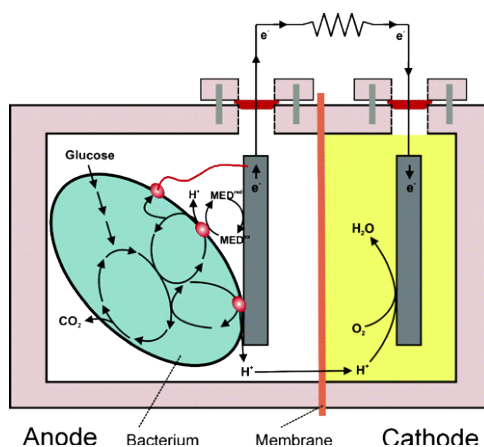


Figure 1-15. Operating principles of a MFC (not to scale). [21] Reused with permission from American Chemical Society.

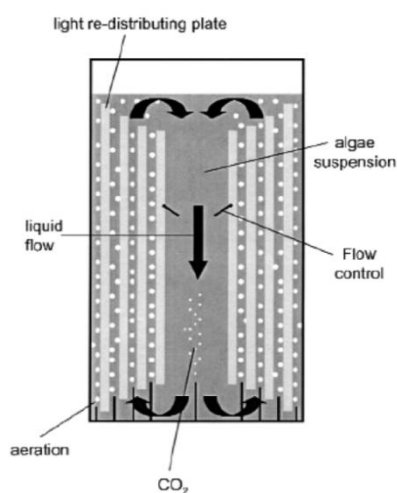


Figure 1-16. Design of a rectangular air-lift photo bioreactor. [63] Reused with permission from John Wiley and Sons.

A bacterium in the anode compartment transferred electrons obtained from an electron donor (glucose) to the anode electrode. This occurred either through direct contact, nanowires, or

mobile electron shuttles (Figure 1-15). During electrons production protons were also produced in excess. These protons migrated through the cation exchange membrane (CEM) into the cathode chamber. The electron flow was from the anode through an external resistance (or load) to the cathode where they reacted with the final electron acceptor (oxygen) and protons.

Bioreactor with implanted cells provided an environment for photo-reactions. The solar energy conversion rate is 10.5%, not considering the metabolism of the photosynthetic cells. However, the metabolism is always the major drawback of photosynthetic cells on chip.

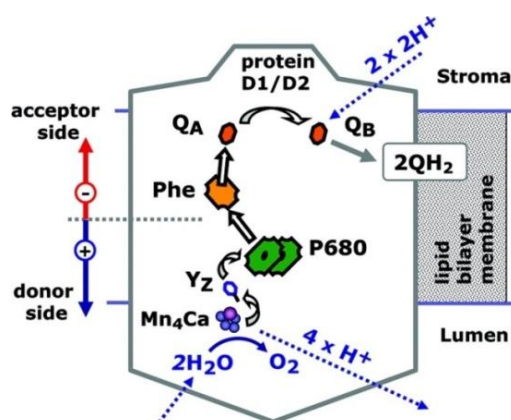


Figure 1-17. Arrangement of redox factors in PSII. The aqueous phases at the acceptor side (stroma) and donor side (lumen) are separated by a lipid bilayer (thylakoid membrane). [64] Reused with permission from American Chemical Society.

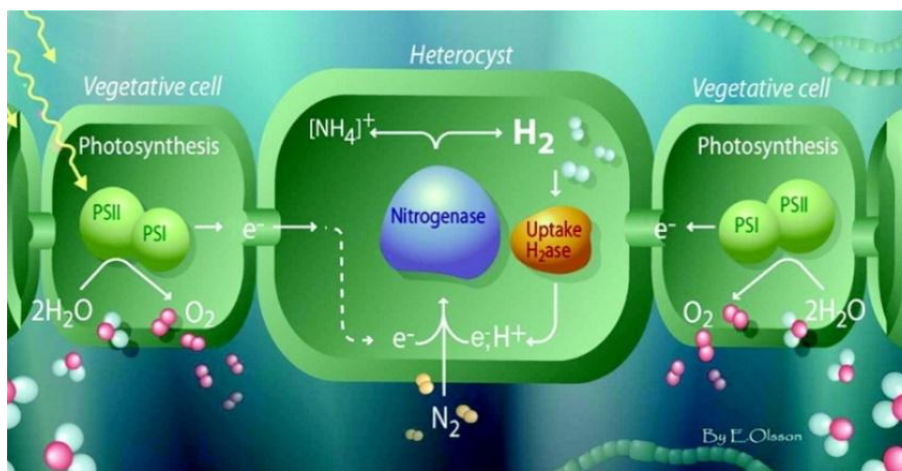


Figure 1-18. Oxygenic photosynthesis takes place in the vegetative cells (yellow, left), separated from the micro-oxic, nitrogen-fixing heterocysts. Heterocyst-specific transcriptional regulation was studied using the green fluorescent protein (bright green). [47] Reused with permission from American Chemical Society.

Many cyanobacterial strains were  $N_2$ -fixing under certain conditions. This occurred in an anaerobic environment achieved by separating  $N_2$  fixation and oxygenic photosynthesis (Figure 1-18) and was accomplished in specialized  $N_2$ -fixing cells called heterocysts.

According to a recent review of artificial ways of biofuel production and light energy utilization, scientists are in search of reliable methods to absorb and reuse light energy effectively with respect to advancements in physics, chemistry, biochemistry and biology.

#### 1.4.4 Type IV: cell-free artificial photosynthesis (light & dark reactions)

To achieve better methods to mimic photosynthesis procedure, scientists found that combining type I and type II could better utilize the photosynthesis principles in a cell-free way.

##### 1.4.4.1 Artificial photosynthesis on chip

An artificial photosynthesis on chip model was published in 2011 as a chemical approach using microfluidics. This mimicking of natural photosynthesis utilizing the NADPH redox reactions of Calvin Cycles could achieve photosynthetic products.

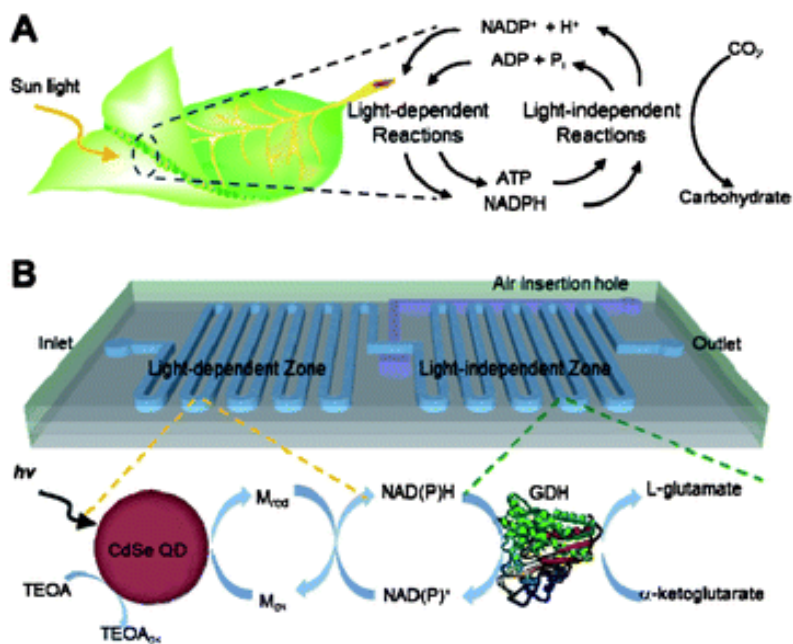


Figure 1-19. Schematic illustrations for (A) natural photosynthesis system and (B) microfluidic artificial photosynthesis system. [29] Reused with permission from Royal Society of Chemistry.

Similar to natural photosynthesis, photochemical regeneration of the NADH cofactor took place in the light-dependent reaction zone, which was then coupled with the light-independent, enzymatic synthesis in the downstream of the microchannel. The yields of both NADH regeneration and L-glutamate synthesis were significantly affected by the retention time and light availability.

As shown in Figure 1-19, this microfluidic device utilized the visible light energy to generate renewable resources. In this specific device, it achieved a chemical conversion from  $\alpha$ -ketoglutarate to L-glutamate, with  $\alpha$ -ketoglutarate as an input chemical. Therefore, unlike the Calvin Cycle using CO<sub>2</sub> and water as base chemical, this device also consumed  $\alpha$ -ketoglutarate as base chemical.



The amino groups were introduced by treatment of the inner side of PDMS microfluidic channels to activate N-hydroxysuccinimide (NHS) by (3-aminopropyl)triethoxysilane (APTES) solution. The microfluidic platform incorporated Cadmium Selenium (CdSe) quantum dots (QDs) and glutamate dehydrogenase (GDH) within the separate microchannel zones. Similar to photosynthesis in green plants, light-driven nicotinamide cofactor (NADH) regeneration took place in the light-dependent reaction zone, which was then coupled with the light-independent, enzymatic synthesis of L-glutamate in the downstream of the microchannel. The triethanolamine (TEOA) was used as sacrificial electron donor, and pentamethyl-cyclopentadienyl rhodium bipyridine was used as electron mediator. The platform was taken under 365 nm UV lamp exhibited distinct red luminescence from 655-QDs along the light-dependent reaction zone, while the inset was an image of the microfluidic platform. The light energy was UV light at 365 nm, which was not normal visible light. In addition, the CO<sub>2</sub> absorption was limited to the T-junction of the air flow and fluid flow.

Unlike the natural photosynthesis using CO<sub>2</sub> to produce organic amino acid, they consumed the energy of visible light by QDs, and involved amino groups' reaction with  $\alpha$ -ketoglutarate,

because one of the supplying chemicals glutamate dehydrogenase was not reusable. Therefore, this chip was not suitable to generate sustainable energy products continuously.

#### 1.4.4.2 Artificial photosynthesis in foam

Another approach was an artificial photosynthesis involves both light reaction and dark reaction, as well as Calvin Cycle and glucose/fructose synthesis with the presence of foam structure made by protein ranspumin-2 (Rsn-2) [28, 65].

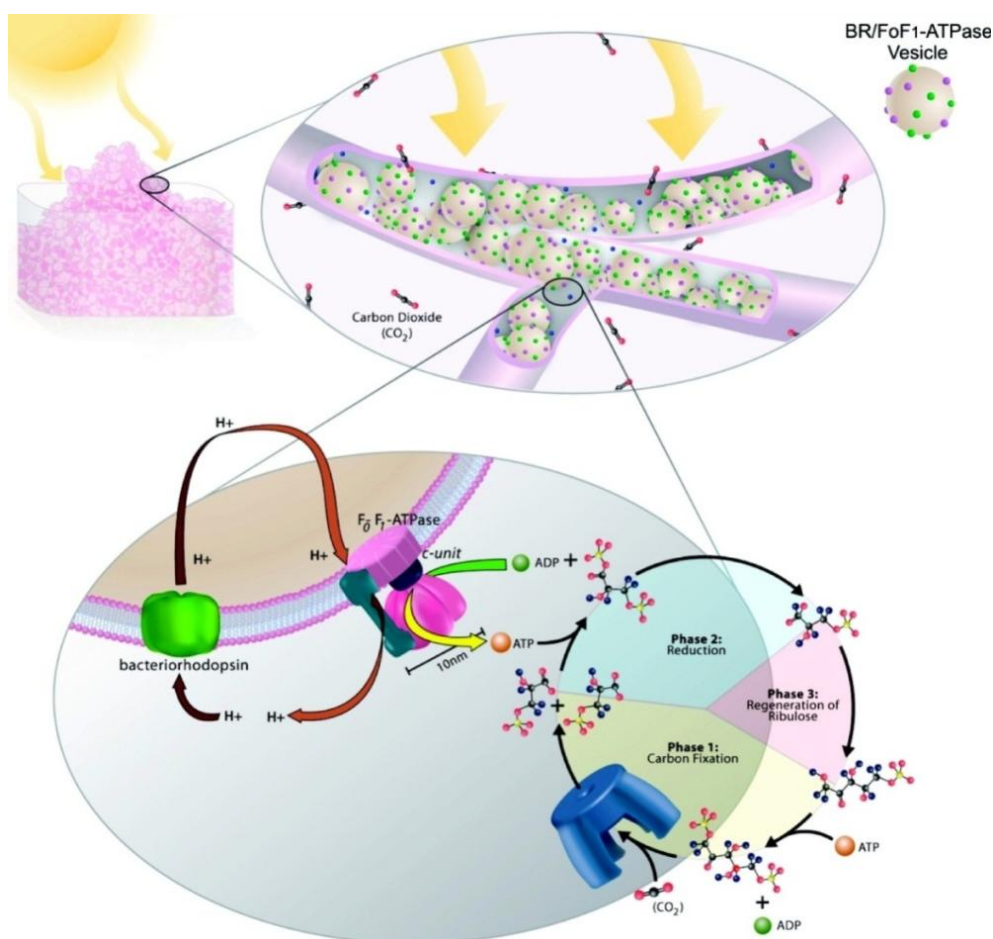


Figure 1-20. An illustration of the BR/FoF1 ATP synthase vesicle solar conversion system coupled to the RuBisCO CBB cycle and trapped within the foam channels.<sup>1</sup> [28] Reused with permission from American Chemical Society.

<sup>1</sup> The RuBP molecule in phase 1 in the CBB cycle has one atom drawn wrong. The RuBP using red atom represent oxygen element O, and black ones as carbon element C, the one above green ADP has two red atoms connected, and one of them is connected to other three carbon atoms. The one connecting three carbon atoms should also be carbon atom, and should be drawn in black color.

The light reaction used light energy conversion proteins/pigments to generate proper chemical status, such as proton gradient or electron flow gradient, to activate ATPase for ATP creation [66, 67]. The foam structure provides a reaction environment for bacteriorhodopsin (BR)-ATPase triblock copolymer vesicles and carbon fixation [68]. In a natural C3 plant leaf, chlorophyll was the light conversion pigment to generate electron flow along the thylakoid membrane, and then used for ATP regeneration in chloroplast. As for the carbon fixation, RuBisCO was common protein to attract CO<sub>2</sub> and ATP for G3P production, just like the RuBisCO in higher plant cells. Since the artificial photosynthesis methods did not involve cell metabolism and DNA translation, RuBisCO had to be supplied into the dark reaction solution environment.

As shown in Figure 1-20, sunlight was converted into ATP which is then used by the Calvin-Benson-Bassham cycle (CBB) enzymes to make sugar from carbon dioxide and NADH [28]. The vesicle structure created a two-chamber system, where the photosynthetic proteins BR and FoF1 ATP synthase was located on the vesicle surface. The BR could absorb sunlight energy and generate proton gradient, which was used to activate the FoF1 ATP synthase to synthesize adenosine diphosphate (ADP) and Pi into ATP. They compared different foam materials to find better ATP synthesis method to increase glucose or fructose synthesis.

The vesicles were mixed with the dark reaction solution. Since the vesicle diameter was around 50~200 nm, the vesicles were almost impossible to be reused or extracted. If the expensive vesicles were not able to recycle, the cost would be highly increased.

The synthesis of vesicles with BR and ATPase was made by commercial triblock copolymer poly(ethyloxazoline)-poly(dimethylsiloxane)-poly(ethyloxazoline) (PEtOz-PDMS-PEtOz), BR from purple membrane (PM) or BR monomer, and ATPase from animal [68-70]. The vesicles had inner side and outer side, while the BR and ATPase had orientation for four possible results. Therefore, accurately control the orientation of the BR and ATPase was critical. Only when the



BR pumps proton into the correct direction, the ATPase can synthesize ATP by rotating the F1 segment.

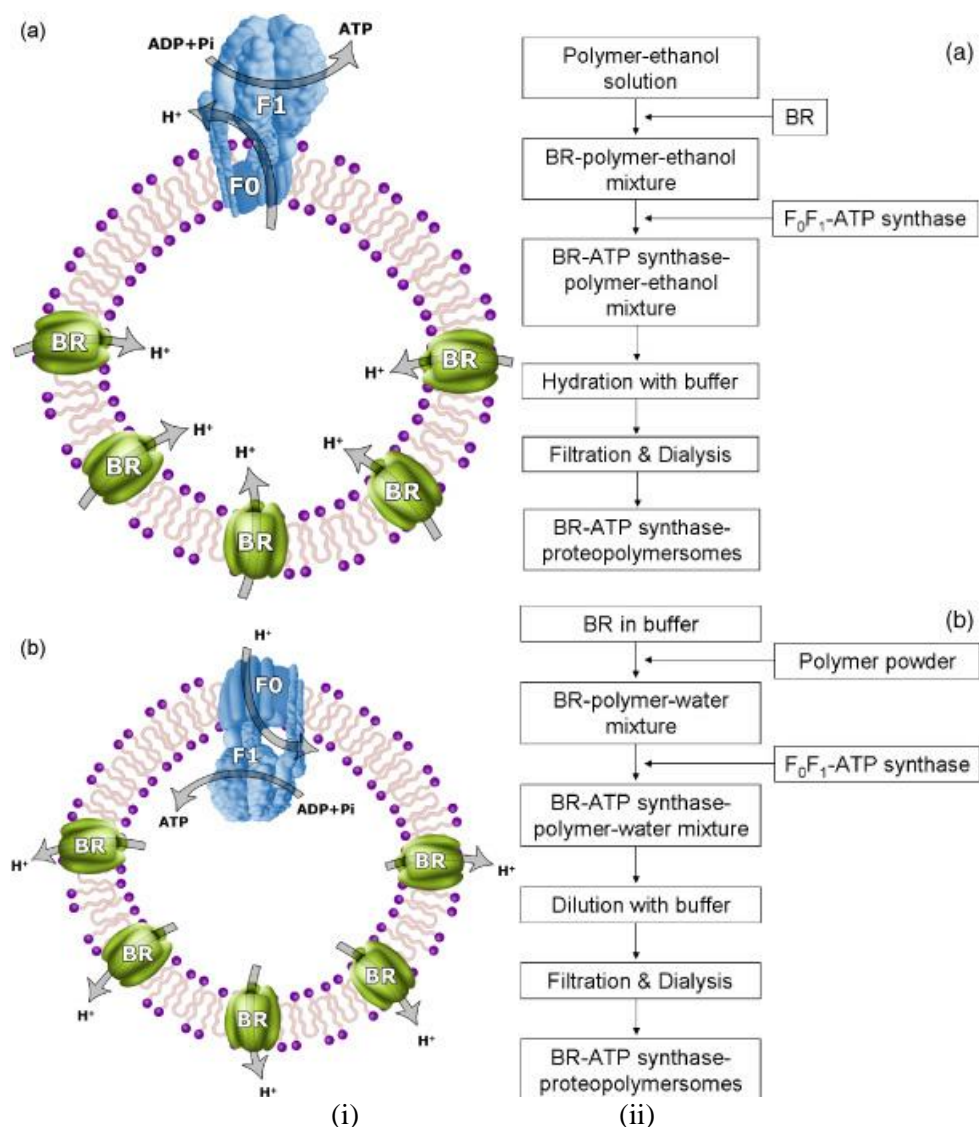


Figure 1-21. (i) Schematic representations of BR-ATP synthase-proteopolymersomes prepared (a) from PM (method A) and from BR monomer (method B), (b) from PM (method B); (ii) Schematic representation of the procedures: (a) the previous method using ethanol (method A); (b) the new method without using ethanol (method B).[69] Reused with permission from IOP Publishing Ltd.

The method A and B are listed in the chart (Figure 1-21) with or without ethanol respectively [69]. Since the BR and ATPase also have hydrophobic and hydrophilic sides, the ethanol can help selecting the orientation of the BR and ATPase.



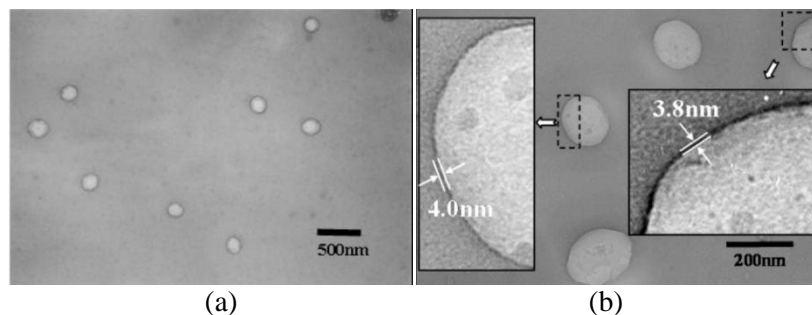


Figure 1-22. TEM of PEToz-PDMS-PEToz vesicles in DI water: (a) low magnification, (b) high magnification. [71] Reused with permission from IOP Publishing Ltd.

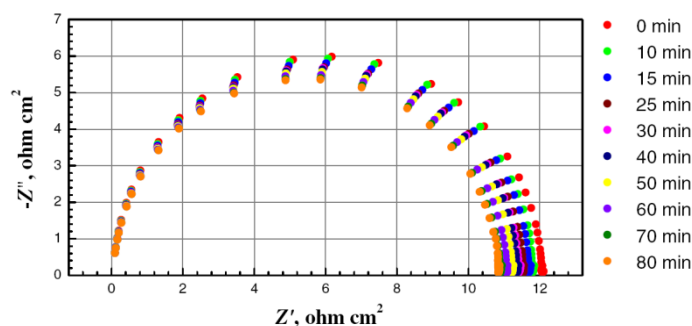


Figure 1-23. Nyquist plots ( $\text{Re}(Z')$  versus  $\text{Im}(Z'')$ ) of a free-standing PEToz-PDMS-PEToz triblock copolymer membrane. [71] Reused with permission from IOP Publishing Ltd.

The vesicles had maximum BR ATPase carrying ability and proton transferring ability due to the dielectric properties of the vesicle membrane triblock copolymer. According to the TEM image of vesicles and the dielectric properties and Nyquist plots of free-standing PEToz-PDMS-PEToz triblock copolymer, the authors concluded a planar membrane capacitance of  $2.58 \times 10^{-7} \sim 2.71 \times 10^{-7} \text{ F/cm}^2$  and a membrane resistance of  $12 \sim 10.8 \Omega \cdot \text{cm}^2$ .

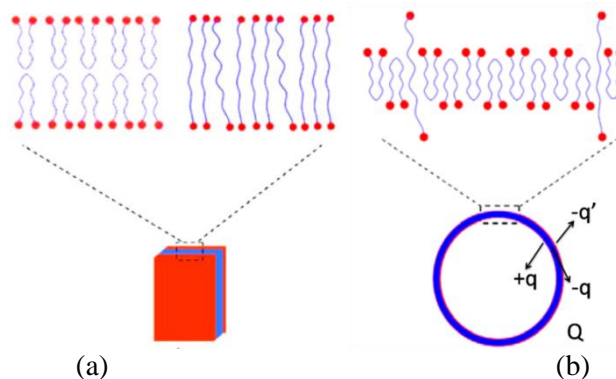


Figure 1-24. Schematics of triblock copolymer membrane in planar membrane (a) and vesicle structure (b) with  $\sim 4 \text{ nm}$  thick wall. [71] Reproduced with permission from IOP Publishing Ltd.

The dielectric properties of triblock copolymer can be measured by EIS experiment. Based on the data, we can use the simple physics method to calculate the capacitance of the triblock copolymer material (Figure 1-24). We assume that the inner wall has a charge +q, the overall charge will be

$$Q = (-q) + (-q')$$

Eq. 1-1

Since the whole vesicle should have same potential,

$$\frac{1}{4\pi\epsilon_0} \cdot \frac{Q}{r_o} + \frac{1}{4\pi\epsilon_0} \cdot \frac{q}{r_i} = 0$$

Eq. 1-2

so

$$q' = \frac{r_o - r_i}{r_o} q$$

Eq. 1-3

The electric potential of whole sphere

$$U = \frac{1}{4\pi\epsilon_0} \cdot \frac{Q}{r_o} + \frac{1}{4\pi\epsilon_0} \cdot \frac{q}{r_o} = \frac{1}{4\pi\epsilon_0} \cdot \frac{r_o - r_i}{r_o r_i} q$$

Eq. 1-4

The capacitance of the thin wall will be

$$C = \frac{q}{U} = \frac{4\pi\epsilon_0\epsilon_r r_o r_i}{r_o - r_i}$$

Eq. 1-5

According to literature, the relative permittivity of triblock copolymer membrane is ~2.7 [72, 73].

In addition, the membrane capacitance was defined without the surface area factor

$$C_{MEM} = \frac{C}{S_{vesicle}} = \frac{C}{4\pi r_o^2} = 5.81 \sim 5.88 \times 10^{-7} \text{F/cm}^2$$

Eq. 1-6

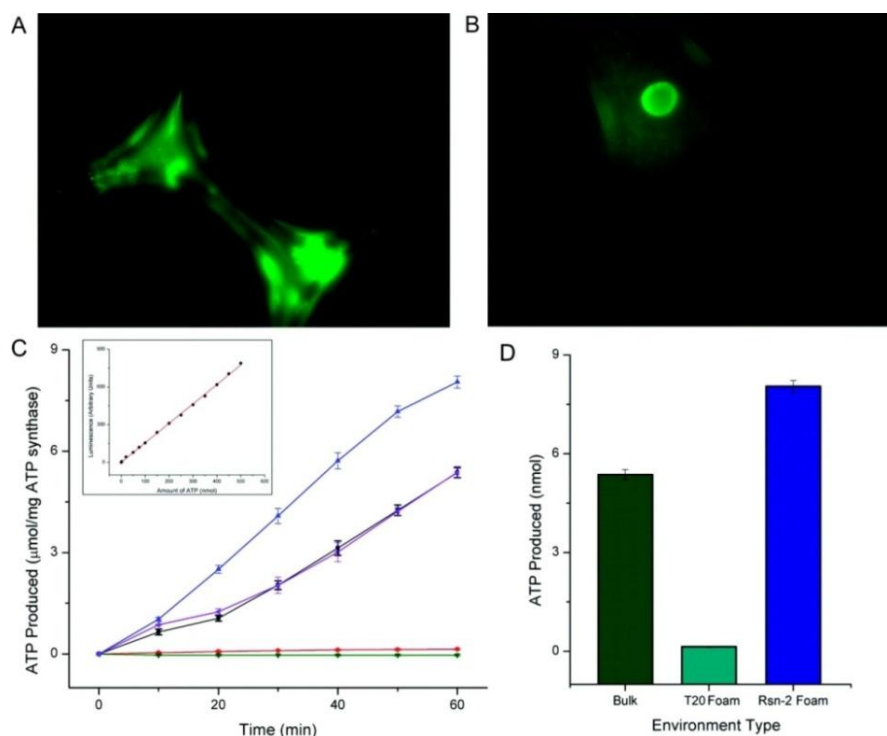


Figure 1-25. Illustration of ATP production. [28] Reused with permission from American Chemical Society.

In Figure 1-25(A), lipid vesicles were formed in the presence of 1 nM QD-565 (green quantum dots used to illuminate the lipid vesicles) and gel purified to separate unincorporated QDs. Eluted vesicles were re-suspended with Rsn-2 and aspirated to create foam. Vesicles actively traveled through the Plateau channels and collected at the nodes. [28] In Figure 1-25(B), large lipid vesicles were readily observed intact within the channels and appeared relatively stationary compared to the smaller flowing vesicle assemblies. [28] In Figure 1-25(C), production of ATP with BR/ATP synthase lipid vesicles in Rsn-2 foam (blue up triangle), in bulk (black square), in deflated Rsn-2 foam (purple left triangle), and in T20 foam (green down triangle) and a control experiment in the dark (red circle) are plotted for comparison. [28] Except the T20 foam, other foam structure proved that the promising ATP production under light emission. In Figure 1-25(D), BR/ATP synthase function in a lipid membrane was limited to the Rsn-2 based foam since the T20 adversely affected coupled FoF1-ATPase/BR vesicle function. [28]

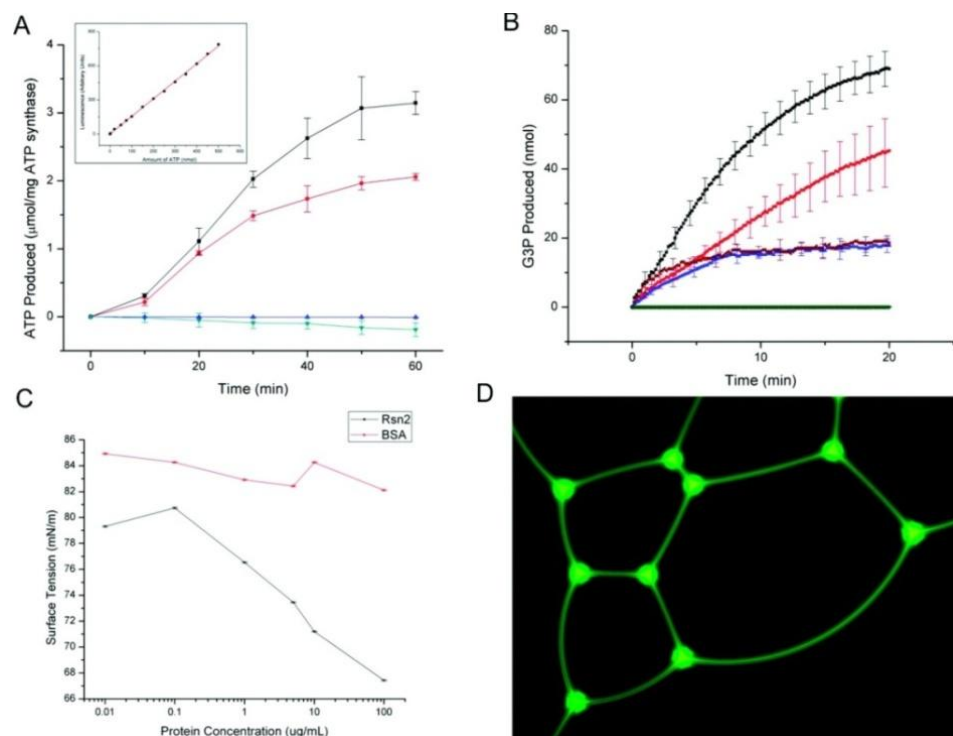


Figure 1-26. G3P production in foam structure. [28] Reused with permission from American Chemical Society.

In Figure 1-26A, ATP synthesis used BR/ATP synthase polymersomes in T20 foam (black square), bulk (red circle), deflated T20 foam (green down triangle), and a control experiment in the dark (blue up triangle) for comparison ( $n = 3$  for each). Inset was the light intensity standard curve created with ATP stock dilutions. [28] The results indicated that the flattened foam structure provide enough ATP synthesis amount. In Figure 1-26B, the foam system contained BR/ATP synthase vesicles, RuBisCO, phosphoglycerate kinase (PGK), glyceraldehydes-3-phosphate dehydrogenase (GAPDH), NADH. These enzymes were converting  $\text{CO}_2$  and RuBP to G3P using photoderived ATP. The RuBisCO-dependent carbon fixation reaction was “fueled” by lipid photophosphorylation vesicles fuel within the Rsn-2 foam (black,  $n = 3$ ) and in bulk (brown,  $n = 3$ ) and the proteopolymersomes within T20 foam (red,  $n = 3$ ) and in bulk (blue,  $n = 3$ ). Control experiments were also performed in the dark (green and purple overlapping at 0,  $n = 3$  for each) and with selectively removed individual components without detectable G3P production. [28] In Figure 1-26C, it demonstrated the surfactant properties of Rsn-2 (black,  $n = 3$ ) and a control with

bovine serum albumin (BSA) (red, n = 3). [28] In Figure 1-26D, fluorescent image showed the polymer vesicles within the T-20 foam. [28]

The dark reaction need resource of CO<sub>2</sub>; however, they used foam structure with air in it, and together with 0.03~0.04% (weight percentage) CO<sub>2</sub> as the only source to provide carbon. Their experiment lasted for 4 hours maximum, and the main reason is the limited carbon source.

#### 1.4.5 Summary of existing artificial photosynthesis

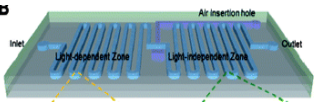

Among all the existing artificial photosynthesis systems or devices, methods of utilizing light energy and creating useful chemical or electrical energy were demonstrated above. Based on the performance and principles of light energy harvesting and light-independent reactions, the published results indicated that the type I and type IV were more useful.

Table 1-1. Comparison of different types of artificial photosynthesis.

	<b>Type I</b>	<b>Type II</b>	<b>Type III</b>	<b>Type IV</b>
Light energy conversion	☺	☹	☺	☺
Light reaction product collection	Hard	N/A	Hard	Hard
Dark reaction product collection	N/A	Hard	Medium	Medium
Dark reaction product format	Gas/ electricity	Gas	Gas/ electricity	Organic compound
Device life-time	Long	Long	Short	Medium
Potential as light energy harvesting	☺	☹	☹	☺
Future cost reduce and commercialize possibility	☺	☹	☹	☺

Type I artificial photosynthesis can be commercialized and product energy product efficiently. Type I, III, and IV involves light energy conversion, so the energy source is clean energy. Type I artificial photosynthesis has been developed into commercial devices with acceptable efficiency to generate electricity or chemical energy. Type III artificial photosynthesis contains photosynthetic cells on chip; therefore, the life-time and the cost of this kind of device are the main obstacle of commercialization. Type IV cell-free artificial photosynthesis has great potential to be a clean energy harvesting method in the future.

Table 1-2. Comparison between cell-free artificial photosynthesis system with other type IV artificial photosynthesis.

	Cell-free artificial photosynthesis system	Other Type IV artificial photosynthesis	
		 [29]	 [28]
Appearance	A whole system with independent light/dark reaction regions	Microfluidic channels with constant $\text{NH}_4^+$ supplies	A beaker with foam and liquid
Light reaction carrier	Planar membrane fixed in devices; BR-ATPase vesicles	CdSe quantum dots in microfluidic channels	BR-ATPase vesicles
Energy from light	$\text{H}^+ \rightarrow \text{ATP}$	QDs $\rightarrow$ NADH	$\text{H}^+ \rightarrow \text{ATP}$
Dark reaction reactant supplies	$\text{CO}_2$ ; constantly supplied into dark reaction	$\text{NH}_4^+$ and $\alpha$ -ketoglutarate supplied to microfluidic channels	$\text{CO}_2$ ; limited $\text{CO}_2$ contained in foams
Dark reaction product	Glucose	L-glutamate	Glucose / fructose

Other type IV cell-free artificial photosynthesis has defects or problems to be a reusable, stable energy harvesting device. The microfluidic CdSe QDs based artificial photosynthesis on chip requires specific nitrogen source to L-glutamate amino acid synthesis. The foam based artificial photosynthesis is limited to beakers and lab conditions, as well as the limited  $\text{CO}_2$  source from foam structure. Our cell-free artificial photosynthesis system is targeted to overcome these problems and improve the artificial photosynthesis system for future commercialization, handling and distributing.

## 1.5 Artificial photosynthesis blueprint

### 1.5.1 Motivations and principles

Our cell-free artificial photosynthesis system will be a platform based on this research principle using both light reaction and dark reactions. We planned to improve the system with better light reaction unit and better dark reaction carbon dioxide supply, as well as an intelligent integration system for better operations and observations.

The basic step for mimicking natural photosynthesis was to produce ATP by artificial light reactions. Researchers had succeeded in producing ATP by embedding BR and FoF1 ATP synthase in a vesicle structure [69, 71, 74, 75]. BR was used to collect green light energy and generates proton gradient, which stimulates FoF1 ATP synthase to attract ADP and Pi (inorganic phosphate,  $\text{HPO}_3\text{O}^{2-}$ ) [3] to produce ATP. The further steps were utilizing the ATP to produce other products, such as glucose or fructose, or use these carbohydrates as precursor to produce biofuels, such as ethanol or DMF, through chemical reactions [24]. The simplest way to produce glucose or fructose was following the C3 plant photosynthesis, Calvin Cycle dark reactions (Figure 1-27):

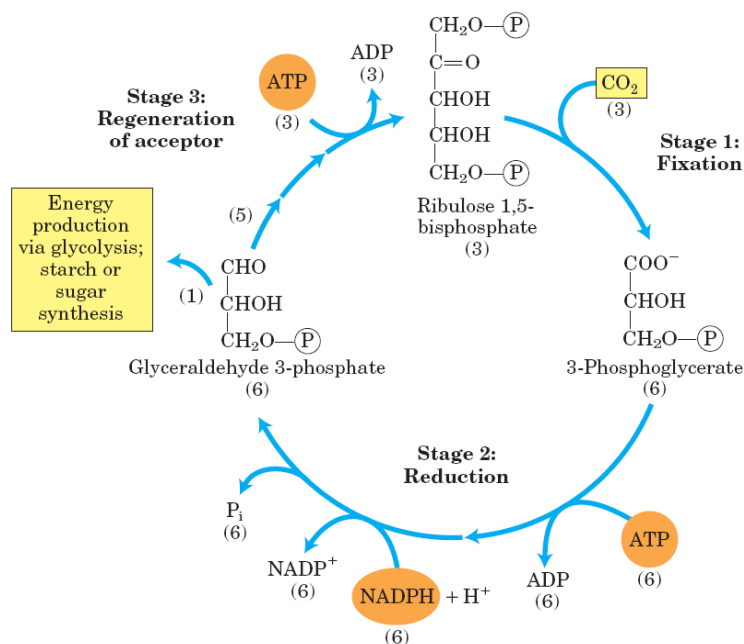
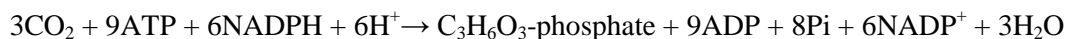


Figure 1-27. Calvin Cycle reactions with molecular quantities. [5] Nelson and Cox, *Lehninger principles of Biochemistry*, 5th Ed., 2008, page 775; Reused with permission from WH Freeman/Worth Publishers.

To simulate the dark reactions in C3 cycle, the carbon fixation enzyme RuBisCO fixed  $\text{CO}_2$  and RuBP. By using ATP offering energy and NADPH oxidizing to  $\text{NADP}^+$ , these reactions produced G3P, and the final output from G3P combination is hexose [28, 76]. With the catalysis of isomerase catalysts, the final product could be glucose or fructose [28].

The above mentioned BR-based artificial photosynthesis is close to natural photosynthesis. However, the process relies on a specially-synthesized vesicle structure for photosynthesis and requires foam architecture to increase reaction area and provide flow channels for vesicles and solutions. The vesicles free float in the aqueous solution and were mixed with photosynthetic proteins and products. Therefore, separation and recycle of vesicles was difficult. Furthermore, the foam structure had poor mechanical strength for long-term outdoor deployment. It was difficult to manufacture and scale-up and product separation was complex due to the mixed solution of vesicles and photosynthetic compounds. A new structure that facilitates product isolation, eases manufacturing, and had reasonable mechanical strength must be developed.

We proposed to use an innovative architecture to support artificial photosynthesis. PEtOz-PDMS-PEtOz or poly(2-methyloxazoline)-poly(dimethylsiloxane)-poly(2-methyloxazoline) (PMOXA-PDMS-PMOXA) triblock polymer embedded with BR and ATP synthases will be created and functioned as mesophyll layer of real leaves for photosynthesis light reactions. A solution with artificial photosynthesis dark reaction chemicals will be embedded, which includes all the protein enzymes such as RuBisCO, catalyzing isomerase and necessary compounds: RuBP and NADPH; and enough amounts of ATP, ADP and Pi to start-up all these carbon fixation reactions. Chromatography gels will also be printed for product transfer and separation. The system was expected to achieve a better photosynthetic way, because it does not have any life-related reactions such as respiration, digestion, reproduction, cell growth and excretion.

## **1.5.2 Artificial photosynthesis reactions assay**

### **(1) BR proton pumping (from light to H<sup>+</sup> gradient)**

The proton pumping activity of BR in the triblock membrane would be monitored using 8-hydroxyprone-1, 3, 6-trisulphonic acid (HPTS) [77]. The pH change inside the triblock membrane and the photo-induced activity will be measured as described in [75].



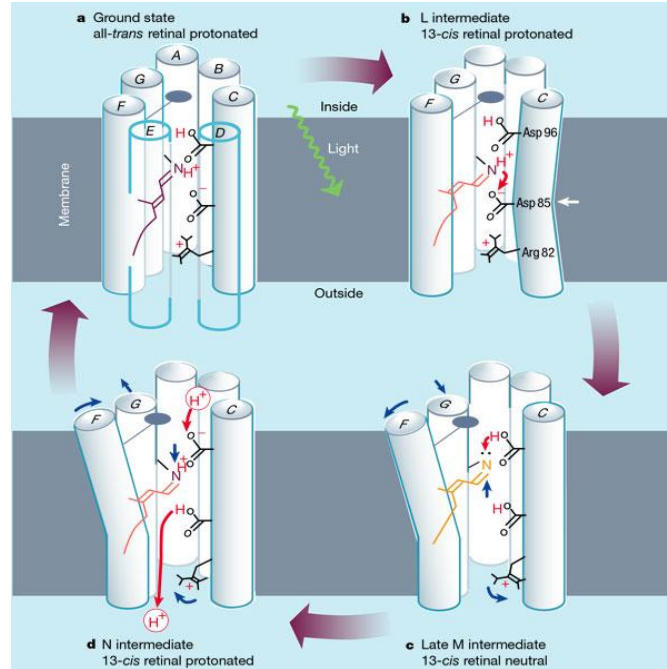


Figure 1-28. Molecular mechanism of proton (H<sup>+</sup>) pumping in bacteriorhodopsin. Retinal is bound in the space between the seven membrane-spanning helices (A to G) by a lysine in helix G [78]. Reused with permission from Nature Publishing Group.

## (2) ATP synthesis (from H<sup>+</sup> to ATP)

The ATP synthesis activity would be measured with a bioluminescence assay kit.

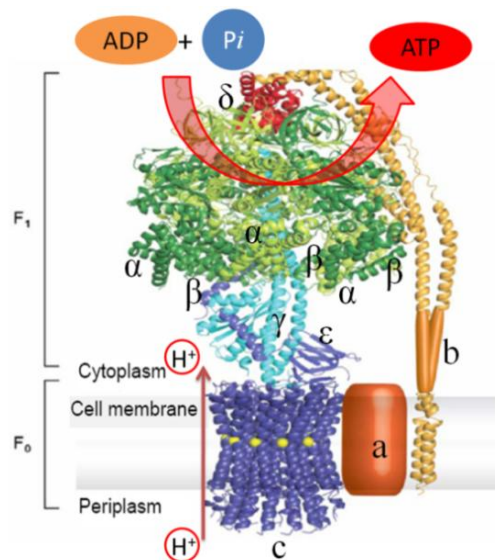


Figure 1-29. An illustration of the F<sub>0</sub>F<sub>1</sub> ATP synthase showing the major component of the structure the rotary part (F<sub>0</sub>) which is embedded in the cell membrane and the stator part (F<sub>1</sub>) which is located in the cytoplasm [79]. Reproduced with permission from Annual Reviews.

Besides proton pumps, ATP synthase generate pmf to motivate protons pumping back across the membrane by Fo section of ATPase (the Fo portion (o: oligomycin) is within the membrane; the F1 portion of the ATP synthase is above the membrane, inside the matrix of the mitochondria). The catalyst of H<sup>+</sup>-ATPase includes three sub-groups at F1 section for ATP synthesis. The core on F1 section helps preventing ATP hydrolysis by F1 section when no light was used to form pmf. Fo section include a, b, and c sub groups (Figure 1-29). Subgroup c is smaller (8 kDa), and extremely hydrophobic, so c contains a cross membrane section, and correspond to F1 section. F1 section contains five different subgroups, and written as  $\alpha_3\beta_3\gamma\delta\epsilon$ . The three nucleotides binding sites were located on three subunit  $\beta$ . During ATP synthesis,  $\alpha_3\beta_3$  subgroups can turn and capture ADP and Pi with proton and water to synthesize ATP. At any time point, the  $\alpha_3\beta_3$  were not at same status, including open (O), loose (L), and tight (T). The proton flow makes  $\gamma$  twisting, and makes O become L, L become T, and T become O. ADP and Pi are first connected to O, and synthesize into ATP at T. Then, ATP can be released at status O.

### **(3) RuBisCO carbon-fixation (from ATP to G3P)**

Carbon-fixing activity and subsequent formation of G3P could be measured. The change in absorbance at 340 nm due to the oxidation of NADH by GAPDH would be monitored using the microplate reader. Glucose production can be detected and measured by many chemical ways, and some of them can be miniaturized and integrated to micro systems we were developing [80].

### **(4) Full glucose synthesis (from G3P to glucose)**

Glucose oxidase forms gluconic acid and hydrogen peroxide from glucose. Hydrogen peroxide reacts with the o-dianisidine in the assay mixture forming a colored product. The oxidized o-dianisidine then reacts with sulfuric acid to form a more stable pink colored product. The intensity of the pink color measured at 540 nm was proportional to the original glucose concentration. The amount of glucose present is quantified by comparison to a standard calibration curve obtained from samples of glucose of known concentration.

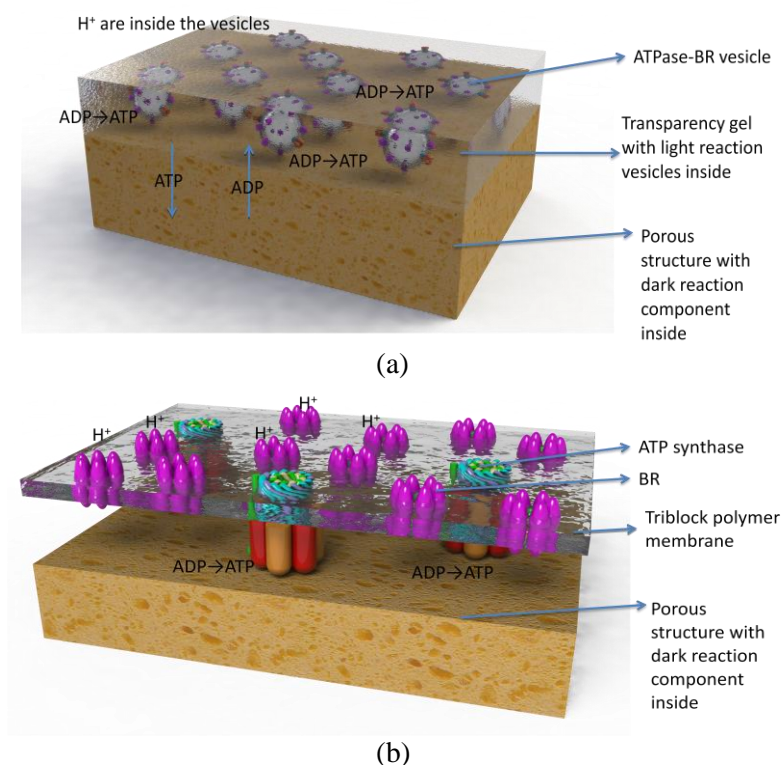


Figure 1-30. (a) Method 1: Artificial light reaction with BR-ATPase vesicles. (b) Method 2: Artificial light reaction with BR-ATPase planar membrane.

Based on the ATP synthesis principles using membrane structure with BR and ATPase, as shown in Figure 1-30a, we can have two basic plans to use light energy for ATP synthesis. In order to fix the light reaction on a device in solid state, we can either use vesicles in a gel structure, or use planar membrane fixed on a certain structure in a device.

## 1.6 The proposed artificial photosynthesis system

The objective of this research is to create a cell-free artificial platform for harvesting light energy and transforming the energy to organic compounds. In order to achieve this objective, we took the approach of mimicking the photosynthetic processes of a plant leaf and integrating them into a compact system. Photosynthesis consists of two parts: light reaction and dark reaction. During the light reaction, light energy turns ADP into ATP, which is used along with carbon dioxide to synthesize organic compounds such as glucose and fructose during the dark reaction. Many people had tried to realize artificial photosynthesis for energy harvesting for decades.

However, most of the previous systems were simply based on light reaction and produce less desirable energy sources such as explosive hydrogen gas and unstable electricity. Other works had been reported that combined both light and dark reactions to produce useful organic compounds, but they were all based on utilizing living cells that were difficult to maintain and were not reusable. We developed cell-free artificial platforms conducting light and dark reactions. To the best of our knowledge, such devices have not been reported so far. These devices were able to harvest and transform the light energy to ATP and also to organic compounds, mimicking a plant leaf. We envisioned integrating the “artificial leaves” to create a compact energy harvesting system with high efficiency. In order to create an artificial photosynthesis device, we had come up with four specific tasks.

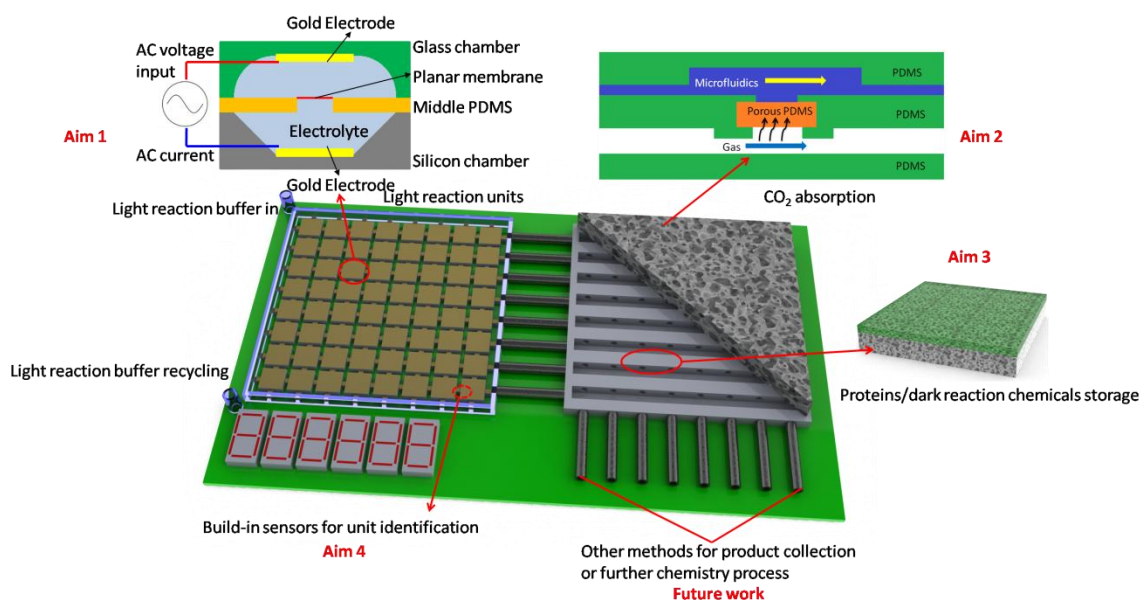


Figure 1-31. Illustration of cell-free artificial photosynthesis system.

### 1.6.1 Aim 1: Light reaction unit

Light reaction was realized in a microfluidic platform that consists of two fluid chambers separated by a planar membrane with embedded proteins that convert light energy into ATP. Four different materials were investigated as potential membrane materials. Since these membrane

materials were very soft, it was challenging to integrate them in a microfluidic platform. Diverse support materials and fabrication techniques was investigated to identify the optimal fabrication process. Once the best membrane material was identified and a microfluidic platform was constructed, we would have light-converting proteins embedded in the membrane followed by the evaluation its light reaction performance.

Light reaction required proteins with light energy conversion ability, and ATP synthase to use the converted energy. Normally this reaction happened on a thin membrane, mimicking thylakoid in chloroplast. Therefore, we needed to create a stable membrane and implant BR and ATPase onto the membrane. To study the membrane, we designed to use fluidic chambers on PCB. By inspecting the impedance of the planar membrane, which functioned as a dielectric layer in the electrolyte, we identified the membrane's electrochemical properties and physical stabilities. To achieve higher efficiency and higher integration purpose, we wanted to further miniaturize the devices with planar membrane to microchip using microfabrication technology. Also, parallel electrodes were plated into the inner side of the microchip to function as a parallel capacitive sensor to monitor the dielectric properties of planar membrane.

### **1.6.2 Aim 2: Dark reaction unit**

Dark reaction was realized in another microfluidic platform that consists of two chambers (one for liquid containing ATP and the other for air flow) separated by a membrane that can transport CO<sub>2</sub> from the air to the liquid chamber. We used porous PDMS as a gas-liquid interface between microfluidic channels to create a “one-way” diffusion path for carbon dioxide. The CO<sub>2</sub> transport was evaluated based on pH change and successful CO<sub>2</sub> transport can produce precursors (C3 compounds) for glucose production.

Nature plants had experienced a long period of evolution time and find several optimal ways of producing nutrition by collecting inorganic molecules or ions from surroundings, such as CO<sub>2</sub> or NH<sub>4</sub><sup>+</sup>. We needed to find a way to mimic the guard cells of leaf. We used porous PDMS as a

gas-liquid interface media, because CO<sub>2</sub> can penetrate through the interconnected pores in porous PDMS; on the other hand, water cannot leak through the porous PDMS because of its hydrophobic property.

### **1.6.3 Aim 3: Organic compound storage platform**

Glucose synthesis and storage unit was developed by mimicking sponge mesophyll found in a leaf (dicotyledons). Chitosan porous structures with interconnected pores were used for this purpose and they would be fabricated by lyophilization after molding-casting or 3D printing.

The glucose synthesis procedure involved reactions that G3P synthesis to hexose: glucose or fructose, which was determined by the catalyzing isomerase. A typical reaction time to synthesis glucose was 4~6 hours. Therefore, we needed to fabricate a space for synthesis reactions and storage. The material we chose was chitosan, which can form some weak hydrogen bond to some proteins, which can reduce the catalyzing protein lost. For storage reason, we needed to build a porous chitosan structure as a “cage” for those dark reaction chemicals. The methods we tried are molding-casting and 3D printing.

### **1.6.4 Aim 4: Simulation of integrated system**

Interconnection and integration of the above-mentioned three key components would be investigated to generate a complete cell-free artificial platform for effective energy harvesting. Seamless interconnection of the three components was necessary for harvesting light energy and transforming the energy to organic compounds. Once this was established we would attempt to integrate multiple devices in an array form for effective energy harvesting. We also proposed to integrate the system with embedded impedance sensors for in-situ monitoring of the function of each unit. The circuits for an integrated light reaction platform was designed and simulated. The digital encode/decode of microchip array was simulated. A high-resolution, low-speed analog-to-digital converter was also designed and simulated for ion channel monitoring purpose.

A piece of leaf contained tens of thousands of cells and numberless chloroplasts. They were working well because plants had life. To build an artificial photosynthesis system, we needed to reproduce the life behavior of plants. Cell-free platform does not have metabolism, neither DNA nor RNA that transfer genetic information or orders. Therefore, we needed to build a microprocessor to deal with all the dielectric sensors, and gave feedback orders to single device, which made the integrated system having the ability to think and behave. An economic method was using VLSI technique to name every unit in binary code, and processed all the electric signals coming from each unit in a digital way.

## **1.7 Arrangement of chapters**

**Chapter 1:** The introduction of photosynthesis and current status in artificial photosynthesis approaches. I also defined new concepts of different types of artificial photosynthesis.

**Chapter 2:** The membrane embedded on PCB, and the mathematical modeling of membrane vibration based on physics principles. The electrochemical impedance spectroscopy to characterize the properties of different membrane materials are carried on PCB based PDMS fluidic system.

**Chapter 3:** The membrane in microfluidic chips, including stability study and ion transfer study. Even though not all of these designs and approaches are necessarily practical, I still explored new method to miniaturize the stable membrane system on microchips and systems with integration and interconnection abilities.

**Chapter 4:** Carbon dioxide absorption study in gas-liquid interface. New applications of porous PDMS cube are studied. Again on miniaturized microfluidic system, the gas-liquid interface technology can benefit not only for specific artificial photosynthesis, but also other applications with gas inquiries.

**Chapter 5:** Glucose synthesis using microfluidic device with gas-liquid interface mechanism. The giant leap to real type IV artificial photosynthesis: from inorganic source with light to

organic compounds. The chemical reactions are well studied before applied into microfluidic systems with carbon dioxide to liquid interface.

**Chapter 6:** The porous platform for organic compound storage platform using additive manufacturing. Additive manufacturing can achieve more than just printing the photosilver mold for PDMS replica molding. The interconnected chitosan porous structure is well studied for dark reaction solution storage and protein preservation.

**Chapter 7:** The integration and interconnection of multiple units. The interconnection and integration helps the system to be easily controlled and examined. The microelectronics is a well approach since we already established miniaturized microchip made by silicon and silicon dioxide.

**Chapter 8:** A summary of the whole research projects.

This research and dissertation concluded most of the research work and detailed planning, experimental analysis with mathematical principles. The dissertation can be used as future work reference and guidance in the field of cell-free artificial photosynthesis system.



## Chapter 2. LIGHT REACTION UNIT: MEMBRANE IN FLUIDIC PCB

The first task in constructing cell-free artificial photosynthesis system from a photosynthesis model is the reproducing of light reaction membrane systems. Light reaction would be realized in a microfluidic platform that consists of two fluid chambers separated by a planar membrane with embedded proteins that convert light energy into ATP. This chapter includes the preliminary experiments and results that presented in conferences and published in journals [81].

Fluidic devices containing lipid or polymer membranes have a wide range of biotechnology applications such as ion channel recording, high-throughput drug screening and artificial photosynthesis [28, 68, 82, 83]. Both vesicular membranes and free-standing planar membranes have been built into fluidics for prototype studies of membrane channel proteins and membrane transport processes. Vesicular membranes are relatively more stable, more facile to fabricate, and easier to be incorporated into fluidic devices than free-standing planar membranes. For example, triblock copolymer vesicular membranes [84] containing the membrane-bound proteins, namely, BR and ATPase, have been incorporated into a foam architecture as an artificial photosynthesis fluidic system [28, 68]. BR absorbs green light and uses the light energy to pump protons across vesicular membranes. The proton gradient then activates ATP synthase, which converts ADP and mono-phosphate  $P_i$  to ATP [28, 69].

Compared to vesicular membranes, free-standing planar membranes are less stable. Traditional free-standing lipid membranes (black lipid membranes, BLM), which suspend a pin hole of the size  $\sim 0.1$ - $1.0$  mm on Teflon or silicon support, are prone to mechanical distortion and become ruptured easily in one single event leading to the loss of membrane electrical resistance in a few minutes to several hours [85-87]. Membrane stability was improved when free-standing membrane was formed on porous alumina or silicon nitride membrane substrate with an array of nano-size pores [88, 89]. In such nano-black lipid membrane systems, each single membrane covering a pore ruptures in a stochastic manner leading to a continuous decrease in overall

membrane resistance over the period of days [88, 89]. The stability of the suspended lipid bilayers depends on membrane composition and increases with decreasing pore size and with increasing the molecular order of the lipids [82, 89, 90].

Free-standing planar membranes on pore support offer some key advantages for fluidics applications: (i) both sides of the membrane are readily accessible for studies of membrane channel proteins and membrane transport processes, (ii) the electrolyte on either side can be conveniently replaced or adjusted, (iii) there is no complication in experiments or data interpretation due to vesicle aggregation or fusion, and (iv) the membrane can be applied to chip technology, especially for the establishment of bio-sensing and high-throughput screening assays. Therefore, it is of interest to develop a new free-standing planar membrane system on nano- or micro-pores with much improved membrane stability.

In this section, we demonstrate the design, fabrication and characterization of the polar lipid fraction E (PLFE) free-standing lipid membranes situated on micro-pores of a PDMS thin film embedded in a printed circuit board (PCB) based fluidic device. In order to fabricate a large number of uniformly produced micron size pinholes on PDMS thin films, we used micro molding method involving photolithography of SU-8 (an epoxy-based negative photoresist polymer) and the use of the positive photoresist polymer S1813 as a dissolvable sacrificial layer between the SU-8 mold and the PDMS thin film. We also used electrochemical impedance spectroscopy (EIS) to demonstrate that PLFE lipids can form free-standing planar membranes over the micro-pores of PDMS thin films. In addition, we used EIS to compare the dielectric properties of PLFE free-standing planar lipid membranes with those obtained from diester lipid membranes (e.g., 1-palmitoyl-2-oleoyl-sn-glycero-3-phosphocholine (POPC) and POPC/1-palmitoyl-2-oleoyl-sn-glycero-3-phosphoserine (POPS)) or triblock copolymer PMOXA-PDMS-PMOXA membranes. Moreover, throughout this paper, the potential application of the PLFE free-standing planar membrane-based fluidics in artificial photosynthesis is discussed.

## 2.1 Introduction on membrane materials

### 2.1.1 PMOXA-PDMS-PMOXA, PEtOz-PDMS-PEtOz, POPC, POPC/POPS (1:1)

Triblock copolymer PMOXA-PDMS-PMOXA (Figure 2-1; MW = 1300-8500-1300 g/mol) was purchased from Polymer Source (Quebec, Canada; sample # P11019-MOXZDMSMOXZ). It contains a hydrophobic layer (dimethylsiloxane) set between two hydrophilic layers (methyloxazoline). Like many other amphiphilic molecules, triblock copolymer can form micelles, vesicles, or planar membranes in aqueous solution [91, 92]. PMOXA-PDMS-PMOXA was dissolved in chloroform (2 wt%) as the stock solution and diluted to 1 wt% with toluene prior to use [69].

POPC and POPS were purchased from Avanti Polar Lipids (Alabaster, AL). These two diester lipids (Figure 2-1) are commonly seen in mammalian or bacterial cells. PLFE bipolar tetraether lipids (Figure 2-2) were isolated from *S. acidocaldarius* as previously described [93]. POPC and POPS stock solutions were made in chloroform. PLFE stock solution was made using a mixture of chloroform : methanol : water (14:5:1, v/v/v).

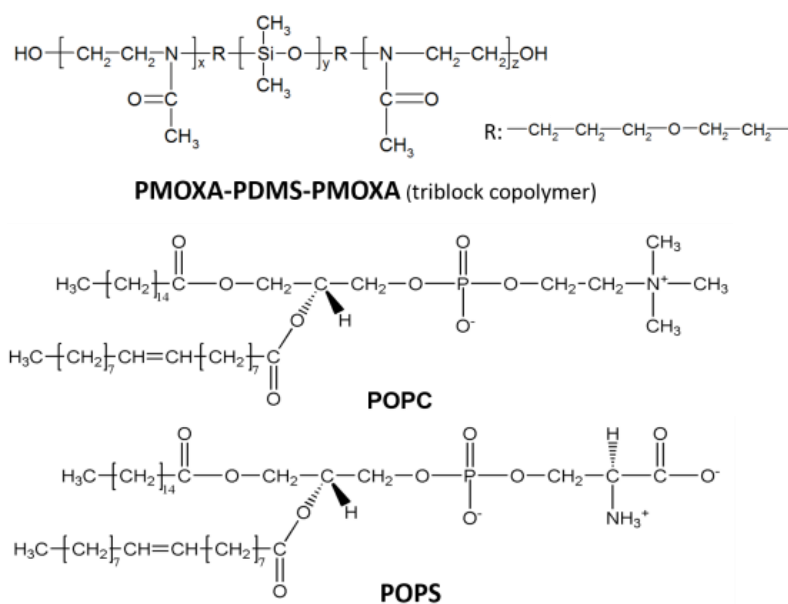


Figure 2-1. Chemical structures of PMOXA-PDMS-PMOXA triblock copolymer, POPC, and POPS.

### 2.1.2 Non-symmetrical lipid: PLFE

In the present study, our membrane design involved the use of archaeal bipolar tetraether lipids. Specifically, we used the polar lipid fraction E (PLFE) isolated from the thermoacidophilic archaeon *Sulfolobus acidocaldarius* (optimum growth: 80°C and pH 2-3) [94] to make free-standing planar membrane on the micro-pores of the PDMS films. PLFE bipolar tetraether lipids are appealing biomaterials and structurally distinctly different from diester lipids found in mammals or bacteria [93, 95]. PLFE is a mixture of calditolglycerocaldarchaeol (also termed glycerol dialkylcalditol tetraether, GDNT) and caldarchaeol (also termed glycerol dialkylglycerol tetraether, GDGT) [96, 97] (Figure 2-2). The GDNT component (~90% of total PLFE) contains phospho-myo-inositol on the glycerol end and  $\beta$ -glucose on the calditol end, whereas the GDGT component (~10% of total PLFE) has phospho-myo-inositol attached to one glycerol and  $\beta$ -D-galactosyl-D-glucose to the other glycerol skeleton. The non-polar regions of these lipids consist of a pair of 40-carbon biphytanyl chains, each of which contains up to four cyclopentane rings. The tetraether linkages, the cyclopentane rings and the lack of C=C bonds in the biphytanyl chains make PLFE lipids chemically much more stable than diester lipids.

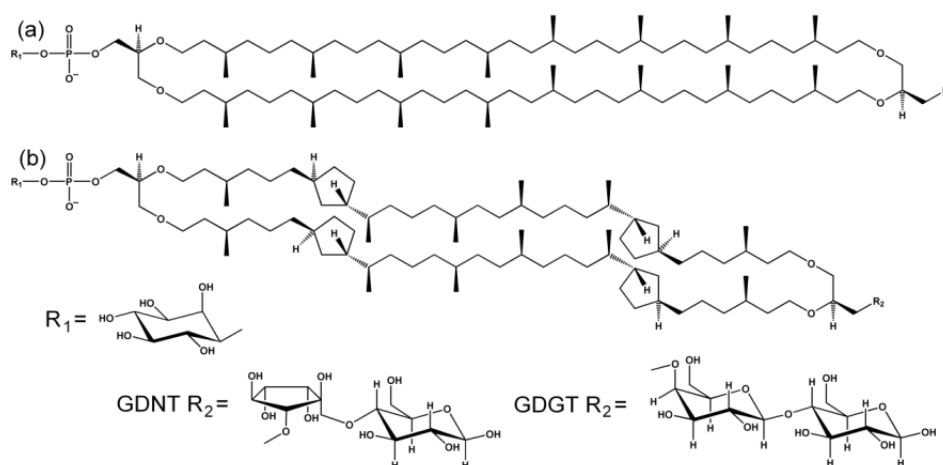


Figure 2-2. Illustrations of the molecular structures of the bipolar tetraether lipids in PLFE isolated from *S. acidocaldarius*. PLFE contains (a) GDGT (or caldarchaeol, ~10%) and (b) GDNT (or calditolglycerocaldarchaeol, ~90%). The number of cyclopentane rings in each biphytanyl chain can vary from 0 to 4. R<sub>1</sub> = myo-inositol, GDGT R<sub>2</sub> =  $\beta$ -D-galactosyl-D-glucose, and GDNT R<sub>2</sub> =  $\beta$ -D-glucose linked to calditol. GDG(N)T-0 and GDG(N)T-4 contain 0 and 4 cyclopentane rings per molecule, respectively. [98] Reprinted with permission from American Chemical Society.

PLFE lipids are able to form vesicles of varying sizes and supported monolayer in the air-water interface [98, 99]. The d-spacing of PLFE lipid membrane is ~4.9 nm at room temperature (~22°C) as revealed by small angle X-ray scattering [100]. PLFE lipid membranes (in either vesicle or supported monolayer form) are extraordinarily stable against chemical, physical and mechanical stressors (e.g., pH, detergents, pro-oxidants, fusogenic compounds, certain phospholipases, pressure, and temperature) (reviewed in [93, 101]). The extraordinary stability of PLFE liposomes can be attributed to the tight and rigid membrane packing due to the presence of tetraether linkages and cyclopentane rings in the bidiphytanyl chains as well as an extensive network of hydrogen bonds created by the sugar and phosphate residues exposed at the outer face of tetraether liposomes (reviewed in [93, 101-103]). This unusually tight and rigid membrane packing in PLFE liposomes is most manifested in the data of volume fluctuations, which are exceedingly low, as compared to those of dipalmitoyl-sn-glycero-3-phosphocholine (DPPC, a diester lipid) bilayers, over a wide range of temperatures [104]. To our knowledge, free-standing PLFE planar lipid membranes have not been reported in the literature. Since it is known that the stability of free-standing planar lipid membranes increases with increasing membrane packing tightness [82] and since PLFE liposomal membranes are more tightly packed than other liposomes, PLFE free-standing planar membranes are expected to be much more stable than those made of diester lipids. Thus, the use of PLFE would alleviate the stability problem of free-standing lipid membranes mentioned earlier.

## **2.2 Electrochemical impedance experiment on planar biomembranes**

### **2.2.1 Selection of PDMS**

PDMS is known to promote the formation of free standing membranes over pinholes due to its ability to conduct spontaneous organic solvent extraction[82]. PDMS can form different shapes by either physics way like molding, or chemical way like dry etching by fluorine-based

reactive ion etching (RIE) or wet etching by a solution of tetrabutylammonium fluoride ( $C_{16}H_{36}FN$ ) in *n*-methyl-2-pyrrolidinone ( $C_5H_9NO$ ) 3:1 v/v NMP:TBAF [105]. PDMS can be easily molded into both macro and micro scales [106]. Additionally, PDMS is optically transparent, which is desirable for certain applications such as artificial photosynthesis. For these reasons, PDMS was chosen as the material to make both fluidic chambers and thin films holding free-standing membranes.

### 2.2.2 Fabrication of PDMS thin film

The PDMS thin film with pinholes for supporting triblock copolymer or lipid membranes was fabricated in cleanroom. The fabrication process is described as follows (Figure 2-3):

(a) Cleaning and dehydration of silicon wafer: A prime-grade 4-inch silicon wafer was cleaned and dehydrated on a hot plate at  $110^{\circ}C$  for 5 min.

(b) SU-8 spin coating: Negative photoresist SU-8 2035 (MicroChem, Newton, MA) was chosen as the molding material. The SU-8 2035 was spin-coated on the silicon wafer at 500 rpm (revolutions per minute) with an acceleration of 100 r/s for 30 s, using a photoresist spinner (CEE, model 100, Rolla, MO). This resulted in an uncured SU-8 layer with a thickness of  $\sim 200\ \mu m$ . The wafer was then soft-baked on a hot plate at  $65^{\circ}C$  for 15 min followed by heating at  $95^{\circ}C$  for 60 min and slow cooling to room temperature.

(c) UV exposure: The wafer with an uncured SU-8 layer was moved to a mask aligner (model 206, OAI, San Jose, CA; UV intensity:  $23.1\ mW/cm^2$ ; wavelength: 365 nm). The SU-8 layer was a negative mask with multiple blank holes to make standing bars for molding the PDMS thin film holes. The total energy required for SU-8 molding was  $500\ mJ/cm^2$ , therefore, the exposure time was set to 21.7 s at  $23.1\ mW/cm^2$  [107]. After the UV exposure, the wafer was placed onto a hot plate baked at  $65^{\circ}C$  for 10 min and then at  $95^{\circ}C$  for 30 min. Post-exposure bake was necessary in order to convert the UV exposed areas to the cured SU-8 (a cross-linked solid structure).

(d) SU-8 developer: When the wafer was cooled down again, it was immersed into a SU-8 developer (MicroChem, Newton, MA) for 10 min to remove the uncured SU-8. This was followed by rinsing first with isopropanol and then deionized water. Finally, the wafer was dried with nitrogen, and a SU-8 mold for the PDMS film was fabricated.

(e) Oxygen plasma treatment of the SU-8 mold: The PDMS thin film with holes would be too thin and fragile to be peeled off from the SU-8 mold. To solve this problem, we used the positive photoresist S1813 (Shipley 1813, MicroChem, Newton, MA) to build a dissolvable sacrificial layer between the SU-8 mold and the PDMS thin film. Before coating the S1813 thin layer, oxygen plasma treatment of the SU-8 surface was performed on a plasma cleaner (model COVANCE, FEMTO Science, Hwaseong-si, Gyeonggi, South Korea) using 110V AC (alternating current) and 50 Hz. Oxygen plasma treatment makes the SU-8 surface more hydrophilic [108] to suit for the coating with S1813.

(f) S1813 sacrificial layer spin coating: After oxygen plasma treatment, positive photoresist S1813 was dispensed onto the center of the cured SU-8 structure. Spinning coating was set at 2500 rpm with an acceleration of 1000 r/s for 60 s. Then, the wafer was hard-baked on a hot plate at 120°C for 5 min. This results in a 4~6  $\mu\text{m}$  S1813 layer on SU-8.

(g) Formation of PDMS thin film: The PDMS pre-polymer (SYLGARD® 184 silicone elastomer, Dow Corning, Midland, MI) and PDMS curing agent (SYLGARD® 184 silicone elastomer curing agent, Dow Corning) were thoroughly mixed at a weight ratio of 10:1 to form the PDMS mixture. The mixture was placed in a vacuum dessicator for 30 min to fully remove the air bubbles. The PDMS mixture was poured slowly onto the center of the S1813/SU-8-coated silicon wafer. Spinning coating was performed at 1500 rpm with an acceleration rate 500 r/s for 60 s, which resulted in a PDMS thin film (thickness ~80-120  $\mu\text{m}$ ) with an array of small holes. The wafer with PDMS was then placed in a 60°C oven for 24 h to allow the PDMS thin film to be cured and solidified.

(h) PDMS film release: The positive photoresist S1813 layer between the silicon wafer and PDMS film was dissolved by acetone. The released PDMS film with multiple pinholes was further cleaned using isopropanol. This method provides an effective way to peel off thin PDMS films from the mold without breaking any micro structure. The resulting PDMS film was cut into multiple single units, each of which contains only one single aperture (diameter: 0.1 or 0.2 mm). For the sake of clarity, Figure 2-3 shows only the fabrication of one single unit.

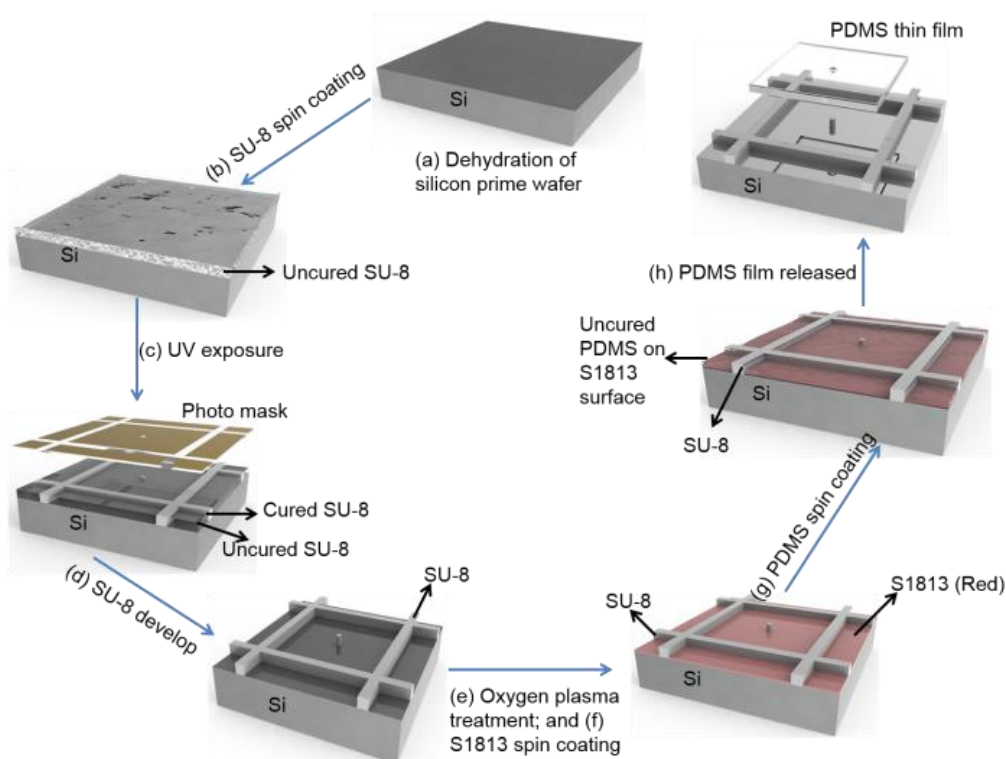


Figure 2-3. PDMS thin film fabrication procedures.

### 2.2.3 Fabrication of PDMS fluidic devices

The fluidic device was also made of PDMS. We designed the 3D structures as the mold of a PDMS fluidic device (Figure 2-4) and then exported them using a stereolithography machine (EnvisionTEC, model Perfactory, Gladbeck, Germany; voxel resolution: 35  $\mu\text{m}$ ). Photo-sensitive polymer photosilver (EnvisionTEC) was used to make the mold of the entire fluidic device (Figure 2-4). The PDMS mixture (described in Section 2.4g) was poured onto the Photosilver



mold and degassed under vacuum for 1 h. The PDMS/photosilver mold was incubated at 60°C for 24 h to allow the PDMS to be cured and solidified. The resulting PDMS chamber can be easily peeled off from the photosilver mold.

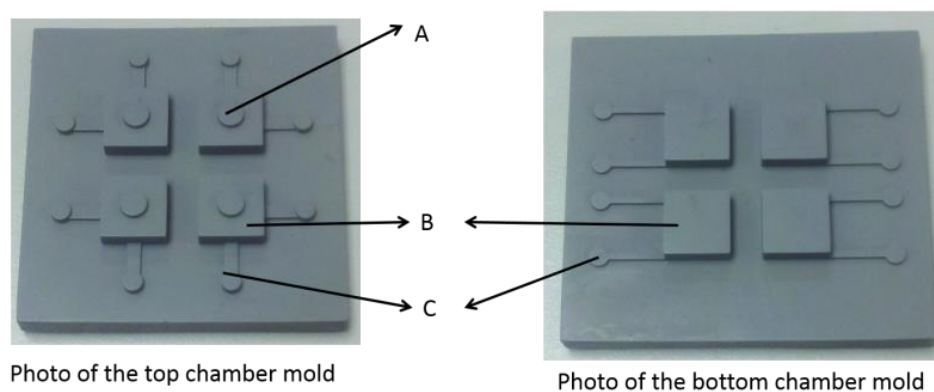


Figure 2-4. 3D lithography of the PDMS chamber mold made by a photopolymer Photosilver.

Each mold contains four identical chamber units (B). The center of each chamber unit contains a reserved window for further applications (for example, allowing green light to go through in order to elicit the light reaction in artificial photosynthesis) (A). There are micro-channels with inlets and outlets (C) associated with each chamber unit.

#### 2.2.4 PCB board and electrodes.

The PCB board was designed using the PCB layout software (PCB Artist) and fabricated by Advanced Circuits (Tempe, AZ). The PCB board contained two electrodes for impedance measurements of the planar membrane. The electrode surface was copper coated with nickel. In the absence of inert metals such as gold and nickel, a copper electrode would be dissolved in the buffer solution during long-term use if a DC (direct current) voltage was continuously applied.

The layout of wires on PCB is determined by voltage, power line and operational temperature, etc. According to Ohm's law and the concept of resistor, we have

$$U = IR = \frac{l\rho}{\delta w}(1 + \alpha\Delta t)$$

where  $U$  is the voltage drop (unit: V),  $I$  is the current on wire (unit: A),  $l$  is the length of wire (unit: m),  $w$  is the width of wire (unit: mm),  $\delta$  is the thickness of copper wire on board (unit: mm),  $\rho$  is the resistivity (unit:  $\Omega \cdot \text{mm}^2/\text{m}$ , and the resistivity of copper is  $0.0175 \Omega \cdot \text{mm}^2/\text{m}$  at  $20^\circ\text{C}$ ; the resistivity of copper is  $0.0189 \Omega \cdot \text{mm}^2/\text{m}$  at  $40^\circ\text{C}$ ),  $\alpha$  is the temperature coefficient of resistor (0.004 for copper), and  $\Delta t$  is the temperature rise of wire (unit:  $^\circ\text{C}$ ). If using  $U/l$  as the voltage drop  $[U]$  on unit length of wire (unit: V/m), we can calculate the wire width as:

$$w = \frac{I\rho}{\delta[U]}(1 + 0.004\Delta t)$$

Eq. 2-2

Assembling of PDMS fluidic chambers, PCB board, and PDMS thin films with planar lipid or copolymer membranes was performed by standard bonding techniques.

Oxygen plasma treatment method was used to bond the PCB board to the PDMS thin films and the PDMS fluidic chambers [109]. Oxygen plasma can turn some of the methyl groups on PDMS surface into hydroxyl groups, which are more hydrophilic and capable of bonding with other plasma-treated PDMS or PCB surface [110].

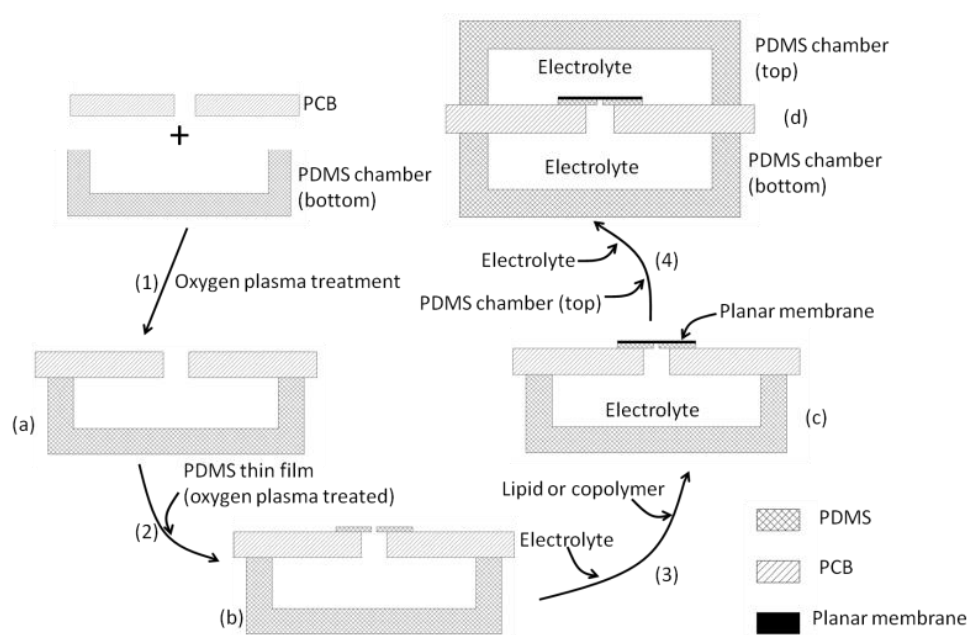


Figure 2-5. Procedures for assembling the fluidics device.

Figure 2-5 describes how the fluidics device is assembled. (1) The bottom part of the PDMS chamber and the PCB board were cleaned, put in the plasma generator, and treated with oxygen plasma for 70 s. Then, the PCB board and the PDMS bottom chamber were compressed together for one minute to have these two components strongly bonded. (2) Oxygen plasma treatment was also applied to the PDMS thin film (5 mm × 5 mm × 100 μm), which was bonded to the PCB board. (3) Electrolyte was introduced to the PDMS chamber, followed by the deposit of lipids or copolymer to generate planar membranes over the micro-hole on the PDMS thin film (see Section 2.2.2). (4) The PDMS top chamber (pre-treated with oxygen plasma) was bonded to the PCB board and filled with electrolyte. Figure 2-6 shows the image of the assembled PCB-based fluidic device. Each PCB board contains four identical PDMS chambers.

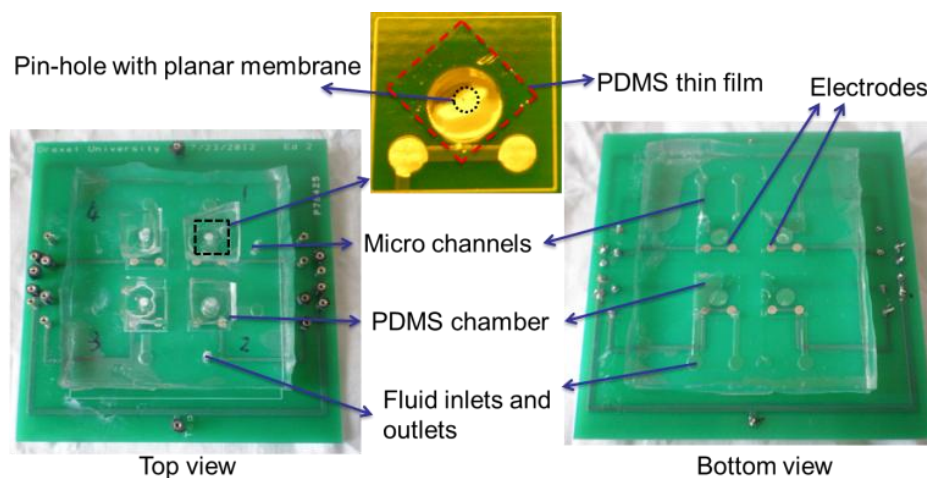


Figure 2-6. Image of the assembled PCB-based fluidic device.

These procedures provided a fast, clean, and convenient bonding method for linking the PCB board to the PDMS thin film or to the PDMS fluidic device. Even though oxygen plasma treatment did not create a permanent bonding, it could last for over two weeks, long enough for the electrochemical measurements which usually take several hours. Both PCB and PDMS surface can be hydroxylized by oxygen plasma treatment (as illustrated in [110]), which makes the surface more hydrophilic. Other than this chemical modification on the surface, we are not

aware that oxygen plasma treatment would introduce any significant chemical impurity to the PCB board or PDMS fluidic device (i.e., PDMS chamber). In this regard, oxygen plasma treatment was better than some other bonding methods such as the use of glues [111].

To enhance the PDMS to PCB bonding, further chemical treatment of PCB surface is necessary, while the pure oxygen plasma treatment can only create hydroxyl group on PDMS side [112-114]. Since the PCB surface is coated with polyamide, we can use saline to activate the polyamide surface to carboxyl groups or hydroxyl groups. First, the PDMS and PCB surface is cleaned and treated by oxygen plasma. Then, the PCB is rinsed in 5% (w/w) (3-aminopropyl)triethoxysilane (APTES) (Sigma Aldrich, US) solution at 80°C. Finally, the PDMS and chemical treated PCB are compressed together in oven at 60°C for 30 min. The PCB and PDMS will have better bonding by saline chemical treatment.

### **2.2.5 Formation of planar membranes**

Assembly b shown in Figure 2-5 was placed on the bottom of a 6-inch Petri-dish and submerged in 10 mM tris(hydroxymethyl)aminomethane (Tris) buffer (pH 7.4) containing 1 M KCl and 1 mM CaCl<sub>2</sub> [71]. Then, a droplet of the triblock copolymer or lipid stock solution was added to the buffer layer. Copolymer or lipid molecules presumably spread over the aqueous surface layer, and when the PDMS thin film was lifted up, polymers or lipids that were near the aperture spontaneously aggregate to form a free-standing planar membrane over the aperture. It is known that diester lipids can form free-standing planar membranes on pinholes in PDMS thin film, silicon dioxide or other semiconductor materials [115, 116]. In this study, we demonstrated that PLFE archaeal tetraether lipids can also form free-standing “planar” membranes on pinholes in PDMS thin films.

### **2.2.6 Impedance measurements**

In each PDMS chamber (Assembly d in Figure 2-5) of the fabricated fluidic PCB board, the PDMS thin film separates the chamber into two compartments, each of which contains an

electrode connected to an external circuit as conceptually illustrated in Figure 2-6. The measurements of potentiostatic electrochemical impedance spectroscopy (PEIS)<sup>2</sup> were performed on an Bio-Logic SAS instrument (model VSP, Claix, France) at room temperature ( $\sim 22^{\circ}\text{C}$ ) in the same Tris buffer as described [71, 117, 118]. The frequency of the AC input signal from the instrument varied from 1 MHz to 10 mHz, and the input signal had a voltage peak of 100 mV (from zero voltage to the peak of the sine wave). In each frequency decade, six sets of voltage and current data were collected. The data acquisition software was able to automatically calculate a fit curve and generate an equivalent circuit with detailed value of each component, such as resistance R, capacitance C and inductance L. The circuit parameters could provide the information about the real and imaginary value of the sample's impedance properties. The data were analyzed and plotted using Matlab.

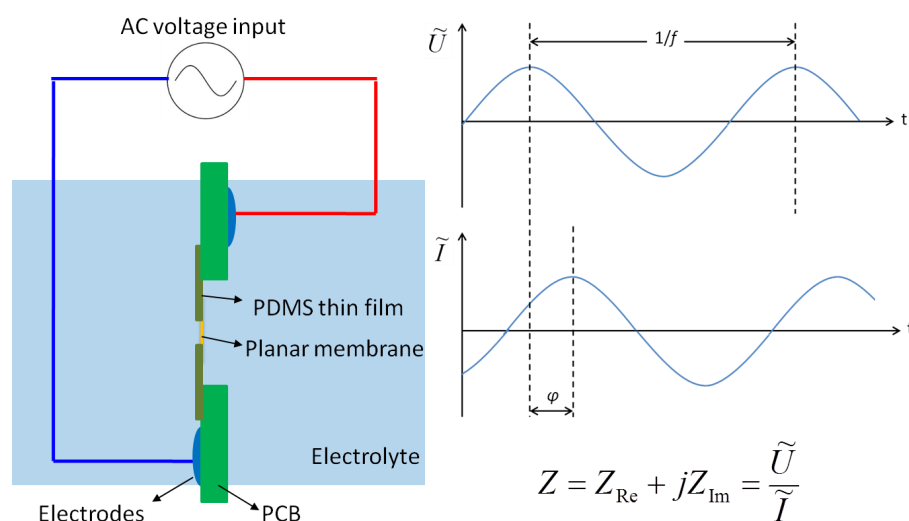


Figure 2-7. Conceptual illustration of the EIS setup for a planar membrane on a PDMS thin film sitting on the PCB board within a PDMS chamber. Impedance ( $Z$ ) is the ratio of voltage ( $U$ ) and current ( $I$ ) at a given frequency ( $f$ ).

<sup>2</sup> PEIS experiment performs the impedance measurements into potentiostatic mode in applying a sinus around a DC potential  $E$  that can be set to a fixed value or relatively to the cell equilibrium potential. For very capacitive or low impedance electrochemical systems, the potential amplitude can lead to a current overflow that can stop the experiment in order to protect the unit from overheating.

## 2.3 EIS result analysis

### 2.3.1 Results

The results obtained from the electrochemical impedance measurements are presented in Figure 2-8. For each membrane studied, the data are displayed using both the complex Nyquist plot (real versus imaginary parts of the impedance, Re vs. Im; Figure 2-8A) and the polar Bode plot (frequency ( $f$ ) versus impedance magnitude ( $|z|$ ) or phase angle ( $\angle\phi$ ); Figure 2-8B and Figure 2-8C, respectively). The Nyquist plots of PLFE and POPC/POPS show compressed semicircles, which could be attributed to the sample's chemical heterogeneity [119]. The magnitude of the impedance ( $|z|$ ) for all membranes examined shows a sigmoidal change with frequency (Figure 2-8B). Similar sigmoidal profiles were previously reported for DPPC monolayer coupled to octadecanethiol monolayer chemisorbed onto gold-coated solid surface [120]. However, the frequency dependence of  $|z|$  for PLFE is significantly different from those obtained from diester lipids and triblock copolymers (Figure 2-8B). The Z magnitude ( $|z|$ ) of PLFE lipid membranes (Figure 2-8B-b) levels off at a frequency  $\sim 102$  Hz whereas  $|z|$  of other lipids levels off at a much higher frequency at  $\sim 10^3$ - $10^4$  Hz (Figure 2-8B-a,c,d). The profile of phase angle versus frequency for PLFE lipid membranes (Figure 2-8C-b) is also distinctly different from those seen from triblock copolymer, POPC, and POPC/POPS mixtures (Figure 2-8C-a,c,d). For triblock copolymer, POPC, and POPC/POPS mixtures, the plot of phase angle versus frequency displays an inverted bell shape, showing a minimal phase angle at  $\sim 50$ - $100$  Hz. In contrast, for PLFE lipid membranes, the phase angle exhibits a biphasic change with frequency at  $10$  Hz and a sharp drop at  $\sim 1$  MHz.

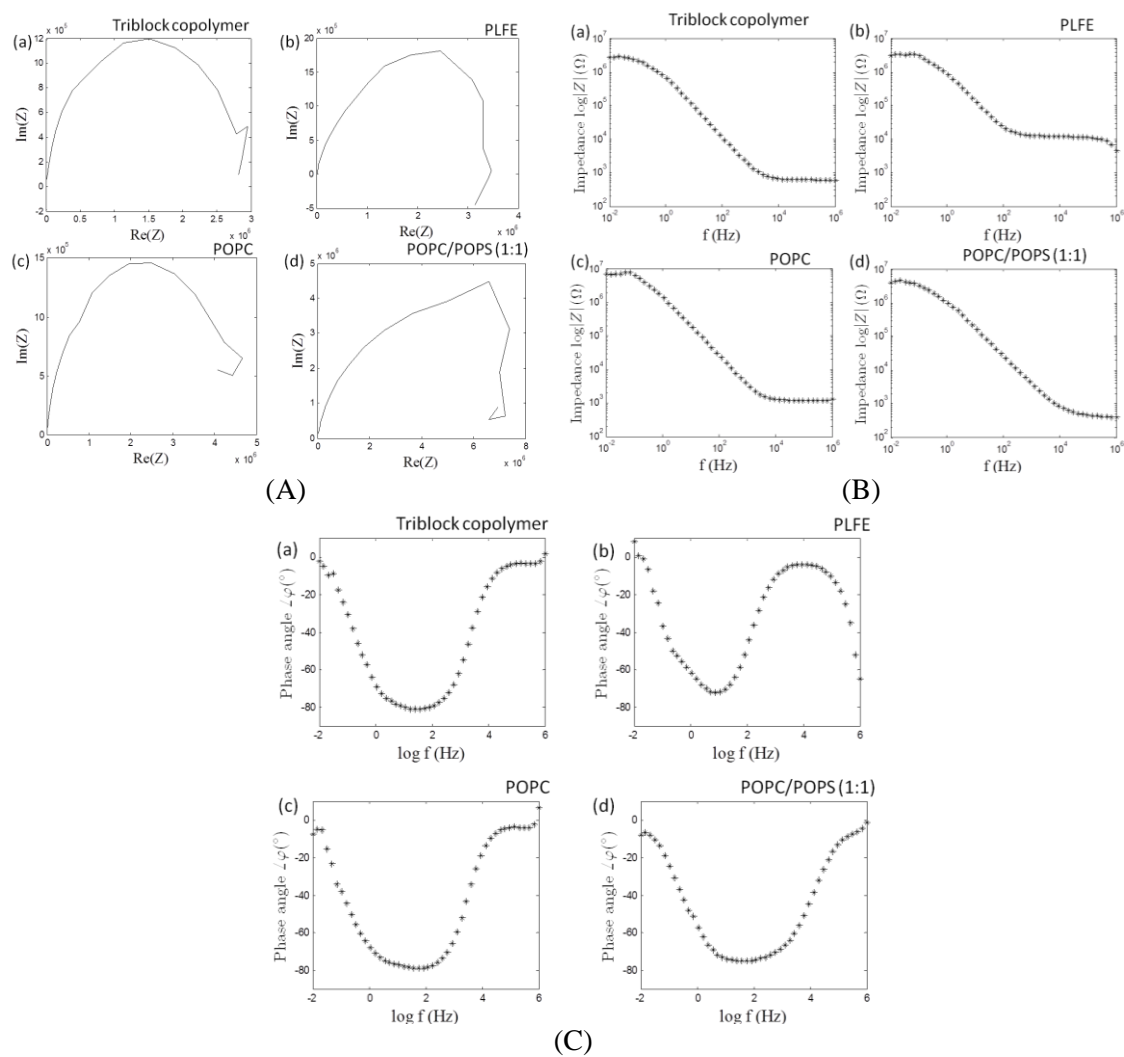


Figure 2-8. (A) Re-vs-Im Nyquist plot of various planar membranes. (B) Frequency ( $f$ ) vs. impedance magnitude ( $|z|$ ) in various planar membranes. (C) Frequency ( $f$ ) vs. phase angle ( $\angle\phi$ ) in various planar membranes.

The impedance equivalent circuits of various membranes (Figure 2-9) were obtained from the best fit of the experimental EIS data (Figure 2-8). The impedance of both triblock copolymer membranes and diester lipid membranes ( $Z_{cp-dl}$ ) can be best described by the equivalent circuit:  $R_1 + C_2 // R_2$  (Figure 2-9a), in good agreement with previous studies [121, 122]. Specifically,

$$Z_{cp-dl} = R_1 + \frac{1}{j\omega C_2 + \frac{1}{R_2}}$$

which can be converted to

$$Z_{cp-dl} = R_1 + \frac{R_2}{1 + (\omega C_2 R_2)^2} - j \frac{\omega C_2 R_2}{1 + (\omega C_2 R_2)^2}$$

Eq. 2-4

where  $\omega = 2\pi f$ .

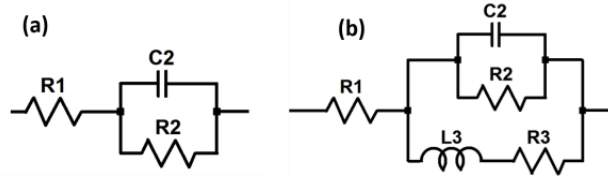


Figure 2-9. (a) Equivalent circuit of triblock copolymer, POPC or POPC/POPS planar membranes:  $R_1 + C_2 // R_2$ ; (b) equivalent circuit of PLFE planar membranes:  $R_1 + C_2 // R_2 // (L_3 + R_3)$ .  $R_1$  is the resistance of the electrolyte.

The impedance of PLFE lipid membranes ( $Z_{PLFE}$ ), on the other hand, can be best described by the equivalent circuit:  $R_1 + C_2 // R_2 // (L_3 + R_3)$  (Figure 2-9b), which can be expressed as

$$Z_{PLFE} = R_1 + \frac{1}{j\omega C_2 + \frac{1}{R_2} + \frac{1}{j\omega L_3 + R_3}}$$

Eq. 2-5

Equation Eq. 2-5 can be rewritten in the form of

$$Z_{PLFE} = R_1 + \frac{R_2^2 R_3 + R_2 R_3^2 + \omega^2 R_2 L_3^2}{(R_2 + R_3 - \omega^2 C_2 R_2 L_3)^2 + \omega^2 (C_2 R_2 R_3 + L_3)^2} + j\omega \frac{R_2^2 L_3 - C_2 R_2^2 (\omega^2 L_3^2 + R_3^2)}{(R_2 + R_3 - \omega^2 C_2 R_2 L_3)^2 + \omega^2 (C_2 R_2 R_3 + L_3)^2}$$

Eq. 2-6

To understand the physical meaning of the equivalent circuit, it is useful to dissect a membrane system into a series of slabs with different dielectric properties (e.g., the bilayer region and the aqueous phase with the electrolyte) [123]. In the equivalent circuit of the triblock copolymer and diester lipid membranes (Figure 2-9a),  $R_1$  can be assigned to the electrolyte, and



C2 and R2 are related to the membrane. Using this equivalent circuit and the EIS data (e.g., Figure 2-8), we determined that the triblock copolymer membrane has a membrane capacitance (C2) of  $0.29 \pm 0.01 \times 10^{-6} \text{ F/cm}^2$  (n=14) and a membrane resistance (R2) of  $7.99 \pm 0.02 \ \Omega \cdot \text{cm}^2$  (n=14), and the POPC membrane has a membrane capacitance (C2) of  $1.89 \pm 0.22 \times 10^{-6} \text{ F/cm}^2$  (n=9) and a membrane resistance (R2) of  $1104 \pm 91 \ \Omega \cdot \text{cm}^2$  (n=9). For the triblock copolymer and diester lipid membranes, the resistance  $R = R1 + R2$  (Figure 2-9a). The capacitance and resistance values of POPC and triblock copolymers obtained from our new fluidic device (Table 2-1) are comparable to those previously reported for free-standing planar membranes on PDMS or Teflon thin films [124-128]. This consistency validates our new PDMS- and PCB-based fluidic membrane design.

Similarly, R1 in the equivalent circuit of the PLFE lipid membrane can be assigned to the electrolyte layer, and the other electrochemical parameters are related to the membrane itself. We found that the PLFE lipid membrane has a membrane resistance (R) of  $4.90 \pm 0.12 \times 10^3 \ \Omega \cdot \text{cm}^2$  (n=12), which is much higher than that seen in triblock copolymer, POPC and POPC/POPS planar membranes (Table 2-1). This large resistance for PLFE suggests that, among the membranes examined in this study, PLFE free-standing planar membrane would be a better lipid matrix for studying channel proteins and trans-membrane events. We also determined the PLFE membrane capacitance (C2) to be  $0.16 \pm 0.02 \times 10^{-6} \text{ F/cm}^2$  (n=12) and the membrane inductance (L3) to be  $1.23 \pm 0.29 \times 10^{-2} \text{ H/cm}$  (n=12) (Table 2-1). Here n is the number of experimental trials. Note that, for PLFE lipid membranes,  $R=R1+R2//R3$  whereas  $R2//R3=(R2 \cdot R3)/(R2+R3)$  (Figure 2-9b). Also note that the measured result of the equivalent circuit has taken into account the impedance of the PDMS thin film and the impedance offset caused by the PCB board which can be considered as a dielectric material. The impedance data of the empty PDMS chamber (without the free-standing planar membranes but with the electrolyte) are presented. The capacitance of the free-standing membrane was determined by comparing the membrane sample with an empty chamber with only the electrolyte (91.6 nF).

Table 2-1. Comparison of electric properties of different planar membranes.

Membrane system	Membrane capacitance from this study ( $\mu\text{F}/\text{cm}^2$ )	Membrane resistance from this study ( $\Omega\cdot\text{cm}^2$ )	Membrane inductance from this study ( $10^{-2}\text{H}/\text{cm}$ )	Membrane capacitance reported by others ( $\mu\text{F}/\text{cm}^2$ )	Membrane resistance reported by others ( $\Omega\cdot\text{cm}^2$ )	Membrane inductance reported by others ( $\text{H}/\text{cm}$ )
Triblock copolymer	0.29±0.01 (n=14)	7.99±0.02 (n=14)	None	0.27 [71]	10.8 [71]	NA
PLFE	0.16±0.02 (n=12)	4901±120 (n=12)	1.23±0.29 (n=12)	NA	NA	NA
POPC	1.89±0.22 (n=9)	1104±91 (n=9)	None	1.2 44, [128] 1.96 [120]	855±490 [128]	NA
POPC/PO PS (molar ratio: 1:1)	1.21±0.17 (n=10)	868±121 (n=10)	None	NA	NA	NA

Note: The errors are the standard deviations from the mean values. NA: not available

### 2.3.2 Discussion

It has long been proposed that archaeal bipolar tetraether lipids are potentially useful biomaterials for technology applications [129-132]. This point was first made based on the fact that tetraether lipids are chemically stable compared to diesters and that tetraether lipids are the major lipid components (e.g., > 90%) in the plasma membrane of thermo acidophilic archaea (such as *S. acidocaldarius*), which thrive at high temperatures (~65~90°C) and acidic conditions (pH 2~3) [133, 134]. This point was further substantiated by studies of tetraether liposomes. Compared to diester liposomes, tetraether liposomes (in particular, PLFE liposomes) exhibit low solute permeability, high stability against autoclaving, detergents, and fusogenic compounds, tight and rigid membrane packing, low enthalpy and volume changes associated with the phase transitions, low compressibility and low relative volume fluctuations (reviewed in [93, 101, 102]). Because tetraether liposomes have such remarkable stability and because they are not toxic to animals [135, 136], many studies have been devoted to use archaeal tetraether liposomes as carriers of therapeutic agents (e.g., [103, 130]).

Here we extended the study of PLFE tetraether lipids from liposomes to free-standing planar membranes. We showed that the intact PLFE lipids (a partially purified tetraether lipid fraction from *S. acidocaldarius*) can form free-standing planar membranes on micro-pores of PDMS thin films. This finding will expand the application scope of PLFE lipids. Planar lipid membranes interposed between two aqueous solutions have been widely used as an experimental model of biomembranes and a platform for technological applications such as water filtration, drug screening and bio-sensing [87, 137, 138]. The major problem of traditional free-standing planar membranes has been their low stability. They are delicate and last for only several hours [87]. Because the stability of free-standing lipid membranes is known to increase with increasing membrane packing tightness [82] and because PLFE lipid membranes are extremely tightly packed (discussed earlier), PLFE free-standing planar membranes are expected to be much more stable than those made of diester lipids. In fact, Melikyan et al. previously showed that black lipid membranes made of hydrolyzed GDNT isolated from *S. acidocaldarius* displayed higher membrane tension (4.3 mN/m) than those made of diester lipids (1.0~2.4 mN/m) [139]. Several previous studies showed that while bipolar tetraether liposomes are tightly packed, membrane bound proteins can still insert into the membranes and retain their enzyme activities or transport functions (reviewed in [95, 140]). It is thus conceivable that membrane proteins can also be reconstituted into a stable PLFE free-standing planar membrane for various applications such as high throughput drug screening, bio-sensing, and artificial photosynthesis.

In terms of studying trans-membrane events and developing new applications, PLFE free-standing planar membranes are more attractive than archaeal lipid-based planar membranes previously reported. Early work on free-standing archaeal lipid membranes used the hydrolytic fraction of GDNT (Figure 2-2) [139, 141-144], which had the sugar and phosphate groups removed. The removal of those moieties eliminates the ability of tetraether lipids to form a hydrogen-bond network in the polar head group regions of the membrane, consequently lowering membrane stability. The electrochemical data of solid-supported (not free-standing) as well as

free-standing planar membranes made of the main tetraether phospholipid (MPL) fraction from the archaeon *Thermoplasma acidophilum* have previously been reported [145, 146]. However, solid-supported planar membranes do not lend free access to both sides of the membrane as free-standing planar membrane does, and MPL from *T. acidophilum* has fewer sugar moieties (thus lower hydrogen bonding capabilities) than PLFE from *S. acidocaldarius* [146].

Of particular interest is also the current finding that PLFE free-standing planar membranes exhibit unusual dielectric properties, compared to the planar membranes composed of diester lipids or triblock copolymers. We showed that the equivalent circuit of PLFE lipid membrane is different from that of diester lipid or triblock copolymer membrane (Figure 2-9). PLFE lipid membrane displays inductance in addition to capacitance and resistance, whereas the other three membranes examined do not display any inductance component (Figure 2-9 and Table 2-1). Additionally, there is a sharp decrease in phase angle with frequency at ~1 MHz for PLFE (Figure 2-8C-b), but this sharp decrease is not observed from the other three membranes examined (Figure 2-8C-a,c,d). The molecular basis of the above mentioned differences in dielectric properties is not known. At present, we can only speculate that these differential effects arise from the differences in membrane structure and membrane physical property (e.g., membrane dipole). An in-depth biophysical study is required in order to provide a mechanistic understanding of why PLFE lipid membranes show different dielectric properties from diester lipid and triblock copolymer membranes.

The ability to form stable free-standing planar membranes makes PLFE lipids particularly attractive for applications in microfluidics platforms (e.g., artificial photosynthesis). However, in the case of artificial photosynthesis, a fluidic device with one planar membrane and two compartments has limited ability for massive production of energy from light via the membrane bound proteins BR and ATP synthase. To increase the efficiency of energy production from planar membrane-based artificial photosynthesis systems, one can decrease the area of the planar membranes over the pinholes or increase the number of individual planar membranes. Therefore,

an integration of a large number of the basic photosynthesis reaction unit is necessary. However, if one of the membranes breaks, the reaction solution in the two separate chambers will be mixed. As a result, the products will be contaminated by the reactants. Therefore, the real time monitoring of the membrane integrity is essential for prolonging the operational life-time of an artificial photosynthesis board. If one of the membranes is broken, the sensors will identify and block the broken unit to prevent any further cross contamination. To construct such devices, the complementary metal–oxide–semiconductor (CMOS) sensors could be employed because of their low noise and fast operational speed. The working frequency of CMOS sensors is around 1 MHz. Interestingly, PLFE's impedance also has an obvious phase shift at 1 MHz (Figure 2-8C-b), which makes PLFE particularly suitable for fabricating integrated micro-fluidic devices such as artificial photosynthesis chips [29]. In essence, the impedance property detected on PLFE lipid membranes can be used as a sensor to inspect in real time the working status of the free-standing planar membrane on the PDMS films of the micro-fluidic device. Without the planar membrane on the pinhole, the frequency response and impedance value of the PDMS thin film became unstable, especially when an AC input voltage signal with 1 MHz frequency was applied.

The work described here can be extended to nano-pores on PDMS thin films in micro-fluidics and eventually add new impetus to the use of microelectromechanical systems and lab-on-chip technology for bio-sensing, bioanalytical chemistry and bioengineering [147, 148].

## **2.4 Mathematical modeling on planar membrane's physical stability**

### **2.4.1 Planar membrane stability factors**

The next task was to study the stability of PLFE, PMOXA-PDMS-PMOXA triblock copolymer, and POPC planar membranes. As stated in PCB-based fluidic devices in this chapter, EIS was able to demonstrate the planar membrane's response and working status. Therefore, we chose to use EIS to study the stability of planar membrane. To achieve a more uniformed and high effective measurement environment, we needed to further miniaturize the device [149-151].

To fabricate a device for long term use, one issue was the stability of planar membranes; another issue was the device's lifetime. Therefore, we used micro device with a sandwich structure made with permanent materials. For example, copper cannot be used as electrode material because Cu, or Al, or Ni would dissolve in electrolyte with small current flow, in long term usage, respectfully. More specifically, only non-electrolysis materials, such as gold (Au) or platinum (Pt), can serve as capacitive sensors.

There are three major factors that may affect the stability of planar membranes:

**(1) Materials.** PLFE, PMOXA-PDMS-PMOXA triblock copolymer, and POPC have different stability based on their own molecular structures. PLFE and POPC are natural materials and form membrane structures spontaneously; however, PMOXA-PDMS-PMOXA is a synthetic copolymer. The common characteristic of these materials is that all three can have selected membrane proteins embedded, such as BR, ATPase, and outer membrane protein F (OmpF) [71, 84, 117].

**(2) Membrane dimensions (aspect ratio).** Our first choice of membrane support was PDMS with a small hole on it. The size of the hole will significantly affect the stability of the planar membrane, which is defined by the aspect ratio (height to diameter ratio) of the hole. It was determined by the fabrication processes of PDMS membrane support.

**(3) Temperatures.** Membrane materials have different mechanical strengths and chemical activities at different temperature. Therefore, we need to study the long term membrane stability at different temperatures, not only the higher temperatures above room temperature, but also the temperatures below room temperature.

## 2.4.2 Membrane vibration

If considering the free membrane vibration model in space, the free membrane model can be analyzed by the vibration function.

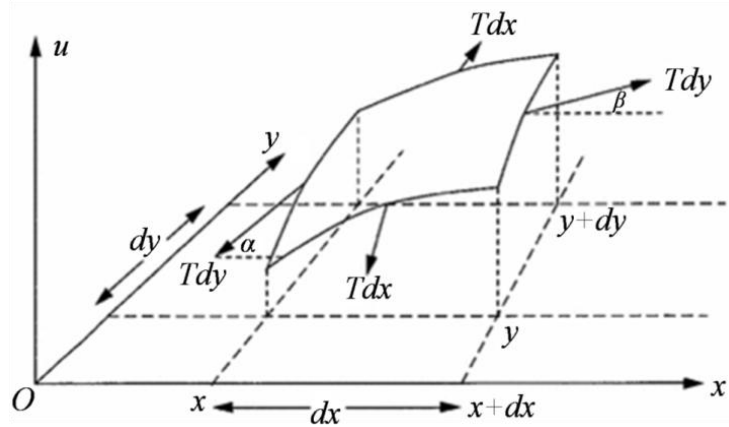


Figure 2-10. Forces on a rectangular membrane element. (Modified from [152] Page 66, Reproduced with permission from Springer-Verlag New York)

We assume that the membrane thickness to be geometric and the membrane to only vibrate in a small range, so the gravity  $mg$  can be ignored. The mathematical model is shown in Figure 2-10.

The angle  $\alpha \approx 0$ , so at the horizontal direction,

$$T \cdot \sin \alpha \approx T \cdot \tan \alpha \approx T \cdot \frac{\partial u}{\partial \vec{n}}$$

Eq. 2-7

where  $\vec{n}$  is the normal direction of the small slice of membrane. The force on the edge of  $x$ , and  $x+dx$  is:

$$-T \frac{\partial u}{\partial x} \Big|_x$$

and

$$-T \frac{\partial u}{\partial x} \Big|_{x+dx}$$

so the total force in the horizontal  $x$  direction is

$$(Tu_{x|x+dx} - Tu_{x|x})dy = Tu_{xx} dx dy$$

Eq. 2-8

and the total force in the horizontal  $y$  direction is

$$Tu_{yy} dx dy$$

The motion function of the membrane in the horizontal direction is

$$\rho \cdot dxdy \cdot u_{tt} = Tu_{xx} dxdy + Tu_{yy} dxdy$$

Eq. 2-9

where  $\rho$  is the mass in unit area. So,

$$\rho u_{tt} - T(u_{xx} + u_{yy}) = 0$$

Eq. 2-10

Then, we use the operator

$$\Delta = \nabla^2 = \frac{\partial^2}{\partial x^2} + \frac{\partial^2}{\partial y^2} + \frac{\partial^2}{\partial z^2}$$

$$\rho u_{tt} - T\Delta u = 0$$

Eq. 2-11

We assume the membrane is uniform, so  $\rho$  is constant. Then,

$$u_{tt} = a^2 \Delta u$$

Eq. 2-12

and we get

$$a^2 = \frac{T}{\rho}$$

Eq. 2-13

which is the vibration transfer speed on the membrane.

When the membrane is embedded in the microchip, external forces are balanced by the microfluidics on both sides of the membrane. If external force exists, and we let the force be  $F(x, y, t)$ , the motion equation becomes the following:

$$u_{tt} - a^2 \Delta u = f(x, y, t)$$

Eq. 2-14

where  $f$  is the external force density on the unit mass in the horizontal direction, and



$$f = \frac{F}{\rho}$$

The condition of free-standing round membrane is studied by Euler in 1764 and F.W. Bessel in 1824. The motion function solution of free-standing round membrane is the problem as:

$$\begin{cases} \frac{\partial^2 u}{\partial t^2} = a^2 \left( \frac{\partial^2 u}{\partial x^2} + \frac{\partial^2 u}{\partial y^2} \right) & (0 \leq x^2 + y^2 < r^2, t > 0) \\ u|_{x^2+y^2=r^2} = 0 & (t \geq 0) \\ u(x, y, t)|_{t=0} = \varphi(x, y) \\ \frac{\partial u(x, y, t)}{\partial t} \Big|_{t=0} = \Psi(x, y) \end{cases}$$

Eq. 2-15

where  $r$  is the radius of round membrane;  $\varphi(x, y)$  and  $\Psi(x, y)$  are known functions. The cylindrical coordinates can be down-graded to two-dimensional problem in polar coordinates.

Let

$$u(x, y, t) = u(\rho, \varphi, t) = T(t)U(\rho, \varphi)$$

Eq. 2-16

and let  $\lambda = k^2$ , to separate parameters

$$T'' + k^2 a^2 T = 0$$

Eq. 2-17

$$\begin{cases} U''_{\rho} + \frac{1}{\rho} U'_{\rho} + \frac{1}{\rho^2} U''_{\varphi} + k^2 U = 0 \\ U|_{\rho=r} = 0 \end{cases}$$

Eq. 2-18

Then, we let

$$U(\rho, \varphi) = R(\rho)\Phi(\varphi)$$

Eq. 2-19

so

$$\Phi'' + v^2 \Phi = 0$$

Eq. 2-20

$$\rho^2 R'' + \rho R' + (k^2 \rho^2 - \nu^2) R = 0$$

Eq. 2-21

and we set

$$k\rho = x$$

$$R(\rho) = y(x)$$

so

$$x^2 \frac{d^2 y}{dx^2} + x \frac{dy}{dx} + (x^2 - \nu^2) y = 0$$

Eq. 2-22

and Eq. 2-22 is  $\nu$ -order Bessel differential equation. The boundary equation is

$$y k \rho |_{\rho=r} = y(kr) = 0$$

Eq. 2-23

The solution to Bessel function is discussed in three conditions as follows:

(1) When  $\nu \neq$  integer number, the solution is

$$y(x) = A J_\nu(x) + B J_{-\nu}(x)$$

Eq. 2-24

where  $J_\nu(x)$  is the  $\nu$  order first type Bessel function.

When  $\nu = n$ , and  $n$  is an integer number,

$$J_{-n}(x) = (-1)^n J_n(x)$$

Eq. 2-25

(2) The second type Bessel function  $N_\nu(x)$ , where  $\nu$  can take any value.

$$y(x) = A J_\nu(x) + B N_\nu(x)$$

Eq. 2-26

and  $N_\nu(x)$  is also named as Neumann function.

(3) The third type Bessel function  $H_\nu(x)$ , also named Hankel function.

For  $\forall \nu$ , the third type is formed by first and second type linearly and independently.

$$\begin{cases} H_\nu^{(1)}(x) = J_\nu(x) + iN_\nu(x) \\ H_\nu^{(2)}(x) = J_\nu(x) - iN_\nu(x) \end{cases}$$

Eq. 2-27

where  $H_\nu^{(1)}(x)$  is the first type Hankel function, and  $H_\nu^{(2)}(x)$  is the second type Hankel function.

So

$$y(x) = AH_\nu^{(1)}(x) + BH_\nu^{(2)}(x)$$

Eq. 2-28

The plotted Bessel function with  $\nu=0,1,2,\dots,5$  is shown in Figure 2-11.

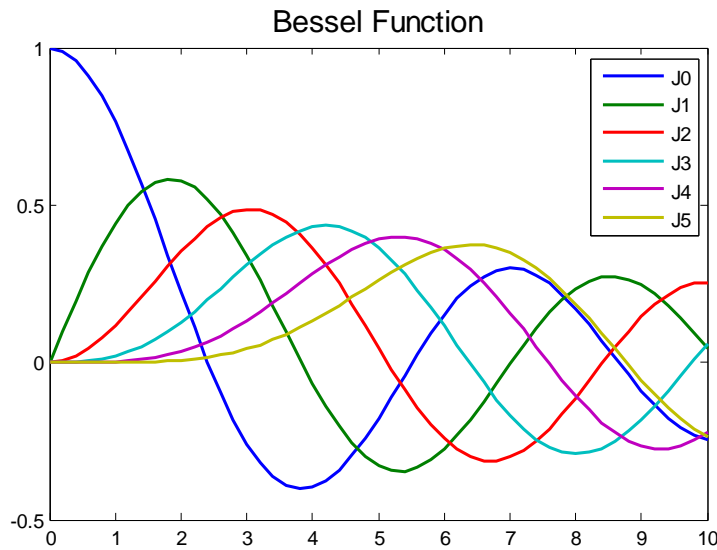


Figure 2-11. Bessel function J0~J5, the solution used in free-standing round membrane function.

### 2.4.3 Round membrane vibration

The analysis of the higher dimension membrane wave function can be decreased to two dimensional membrane analysis. The motion function and wave function are similar and extracted from the theories of higher dimension wave function.

#### 2.4.3.1 Higher dimensional wave function

Assume there are  $n$  parameters,  $x_1, x_2, \dots, x_n$ , and the function

$$u = u(t, x) = u(t, x_1, x_2, \dots, x_n)$$

Eq. 2-29

so we can have the higher dimension wave function

$$u_{tt} - c^2 \Delta u = 0$$

Eq. 2-30

where  $c$  is a positive normal number. The wave function can be written as

$$u_{tt} - c^2 \Delta u = u_{tt} - c^2 \sum_{i=1}^n u_{x_i x_i}$$

Eq. 2-31

if  $n = 1$ , the function represents the vibration wave on a string; if  $n = 2$ , the function represents the vibration wave on a membrane; if  $n = 3$ , the function represents the transportation of light wave, or known as electromagnetic wave.

In order to study this problem, basic assumptions of membrane vibration are made, and are listed below along with the prerequisites:

- (1) The membrane is uniform, and the surface density  $\rho$  is defined as mass over an area; and we can let  $\rho = 1$ ;
- (2) The membrane thickness is small, and can be considered as geometric surface;
- (3) The equilibrium position of the membrane is on the flat plane, so each point on the membrane presents only a small movement or vibration that is normal to the direction of this flat plane;
- (4) The membrane can be applied to an external force  $F$ , and the force  $F$  direction is vertical to the equilibrium flat plane;
- (5) The membrane is soft, which means no resistance force is generated when the curvature or shape shift occurs.

We can plot the force analysis on Figure 2-12 below. We assume the balanced or equilibrium flat plane is  $Ox_1x_2$  plane, and  $u(t, x_1, x_2)$  represents the position shift of each point on  $(x_1, x_2)$  at the time  $t$ , so the tension  $T$  at any point of the membrane is constant. If we have a cut length of  $l$ ,

the tension force  $T \propto l$ , which is perpendicular to both the direction of  $\vec{l}$  and the normal direction  $\vec{v}$  of the curvature surface, and can be written as

$$\vec{T} = \sigma \vec{l} \times \vec{v}$$

Eq. 2-32

where  $\sigma$  is the surface tension force coefficient, another constant related to the membrane's strength properties.

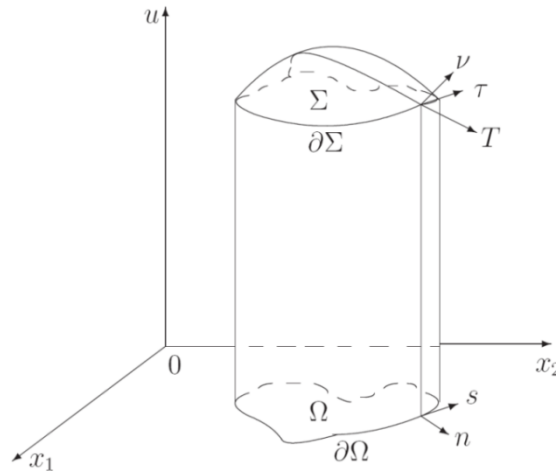


Figure 2-12. Force analysis on a small area of a round membrane element. This model is similar to our situation to analyze the lipid or copolymer membrane on the small hole.

We take a small area  $\Sigma$  on the membrane, and the projection area on the  $Ox_1x_2$  plane is  $\Omega$ . The time during this vibration goes from  $t$  to  $t + \Delta t$ , and  $\Delta t$  is small. The impulse on the membrane results in a momentum change during the time  $\Delta t$ . The direction of tension  $\vec{T}$  is the same as the direction of  $\vec{\tau} \times \vec{v}$ . The function of that small area  $\Sigma$  is  $u(t, x_1, x_2) = u$ ; and the direction of the normal vector  $\vec{v}$  of the curvature surface is  $(-u_{x_1}, -u_{x_2}, 1)$ .

∴ the direction of  $\vec{s}$  is

$$(\cos(x_1, s), \cos(x_2, s), 0)$$

∴ the direction of  $\vec{\tau}$  is

$$\left( \cos(x_1, s), \cos(x_2, s), \frac{\partial u}{\partial s} \right)$$

∴ the direction of  $\vec{\tau} \times \vec{\nu}$  is  $(a_1, a_2, a_3)$ , with

$$a_1 = \cos(x_2, s) + \frac{\partial u}{\partial s} u_{x_2}$$

Eq. 2-33

$$a_2 = -\cos(x_1, s) + \frac{\partial u}{\partial s} u_{x_1}$$

Eq. 2-34

$$a_3 = u_{x_1} \cos(x_2, s) - u_{x_2} \cos(x_1, s) = u_{x_1} \cos(x_1, n) - u_{x_2} \cos(x_2, n) = \frac{\partial u}{\partial n}$$

Eq. 2-35

∴ the vertical component of T

$$T_n = \frac{a_3}{\sqrt{a_1^2 + a_2^2 + a_3^2}} T$$

Eq. 2-36

∴  $u_{x_1}$ ,  $u_{x_2}$ , and  $\frac{\partial u}{\partial s}$  are small variables,

∴

$$T_u \approx T \cdot \frac{\partial u}{\partial n}$$

Eq. 2-37

∴ the composition of tension is the integral of the tension along the curve  $\partial\Sigma$

$$\int_{\partial\Omega} T \frac{\partial u}{\partial n} ds$$

and the composition of external force is

$$\iint_{\Omega} F(t, x_1, x_2) dx_1 dx_2$$

∴ the impulse on  $\Sigma$  during the time  $\Delta t$  is

$$\int_t^{t+\Delta t} \left[ \int_{\partial\Omega} T \frac{\partial u}{\partial n} ds + \iint_{\Omega} F(t, x_1, x_2) dx_1 dx_2 \right] dt$$

the momentum variation on  $\Sigma$  during the time  $\Delta t$  is

$$\iint_{\Omega} \left[ \frac{\partial u}{\partial t}(t + \Delta t, x_1, x_2) - \frac{\partial u}{\partial t}(t, x_1, x_2) \right] dx_1 dx_2$$

and during time  $\Delta t$ , the impulse on  $\Sigma$  is equal to the momentum variation on  $\Sigma$ .

$$\begin{aligned} \int_t^{t+\Delta t} \left[ \int_{\partial\Omega} T \frac{\partial u}{\partial n} ds + \iint_{\Omega} F(t, x_1, x_2) dx_1 dx_2 \right] dt = \\ \iint_{\Omega} \left[ \frac{\partial u}{\partial t}(t + \Delta t, x_1, x_2) - \frac{\partial u}{\partial t}(t, x_1, x_2) \right] dx_1 dx_2 \end{aligned}$$

Eq. 2-38

We assume the membrane is complete and smooth, so the second order differential of  $u$  on  $x_1$ , and  $x_2$  are continuous. Therefore, we use the Green equation:

$$\int_{\partial D} P dx + Q dy = \iint_D \left( \frac{\partial Q}{\partial x} - \frac{\partial P}{\partial y} \right) dx dy$$

Eq. 2-39

where  $D \subset R^2$  has boundaries,  $\partial D$  is a smooth curve with direction, functions  $P(x, y)$ , and  $Q(x, y)$  are continuous and can be differentiated on the domain  $D$ , and are also continuous on the closed domain  $\bar{D} = D \cup \partial D$ ,

$\therefore$

$$\int_{\partial\Omega} T \frac{\partial u}{\partial n} ds = \iint_{\Omega} T \cdot \left( \frac{\partial^2 u}{\partial x_1^2} - \frac{\partial^2 u}{\partial x_2^2} \right) dx dy$$

Eq. 2-40

Then, the momentum theory as Eq. 2-38,

$$\iint_t^{t+\Delta t} \left\{ \iint_{\Omega} \left[ T \cdot \left( \frac{\partial^2 u}{\partial x_1^2} - \frac{\partial^2 u}{\partial x_2^2} \right) + F(t, x_1, x_2) - \frac{\partial^2 u}{\partial t^2} \right] dx_1 dx_2 \right\} dt = 0$$

Eq. 2-41

Since the  $\Delta t$  and  $\Omega$  can be any value and anywhere, so the membrane vibration function is

$$\frac{\partial^2 u}{\partial t^2} = T \cdot \left( \frac{\partial^2 u}{\partial x_1^2} - \frac{\partial^2 u}{\partial x_2^2} \right) + F(t, x_1, x_2)$$

Eq. 2-42

By setting  $T = c^2$ ,  $f = F$ , we can get the standard equation

$$\frac{\partial^2 u}{\partial t^2} = c^2 \cdot \left( \frac{\partial^2 u}{\partial x_1^2} - \frac{\partial^2 u}{\partial x_2^2} \right) + f$$

Eq. 2-43

where  $f$  is a free term. If  $f$  exist, this represents a forced vibration. In our situation however, a free-standing membrane has no external forced behavior, which means  $f = 0$ .

∴

$$\frac{\partial^2 u}{\partial t^2} = c^2 \cdot \left( \frac{\partial^2 u}{\partial x_1^2} - \frac{\partial^2 u}{\partial x_2^2} \right)$$

Eq. 2-44

This equation represents our model on free-standing membrane on a small hole.

### 2.4.3.2 The solution Cauchy problem

To find a solution to this membrane vibration problem, we need to establish the boundary conditions and initial condition, including the initial position and velocity. So we can have the boundary condition as

$$\begin{cases} u(0, x) = \varphi(x) \\ \frac{\partial u}{\partial t}(0, x) = \Psi(x) \end{cases}$$

Eq. 2-45

This Eq. 2-45 is known as the Cauchy problem of the vibration function. There are three types of the boundary conditions.

(1) The first-type of boundary condition, where the boundary is changed following a known function (t)

$$u(t, x)|_{\partial\Omega} = 0$$

Eq. 2-46



or

$$u(t, x)|_{\partial\Omega} = \mu(t, x)$$

Eq. 2-47

where  $\mu(t, x)$  is a known function.

(2) The second-type of boundary condition, where the boundary can be moved along the cylindrical surface without friction force.

$$\left. \frac{\partial u}{\partial n} \right|_{\partial\Omega} = 0$$

Eq. 2-48

or

$$\left. \frac{\partial u}{\partial n} \right|_{\partial\Omega} = \mu(t, x)$$

Eq. 2-49

where  $\mu(t, x)$  is a known function.

(3) The third-type of boundary condition, where the boundary is fixed on a elastic support.

$$\left( \frac{\partial u}{\partial n} + \sigma u \right) \Big|_{\partial\Omega} = 0$$

Eq. 2-50

where  $\sigma$  is a known positive normal number, or

$$\left( \frac{\partial u}{\partial n} + \sigma u \right) \Big|_{\partial\Omega} = \mu(t, x)$$

Eq. 2-51

where  $\mu(t, x)$  is a known function.

This third-type condition is applied to our condition that the lipid or copolymer membrane is covered on the PDMS thin film support with a small hole. The support is an elastic structure and the membrane is not moving along the inner cylindrical surface.

### 2.4.3.3 High dimensional Cauchy problem and Poisson average spherical method

We use the Poisson average spherical method to study the high dimensional Cauchy problem.

The three-dimensional vibration function is

$$\begin{cases} u_{tt} - c^2(u_{x_1x_1} + u_{x_2x_2} + u_{x_3x_3}) = 0 \\ u(0, x) = \varphi(x) \\ u_t(0, x) = \Psi(x) \end{cases}$$

Eq. 2-52

Let  $\varphi(x)$  and  $\Psi(x)$  be spherically symmetric,

$\therefore \varphi$  and  $\Psi$  are only functions of  $r = \sqrt{x_1^2 + x_2^2 + x_3^2}$ ,

$\therefore$  we can change it to the function about  $t$  and  $r$ , since  $u = u(t, r)$ ,

$$u_{tt} = c^2 \left( u_{rr} + \frac{2}{r} u_r \right)$$

Eq. 2-53

Let  $v = ru$

$\therefore$

$$v_{tt} = c^2 v_{rr}$$

Eq. 2-54

The one dimension vibration function is solving for the solution  $v$ .

The higher dimension problem is

$$\begin{cases} u_{tt} = c^2 \Delta u \\ u(0, x) = \varphi(x) \\ u_t(0, x) = \Psi(x) \end{cases}$$

Eq. 2-55

The function  $h(x) = h(x_1, x_2, \dots, x_n)$  is continuous on  $R^n$ , and then we take the average on a spherical surface, with a center of  $x$ , and radius of  $r$ .

$$M_h(x, r) = \frac{1}{w_n \gamma^{n-1}} \int_{|y-x|=r} h(y) dS_y$$

Eq. 2-56

which is correlated to function  $h$ .

Let  $y = x + r\xi$ , with  $|\xi| = 1$ ,

$\therefore$

$$M_h(x, r) = \frac{1}{w_n} \int_{|\xi|=1} h(x + r\xi) dS_\xi$$

Eq. 2-57

Originally,  $r > 0$ , but now  $r$  can be extended to all real numbers.

$\therefore$  using  $-r$  to replace  $r$ , we can eliminate  $-\xi$ ,

$\therefore M_h(x, r)$  is an even function about  $r$ ;

and also

$$h \in C^s(R^n) \Rightarrow M_h \in C^s(R^{n+1})$$

as for  $h \in C^s(R^n)$ , according to divergence theorem (Gaussian theorem),

$$\iiint_V \nabla \cdot \vec{F} dV = \oiint_S \vec{F} \cdot d\vec{S}$$

Eq. 2-58

and we can have

$$\begin{aligned} \frac{\partial}{\partial r} M_h(x, r) &= \frac{1}{w_n} \int_{|\xi|=1} \sum_{i=1}^n h_{x_i}(x + r\xi) \xi_i dS_\xi \\ &= \frac{1}{w_n} \int_{|\xi|<1} \Delta_x h(x + r\xi) dS_\xi \\ &= \frac{r^{1-n}}{w_n} \Delta_x \int_{|y-x|<r} h(y) dy \\ &= \frac{r^{1-n}}{w_n} \Delta_x \int_0^r d\rho \int_{|y-x|=\rho} h(y) dS_y \\ &= r^{1-n} \Delta_x \int_0^r \rho^{n-1} M_h(x, \rho) d\rho \end{aligned}$$

Eq. 2-59

then we multiply  $r^{n-1}$  on both sides of Eq. 2-59, and differentiated about  $r$ ,

$$\frac{\partial}{\partial r} \left( r^{n-1} \frac{\partial}{\partial r} M_h(x, r) \right) = \Delta_x r^{n-1} M_h(x, r)$$

Eq. 2-60

$\therefore \forall$  average spherical  $M_h$  of function  $h \in C^2(R^n)$ ,  $M_h$  satisfies Darboux equation

$$\left( \frac{\partial^2}{\partial r^2} + \frac{n-1}{r} \frac{\partial}{\partial r} \right) M_h(x, r) = \Delta_x M_h(x, r)$$

Eq. 2-61

with the fact that  $M_h(x, r)$  is an even function, we can find the initial value to be

$$\begin{aligned} M_h(x, 0) &= h(x) \\ \frac{\partial}{\partial r} M_h(x, r) \Big|_{r=0} &= 0 \end{aligned}$$

Eq. 2-62

As the spherical average, we separate the vibration function to a initial value problem of two hyperbolic function with its own independent variables.

Let  $u(x, t)$  to be the solution of

$$\begin{cases} u_{tt} = c^2 \Delta u \\ u(0, x) = \varphi(x) \\ u_t(0, x) = \Psi(x) \end{cases}$$

Eq. 2-63

in the domain of half space  $x \in R^n$ ,  $t \geq 0$ , and belongs to  $C^2$  type solution. We take  $u$  as the function of  $x$ , and take the spherical average

$$M_u(x, r, t) = \frac{1}{w_n} \int_{|\xi|=1} u(x + r\xi, t) dS_\xi$$

Eq. 2-64

$\therefore$

$$M_u(x, 0, t) = u(x, t)$$

Eq. 2-65

$\therefore$  we can get  $u$  from  $M_u$ , according to the Darboux function,

$$\Delta_x M_u = \left( \frac{\partial^2}{\partial r^2} + \frac{n-1}{r} \frac{\partial}{\partial r} \right) M_u$$

Eq. 2-66

and according to Eq. 2-63 and Eq. 2-64, we have

$$\begin{aligned} \Delta_x M_u &= \frac{1}{w_n} \int_{|\xi|=1} \Delta_x u(x + r\xi, t) dS_\xi \\ &= \frac{1}{c^2} \frac{\partial^2}{\partial t^2} \frac{1}{w_n} \int_{|\xi|=1} u(x + r\xi, t) dS_\xi \\ &= \frac{1}{c^2} \frac{\partial^2}{\partial t^2} M_u \end{aligned}$$

Eq. 2-67

∴ with a fixed  $x$ ,  $M_u(x, r, t)$  is the function of two scalar quantity variables  $r$  and  $t$ , and is the solution of the Euler-Poisson-Darboux function

$$\frac{\partial^2}{\partial t^2} M_u = c^2 \left( \frac{\partial^2}{\partial r^2} + \frac{n-1}{r} \frac{\partial}{\partial r} \right) M_u$$

Eq. 2-68

where  $n$  is the dimension number of the  $x$  space.

When  $t = 0$ ,  $M_u$  is the solution of a known initial condition

$$\begin{cases} M_u = M_\varphi(x, r) \\ \frac{\partial}{\partial r} M_u = M_\psi(x, r) \end{cases}$$

Eq. 2-69

when the dimension number  $n = 3$ ,

$$\begin{aligned} \frac{\partial^2}{\partial t^2} (rM_u) &= c^2 \left( r \frac{\partial^2}{\partial r^2} M_u + 2 \frac{\partial}{\partial r} M_u \right) \\ &= c^2 \frac{\partial^2}{\partial r^2} (rM_u) \end{aligned}$$

Eq. 2-70

In this case,  $rM_u(x, r, t)$  is the initial value's solution of one dimensional vibration function at time  $t = 0$ .

$$\begin{cases} r \cdot M_u = rM_\varphi(x, r) \\ \frac{\partial}{\partial t} rM_u = rM_\Psi(x, r) \end{cases}$$

Eq. 2-71

By the existing D'Alembert equation, one dimension vibration function

$$\begin{cases} u_{tt} = a^2 u_{xx} \\ u(0, x) = \varphi(x) \\ u_t(0, x) = \Psi(x) \end{cases}$$

Eq. 2-72

has the solution

$$u(x, t) = \frac{1}{2} [\varphi(x + at) + \varphi(x - at)] + \frac{1}{2a} \int_{x-at}^{x+at} \Psi(\tau) d\tau$$

Eq. 2-73

∴ according to D'Alembert equation, we get

$$rM_u(x, r, t) = \frac{1}{2} [(r + ct)M_\varphi(x, r + ct) + (r - ct)M_\varphi(x, r - ct)] + \frac{1}{2c} \int_{ct-r}^{ct+r} \xi M_\Psi(x, \xi) d\xi$$

Eq. 2-74

then we utilize the fact that both  $M_\varphi(x, r)$  and  $M_\Psi(x, r)$  are even functions of  $r$ ,

$$M_u(x, r, t) = \frac{1}{2r} [(ct + r)M_\varphi(x, ct + r) - (ct - r)M_\varphi(x, ct - r)] + \frac{1}{2rc} \int_{ct-r}^{ct+r} \xi M_\Psi(x, \xi) d\xi$$

Eq. 2-75

Let  $r \rightarrow 0$ , we can replace the differential of  $r$  to the differential of  $ct$ , so we can get the Poisson function

$$\begin{aligned} u(x, t) &= tM_\Psi(x, ct) + \frac{\partial}{\partial t} (tM_\varphi(x, ct)) \\ &= \frac{1}{4\pi c^2 t} \int_{|y-x|=ct} \Psi(y) dS_y + \frac{\partial}{\partial t} \left( \frac{1}{4\pi c^2 t} \int_{|y-x|=ct} \varphi(y) dS_y \right) \end{aligned}$$

Eq. 2-76

When  $n = 3$ , this becomes a Cauchy problem. With  $\forall t \geq 0$ , the solution  $u$  belonging to  $C^2$  type can be and only can be presented by the Poisson equation.

### 2.4.3.4 Hadamard method of decreasing dimension

Considering the two dimensional problem

$$\begin{cases} u_{tt} - c^2(u_{x_1x_1} + u_{x_2x_2}) = 0 \\ u(0, x_1, x_2) = \varphi(x_1, x_2) \\ u_t(0, x_1, x_2) = \Psi(x_1, x_2) \end{cases}$$

Eq. 2-77

the main idea is to take this partial differential equation's solution as the specific solution of another solvable function group with more variables. For instance, the solution  $u(t, x_1, x_2)$  of this Cauchy problem at  $n = 2$ , can be treated as a solution without  $x_3$  at  $n = 3$ .

$\therefore$  as for  $x_3 = 0$ , and  $\varphi(y) = \varphi(y_1, y_2)$ , and  $\Psi(y) = \Psi(y_1, y_2)$ , from the solution  $u(t, x_1, x_2)$  got from Poisson equation, and the surface integral on the spherical area

$$|y - x| = \sqrt{(y_1 - x_1)^2 + (y_2 - x_2)^2 + y_3^2} = ct$$

Eq. 2-78

because on this spherical surface

$$\begin{aligned} dS_y &= \sqrt{1 + \left(\frac{\partial y_3}{\partial y_1}\right)^2 + \left(\frac{\partial y_3}{\partial y_2}\right)^2} dy_1 dy_2 \\ &= \frac{ct}{|y_3|} dy_1 dy_2 \end{aligned}$$

Eq. 2-79

also the points  $(y_1, y_2, y_3)$  and  $(y_1, y_2, -y_3)$  contributes equally to the integral.

$\therefore$

$$u(t, x_1, x_2) = \frac{1}{2\pi c} \iint_{r < ct} \frac{\Psi(y_1, y_2)}{\sqrt{c^2 t^2 - r^2}} dy_1 dy_2 + \frac{\partial}{\partial t} \frac{1}{2\pi c} \iint_{r < ct} \frac{\varphi(y_1, y_2)}{\sqrt{c^2 t^2 - r^2}} dy_1 dy_2$$

Eq. 2-80

where  $r = \sqrt{(x_1 - y_1)^2 + (x_2 - y_2)^2}$ , and the dependent domain of point  $(t, x_1, x_2)$  about the initial value is the round domain on the current  $y_1 y_2$  plane with  $r \leq ct$ .

### 2.4.3.5 Cauchy problem of non-uniform order vibration equation

The principle concept in order to solve the Cauchy problem of non-uniform order vibration equation is to get the uniform order Poisson function, and then satisfy the initial condition. The Cauchy problem is

$$\begin{cases} u_{tt} = c^2(u_{x_1x_1} + u_{x_2x_2} + u_{x_3x_3}) + f(t, x_1, x_2, x_3) \\ u(0, x) = \varphi(x) \\ u_t(0, x) = \Psi(x) \end{cases}$$

Eq. 2-81

First, we solve for the uniform order function

$$\begin{cases} u_{tt} = c^2(u_{x_1x_1} + u_{x_2x_2} + u_{x_3x_3}) \\ u(0, x) = \varphi(x) \\ u_t(0, x) = \Psi(x) \end{cases}$$

Eq. 2-82

with a solution of  $w(t, x_1, x_2, x_3; \tau)$ ; and then take the integral about  $\tau$ , get

$$u(t, x_1, x_2, x_3) = \int_0^t w(t, x_1, x_2, x_3; \tau) d\tau$$

Eq. 2-83

We can verify that the solution satisfies the following conditions.

(1) Satisfying  $u|_{t=0} = 0$ .

This is satisfied on Eq. 2-82 and Eq. 2-83.

(2) Proof of  $u_t|_{t=0} = 0$ .

∴

$$\frac{\partial u}{\partial t} = w(t, x_1, x_2, x_3; t) + \int_0^t \frac{\partial w(t, x_1, x_2, x_3; \tau)}{\partial t} d\tau$$

Eq. 2-84

using the condition of  $w|_{t=\tau} = 0$ .

$$w(t, x_1, x_2, x_3; \tau)|_{t=\tau} = 0$$

Eq. 2-85



∴

$$w(t, x_1, x_2, x_3; t) = 0$$

Eq. 2-86

∴

$$\frac{\partial u}{\partial t} = \int_0^t \frac{\partial w}{\partial t} d\tau$$

Eq. 2-87

∴

$$u_t|_{t=\tau} = 0$$

Eq. 2-88

(3) Proof the solution satisfied to the non-uniform order function.

We take the derivative of the Eq. 2-84 on  $t$ , so we can get the solution

$$\begin{aligned} \frac{\partial^2 u}{\partial t^2} &= \frac{\partial w(t, x_1, x_2, x_3; t)}{\partial t} \Big|_{\tau=t} + \int_0^t \frac{\partial^2 w(t, x_1, x_2, x_3; \tau)}{\partial t^2} d\tau \\ &= f(t, x_1, x_2, x_3) + c^2 \Delta \int_0^t w d\tau \\ &= c^2 \Delta u + f \end{aligned}$$

Eq. 2-89

Based on the Poisson function, this solution indicates that it has

$$w(t, x_1, x_2, x_3; \tau) = \frac{1}{4\pi c} \iint_{|y-x|=a(t-\tau)} \left[ \frac{f(\tau, \xi, \eta, \zeta)}{r} \right]_{r=c(t-\tau)} dS_y$$

Eq. 2-90

∴

$$u(t, x_1, x_2, x_3) = \frac{1}{4\pi c} \int_0^t \left[ \iint_{|y-x|=a(t-\tau)} \left[ \frac{f(\tau, \xi, \eta, \zeta)}{r} \right]_{r=c(t-\tau)} dS_y \right] d\tau$$

Eq. 2-91

With

$$\tau = t - \frac{r}{c}$$

Eq. 2-92

we have

$$\begin{aligned} u(t, x_1, x_2, x_3) &= \frac{1}{4\pi c^2} \int_0^{ct} \left[ \iint_{|y-x|=r} \frac{f\left(t - \frac{r}{c}, \xi, \eta, \zeta\right)}{r} dS_y \right] dr \\ &= \frac{1}{4\pi c^2} \iiint_{r \leq ct} \frac{f\left(t - \frac{r}{c}, \xi, \eta, \zeta\right)}{r} dV \end{aligned}$$

Eq. 2-93

which is integral about  $dV$  in a sphere with a center of  $(x_1, x_2, x_3)$ , and a radius of  $ct$ .

At time  $t$ , the value of  $u$  at  $M(x_1, x_2, x_3)$  is presented by the volumetric integral of  $f$  at time  $\tau = t - \frac{r}{c}$  in this sphere.

## 2.5 Contributions

### 2.5.1 Fluidic PCB for Basic EIS properties of planar membranes

In this study, using EIS, we demonstrated that PLFE archaeal tetraether lipids can form free-standing planar membranes on micro-pores of PDMS thin films in a home-built PCB-based fluidic device. The fabrication of the PDMS thin film and the fluidics was facilitated by the use of an S1813 sacrificial layer and oxygen plasma treatment. Compared to the planar membranes of diester lipids (POPC and POPC/POPS) and triblock copolymers (PMOXA-PDMS-PMOXA) made with the same method and device, PLFE free-standing planar membrane exhibits unusual dielectric properties, showing an inductance component, a large membrane resistance, and a sharp drop in phase angle with electrical signal inputs at frequency at  $\sim 1$  MHz. The large resistance suggests that, among the membranes examined, PLFE free-standing planar membrane is a better lipid matrix for studying channel proteins and trans-membrane events. The inductance component and the sharp drop in phase angle can be developed as a sensor to monitor the PLFE membrane status in the fluidics platform. Based on our current knowledge of bipolar tetraether lipids and

lipid vesicles, PLFE free-standing planar membranes situated in the PDMS- and PCB-based fluidics are expected to be stable and thus suitable for various applications such as high-throughput drug screening and artificial photosynthesis.

### **2.5.2 Extended modeling of round planar thin membranes**

The model we presented here illustrated the vibration behavior of a free-standing membrane on a small hole, same as our experiment of planar membrane status. The planar membrane has a smaller vibration resistivity compared to the vesicle structure, or the membrane with curvature. Besides, the free-standing planar membrane can generate vibration voluntarily, by stimulated by random vibration source from the solution environment. The differential equations can describe the vibration displacement and speed, etc., which represent the stability of free-standing planar membranes. However, due to the uncertainty and uniqueness of each membrane, we only considered geometric membrane, without the physical and chemical properties of the membranes. Therefore, we needed to study the stability of different membrane materials. According to the geometric model of the membrane vibration, the stability can be determined by the external vibration source, membrane extension coefficient, and the round membrane diameter, etc. The correlated experiments on the stability of membranes can be designed by different parameters.

## **Chapter 3. LIGHT REACTION UNIT: MEMBRANE IN MICROFLUIDICS**

### **3.1 Microchip EIS principle**

#### **3.1.1 Existing microchip technologies in EIS**

Microchip with biomembranes or living cells miniaturizes bioreactors for biochemistry and biological experiments, where microchip can achieve higher production rate, higher energy density, higher successful probability and lower cost. However, the sensing with or without actuators, and the data collection from miniaturized microchip becomes a challenging topic in lab-on-chip system [153-156]. The sensing in microfluidic system includes static sensing and dynamic sensing [155, 157]. Static sensing illustrates the static data or intrinsic parameters of a microfluidic system, such as microfluid pressure [158-160], or intrinsic frequency of micromechanical structures [154]. On the other hand, dynamic sensing demonstrates the real-time status in a microfluidic system [161-163], such as the completeness of a biomembrane by time [81, 157]. Dynamic sensing without jeopardizing the cell behavior or bio-reaction procedure requires harmless and contamination-free sensors needs to be build in microchip, either by traditional microfabrication [153, 164-167] or advanced techniques such as additive manufacturing (AM) [168].

One of the reliable sensor is monitoring the impedance properties of the biomembrane structure or target objects as dielectric materials, by fabricating capacitive sensors on the microchip [165, 169, 170]. Biomembranes normally have higher impedance compared to electrolyte, and different membranes have their own ranges of capacitances and resistances. Based on this reason, biomembranes can be used as the dielectric layer between two capacitor electrodes [171]. Capacitive sensing can apply to micro channels with electrolyte included microfluidic systems, including cell cytometry and monitoring [172], fluid parameter analysis [159, 160, 167], DNA detection [173, 174], or antigen-antibody characterization [175-177], etc. Our biomembrane monitoring platform was built on silicon wafer and glass, which could also be

fully interfacing with possible integrated circuits [154, 178], such as digital amplifiers [154, 169] and signal filters [154].

A thin film with a micro or nano size hole was required to support a biomembranes for bio-reactions. The selection of this thin film was based on the biomembranes' materials. For example, silicon nitride [90], Teflon [71], or PDMS [81] can be used to support phospholipid bilayer membrane. Many methods and technologies had already been developed to create micro and nano holes array [179, 180], such as ion beam [181] and electron beam lithography [182, 183], stamp imprint [184, 185], and soft-lithography [107, 186], etc. For our studying on PLFE, PMOXA-PDMS-PMOXA triblock copolymer, POPC, POPC/POPS (1:1), we use double-sided PDMS replica molding on negative photoresist SU-8.

The PDMS thin film with micro size hole was capable to support biomembrane in both single-membrane structure and dual-membrane structure. Single-membrane can separate two compartments, while dual-membrane can create three compartments, including a compartment with pre-definable diameter and volume in the middle layer. The dimension of this middle compartment was determined by the size of PDMS micro hole, which was related to a controllable dimension of SU-8 micro mold array during photolithography [107].

The dual-membrane structure has been made for the purpose of gas-liquid interface. However, the fabrication of a Langmuir-Blodgett film [187] dual-membrane that proper for biochemical reactions and membrane protein implantation is still challenging. For example, a kind of dual-membrane cell is made by assembling two casted copolymer films [188, 189]. However, this kind of film is not a single layer membrane. Another example is assembling two single layer membranes within two inlets and two outlets microfluidic system [190, 191]. However, when the two single layer membranes are formed, two membranes contacted and directly merged, without fluid or space between the two membranes. More applications in fuel cells or gas-liquid contactors are using commercially available porous membranes to make dual-membrane systems

[192, 193]. However, the porous membranes are not Langmuir-Blodgett film, which is suitable to obtain membrane proteins.

Energy harvesting by artificial photosynthesis process converting the solar energy into chemical energy gains much attention due to its superiority in storage [28]. For example, artificial planar membrane made of triblock copolymer can carry membrane proteins such as BR and ATPase, which converts solar energy into chemical energy as ATP [69]. With the development of biomaterials, the challenge nowadays is to build these materials into reliable energy harvesting devices.

### 3.1.2 EIS principle in microchip

The dielectric properties of planar membrane are measured by EIS [194, 195] as shown in Figure 3-1a. A sinusoidal voltage is applied between two electrodes and the consequent current follows the sinusoid waveform but with a phase delay as in Figure 3-1b. Based on these frequency responses, the equivalent capacitance and resistance characteristics of the planar membrane could be obtained [196].

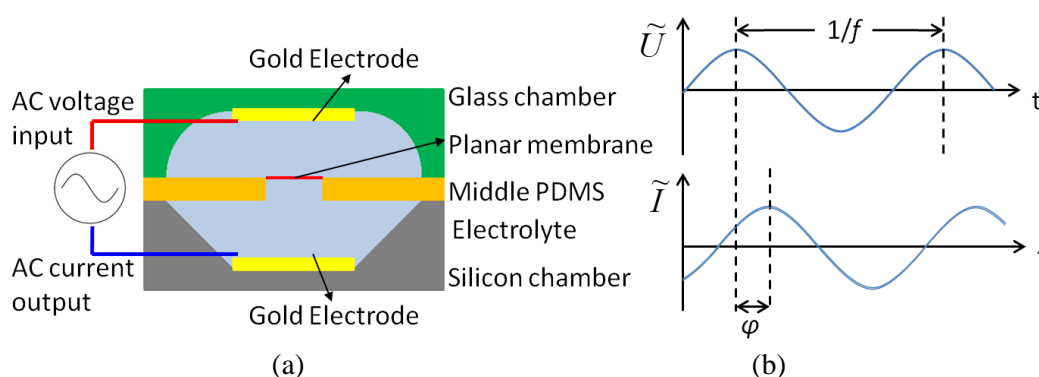


Figure 3-1. Illustration of EIS principles for planar membrane imbedded in a microchip.

The voltage source

$$V(t) = V_A \sin(\omega t)$$

Eq. 3-1

where radial frequency  $\omega=2\pi f$ . The membrane in microchip has capacitance and resistance, but no time related non-linear component. The result-in current response

$$I(t) = I_A \sin(\omega t + \varphi)$$

Eq. 3-2

where  $\varphi$  is the phase shift, so the impedance

$$Z = \frac{V(t)}{I(t)} = \frac{V_A \sin(\omega t)}{I_A \sin(\omega t + \varphi)}$$

Eq. 3-3

The magnitude

$$|Z| = \frac{V_A}{I_A}$$

Eq. 3-4

Based on Euler's relationship

$$e^{j\phi} = \cos \phi + j \sin \phi$$

Eq. 3-5

the voltage input and current can be written as

$$V(t) = V_A e^{j\omega t}$$

Eq. 3-6

$$I(t) = I_A e^{j(\omega t - \varphi)}$$

Eq. 3-7

so the impedance

$$Z = |Z|e^{j\varphi} = |Z|(\cos \varphi + j \sin \varphi) = Z_{Re} + jZ_{Im}$$

Eq. 3-8

and the phase shift angle

$$\varphi = \arctan \frac{Z_{Im}}{Z_{Re}}$$

Eq. 3-9

The equivalent circuit includes the R/C model of the membrane and the resistance model of the microchip itself with electrolyte. The equivalent circuit of a single or dual-membrane in microchip is summarized below.

The membrane follows  $R_M//C_M$ , and dual membrane follows Voigt's structure  $R_M//C_M + R_M//C_M$ . We used  $R_E$  to represent the resistance of electrolyte. Since the electrolyte was distributed in microchip in two cavities, we used  $R_E/2$  to represent electrolyte on each side<sup>3</sup>.

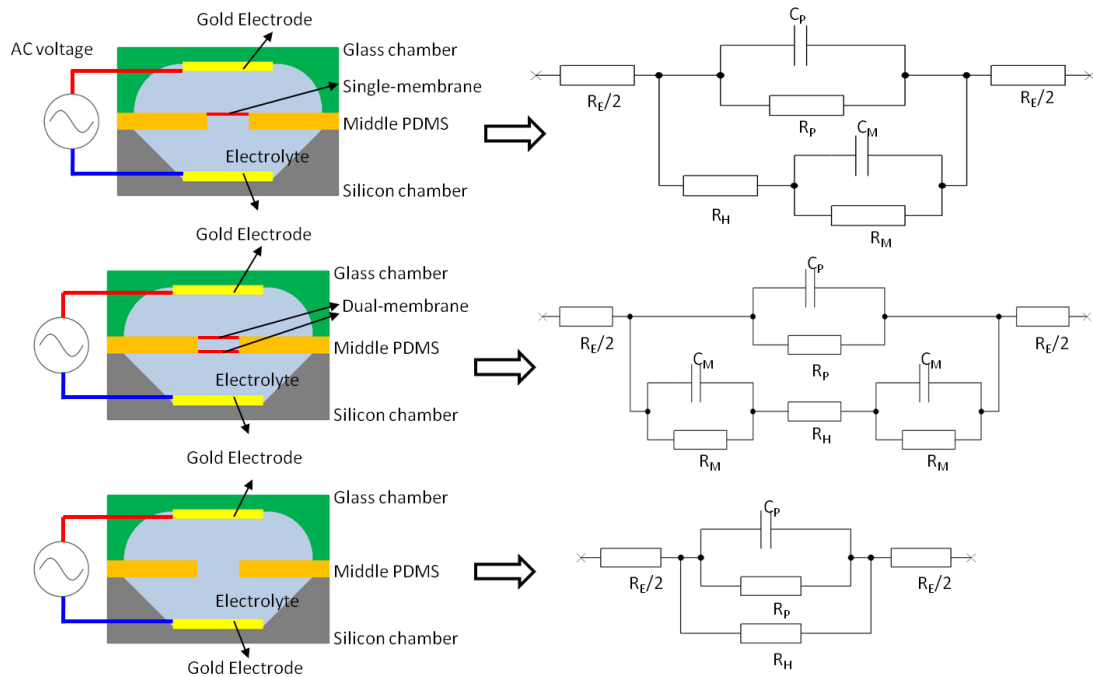


Figure 3-2. The equivalent circuit for single-membrane, dual-membrane, and empty group in microchip.

The impedance of single-membrane is:

$$Z_S(j\omega) = R_H + C_M // R_M = R_H + \frac{1}{R_M + \frac{1}{j\omega C_M}}$$

$$Z_S(j\omega) = R_H + \frac{R_M}{1 + (\omega C_M R_M)^2} - j \frac{\omega C_M R_M^2}{1 + (\omega C_M R_M)^2}$$

Eq. 3-10

while the impedance of dual-membrane is:

<sup>3</sup> The  $R_E/2$  was connected in series in the equivalent circuit, so no affect if the resistance of electrolyte on the two sides of membrane were different.



$$Z_D(j\omega) = R_H + C_{M1} // R_{M1} + C_{M2} // R_{M2} = R_H + \frac{1}{R_{M1} + \frac{1}{j\omega C_{M1}}} + \frac{1}{R_{M2} + \frac{1}{j\omega C_{M2}}}$$

Eq. 3-11

The empty group impedance is:

$$Z_E(j\omega) = R_H$$

Eq. 3-12

The EIS frequency response by Bode plot can be used to determine each capacitance and resistance by the form of real and imaginary part.

### 3.2 Microchip Fabrication

The fabrication processes of microchip was planned based on the facilities and equipment we have in microfabrication.

Our device consisted of three layers: top glass layer with a micro chamber, middle PDMS layer with a through hole where a biomembrane was placed, and bottom silicon layer with the other micro chamber. The top and bottom chambers had Cr/Au electrodes for impedance measurement. The glass and silicon chambers were fabricated by standard photolithography and wet etching techniques (buffered oxide etching (BOE) for glass and KOH etching for silicon). Cr/Au electrodes (~ 50 nm thick) were patterned on the chambers using lift-off technique.

PDMS layer with a through-hole was then fabricated by replica molding using U-8 molds by photolithography. Three different biomembranes were used in this study: PMOXA-PDMS-PMOXA, POPC membrane, and POPC/POPS (1:1). These biomembranes were placed on the PDMS through-hole by drop casting on top of water surface in a Petri-dish (Figure 3-7g). Final, the PDMS layer was bonded to the top glass chamber and the bottom silicon wafer after the oxygen plasma treatment.

### 3.2.1 Bottom silicon fabrication

The bottom silicon chamber was fabricated by photolithography and KOH wet etching, followed by gold electrode deposition. We used 3-inch silicon wafer (<100> P-type wafer) with 1 $\mu$ m oxidized layer.

#### (1) Photoresist deposition

Positive photoresist S1827 was dispensed onto the center of the polished side of 3-inch silicon wafer (single-side-polished (SSP) wafer with 1 $\mu$ m silicon dioxide). Spin coating was set at 2000 rpm with an acceleration of 1000 r/s for 60 s. The wafer was hard-baked at 120 °C for 5 min, which resulted in a  $\sim$ 4  $\mu$ m S1827 layer. Positive photoresist S1827 was spin coated on the unpolished side of the silicon wafer. Spin coating was set at 3000 rpm with acceleration of 1000r/s for 60s. The wafer was hard-baked at 95°C for 90 seconds.

#### (2) Wafer exposure

The wafer was put on a vacuum chuck (polished side up), and a photo mask with micro device pattern was fixed on the top of wafer. The measured UV intensity was 21.6 mW/cm<sup>2</sup>, so the exposure time was set 9.3 s to reach 200 mJ/cm<sup>2</sup>. The wafer was put in developer 351, to remove the exposed photoresist. Then, the wafer was rinsed in DI water and dried by nitrogen. The wafer was hard-baked on hot plate for 2 min for 120°C.

#### (3) Oxide etching

The wafer was immersed in BOE to etch the polished surface silicon dioxide layer. After the unprotected oxide layer was removed, the photoresist defined pattern will be left with SiO<sub>2</sub> on it. The silicon dioxide was used as a layer of mask for KOH etching of silicon [197].

#### (4) Photoresist remove

The remaining photoresist 1827 needed to be removed before KOH cavity etching. The wafer was washed by acetone to remove photoresist on both the polished and unpolished sides. Then, the wafer was rinsed with isopropanol, and dried by nitrogen gun.

### (5) Si etching

The wafer was fully immersed in 49% (w/w) KOH with 0.5% (v/v) isopropanol on a hotplate of 65°C, holding by a Teflon wafer dipper; at the same time, a magnetic stir bar was stirring at 100 r/min. After 4 hours etching, the resulting cavity had a depth of 125  $\mu\text{m}$  with a relatively flat bottom surface.

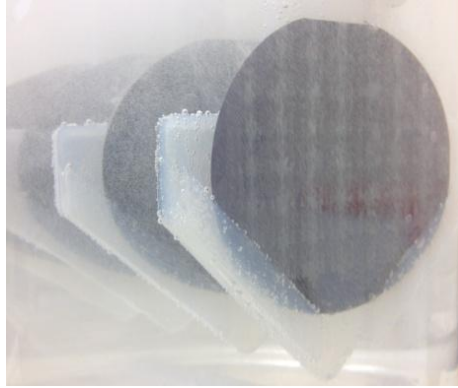


Figure 3-3. Silicon wafer in KOH etching.

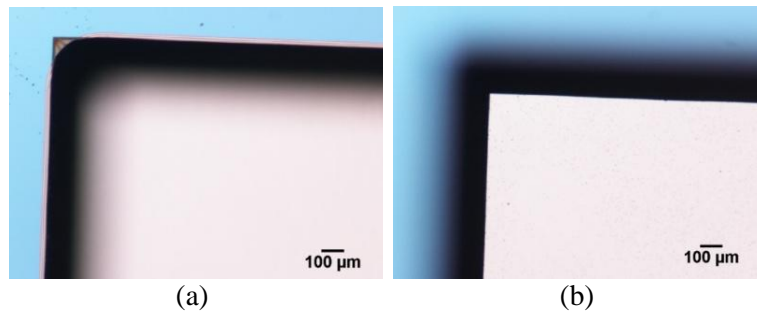


Figure 3-4. KOH etched silicon focus planes, (a) top edge (b) bottom edge.

The KOH etching was added isopropanol to improve the roughness of etched silicon bottom surface. Based on experimental experience, 49% (w/w) KOH with 0.5% (v/v) isopropanol at 65°C in etching will have a surface roughness less than 1  $\mu\text{m}$ . The wet etching depth can be measured by optical microscope, the measured depth based on the focus plane at top surface edge and bottom surface was measured as 125  $\mu\text{m}$ .

### (6) Photoresist deposition

Positive photoresist S1827 was dispensed onto the center of the polished side of 3-inch

silicon wafer. Spin coating was set at 2000 rpm with an acceleration of 1000 r/s for 60 s. the wafer was hard-baked at 120 °C for 5 min, which resulted in a  $\sim 4 \mu\text{m}$  S1827 layer.

### **(7) Wafer exposure**

The wafer was put on a vacuum chuck (polished side up), and a photo mask with micro device pattern was fixed on the top of wafer. The mask had to put to the same place as the first time exposure. We designed two alignment marks on the two sides of photo mask. The measured UV intensity was  $21.6 \text{ mW/cm}^2$ , so the exposure time was set 9.3 s to reach  $200 \text{ mJ/cm}^2$ . The wafer was put in developer 351, to remove the exposed photoresist. Then, the wafer was rinsed in DI water and dried by nitrogen. The wafer was hard-baked on hot plate for 2 min for  $120^\circ\text{C}$ .

The alignment marks were located at the two edges of wafer with two crosses and triangle shape. The second layer will be covered by the alignment marks if the three dimensions (X-axis, Y-axis, and twist angle) were all aligned.

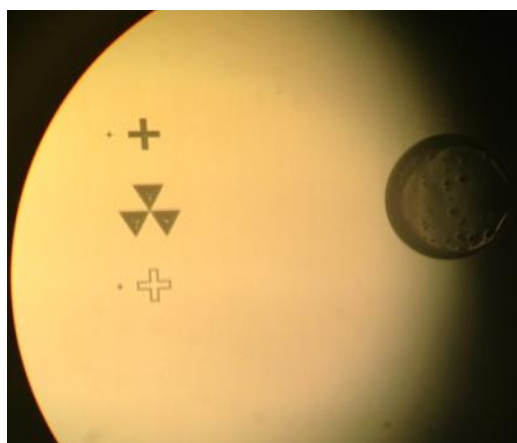


Figure 3-5. Mask alignment by alignment mark during secondary photolithography.

### **(8) Metal evaporation and lift-off**

A thin layer of chrome (15 nm) and gold (50 nm) was coated on the wafer by metal evaporation. The existence of chrome can benefit the attachment between gold and silicon. The sacrificial layer S1827 was removed in acetone that half immersed in sonicator, that the unwanted gold will be broken into small pieces and released from the wafer.

### **(9) Dicing and wiring**

After metal lift-off, the wafer and glass slide were diced into 9 mm × 9 mm single devices using dicing saw (Kulicke & Soffa ®, model 7300csp, Fort Washington, PA). Then the devices were soldered to aluminum wire.

### **3.2.2 Top glass fabrication**

The glass was standard microscope glass slide (75 mm × 50 mm). The mask for etching was positive photoresist S1827 [198].

#### **(1) Photoresist deposition**

Positive photoresist S1827 was dispensed onto the center of the glass slide. Spin coating was set at 2000 rpm with an acceleration of 1000 r/s for 60 s. The glass slide was hard-baked at 120 °C for 5 min, which resulted in a ~4 μm S1827 layer.

#### **(2) UV exposure**

The glass slide was put on a vacuum chuck (the side with photoresist up), and a photo mask with microdevice pattern was fixed on the top of wafer. The measured UV intensity was 21.6 mW/cm<sup>2</sup>, so the exposure time was set 13.9 s to reach 300 mJ/cm<sup>2</sup>. The glass required a 1.5 times higher UV dose compared to silicon wafer. The glass slide was put in developer 351, to remove the exposed photoresist. Then, the glass slide was rinsed in DI water and dried by nitrogen. The glass slide was hard-baked on hot plate for 2 min for 120°C.

#### **(3) Photoresist deposition**

To protect the other side of glass during BOE etching, we deposit another layer of photoresist on the other side. Positive photoresist S1827 was dispensed onto the back side of glass slide. Spin coating was set at 2000 rpm with an acceleration of 1000 r/s for 60 s. The glass was hard-baked at 120 °C for 5 min, which resulted in a ~4 μm S1827 layer.

#### **(4) Oxide etching**

The glass slide was moved to BOE etching for 40 min, which resulted in a chamber with

depth of  $\sim 75\mu\text{m}$ .

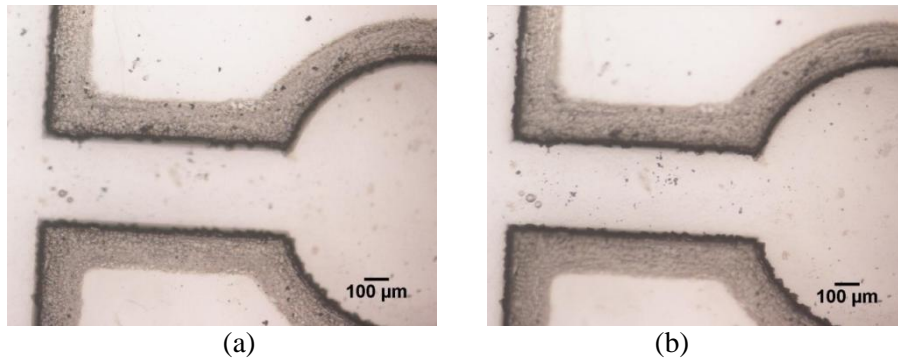


Figure 3-6. BOE etched glass slide focus planes, (a) top edge (b) bottom edge.

#### (5) Photoresist remove

Sometimes the structure of photoresist layer after BOE etching was broken, so we need to remove the S1827 layer and deposit new photoresist again form metal deposition. The glass slide was washed by acetone to remove photoresist on both sides. Then, the wafer was rinsed with isopropanol, and dried by nitrogen gun.

#### (6) Photoresist deposition

Positive photoresist S1827 was dispensed onto the back side of glass slide. Spin coating was set at 2000 rpm with an acceleration of 1000 r/s for 60 s. The glass slide was hard-baked at 120 °C for 5 min, which resulted in a  $\sim 4\mu\text{m}$  S1827 layer.

#### (7) Wafer exposure

The glass slide was put on a vacuum chuck (the side with photoresist up), and a photo mask with microdevice pattern was fixed on the top of wafer. The mask had to put to the same place as the first time exposure. We designed two alignment marks on the two sides of photo mask. The measured UV intensity was  $21.6\text{ mW/cm}^2$ , so the exposure time was set 13.9 s to reach  $300\text{ mJ/cm}^2$ . The glass required a 1.5 time higher UV dose compared to silicon wafer. The glass slide was put in developer 351, to remove the exposed photoresist. Then, the glass slide was rinsed in DI water and dried by nitrogen. The glass slide was hard-baked on hot plate for 2 min for 120°C.

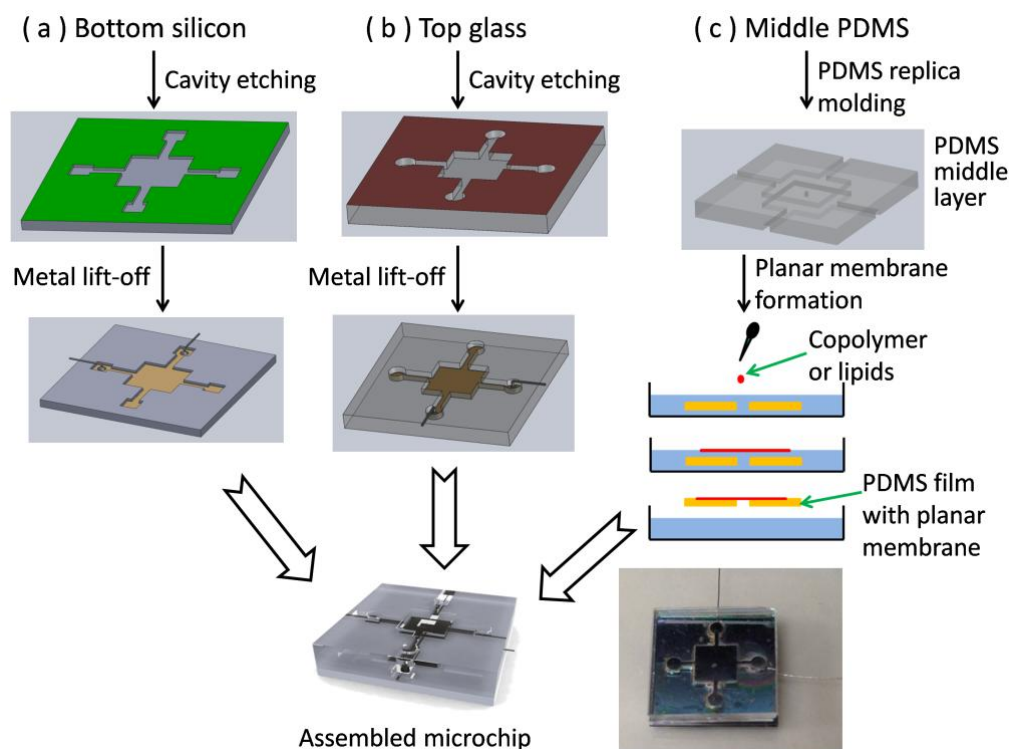


Figure 3-7. Fabrication process flow of microchip.

### (8) Metal evaporation and lift-off

A thin layer of chrome (15 nm) and gold (50 nm) was coated on the glass slide (the side with photoresist pattern) by metal evaporation. The existence of chrome can benefit the attachment between gold and glass. The sacrificial layer S1827 was removed in acetone that half immersed in sonicator, that the unwanted gold will be broken into small pieces and released from the glass slide.

### (9) Dicing and wiring

After metal lift-off, the wafer and glass slide were diced into  $9\text{ mm} \times 9\text{ mm}$  single devices using dicing saw (Kulicke & Soffa®, model 7300csp, Fort Washington, PA).

### 3.2.3 Microchip dicing and wiring

After metal lift-off, the wafer and glass slide were diced into  $9\text{ mm} \times 9\text{ mm}$  single devices using dicing saw (Kulicke & Soffa®, model 7300csp, Fort Washington, PA). The blue film is

attached to the wafer or glass first, and proper saw is selected to cut silicon or silicon dioxide. After the path is finalized and aligned, the wafer and glass is cut into single devices.

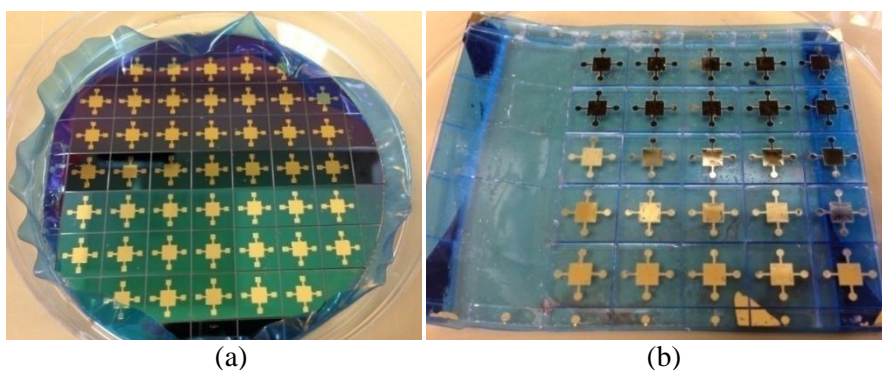


Figure 3-8. (a) Diced silicon microchip (9\*9mm) by dicing saw. (b) Diced glass slide (9\*9mm) by dicing saw.

The glass transfers heat slower than silicon wafer, so the heat will melt the Au on glass, if the soldering iron touches the Au electrodes. Put proper amount of solder paste on the wire. Use soldering iron on the wire but not directly on the solder paste. When the solder paste is about to melt, move the solder wire directly to the surface of Au on the glass, and the wire will be soldered to the Au electrode.

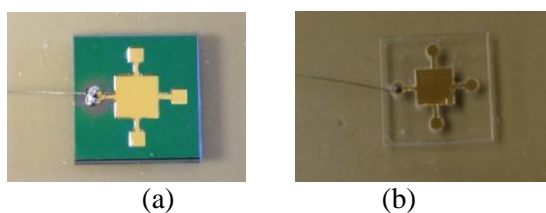


Figure 3-9. Aluminum wires are soldered on (a) bottom layer silicon electrode; and (b) top layer glass electrode.

The silicon transfers heat faster than silicon wafer, so the heat is not enough to melt the solder paste if it is stick to the wire. Put small amount of solder paste on the Au electrodes on the silicon wafer. Immerse the thin wire into the solder paste, and use soldering iron to touch the surface of solder paste. When the solder paste begins to melt, remove the soldering iron and let the solder melt and become solid again, the wire will embedded in the solder paste.



The amount of solder paste we used was limited, because we don't want a very large solder ball on the device. The remaining solder ball height is 150  $\mu\text{m}$ ~200  $\mu\text{m}$ , which can be fully covered by the middle layer PDMS with cavity pattern because of the elasticity of PDMS. The measurement of microscale electrodes and wires need specific method to reach a reasonable data [199]. The soldered wire-to-electrode resistance on glass is  $4.8 \pm 0.9 \Omega$  measured by Van der Pauw method [200, 201]; while the wire-to-electrode resistance on silicon is  $4.5 \pm 0.9 \Omega$ .

$$R = \frac{1}{4} \left[ \frac{V_{12}}{I_{34}} + \frac{V_{23}}{I_{41}} + \frac{V_{34}}{I_{12}} + \frac{V_{41}}{I_{23}} \right]$$

Eq. 3-13

and

$$R_s = \frac{\pi}{\ln 2} F(Q) R$$

Eq. 3-14

where  $F(Q)$  is the correction factor that depends on the geometry. For a square,  $F(Q) = 1$ . The measure contact is on the side of the samples.

### 3.2.4 Middle layer PDMS: double-sided mold replica

In our microchip structure, the middle layer PDMS thin film with small hole needs to be bonded to glass and silicon on both sides, so the two sides needs to be flat enough to bond to the flat surface of glass and silicon.

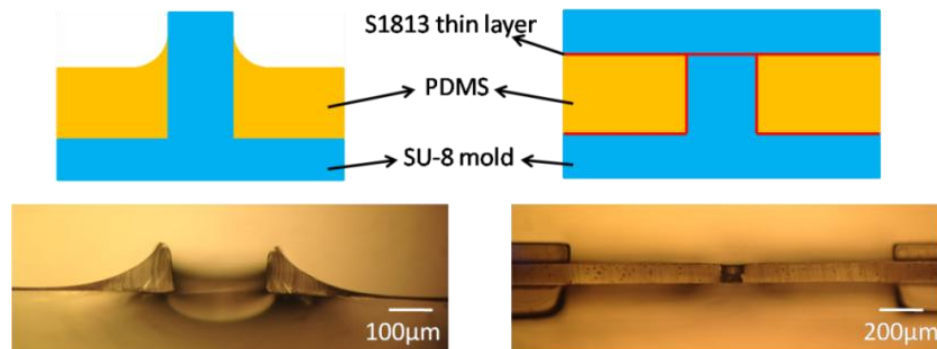


Figure 3-10. PDMS replica molding by clamping molding to avoid the cliff on edge.

Traditional method on PDMS mold replica using SU-8 as molding layer will create cliff structure at the edge of SU-8 cylindrical structure, because of the surface tension and capillary effect of the uncured PDMS pre-polymer mixture. Therefore, we improved PDMS replica molding by clamping method as shown in Figure 3-10.

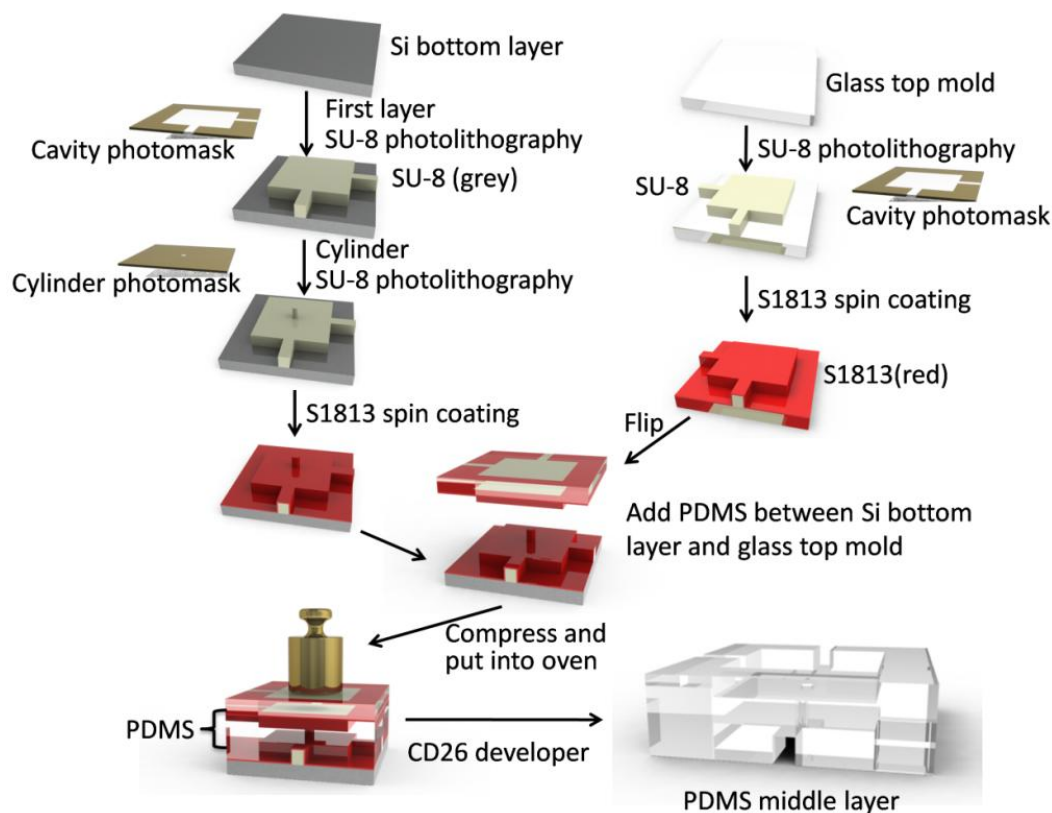


Figure 3-11. Fabrication process flow of double-sided PDMS replica molding by SU-8 molds.

The double-sided molding used SU-8 micro molding on both silicon and glass. The transparency of glass allowed us to align the glass layer to the silicon during the PDMS molding step (Figure 3-11).

### 3.2.4.1 Bottom mold:

#### (1) First layer SU-8

We used SU-8 2035 on a clean and dehydrated prime silicon wafer. The SU-8 2035 was spin coated at 500 rpm with an acceleration of 100 r/s for 30 s. This uncured SU-8 layer was around 200  $\mu\text{m}$  in thickness. Then the wafer was soft baked at 65°C for 15 min and followed by 95°C for

60 min. After the wafer with uncured SU-8 was cool down to room temperature, the wafer was moved to a mask aligner and covered with a negative photo mask with patterned cavity and channel structure. The exposure time was set to 23.2 s at  $21.55 \text{ mW/cm}^2$ , which provided a total dose of  $500 \text{ mJ/cm}^2$  on the wafer. After the first UV exposure, the wafer was transferred to a hot plate for post exposure bake at  $65^\circ\text{C}$  for 10 min and followed by  $95^\circ\text{C}$  for 30 min. After the wafer cooled down to room temperature after post bake, the wafer was immersed in SU-8 developer for 20 min to remove the uncured SU-8. Then the wafer with SU-8 pattern was cleaned by isopropanol and DI water, and dried with nitrogen gun.

### **(2) Second layer SU-8**

The SU-8 cylindrical mold is the core of SU-8 double-sided molding, which requires a better strength and adhesions. We used SU-8 3035 with improved adhesion to spin coating on the wafer at 1000 rpm with acceleration of 200 r/s for 30 s. This uncured SU-8 layer was around  $80 \mu\text{m}$  in thickness. Then the wafer was again soft baked at  $65^\circ\text{C}$  for 15 min and followed by  $95^\circ\text{C}$  for 45 min. After the wafer with uncured SU-8 was cool down to room temperature, the wafer was moved to a mask aligner and covered with a negative photo mask with patterned micro hole array (diameter  $100 \mu\text{m}$ ) and alignment marks. After alignments using microscope, the exposure time was set to 16.6 s at  $21.55 \text{ mW/cm}^2$ , which provided a total dose of  $250 \text{ mJ/cm}^2$  on the wafer. After the first UV exposure, the wafer was transferred to a hot plate for post exposure bake at  $65^\circ\text{C}$  for 5 min and followed by  $95^\circ\text{C}$  for 15 min. After the wafer cooled down to room temperature after post bake, the wafer was immersed in SU-8 developer for 10 min to remove the uncured SU-8. Then the wafer with SU-8 pattern was cleaned by isopropanol and DI water, and dried with nitrogen gun.

### **(3) S1813 sacrificial layer**

Positive photoresist S1813 was dispensed onto the center of the cured SU-8 structure. Spin coating was set at 3000 rpm with an acceleration of 1000 r/s for 60 s. Then, the wafer was hard-

baked at 120 °C for 5 min, which resulted in a 2 μm S1813 layer on SU-8. After S1813 coating step, this wafer was ready to be one of the mold in our double-sided molding for PDMS.

### **3.2.4.2 Top mold:**

#### **(1) SU-8 layer**

We used P-20 to increase the adhesion between SU-8 2035 and glass. The standard microscope glass slide (75 mm × 50 mm) was cleaned and dehydrated at 110°C for 5 min. After the glass cooled down to room temperature, a SU-8 primer P-20 (ShinEtsu MicroSi, Inc., Phoenix, AZ) was spin coated on the glass surface at 3000 rpm with an acceleration of 1000 r/s for 10 s. The surface of glass showed a flash of color change, and remained transparent again. The SU-8 2035 was spin coated onto the P-20 coated glass, at 500 rpm with an acceleration of 100 r/s for 30 s. This uncured SU-8 layer was around 200 μm in thickness. Then the glass was soft baked at 65°C for 15 min and followed by 95°C for 60 min. After the glass with uncured SU-8 was cool down to room temperature, the glass slide was moved to a mask aligner and covered with a negative photo mask with patterned cavity and channel structure. The exposure time was set to 23.7 s at 21.55 mW/cm<sup>2</sup>, which provided a total dose of 550 mJ/cm<sup>2</sup> on the glass slide, because the exposure of SU-8 on glass requires larger dose than SU-8 on silicon wafer. After the first UV exposure, the glass was transferred to a hot plate for post exposure bake at 65°C for 10 min and followed by 95°C for 30 min. The SU-8 pattern showed transparent light yellow color under the cleanroom light. After the glass cooled down to room temperature after post bake, the glass slide was immersed in SU-8 developer for 20 min to remove the uncured SU-8. Then the glass with SU-8 pattern was cleaned by isopropanol and DI water, and dried with nitrogen gun.

#### **(2) S1813 sacrificial layer**

Direct peeling off of PDMS from double side SU-8 molds was too difficult to protect the

completeness of PDMS film, so we need a sacrificial layer between SU-8 and PDMS [202-205]<sup>4</sup>. PDMS Positive photoresist S1813 was dispensed onto the cured SU-8 structure. Spin coating was set at 3000 rpm with an acceleration of 1000 r/s for 60 s. Then, the glass slide was hard-baked at 120°C for 5 min, which resulted in a 2 µm S1813 layer on SU-8. After S1813 coating step, this glass slide with SU-8 pattern was ready to be the other one of the mold in our double-sided molding for PDMS.

### **3.2.4.3 Clamping molding:**

#### **(1) Si and glass alignment**

PDMS pre-polymer and curing agent mixture was poured between the top glass and bottom silicon with SU-8 mold. The top glass was aligned to the bottom silicon by the alignment mark on the edge of the wafer.

#### **(2) PDMS clamping molding**

A 200 g mass weight was put on the top of glass slide, before the molds and PDMS moved into an oven of 65°C for 4 hours to allow the PDMS fully cured.

#### **(3) PDMS release**

After the two molds and PDMS was taken out from the oven and cooled down to room temperature, the molds was moved exposed to UV at a dose of 300 mJ/cm<sup>2</sup>, with the glass side up. The positive photoresist S1813 is referred as DQN (photo-active compound (diazoquinones, DQ) and matrix material (N)). The UV exposure can benefit the S1813 removing by positive photoresist developer. The S1813 between PDMS and SU-8 mold was then removed by CD-26 developer (Microposit, Marlborough, MA), and cleaned by isopropanol.

---

<sup>4</sup> The reference: “Anderson, Janelle R., Daniel T. Chiu, Hongkai Wu, O. J. Schueller, and George M. Whitesides. "Fabrication of microfluidic systems in poly (dimethylsiloxane)." *Electrophoresis* 21, no. 1 (2000): 27-40.” was imported from *Electrophoresis* journal, but the authors shown on paper was: “J. Cooper McDonald, David C. Duffy, Janelle R. Anderson, Daniel T. Chiu, Hongkai Wu, Olivier J.A. Schueller, and George M. Whitesides”.

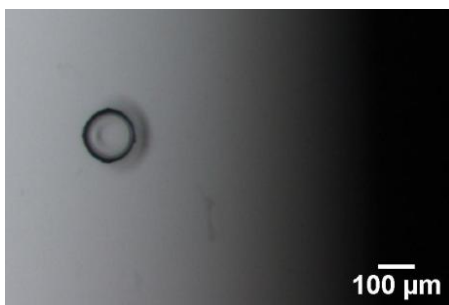


Figure 3-12. SU-8 pillar on wafer used for double-sided replica molding.

### 3.2.5 Middle layer PDMS: laser drilling

One issue in membrane stability study is the affect of different aspect ratios. We used SU-8 molding method to create the small through hole of 100  $\mu\text{m}$  and 200  $\mu\text{m}$ ; and we used laser drilling method to create 20  $\mu\text{m}$  holes on the same molded PDMS. In this molding, the SU-8 pillar for through-hole molding is not used. Only a comparison label is marked on the PDMS thin film, which can locate the coordinate on laser unit, and estimate the target. The laser drilled small hole is a cone-shape hole rather than a straight cylindrical hole. I took a cut on the laser-drilled hole by surgical blade on a 10~20  $\mu\text{m}$  dot under a 20 $\times$  microscope, and got the cross-section image of a laser-drilled hole in PDMS thin film (Figure 3-13). According to the optical microscope image, the cone has a maximum diameter of 18  $\mu\text{m}$  and a height of 153  $\mu\text{m}$ ; therefore, the laser-drilled hole has a slope angle of  $\sim 86.6^\circ$ . This angle is depends on the impact energy, impact quantities of laser, and the properties of PDMS.

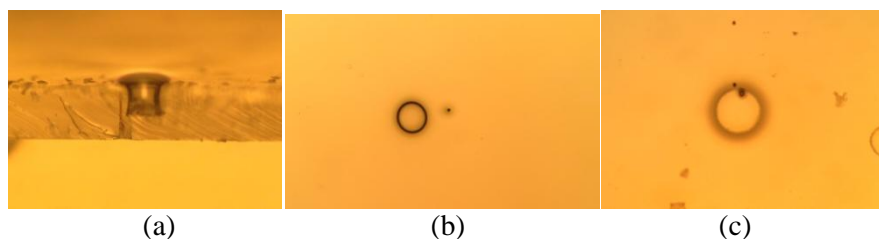


Figure 3-13. (a) The cross-section view of a non-through hole drilled by laser; (b) One laser shot compared to the 200  $\mu\text{m}$  through hole mark; (c) Through hole by laser drilling on PDMS thin film.

The excimer laser system usually consists of two major parts: micromachining station and laser unit. In this work, the excimer laser micromachining station (Rapid X 250, Resonetics, NH)

and the stand-alone gas type ultraviolet laser unit (COMPex Pro 110F, Coherent, Germany) were used to fabricate tiny holes on PDMS membranes. Argon fluoride (ArF) gas mixture (0.17% F<sub>2</sub>, 5.33% Ar, 16.5% He and Ne) was connected to generate 193 nm wavelength excimer laser. The entire optical path of ArF excimer laser was purged with nitrogen to prevent ozone generation by a reacting ArF excimer laser with oxygen in the air. Three sets of turning mirrors are placed in micromachining station to deliver laser beam onto sample stage. The amount of demagnification was selected with combination of three different focal lengths. In this experiment, the demagnification was set as 25×, therefore, the final dimension of the focused beam dimension was reduced by 25 times from the original dimension of a stainless steel mask.

The system runs with energy constant mode to apply a fixed energy value. In addition, to apply an excimer laser with lower energy, a 60% transmission rate attenuator was equipped. The ablation depth can be adjusted by controlling the number of laser shots. A microscope with a charge-coupled device (CCD) camera provides a magnified view of the sample on the monitor to fine out the exact ablation spot. After sample loading, the sample stage was moved by controlling electrical motors along 3 axes: X, Y, Z. Then, we applied these laser ablation conditions to create a tiny hole on PDMS membranes with fluency of 21.75 J/cm<sup>2</sup>, frequency of 100 Hz, and number of shot of 1000.

### **3.2.6 Membrane formation**

To form free-standing membrane on the middle layer PDMS thin film support, we used the method invented by Langmuir. The membrane material in organic solvent was dipped on the surface of water, and forms a planar membrane. Then the PDMS thin film support was lifted up and the lipid or copolymer covered the surface of the PDMS thin film, where the free-standing membrane was formed over the small hole on PDMS thin film.

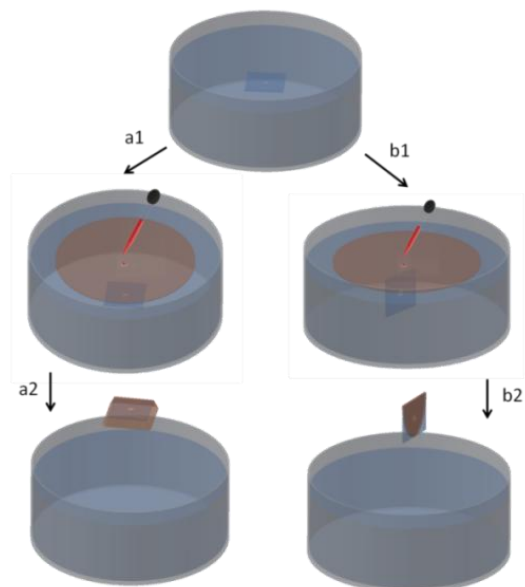


Figure 3-14. Free-standing membrane formation procedure. Step a1~a2: single membrane; step b1~b2: dual-membrane.

This Langmuir method can be used to make either single-membrane or dual-membrane in a microchip device. To prepare a single membrane, the PDMS thin film was horizontally submerged in water, and triblock copolymer or lipid solution in organic solvent was dropped on the water surface. Then, the PDMS thin film was lifted up horizontally with planar membrane covered on top. On the another hand, the formation of dual-membrane was using the same procedure, except the PDMS thin film was lifted up vertically to allow the planar membrane to cover on both sides of PDMS thin film.

### 3.2.7 Temperature control

To achieve a certain temperature to measure the membrane impedance, the assembled devices were connected to the wire on impedance spectroscopy, and immersed in water baths (Fisher Scientific Isotemp Economy, Model 105, Dubuque, Iowa). The temperature of water was read from a mercury thermometer in the water bath.

The higher temperature than room temperature can be achieved by water bath; on the other hand, we need to use cool plate to reach a temperature lower than room temperature. The cold



plate cooler (Model: CP-031, Serial No. 0285, TE technology, Inc, Traverse City, Michigan) was using the principle of Peltier effect in semiconductor. The power source (DC power supply, SPS-3610, GW Instek, Taiwan) provide voltage and current for semiconductor.

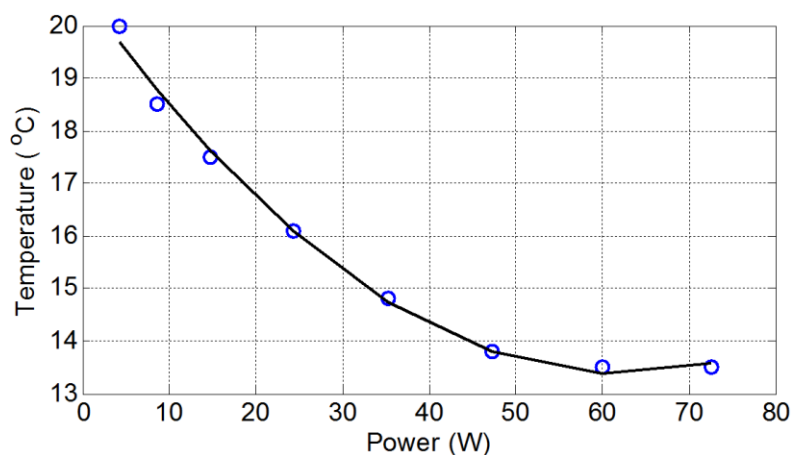


Figure 3-15. Temperature of cooling plate water bath determined by power (current and voltage).

### 3.3 Electrochemical impedance measurement results

The Cr/Au electrode was soldered to metal wires and then used for EIS measurement. We still used 1 M KCl, 1 mM CaCl<sub>2</sub>, and 10 mM Tris solution as electrolyte. A sinusoidal voltage (amplitude 100 mV) was applied with a frequency sweep from 1 MHz to 10 mHz. Based on the input voltage and output current, we calculated the capacitances and resistances of the equivalent circuit as shown in Table 3-1 and compared the values with literature.

Table 3-1. Dielectric properties of four different membrane materials\*

	PMOXA-PDMS- PMOXA	POPC	POPC/POPS (1:1)	PLFE
Capacitance ( $\mu\text{F}/\text{cm}^2$ )	$2.872 \times 10^{-1}$ (n=18)	1.805 (n=15)	1.301 (n=9)	$1.624 \pm 0.14 \times 10^{-1}$ (n=15)
Resistance ( $\Omega \cdot \text{cm}^2$ )	7.720 (n=18)	$1.138 \times 10^3$ (n=15)	$1.263 \times 10^3$ (n=9)	$4.923 \pm 0.12 \times 10^3$ (n=15)
Reference Capacitance ( $\mu\text{F}/\text{cm}^2$ )	$2.71 \times 10^{-1}$ [71]	1.2~1.96 [128]	NA	$0.16 \pm 0.02$ [81]
Reference Resistance ( $\Omega \cdot \text{cm}^2$ )	10.8 [71]	$855 \pm 490$ [128]	NA	$4901 \pm 120$ [81]

\* n represents the number of experiment trials.

The dielectric properties measurements of three planar biomembranes used in this study were shown in Table 3-1. The similar variations of the impedance and phase angle with increasing applied frequency for three planar membranes indicated that the tri-block copolymers were capable of substituting the natural lipid (POPC/POPS (1:1)) for the photosynthesis membranes. Moreover, the overall impedance ( $\|Z\| = \sqrt{\text{Re}^2 + \text{Im}^2}$ ) for the tri-block copolymer membrane was much larger than the natural lipid membranes and thus would be easier to monitor using the embedded parallel capacitor sensors.

### 3.3.1 Experimental setup

### 3.3.2 Single membrane EIS results

The single membrane on microchip EIS result of Nyquist plot and Bode plot are similar to the EIS results of single membrane on PCB fluidic device.

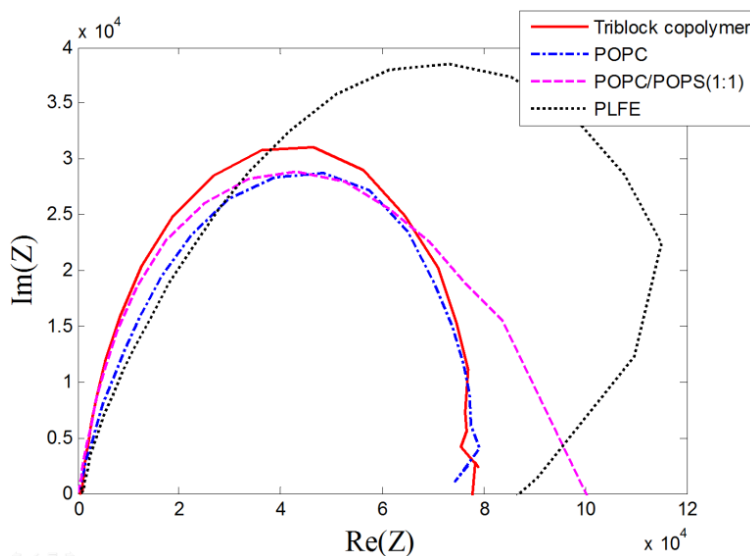


Figure 3-16. Nyquist plot of four different materials single membrane.

The Nyquist plot of triblock copolymer PMOXA-PDMS-PMOXA, PLFE, POPC, POPC/POPS (1:1) has similar results to PCB fluidic device results. The curve represents the

resistance and capacitance properties of these four membranes. PLFE showed a higher capacitance compared to the other three.

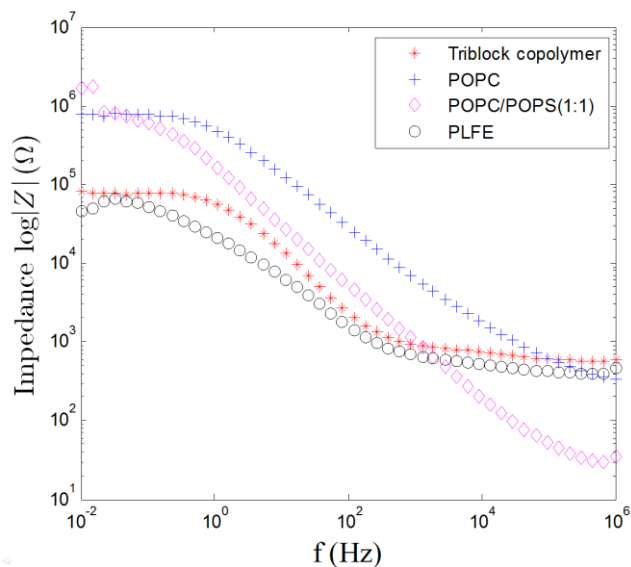


Figure 3-17. Amplitude impedance in Bode plot of the four different materials single membrane.

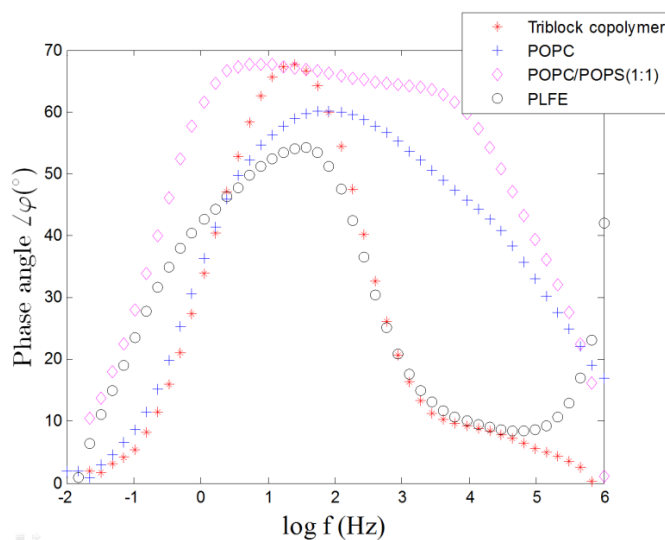


Figure 3-18. Phase frequency response in Bode plot of four different materials single membrane.

In the Bode plot of PLFE, it also showed a phase angle increase at mega hertz range, while triblock copolymer, POPC, and POPC/POPS (1:1) doesn't have the large phase angle difference at 1 MHz. The Bode plots indicated that PLFE and PMOXA-PDMS-PMOXA triblock copolymer are good candidates as dielectric sensor material in capacitive sensor micro devices.

The EIS results of planar membranes on microchip were more stable than the fluidic device on PCB.

### 3.3.3 SPICE simulation results

To verify the experimental results from microchip with planar membranes, I put equivalent resistor and capacitor in SPICE simulation, based on the data from Table 3-1.

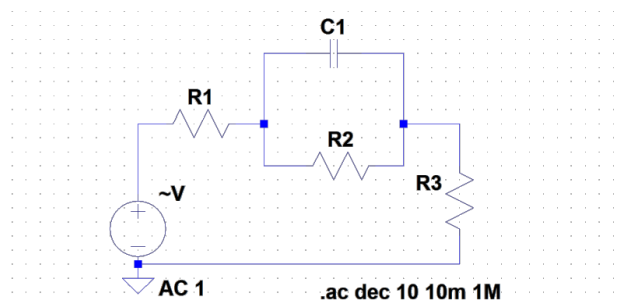
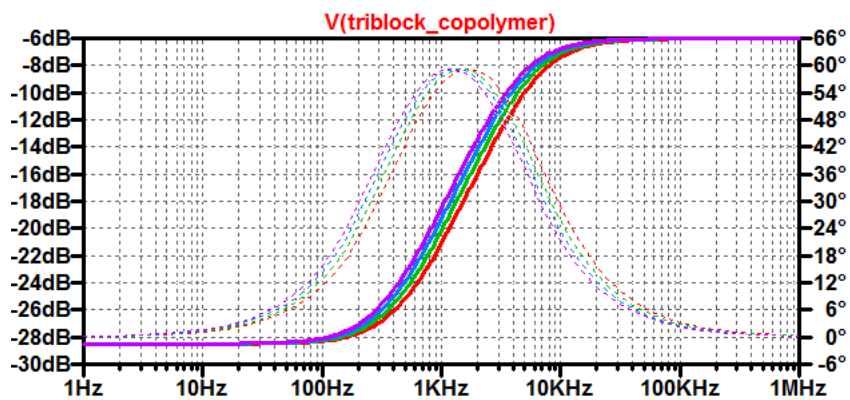
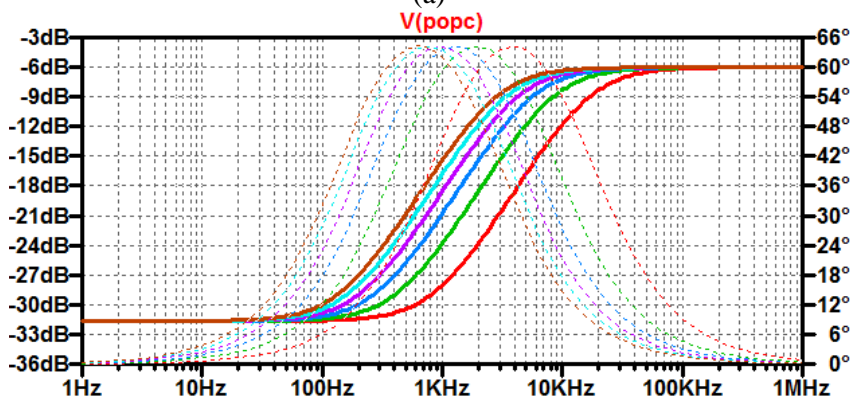


Figure 3-19. LTspice simulation circuit (schematic).



(a)



(b)

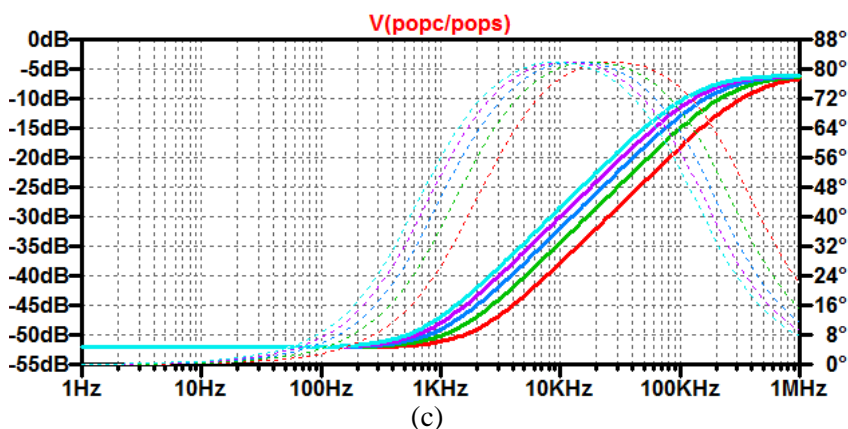


Figure 3-20. Planar membrane Bode plot simulation by LTspice: (a) PMOXA-PDMS-PMOXA triblock copolymer; (b) POPC; (c) POPC/POPS (1:1).

With a sweeping data of capacitor, we can find the range of PMOXA-PDMS-PMOXA, POPC, and POPC/POPS (1:1) are similar to the experimental Bode plot results in Figure 3-17 and Figure 3-18. LTspice can fully shows the simulation results just as Cadence Virtuoso; hence, the integration system simulation can also be designed in LTspice schematically.

### 3.3.4 Control groups for microchip EIS

The microchip EIS includes the impedance information of the microchip itself. The control groups were used to determine the intrinsic impedance, frequency response of the microchip with electrolyte, but no membrane materials presenting. Since the membrane materials were not conductive, the impedance of the experimental devices was significant in impedance amplitude variation and phase shift. On the other hand, the microchip without membrane materials was conductive, because the electrolyte was 1 mol/L KCl solution, which was highly conductive. Even though the small dimension of the electrolyte in microchip cavities, the resistance of the electrolyte was still far less than the resistance of the membrane materials. As for the capacitance of the microchip, the capacitance of microchip was much larger than the capacitance of fluidic chambers on PCB. The two gold electrodes were parallel to the membrane material, that formed a good capacitor structure of two plates with dielectric material between the two plates. Luckily,

according to our equivalent circuit model of this microchip structure, the equivalent capacitor of the microchip was parallel to the membrane's RC model.

In order to rule out the resistance and capacitance data of the microchip itself, we needed the EIS data of an empty group of microchip with electrolyte.

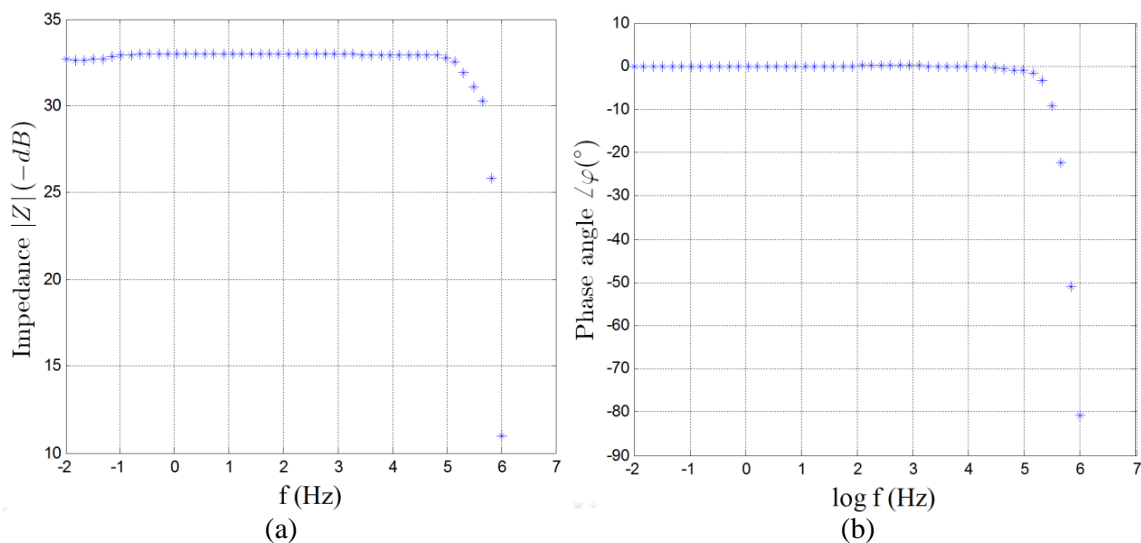


Figure 3-21. Frequency response of empty microchip (a) impedance amplitude; (b) phase angle.

The frequency response of control group represented a amplitude variation and phase angle shift of  $90^\circ$  at 1  $MHz$ . To verify the experimental results, as well as the equivalent circuit of control group or empty microchip with electrolyte only, we used SPICE simulation to test the frequency response of control group.

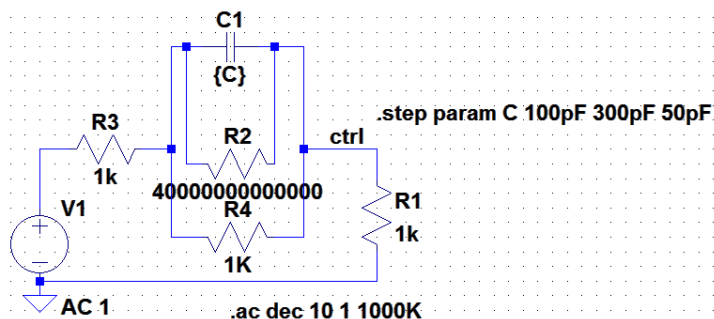


Figure 3-22. Schematic of equivalent circuit of control group.

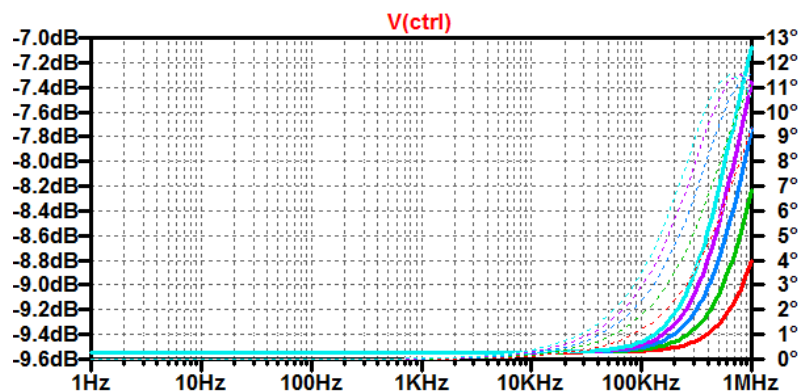


Figure 3-23. SPICE simulation of Bode plot of control group.

The equivalent circuit of control group includes the RC model of microchip and electrolyte with 1 K $\Omega$ . For different capacitance range, we used a variation of microchip capacitance of 100 pF, 150 pF, 200 pF, 250 pF, and 300 pF<sup>5</sup>. The Bode plot of this circuit showed similar amplitude variation and phase angle change at 1 MHz.

### 3.3.5 Dual-membrane EIS results

The dual-membrane structure also can be assembled into microchip devices with top glass cavity and bottom silicon cavity. In our research target, we want to fabricate a two layers of membranes with BR and FoF1 ATP synthase on each layer of membrane, which were both fitted in a micro chip (Figure 3-24).

The membrane with BR can pump the protons from glass cavity into PDMS middle layer chamber. The small volume of PDMS chamber can provide a faster pH gradient change. On the other membrane with FoF1 ATPase, proton gradient activates the ATPase and synthesize ATP in the silicon cavity.

Based on the equivalent circuit in Figure 3-2, dual-membrane can be modeled as two sets of resistor parallel with capacitor, as demonstrated in Voigt's structure [206]. The two semi-circles in Nyquist plot represent two separate membrane along each side of the PDMS thin film.

<sup>5</sup> The run option in schematic “.step param C 100pF 300pF 50pF” represents C variation from 100 pF to 300pF with a step of 50 pF.

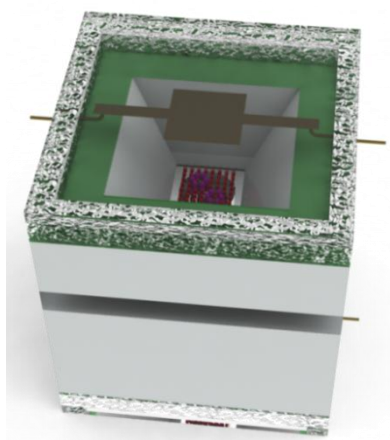


Figure 3-24. Schematic of membrane systems embedded in microchip based on SOI wafer fabrication (SOIMUMP) technique.

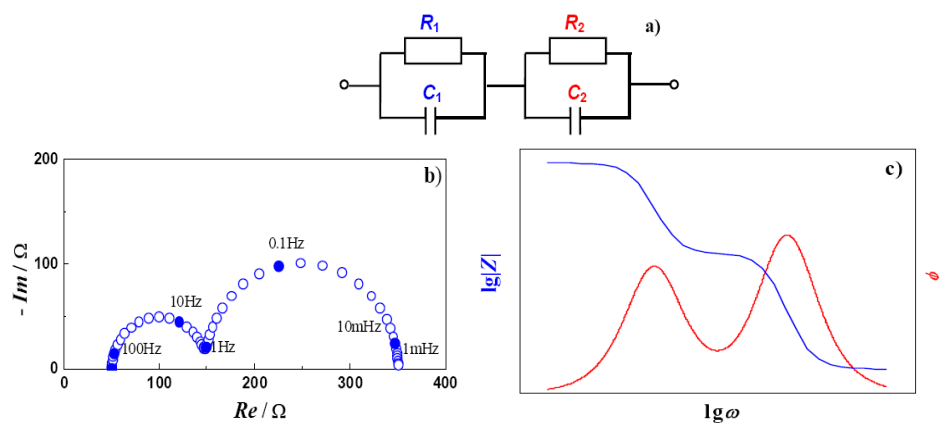


Figure 3-25. Equivalent circuit of two time constants model with Voigt's structure [R/C R/C] (a) and its graphical impedance presentation: complex plane impedance diagram (b); Bode plots (c) [206]. Reuse permission by Springer Science & Business Media.

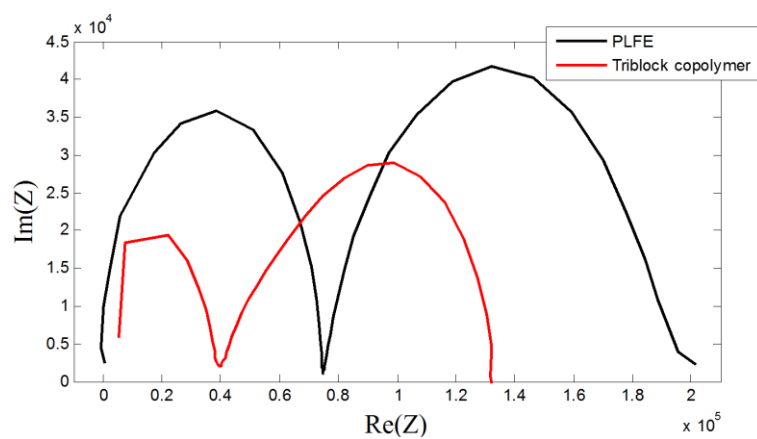


Figure 3-26. Nyquist plot of dual-membrane of two time constants model with Voigt's structure [R/C+R/C]



The Nyquist plot of PLFE and triblock copolymer PMOXA-PDMS-PMOXA fits to the Voigt's structure with different radius of the two hemi circles.

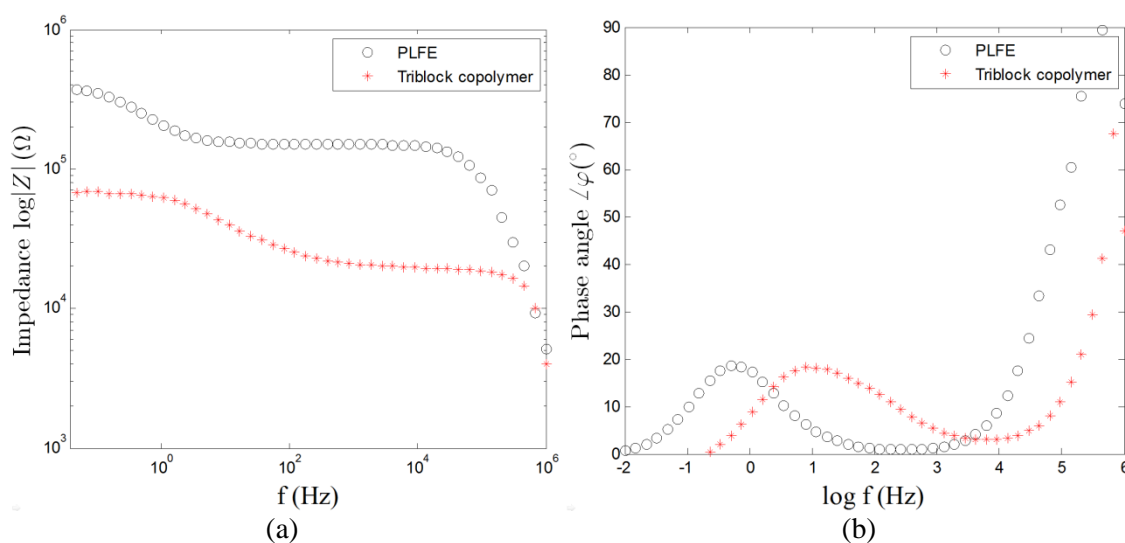


Figure 3-27. (a) Amplitude impedance's frequency response of Bode plot of dual-membrane structure; (b) Phase angle's frequency response of Bode plot of dual-membrane structure.

The Bode plot showed two cut-off frequencies in amplitude impedance's frequency response, and two peak frequencies in phase angle's frequency response; and these two sets of frequencies are equal to each other. The value of this frequency is determined by the materials intrinsic resistance and capacitance, which explains the difference of cut-off frequencies of PLFE and triblock copolymer.

The Nyquist plot was generated for each biomembrane and an equivalent RC circuit was produced based on the best fitting. Based on the experiment data, simulation program with integrated circuit emphasis (SPICE) was used to illustrate the frequency response (Figure 3-20). The Bode plot of the triblock copolymer showed much less variation with the frequency change indicating that the triblock copolymer was more stable than other lipid membranes in terms of frequency response. Another important observation was that the triblock copolymer has a narrower bandwidth (better sensitivity).

### 3.4 Membrane stability EIS results

#### 3.4.1 Definition of stability

The stability can be represented and evaluated by the impedance variance with time. The membrane with higher impedance variation rate represents a lower stability. To define a parameter showing the stability of membranes, we normalized the stability  $\xi$  with the maximum impedance of the certain membrane, so the stability  $\xi$  will be a number between 0 to 1, and higher the  $\xi$  represent a better stability.

$$\text{stability } (\xi) = 1 - \frac{1}{Z_{\text{stable}}} \cdot \frac{dZ(t)}{dt} = 1 - \frac{|Z(t) - Z_{\text{stable}}|}{Z_{\text{stable}} \cdot \Delta t}$$

Eq. 3-15

where  $Z$  is the impedance of a certain membrane, and  $Z_{\text{stable}}$  is the stable value of the membrane, which is closer to the theoretical impedance value of the membrane,  $dZ(t)/dt$  represent the impedance variation by time. In order to find the stable value  $Z_{\text{stable}}$ , we selected the mode (the most common value) of the impedance set, which was the number that shows highest frequency in a  $\pm 2.5\%$  range of the theoretical impedance value.

#### 3.4.2 EIS results for long term

For the long term planar membrane stability study, we chose three kinds of materials: triblock copolymer, PLFE, and POPC. Similar to the EIS measurement of membranes, the stability measurement was carried by the similar parameters on microchip. The input signal was sinusoidal voltage with 100 mV amplitude, and frequency change from 1 MHz to 10 mHz. The resulting current was 5 nA to 10  $\mu$ A. We plotted the 3D figure of EIS data results vs. frequency and time. All experiment were carried by identical microchips with uniform PDMS thin films, and carried in same environment. The higher temperature condition of membranes was achieved by immersing the microchip, wires with banana clips in water bath.

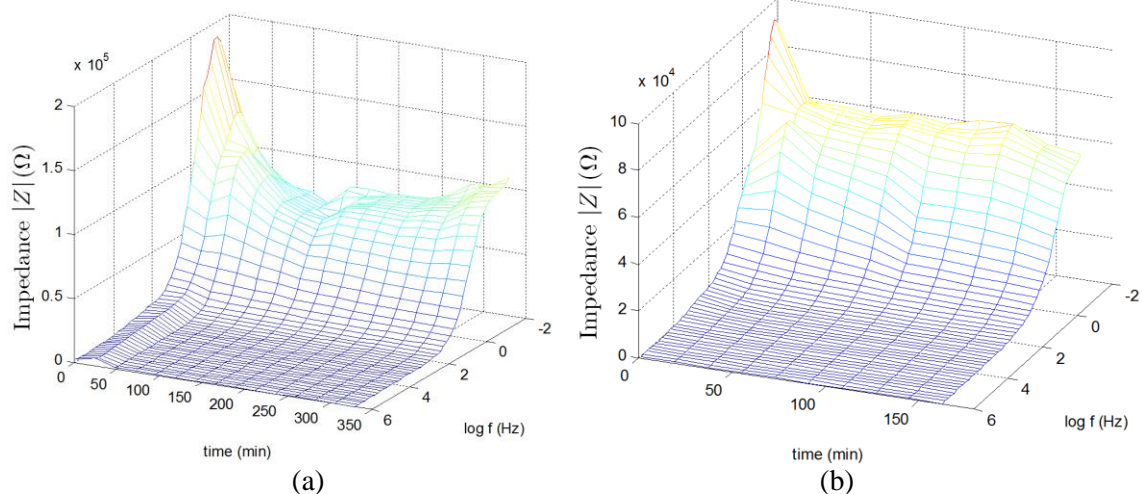


Figure 3-28. Impedance of triblock copolymer at (a) room temperature ( $\sim 23^\circ\text{C}$ ); (b)  $51^\circ\text{C}$ .

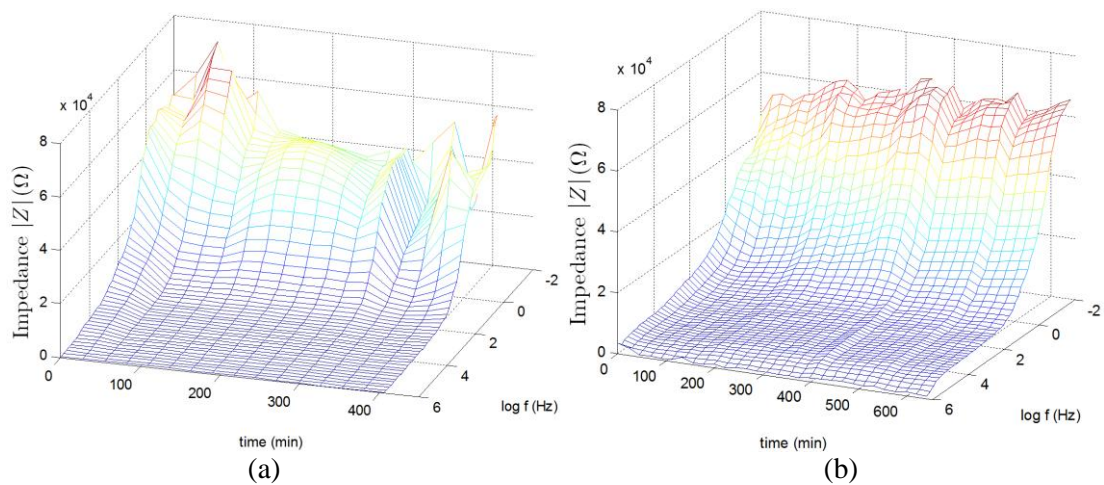


Figure 3-29. Impedance of PLFE at (a) room temperature ( $\sim 23^\circ\text{C}$ ); (b)  $39^\circ\text{C}$ .

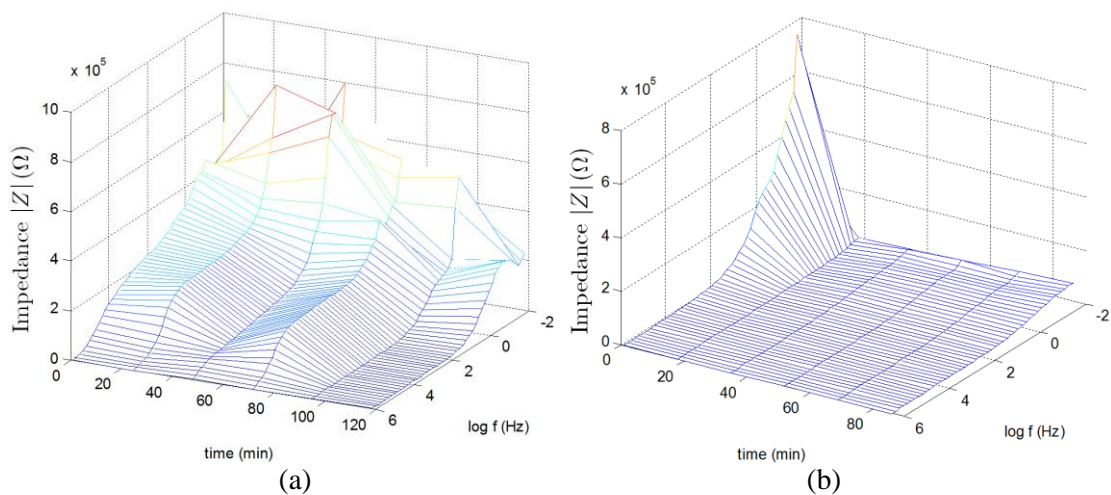


Figure 3-30. Impedance of POPC at (a) room temperature ( $\sim 23^\circ\text{C}$ ); (b)  $50^\circ\text{C}$ .

The PMOXA-PDMS-PMOXA triblock copolymer and PLFE demonstrated a relatively stable status for hours. However, POPC can only keep membrane status within one hour. PLFE at room temperature and  $\sim 40^{\circ}\text{C}$  lasted for 4~7 hours with a stable impedance. External disturbance can cause impedance variation, so we keep the experimental setups stable at water bath. A radio free environment was preferred because electromagnetic waves may cause interference of the AC current collection procedure, because the wires and banana clips worked as antenna to receive electromagnetic wave signals. The PMOXA-PDMS-PMOXA triblock copolymer didn't reach the stable impedance within 30~60 min. Since the triblock copolymer was not natural lipid, the polymerization procedure would consume a certain time to form a stable membrane structure. Besides, the polymerization of middle PDMS chains needs a chemical reaction time during the formation of planar membrane in electrolyte environment. The EIS results of triblock copolymer at room temperature ( $\sim 21^{\circ}\text{C}$ ) or  $51^{\circ}\text{C}$  both showed a higher impedance data at the beginning of membrane formation. If the copolymer had stack of multi-layer or micelles structure on the planar membrane, the dielectric coefficient would be much larger than the single layer planar membrane, so that the impedance data collected by parallel capacitive electrodes would be larger than the planar membrane. The stabilization procedure of triblock copolymer existed in every temperature steps of the EIS experiment on planar membranes. Therefore we can conclude that PLFE was a better choice for constructing planar membrane on microchips. POPC showed the least stable time, especially at higher temperature.

### **3.4.3 Difference materials**

The individual 3D plots demonstrated the trends of each kind of membrane's stability by time and frequencies. To better demonstrate the difference between materials, we plotted different materials' impedance trends at same temperature.

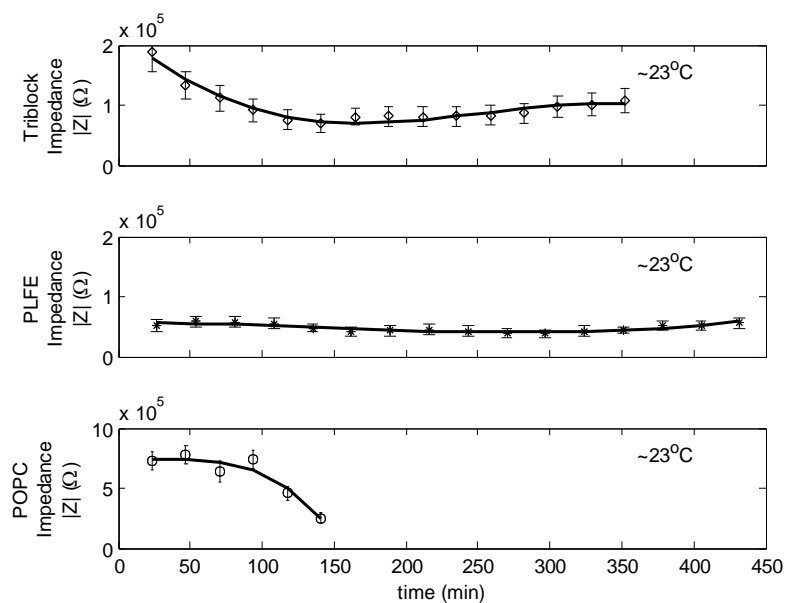


Figure 3-31. Impedance data of different materials at room temperature ( $\sim 23^{\circ}\text{C}$ ).

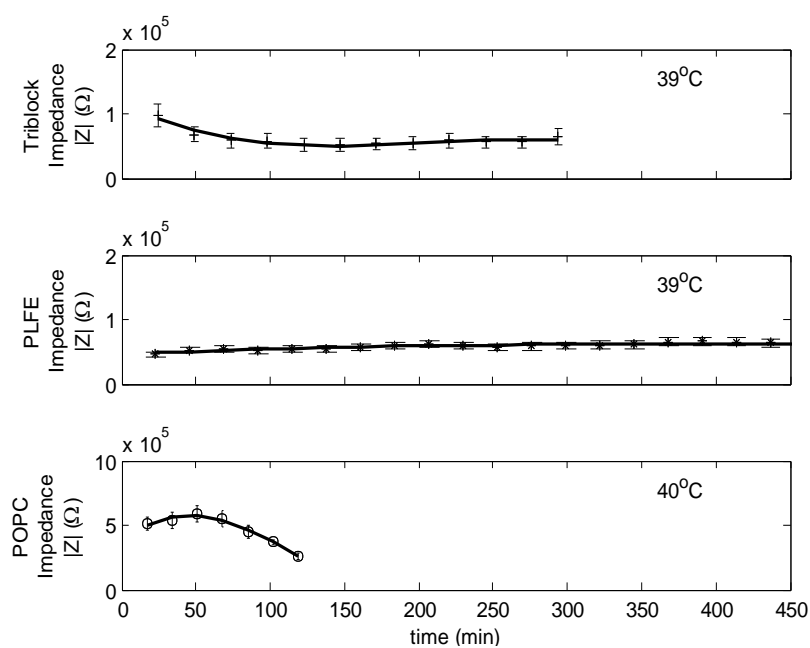


Figure 3-32. Impedance data of different materials at  $\sim 40^{\circ}\text{C}$ .

The trends of PMOXA-PDMS-PMOXA triblock copolymer, PLFE, and POPC were same at both room temperature ( $\sim 23^{\circ}\text{C}$ ) and  $\sim 40^{\circ}\text{C}$ . PLFE had the longest stability, comparing to triblock copolymer and POPC. We further studied the long term stability of PLFE at  $39^{\circ}\text{C}$ .

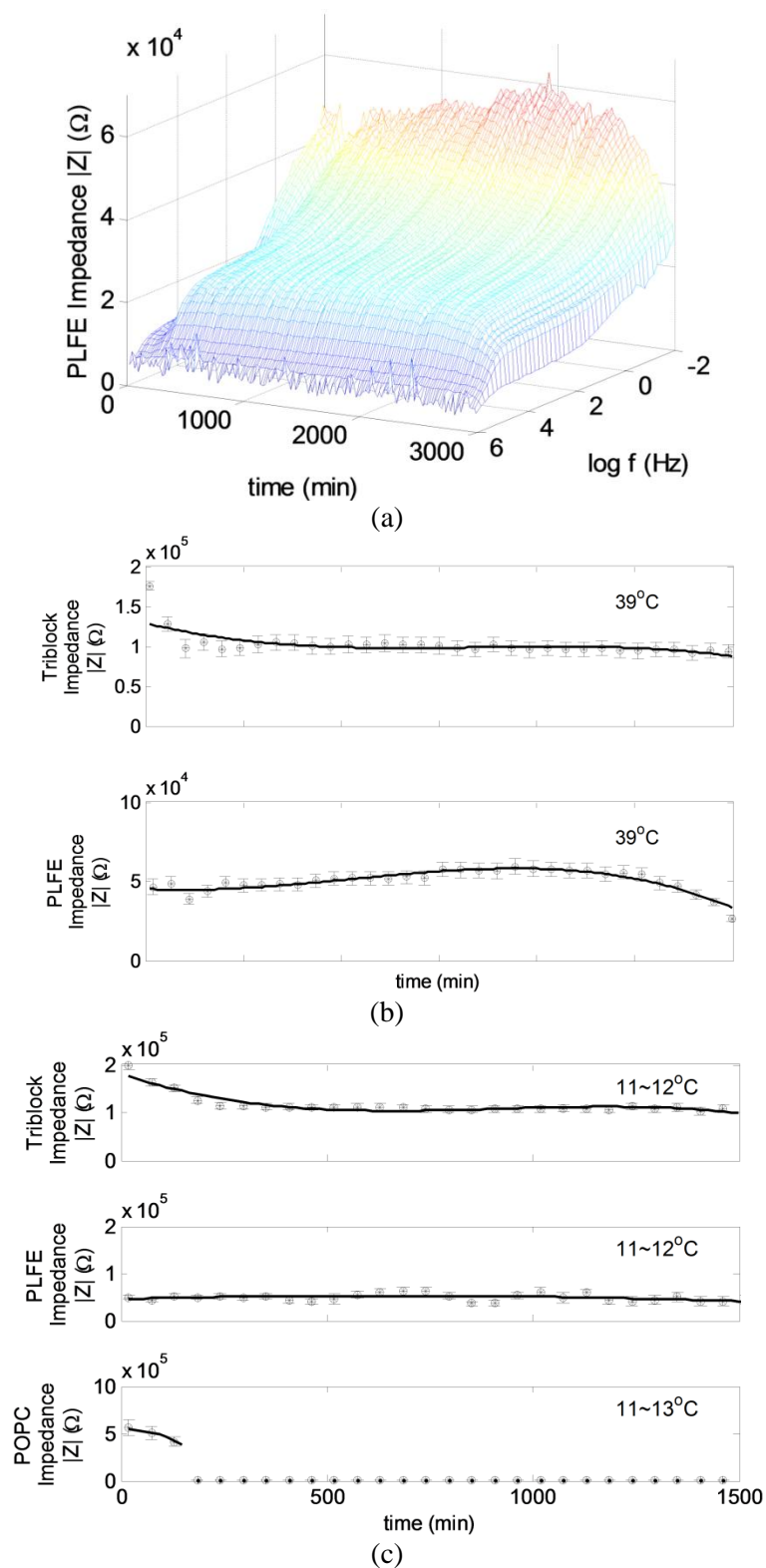


Figure 3-33. (a) Impedance of PLFE at 39°C in long term stability study; (b) Impedance of PLFE and triblock copolymer at 39°C in long term stability study; (c) Impedance of PLFE and triblock copolymer at 11~13°C in long term stability study.

PLFE showed stability at around 50 hours. The decreasing of impedance value was shown after 50 hours, which indicated that the membrane began to decay as stability decreasing.

### 3.4.4 Difference of temperatures

In the mathematical model, we discussed the geometry affects of the membrane stability. Generally, materials mechanical properties was sensitive to temperatures. We put the whole microchip with planar membranes in water bath to achieve higher temperature. We used the concept of membrane stability  $\xi$ , a number from 0~1 to represent the stability of low to high.

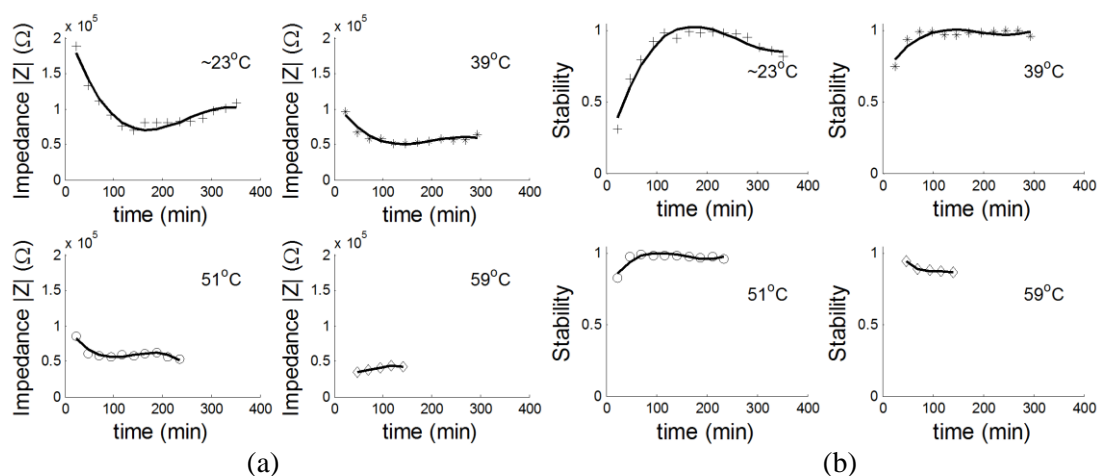


Figure 3-34. (a) Impedance of triblock copolymer at different temperatures; (b) Defined stability of triblock copolymer at different temperatures.

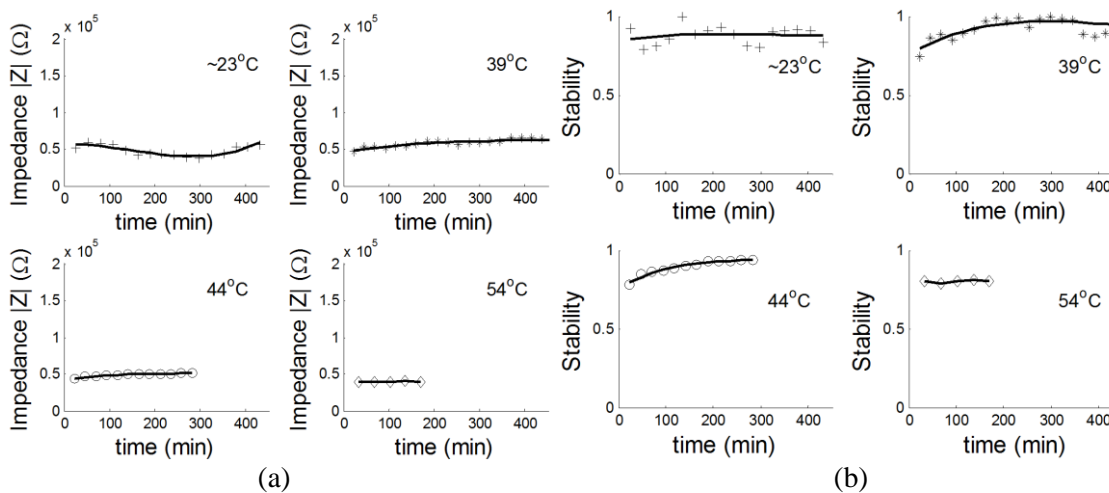


Figure 3-35. (a) Impedance of PLFE at different temperatures; (b) Defined stability of PLFE at different temperatures.

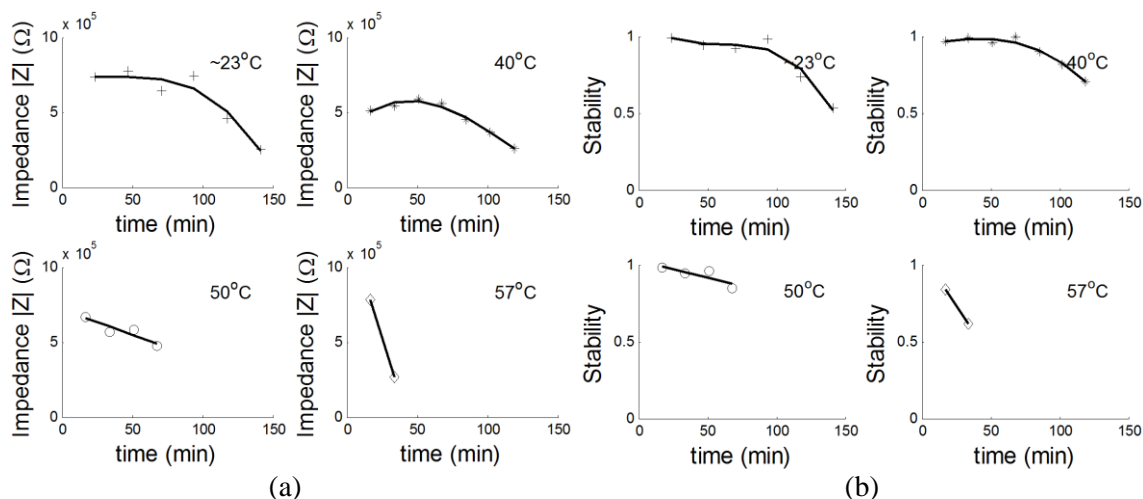


Figure 3-36. (a) Impedance of POPC at different temperatures; (b) Defined stability of POPC at different temperatures.

Both of PMOXA-PDMS-PMOXA triblock copolymer, and POPC showed lower stability at higher temperature. However, PLFE seemed have best stability at the temperature around  $39^\circ\text{C}$ . POPC had the lowest stability in all three materials, and it had almost no stability at higher temperature.

### 3.4.5 Difference in membrane dimension (hole size)

We selected different hole sizes for different membrane materials:  $20\ \mu\text{m}$ ,  $100\ \mu\text{m}$ , and  $200\ \mu\text{m}$ . The  $20\ \mu\text{m}$  holes were drilled by eximer laser, while the  $100$  and  $200\ \mu\text{m}$  holes were made by soft-lithography.

The impedance of membrane was related to the surface area of the membrane itself. Therefore, the impedance data we got included the difference of capacitance value on different hole sizes. The capacitance was proportional to the surface area, that indirectly proportional to the square of hole diameter. The impedance introduced by capacitance was

$$Z_C = \frac{1}{j\omega C}$$



The capacitance of 100  $\mu\text{m}$  diameter membrane was 25 times larger compared to the capacitance of 20  $\mu\text{m}$  diameter membrane; and the capacitance of 200  $\mu\text{m}$  diameter membrane was 4 times larger compared to the capacitance of 100  $\mu\text{m}$  diameter membrane. In order to have a better comparison of the impedance value of the membrane at different hole sizes, we normalized the impedance value to the equivalent impedance value at a hole size of 100  $\mu\text{m}$  in diameter. Hence, the impedance values of 20  $\mu\text{m}$  diameter membrane were divided by 25; while the impedance values of 200  $\mu\text{m}$  diameter membrane were timed by a factor of 4. The unit of these values were the equivalent impedance at a diameter of 100  $\mu\text{m}$ , using the symbol of “ $\Omega/(D=100\ \mu\text{m})$ ”.

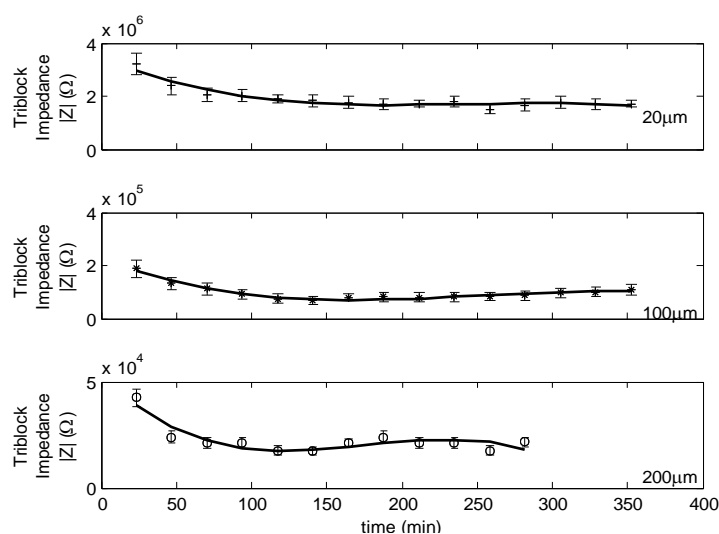


Figure 3-37. Impedance of triblock copolymer with different membrane diameters.

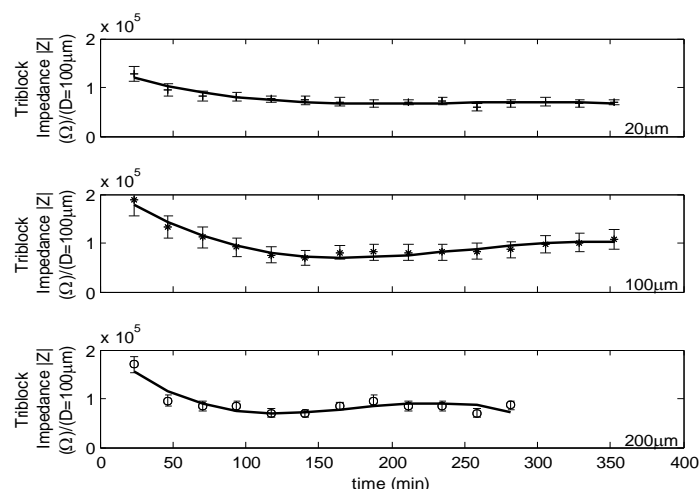


Figure 3-38. Impedance of triblock copolymer with equivalent membrane diameter of 100  $\mu\text{m}$ .

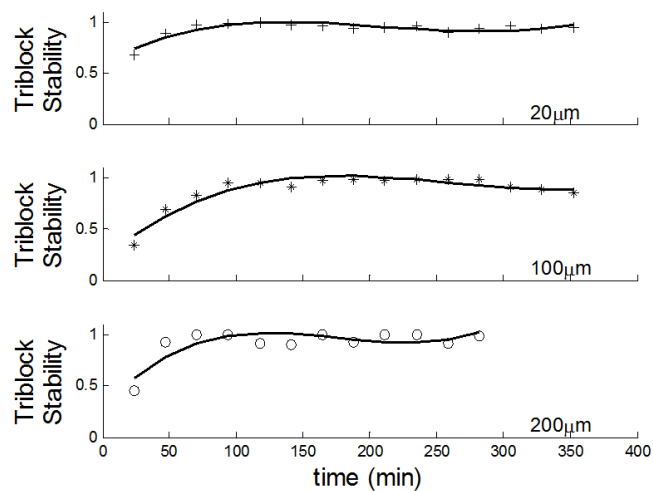


Figure 3-39. Defined stability of triblock copolymer with different membrane diameters.

The PMOXA-PDMS-PMOXA triblock copolymer still showed a higher impedance before stabilization. The smaller hole diameter provided a smaller aspect ratio (diameter to height) of planar membrane.

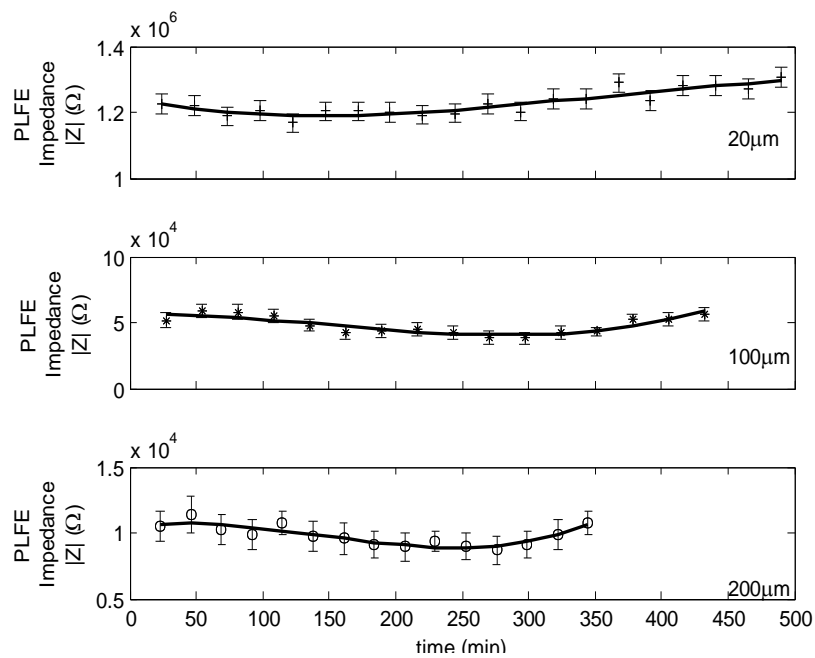


Figure 3-40. Impedance of PLFE with different membrane diameters.

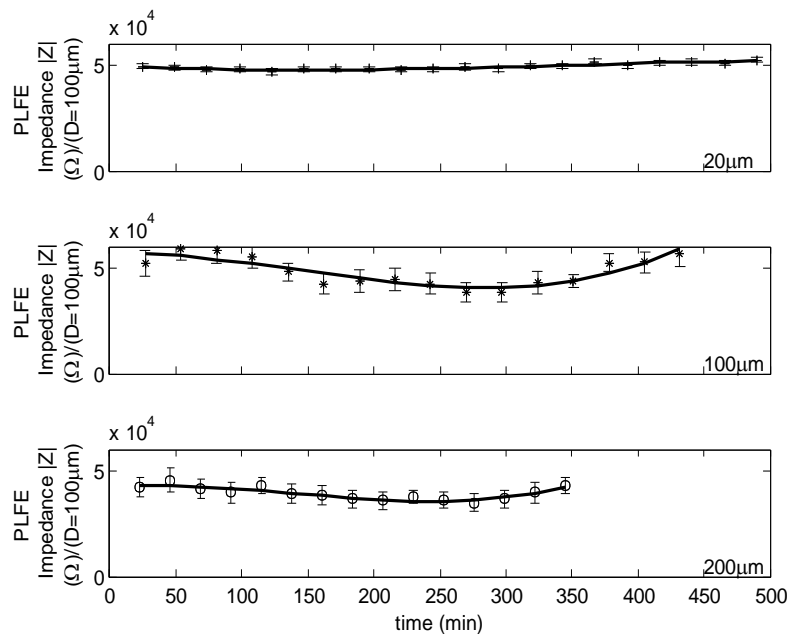


Figure 3-41. Impedance of PLFE with equivalent membrane diameter of 100  $\mu\text{m}$ .

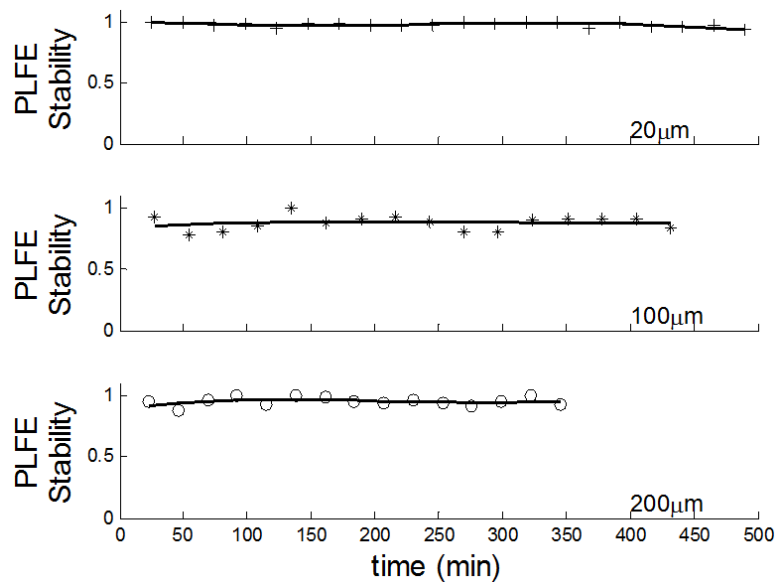


Figure 3-42. Defined stability of PLFE with different membrane diameters.

The PLFE planar membrane demonstrated a relatively stable status in all three different hole diameters. The higher aspect ratio illustrated a lower stability, due to the mechanical strength of Langmuir-Blodgett membranes.

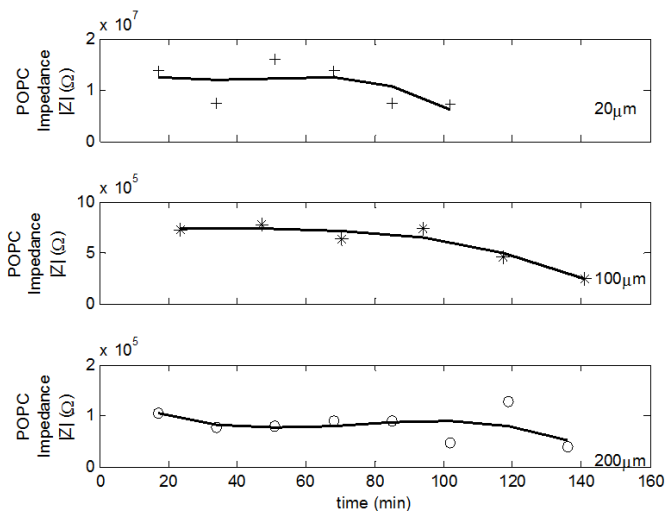


Figure 3-43. Impedance of POPC with different membrane diameters.

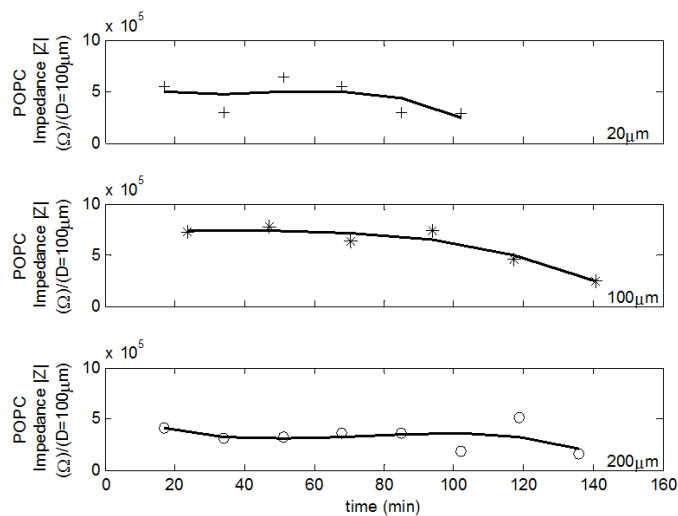
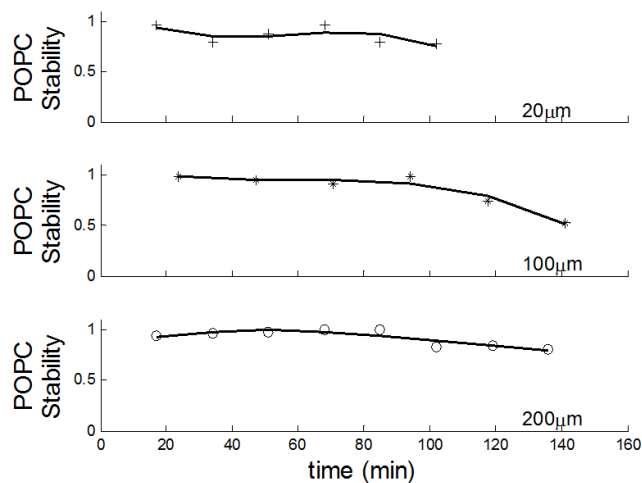
Figure 3-44. Impedance of POPC with equivalent membrane diameter of 100  $\mu\text{m}$ .

Figure 3-45. Defined stability of POPC with different membrane diameters.

POPC at smaller hole size of 20  $\mu\text{m}$  illustrated a shorter stable time. POPC was the least stable membrane material among all three kinds of Langmuir-Blodgett membranes. When the hole size reduced to 20  $\mu\text{m}$ , POPC was harder to form a uniformed Langmuir-Blodgett planar membranes. The POPC was unstable if the planar membrane was incomplete or un-uniform. The stability data of POPC on hole sizes of 100  $\mu\text{m}$  and 200  $\mu\text{m}$  demonstrated a reasonable stability trends, and implied that the POPC membrane was formed in short term.

### **3.5 Proteins in planar membrane**

To mimic or partially mimic the cell function, ion channel is the first step to achieve cell or cell membrane functions. The common protein used for ion channel formation and ion transfer detection are alamethicin and gramicidin [207, 208].

#### **3.5.1 Ion channel protein alamethicin**

The presence of ion channel in membrane on microchip can realize partial of the cell functions. Alamethicin (Sigma Aldrich) is a trans-membrane peptide (20-amino acid peptide antibiotic) with ability of ion transfer [207, 209-211]; however, the status of open or close of the ion channel is voltage-dependent [212-215]. The common ion channel for mimicking ion channel includes alamethicin, gramicidin, and BR, etc [216]. Once a planar membrane was formed by Langmuir-Blodgett method, the side by dropping the planar membrane with extra cover on the membrane support was referred as *cis* side, while the opposite side was called *trans* side. Alamethicin was required to added to the *cis* side of the membrane [88, 217]; gramicidin needed to be added at both *cis* and *trans* sides of the membrane [88]. Bacteriorhodopsin is a protein with proton transfer ability after absorbing the energy from green light, which is commonly used in artificial photosynthesis for ATP synthesis [69, 71, 75, 218]. The transfer of metallic ions like potassium is mimicking the ion transfer function of cell membrane. In this paper, we report the function of potassium ion transfer using alamethicin.

### 3.5.2 Experimental procedure

Alamethicin was dissolved in ethanol solution with water at a concentration of 5.09  $\mu\text{mol/L}$ . To achieve a final concentration of  $\sim 10^{-7}$  mol/L, around 10 times of electrolyte solution was mixed with alamethicin solution, and distributed on the *cis* side of the membrane after the PLFE membrane was formed on the middle layer PDMS hole.

Similar to the planar membrane experiment, we used microchip with Bio-Logic SAS instrument (model VSP, Claix, France) for cyclic voltammetry<sup>6</sup> (CV) and chronoamperometry /chronocoulometry<sup>7</sup> (CA) test for current. The equipment has a voltage range of 20 V with a resolution of 5  $\mu\text{V}$ , current range of 10  $\mu\text{A}$  to 1 A, and low current range of 1  $\mu\text{A}$  to 1 nA with a resolution of 76 fA.

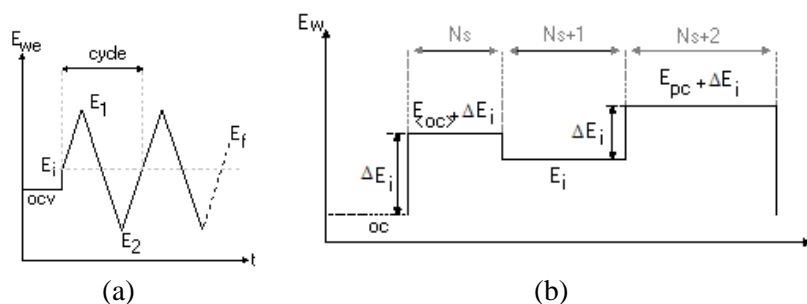


Figure 3-46. (a) CV input signal; (b) CA input signal.

In the CV settings,  $E_i$  was the middle line of the voltage input,  $E_1$  and  $E_2$  were the upper limit and lower limit of the voltage input, defined as  $\pm 150$  mV in CV experiment. The repeat times was set as 3 times, and current was recorded at last 50% of the step duration. The sweeping speed was 10 mV/s.

<sup>6</sup> CV is the most widely used technique for acquiring qualitative information about electrochemical reactions. CV provides information on redox processes, heterogeneous electron-transfer reactions and adsorption processes. It offers a rapid location of redox potential of the electroactive species. CV consists of scanning linearly the potential of a stationary working electrode using a triangular potential wave form. During the potential sweep, the potentiostat measures the current resulting from electrochemical reactions. The cyclic voltammogram is a current response as a function of the applied potential.

<sup>7</sup> The basis of the controlled-potential techniques is the measurement of the current response to an applied potential step. Chronoamperometry involves stepping the potential of the working electrode from an initial potential, at which no faradic reaction occurs, to a potential  $E_i$  at which the faradic reaction occurs. The current-time response reflects the change in the concentration gradient in the vicinity of the surface.

In the CA settings, the  $E_i$  was related to the reference  $V_{ref}$  with +70 mV. The time was set to 2 seconds, and data was recorded every 0.02 s.

### 3.5.3 Experimental results

Alamethicin was added to top side of the membrane with a final concentration of  $2.54 \times 10^{-7}$  mol/L. We used the same microchip for ion channel formation and ion transfer detection. Alamethicin is voltage dependent ion channel protein, so we used CV triangular wave voltage signal with peak voltage of  $\pm 100$  mV, with a sweeping speed of 10 mV/s.

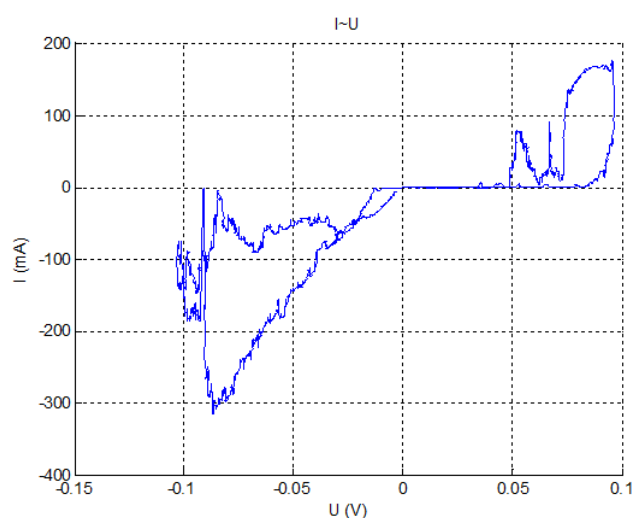


Figure 3-47. Current-voltage curve of alamethicin on planar membrane in microchip in CV experiment.

The open and close status of alamethicin ion channels on membrane is random, so we used CA with a constant voltage of 70 mV for 2 seconds per cycle. We recorded current data every 0.02 s. We deposited the alamethicin at *cis* side of the planar membrane, therefore the threshold of two sides were different. Alamethicin model was established by the voltage-dependent current response, with four to six molecules forming an ion channel [217]. The current-voltage curve by sweeping rate around 20 mV/s demonstrated a difference between rising and falling of the voltage, which was also shown in our experiment in Figure 3-47. The threshold voltage was related to the concentration of alamethicin and the concentration of electrolyte [217].

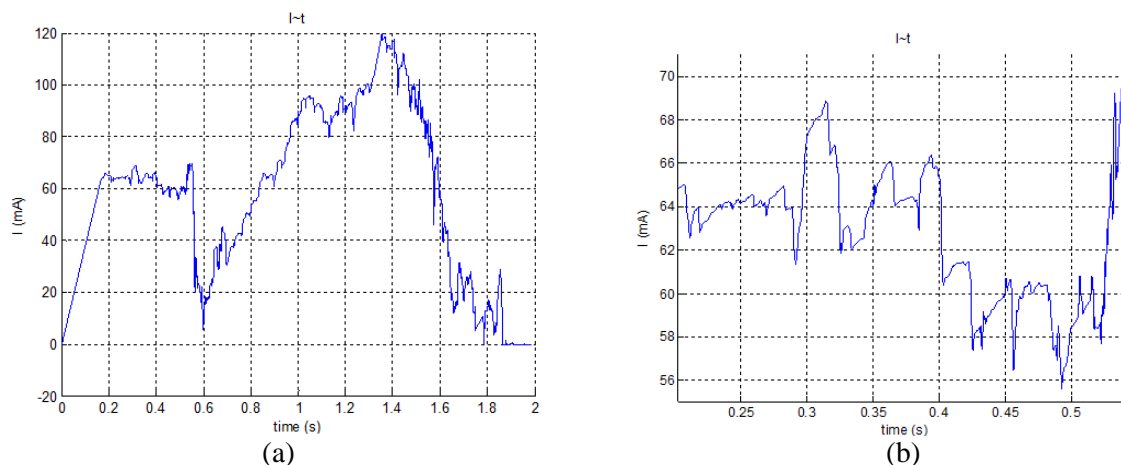


Figure 3-48. Current trace of alamethicin ion channel on planar membrane in microchip in CA experiment: (a) 0~2 s; (b) 0.2~0.55 s.

Alamethicin was a peptide that integrated into the PLFE membrane voluntarily. The experiment of recording current trace can show the single pore channels at nano sized BLM. Based on the current trace and correlated current histogram, the opening status of alamethicin ion channels can be revealed [88]. The CA experiment was carried in the same situation as CV experiment. The constant voltage was set as +70 mV, which was larger than the activation voltage of alamethicin ion channels. However, the quantity of the ion channels opening was randomly distributed among the lipid membrane surface. According to the current-time curve within several seconds in Figure 3-48, the current response illustrated quantum steps of current, which represented the quantities of the opening ion channels. The multi-level current can be counted for histogram to demonstrate the opening status of ion channels among the membrane.

Based on the current data from 0~2 seconds, we calculated the frequency numbers of each current range as the corresponding current amplitude histogram. Similar to the ion channel on black lipid membranes, the alamethicin also generated ion channels on PLFE membrane in a microchip. However, to determine the properties of the ion channels other than alamethicin, such as BR and ATPase, further experiments are necessary with multiple conditions, such as the protein concentration, electrolyte composition, temperature, pH, and membrane dimensions, etc.



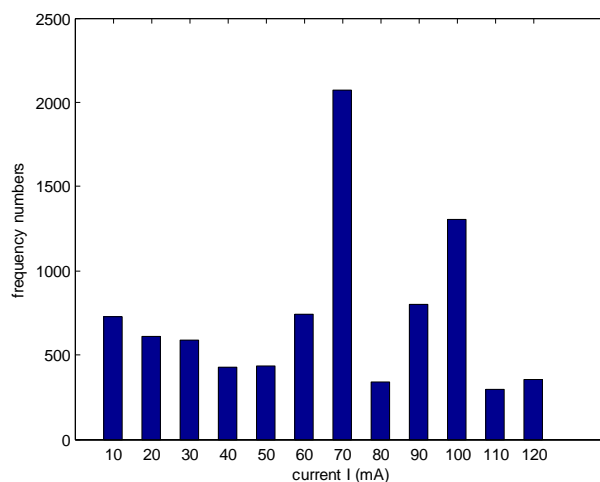


Figure 3-49. Corresponding current amplitude histogram within 2 s in CA experiment.

### 3.5.4 Further experimental device

The micro devices were suitable in EIS testing planar membrane properties; however, in ion channel testing, we need a larger volume of electrolyte to provide sufficient protein concentration in forming ion channels. Therefore, I designed new larger scale fluidic devices for ion channel testing with the capability of forming different diameters of membranes.



Figure 3-50. Photo of PCB fluidic testing board for ion channels on planar membrane.

The new device was PCB based fluidic platform similar to larger scale planar membrane testing described before. The connections were user-friendly and good for demonstration and

measurement. Each unit was measured as 1 inch by 1 inch, and the compartment in each unit was  $1\text{ cm} \times 1\text{ cm} \times 4\sim 5\text{ mm}$ . Each mold had four fluidic channels for the convenience of injecting electrolyte and venting. The top observing window can be used to paste lipid material onto the middle layer PDMS with small hole in it. Copper / nickel electrodes were embedded in PCB and connected to common power input/output. The wire layout of units were designed to reduce capacitance and interference between testing units and groups with electric signals  $<150\text{ MHz}$ . The maximum wire resistance was measured as  $\sim 0.71\ \Omega$ .

## **3.6 Contributions**

### **3.6.1 Planar membrane stability**

The EIS data of three different membrane materials, PMOXA-PDMS-PMOXA triblock copolymer, PLFE, and POPC, were studied and recorded. Based on the equivalent circuit of membrane on the micro device, we established a database of the membrane materials' frequency response that range from 1 MHz down to 10 mHz, as well as the current, resistance, capacitance and time elements. All data were recorded following the mathematical principles of data processing and theory of possibilities.

In addition to plotting the images and fitting the curves in Nyquist plot and Bode plot, I used 3D mesh to represent the stability of planar membrane materials. The trends can better demonstrate the stability trends over time. By the new definition of the stability of the planar membrane, the figures can indicate the stability trends of a single membrane material.

### **3.6.2 Microfabrication method improvement**

The fabrication of micro devices involves microfabrication on silicon, glass, and PDMS, as well as dicing and assembling. Two major improvements were made in the microfabrication methods of the device components.

First, I improved the PDMS replica molding in middle layer PDMS fabrication. The double-sided replica molding can prevent the formation of cliff structures due to the surface tension and capillary effect of the uncured PDMS mixture. The introduced sacrificial layer S1813 was important for PDMS release from the two aligned molds.

Second, the method of lifting the PDMS middle layer from petri-dish to form a planar membrane was extended to forming a dual-membrane structure. The formation of two parallel membranes on a micro device can improve the biochemical functions of the micro device with proper membranes and functional membrane proteins. EIS data of the dual-membrane were also collected for comparison with the single-membrane structure. PLFE and triblock copolymer showed better dielectric properties in forming a planar membrane on a micro device.

### **3.6.3 Planar membrane on microchip with ion channels**

Alamethicin was embedded in the PLFE membrane on a micro device and formed ion channels through the planar membrane. Before adding BR and ATPase onto the membrane, we first used a simple ion channel to demonstrate ion transfer abilities on planar membranes. Alamethicin, gramicidin and BR have similar properties. The CA and CV experiments on alamethicin displayed an ion channel, which also proved that the micro devices were able to test ion channels. Further experiments with BR or ATPase can be performed in a similar way with fluorescence testing for ATP production.

## Chapter 4. DARK REACTION UNIT: CO<sub>2</sub> ABSORPTION

The photosynthesis requires CO<sub>2</sub> and water supply. Water is absorbed by plant roots, while the gas exchange mechanism in plant leaf relies on stoma formed by two guard cells. The area of stomata are around 1% of the area of leaf; however, the evaporation ability of stomata can reach 50~100% compared to the water evaporation ability with same area of water [6]. The task in this chapter is to achieve this gas exchange function in artificial photosynthesis system, mimicking the stomata function from lotus leaf [219]. This chapter contains published contents from Hilton Head conference 2014 [220] and MicroTAS conference 2015 [221].

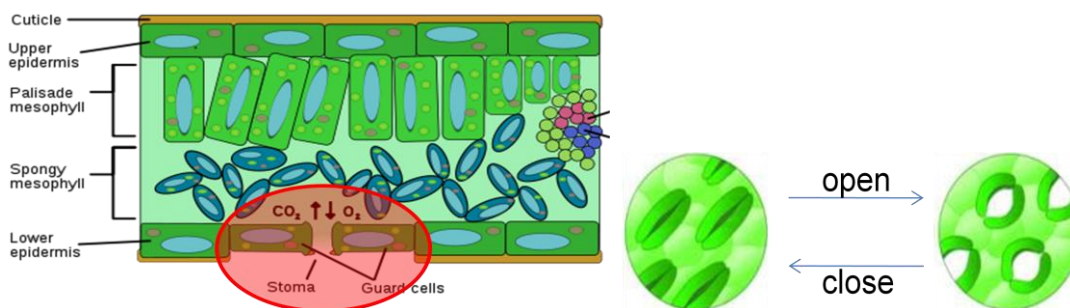


Figure 4-1. Dicotyledons (or dicots) leaf structure: a typical C<sub>3</sub> plant leaf cross-section view [5]. Reproduced with permission from MacMillan.

Some microfluidic devices require specific gas composition in liquid. For example, microfluidic platforms for cell culture [222, 223], organ on a chip systems [224-226], and cell-based sensing devices [227] require oxygen and carbon dioxide exchange for the metabolism of the cells. Another example is an artificial photosynthesis system for energy harvesting that requires constant supply of CO<sub>2</sub> [228, 229]. With the rapid growth of these research areas, there is an increasing need for effective gas-liquid interfaces in microfluidic devices.

Currently, creating a gas-liquid interface in microfluidic channels remains challenging [230-233]. There are two approaches to provide a desired gas composition in liquid in microchannels. One is to generate gas bubbles in microfluidic systems [234-236]; the other is to let the gas diffuse into fluidic channels through semi-permeable or porous materials [237]. The bubble

generation approach is relatively easy to implement [238-242], but the bubbles can interrupt the fluid flow [243, 244] and also affect cellular metabolism, causing cell damaging [245]. Thus, diffusion through semi-permeable or porous materials is preferable in most applications. Various materials have been explored for this purpose including protein thin film [28], hollow fibers or filters [246], and polymers membranes such as PDMS [247, 248]. PDMS-based microfluidic devices can utilize the gas permeability of the PDMS itself as a thin film structure [225, 247, 249]. Multiple bonding choices can be applied to different structures with same material. The gas permeability through PDMS from high to low is in the order as: toluene, trichloroethylene, dimethyl sulfide, ethylene, carbon dioxide and oxygen [250, 251]. PDMS is most commonly used because of its relatively high gas permeability and convenient manufacturability via replica molding. However, in order to achieve sufficient gas diffusion through PDMS, it has to be a thin membrane, which is not desirable in some applications due to the lack of structural rigidity. Here we present a novel method of creating a gas-liquid interface using porous PDMS and demonstrate its utility in an artificial photosynthesis system.

We present a novel method of creating a gas-liquid interface using porous PDMS, especially for artificial photosynthesis system. Porous PDMS provides enough contact between gas and liquid media while effectively preventing water leakage and evaporation due to its hydrophobic property [252].

We used sugar leaching method to make porous PDMS cubes, and starch leaching method to make porous PDMS film. The sugar cubes are sugar particles with interconnected empty spaces. Liquid PDMS elastomer with curing agent can fill into the empty spaces among sugar particles. After the PDMS curing, the sugar can be removed by hot water. Rice paper is a porous film of starch, which can be cut into dissolvable monomer glucose with the presence of amylase.

We reported different structures of porous PDMS in either cube structure or film structure. To study the feasibility of porous PDMS as interface media, carbon dioxide absorption was analyzed, and further dark reactions in photosynthesis was performed in microchannel with porous PDMS.

First, we demonstrated a microfluidic device with connected porous PDMS cubes exposed to air. We had a fluidic channel volume of 600  $\mu\text{L}$  to meet the requirement of chemical reactions and detection for pH and further glucose synthesis. The pH was detected by Matlab video and image processing. Then, we used porous PDMS film to compare with porous PDMS cubes for absorbing the  $\text{CO}_2$  from air. Even though the microchannel with porous PDMS film had higher  $\text{CO}_2$  absorption rate, the microfluidic channels with porous PDMS cubes absorbed  $\text{CO}_2$  from air continuously for hours with little liquid evaporation. Therefore, we selected fluidic channel with porous PDMS cubes for the biological reactions of an artificial photosynthesis with glucose synthesis. We used BR-ATP synthesis triblock copolymer vesicles as light reaction source for ATP synthesis, and used carbon fixation enzyme RuBisCO with glucose catalyzing isomerase to produce glucose from  $\text{CO}_2$  and water. The glucose produced in static flow in 4 hours was 3.525  $\mu\text{g/mL}$ ; and the glucose concentration in dynamic flow of 50  $\mu\text{L/min}$  in 3 hours was 5.559  $\mu\text{g/mL}$ . The experimental results indicated that our gas-liquid interface made with porous PDMS cubes could allow  $\text{CO}_2$  penetration constantly to the liquid mixture to perform glucose synthesis reactions.

## **4.1 Gas permeability and diffusivity in gas-liquid interface**

The gas permeability and diffusivity of an interface material is critical under a gas-liquid exchange structure. Our liquid environment is neutral, even though  $\text{CO}_2$  have higher absorption ratio in alkaline solutions [253, 254]. Our experiments of  $\text{CO}_2$  diffusion in porous PDMS was done by analyzing the absorbing ratio of  $\text{CO}_2$  in solution. Theoretical model of gas diffusion in porous media had been developed several decades before [255, 256].

## **4.2 Porous PDMS and sugar leaching**

### **4.2.1 Porous PDMS cubes fabrication**

We prepared two different kinds of porous PDMS structures: cubes and films. The

microfluidic device with gas channel and liquid channel will be using porous PDMS discs, which was cut from porous PDMS cube. The microfluidic channel bonded with porous PDMS film was an molded PDMS channel attached to one piece of porous PDMS film on the bottom side.

First, porous PDMS cubes were fabricated by sugar leaching technique where sugar cubes were used as sacrificial materials [230]. The sugar particles in sugar cubes were connected together; therefore, the created porous PDMS had interconnected micro pores after the removal of sugar. PDMS pre-polymer and curing agent were mixed at 10:1 mass ratio and degassed in vacuum. Sugar cubes ( $15 \times 15 \times 10 \text{ mm}^3$ ) were then immersed in the mixture with a depth of 3 mm in a vacuum container for 1 hour allowing the sugar cubes fully filled with PDMS by capillary effect. The PDMS with sugar cube was then cured in an oven at  $60^\circ\text{C}$  for 24 hours.

To prepare the porous PDMS disc, the cured PDMS-sugar cubes were cut into a cylindrical disc shape (diameter = 3 mm, height = 2 mm) and washed in  $50^\circ\text{C}$  water to remove the sugar followed by air dry.

Two main properties that characterize porous structures are porosity and average pore size. The average pore size could be roughly observed by the optical microscope image of the cross-section of the porous PDMS, which was around  $150\sim 200 \mu\text{m}$ , mainly depends on the sugar particle size. The porosity was defined as the empty space volume over the total volume of a material. By measuring the mass of a certain block of porous PDMS, we could calculate the existing PDMS volume (the density of pure PDMS is  $0.965 \times 10^3 \text{ kg/m}^3$ ). The PDMS block's volume was measured by the out profile's dimensions. We measured 20 different porous PDMS samples to reduce the errors. The porosity of the porous PDMS was calculated as  $69.8 \pm 0.2\%$  (the density of original PDMS is  $0.965 \times 10^3 \text{ kg/m}^3$  after curing) .

#### **4.2.2 Porous PDMS film fabrication**

The porous PDMS film requires similar leaching technology as the fabrication of porous PDMS cube. In order to create porous film, we need to use a dissolvable porous film as sacrificial

material, and rice paper became a good candidate for this purpose.

Sugar leaching technique was very simple but cannot produce a film structure, which was often desired for gas-liquid interface. Especially we wanted to create a microfluidic channel with porous PDMS film on one side for gas-liquid interface by air.

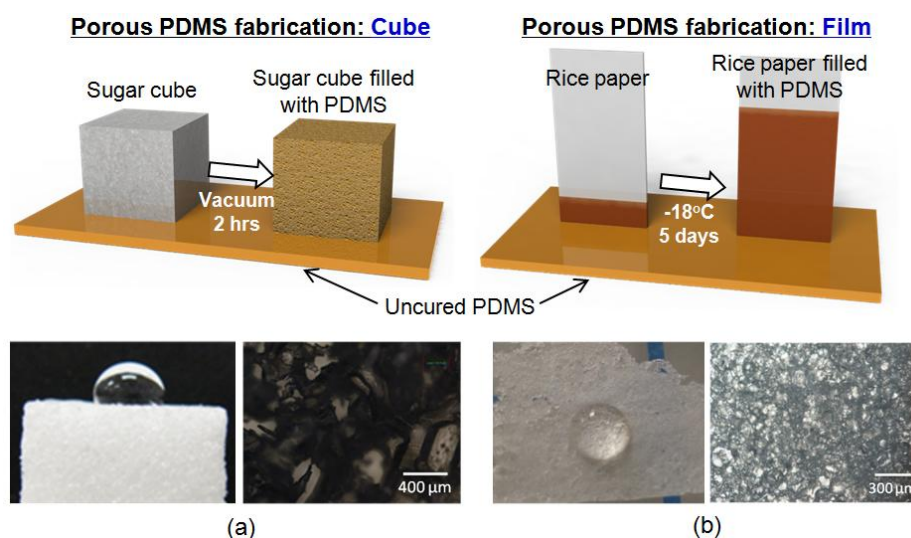


Figure 4-2. Illustration of facilitating capillary rise of PDMS in sugar cube and rice paper. (a) Hydrophobic surface of porous PDMS cube; (b) Optical microscope image of porous PDMS cube; (c) Hydrophobic surface of porous PDMS film; (d) Optical microscope image of porous PDMS thin film.

Inspired by the sugar leaching technique, we used porous rice paper as sacrificial material to create porous PDMS films. Edible porous rice papers are commonly used for wrapping foods and candies. Although they have a highly porous structure, it turned out that the capillary rise of PDMS in rice papers was much slower than in sugar cubes. This may be because the pores are not as well interconnected as in sugar cubes. As a result, PDMS was cured while it was still climbing through the rice paper by capillary force. In order to overcome this issue, we conducted the capillary filling step in a freezer at  $-18^{\circ}\text{C}$ . This way curing was prevented until capillary filling was completed in the rice paper (width: 2 cm; length: 6 cm). After 5 days, the PDMS-rice paper composite material was moved to an oven for curing at  $60^{\circ}\text{C}$  for 4 hours. Finally, the rice paper was dissolved in 10%  $\alpha$ -amylase at  $36^{\circ}\text{C}$ , followed by rinsing the film in deionized water to fully remove the remaining  $\alpha$ -amylase. Then the porous PDMS film was stored in a clean environment



for air dry.

The capillary effect in porous media was different from the case in microchannels [257, 258]. The rising time of liquid in porous media was proportional to the square root of immersing time. It turned out that the capillary rise of PDMS in rice papers was much slower than in sugar cubes. As a result, curing occurred before filling the desired area with PDMS at room temperature, because PDMS mixed with curing agent would be cured in 2 days at 25°C (Table 4-2). In order to overcome this issue, we kept the setup of rice paper hanging with one ending immersed in liquid PDMS mixture in a freezer at -18°C. This way curing was prevented while capillary rise was completed to fill the desired area of rice paper (width: 2 cm; length: 6 cm). After 5 days, the PDMS-rice paper composite material was moved to an oven at 60°C for 4 hours. Finally, the rice paper was dissolved in 10%  $\alpha$ -amylase at 36°C, followed by rinsing the film in DI water to fully remove the remaining  $\alpha$ -amylase. Then the porous PDMS film was stored in a clean environment for air dry.

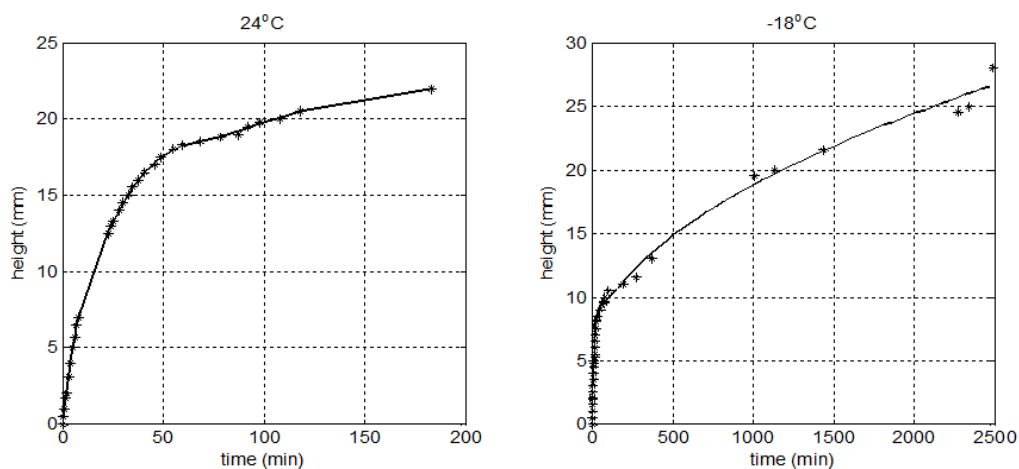


Figure 4-3. Capillary effect of uncured PDMS on porous rice paper at room temperature (24°C) and freezer (-18°C).

As long as the PDMS remained liquid status, the capillary effect would continue in the porous rice paper. According to the theory of capillary effect in porous media, the height of absorbed PDMS was proportional to the square root of time.

The volume of absorbed liquid was

$$V = A \cdot S \cdot \sqrt{t}$$

Eq. 4-1

where A was the cross-section area of porous media to liquid; S was the sorptivity of medium. In this situation, the S was the coefficient between PDMS liquid to sugar cube or porous rice paper. The size of the rice paper of  $67.2 \times 35.6$  mm was around 0.2 g.

Table 4-1. Thickness measurement of porous PDMS film.

Quantity	Thickness (mm)	Average thickness (mm)
1	0.11	0.11
2	0.22	0.11
3	0.35	0.1167
4	0.47	0.1175
6	0.71	0.1183

The average thickness of porous PDMS film was  $0.1145 \pm 0.0041$  mm. Considering the PDMS density of  $0.965 \times 10^3$  kg/m<sup>3</sup>, the porosity of porous PDMS film was

$$\phi = 1 - \frac{m/\rho}{vol} = 1 - 0.7866 = 21.3\%$$

Eq. 4-2

For porous PDMS film, cross-section area was

$$A_{\text{film}} \approx 67.2\text{mm} \times 0.11\text{mm}$$

Eq. 4-3

Comparing to porous PDMS cube with porosity of  $69.8 \pm 0.2\%$ , the cross-section area of porous PDMS cube was

$$A_{\text{cube}} \approx 10\text{mm} \times 10\text{mm}$$

Eq. 4-4

For porous media,

$$\phi \cdot A \cdot h(t) = A \cdot S \cdot \sqrt{t}$$

Eq. 4-5

So

$$h(t) = \frac{S}{\phi} \sqrt{t}$$

Eq. 4-6

therefore, the porous PDMS cube with larger porosity will have slower PDMS rising speed.

Based on the polynomial fitting of the capillary PDMS rising in porous media, we can get the height (h, mm) to time (t, min) relationship in liquid PDMS absorption.

$$\begin{cases} h = 4.42\sqrt{t}, & \text{porous PDMS film at } 24^{\circ}\text{C} \\ h = 0.31\sqrt{t}, & \text{porous PDMS film at } -18^{\circ}\text{C} \\ h = 1.29\sqrt{t}, & \text{porous PDMS cube at } 24^{\circ}\text{C} \end{cases}$$

Eq. 4-7

The fitting curve was plotted based on Taylor expansion

$$f(x) = f(a) + \frac{f'(a)}{1!}(x-a) + \frac{f''(a)}{2!}(x-a)^2 + \dots + \frac{f^{(n)}(a)}{n!}(x-a)^n$$

Eq. 4-8

of the square root of time at the point of  $a = 1$ .

$$\sqrt{t} = 1 + \frac{1}{2}(x-1) + \dots + \frac{1}{2^n} \cdot \prod_{k=2}^n (2k-3) \cdot \frac{(-1)^{n+1}}{n!} (x-1)^n, \quad (n \geq 2)$$

Eq. 4-9

More data was collected at the beginning of PDMS absorption at  $-18^{\circ}\text{C}$ .

Table 4-2. PDMS (Sylgard 184 silicone elastomer to PDMS curing agent weight ratio 10:1) curing time with temperature.

Temperature	Curing time
150°C	10 min
125°C	25 min
100°C	45 min
65°C	~2 hours
25°C	~48 hours
4 °C	~5 days
-18°C	>6 months

## 4.3 pH indicator

### 4.3.1 pH sensitive pigment

Bromothymol blue solution (BTB, Sigma Aldrich) was used as CO<sub>2</sub> absorption indicator [231]. In the neutral (pH = 7) solution, the color is dark green and close to blue. Once it accepts protons, the color changes to yellow; and it changes to blue if lose protons. The color of BTB solution depends on the solution's pH value: pH < 6.0 (yellow); 6.0 < pH < 7.6 (color change from yellow to green to blue); pH > 7.6 (blue). The microchannel inlet was connected to a syringe with BTB solution. The liquid's initial color was adjusted to blue by adding pH buffers, in order to reach the larger capacity of CO<sub>2</sub> absorption and the corresponding pH value change.

If using the color change from blue to green to yellow to identify the pH, the data is not accurate enough to calculate the exact amount of CO<sub>2</sub> absorbed. Therefore, we recorded the video of the color change procedure, and used Matlab to analyze the color image changing sections.

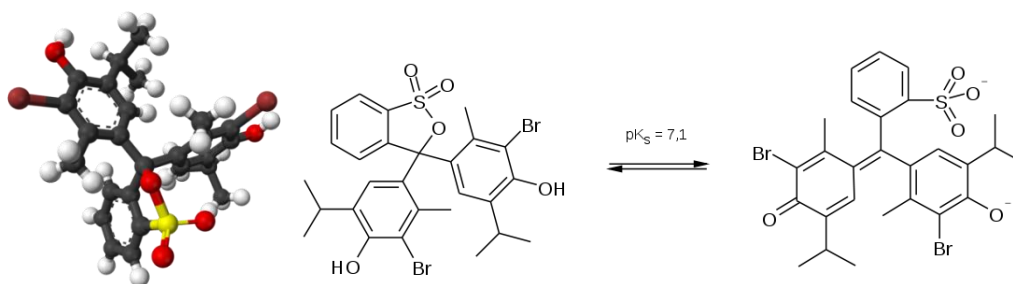


Figure 4-4. BTB structure; BTB structure is changed in different pH environment. Reused with permission from Wikipedia.

The color alteration of the BTB was monitored over time at different flow rates (8~30  $\mu\text{L}/\text{min}$ ) in addition to the static condition. However, if using the color change from blue to green to yellow to identify the pH, the data is not accurate enough to calculate the exact amount of CO<sub>2</sub> absorbed. Therefore, we recorded the video of the color change process, and used Matlab to analyze the pixels of the color changing region. PDMS is clear and optically transparent to any light wavelength of 240~1100 nm, which contained the BTB color change wavelength.

### 4.3.2 Color analysis by Matlab

The color images were imported into Matlab and isolated into red, green, and blue (RGB) color map. By comparing the data of gray map and RGB map, the fluid's color was represented by relative intensity numbers from 0 to 255 of each pixel, where 0 is black, and 255 is white. The algorithm we used was demonstrated in Figure 4-5 by flow chart. The first step was changing the video into image frames. The “.mov” file was changed into “.avi” file, and then cut into 8 frames per second; in another word, between two images, the time step was 0.125 s. Matlab could change each color image into gray map to roughly tell the difference when the pH color changed.

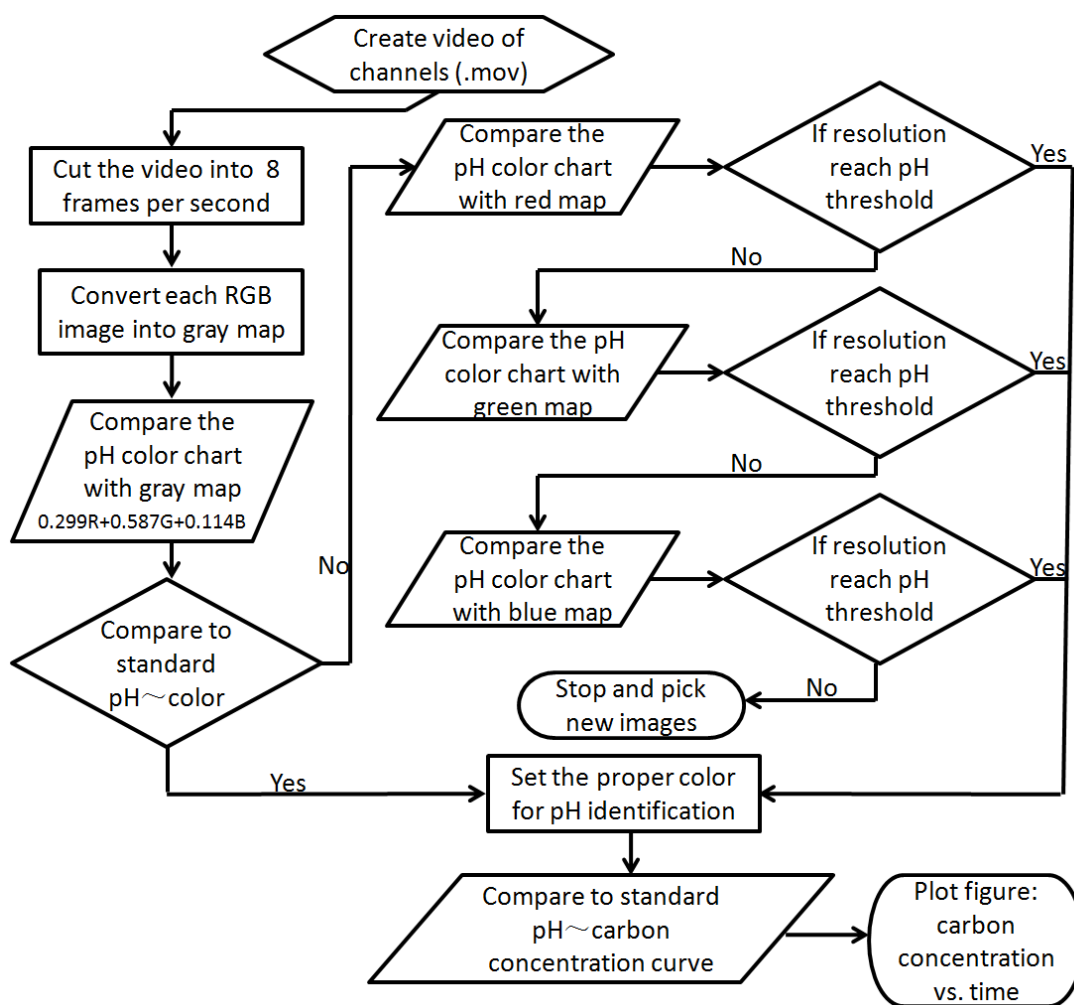


Figure 4-5. Algorithm of the fluid's pH identification by Matlab.

In order to improve the accuracy of the image matrix's relative intensity numbers representing the pH value, we used four comparisons: gray map, red, green, and blue maps. A pre-set relative intensity threshold was established to identify the best resolution of pH value correlating with the image's relative intensity number. If a single color map could not represent pH value in some part of the pH, we could use other color maps to further divide the color into intensity numbers.

### 4.3.3 Carbon absorption amount by pH value

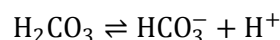
At room temperature, CO<sub>2</sub> dissolves in water to form carbonic acid (H<sub>2</sub>CO<sub>3</sub>) that gradually changes pH value of the solution, which contains H<sup>+</sup>, CO<sub>2</sub>, H<sub>2</sub>CO<sub>3</sub>, HCO<sub>3</sub><sup>-</sup>, and CO<sub>3</sub><sup>2-</sup>. The pH value is defined by the proton H<sup>+</sup> concentration in the solution; however, measuring the H<sup>+</sup> concentration was difficult in microfluidic environment, so we used the data for other negative ions. The hydration equilibrium constant (K<sub>h</sub>) of CO<sub>2</sub> and H<sub>2</sub>CO<sub>3</sub> in water (25°C) is:

$$K_h = \frac{[H_2CO_3]}{[CO_2]} = 1.70 \times 10^{-3}$$

Eq. 4-10

where the “[ ]” represents the compound concentration [5].

The hydrolysis of H<sub>2</sub>CO<sub>3</sub> in water follows the dissociation equation below:



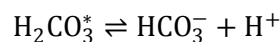
Eq. 4-11

and the dissociation constant (K<sub>a1</sub>) of this reaction at 25°C is [5]:

$$K_{a1} = 2.5 \times 10^{-4} \text{ mol/L}$$

$$pK_{a1} = 3.6$$

However, when [H<sub>2</sub>CO<sub>3</sub>] ≪ [CO<sub>2</sub>], the dissociation of H<sub>2</sub>CO<sub>3</sub> in water follows:



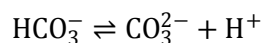
Eq. 4-12

The dissociation constant ( $K_{a(\text{app})}$ ) of this reaction at 25°C is:

$$K_{a(\text{app})} = 4.6 \times 10^{-7} \text{ mol/L}$$

$$\text{p}K_{a(\text{app})} = 6.3$$

The further hydrolysis of  $\text{HCO}_3^-$  is:



Eq. 4-13

The dissociation constants ( $K_{a2}$ ) of this reaction at 25°C are [5]:

$$K_{a2} = 4.69 \times 10^{-11} \text{ mol/L}$$

$$\text{p}K_{a2} = 10.329$$

Finally, the pH value can be related to the concentration of carbon-containing species by Henderson-Hasselbach equation [5],

$$\text{pH} = \text{p}K_a + \log \frac{[\text{HCO}_3^-]}{[\text{H}_2\text{CO}_3]}$$

Eq. 4-14

This equation was used to calculate the overall concentration of the absorbed carbon in the solution, as shown in Figure 4-18. The concentration of  $\text{CO}_2$  molecule,  $\text{H}_2\text{CO}_3$ ,  $\text{HCO}_3^-$ , and  $\text{CO}_3^{2-}$  can be calculated individually. According to Eq. 4-14, the concentration of  $\text{H}_2\text{CO}_3$  and  $\text{HCO}_3^-$  was obtained from the pH value. Based on Eq. 4-13, the concentration of  $\text{CO}_3^{2-}$  was much smaller than any other ions in the water. Because the unhydrolyzed  $\text{CO}_2$  keep the molecule status in the water and not affecting the proton's concentration,  $\text{CO}_2$  molecule didn't affect the pH value of the fluid. The concentration of  $\text{CO}_2$  molecules was calculated by the hydration equilibrium constant  $K_h$  in Eq. 4-10. For example, we listed some concentrations with different pH values in Table 4-3.

The overall carbon concentration was the combination of  $\text{CO}_2$  molecule,  $\text{H}_2\text{CO}_3$ ,  $\text{HCO}_3^-$ , and  $\text{CO}_3^{2-}$ . Therefore, the overall carbon atom that absorbed into the fluid was defined as carbon fixation rate, represented by “[C]”.

Table 4-3. Absorbed  $\text{CO}_2$ ,  $\text{H}_2\text{CO}_3$ ,  $\text{HCO}_3^-$ , and  $\text{CO}_3^{2-}$  concentration (unit: mol/L) with the change of pH.

pH	$[\text{CO}_2]$	$[\text{H}_2\text{CO}_3]$	$[\text{HCO}_3^-]$	$[\text{CO}_3^{2-}]$
7.00	$3.36 \times 10^{-10}$	$5.71 \times 10^{-13}$	$1.42 \times 10^{-9}$	$7.90 \times 10^{-13}$
6.94	$3.36 \times 10^{-9}$	$5.71 \times 10^{-12}$	$5.90 \times 10^{-9}$	$1.90 \times 10^{-12}$
6.81	$3.36 \times 10^{-8}$	$5.71 \times 10^{-11}$	$9.16 \times 10^{-8}$	$3.30 \times 10^{-11}$
6.42	$3.36 \times 10^{-7}$	$5.71 \times 10^{-10}$	$3.78 \times 10^{-7}$	$4.53 \times 10^{-11}$
5.92	$3.36 \times 10^{-6}$	$5.71 \times 10^{-9}$	$1.19 \times 10^{-6}$	$5.57 \times 10^{-11}$
5.65	$1.18 \times 10^{-5}$	$2.00 \times 10^{-8}$	$2.23 \times 10^{-6}$	$5.60 \times 10^{-11}$
5.42	$3.36 \times 10^{-5}$	$5.71 \times 10^{-8}$	$3.78 \times 10^{-6}$	$5.61 \times 10^{-11}$
4.92	$3.36 \times 10^{-4}$	$5.71 \times 10^{-7}$	$1.19 \times 10^{-5}$	$5.61 \times 10^{-11}$
4.42	$3.36 \times 10^{-3}$	$5.71 \times 10^{-6}$	$3.78 \times 10^{-5}$	$5.61 \times 10^{-11}$
3.92	$3.36 \times 10^{-2}$	$5.71 \times 10^{-5}$	$1.20 \times 10^{-4}$	$5.61 \times 10^{-11}$
3.72	$8.40 \times 10^{-2}$	$1.43 \times 10^{-4}$	$1.89 \times 10^{-4}$	$5.61 \times 10^{-11}$
3.42	$3.36 \times 10^{-1}$	$5.71 \times 10^{-4}$	$3.78 \times 10^{-4}$	$5.61 \times 10^{-11}$

The overall carbon concentration was the combination of  $\text{CO}_2$  molecule,  $\text{H}_2\text{CO}_3$ ,  $\text{HCO}_3^-$ , and  $\text{CO}_3^{2-}$ . Therefore, the overall carbon atom that absorbed into the fluid was defined as carbon fixation rate.

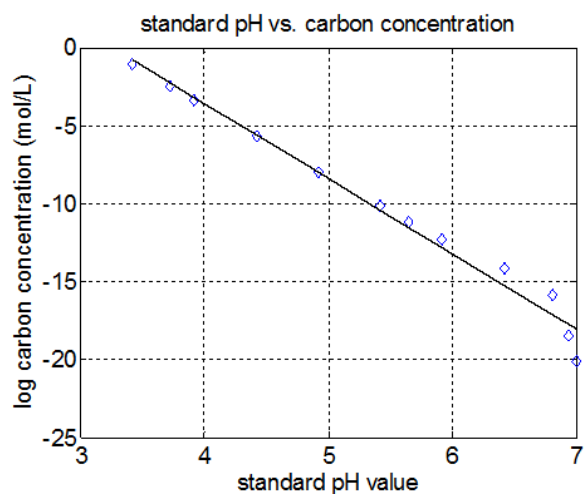


Figure 4-6. Theoretical carbon concentration with standard pH value by Henderson-Hasselbach equation.

#### 4.3.4 Channel pH color identification

The carbon absorbed can be calculated by the integral of all the carbon at every point. However, calculating the average pH value can also be used to calculate the carbon concentration.



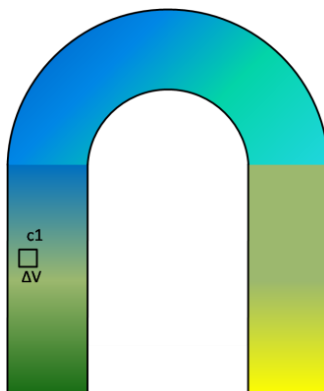


Figure 4-7. Illustration of calculation CO<sub>2</sub> absorbed by channel pH color.

**Hypothesis.** The overall carbon concentration is the accumulation of every point of the fluidic channel, which is also can be calculated by the average pH of the whole channel.

**Proof.** The over carbon concentration and pH has the relationship of

$$\text{pH} \propto \log [C]$$

the carbon concentration of integral of every point is

$$\frac{c_1 \cdot \Delta V + c_2 \cdot \Delta V + \dots}{V}$$

The logarithm of concentration is proportional to the pH value, so we can discuss the average value of pH and the average value of carbon concentration.

$$\log \frac{\Delta V}{V} \cdot \sum_i^n c_i$$

we consider the pH of each point on the fluidic channel

$$\begin{aligned} & \log c_1 + \frac{1}{c_1} (c - c_1) - \frac{1}{c_1^2} \frac{(c - c_1)^2}{2} + \dots \\ & + \log c_2 + \frac{1}{c_2} (c - c_2) - \frac{1}{c_2^2} \frac{(c - c_2)^2}{2} + \dots \\ & + \dots \end{aligned}$$

Considering the fact that  $c - c_1 \ll c_1$ ,  $c - c_2 \ll c_2$ , ..., we take the first term of each line, so

$$\log \frac{\Delta V(c_1 + c_2 + \dots)}{V} = \log \frac{n \cdot \Delta V}{V} + \sum_i^n \log c_i$$

Eq. 4-15

can represent the average carbon concentration.

Therefore, by calculating the average pH value of the fluid channel can also be used to calculate the total carbon concentration in fluidic channel. ■

### 4.3.5 Comparison pH color bar

We put two standard color bars (one for a broad range, pH of 4, 7, 10, and the other for a narrow range, pH of 6, 7, 7.6) next to the test channel for Matlab image comparison in order to minimize the error due to external light intensity change during experiments.

The two sets of color bars has different pH values: left side pH was 4 (light yellow), 7 (green), 10 (blue); and right side pH was 6 (light yellow-green), 7 (green), 7.6 (royal blue). The image color of the fluid channel was compared to the two sets of color bar real time to tell the pH value. This method did not require sample extraction from the fluid channel, especially during the dynamic flow experiment.

Different pH value indicated a certain concentration combination of  $\text{CO}_2$  molecule,  $\text{H}_2\text{CO}_3$ ,  $\text{HCO}_3^-$ , and  $\text{CO}_3^{2-}$ . The overall carbon concentration was defined as the total  $\text{CO}_2$  dissolved and hydrolyzed in water. Based on the pH value, we could calculate the theoretical overall carbon concentration absorbed in liquid.

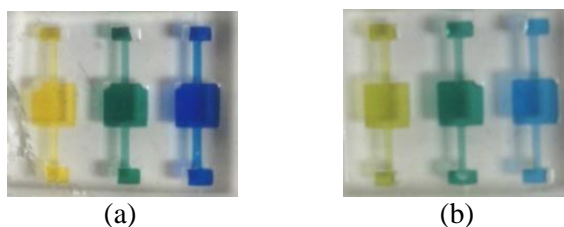


Figure 4-8. Standard pH color bar for image processing; (a) yellow: pH=4, green: pH=7, blue: pH=10; (b) yellow: pH=6, green: pH=7, blue: pH=7.6.

Color images were imported to Matlab and converted to gray images. The standard pH to color bar with pH of 4, 7, 10, and 6, 7, 7.6, were also converted to related color map, which can minimize the error of the light change during the long term experiment, since the gray color map was synchronized with the color of fluid in microchannels. The standard pH color bar was made by buffer solution with pH of  $4.01 \pm 0.01$ ,  $7.01 \pm 0.01$ , and  $10.01 \pm 0.01$  at  $25^\circ\text{C}$ . The pH value of each color block was measured by pH pen (EcoSense® pH 10A, YSI Inc, Yellow Springs, OH).

The image frame of standard color bar showed an gray image number difference of 40/255 for the pH difference of 2. Therefore, the resolution of pH identification by this image processing method ( $\Delta\text{pH}/\text{pixel}$ ) is 0.05.

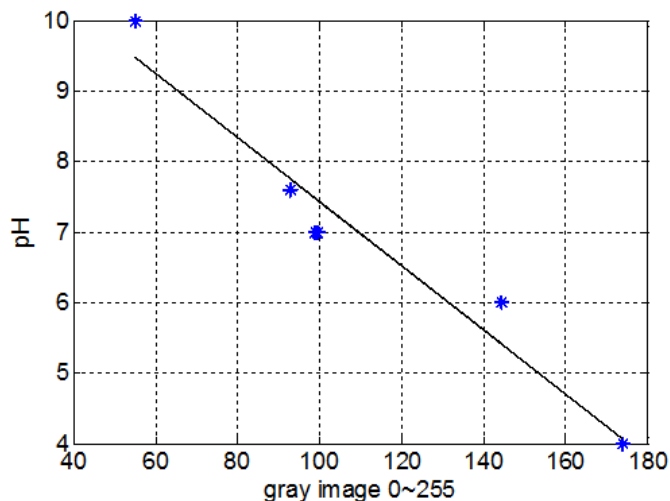


Figure 4-9. Standard pH to color bar for image analysis calibration with gray image color.

Based on the standard color bar, the gray image can be correlated with the pH value of the fluid. The gray map intensity number from 0~255, the white color is 0; while the black color is 255. Gray map is transferred by the RGB color map by the relation of:

$$\text{Gray} = 0.299 \times R + 0.587 \times G + 0.114 \times B$$

Eq. 4-16

where R, G, and B are also from 0~255.

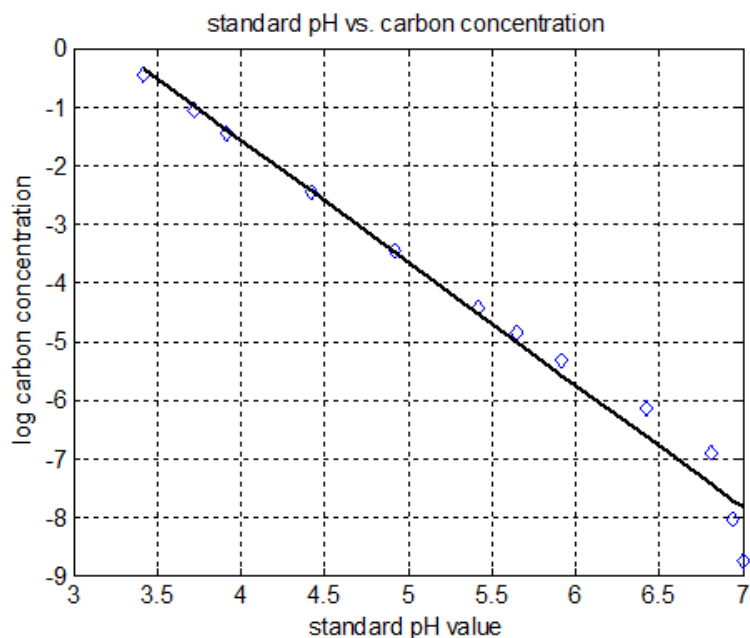


Figure 4-10. Theoretical carbon concentration with standard pH value by Henderson-Hasselbach equation.

Different pH value indicates a certain concentration combination of  $\text{CO}_2$  molecule,  $\text{H}_2\text{CO}_3$ ,  $\text{HCO}_3^-$ , and  $\text{CO}_3^{2-}$ . The overall carbon concentration will be the total  $\text{CO}_2$  dissolved and hydrolyzed in water. As shown on Figure 4-10, based on the pH value, we can calculate the theoretical overall carbon concentration absorbed in liquid.

## 4.4 PDMS molding replica and stereolithography

### 4.4.1 Mold 3D stereolithography

The microfluidic channels can be made by either traditional microfabrication method, or advanced manufacturing methods as 3D stereolithography or 3D printing. The 3D printing requires removable material or structure as mold. The 3D stereolithography mold can be released after PDMS replica molding; on the other hand, the 3D wax printed mold can be dissolved in acetone. Therefore, 3D printed wax mold can be used as further supporting structure inside a PDMS replica.

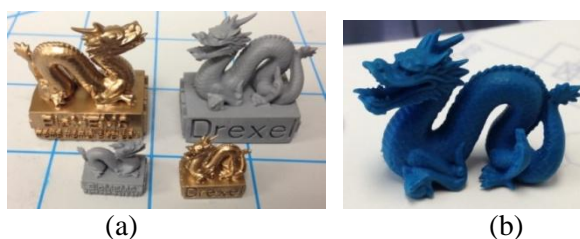


Figure 4-11. (a) 3D stereolithography product of dragon, gray photosilver (left) and coated with gold paint (right); (b) 3D wax printed dragon by Solidscape®.

The porous PDMS was then sealed inside PDMS channels manufactured by stereolithographically defined molds (Figure 4-12).

#### 4.4.2 Fluidic device fabrication

The flow channels for evaluating gas-liquid interface consisted of three parts: a meander channel for fluid flow made of PDMS, a flat layer of PDMS with four through-holes placed on top of the flow channel layer, and porous PDMS cubes placed on the through-holes. The fabrication procedure is demonstrated in Figure 4-12.

The flow channel was made by PDMS replica molding using 3D printed molds. PDMS was selected as channel materials because it can be readily bonded to another PDMS layer including porous PDMS cubes/films it is also optically transparent to the light with a wavelength from 240 nm to 1100 nm, which is necessary for photosynthesis process. The mold for PDMS channel was made of a photopolymer (commercial name: Photosilver, EnvisionTEC, Dearborn, MI) using a 3D printer (EnvisionTEC®, model: Perfactory, Dearborn, MI). Since the detection of the products of artificial photosynthesis requires at least 200  $\mu\text{L}$  of liquid sample, the PDMS channel was designed to have an internal volume of  $\sim 600 \mu\text{L}$ . Zig-zag shape structures were added to the surface of fluidic channel to promote mixing, which would benefit the carbon fixation enzyme reactions, enhancing the chance of  $\text{CO}_2$  and adenosine triphosphate (ATP) attraction by the enzyme ribulose-1,5-bisphosphate carboxylase/oxygenase (RuBisCO). The PDMS flow channel had a width of 1.5 mm and a height of 0.8 mm. Four square patterns (3 mm  $\times$  3 mm) were added to the channel for alignment with porous PDMS cubes and for image processing.

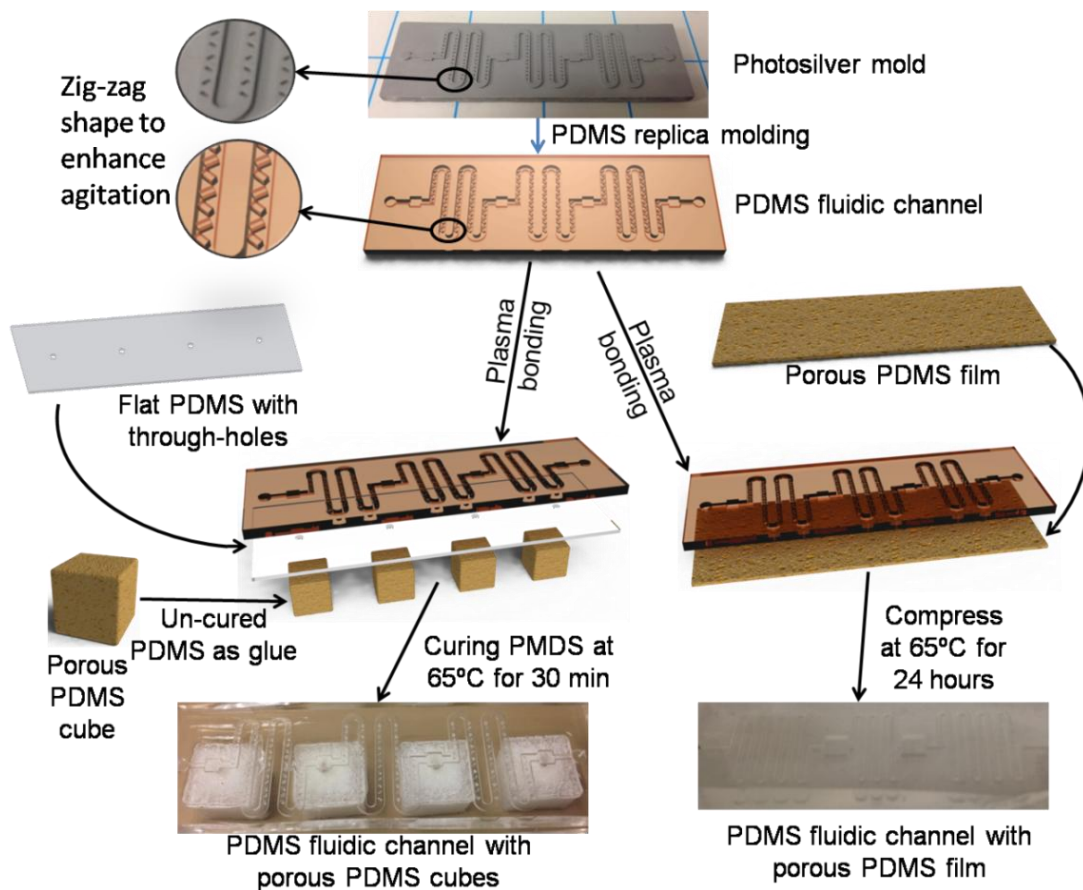


Figure 4-12. Fabrication process flow of fluidic channels with porous PDMS cubes and film.

Tridecafluoro-1,1,2,2-tetrahydrooctyl-1-trichlorosilane (TFOCS, Fisher Scientific) was coated on the surface of the molds for easy release of PDMS. 0.3 mL of TFOCS was dropped on the surface of a petri-dish, with the mold placed next to the droplets. Then, the petri-dish was moved into a vacuum chamber for 30 min. The TFOCS fully evaporated and formed a Teflon-like surface on the photosilver mold. After the mold was prepared, standard PDMS replica molding was conducted to fabricate microchannels. PDMS pre-polymer and the curing agent were mixed at a weight ratio of 10:1. The mixture was then placed in a vacuum container for 30 min to remove all the air bubbles. The degassed PDMS mixture was poured onto the mold and placed in a 60°C oven for 24 hours for the solidification of PDMS. A flat layer of PDMS (500  $\mu\text{m}$  thick) was also prepared and through-holes were created by hole punch. This flat PDMS layer was then bonded to the channel layer after air plasma treatment (Femto Science, Model: CUTE, Serial

number: FS15-031, Korea). The same method was attempted for bonding porous PDMS cubes to the channel but the bonding result was poor due to the rough surface of porous PDMS cubes. As an alternative, we used uncured PDMS as a glue. A mixture of PDMS pre-polymer and curing agent was put on a hot plate and the temperature was increased gradually to 55°C with constant stirring. The PDMS mixture would become like a gel with higher viscosity. The gel-like mixture was applied to the edge of porous PDMS cubes placed on the flat PDMS layer. Then, the whole device was moved to the oven at 65°C for 30 min for curing. For the device for testing porous PDMS film, the flat PDMS layer was not used. The porous PDMS film was directly attached to a PDMS microchannel via plasma treatment, followed by compressing in an oven at 65° for 24 hours.

#### **4.4.3 Fluidic agitation simulation**

The existence of the PDMS pillar is used to create possible agitation or mixing vortex in the microfluidic channels for low Reynolds number fluidic situation, such as chaotic mixers in microchannels [259-264]. We selected an easier pillar bar structure to achieve mixing and agitation for the glucose synthesis solution. The micro pillar bars are molded by the 0.2 mm × 2.2 mm × 0.4 mm empty cavities in the 3D printed photosilver mold. The simulation is applied with water-like fluid properties with a flow rate of 50 µL/min; and the cross-section area of 3 mm<sup>2</sup>.

The effect of pillar bars and cylindrical obstacles inside the top surface of fluidic flow can create similar mixing effect for low Reynolds number fluid. However, the cylindrical pillars does not mix the fluid flow located on different streamlines. Therefore, the agitation effect of the pillar bars is better than the cylindrical pillars. The chance of collecting CO<sub>2</sub> and ATP still exist, because the diffusion of CO<sub>2</sub> and ATP at 2 mm range is still dominating the chemical reactions. The fluid shows low turbulence in the square watching window, which guarantees the image processing for comparison at the window blocks.

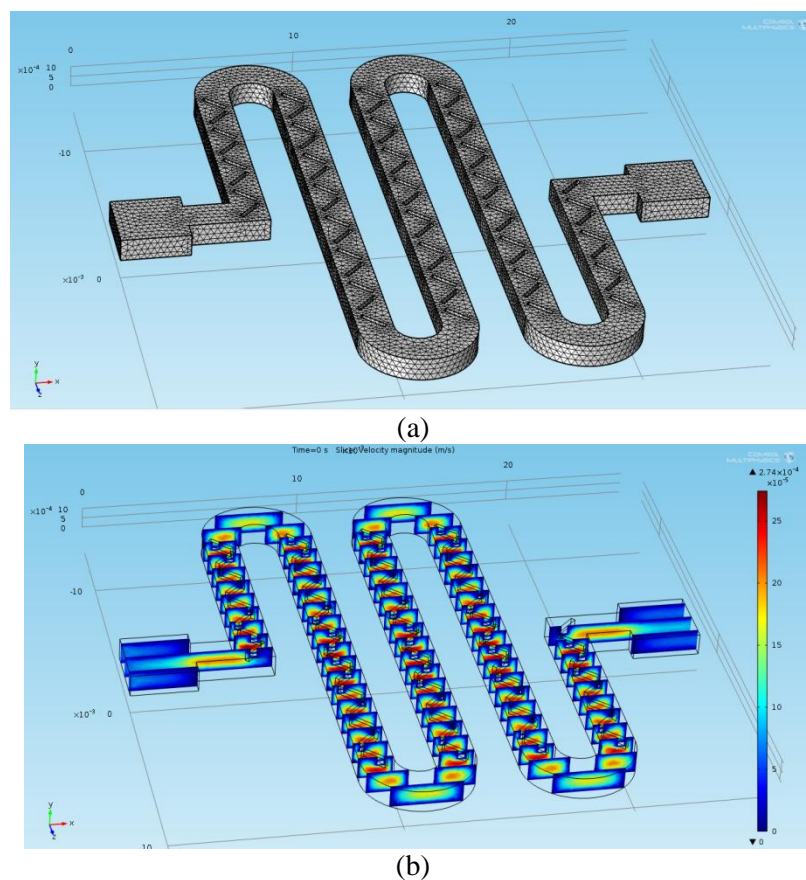


Figure 4-13. (a) Mesh analysis of the fluid in microfluidic channels with pillar bars; (b) Flow velocity profile in microchannel with pillar bar.

On the fabrication side, cylindrical obstacles are easier for the PDMS to peel off because of the less of rigidity on the edges. However, the ridges with micro pillar bars are broadly selected for agitation use. Besides, since we already solved the photosilver mold surface coating for PDMS separation, the dimension and geometry of the pillars are flexible in various designs.

## 4.5 Porous PDMS disc between gas channel and flow channel

### 4.5.1 Experimental

In order to test the gas-liquid interface performance, we used the dual-channel model to test the gas-liquid interface through porous PDMS [265]. The liquid with BTB was applied to one channel using a syringe pump, and  $\text{CO}_2$  was imported to the other channel using a glass flask



filled with dry ice. The flow rate of  $\text{CO}_2$  was considered constant during the dry ice sublimation because of the significant smaller gas channel volume compared to the glass flask.

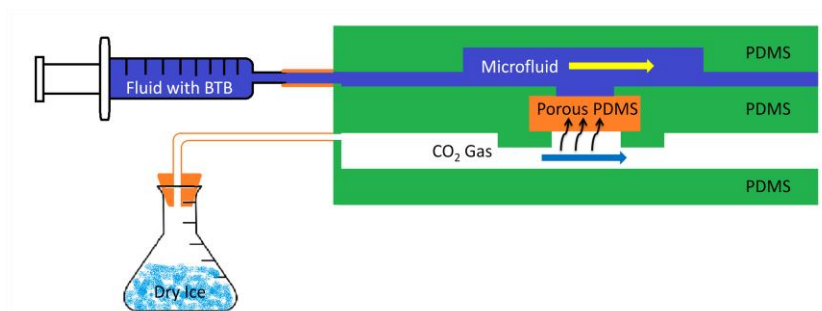


Figure 4-14. Experiment setup of gas-liquid interface using dry ice as  $\text{CO}_2$  source.

The porous PDMS (see below for its fabrication) was “locked” in to solid PDMS layers as shown in Figure 4-14. Extra solid PDMS surrounding the porous PDMS was necessary for this purpose and it was permanently bonded to the middle layer PDMS after plasma treatment (Femto Science, Model: CUTE, Serial number: FS15-031, Korea). Porous PDMS has some advantages for gas penetration for microfluidics. First, porous PDMS provides direct contact between liquid and air environment. Interconnected pores created multiple random paths between air and liquid. Second, porous PDMS can be easily connected with PDMS microfluidic channels, since they share the same material PDMS. Third, porous PDMS is soft, flexible, and compressible, so the porous PDMS cube or disc can be compressed to change pore sizes and porosity in a certain range.

$\text{CO}_2$  was introduced into the lower layer of the microchannel.  $\text{CO}_2$  molecules penetrated through the porous PDMS layer, and then continuously diffused into the fluid in the upper channel. A pH sensitive pigment was added in the fluid to monitor the color change during the  $\text{CO}_2$  absorption process.

The fluid with BTB was connected to the inlet. Syringe pump (Harvard Apparatus Pump, Holliston, MA) was set with a flow rate from 8~30  $\mu\text{L}/\text{min}$  with a step of 2  $\mu\text{L}/\text{min}$ . The whole color change was recorded by a high-resolution camera for further image processing. Therefore, a

white background was placed behind the experimental device, and the lighting conditions as well as the camera were fixed during all the experiment process.

## 4.5.2 Results

The flow rate was set to moderate; otherwise, the pressure tends to increase with higher flow rate. Once the pressure reached the maximum threshold that the porous PDMS could hold, the fluid would overcome the hydrophobic resistance of the porous PDMS layer and penetrate through the porous PDMS disc layer.

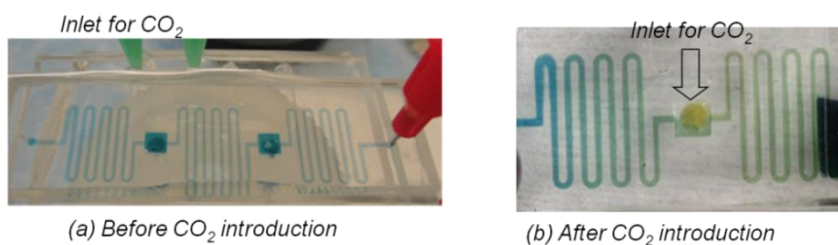


Figure 4-15. BTB color alteration before and after introducing CO<sub>2</sub>.

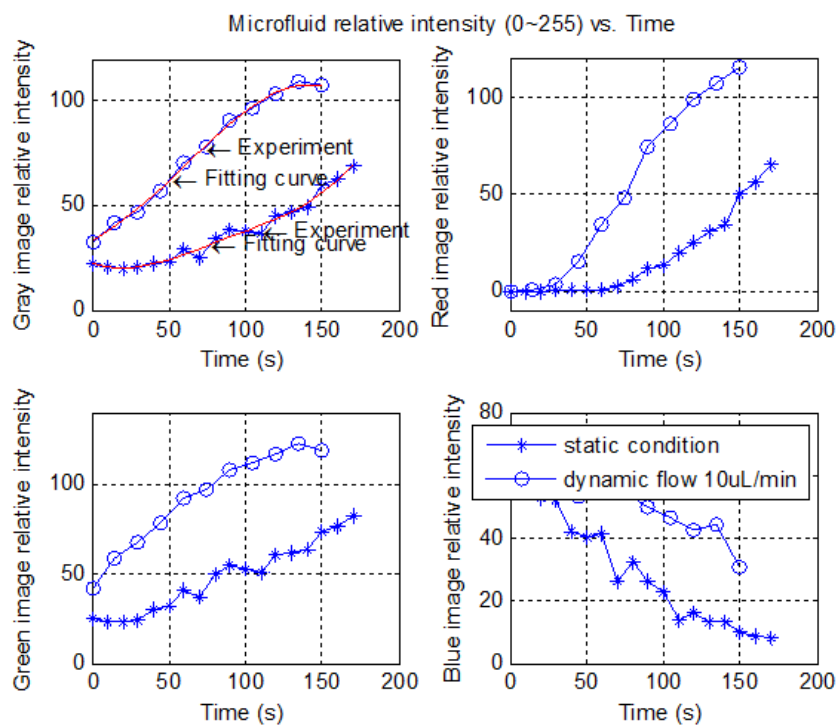


Figure 4-16. RGB color intensity comparison results.

For example, when the color was green or blue, the red map's data of each image pixel were almost same by the changing of time, which meant the red map data could not identify the pH value during that small period of time. Therefore, we should continue to use the green and blue map to identify the pH value during that period of time. These data were then analyzed to calculate the fluid's pH value (Figure 4-17) by comparing the fluid's color with standard BTB color chart.

These data were then analyzed to calculate the fluid's pH value (Figure 4-17) by comparing the fluid's color with standard BTB color chart (Figure 4-15c). The data of static condition and one of the dynamic conditions (10  $\mu\text{L}/\text{min}$ ) were shown in this paper for clearer demonstration. The static case data indicated that  $\text{CO}_2$  was dissolved and diffused into the liquid channel through porous PDMS; the dynamic flow case showed faster transfer of  $\text{CO}_2$ .

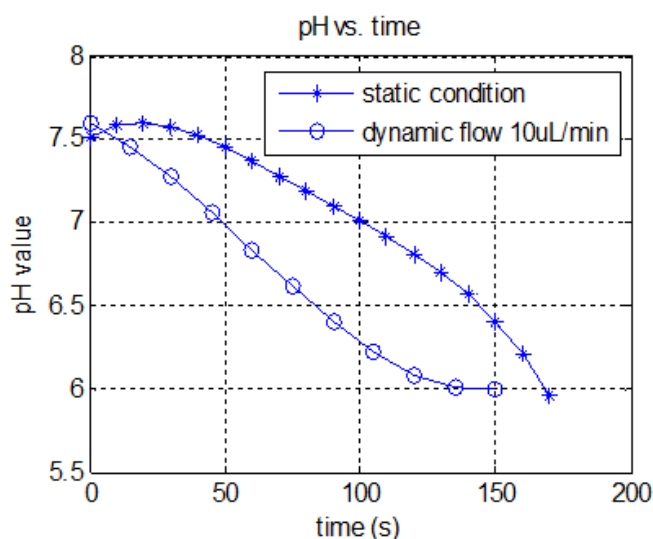


Figure 4-17. pH value change over time in static and dynamic conditions.

As observed in Figure 4-17 the dynamic fluid condition presented a faster  $\text{CO}_2$  transfer compared with the static fluid condition. With the consumption of  $\text{CO}_2$ , more  $\text{CO}_2$  molecules would be hydrolyzed into  $\text{HCO}_3^-$ , and the equilibrium would continue to shift to create more  $\text{HCO}_3^-$ , allowing more  $\text{CO}_2$  molecules to diffuse into the fluid.

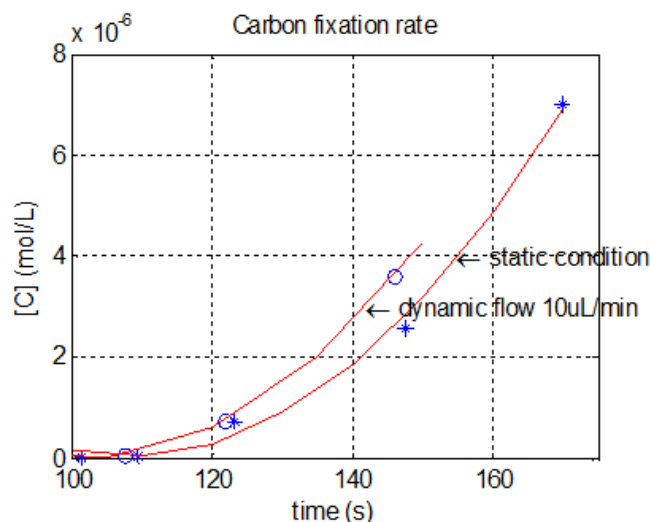


Figure 4-18. Carbon concentration in the liquid chamber.

Considering the microchannel dimensions, the average  $\text{CO}_2$  absorption rates was 13.7  $\mu\text{mol}/(\text{L}\cdot\text{min})$  in static condition and increased to 18.2  $\mu\text{mol}/(\text{L}\cdot\text{min})$  under fluid flow rate of 8~10  $\mu\text{L}/\text{min}$ .

We developed a novel method of creating a gas-liquid interface in microchannel systems using porous PDMS and demonstrated its performance using  $\text{CO}_2$  absorption. We believed that this gas-liquid interface method could be applied to many applications in lab-on-a-chip systems, especially in artificial photosynthesis systems, which is our ultimate target system. Such system will simulate the leaf function: absorbing  $\text{CO}_2$  with less water evaporation.

#### 4.6 $\text{CO}_2$ absorption with porous PDMS cube

The final goal is fabricating a device that can absorb carbon dioxide from air without solution's water leakage and evaporation. Other than porous PDMS, other hydrophobic porous material can be considered as potential candidate to be built in devices.

As for porous PDMS, we can further modify the microchannel dimensions and the inlet flow rate to increase the  $\text{CO}_2$  absorption rate. Besides, the porosity and average pore size may also affect the  $\text{CO}_2$  penetration rate as well as the absorption rate. Theoretical analysis and simulations can find a theoretical saturation state of maximum  $\text{CO}_2$  absorption in microchannels.

### 4.6.1 Experimental

The experiment was conducted in a plastic container connected to a CO<sub>2</sub> gas cylinder. The BTB solution inlet was connected to a 5 mL syringe placed on a syringe pump (Harvard Apparatus, Holliston, MA) (Figure 4-19). We observed the color change of BTB solution for static condition (no flow) and dynamic conditions (flow rates of 20, 40, 60, 80, and 160  $\mu\text{L}/\text{min}$ ). For accurate measurement, we recorded the video of the color change, and used Matlab to analyze the data.

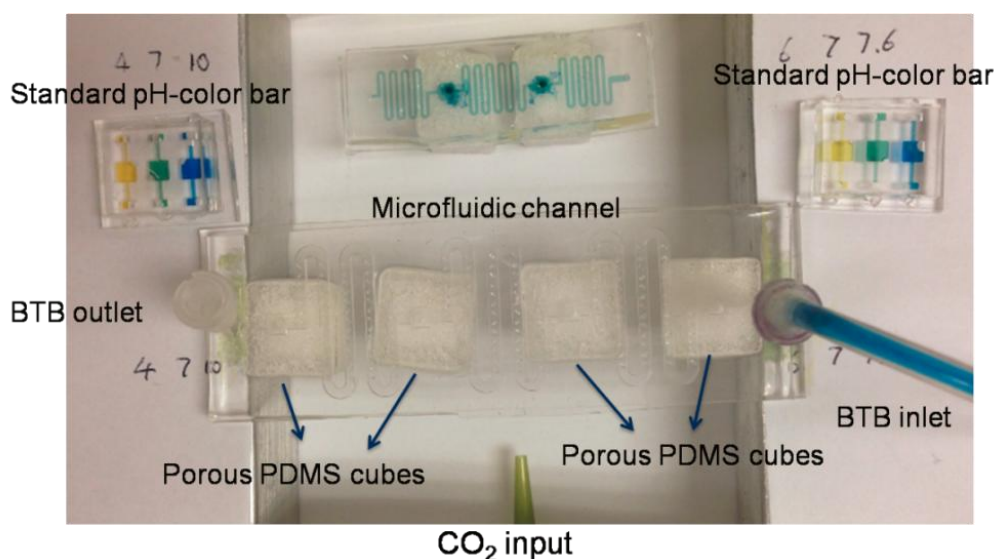


Figure 4-19. Experimental setup for CO<sub>2</sub> absorption in a flow channel with porous PDMS cubes.

### 4.6.2 Static fluidic status

The color image is imported to Matlab and converted to gray image. The standard color bar with pH of 4, 7, 10, and 6, 7, 7.6, were also converted to related color map, which can minimize the error of the light change during the long term experiment, since the gray color map was synchronized with the color of fluid in microchannels.

In microfluidic channels, the molecules diffusion is the normal way. However, in our pH variation in fluidic channels involves CO<sub>2</sub> absorption and diffusion. Considering the CO<sub>2</sub>

diffusion in water, the diffusion coefficient is  $1.92 \times 10^{-5} \text{ cm}^2/\text{s}$ . At 30 min when the fluid channel turns to green, the diffusion distance of  $\text{CO}_2$  is

$$\sqrt{2Dt} = 2.4 \text{ mm}$$

However, BTB responds to weak acid solution with the presence of  $\text{H}_3\text{O}^+$ . The  $\text{H}^+$  has unusual high diffusion coefficient than other molecules or atoms, because the  $\text{H}^+$  is “passing” in the aqueous solution rather than “moving”.

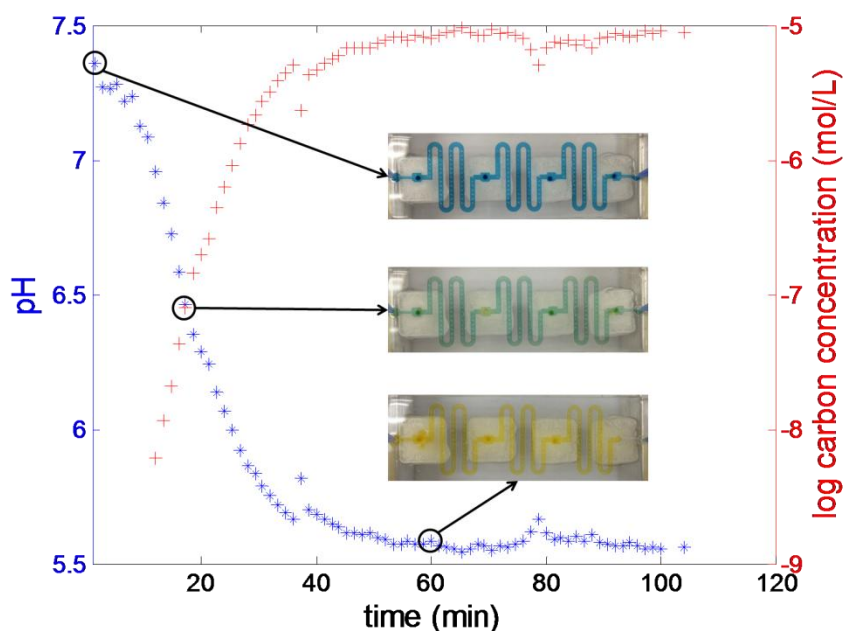


Figure 4-20. pH value and carbon concentration change with time in static flow in PDMS microchannel.

Figure 4-20 shows the  $\text{CO}_2$  absorption results for channels with PDMS cubes as a gas-liquid interface. Under static condition (no flow), the pH value and carbon concentration became saturated after about 60 min (Figure 6a). The saturated carbon concentration was  $8.08 \times 10^{-6} \text{ mol/L}$  (the log carbon concentration average after saturation was -5.10). Since the volume of microfluidic channel was  $\sim 600 \mu\text{L}$ , the average  $\text{CO}_2$  absorption rate was around  $1.3 \mu\text{mol}/(\text{L} \cdot \text{min})$ .

### 4.6.3 Dynamic flow status

In addition to static flow status, we used dynamic flow to test the  $\text{CO}_2$  absorption rate. Absorption and diffusion rate is determined by the concentration gradient in fluid. During the

static flow status, the diffusion rate decreased due to the length of fluidic channel and diffused CO<sub>2</sub>. In dynamic flow status, new fluid without CO<sub>2</sub> was introduced to the open window to porous PDMS, so the diffusion rate of CO<sub>2</sub> would be larger than the static flow status.

In dynamic flow condition, the carbon concentration reached a steady-state much faster (only about 1 min) and the value was lower than static condition. Figure 4-21 demonstrates the steady-state pH value and carbon concentration as a function of flow rate. For example, under a flow rate of 160  $\mu\text{L}/\text{min}$ , the carbon concentration became stable after about 1 min and the value was  $1.81 \times 10^{-6}$  mol/L (the log carbon concentration average after stable status was -6.74). The average CO<sub>2</sub> absorption rate was around 1.81  $\mu\text{mol}/(\text{L} \cdot \text{min})$ . When the flow rate was reduced to 80  $\mu\text{L}/\text{min}$ , the carbon concentration became stable after about 1.5 min and the value was  $2.37 \times 10^{-6}$  mol/L (the log carbon concentration average after stable status was -6.63). The average CO<sub>2</sub> absorption rate was around 1.60  $\mu\text{mol}/(\text{L} \cdot \text{min})$ , which was slightly higher than that of static case.

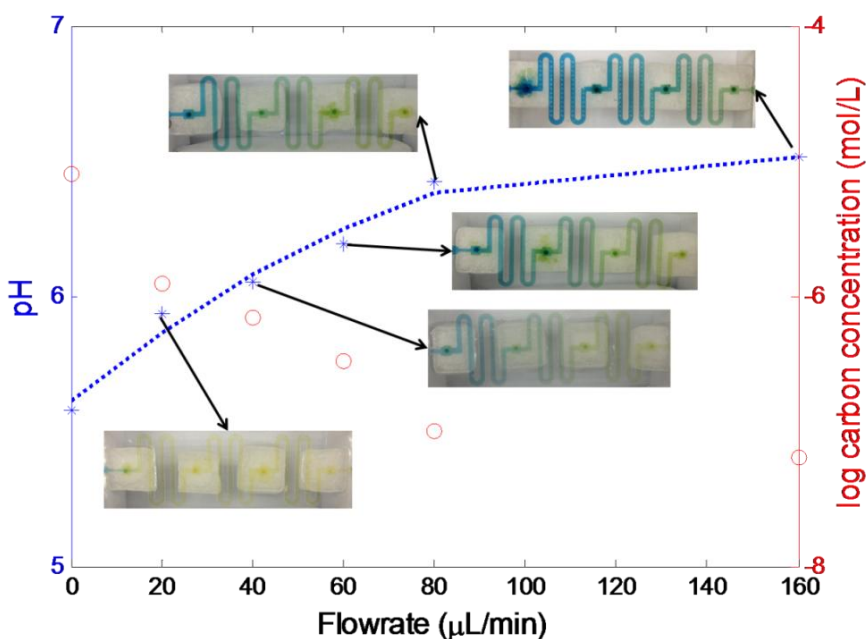


Figure 4-21. Fluid pH value at stable status of different flow rates.

We used different flow rates of fluid to find out the final pH value after stabilization. The slow flow rate had more flow time and CO<sub>2</sub> absorption time. The faster flow rate generated a

gradually pH variation along the channel.

In dynamic flow condition, the  $\text{CO}_2$  absorption rate was higher than static flow condition.  $\text{CO}_2$  molecules passed through the porous PDMS and dissolved into fluidic at the contact point (shown as round dot in Figure 4-20 and Figure 4-21) between fluidic channel and porous PDMS cubes. At each contact point, the pH change depends on the diffusion of  $\text{HCO}_3^-$  and  $\text{H}_3\text{O}^+$ . In static flow condition,  $\text{CO}_2$  diffusion rate decreased gradually with the increasing of the  $\text{HCO}_3^-$  concentration. On the other hand, in dynamic flow condition, the fluid was continuously pumped into the fluidic channel, so the increasing of  $\text{HCO}_3^-$  concentration was much slower than in static flow condition. Therefore, in dynamic flow condition, the diffusion rate of  $\text{CO}_2$  molecules,  $\text{HCO}_3^-$  and  $\text{H}_3\text{O}^+$  were faster than in static flow condition.

#### 4.6.4 Parylene-C coated porous PDMS cubes

PDMS is also a kind of material for  $\text{CO}_2$  to diffuse, so I tried parylene-C coating over the PDMS fluid channel with porous PDMS cubes. The parylene-C can generate a thin layer of protection on the channel and porous cubes. We tried the dynamic flow in parylene-C coated channel with porous PDMS cubes at  $20 \mu\text{L}/\text{min}$ ,  $40 \mu\text{L}/\text{min}$ , and  $80 \mu\text{L}/\text{min}$ .

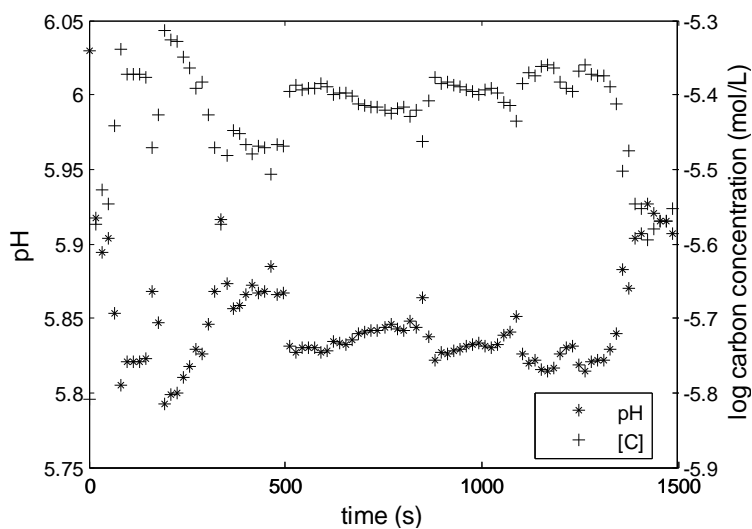


Figure 4-22. pH value and carbon concentration change with time in dynamic flow at  $20 \mu\text{L}/\text{min}$  in parylene-C coated fluidic channel with porous PDMS cubes.



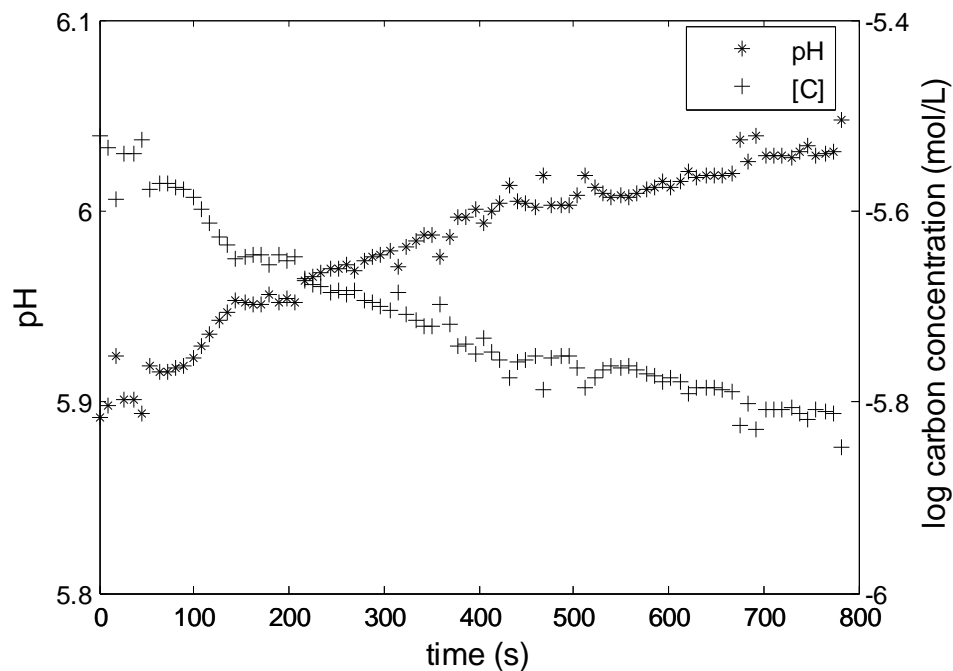


Figure 4-23. pH value and carbon concentration change with time in dynamic flow at 40  $\mu\text{L}/\text{min}$  in parylene-C coated fluidic channel with porous PDMS cubes.

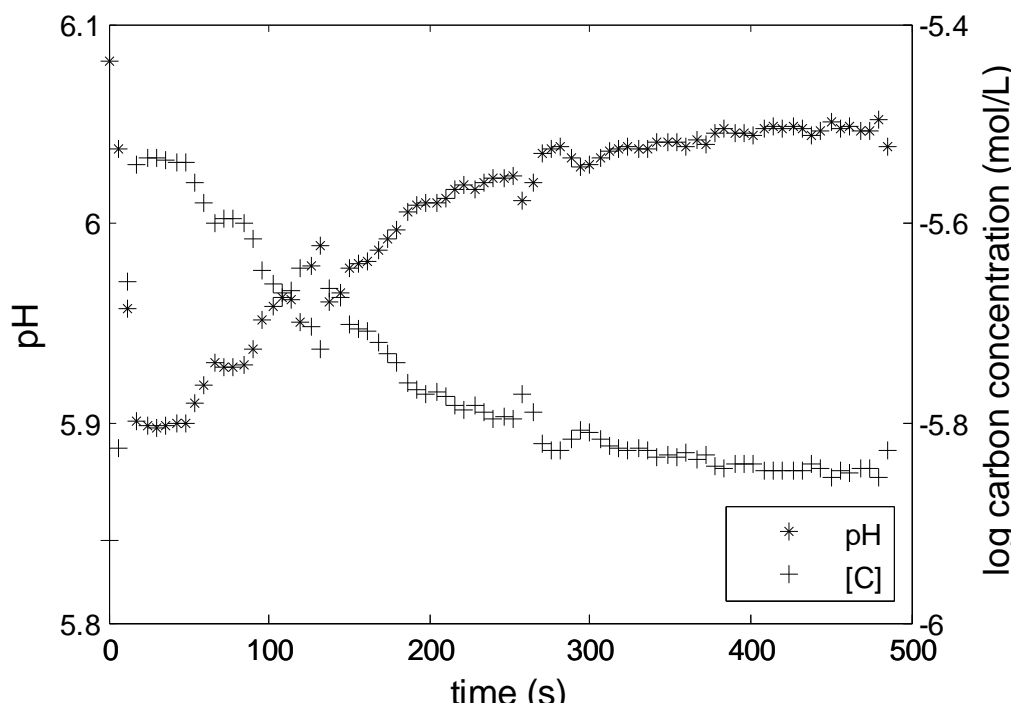


Figure 4-24. pH value and carbon concentration change with time in dynamic flow at 80  $\mu\text{L}/\text{min}$  in parylene-C coated fluidic channel with porous PDMS cubes.

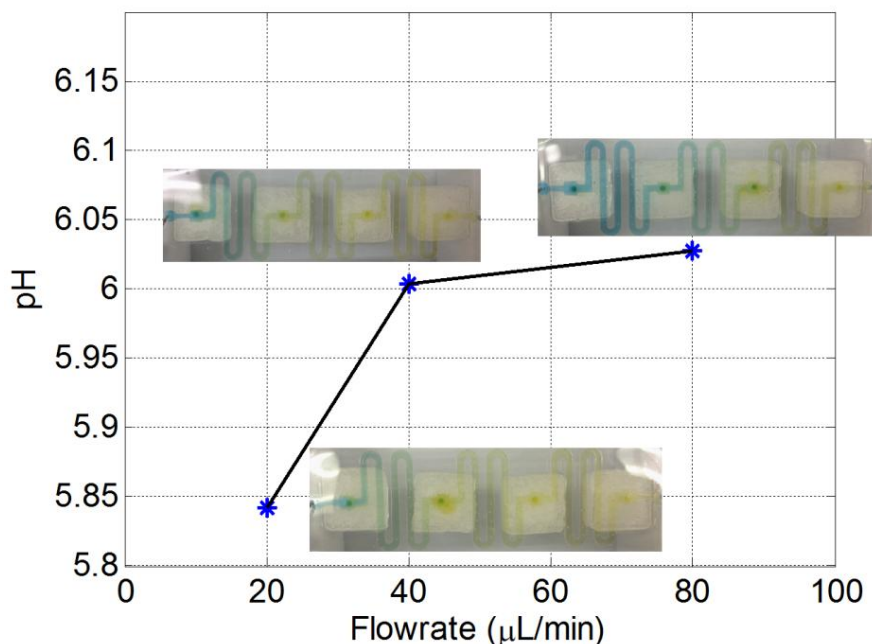


Figure 4-25. Fluid pH value at stable status of different flow rates in parylene-C coated fluidic channel with porous PDMS cubes.

The parylene-C coated fluidic channel were similar to the prime PDMS channels. Parylene-C did not change the properties of porous PDMS.

## 4.7 CO<sub>2</sub> absorption with porous PDMS film

### 4.7.1 Experimental

We evaluated the porous PDMS thin film and the PDMS cube as gas-liquid interface by measuring CO<sub>2</sub> penetration through them. The porous PDMS cube was bonded to an opening on the bottom of a PDMS microchannel using PDMS mixture; on the other hand, porous PDMS film was attached to a PDMS microchannel opening after plasma treatment for 2 min, followed by compressing in an oven at 65°C for 24 hours.

CO<sub>2</sub> molecules penetrated through the porous PDMS layer, and then continuously diffused into the fluid in the upper channel. The pH sensitive pigment BTB was added in the fluid as CO<sub>2</sub> absorption indicator as the experiment before.

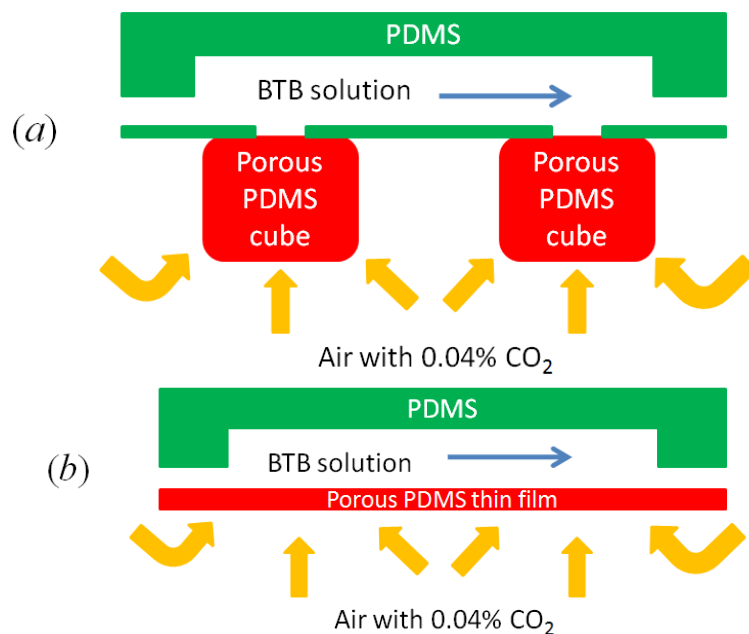


Figure 4-26. Schematic comparison of CO<sub>2</sub> absorption in a microchannel through (a) porous PDMS cube, and (b) porous PDMS thin film.

At room temperature, CO<sub>2</sub> dissolves in water to form carbonic acid (H<sub>2</sub>CO<sub>3</sub>) that gradually changes pH value of the solution, which contains H<sup>+</sup>, CO<sub>2</sub>, H<sub>2</sub>CO<sub>3</sub>, HCO<sub>3</sub><sup>-</sup>, and CO<sub>3</sub><sup>2-</sup>. The hydration equilibrium constant ( $K_h$ ) defined as the concentration ratio of H<sub>2</sub>CO<sub>3</sub> and CO<sub>2</sub> in water (25°C) is  $1.7 \times 10^{-3}$ . Therefore, the pH value can be related to the concentration of carbon-containing species by Henderson-Hasselbach equation.

Similar to porous PDMS film, we can also make porous parylene-C using starch leaching method. Unlike the capillary absorption of liquid PDMS, parylene-C was coated on the surface of starch with a thickness of 1 μm. In order to have a better attachment between PDMS fluidic channel to porous parylene-C, we attached the rice paper to PDMS fluidic channel first. Then, parylene-C was coated on all the surfaces of the device. After parylene-C coating, the whole device was rinsed in 5% α-amylase solution to dissolve the starch.

#### 4.7.2 Results

The microfluidic channels with porous PDMS film had much faster CO<sub>2</sub> absorption rate than the microfluidic channels with porous PDMS cubes. The fluid color changed to yellow at 12 min,

even though some liquid evaporation was observed, because the thickness of porous PDMS film was around 0.3~0.4 mm.

Figure 4-27 shows the CO<sub>2</sub> absorption results for channels with PDMS films as a gas-liquid interface. Experiments were conducted only under static conditions in this case. The fluid color changed from green to yellow after 12 min. The CO<sub>2</sub> absorbed in the channel with porous PDMS film reached  $1.18 \times 10^{-5}$  mol/L in 12 min, so the average CO<sub>2</sub> absorption rate was 9.83  $\mu\text{mol}/(\text{L} \cdot \text{min})$ . While porous PDMS film can provide faster CO<sub>2</sub> absorption than porous PDMS cubes, fluid leakage was observed during the experiment.

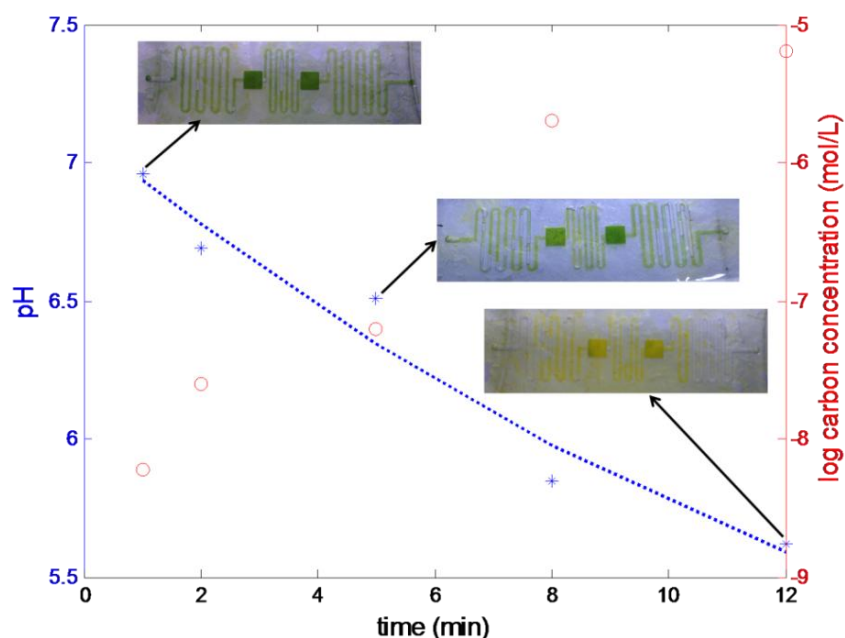


Figure 4-27. CO<sub>2</sub> absorption result for porous PDMS cubes and porous PDMS film.

According to literature, people usually used PDMS thin film as gas-liquid interface method [245, 247, 250]. A PDMS thin film with 225  $\mu\text{m}$  in thickness can have CO<sub>2</sub> penetration rate of 0.045  $\mu\text{mol}/(\text{L} \cdot \text{min})$  [250]. A PDMS thin film with 127  $\mu\text{m}$  in thickness can reach 0.056  $\mu\text{mol}/(\text{L} \cdot \text{min})$  [245]. The thicker PDMS thin film has slower gas permeability [247]. This CO<sub>2</sub> absorption rate demonstrated with PDMS thin film was already suitable to most biological reactions and cell growth or reactions [266]. Our porous PDMS cubes as gas-liquid interface

media can reach a CO<sub>2</sub> absorption rate up to 1.81 μmol/(L·min). Not only the CO<sub>2</sub> penetration ratio through PDMS thin film was limited, but also the mechanical strength of PDMS thin film was limited. Therefore, our device with porous PDMS cubes have a better performance as gas-liquid interface media for CO<sub>2</sub> absorption.

The results of CO<sub>2</sub> absorption on porous PDMS cubes and porous PDMS film indicated that the porous PDMS film can provide faster CO<sub>2</sub> diffusion. However, porous PDMS film showed issues such as leakage and evaporation.

#### **4.8 Discussion and conclusion**

Gas-liquid interface approaches in microfluidic systems using porous PDMS provides a direct contact between liquid and air. Porous PDMS is the same materials as PDMS channel broadly used in microfluidic society. Porous PDMS have better CO<sub>2</sub> absorption, however, porous PDMS cannot prevent water evaporation; even though PDMS itself can also have water penetrated slowly. If we consider the gas-liquid interface in dynamic flow in microchannel, water leakage problem is more important than long-term water evaporation. Since PDMS is hydrophobic, the porous PDMS also shown hydrophobic property on surface. Porous PDMS is not the only way for gas-liquid interface media. Some people presented other porous materials embedded in micro or macro scale fluidic systems [230, 250]. The materials and structures were determined by specific applications and chemical purposes. Some other researchers used PDMS thin film as a slow gas-liquid interface media [231, 247]; however, not only the penetration ratio of the gas through PDMS thin film was limited, but also the mechanical strength of PDMS thin film was limited.

There were many approaches for gas-liquid interface, for either gas absorption for chemical reactors, or multi-gas sorting and chromatography. The applications of PDMS provided plenty of choices for gas penetration and diffusion applications. The gas bubbles introduced into microfluidic system provides more gas diffusion and absorption. Mathematical modeling of the

gas bubble shape with dissolving rate was established by CO<sub>2</sub> bubbles in aqueous microfluidic channel [240]. With a proper channel length, flow rate and wetting diameter, the CO<sub>2</sub> captured in gas bubbles can be fully dissolved in liquid. By measuring the decreasing size of the bubbles, the gas absorption rate can be estimated together with the pressure drop in microfluidic channels. The gas choices was limited to water soluble gas, such as CO<sub>2</sub>, ammonia (NH<sub>3</sub>), for inorganic chemical reactions [236, 241]. Another high efficient gas liquid interface media is hollow fiber, which was studied and applied to gas absorption and filtration decades ago [267]. Hollow fiber is commercially available filter with variety of hole sizes and porosities. The major advantages of hollow fiber is providing large equivalent contact surface area with limited dimension of fibers. For example, a hollow fiber membrane module with 0.0254 m in diameter and 0.2 m in length can have 2324 m<sup>2</sup>/m<sup>3</sup> effective surface area. However, hollow fibers requires special fluidic reactors for gas liquid interface. Besides, different types and dimensions of hollow fibers have different porosity, as well as the average mean path for gas molecules. Therefore, the uncertainty and instability of the hollow fibers are not the first choice of gas liquid interface in microfluidic environment.

The best existing gas-liquid interface choice is using polymer thin film, such as Teflon, polyisoprene (PI), polyurethane (PU), PDMS, etc [247, 268]. Thicker the PDMS thin film will have a slower gas permeability. The gas permeability of PDMS was measured by the gas penetrating coefficient of the difference of gas pressure. A PDMS thin film with 225 μm in thickness can have CO<sub>2</sub> penetration rate of 12 g/(m<sup>2</sup>·h) [250]. The PDMS thin film separating gas channel and aqueous channel with thickness of 127 μm showed a slow pH change from 8.3 (using alkaline solution at beginning) to 4.5 within 1000 s with a contact area of 100 mm<sup>2</sup> [237], the carbon absorption rate was around 0.056 μmol/(L·min). This CO<sub>2</sub> absorption rate demonstrated with PDMS thin film was already suitable to most biological reactions and cell growth or reactions [237]. Compared to the CO<sub>2</sub> absorption rate of our porous PDMS cubes 2.370×10<sup>-7</sup> μmol/(L·min) and porous PDMS film 0.983 μmol/(L·min), the PDMS thin film with thickness of

127  $\mu\text{m}$  had a slower  $\text{CO}_2$  absorption rate. A recent approach using silicone microcapsules for  $\text{CO}_2$  absorption was described as an efficient gas-liquid interface method [234]. The microcapsules were generated by the similar method of droplet generation in microfluidics, with UV curable silicone as surfactant instead of oil or lipids. The generated microcapsules had diameter of  $600 \pm 6 \mu\text{m}$ , and wall thickness of  $32 \pm 1 \mu\text{m}$ . The  $\text{CO}_2$  absorption rate was measured as  $800 \sim 1000 \mu\text{mol}/(\text{L} \cdot \text{min})$  [234], which had much faster  $\text{CO}_2$  absorption rate than ours. However, this method only applies to the application of  $\text{CO}_2$  absorption in vesicle structure with the presence of cured silicone vesicles.

Other than PDMS, people had also tried some other material to form foam structures form gas-liquid interface, such as protein ranspumin-2 based foam [28]. The foam contains gas with  $\text{CO}_2$ , and the liquid solution were squeezed to the space between foams. The  $\text{CO}_2$  molecules could penetrate the protein foam membrane and dissolved into the aqueous solution for further carbon fixation and organic chemical synthesis reactions. The final product organic glucose reached  $60 \pm 6 \text{ nmol}$  within 4 hours reactions [28], so the  $\text{CO}_2$  absorption rate was approximately  $1.5 \times 10^{-4} \mu\text{mol}/(\text{L} \cdot \text{min})$ . However, after all of the  $\text{CO}_2$  in foam were absorbed, there was no continuous supply of  $\text{CO}_2$ , unless the used foam were broken and new foam were regenerated after all  $\text{CO}_2$  were consumed.

The experiment of 600  $\mu\text{L}$  microfluidic channel with porous PDMS cubes absorbing  $\text{CO}_2$  indicated that porous PDMS cubes are capable for  $\text{CO}_2$  penetration and little water leakage in a flow rate between 0 to 160  $\mu\text{L}/\text{min}$ . The volume of 600  $\mu\text{L}$  is prepared for artificial photosynthesis glucose synthesis purpose.

We demonstrated another gas liquid interface method with porous PDMS, combining the advantages of porous material and PDMS thin films. The experiment of 600  $\mu\text{L}$  microfluidic channel with porous PDMS cubes absorbing  $\text{CO}_2$  indicated that porous PDMS cubes are capable for  $\text{CO}_2$  penetration and little water leakage in a flow rate between 0 to 160  $\mu\text{L}/\text{min}$ . The volume of 600  $\mu\text{L}$  is prepared for artificial photosynthesis glucose synthesis purpose. The  $\text{CO}_2$  absorption

rate at a flow rate of 80  $\mu\text{L}/\text{min}$  reaches  $2.370 \times 10^{-7} \mu\text{mol}/(\text{L} \cdot \text{min})$ . Besides porous PDMS cubes, we also fabricated porous PDMS film using a similar way as leaching methods. Since the porous PDMS film has thinner thickness than porous PDMS cubes, the  $\text{CO}_2$  penetrating faster than porous PDMS cubes. However, porous PDMS film doesn't have long-term gas-liquid interface ability, because water leakage and evaporation is obvious for microfluidics.

Besides porous PDMS cubes, we also fabricated porous PDMS film using a similar way as leaching methods. Since the porous PDMS film has thinner thickness than porous PDMS cubes, the  $\text{CO}_2$  penetrating faster than porous PDMS cubes. However, porous PDMS film doesn't have long-term gas-liquid interface ability, because water leakage and evaporation is obvious for microfluidics. For artificial photosynthesis applications, we need a balance between  $\text{CO}_2$  absorption ability and liquid preservation ability. The light and dark reaction in artificial photosynthesis requires a stable pH and temperature environment under green light, because photosynthetic enzymes are sensitive chemicals in buffer solution. Therefore, we select a 600  $\mu\text{L}$  microfluidic channel with four porous PDMS cubes for glucose synthesis experiment.

We developed a novel method of creating a gas-liquid interface in microchannel systems using porous PDMS and demonstrated its performance using  $\text{CO}_2$  absorption. It is expected that the high  $\text{CO}_2$  absorption/penetration ability of the porous PDMS thin film can facilitate effective  $\text{CO}_2$  absorption from the air for diverse microfluidic cell culture platforms.

## **4.9 Contributions**

### **4.9.1 Real-time pH monitoring by cell-phone with Matlab**

Matlab image processing involves smart phone and programming indicated many advantages in fast and accurate pH monitoring. We used a smart phone to take photos/videos to observe the color change and pH value, which required no liquid extraction from the fluidic channel. Traditional accurate pH monitoring using fluorescence requires a certain volume of liquid for optical density measurement.



The method I used here can calculate pH value in a short time at an acceptable accuracy. The future of analysis using a smart phone will become a popular topic. This observation and measurement technique may even further be applied to determine the concentrations of other chemicals, such as glucose and certain ions, as well as meeting other specific purposes. With the broad use of smart phones, more useful fluidic devices that can be connected to smart phones will allow fast chemical analysis and may become a promising industry in the near future, especially in medical devices and point-of-care applications.

#### **4.9.2 Gas-liquid interface by porous PDMS**

I used porous PDMS cubes as gas-liquid interface for CO<sub>2</sub> absorption into fluidic channels. The experiments indicated that the porous PDMS cubes are better than other gas-liquid interface methods. In addition to porous PDMS cubes and films, I also explored methods of making porous parylene-C cubes and porous parylene-C films. Porous parylene-C showed similar gas-liquid interface results as porous PDMS.

## Chapter 5. DARK REACTION UNIT: GLUCOSE SYNTHESIS

After we evaluated the  $\text{CO}_2$  absorption in microfluidic channel with porous PDMS cube, we used this device to perform artificial photosynthesis of glucose.

### 5.1 ATP synthesis materials

Artificial photosynthesis includes light reaction and dark reaction as natural photosynthesis. The light reaction convert light energy into high energy chemical's energy in ATP. The pigment BR can absorb green light energy and generate proton gradient, which can be used to activate ATP synthase to create ATP from ADP and Pi. ATP synthesis is achieved by BR-ATP synthase on PMOXA-PDMS-PMOXA triblock copolymer vesicles under green light [28].

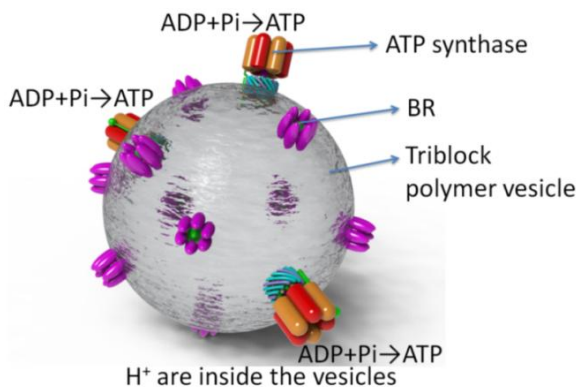


Figure 5-1. Illustration of BR-ATPase triblock copolymer vesicle structure.

The PMOXA-PDMS-PMOXA triblock copolymer vesicles with BR and FoF1 ATP synthase (Figure 5-1) can achieve light reactions in artificial photosynthesis. BR absorbed green light energy and pumped protons ( $\text{H}^+$ ) to the inside of the vesicles [78], which resulted in an increase of the pH value in the buffer solution, as shown in Figure 5-2. This pH gradient between the inside and outside of vesicles activated the FoF1 ATP synthase to synthesize ATP from ADP and Pi (Figure 5-3). The generated ATP will be the major energy source for further carbon fixation and glucose synthesis reactions.

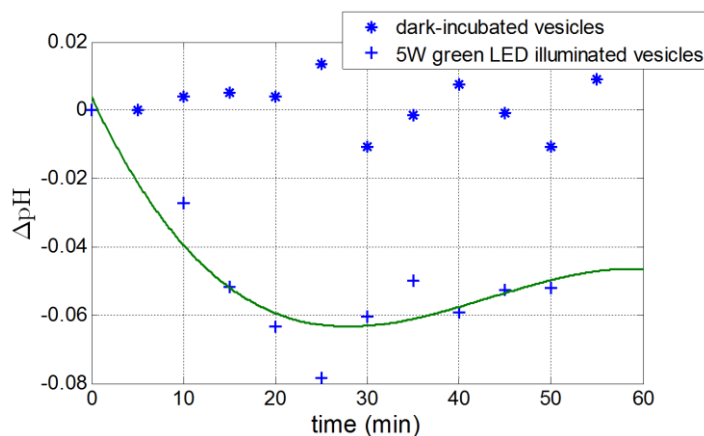


Figure 5-2. pH difference between inside and outside of the vesicles.

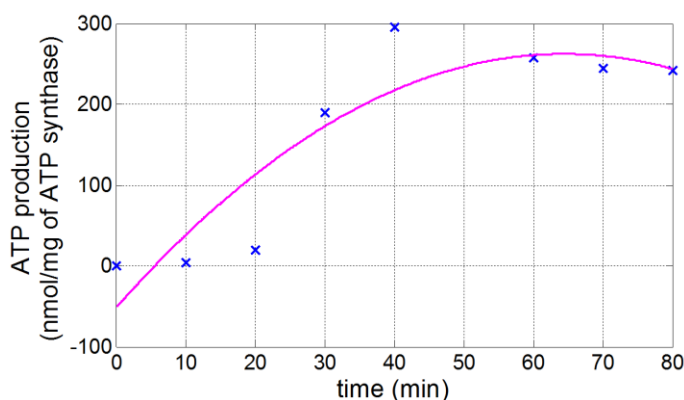


Figure 5-3. ATP synthesis amount by BR-ATPase triblock copolymer vesicles under 5W green LED.

### 5.1.1 Buffer solution

First, the buffer for dialysis is made for BR and ATP synthase. 20 mM 3-(N-morpholino) propanesulfonic acid (MOPS) (4.186 g, 209.2633 g/mol), 50 mM  $\text{Na}_2\text{SO}_4$  (7.103 g, 142.04 g/mol), 50 mM  $\text{K}_2\text{SO}_4$  (8.713 g, 174.259 g/mol), 2.5 mM  $\text{MgSO}_4$  (0.301 g, 120.366 g/mol), 0.25 mM dithiothreitol (DTT) (0.039 g, 154.25 g/mol), 0.2 mM ethylene-diaminetetra-acetic acid (EDTA) (0.075 g, 292.24 g/mol) were measured and placed in a beaker. Then, 1000 mL ID water was added to the beaker, and the pH was adjusted to around 7.3 by adding NaOH solution. [218] Second, the buffer for BR (same with dialysis buffer) was made by adding 200 $\mu\text{L}$  buffer into the BR vial (total BR monomer weight was 5mg), where the concentration of BR is 25mg/ mL. [218] This buffer solution needs to be replaced after 24 hours in order to keep the functionality. Third,

buffer for ATP synthase (Same with dialysis buffer) was made by measuring 950 $\mu$ L of the same buffer above into a test tube. Then, 50  $\mu$ L FoF1-ATP synthase (original concentration is 44.5mg/ml) was diluted, where the FoF1-ATP synthase concentration is 2.225 mg/mL. [218] Fourth, ADP solution was prepared by measuring 0.08544 g ADP (0.0002 mol, 427.201 g/mol), and about 1 mL DI water was added to make the solution into an ADP concentration of 0.2 mol/L. [218] Finally, monopotassium phosphate ( $\text{KH}_2\text{PO}_4$ ) solution preparation was made by measuring 0.06804g  $\text{KH}_2\text{PO}_4$  (0.0005 mol, 136.086 g/mol), and about 1 mL DI water was added to make the  $\text{KH}_2\text{PO}_4$  concentration as 0.5 mol/L. [218]

### 5.1.2 Vesicle preparation

To prepare the BR-ATP synthase copolymer vesicles, 10 mg triblock copolymer was placed in small centrifuge tube. Then, 68.5  $\mu$ L BR monomer solution was slowly added into the tube. The centrifuge procedure continued for 0.5 hour. After the centrifuge finished, 0.59 mg sodium cholate ( $\text{C}_{24}\text{H}_{39}\text{O}_5\text{Na}$ , 430.55 g/mol) and 0.29 mg sodium deoxycholate ( $\text{C}_{24}\text{H}_{39}\text{O}_4\text{Na}$ , 414.55 g/mol) were added into the BR and copolymer structure and kept vibrating for 2 hours in the dark to get a homogeneous solution. [218] The sodium cholate and sodium deoxycholate were used to help the formation of copolymer vesicles. After diluting in synthesis assay, the sodium cholate and sodium deoxycholate can be eliminated by multiple time diluting procedures.

To add ATP synthase into the vesicles, 230  $\mu$ L of FoF1-ATP synthase ( $2.225\text{mg/ml} \times 230 \mu\text{L} = 511.75 \mu\text{g}$ ) was placed in a test tube. Then, 1.98 mg sodium cholate and 0.96 mg sodium deoxycholate were added into ATP synthase and kept vibrating for 0.5 hour. Then, ATP synthase and sodium deoxycholate mixture was slowly added into the polymer and BR mixture. After vibrating for half a hour, a slow drop wise of this protein – polymer mixture was added into the dialysis buffer, and placed in small centrifuge tube, whereas the total volume of this mixture was 2 mL. To create BR-ATP synthase proteopolymersomes, the mixing was performed by adding the droplets at a ratio of 10  $\mu$ L per 30 seconds, with a total mixing time of 2.5 hours. Syringe

filtration through a membrane with pore size of 0.2  $\mu\text{m}$  was used to remove non-functional multi-lamellar vesicles and other aggregates. [218]

All polymersome suspensions were dialyzed while stirring by rotor at 4°C in the dark for 2 days. The dialysis tube (12000Da) containing the sample was placed in the beaker. Buffer was used as the solution for dialysis. This experiment was operated in the refrigerator, and the buffer was replaced in every 24 hours. [218]

### **5.1.3 ATP synthesis assay**

After the ATP synthesis, no inhibitor was added into the reaction to stop further ATP synthesis. The reaction mixture in bulk-vesicle solution contained 400  $\mu\text{L}$  of BR-ATP synthase proteo-polymersome solution, 40  $\mu\text{L}$  of 0.2 M ADP, 40  $\mu\text{L}$  of 0.5 M  $\text{KH}_2\text{PO}_4$ , which was placed in the short glass tube. The ADP and  $\text{KH}_2\text{PO}_4$  were incorporated into the proteopolymersomes by vigorous mixing. The samples were illuminated by a 5.0 W green LED ( $\lambda=570\text{nm}$ ). After incubation for 15~20 min at 35°C under continuous illumination, ATP synthesis reaction was initiated by the addition of 0.96 mg  $\text{MgSO}_4$  (0.017 mol/L, same concentration with ADP, 0.008 mmol, 120 g/mol). To measure ATP synthesis activity, a bioluminescence assay kit (Sigma Aldrich, catalog number FLAAM-1VL) with luciferin and luciferase were used. At the same intervals (10 min), 40  $\mu\text{L}$  aliquots of reaction mixture are taken out and rapidly mix with 40  $\mu\text{L}$  ATP assay mix and immediately measured the amount of light produced. [218]

## **5.2 Glucose synthesis materials**

### **5.2.1 Buffer solution**

To make the buffer for glucose synthesis, 0.6057g Tris-base (0.1mol/L), 0.0238g  $\text{MgCl}_2$  (5 mmol/L), 0.330g  $\text{KHCO}_3$  (66 mmol/L) and 0.039g DTT (5 mmol/L) were added into the beaker (100mL) and then added 50mL DI water. The pH of the buffer was measured and adjusted to 7.8 by adding the HCl or NaOH solution. [218]

## 5.2.2 Enzymes mixing

520  $\mu\text{L}$  of the buffer was transferred into tube (1.5 mL) before adding the following carbon fixation enzymes: 0.8  $\mu\text{L}$  triose phosphate isomerase (TPI, Sigma Aldrich) (12 units, Sigma Aldrich), 1  $\mu\text{L}$  fructose-1,6-bisphosphatase (F1,6BPase) (12 units, Cayman Chemical Co., Ann Arbor, MI), 1.6  $\mu\text{L}$  phosphoglucose isomerase (PGI, Sigma Aldrich) (12 units, Sigma Aldrich), 0.15 mg aldolase (0.8 units, MP Biomedicals LLC, Solon, OH), 1 mg glucose-6-phosphatase (G6Pase) (0.12 units, Sigma Aldrich). 0.08mg glyceraldehydes-3-phosphate dehydrogenase (GAPDH) (4 units), 0.18 mg nicotinamide adenine dinucleotide hydrogen (NADH) (250 nmol, Sigma Aldrich), 1.6  $\mu\text{L}$  phosphoglycerate kinase (PGK) (8 units, Sigma Aldrich), 0.500 mg of RuBisCO, (Sigma Aldrich) and 0.22 mg RuBP (Sigma Aldrich) (400 nmol). [218]

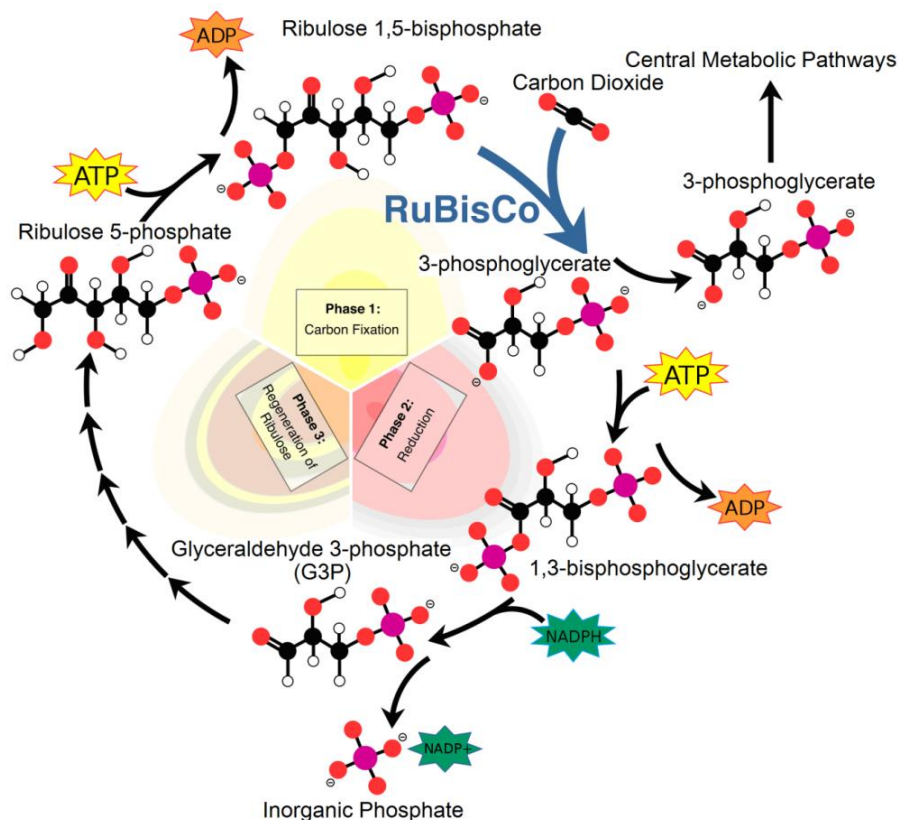


Figure 5-4. Three phase reactions in Calvin Cycle of 3PG synthesis for glucose/fructose synthesis. Reproduced from [5] Nelson and Cox, Lehninger principles of Biochemistry, 5th Ed., 2008; Reproduced with permission from WH Freeman/Worth Publishers.

### 5.2.3 Glucose synthesis assay

The glucose synthesis assay was carried out after the preparation of the carbon fixation enzymes. 520  $\mu\text{L}$  of above enzyme complex and 600  $\mu\text{L}$  polymersome mixture were added into the glass tube, and mixed using a small magnetic stirring bar. The samples were illuminated by a 5.0W green LED ( $\lambda=570\text{nm}$ ). After incubation for 15~20 min at 30°C under continuous illumination, ATP synthesis reaction is initiated by the addition of 2.24 mg  $\text{MgSO}_4$  (0.0166 mol/L, same concentration with ADP). At different time points (0 hour, 1 hour, 3 hours, 5 hours, 7 hours), 200  $\mu\text{L}$  of samples were taken out and put in the centrifugal filter. After 15 min centrifuge, 100  $\mu\text{L}$  sample and 200  $\mu\text{L}$  glucose assay (GAGO20, Sigma Aldrich, catalog number GAGO20-1KT) were added into the tube in 37°C water bath. After 30 min, 200  $\mu\text{L}$  sulfuric acid was added into the mixture, in order to show the color change of o-dianisidine from brown color to pink color. Then, the sample with assay and sulfuric acid was mixed completely by vortex, and the absorbance measurement for glucose production on each sample was measured right after mixing. The control group in glucose synthesis assay included another sample with 520  $\mu\text{L}$  enzyme complex and 600  $\mu\text{L}$  polymersome mixture with same reaction conditions except for the LED illumination. [218] The solution will be transferred to 96-well round bottom assay plate (Corning Incorporated, Corning, NY), and the absorbance at 540 nm will be measured by microplate reader (Synergy Mx, BioTek Instruments Inc., Winooski, VT).

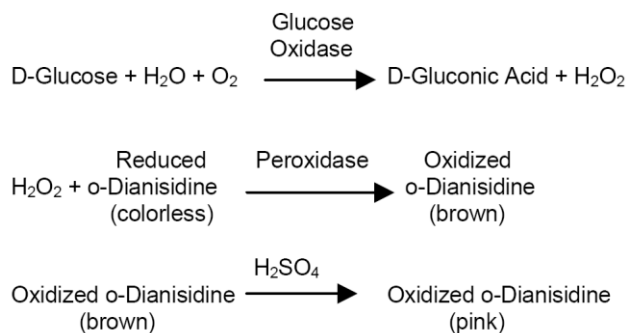


Figure 5-5. Glucose assay principle using o-dianisidine as redox indicator. Reused with permission from Sigma Aldrich.

Glucose is oxidized to gluconic acid and hydrogen peroxide ( $\text{H}_2\text{O}_2$ ) by glucose oxidase, so the detection of glucose concentration is changed to detect the amount of  $\text{H}_2\text{O}_2$  generated.  $\text{H}_2\text{O}_2$  can be reacted with o-dianisidine by the catalyze of peroxidase to produce a brown color product of oxidized o-dianisidine. After adding 6 mol/L  $\text{H}_2\text{SO}_4$  solution, the brown color will become pink color, and ready for optical density measurement. The density of the pink color at luminance of 540 nm is proportional to the glucose concentration. Therefore, we can use the microplate reader to collect optical density (OD) value and compare the results to standard glucose vs. OD value calibration curve to find out the original glucose concentration.

### 5.3 Experimental

The fluidic channel with porous PDMS cubes was placed in a plastic container connected to  $\text{CO}_2$  supply (Figure 5-6). The  $\text{CO}_2$  was generated by sublimation of dry ice. In order to reduce the effect of the low temperature of dry ice on  $\text{CO}_2$  absorption experiment, we used a 0.5 m long tube to provide the gas into the plastic container. The temperature in the container during experiment remained at room temperature ( $27^\circ\text{C}$ ). The light source was a 5 W green LED lamp with a wavelength around 570 nm, located at a distance of approximately 10 cm from the fluidic channel.

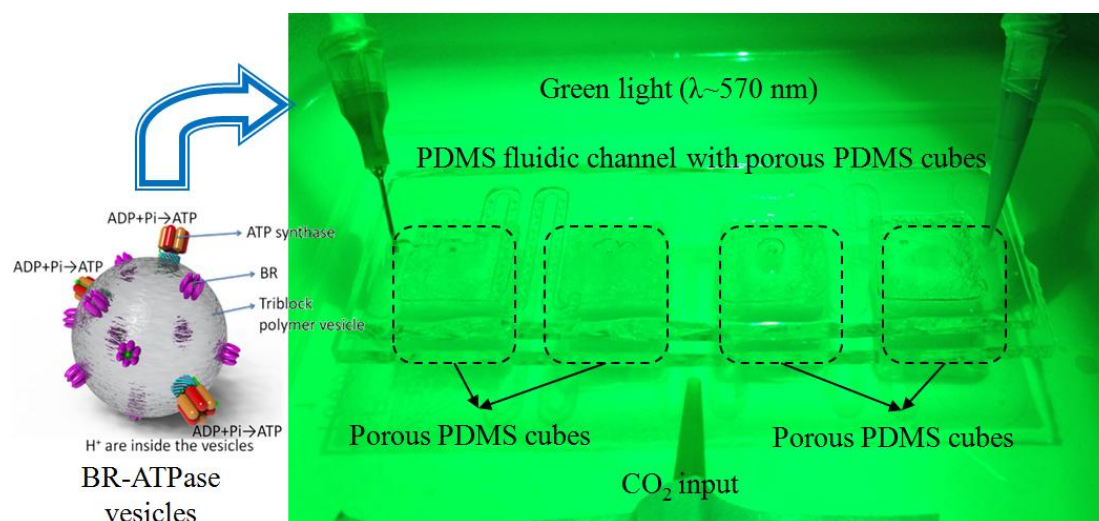


Figure 5-6. Experimental setup for glucose synthesis analysis.



The vesicle buffers with carbon fixation enzymes buffer were mixed under the green LED lamp for 15 min to initiate the glucose synthesis procedure. Then, the mixture was transferred into a 3 mL syringe with internal diameter of 9.883 mm. The solution was injected to the PDMS channel with a flow rate set by the syringe pump.

We tried both static and dynamic flow conditions. In static condition, the inlet and outlet of the PDMS channel were sealed after the fluid was filled in the channel. The porous PDMS cubes were exposed to CO<sub>2</sub> environment. In dynamic condition, the fluid was pumped into the channel at a flow rate of 50 μL/min. After the fluid fully filled the PDMS channel and the outlet reservoir, the syringe pumping direction was reversed, so that the glucose synthesis solution was flowing back and forth in the PDMS channel. This procedure was repeated multiple times for 3 hours then the solution was extracted and mixed with glucose assay solution (GAGO20, Sigma Aldrich, catalog number GAGO20-1KT) for 30 min at 37°C, followed by centrifuging at 5000 rpm for 10 min. Filtering was necessary to remove solid residuals produced during the reaction of the photosynthesis solution with glucose assay kit solution. After syringe filtration with a 2.0 μm membrane filter, the extracted solution would not contain the vesicles.

Glucose was oxidized to gluconic acid and hydrogen peroxide (H<sub>2</sub>O<sub>2</sub>) by glucose oxidase. The detection of glucose concentration was accomplished by measuring the amount of H<sub>2</sub>O<sub>2</sub>. H<sub>2</sub>O<sub>2</sub> reacted with o-dianisidine by the catalysis of peroxidase to produce oxidized o-dianisidine with brown color. Then, 2.0 mL of diluted 6 mol/L sulfuric acid (H<sub>2</sub>SO<sub>4</sub>) solution was added to the extracted solution in test tube to generate pink color oxidized o-dianisidine. The density of the pink color at luminance of 540 nm was proportional to the glucose concentration. 200 μL of the solution was carefully dropped in 96-well plate for optical density reading right after the pink color generated. We used the microplate reader (Synergy Mx, BioTek Instruments Inc., Winooski, VT) to collect OD<sub>540</sub> value and compared to standard glucose vs. OD<sub>540</sub> value calibration curve (Figure 5-7) to find out the original glucose concentration.

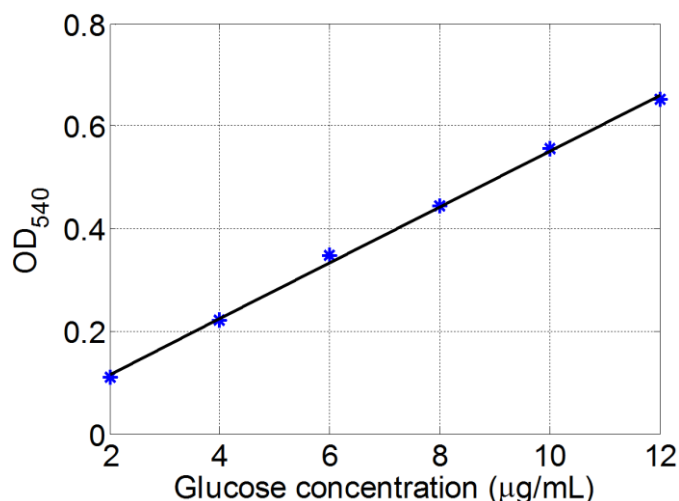


Figure 5-7. Optical density value change at different glucose concentration with an emission at 540 nm.

The method of optical density can be used to identify the glucose concentration. Based on the six data sets of standard glucose concentration (2, 4, 6, 8, 10, 12 µg/mL) to OD value, the linear fitting function was

$$f(x) = 0.05449x + 0.007267$$

Eq. 5-1

where the coefficients had 95% confidence bounds, with a linear fitting correlation coefficient  $R^2=0.9983$ ; adjusted  $R^2=0.9979$ . Considering the correlation of the fitting, correlation coefficient  $R \approx 0.999$ , with  $n=6$ , from the relative coefficient table  $R_{0.01}(4)=0.917$  (the table in Appendix IV “Table of correlation significance test threshold value of the correlation coefficient”); while  $R > R_{0.01}(4)$ , the linearity of this fitting is acceptable in significance test.

## 5.4 Results

We used the average value of two sets of OD reading results. Before we added the solution into PDMS channel, the initial stirring under 5W green LED light can also absorb some of the  $\text{CO}_2$  from air but the amount of glucose created by  $\text{CO}_2$  from air was minimal. The glucose generated during initial stirring was measured as “Initial” in Table 1. The  $\text{OD}_{540}$  value in standard glucose concentration is the average  $\text{OD}_{540}$  value (“after 4 hours” data for static flow, and “after 3 hours” data for dynamic flow) minus the pure  $\text{H}_2\text{O}$   $\text{OD}_{540}$  value in Table 1. Comparing the  $\text{OD}_{540}$

value to the standard fitting line in Figure 5, the glucose concentration in static flow after 4 hours was  $3.53 \pm 0.06 \mu\text{g/mL}$ ; and the glucose concentration in dynamic flow was  $5.56 \pm 0.17 \mu\text{g/mL}$ .

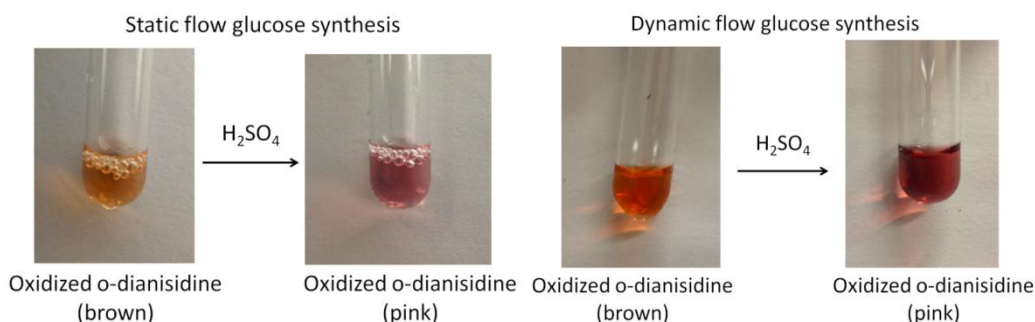


Figure 5-8. Glucose assay of static flow and dynamic flow at  $50 \mu\text{L}/\text{min}$  using oxidized o-dianisidine color change by adding sulfuric acid.

Table 5-1. Microplate optical density (OD) value reading with emission at 540 nm

	H <sub>2</sub> O	0 hour	4 hour	Glucose* concentration
Static flow	0.054	0.068	0.249	$3.53 \pm 0.06$ $\mu\text{g/mL}$
	0.054	0.062	0.257	
	H <sub>2</sub> O	0 hour	3 hour	Glucose* concentration
Dynamic flow $50 \mu\text{L}/\text{min}$	0.043	0.045	0.368	$5.56 \pm 0.17$ $\mu\text{g/mL}$
	0.043	0.045	0.338	

\* The molar mass of glucose ( $\text{C}_6\text{H}_{12}\text{O}_6$ ) is 180 g/mol.

The  $\text{CO}_2$  absorbed in static condition in 4 hours was around  $312 \mu\text{mol/L}$ . The synthesized glucose was  $19.6 \mu\text{mol/L}$ , so the  $\text{CO}_2$  conversion rate of carbon-fixation enzyme RuBisCO was  $\sim 37.7\%$ . On the other hand, the  $\text{CO}_2$  absorbed in dynamic condition in 3 hours was around  $270 \mu\text{mol/L}$ . The synthesized glucose was  $30.88 \mu\text{mol/L}$ , so the  $\text{CO}_2$  conversion rate of carbon-fixation enzyme RuBisCO was  $\sim 68.6\%$ . The dynamic fluid had higher carbon fixation rate because the zig-zag shape structure in the fluid channel facilitated the mixing of dynamic fluid. More agitation of the reaction solution can benefit the RuBisCO's possibilities to combine with  $\text{CO}_2$  and ATP.

## 5.5 Discussion and conclusion

For artificial photosynthesis applications, we need a balance between CO<sub>2</sub> absorption ability and liquid preservation ability. The light and dark reaction in artificial photosynthesis requires a stable pH and temperature environment under green light, because photosynthetic enzymes are sensitive chemicals in buffer solution. Therefore, we select 600 μL microfluidic channel with four porous PDMS cubes for glucose synthesis experiment.

Some previous artificial photosynthesis approaches following the similar Calvin Cycle reaction principles have limitations on carbon fixation, especially for long term CO<sub>2</sub> input into the reaction solution. Some researchers successfully achieved artificial photosynthesis in bubble structure, where the CO<sub>2</sub> was captured in the bubble architecture. The amount of CO<sub>2</sub> to the system was limited to the CO<sub>2</sub> inside the bubbles [28, 68]. Otherwise, people tried to create constant CO<sub>2</sub> input to the reaction solution for hours, they have to use test tubes or beakers to create openings to the air, which was not suitable for a device that can be produced or transported [218]. In our microfluidic channel devices, the porous PDMS cubes can provide constant CO<sub>2</sub> input to the photosynthetic reaction solution for long-term glucose synthesis.

The glucose synthesis concentration in static flow is lower than the concentration in dynamic flow of 50 μL/min, because the dynamic flow can absorb more CO<sub>2</sub> than static flow condition. The dynamic flow keeps a more steady CO<sub>2</sub> concentration gradient, which will be better for CO<sub>2</sub> absorption through this porous PDMS cube gas-liquid interface.

The glucose synthesis solution is using BR-ATP synthase vesicles as ATP synthesis source, and carbon fixation enzymes as dark reaction by Calvin Cycle principle. The vesicles are formed by PMOXA-PDMS-PMOXA triblock copolymer. Since the reaction was successfully procedure, the successful result indicated that the middle chain PDMS in triblock copolymer will not react with the PDMS on microfluidic channel, neither attracted by the pillars on top ceiling of the microfluidic channel, nor broken or squeezed inside the fluidic channel.

During the glucose synthesis, ATP synthesis and dark reaction were happening at the same time, as long as the green light was over the top of PDMS microfluidic channel. The ATP synthase concentration and ATP synthesis efficiency can also affect the glucose synthesis efficiency, sometimes dominating the glucose synthesis procedure. Besides, the energy input of green LED will also affect the BR proton transfer efficiency, as well as ATP synthesis efficiency. The distance of the LED source to the solution will determine the irradiance and light luminous intensity. Therefore, further study on the quantity of light luminous needs to be determined. During the previous experiment experiences [218], the ATP synthesis from ADP and  $P_i$  are not necessarily have 100% recycle rate, which will also limit the ATP synthesis efficiency. The reducing of ADP reuse ratio will results in a decreasing ATP synthesis rate, and further dominating the lower glucose synthesis rate.

The carbon fixation enzymes are floating with BR-ATP synthase vesicles in the solution at a pH around 7.5. The enzymes are sensitive to temperature and pH value, because the enzymes are proteins in solution, and the activities are related to temperature and pH. Using dry ice as  $CO_2$  source will slightly change the environment temperature, as well as pH of the solution. One standard atmosphere pressure of  $CO_2$  will result in a saturated pH of 5.6~6.5, which may affect the enzymes activities.

The fluid mixing and diffusion properties are significant factors in glucose synthesis. The prime enzyme in carbon fixation, RuBisCO, dominates the carbon fixation rate and glucose synthesis efficiency. The chance of RuBisCO capturing ATP and  $CO_2$  at same time is the most important factor in glucose synthesis rate. Therefore, the agitation of the fluid will benefit the chance of RuBisCO capturing one molecule of ATP and one molecule of  $CO_2$  at once. If the capturing process is successful, the byproduct RuBP can be reused to Calvin Cycle for further  $CO_2$  capture.

We developed a novel method of creating a gas-liquid interface in microchannel systems using porous PDMS and demonstrated its performance using  $CO_2$  absorption. We believed that

this gas-liquid interface method could be applied to many applications in lab-on-a-chip systems, especially in artificial photosynthesis systems, which is our ultimate target system. Our microfluidic channels with porous PDMS cubes are able to simulate the leaf function: absorbing CO<sub>2</sub> with less water evaporation and glucose synthesis. The CO<sub>2</sub> absorption ratio and glucose synthesis amount can be improved by alternating the dimensions of porous PDMS cubes.

Our fluidic device with porous PDMS cubes offered some key advantages for artificial photosynthesis reactions: (i) the porous PDMS cubes provided continuous CO<sub>2</sub> supply to fluidic channel, (ii) the PDMS fluidic device was easier for handling than foam bubble structure in beakers, and (iii) PDMS was lower in cost and more convenient in fabrication processes than protein based foam. Therefore, our PDMS device with porous PDMS cubes brings the artificial photosynthesis from laboratory to a practical platform or device for usage.

## **5.6 Contributions**

A new light energy harvesting device was designed, fabricated and tested with glucose synthesis experiment. The fluidic channel with porous PDMS cubes was capable to absorb sufficient CO<sub>2</sub> for carbon fixation in glucose synthesis. Comparing the glucose or fructose synthesis in Rsn-2 foam, the porous PDMS was able to capture CO<sub>2</sub> continuously. Further experiments can determine the role of temperature, pH value, light source intensity, and air source's affect in carbon fixation in glucose synthesis reactions.

## Chapter 6. ORGANIC COMPOUND STORAGE PLATFORM

We originally proposed an artificial photosynthesis fabrication platform using Calvin Cycle principles based on additive manufacturing technology. We were planning to use an innovative tree-leaf-like architecture with multi-layer interconnected channels and micro-porous structures to support artificial photosynthesis for organic compound production. The main objective in this task was to create a 3D interconnected chitosan porous structure using additive manufacturing technology. This chapter contains the published contents in journal papers [269].

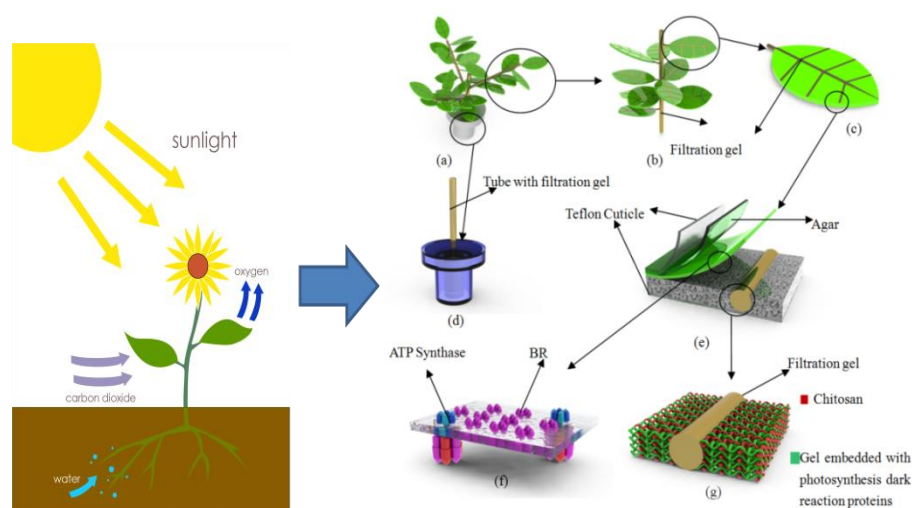


Figure 6-1. Illustration graph of a leaf-like device from the principle of photosynthesis. ([5] Reused with permission from MacMillan.) (a) artificial tree with photosynthetic leaves; (b) artificial tree branch; (c) artificial leaves with filtration channels; (d) product collection container; (e) layers' structure of artificial leaves; (f) triblock membrane; (g) porous structure with “dark reaction” solutions.

We planned to print the main structure of our whole artificial photosynthesis device using a specifically designed rapid prototyping (RP) system. We planned to make the interconnected channels with micro porous chitosan. Another layer of PEtOz-PDMS-PEtOz or PMOXA-PDMS-PMOXA triblock polymer embedded with BR and ATPase was going to be created and function as the mesophyll layer of natural leaves for photosynthesis light reactions. The artificial photosynthesis dark reaction was planned to be embedded in the chitosan layers and channels. The solution included all carbon fixation proteins such as RuBisCO, glucose or fructose

isomerase and other necessary organic compounds: RuBP and NADP<sup>+</sup>, and enough amounts of ATP, ADP and Pi (inorganic phosphate, HPO<sub>3</sub>O<sup>2-</sup>) as start-up for all these carbon fixation reactions. The carbon fixation enzyme RuBisCO fixed CO<sub>2</sub> and RuBP. By using ATP offering energy and NADPH oxidizing to NADP<sup>+</sup>, these reactions produced G3P, and the final output from G3P combination was hexose such as glucose or fructose. With the catalysis of isomerase catalysts, the final product could be either glucose or fructose [28]. The system was able to achieve high photosynthetic efficiency because it did not have any life-related activities such as respiration, digestion, reproduction, growth and excretion.

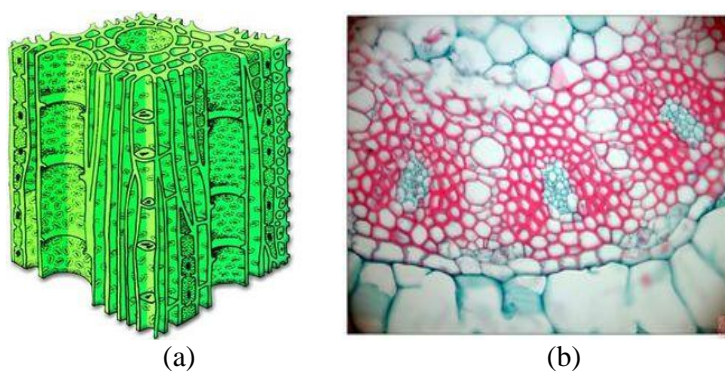


Figure 6-2. Image of plant (a) sieve tube; and (b) vascular bundle [5]. Reused with permission from MacMillan.

To mimic natural leaves, an artificial leaf/tree design was illustrated in Figure 6-1. In Figure 6-1a and Figure 6-1b, the main branches and stems (called channels) on the leaves would be used to supply photosynthesis proteins and enzymes and collect the sugar products. In order to simplify final product separation, the branches/channels of the leaf were connected to a chromatographic column which contains the gel for glucose-size molecule isolation (Figure 6-1b and Figure 6-1c). The filtration gel size was controlled to be bigger than glucose and smaller than proteins and enzymes, so that the isolation of the final product could be simplified in only one step. Figure 6-1e showed the multi-layer feature of the artificial leaf consists of top Teflon cuticle layer, agar layer, triblock membrane layer, interconnected channels and micro-porous layers, and bottom Teflon cuticle layer. Among these five layers, the main challenges were to make the dark



reaction layer (channels and reaction gels) and fabricate the light reaction layer (triblock membrane layer). In the dark-reaction layer, there were three materials: chitosan, hydrogel and filtration gel (Figure 6-1g). The Calvin Cycle reaction solution was embedded in hydrogel and kept inside the chitosan-formed interconnected channels. While giving enough space for photosynthesis, the structure could also facilitate air exchange and glucose product pre-isolation. The chitosan structure's micro-pores would make it flexible, thus the produced "artificial leaf" could be soft and could be folded for easier transportation. On the top of the micro-porous chitosan, channel layer would be a triblock polymer membrane layer which combines photosynthesis pigment BR and FoF1 ATP synthase. Above the triblock polymer membrane, a layer of ~10 nm thick phytagar would be coated. Phytagar does not have great mechanical strength, but it was able to act as a solid/gel medium for energy exchange of protons produced by light collection pigments.

In natural leaves, there is a layer of spongy mesophyll cells. The spongy mesophyll cells form an interconnected porous structure that facilitates photosynthetic dark reactions. In some previous work, scientists had compared the artificial photosynthesis efficiency of pure liquid solution to the foam structure with dark reaction components. The results showed that the foam structure had three times greater the glucose production than in bulk solution without foams [28]. The foam architecture could increase the carbon fixation reaction area to contact the carbon dioxide and provide flow channels for vesicles and solutions. Therefore, it was important to have a structure that facilitated the flow of reactants and exchange of energy and mass. Making the porous structure with interconnected inner channels was a big challenge for the successful fabrication of an artificial photosynthesis system.

## **6.1 Physics and chemistry properties of chitosan**

The main structure in this novel artificial photosynthesis device was a chitosan porous scaffold with micro-pores. The porous structure was employed to increase the interface of

reactions among carbon fixation compounds, carbon dioxide and enzymes in the dark reaction solution [270].

Every repeating monomer in chitosan had one amino group (Figure 6-3) which was capable of creating hydrogen bonds with the enzymes in the artificial photosynthesis dark reaction [271]. Even though hydrogen bonds are rather weak, those bonds still helped to prevent enzyme loss [272-274]. Moreover, chitosan through lyophilization could create porous structures, which became the media that allowed the air exchange between the atmosphere and this artificial photosynthesis device [275]. In addition, the porosity, average pore size, and pores orientations can be modified by different chitosan recipes and cross linking methods [276-282].

The porous structure was used to hold the dark reaction solution and provide a larger interface between carbon dioxide and the carbon fixation compounds and enzymes. We chose chitosan as the frame structure material [283, 284]. Chitosan, a deacetylated derivative of chitin commonly found in the shells of crustaceans, was an attractive candidate as a natural biopolymer hydrogel.

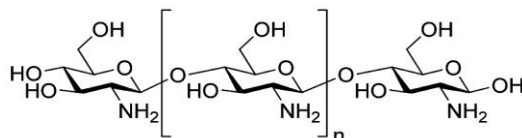


Figure 6-3. Molecular structure of chitosan [285]. Reused with permission from Wikipedia.

Chitosan has been extensively used for many purposes. It is used as a cosmetics additive, in food and nutrition supplements, and in medical care [286-291]. Chitosan was a candidate material in RP or other RP methods, but the details of printing chitosan in different concentrations were not the same. According to experiments in which chitosan was fabricated with NaOH as the bath solution, even the same concentration of NaOH and the same concentration of chitosan could lead to different results [287, 292-294]. Other cross-linking methods also could be applied on chitosan gels to form chitosan scaffolds before lyophilization [295-298], even using advanced chemical

method like electrochemical electroplating [299-304]. Chitosan would become solid once the pH value increased in the surrounding solution near the electrodes [305].

Figure 6-4 shows a scanning electron microscope (SEM) image of the internal morphology of chitosan's micro-porous structure produced by the lyophilization process using liquid nitrogen in freezing. The average diameter of the micro-pores was around 5~10  $\mu\text{m}$  (Figure 6-4a), and the overall morphology and orientation of micro-porous structure could be regulated.

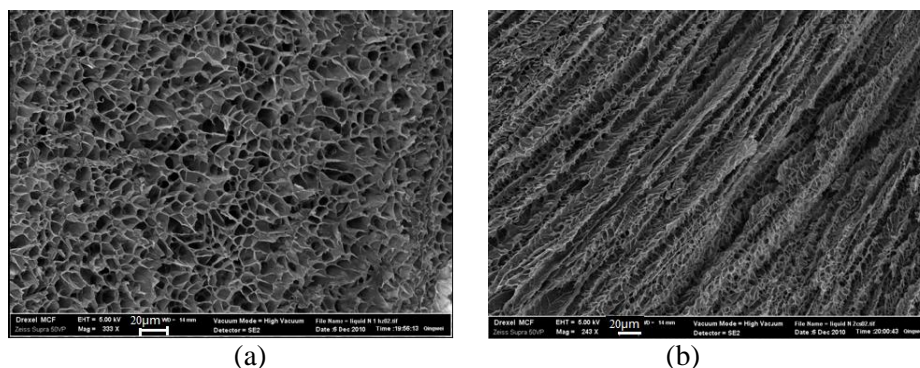


Figure 6-4. Morphology of micro-porous chitosan produced by liquid nitrogen lyophilization process: (a) Cross-section view; (b) Perpendicular section view.

In RP, the material's properties, especially the viscosity and density of the material, were critical to the printing parameters and the printed result [306]. Since the concentration data of existing experiments were reliable, we prepared chitosan samples and tested the viscosity. First, we separated samples into three groups based on their molecular weights: high molecular weight was 310,000 g/mol to > 375,000 g/mol; medium molecular weight was 190,000-310,000 g/mol; and low molecular weight was 50,000~190,000 g/mol. We placed 0.1 g, 0.15 g, 0.2 g, 0.25 g, 0.3 g of high molecular weight chitosan in the proper amount of 70%  $\text{CH}_3\text{COOH}$  (acetic acid) to make each sample become 10 g; we placed 0.4 g, 0.5 g, 0.6 g, 0.7 g, 0.8 g, 0.9 g of medium molecular weight chitosan in proper amount of 70% acetic acid to make each sample become 10 g; then, we put 0.7 g, 0.8 g, 0.9 g, 1.0 g, 1.1 g, 1.2 g, 1.3 g of low molecular weight chitosan in proper amount of 70% acetic acid to make each sample become 10 g. Then, we measured the

viscosity for each sample with a rheometer (Brookfield Viscometer DV-II+Pro). To measure each sample, we selected proper shear rate, as the samples were non-Newtonian fluids.

The chitosan samples with higher chitosan concentration in 70% acetic acid solution were more viscous than the chitosan samples with lower chitosan concentration in the same 70% acetic acid solution. Increasing the acetic acid concentration would also increase the viscosity of chitosan sample, but the solubility of high concentration acetic acid was limited [307]. Chitosan was not soluble in glacial acetic acid, but it could form hydrogel in an acetic acid solution with water. The concentration of water would make the solution become gel and determine the viscosity as well as the surface tension of the gel [308]. We found that the chitosan's molecular weight played an important role in determining the viscosity in printing material. Since the molecular weight for different batches of chitosan could vary greatly, the material tests before printing were necessary.

Chitosan can be cross linked by glutaraldehyde, formula  $\text{CH}_2(\text{CH}_2\text{CHO})_2$  [309, 310]. Using 1.5 wt% chitosan in 1% acetic acid with 1 mL 25% glutaraldehyde would form chitosan in hydrogel status.

Table 6-1. Chitosan porosity after lyophilization.

Materials	Sample #	Gel (g)	Lyophilization (g)	Gel volume (mL)	Lyophilization volume (mL)	Porosity
Chitosan	1	4.069	0.077	4	0.0604	98.49%
	2	4.640	0.085	4.5	0.0667	98.51%
	3	4.988	0.092	5	0.0722	98.56%
Chitosan + glutaraldehyde	1	4.951	0.177	5	0.1315	97.37%
	2	3.951	0.146	4	0.1085	97.29%
	3	4.386	0.157	4.5	0.1166	97.41%

The density of gel was calculated as around  $1.369 \text{ g/cm}^3$ .

## 6.2 Rapid prototyping technology

Rapid prototyping technology is a fast way to create a prototype with direct manufacturing methods. Rapid prototyping includes subtractive manufacturing and additive manufacturing (AM).

American Society for Testing and Materials (ASTM) International defines AM as the “process of joining materials to make objects from 3D model data, usually layer upon layer, as opposed to subtractive manufacturing methodologies. Synonyms: additive fabrication, additive processes, additive techniques, additive layer manufacturing, layer manufacturing and freeform fabrication.” Additive manufacturing is the method of building subjects by adding thin layers of materials as bases for additional layers. Subtractive manufacturing, such as CNC milling, is the method of machining subjects by removing materials from a block of material and leaving the wanted material. Subtractive manufacturing not only consumes more materials than additive manufacturing, it also has some limitations in making complicated internal structures because of the movement limitations of milling or drilling tools.



Figure 6-5. Rapid prototyping: (a) subtractive manufacturing; (b) additive manufacturing.

### 6.3 Additive manufacturing: 3D printing

Additive manufacturing is a kind of prototyping technique by adding structural materials to form 3D structure which is broadly used in biomaterials 3D printing for tissue engineering scaffolds fabrication. There are different types of additive manufacturing, mainly divided in high resolution methods, such as two-photon polymerization [311, 312], and micro-stereolithography [313]; and lower resolution methods, such as bio-printers [314], and many other user-developed 3D printers [315, 316]. Based on the materials, the 3D printers can also be categorized by photo polymer-based, powder-based, molten materials based, and solid sheets based. The well-known molten materials is acrylonitrile butadiene styrene (ABS), or PCL, etc, using the fused deposition modeling (FDM) to construct complex 3D structures. The ABS printing in FDM has limitations

in building speed, accuracy, and material density. Besides, the melding filaments cannot form sharp external corners, which are determined by the acceleration and deceleration of FDM dispensing nozzles. We mentioned photo polymer based EnvisionTEC perfactory 3D printer for microfluidic channels in PDMS molding for gas-liquid interface. The dynamic masks for each layer was projected by liquid crystal display (LCD) screen. For most of the self-prepared gel or liquid, using extrusion nozzles as printing head was the best choice. The extrusion based 3D printing system includes material loading, liquefaction, pressure to nozzles, extrusion, plot path, solid bonding, and support structure. The principles of extrusion processes followed the fluid dynamics principles, sometimes belonged to microfluidics if the nozzle cavities were small enough to have low Reynolds numbers.

3D printing is fabrication of an object by direct deposition of structural materials. The movement of the automatic AM machine's printing nozzles and dispensing activities must follow a computer-designed program. Therefore, the technique of computer-aided design (CAD) and correlated G-code programming were introduced and embedded into 3D printers [317]. The principle of printing CAD file is to slice the CAD model into layers, and import the model data into the 3D printers layer by layer, which translated the model's digital information into G-code that could be operated by a computer program similar to CNC. Then the sliced coordinate information in G-code controls the horizontal movements of nozzles and biomaterials for each layer.

Commercially available 3D printing machines can only handle one or two kinds of pre-defined or pre-loaded materials (structural material and sacrificial material) with specified parameters. They must have specifically designed programs consisting of printing parameters and printing nozzles for each printing material [292, 293, 318]. However, user-prepared biomaterials, for example, polycaprolactone (PCL) in acetic acid solution, could have different weight concentrations which would result in different fluidic properties, including viscosity, surface tension coefficient, solidification coefficient in air, and density, etc. The variable fluidic

properties cannot fit the pre-defined printing parameters in commercial 3D printers. Due to this limitation, most user-prepared biomaterials are not suitable for commercially available 3D printers. In order to achieve a successful printing of novel biomaterials, a printing machine with special printing nozzles, which could be used for different printing materials, was necessary [319]. The new 3D printing technique that prints multiple building materials simultaneously was named heterogeneous printing.

Introducing pneumatic valve or piezoelectric nozzles into 3D printing could overcome some limitations and provide a great opportunity for bio-fabrication with different biomaterials. The research on using pneumatic dispensing valves as additive manufacturing nozzles in 3D printing has attracted much interest [315, 316, 320-323]; however, programming and controlling the pneumatic valve dispenser's movement is still a big technical challenge. Due to the property variation of different materials, the 3D printer's settings, including printing speed and model, has to be modified to fit for the printing biomaterial and the physical properties of pneumatic valve dispenser. Each user-prepared material has a unique viscosity and surface tension coefficient, so different biomaterials cannot share the same G-code or valve dispenser's working status for the same CAD model. Thus, the heterogeneous printing of multiple biomaterials is still a difficult task, because the rules of computer numerical control (CNC) G-code programming have to perfectly match with the physical properties of pneumatic valve dispenser. Current research mainly focused on the properties' studies of new biomaterials rather than the universal printing design rules [322]. For example, polycaprolactone with or without hydroxyapatite was 3D printed for bone tissue scaffolds, while the biocompatibility of the scaffolds for tissue engineering was thoroughly studied. The 3D printing scaffolds preparation methods were still limited in printing those biomaterials with different polycaprolactone/hydroxyapatite concentration or different viscosities and surface tension coefficients [316, 321]. Engineered Fluid Dispensing (EFD) pneumatic valve dispensers were popular for 3D printing. Therefore, researches in bio-fabrication or biomaterial studies were also using EFD pneumatic valve to build up 3D scaffolds [315]. With

standard designed pistons and valves, EFD pneumatic valve dispensers could be used in additive manufacturing with different biomaterials, such as alginate and chitosan [324]. During printing process, the dispensing nozzle provides the control in horizontal level printing, while the movement of substrate responds to the G-code order to move in vertical direction. Normally, the programming of the dispenser's movement was based on CNC controlling system and the stage of printing substrate, while the programming of printing model was based on a CAD model. The substrate's vertical movement provided the possibility of optional printing environment control. For example, alginate hydrogel required calcium ion as cross-linking agent, chitosan hydrogel needed sodium hydroxide or sodium poly(tri-phosphate) for further cross-linking [325]. The substrate's vertical movement thus can function as additional cross-linker bath for the hydrogel cross-linking. Therefore, the programming of nozzle's movement and the study of printing materials' physical properties became the first task of 3D printing.

In this section, we provide mathematical models for CAD model designing and the pneumatic valve dispenser's physical properties, which could further provide a universal design rule for different materials' 3D printing. We studied the EFD pneumatic valve dispenser's physical structure and established a mathematical model to improve setting up routine programming rules for nozzle and CAD model analysis. The mathematical models of viscous material printing by pneumatic valve dispenser were based on the structure and operation principle of pneumatic valves and the properties of viscous fluid inside the dispenser during printing. Based on our model, we could decide the nozzle movement's programming rules, the CAD model and CNC controlling G-code's writing rules and other physical parameters of the pneumatic dispensing valve. PCL in acetic acid solution and sucrose with buffer solution mixture were used to test our model. Within the allowance of experimental error, our model provided a general design rule for main parameters in G-code and the pneumatic valve dispenser's working status for printing biomaterials.



## 6.4 Preliminary research on heterogeneous printing

### 6.4.1 Preliminary printing study

To develop a 3D printing system that could perform heterogeneous printing, we tested different self-prepared materials, including polyethylene glycol (PEG), PCL, and sucrose. This method of using printing nozzles was called as direct-write fabrication process (DWFP).

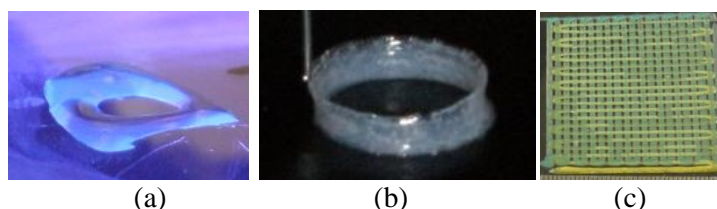


Figure 6-6. Preliminary printing examples, (a) PEG; (b) PCL in 40% acetic acid; (c) two kinds of colored PCL in 42% acetic acid.

The heterogeneous printing technology has been developed in recent years and commercialized for specific materials, such as ABS and PLA, with the method of FDM. However, for printing self-prepared materials, FDM has very limited ability to handle all of the printing parameters [326-328].

### 6.4.2 Existing problems

#### 6.4.2.1 Selection of printing materials

The uncertainty of self-prepared materials in printing causes unpredictable failures. Most polymer printing requires a curing procedure during the printing processes. Different polymer molecule weights at different temperatures have different curing conditions. The self-prepared materials need pre-printing experiments to test the viscosity and required printing parameters.

One critical issue that must be determined is whether or not the materials contain water or other evaporable solvents. Water in a liquid state in a material is not easy to cure or cross-link. The water needs to be evaporated or combined with other chemicals to become a hydrate compound.

#### 6.4.2.2 Printing parameters

EFD dispensing valves have controllers, valves, and motors that are connected together. The printing parameters cannot be taken individually during the printing processes. The step times, valve dispensing pressure, and motors are related to surface tension and viscosity.

#### 6.4.2.3 Feedback from printed lines

The printed lines are attached to substrate, while the needle tip on the dispensing valve rise a certain height  $\Delta h$ . This height is an absolute value rather than the relative height to the printed lines. Therefore, the pre-defined  $\Delta h$  forms an open-loop system without feedback or compensation.

#### 6.4.2.4 Multiple nozzles

When performing heterogeneous printing with two nozzles, the printer requires an offset during switching between the two nozzles [329, 330]. By the mathematical definition of space distance, the offset is the 3D distance between two nozzle tip dispensers is:

$$\sqrt{\Delta X^2 + \Delta Y^2 + \Delta Z^2}$$

Therefore, before calibrating the two nozzles in XY direction, the two needle tips need to be placed in the same horizontal plane. This calibration procedure needs to be considered in the heterogeneous printing code.

#### 6.4.2.5 Follow-up problem after nozzle extrusion

The materials need to be solidified after extrusion from nozzle, but the materials inside of the nozzle need to be kept liquid. This phenomenon requires accurate control and manipulation of the materials' solidification conditions. Theoretically, this cannot be achieved due to the physics of curing conditions. Temperature fields and electromagnetic fields (except for lasers), are not discrete in the 3D space. Even with a method to comprise the printing field into relatively stable points to maintain an appropriate threshold for curing, the curing outside the nozzle tip is not stabilized due to the stability of differential equations of the heat field or electromagnetic fields.

In addition, the approach to stable status requires many experimental trials to establish a database for comparisons.

#### **6.4.2.6 Other system problems**

Other control and integration problems exist for 3D printing system. These problems include power communication and exchanging, command exchanging between hardware and software, coding and decoding text files and G-code, and the motor's power connection to the TTL signal from valve controller. There are a lot of unsolved problems to solve before building a heterogeneous 3D printing system to print self-prepared materials with UV curing or heat curing.

### **6.5 Theories: 3D printing by pneumatic valve dispenser**

#### **6.5.1 Fluid mechanics analysis inside dispenser**

Our 3D additive manufacturing machine had a precisely controlled pneumatic valve dispenser based on a CNC controlling system. As shown in Figure 6-7, this machine used G-code as the input command to control the movement of motor-arms in X-Y-Z direction. Parameters in 3D printing included the G-code parameters and hardware parameters. The G-code contained the feed rate of nozzle, which had the same motion as the X-Y-Z stage. The G-code was imported into CNC interface software named Mach3 (Newfangled Solutions LLC, Livermore Falls, ME). Mach3 translated the feed rate information into transistor-transistor logic (TTL) signals, and sent command to the X-Y-Z motors via power electronic break-out circuit board. The feed rate determined the speed of the nozzles. At the same time, the other nozzle controlling parameters were also sent out by Mach3 software. By the pulse-width modulation (PWM) method, the electric signals with the stage motor command and the pneumatic nozzle activation information was sent out. For example, a cylindrical CAD model with 8 mm in diameter and 4 mm in height was sliced into layers and translated into G-code. The wall thickness was mainly determined by the nozzle inner diameter. The printing layer distances in the height direction (z-direction) was set to 0.10 mm by G-code, and the liquid back pressure was set to about 40 psi by the compressed air

pressure regulator. In this condition, the liquid could be printed continuously and the designed structure was built layer by layer.

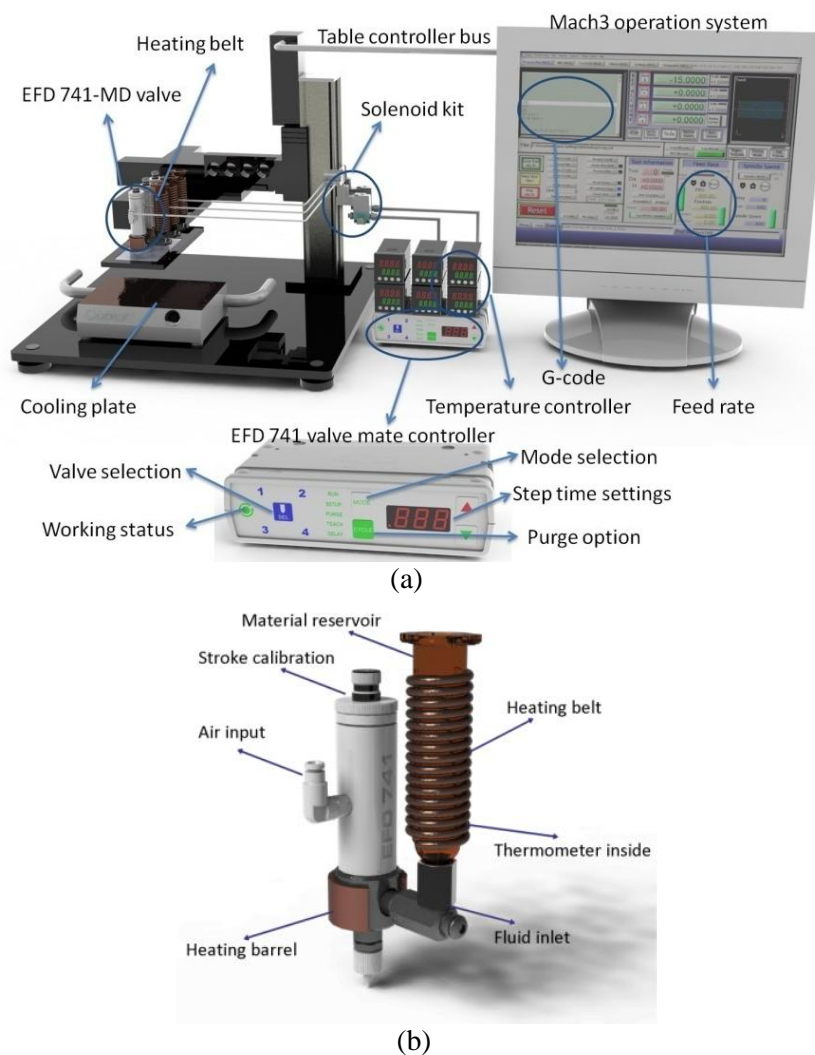


Figure 6-7. (a) EFD valve printing system setup; (b) EFD valve with material reservoir

One of the hardware parameters was the EFD 8000 controller dispensing step time, which was normally set as 0.100 seconds for PCL or 0.200 to 0.250 seconds for sucrose mixtures. This value represents the period of valve's stroking speed. Another manually controlled parameter was the initial air pressure for the valve and the air pressure for the reservoir connected to the inlet of the valve. The EFD 741MD valve required an initial air pressure of about 70~75 psi, which was kept constant when the valve was working. The reservoir's flow back pressure could vary from

0~100 psi, which was controlled by an air pressure regulator. The active pressure on the EFD 741MD valve cannot exceed 100 psi. Pressures above 100 psi would damage the valve. The back flow pressure affected the amount of materials coming out of the valve tip during a certain unit time. The fluid with higher viscosity required larger fluid back pressure to print a certain amount of material. Last but not least, there were two more temperature parameters controlled by thermal controllers' (Omega Engineering, Inc) temperature setting.

There were two thermal controllers and heating devices needed for one printing valve containing sucrose mixtures. One heating element heated up the reservoir using a heating belt, and the other heated up the EFD nozzle using a heating barrel. The heating devices were directly plugged into an AC 110 V power outlet. One of the wires was connected to a thermal controller which served as a relay switch for the heating device. After manually setting the target temperature, another thermal couple was connected to the thermal input of the controller, and then the controller automatically triggered the relay output to turn on and off the heating device to keep it at a stable temperature.

## **6.5.2 Mathematical modeling**

### **6.5.2.1 Material properties**

The mathematical modeling mainly considered material properties, mathematical modeling parameters, and feed rate in G-code and EFD 741MD valve extrusion behavior. These factors determined the scaffold line width, printing line spacing, scaffold layer thickness, etc.

For viscous material printing, the material parameters that had major effect on final samples were viscosity  $\mu$ , density  $\rho$ , and surface tension coefficient  $\sigma$ . The print head moving speed was decided by the solidification time, which was defined as:

$$t_s = C \left( \frac{V}{A_r} \right)^n$$

where  $V$  is the volume of printed lines;  $A_r$  is the surface area of printed lines;  $C$  is the solidification coefficient [331]. For most solutions, the viscosity and the surface tension of the contact surface between liquid and air were not independent.

$$\mu = Ae^{-\frac{B}{\sigma}}$$

Eq. 6-2

where  $A$  and  $B$  are constants for a certain printing material [332, 333]. However, they could change due to different samples or different concentrations of the samples. PCL samples with higher concentration in acetic acid resulted in higher viscosity, higher surface tension coefficient and lower solidification coefficient compared to low PCL concentration in acetic acid.

### 6.5.2.2 Mathematical modeling parameters

According to the structure of the EFD 741MD valve, the basic parameters are the needle tip inner diameter  $D$  and the needle tip inner radius  $r = D/2$ ; the piston and needle's radius  $R_1$ ; the tip adaptor's radius (around the piston and needle)  $R_2$ ; the stroke length of piston and needle  $S$ , which is decided by initial setting of stroke calibration and stroke reference. Other EFD parameters include the controller's step time  $t$ , which is the stroke time of piston inside the EFD valve.

### 6.5.2.3 Feedrate in G-code

The G-code was loaded into CNC controller program Mach3. The feedrate,  $Fr$ , in G-code was adjustable by percentage in Mach3. In order to match the printed lines and needle tip inner diameter, the speed of needle tip was  $v=Fr$ . So

$$\frac{V}{t} = (\pi r^2)v$$

Eq. 6-3

where  $V$  is the printed line's volume. So

$$F_r = \frac{4V}{\pi D^2 t}$$

Eq. 6-4

$V$  is related to the EFD calibration stroke length  $S$ , since the piston's diameter was fixed inside the dispenser. Therefore, the feed rate was a function of the CAD model and the nozzle's geometric parameters.

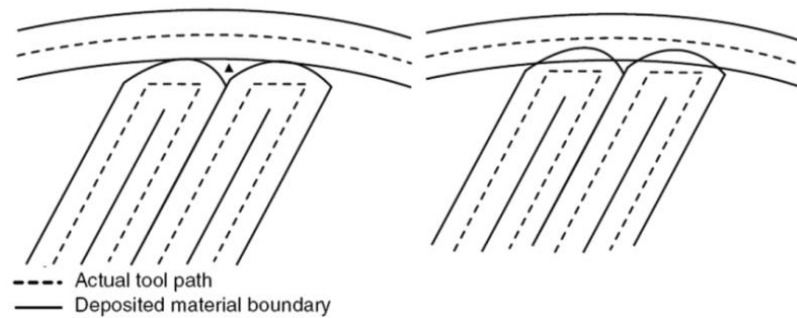


Figure 6-8. The printing path: actual tool path and the printed material boundary.

The actual tool path is driven by G-code, while the deposited material boundary will be spread to the material boundary. The line width is determined by the feedrate, the nozzle dispensing pressure, and the material surface tension. However, if the material cannot turn into solid quickly, the line width may further change after another layer is deposited onto the printed lines.

### 6.5.3 Scaffold printing modeling

#### 6.5.3.1 Maximum line distance

In order to print a 3D structure using additive manufacturing without support material, the line distance has a maximum allowance to support the upper layers. Before the bottom layers becomes completely solid, the upper layers had the tendency to collapse [334].

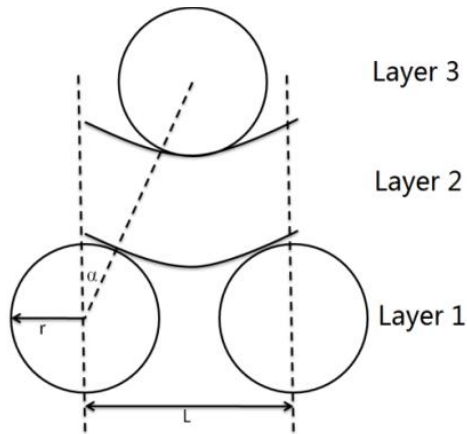


Figure 6-9. Model for maximum line distance without support material

The maximum line distance without support material has geometry relationships with the upper layer's diameter and the tangent line between layers. In order to keep the middle layer stable, the height increment in the Z direction should decide the Z coordinates in the G-code. As shown in the Figure 6-9, L was the distance between two neighbor lines' centers. The geometry relationship was:

$$2h = 4r \cos \alpha$$

Eq. 6-5

$$\sin \alpha \leq \frac{L/2}{4r} = \frac{L}{8r}$$

Eq. 6-6

By using the above two relationships, we get:

$$L \leq \sqrt{64r^2 - 16h^2}$$

Eq. 6-7

### 6.5.3.2 Z increment in G-code

In normal conditions, the upper layer's viscous fluid melted and covered the lower supporting layer. The fluid was collapsing because of the fluid's density and surface tension. When the surface tension and supporting force overcomes the gravity of acting on the upper layer [318], the fluid can solidify and keep its shape. This requires a faster solidification time. The increment in Z direction therefore would be:



$$h = 2r - \Delta h = 2r - (r - r \cos \alpha) = r(1 + \cos \alpha)$$

Eq. 6-8

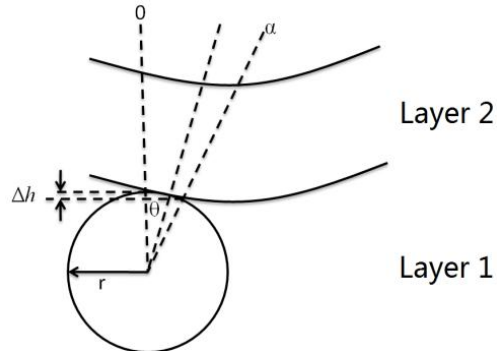


Figure 6-10. Model for height increment in Z direction

The forces of the contacted area were balanced in the tangent direction, including the projection of gravity  $mg$  and surface tension  $T$ .

$$mg \cos \theta = 2T \sin \frac{\Delta \theta}{2}$$

Eq. 6-9

where  $\Delta \theta$  is very small, and  $\sin \Delta \theta \approx \Delta \theta$ . In this equation, the gravity and surface tension are:

$$mg = \rho g \cdot \pi r^2 \cdot r \cdot d\theta$$

Eq. 6-10

$$T = \sigma \cdot 2\pi \cdot r(\theta + d\theta)$$

Eq. 6-11

so

$$\pi \rho g r^3 \cos \theta d\theta = 2\pi \sigma r \theta d\theta + o_{(d\theta)}^2$$

Eq. 6-12

and  $\theta$  increases from 0 to  $\alpha$ . By solving this differential equation:

$$\int_0^\alpha \pi \rho g r^3 \cos \theta d\theta = \int_0^\alpha 2\pi \sigma r \theta d\theta$$

Eq. 6-13

$$\pi\rho gr^3(\sin\theta)|_0^\alpha = \pi\sigma r\theta^2|_0^\alpha$$

Eq. 6-14

$$\pi\rho gr^3 \sin\alpha = \pi\sigma r\alpha^2$$

Eq. 6-15

so

$$\frac{\alpha^2}{\sin\alpha} = \frac{\rho gr^2}{\sigma}$$

Eq. 6-16

Therefore, the height for G-code in Z direction should be

$$h = r(1 + \cos\alpha)$$

Eq. 6-17

where  $\alpha$  required the relationship of

$$\frac{\alpha^2}{\sin\alpha} = \frac{\rho gr^2}{\sigma}$$

Based on this modeling equation, we found the proper way to code the nozzle pathway of the printing machine. The maximum line width model gave a coding principle for making multi-layer structures, and the second model gave a coding principle for layer thickness and needle increments in the vertical direction.

#### 6.5.4 Modeling of EFD 741 MD valve extrusion behavior

The viscous fluid in the EFD pneumatic valve formed flow with no turbulence. The fluid was driven not only by the reservoir back pressure, but also by the additional pressure caused by the movement of the piston and needle. Modeling the fluid behavior inside the pneumatic valve was important because the additional pressure plays a significant role in dispensing extremely viscous fluid. Because of the extremely high viscosity, the fluid velocity in the direction of the radius and the vortex could be ignored. Only velocity in vertical direction UR would be analyzed.

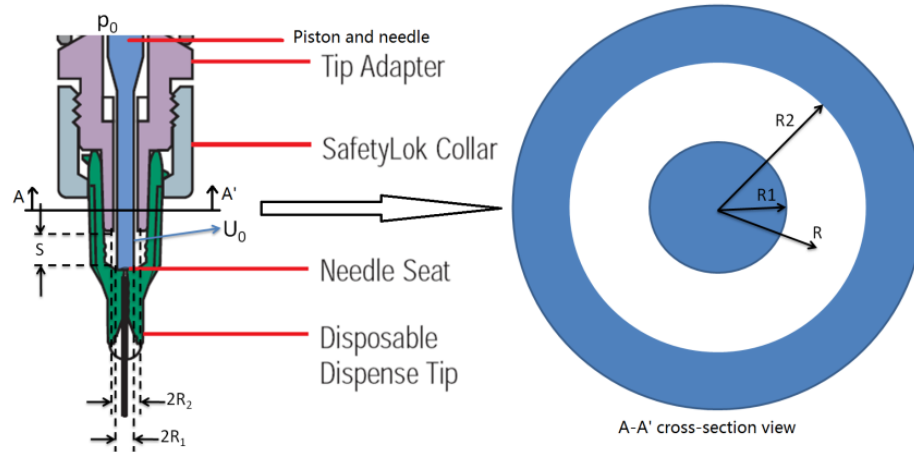


Figure 6-11. Model of viscous fluid flow in 741MD pneumatic valve. Reproduced with permission from EFD®.

The inner piston and needle velocity after calibration was

$$U_0 = \frac{S}{t}$$

Eq. 6-18

where  $S$  is the stroke length after calibration, and  $t$  is the step time of EFD controller.

The extreme viscous fluid in the valve was an incompressible non-Newtonian fluid. We assumed that the back pressure and temperature was constant among the fluid flow inside the valve, and the viscosity and the density were constant along the concentric flow channel. The radius of the piston and needle was  $R_1$ , and the tip adaptor's inner radius was  $R_2$ . From the continuity equation, we got:

$$\nabla^2 U = \frac{1}{R} \cdot \frac{\partial}{\partial R} \left( R \cdot \frac{\partial U}{\partial R} \right) = 0$$

Eq. 6-19

and it was independent from the fluid properties [335]. We assumed that the laminar fluid on the stroking needle had the same velocity at the surface of piston and needle; the velocity on tip adaptor's inner surface also had the same velocity with tip adaptor, which was zero, so the solution  $U_{(R)}$  had the format of

$$U_{(R)} = C_1 \ln(R) + C_2$$

Eq. 6-20

and the boundary conditions were:

$$\begin{cases} U_{(R_1)} = U_0 \\ U_{(R_2)} = 0 \end{cases}$$

Eq. 6-21

then we got C1 and C2:

$$\begin{cases} C_1 = \frac{U_0}{\ln(R_1/R_2)} \\ C_2 = -C_1 \ln(R_2) \end{cases}$$

Eq. 6-22

so

$$U_{(R)} = U_0 \frac{\ln(R_2/R)}{\ln(R_2/R_1)}$$

Eq. 6-23

and shear stress

$$\tau = -\frac{\mu U_0}{R \ln(R_2/R_1)}$$

Eq. 6-24

The dispensing rate was the volume of printed material in a unit time, which would affect the feedrate mentioned before. The dispensing rate was

$$\begin{aligned} \frac{V}{t} &= \int_{R_1}^{R_2} U_{(R)} \cdot [(R + dR)^2 - R^2] \\ &= \int_{R_1}^{R_2} U_{(R)} \cdot 2\pi R dR \end{aligned}$$

Eq. 6-25

By adding equation Eq. 6-23 into the dispensing rate Eq. 6-25, we got

$$\begin{aligned}
\frac{V}{t} &= \frac{2\pi U_0}{\ln(R_2/R_1)} \cdot \int_{R_1}^{R_2} \ln\left(\frac{R_2}{R}\right) \cdot R dR \\
&= \frac{2\pi U_0}{\ln(R_2/R_1)} \int_{R_1}^{R_2} (R \ln R_2 - R \ln R) dR \\
&= \frac{2\pi U_0}{\ln(R_2/R_1)} \left( \ln R_2 \cdot \int_{R_1}^{R_2} R dR - \int_{R_1}^{R_2} R \ln R dR \right) \\
&= \frac{2\pi U_0}{\ln(R_2/R_1)} \left[ \frac{(R_2^2 - R_1^2) \ln R_2}{2} \right] - \frac{2\pi U_0}{\ln(R_2/R_1)} \cdot \left( \frac{R_2^2 \ln R_2 - R_1^2 \ln R_1}{2} - \frac{R_2^2 - R_1^2}{4} \right) \\
&= \frac{2\pi U_0}{\ln(R_2/R_1)} \cdot \left[ \frac{R_1^2 \ln(R_1/R_2)}{2} + \frac{R_2^2 - R_1^2}{4} \right] \\
&= -\pi U_0 R_1^2 + \frac{\pi U_0 (R_2^2 - R_1^2)}{2 \ln(R_2/R_1)}
\end{aligned}$$

Eq. 6-26

The additional pressure caused by the piston and needle was

$$\frac{\mu U_0}{\ln(R_2/R_1)} \cdot \frac{-\int_{R_1}^{R_2} \frac{1}{R} \cdot 2\pi R dR}{\pi(R_2^2 - R_1^2)} = \frac{2\mu}{(R_1 + R_2) \ln(R_2/R_1)} \cdot \frac{S}{t}$$

Eq. 6-27

so the final pressure

$$p = p_0 + \rho g l + \frac{2\mu S}{(R_1 + R_2) t \ln(R_2/R_1)}$$

Eq. 6-28

where  $l$  is the length of vertical height of fluid in the pneumatic valve. According to the result, less step time  $t$  will give larger additional pressure at the dispensing outlet of needle tip. The last term will have a greater effect if the viscosity  $\mu$  is greater.

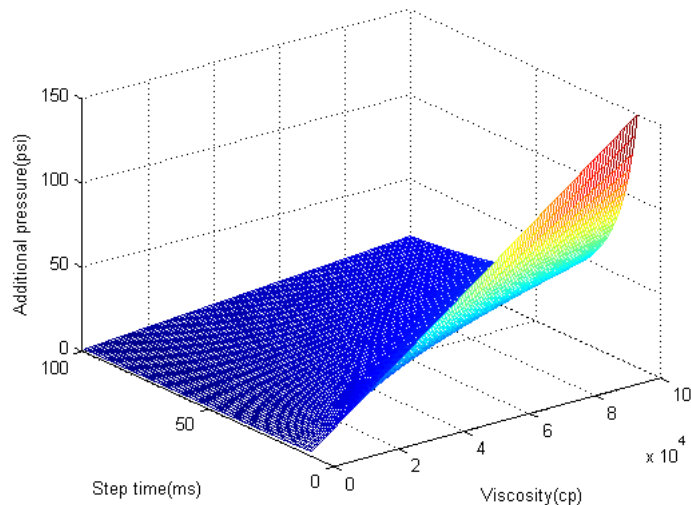


Figure 6-12. Additional pressure's relationship to material viscosity and controller step time.

Applying our step time and the viscosity of the PCL samples, we take step time as 40 ms. Viscosity can be up to 1,000~10,000 cp, which makes the additional pressure vary from 1 psi to 37.19 psi. Compared to the reservoir back pressure  $p_0$  which is 40~60 psi, the additional pressure cannot be ignored.

## 6.6 Other materials used in printing

Our research was focused on additive manufacturing using high viscosity fluid. The pneumatic valve EFD 741MD required a minimum of 70 psi activation air pressure. Pulsed activation air was used to give the material external pressure and drive the materials out of the valve during the printing.

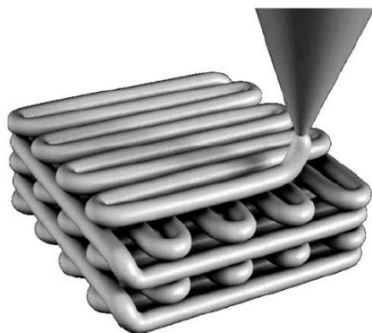


Figure 6-13. The deposition of a meander scaffold using dispensing valve [336]. Reused with permission from Springer.

Our printing materials were a sucrose mixture and several high concentration of PCL solutions that allowed the solvent to evaporate faster than the lower concentration materials. In all of our experiments, the printed lines of sucrose became solid in 3~5 seconds, and the PCL printed lines became solid without any curing agent within 8~10 seconds. The solidification time varies for different PCL concentrations because the evaporation time of acetic acid changes for different PCL concentrations. When printing the cylinder scaffold using either the PCL solution or the sucrose mixture, the printing nozzle circulated around the cylinder line and each layer solidified within 10 seconds. It therefore could support the deposition of the upper layers deposition. The upper layers stuck to the lower layers after solidification, forming the whole model structure. Our experiments showed that the materials in the lower layers were strong enough to act as supporting substrates for further printing.

### **6.6.1 Sucrose printing results by height increment and line distance model**

Sucrose is one of the most popular materials used as porogen building material for porogen-based tissue engineering scaffolds fabrication [319]. However, pure sucrose was not suitable for 3D solid freeform fabrication, because its decomposition temperature is 186°C. It is therefore difficult to avoid decomposition during heating or warming in the sucrose reservoir [319]. Therefore, sucrose mixtures with other materials were studied as porogen building materials [319]. A mixture of sucrose with honey, aluminum sulfate, and butter was developed for solid freeform fabrication of a porogen for bone scaffold fabrication. The highly biocompatible and water soluble sucrose porogen was successfully printed using a reduced melting temperature [319]. However, the viscosity and surface tension coefficient varied greatly with different ratios of each component in the mixture. When the mixture was dispensed from the EFD pneumatic valve dispenser, the viscous fluid would solidify within 3~5 seconds at room temperature. During the printing process, the valve dispenser was heated up to assure that the viscous fluid could be printed smoothly and uniformly.

In this work, the sucrose mixture was prepared of sucrose, honey, aluminum sulfate, and butter with the weight ratio of 90:4:5:1 at 60°C. The temperature of the printing reservoir was 60°C; and the EFD 741MD pneumatic valve was heated to 70°C. The feedrate was set to 90% in the Mach3 software, with the controller step time as 80 ms. The first CAD model we used was a cylindrical tube with a diameter of 20 mm. The wall thickness was equal to the printing line's diameter of 2 mm. After 15 layers, the 3D structure was formed by continuous printing by the pneumatic valve dispenser (Figure 6-14a). The model design rules were restricted by Eq. 6-7, which required the feed rate of the nozzle to be 90% of the default velocity, with a pneumatic valve stroke time period of 80 ms.

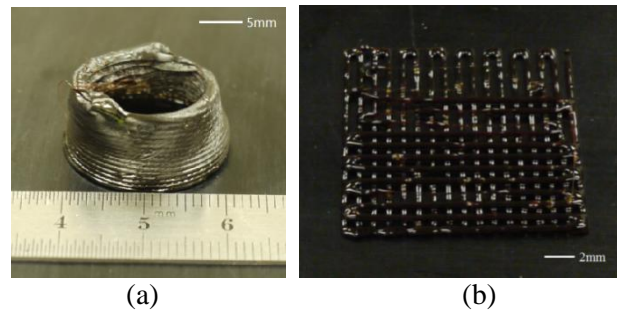


Figure 6-14. Sucrose printing results (a: cylinder; b: meander mesh).

The second printing model was a meander mesh structure of a 16 mm by 16 mm pad with a 0.5 mm line width. The printed sucrose solidified within 5 seconds on the substrate (Figure 6-14b). The results showed that high viscosity and surface tension would allow the upper layer material to stand on the lower layer material. The images of the printed sucrose (Figure 6-14) showed that high surface tension can hold the upper layers without supporting material. The sucrose fluid solidified after being held together by the surface tension. Based on the requirement of equation Eq. 6-16 and Eq. 6-17, the height increment of 0.5 mm was sufficient to allow the upper layers to be suspended on the lower layers.



### 6.6.2 PCL printing by pneumatic valve dispenser extrusion model

PCL can be easily dissolved in glacial acetic acid with up to a 43% weight concentration. The viscous flow at a weight concentration of 42% (w/w) was applied to a valve needle whose diameter was larger than 200  $\mu\text{m}$  without clogging. In our experiments, PCL was dissolved in glacial acetic acid. The glacial acetic acid acted as a solvent. It can evaporate at room temperature within 1 minute due to its low melting point (16.5°C) and it leaves PCL as a solid 3D structure without cracking.

For PCL printing, mesh layers models with 100 to 200 micron line width and 100 to 200 micron line space were built in CAD files. The 741 MD valve dispenser was used to directly write the PCL lines on a plastic film substrate layer by layer. The sliced CAD model followed the requirement by geometric relationships in the Z-increment model. Then the printed samples were inspected under an optical microscope (Figure 6-15a~e). (a) PCL sample 1 microscope view: G-code feedrate of 90%; layer thickness of 0.05mm; PCL concentration of 42%(w/w); needle tip inner diameter of 250 micron; reservoir back pressure of 45 psi; EFD controller step time of 70 ms. (b) PCL sample 2 microscope view: G-code feedrate of 90%; layer thickness of 0.10 mm; PCL concentration of 42%(w/w); needle tip inner diameter of 250 micron; reservoir back pressure of 50 psi; EFD controller step time of 70 ms. (c) PCL sample 3 microscope view: G-code feedrate of 90%; layer thickness of 0.05 mm; PCL concentration of 42%(w/w); needle tip inner diameter of 250 micron; reservoir back pressure of 40 psi; EFD controller step time of 70 ms. (d) PCL sample 4 microscope view: G-code feedrate of 120%; layer thickness of 0.08 mm; PCL concentration of 42%(w/w); needle tip inner diameter of 250 micron; reservoir back pressure of 40 psi; EFD controller step time of 70 ms. (e) Optimized parameters: G-code feedrate of 90%; layer thickness of 0.15 mm; PCL concentration of 42%(w/w); needle tip inner diameter of 200 micron; reservoir back pressure of 48 psi; EFD controller step time of 67 ms.

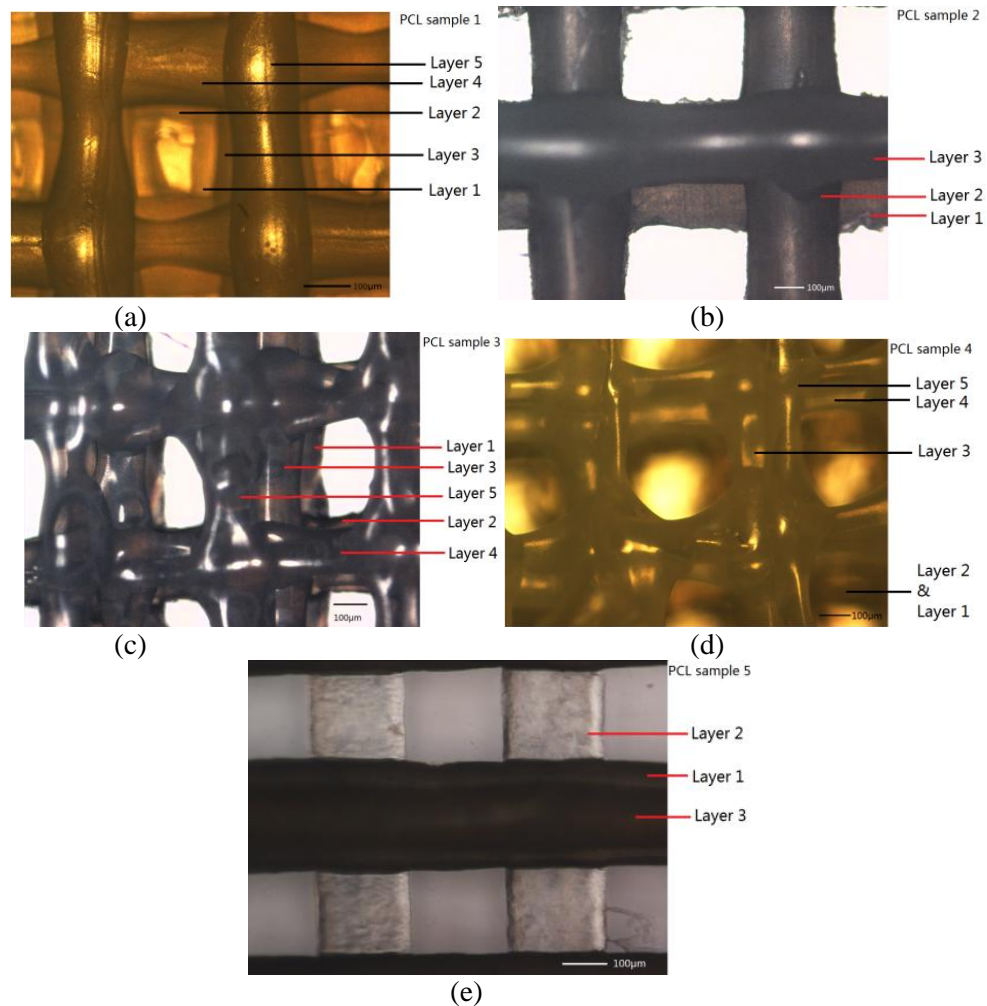


Figure 6-15. Optical microscope view of PCL sample with different G-code federate, layer thickness, PCL concentration, needle tip inner diameter, reservoir back pressure, and EFD controller step time.

Comparing Figure 6-15a and Figure 6-15b presented different layer thickness in the CAD models, the result showed that the 42% PCL-acetic acid and a 0.070 s controller step time is proper for printing continuous PCL lines. The back pressure had an allowance of 45~50 psi, and this range had almost no affect on the printed results. However, the 50 psi back pressure provided larger line width and led to a longer solidification time. Therefore, sample 2 (Figure 6-15b) cannot support more layers compared to sample 1 (Figure 6-15a). In sample 3 (Figure 6-15c), the

PCL back pressure was reduced to 40 psi. According

$$p = p_0 + \rho g l + \frac{2\mu S}{(R_1 + R_2)t \ln(R_2/R_1)}$$

the deposited materials would have smaller volume and line width. The feedrate speed and model

layer thickness was proper to support a five-layer 3D structure without collapse. However, the printed lines were not perfect round lines as in sample 1 (Figure 6-15a) and sample 2 (Figure 6-15b). Sample 4 (Figure 6-15d) had a higher layer thickness and a faster nozzle feed speed. The printed lines became dashes at some places, and the suspended structure was not aligned to the lower layer because the moving speed caused less materials to be placed on the notch of the lower layers' conjunction points.

To summarize, when the controller's step time decreased, the EFD nozzle's central piston moved faster. Based on the mathematical model we established for the EFD 741MD valve extrusion behavior, additional pressure was applied on the PCL solution sample in the cavity. In the Eq. 6-28, the material's density was constant during the printing procedure, and the other forces were not changing over time, so the pressure gradient  $\nabla p$  was related to velocity field. In this condition, the boundary layer's velocity was driven by the inner moving piston in the EFD 741MD valve dispenser, so the speed of valve motivation decided the pressure gradient. Therefore, the controller's step time could control the amount of printed material. According to the mathematical modeling equation Eq. 6-3, Eq. 6-16, and Eq. 6-28, the optimized parameters were 48 psi material back pressure, a 0.15 mm Z increment in G-code, and a valve controller step time of 67 ms. This was solved from the numerical solution of Eq. 6-28. The printed results were shown in Figure 6-15e by optical microscope, which provides straight lines in 3 layers. The alignment in conjunctions had not caused any deformation of layer 3, because the pressure caused by controller step time fits the requirement for keeping the 3D suspended lines connected to lower layers.

The 3D additive manufacturing machine with multiple user-developed biomaterials is possible to use even though those materials had different fluidic properties and physical properties. The needle tip inner diameter was able to determine the line width. The thinner tip needed higher minimum flow back pressure, as well as thinner layer thickness in the original CAD model to drive the material out. The material concentration decided solidification time,

normally, 40% PCL-acetic acid solution was proper for printing a 3D suspension structure, and short solidification time can significantly reduce the tendency of viscous liquid to collapse. According to the mathematical model and the comparison results of the experiments, the EFD controller step time was the most important factor to decide the material quantity. The viscous fluid continuity equation inferred that the laminar fluid layer velocity causes additional pressure and this pressure cannot be neglected compared to flow back pressure provided by air pressure regulator.

## **6.7 Conclusions in 3D printing viscous materials**

Our work established a mathematical model of fluidic behavior in a pneumatic valve and the relationships with fluid properties in additive manufacturing. The relationships may lead to a recipe for printing other 3D additive manufacturing materials in the future. The input of fluid density, viscosity and surface tension may be able to automatically generate the G-code increment in the Z direction and the controller settings for the valve. The settings include but are not limited to step time and feedrate percentage. For further research, specific software can be developed to solve the problems of parameters settings and generate a recipe for certain kinds of printing material, which would contribute to the additive manufacturing and fabrication machine. By using a recipe generating software, new 3D additive manufacturing machine can handle multiple self-prepared printing materials with accurate CAD model slicing and print head pathway coding.

## **6.8 Chitosan structure fabrication: casting**

There were two ways to form the chitosan scaffold: using 3D printing and casting. When we had the cross-linked chitosan hydrogel, we directly moved them to lyophilization facilities with pre-freezing media. The pre-freezing process was critical to determine the pore size and usually there were two ways to pre-freeze: using dry ice or liquid nitrogen. Liquid nitrogen would freeze water much faster than dry ice. After pre-freezing the water in chitosan hydrogel formed small

crystal-like ice which would sublime to H<sub>2</sub>O gas. The water gas was eliminated by vacuum and leaved the space with pore structure.

To make a chitosan scaffold by molding and casting, we needed to build a mold for the chitosan that was flexible and stable during the lyophilization process [337, 338]. Therefore, we chose PDMS as the chitosan molding material. However, to make the PDMS opposite mold, we need another mold with the proper scaffold structure for PDMS.

### **6.8.1 ABS Mold Printing**

We used Solidworks to design 3D structures for the PDMS molds, and then exported the 3D designs into STL (stereo-lithography) files. STL files are binary code files that can be read by our ABS prototyping machine (Stratasys Dimension 3D printer). ABS is a thermoplastic that can be heated up to become a highly viscous fluid that can be printed out from a nozzle. When the temperatures lower, it again becomes solid and the printed lines stick to each other to form strong 3D physical structures.

### **6.8.2 PDMS Molding**

After an ABS molding was prepared, we needed to make PDMS, as it was softer and more suitable for the chitosan hydrogel. PDMS and chitosan were put together for lyophilization (Model: Freezone 6 Plus, Labconco, Kansas City, MO). PDMS does not change its properties during lyophilization, which means one piece of PDMS can be used multiple times for the chitosan lyophilization process.

First, we mixed PDMS (Dow Corning) and the PDMS curing agent (Dow Corning) at a weight ratio of 10:1, and stirred well with glass rod for 10 min. Then we poured the PDMS mixture into a petri-dish with the ABS mold in it. Then we put the mixture into a vacuum for 1 hour and kept the petri-dish in a 60°C oven for 24 hours to allow PDMS fully curing. Finally, we peeled off the PDMS from the ABS mold. Then, it was ready to be used as the opposite mold for a chitosan hydrogel casting.

PDMS does not have major deformation in liquid nitrogen or during the lyophilization procedure that takes over 24 hours. Therefore, PDMS would not damage chitosan's channel structure after lyophilization.

### 6.8.3 Chitosan Casting and Lyophilization

We prepared the chitosan hydrogel, poured the chitosan onto the PDMS mold in the petri-dish and stored the mixed solution in a refrigerator at 4°C for 20 h to allow glutaraldehyde to cross-link the chitosan-gelatin hydrogel. The cross-linked chitosan hydrogel was then immersed in liquid nitrogen (-196°C) for 1 h for pre-freezing process to force the water to become solid, interconnected micro ice. Chitosan and gelatin's porous structure with an internal channel structure was obtained after freeze-drying for 24 h.

### 6.8.4 Casting Results

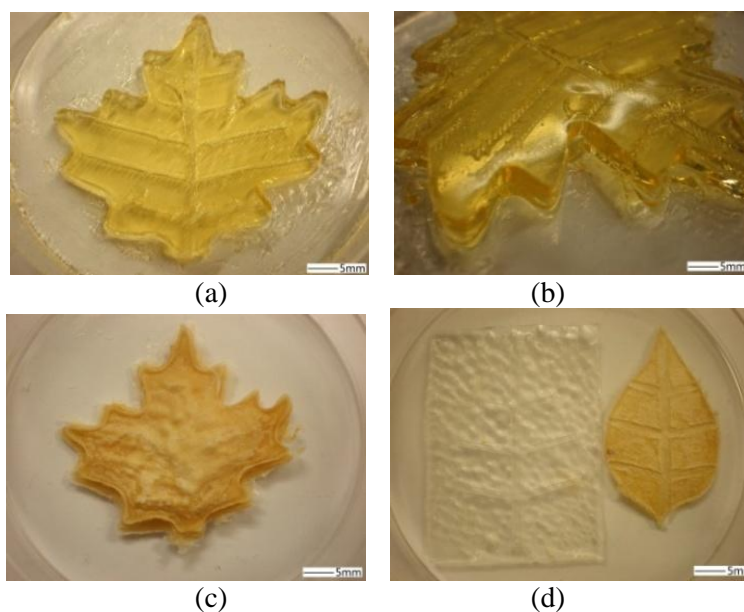


Figure 6-16. Chitosan printing and casting in leaf-shape results: (a) chitosan gel; (b) chitosan with internal channels; (c) chitosan after lyophilization; (d) PDMS mold and casted chitosan after lyophilization.

Figure 6-16a-c were the results of casting procedure of medium molecular weight chitosan hydrogel with a leaf-shape molding and cutting. Figure 6-16b shows the internal channels made by PDMS molding within the leaf-shape; the internal channels were formed by the PDMS

opposite mold, and then stuck to another piece of flat chitosan hydrogel before the lyophilization process, so the two pieces of chitosan hydrogel were bonded with each other and become one piece with internal channels after the lyophilization process. Figure 6-16c and Figure 6-16d showed that the leaf-shape porous chitosan structure after lyophilization.

Since we were using this porous structure in an artificial photosynthesis micro-fluidic device as the media between atmosphere and fluid reaction region, the pore sizes were critical for carbon dioxide penetration and exchange.

## 6.9 Chitosan structure fabrication: rapid prototyping

Before printing, we designed the 3D multi-layer leaf structure in CAD software, and then used our heterogeneous materials printing algorithm to generate sliced G-code files to guide the movement of the nozzles array. Our own RP machine could perform heterogeneous 3D building with extremely high viscous fluid materials. The chitosan structure with channels printing followed the pre-loaded G-code generated from a CAD STL file of the artificial leaf. After building the whole micro channels structure, we generated micro-size porous structure for dark reaction by lyophilization.

### 6.9.1 Chitosan Printing without Support Material

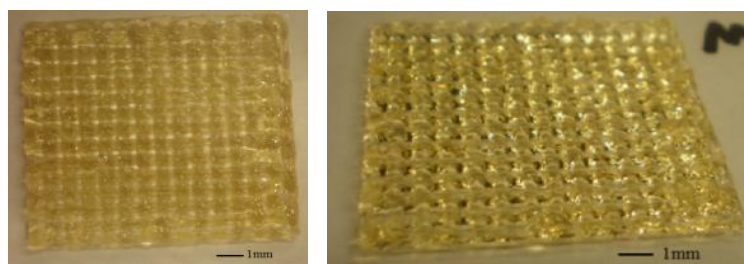


Figure 6-17. Front view and side views of 5 layers chitosan scaffold with 7% (wt%) medium molecular weight chitosan.

Chitosan samples were prepared for RP by a self-made heterogeneous printing machine with a EFD pneumatic valve as the printing head. According to the viscosity test, we found that the

sample with higher viscosity and reasonable surface tension to hold the 3D structure had the following properties: 7 wt% medium molecular weight chitosan with 90% of acetic acid.

As shown by the printed samples in Figure 6-17, the highly viscous chitosan sample could hold its structure for several hours before further processes such as lyophilization, but for massive production or lower viscosity and concentration of chitosan printing, additional support material was required.

### 6.9.2 Chitosan Printing with Sodium Bicarbonate as Support Material

We found a better way to form a solid 3D structure for the chitosan scaffold by using sodium bicarbonate  $\text{NaHCO}_3$  to react with acetic acid. The extra  $\text{NaHCO}_3$  would function as support material to support the upper layers without falling or collapsing during the printing progress. In addition, the  $\text{NaHCO}_3$  can react with the remaining acetic acid and neutralize the cross-linked chitosan, by converting the  $-\text{NH}_3^+$  groups back to amino groups  $-\text{NH}_2$ . The code used in this printing method was layer-by-layer printing code. Therefore, the wait time between layers is about 3 min which was long enough to deposit  $\text{NaHCO}_3$  powder.

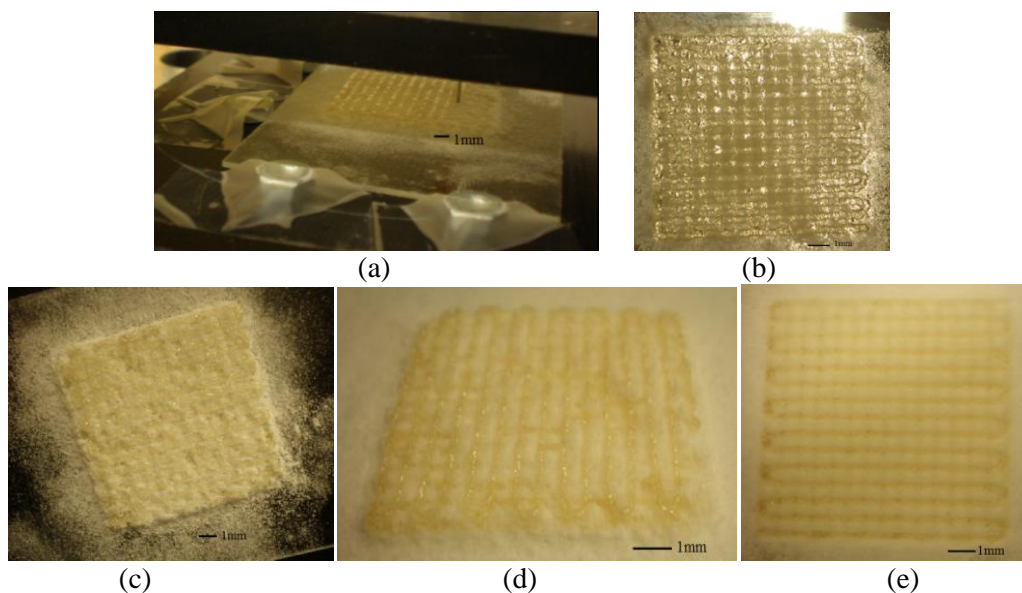


Figure 6-18. Chitosan printing results using sodium bicarbonate as a support material: (a) second layer printing after adding sodium bicarbonate on the first layer; (b) interconnection between printed first layer and second layer; (c) two layers chitosan with support material; (d) side view of four layers of chitosan scaffold with support material; (e) back view of four layers of chitosan scaffold with support material.



The printing condition was set for printing extremely highly viscous fluid: back pressure for the chitosan sample was set around 20 psi. The EFD valve controller's step time was set to 0.070 s to drive enough chitosan in a unit time to form a continuous stream line. The most important parameter of the Z direction space, the initial space between needle tip and substrate, was around 0.8 mm. After the first layer was printed, we put a sufficient amount of  $\text{NaHCO}_3$  powder onto the printed layer. The  $\text{NaHCO}_3$  powder would make this layer become a new flat surface for printing the next layer. The printed chitosan scaffold had a line space of 2 mm, and a layer thickness of 0.3 mm with the needle tip inner diameter equal to 300  $\mu\text{m}$ .

When printing the second layer, the needle went over the first layer with a space around 0.5 mm. In this condition, the second layer would not collapse or spread. The extra  $\text{NaHCO}_3$  not only filled the spaces between lines on the first layer, but also reacted with the  $\text{CH}_3\text{COOH}$  of the printed structure's surface on both the first layer and the second layer. This constrained the second layer's structure. The second layer was inter-connected with the first layer. As shown in Figure 6-18b, the connection of horizontal and vertical lines between the layers was clear in color, so that the first layer's chitosan was fully contacted with second layer's chitosan. After four layers, the scaffold was about 3 mm in height. The bottom structure could still hold the shape.

From the final four layers of the chitosan scaffold, Figure 6-18d indicated that the weak acid  $\text{CH}_3\text{COOH}$  in the chitosan sample could be neutralized by  $\text{NaHCO}_3$ . In Figure 6-18e, the back view of the scaffold showed that the upper layers did not collapse, and the final scaffold was strong because of the existing of  $\text{CH}_3\text{COONa}$  crystal.

## **6.10 Assembling onto artificial photosynthesis board**

The porous chitosan structure can be made by either molding-casting or 3D printing. The lyophilization is a fully developed technique to create porous structure. Therefore, the final step is assembling the porous chitosan structure to the glucose or fructose synthesis and a storage region on a fully developed artificial photosynthesis board.

According to my previous experiment, the porous chitosan structure can fully contact and be bonded to a wafer, PCB and glass, which make the design of a photosynthesis storage region very flexible.

## **6.11 Contributions**

### **6.11.1 Technical improvement on 3D printing**

3D printing technology is facing multiple obstacles during development. Current 3D printing technologies are mainly used in object demonstration or trials, because any product tolerance will be passed onto next level applications. The uncertainty of 3D printing issues will affect the applications of 3D printed parts. Our mathematical modeling and experiment provided an improvement to FDM.

In pneumatic valve dispensing FDM, the height increase modeling was always a constant, which was not suitable for self-prepared viscous materials. The mathematical modeling algorithm can be written as software to operate a 3D printer for self-prepared materials in FDM. By using a recipe generating software, new 3D additive manufacturing machine can be made to handle multiple self-prepared printing materials with accurate CAD model slicing and print head pathway coding.

### **6.11.2 Chitosan printing with powder support material**

The chitosan-acetic acid solution was printed following the mathematical model of viscous material printing. By adding sodium bicarbonate powder to printed chitosan gel, I provided a new strategy of adding support structure to FDM. Other kinds of chemical gels in FDM can use similar cross-linking or curing methods, such as a chemical reaction that involves pH variation, hydroxide reactions, or carboxyl reactions.

## Chapter 7. SIMULATION OF INTEGRATED SYSTEM

### 7.1 Motivation of integrated system

After building the light reaction units and dark reaction units, we come to the final task of interconnecting and integrating the whole system. In the higher plants, leaf cells are connected and operated by the plant itself. The behaviors of plants include ion transfer and pumping, photorespiration, falling leaves, and transpiration. Plant has no nerve cells in it, so every movement was triggered by genetic reasons, external stimulations, chemicals reactions, or  $\text{Ca}^{2+}$  channels and chemical gradients.

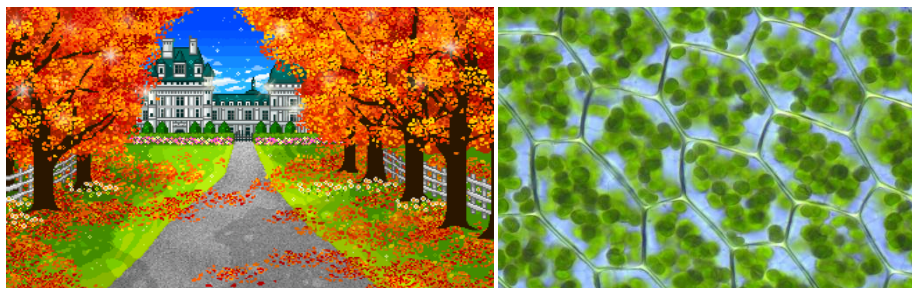


Figure 7-1. Demonstration of tree falling and plant cells interconnection. Reused with permission from Wikipedia.

Our current light reaction unit has enough inlets and outlets to connect to each other. Therefore, we were building an integrated system synthesizing both microfluidics and microelectronics together, which had been studied and developed within the past ten years [339-342]. The integration of PDMS based microfluidics systems were also challenging [343-347]. However, different connection ways would result in different performance. Further research would be based on how to connect the reaction microchips together and what kinds of layout should we use.

### 7.2 Integrate light reaction units

The final output of artificial photosynthesis system would include integrated microfluidic chips with proper sensors to partially achieve artificial intelligent [348, 349]. The inspection of

membrane impedance and ion channels required capacitive sensors and current sensing and amplification circuits. In the EIS experiments, we used potentiostat equipment to measure the impedance and ion transferring current [350]; however, we cannot carry the equipment with artificial photosynthesis system all the time. Therefore, I designed the integrated circuits for microchip and ion channel monitoring.

The first part was used to identify the microchip in array with binary coding. The hierarchy designs and simulations of microelectronic circuit provided an efficient way to manipulate the electrical signals on microchips for better operation and integration. The real-time observation of the working status of microchips with planar membranes or microfluidics with dark reaction solutions was necessary in integration. In mixed-mode microelectronics, we were having digital signals of the identification of each microchip, and analog signals that applying to the microchip for electrochemical impedance measurement dynamically. The digital signals needed logic units to process the digital transistor-transistor logic (TTL) signal to tell the working status, while the analog signals required proper amplifiers to enlarge the signals and process the output results from comparators. Therefore, our hierarchy design and simulations were from basic digital logic gates to units, to analog amplifiers with proper bandwidth for microchip.

The second part was used to amplify the current signal and recognize the ion transfer. After membrane stability study, we were able to add proteins in planar membrane to form ion channels. The current passing the membrane was limited; therefore, an proper amplifier with digital-to-analog converter (DAC) and analog-to-digital converter (ADC) were necessary to analysis the ion channels on microchip to achieve cell function on this cell-free platform. The amplifier can enlarge the current, and ADC can change the current amplitude into digital numbers for comparison.

Integration of multiple reaction units was similar to assembling multiple photosynthetic cells to a leaf. The ideal situation was giving each unit a label to identify themselves. Sensor array always come together with actuators [163, 351-355]. The embedded parallel capacitive sensors in

each light reaction unit could work as identification method to name each of them [356, 357]. The light reaction unit had two isolated chambers, after integration, one broken unit would result in a mixing or diffusion between the two chambers, which may contaminate other surrounding units. Therefore, proper single-unit identification and working status monitoring was necessary [358-360], especially packaging and integration for sensor array [361-363].

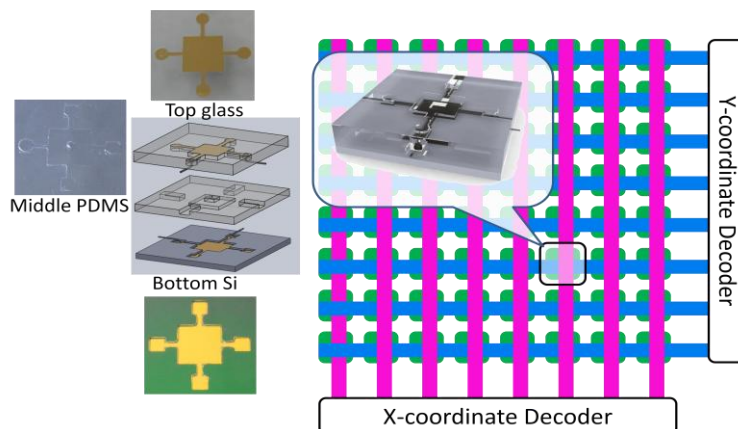


Figure 7-2. Illustration of single unit's X and Y coordinate identification. Blue and red wires represent different metal layers.

To identify a malfunction unit among the microchip array, extraordinary signals should be sent to two decoders. As demonstrated in Figure 7-2, the first layer metal (blue) can recognize the column number of the malfunction unit, while the second layer metal (purple) can recognize the row number of the malfunction unit. I planned to use binary code to represent the numbers of row and column. Take  $8 \times 8$  microchip array as example, each microchip can be named by X and Y coordinates, and each coordinate can be coded by a 3-bit binary code, so each microchip can be named by a 6-bit binary code. The complementary metal–oxide–semiconductor (CMOS) microchip can be further fabricated by 0.18  $\mu\text{m}$  CMOS technology.

### 7.3 Principle: increase SNR

The repeating cycle is also a factor need to be considered during measurement. Signal to noise ratio (SNR) can vary depends on the repeating cycles.

### 7.3.1 Mathematical analysis and proof of increasing SNR

**Theorem 1.** If random variables  $X \sim N(\mu, \sigma^2)$ , then the linear function of  $X$ ,  $Y = aX + b$  ( $a \neq 0$ ), will also follow normal distribution.

**Proof.** The probability density is

$$f_X(x) = \frac{1}{\sqrt{2\pi}\sigma} e^{-\frac{(x-\mu)^2}{2\sigma^2}} \quad (-\infty < x < +\infty)$$

Eq. 7-1

Let

$$y = g(x) = ax + b$$

Eq. 7-2

its inverse function is

$$x = h(y) = \frac{y-b}{a}$$

Eq. 7-3

and

$$h'(y) = \frac{1}{a}$$

Eq. 7-4

$\therefore$  the probability density of  $Y = aX + b$  is

$$\begin{aligned} f_Y(y) &= \frac{1}{|a|} f_X\left(\frac{y-b}{a}\right) = \frac{1}{|a|} \frac{1}{\sqrt{2\pi}\sigma} e^{-\frac{\left(\frac{y-b}{a}-\mu\right)^2}{2\sigma^2}} \\ &= \frac{1}{\sqrt{2\pi}\sigma|a|} e^{-\frac{(y-(b+a\mu))^2}{2(a\sigma)^2}} \quad (-\infty < y < +\infty) \end{aligned}$$

Eq. 7-5

$\therefore$  if the random variables  $X \sim N(\mu, \sigma^2)$ , then the linear function of  $X$ ,  $Y = aX + b$  ( $a \neq 0$ ), will also follow normal distribution, and  $Y \sim N(a\mu + b, (a\sigma)^2)$ . ■

**Theorem 2.** If random variables  $X$  has a probability density  $f_X(x)$ ,  $-\infty < x < +\infty$ , and if function  $y = g(x)$  is derivable everywhere, and always has  $g'(x) > 0$ , (or always has  $g'(x) < 0$ ), then  $Y = g(X)$  is continuous random variables, and its probability density is

$$f_Y(y) = \begin{cases} f_X[h(y)]|h'(y)|, & \alpha < y < \beta \\ 0, & \text{else.} \end{cases}$$

Eq. 7-6

where  $\alpha = \min\{g(-\infty), g(+\infty)\}$ ,  $\beta = \max\{g(-\infty), g(+\infty)\}$ ,  $x = h(y)$  is the inverse function of  $y = g(x)$ .

**Proof.** Let  $g'(x) > 0$ , from Inverse function theorem, we know that the inverse function of  $y = g(x)$  exist, which is  $x = h(y)$ , and derivable everywhere, and increases monotonically on  $(\alpha, \beta)$ , and  $h'(y) > 0$ .

Because  $y = g(x)$  gets value in domain  $(\alpha, \beta)$ , when  $y < \alpha$ ,

$$F_Y(y) = P\{Y \leq y\} = 0$$

Eq. 7-7

when  $y \geq \beta$ ,

$$F_Y(y) = P\{Y \leq y\} = 1$$

Eq. 7-8

When  $\alpha \leq y < \beta$ ,

$$\begin{aligned} F_Y(y) &= P\{g(X) \leq y\} = P\{X \leq h(y)\} \\ &= \int_{-\infty}^{h(y)} f_X(x) dx \end{aligned}$$

Eq. 7-9

so  $Y$ 's probability density

$$f_Y(y) = \begin{cases} f_X[h(y)]|h'(y)|, & \alpha < y < \beta \\ 0, & \text{else.} \end{cases}$$

Eq. 7-10

and similarly, when  $g'(x) < 0$ ,

$$f_Y(y) = \begin{cases} f_X[h(y)][-h'(y)], & \alpha < y < \beta \\ 0, & \text{else.} \end{cases}$$

Eq. 7-11

where  $h'(y) < 0$ . ■

### 7.3.2 Increasing SNR by increasing repeat times

To exam the bio-membrane properties on chip, we need to consider possible noises generated together with signals. There are many ways to increase SNR. Here we only list one method to extract small signal from strong noise background. We suppose the noise energy  $|A|^2$  is much larger than the signal energy. If  $s$  is our signal,  $n$  is a random noise. After transmission, the accepted is:  $X = n + s$ . Consider the noise  $n$  follows normal distribution  $\sim N(0, \sigma^2)$ .  $\sigma^2$  is the average power of noise. Then, the linear function of  $n$ ,  $X = n + s$  also follows normal distribution (**Theorem 1**), the probability density is

$$f_X(x) = \frac{1}{\sqrt{2\pi}\sigma} e^{-\frac{(x-s)^2}{2\sigma^2}} \quad x \in R$$

Eq. 7-12

Suppose the signal is repeated sending out, so the accepted signal is in a sequence:

$$X_k = n_k + s, \quad k = 1, 2, \dots, m,$$

Eq. 7-13

And suppose the time between sending each one is separate, so we can assume that  $\{X_k\}, k = 1, 2, \dots, m$ , can be considered as independent to each other. At the same time,  $X_k$  follows normal distribution  $\sim N(s, \sigma^2)$ . Then we add them, let:

$$Y = \sum_{k=1}^m X_k$$

Eq. 7-14

So  $Y$  still follows normal distribution  $\sim N(ms, m\sigma^2)$  (**Theorem 2**), where “ $ms$ ” represent signal attitude after  $m$  times superposition, “ $m\sigma^2$ ” represent the average power of noise after  $m$  times



superposition.

If using  $\left(\frac{s}{\sigma}\right)^2$  to represent the SNR of  $Xs$ , the SNR after superposition is changed to:

$$\left(\frac{S}{N}\right)_m^2 = \left(\frac{ms}{\sqrt{m}\sigma}\right)^2 = m \left(\frac{s}{\sigma}\right)^2$$

Eq. 7-15

After  $m$  time's superposition, the SNR increased to:

$$SNR = 10 \log \frac{(S/N)_m^2}{(s/\sigma)^2} = 10 \log m$$

Eq. 7-16

so by increasing  $m$ , the SNR will increase. Then the signals can be extracted from noise.

## 7.4 Capacitive sensor

### 7.4.1 Current mirror and amplification

The current through our light reaction microchip with biomembranes is low, so that any interference of the device may cause false measurement of the current. Therefore, we use current mirror to take sample of the current and amplify the current properly.

The sampled current is determined by the dimensions of CMOS transistors [364]. The N-type metal–oxide–semiconductor field-effect transistor (NMOS) transistor size determines the source/drain current by the size of polysilicon gate size. The schematic circuit simulation of NMOS shows that the current  $I_{DS}$  can be modified by changing width  $W$  and length  $L$ .

$$I_{DS} = k' \frac{W}{L} \left( V_{GT} \cdot V_{min} - \frac{V_{min}^2}{2} \right) (1 + \lambda V_{DS})$$

Eq. 7-17

where  $k' = \mu_n C_{ox}$ ; the coefficients are parameters in CMOS transistors. The excess voltage

$$V_{GT} = V_{GS} - V_{TH}$$

Eq. 7-18

and

$$V_{min} = \min(V_{GT}, V_{DS}, V_{DSAT})$$

Eq. 7-19

At saturation status,  $V_{min}=V_{GT}$ ; at linear status,  $V_{min}=V_{DS}$ ; at square ( $x^2$ ) status,  $V_{min}=V_{DSAT}$ .

Before I finalize the schematic of the current mirror for microfluidic chip, I present the simple model of NMOS first.

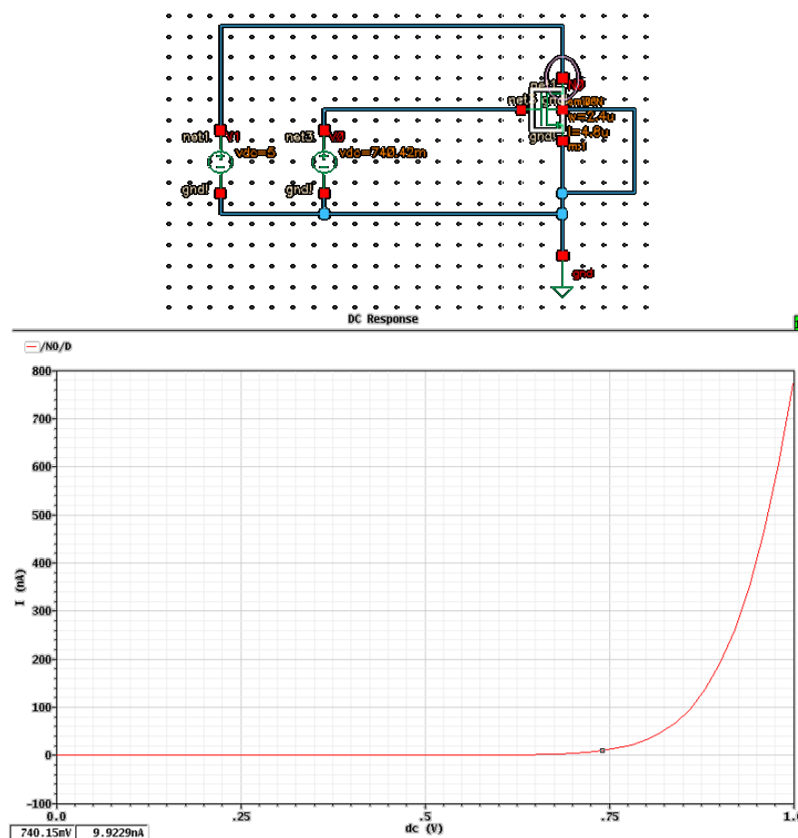


Figure 7-3. Schematic simulation of NMOS with  $W = 2.4 \mu\text{m}$  and  $L = 4.8 \mu\text{m}$ .

In first situation, the gate size is set as  $W = L = 2.4 \mu\text{m}$ , and  $V_g$  (the  $V_0$  in schematic above) is set from 0 ~ 1 V; the relationship of  $V_g \sim I_1$  figure is plotted. Based on the result, when  $I_1 = 10 \text{ nA}$ , the  $V_g$  is about 740 mV. Then the  $V_g$  is set as 740 mV, and the gate width is changed from  $w$  to  $2w = 4.8 \mu\text{m}$ , so the new  $I_2$  is shown as 136 nA. Then the width  $W$  is changed back to  $2.4 \mu\text{m}$ , and  $L = 4.8 \mu\text{m}$ , the new  $I_3$  in simulation become 4.66 nA.

Table 7-1. Relationship between current and W/L in NMOS.

No.	W	L	I <sub>DS</sub>
(1)	W <sub>0</sub>	L <sub>0</sub>	10 nA
(2)	2W <sub>0</sub>	L <sub>0</sub>	136.09 nA
(3)	W <sub>0</sub>	2L <sub>0</sub>	4.66 nA

Comparing I<sub>1</sub> and I<sub>2</sub>, the only difference is the width changing from W to 2W, with a result of I<sub>1</sub> = 10 nA, I<sub>2</sub> = 136.09 nA; comparing I<sub>1</sub> and I<sub>3</sub>, the only difference is the length changing from L to 2L, with a result of I<sub>1</sub> = 10 nA, I<sub>3</sub> = 4.66 nA. To find out the position for current adjust back to 10 nA, we use the two sets of data to find  $x$  on width (I<sub>1</sub> and I<sub>3</sub>) and length (I<sub>1</sub> and I<sub>3</sub>). In the Cadence layout, 1W = 1L = 4 λ, where λ is the minimum step length in MOS fabrication. I use linear fitting to the two sets of points, in comparing I<sub>1</sub> and I<sub>2</sub>, for I = 0,

$$\frac{136.09 - 10}{W} = \frac{10}{W - x}$$

so  $x = 0.92 W = 3.68 \lambda$ . On the other hand in comparing I<sub>1</sub> and I<sub>3</sub>, for I = 0,

$$\frac{10 - 4.66}{L} = \frac{10}{x - L}$$

so  $x = 2.87 L = 11.49 \lambda$ .

In order to increase the sampled current, we use amplified current mirror. In the current mirror SPICE schematic simulation, the original current I<sub>dc</sub> is set to 10 nA. The gate voltage input to the NMOS V<sub>b</sub> above current mirror (connected to V<sub>dd</sub>) is set to constant, and try the general value of V<sub>b</sub>.

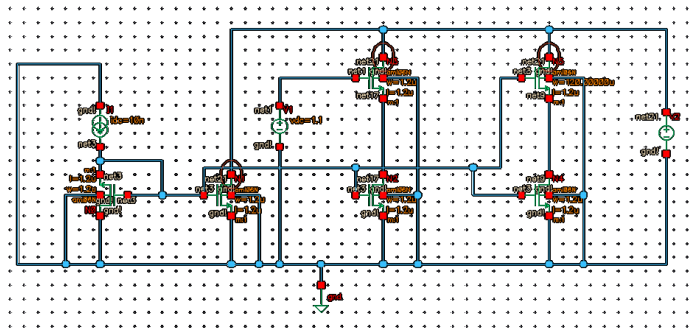


Figure 7-4. Schematic simulation of current mirror.

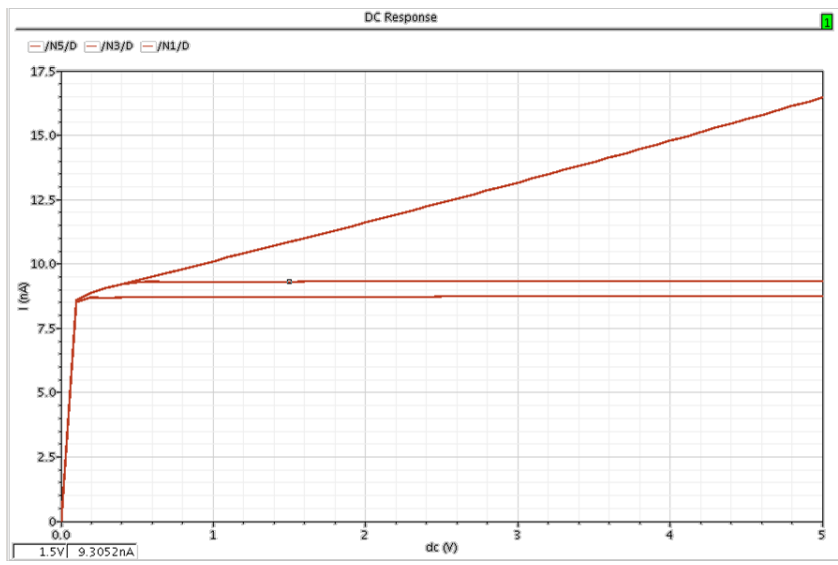


Figure 7-5. Schematic simulation result of  $V_b$  in current mirror.

The value of  $V_b$  is set to between 0.5 to 1.5, and the variable  $V_b$  is defined as “parameter a”, so the Hspice can simulate different  $V_b$  values and plot in one figure. The plot axis is the  $I_{out}$  vs.  $V_{out}$  with a step of  $V_b$  of 0.05 V.

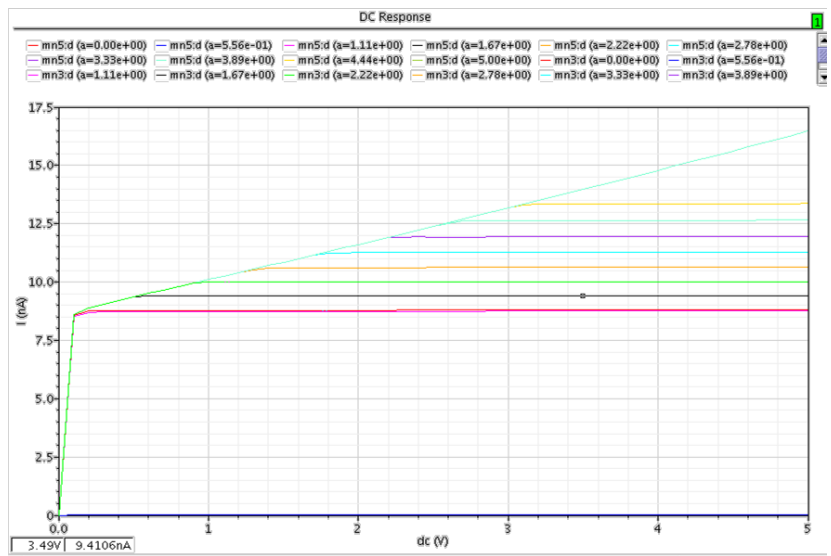


Figure 7-6. Schematic simulation result of  $V_b$  in current mirror with a step of  $V_b$  of 0.05 V.

The plotted  $I_{out}$  vs.  $V_{out}$  indicate that the required  $V_b$  is about 0.95 V. At  $V_b = 2.22$  V, the resulted  $I_{out} = 10$  nA.

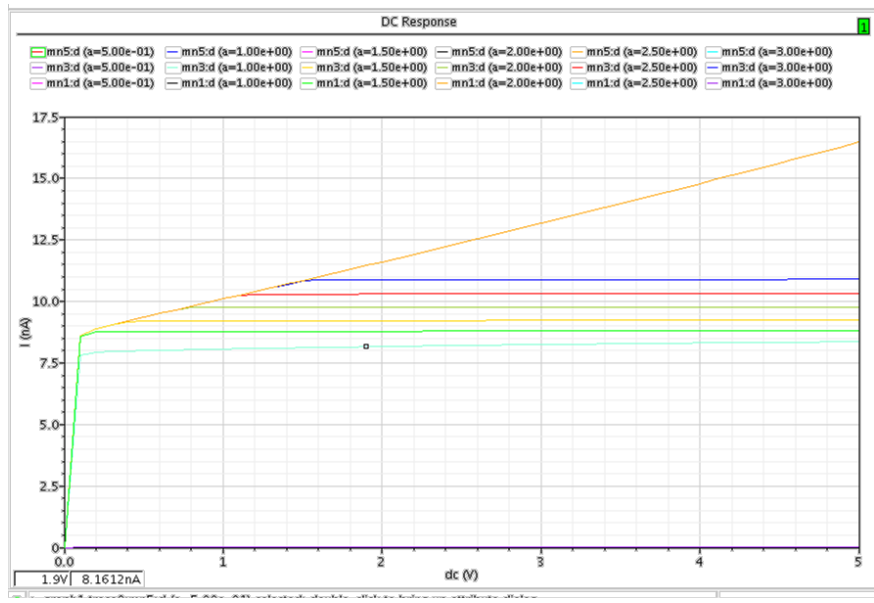


Figure 7-7. Schematic simulation result of  $V_b$  in current mirror with a step of  $V_b$  of 0.5 V.

Then, I change the  $V_b$  step to 0.5 V , the simulated result shows that the green line overlaps the first transistor's line.

Using the current mirror can copy the current and amplify the current in a certain gain. The schematic simulation of current mirror gain is shown below.

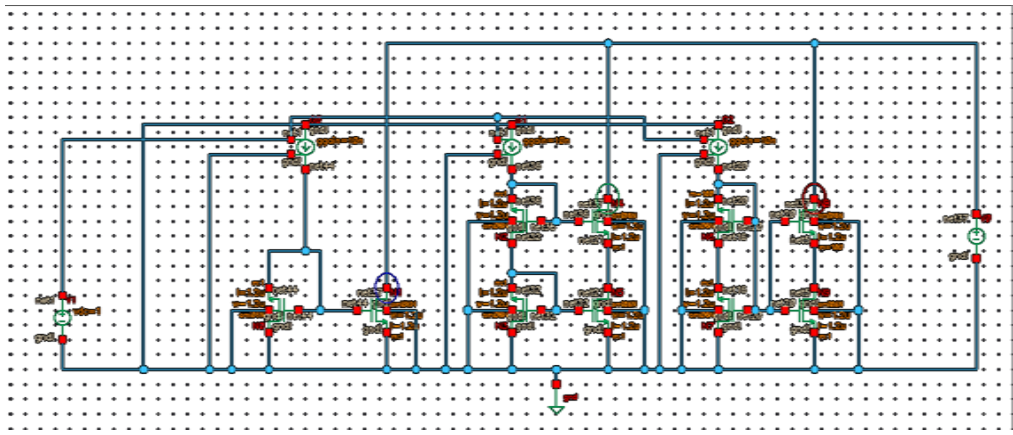


Figure 7-8. Schematic simulation of current mirror gain.

The  $V_{in}$  is set as 1 V, and the gain of VCCS is 10 nA/V, so the controlled current is 10 nA. The simulation result of DC response is plotted in  $I_{out}$  vs.  $V_{dc}$  curve.

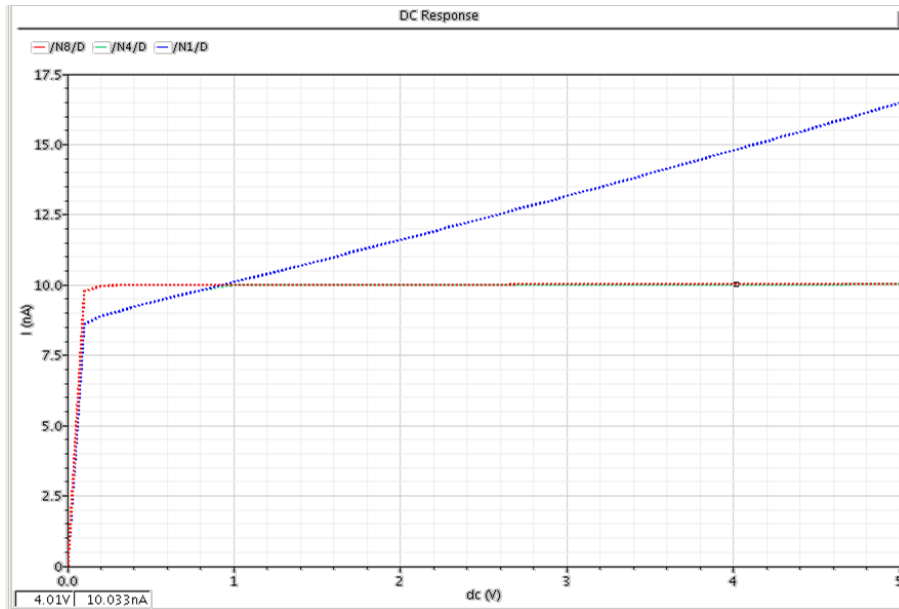


Figure 7-9. DC response of current mirror using VCCS of 10 nA.

## 7.4.2 Basic logic units

Similar as EIS for planar membrane on microchip, the capacitive sensor on each chip is connected to digital circuits for inspection and calculation. The digital algorithm is achieved by logic units conducting logic calculations including inverting, AND, OR, XOR, etc. The simple logic units are simulated in both of LTspice and Hspice.

### 7.4.2.1 Inverter

Starting with the basic logic gate inverter, inverter inverts the TTL logic voltage. Inverter is a basic component in VLSI design, which can be an end output to make other basic logic units, such as AND gate, OR gate and XOR gate. The schematic is the structure of logic gates with transistors and the layout demonstrate the CMOS transistors on P-type wafer.

First, the schematic structure of an inverter is drawn in Cadence Virtuoso. The width and length of P-type metal–oxide–semiconductor field-effect transistor (PMOS) and NMOS are unit sizes that defined by “ami06N”. Then, a symbol of inverter is created for further usage.

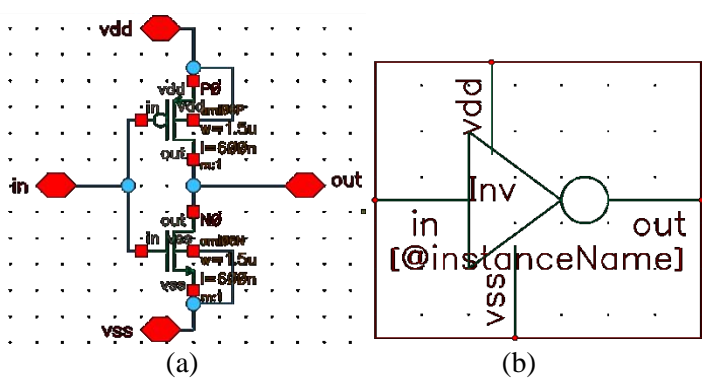


Figure 7-10. Unit sized inverter: (a) schematic; (b) symbol.

In the schematic and symbol design, “vdd” is the 5V supply on the inverter; “vss” is connected to ground; “in” is the input of inverter; and “out” is the output of the inverter. Then, a test file is created for testing the schematic of inverter with unit sizes.

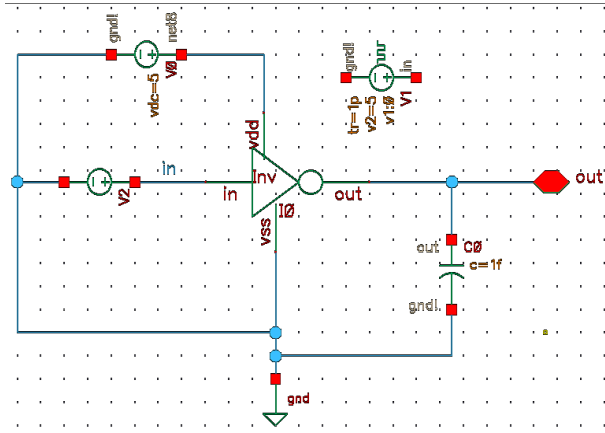


Figure 7-11. Testing schematic for unit-sized inverter.

The inverter is connected to vdd of 5V, vss to ground (gnd), and a capacitor of 1 fF as external load. To run the simulation, the variable V2 is set as a sweeping voltage source from 0V to 5V, and the input vs. output of the inverter is plotted in DC response figure.

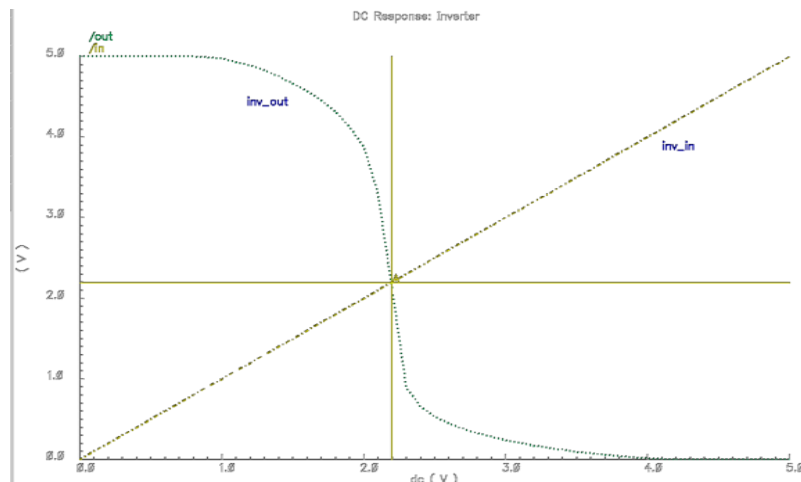


Figure 7-12. Simulation results of a unit-sized inverter with dc 0~5 V input.

Similar to DC response, I change the variable to pulse voltage for simulation. The pulse is a square wave signal with minimum voltage of 0 V, maximum voltage of 5 V, period of 4 ns, rising time and falling time of 1 ps, and delay time of 1 ns. The simulation time is set as 8 ns and plotted in transient response figure.

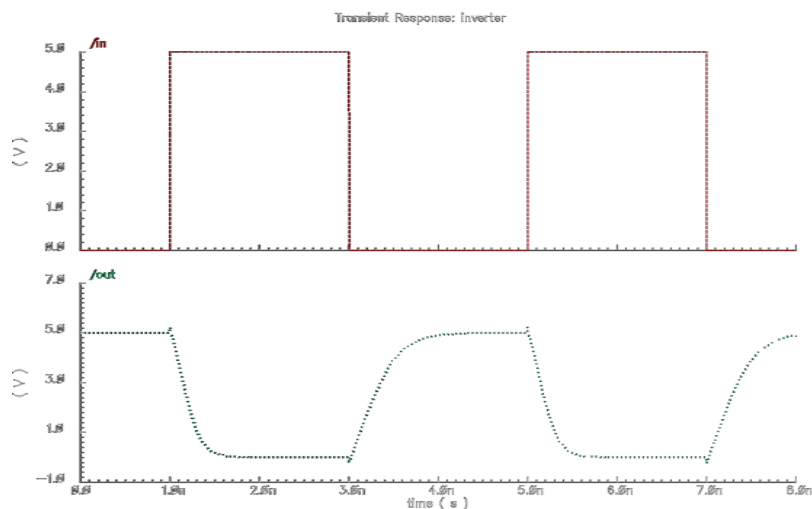


Figure 7-13. Simulation results of a unit-sized inverter with pulse voltage input.

Final, the layout structure for inverter is drawn in Cadence Virtuoso Layout. The layout is the real distribution of transistors which can be fabricated into CMOS chip. The sizes of transistors are determined in the schematic simulations.



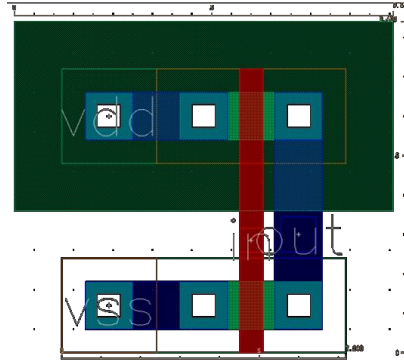


Figure 7-14. Layout of a unit-sized inverter.

The size of NMOS transistors is  $3600 \text{ nm} \times 7200 \text{ nm}$ , and the total dimension of this inverter is  $8400 \text{ nm} \times 9600 \text{ nm}$ . The top part of the layout represents a PMOS (PNP), and the bottom part represents a NMOS (NPN). The PMOS is larger than NMOS because on P-type silicon, the PMOS requires a larger N-well to support the PMOS.

The blue region represents the metal layer 1; pink region represents metal layer 2; red region represents polysilicon; black squares represent contacts and vias; the green boundary rectangular represents N-substrate; the orange boundary rectangular represents P-substrate; the green filled rectangular region represents N-well used for PMOS; the blue square represents input or output pins; the NMOS does not need to draw a P-well because the layout was for P-type wafer.

#### 7.4.2.2 Switch with clear function

Based on the structure of inverter, I can further make voltage buffers, and switches. An inverter can also be seen as a switch with open or close status controlled by gate voltage (1 or 0). If we want a switch to turn on or off and with a function of clearing to 0, we can use the inverter. Instead of connect the source of PMOS to “ $5 \text{ V } V_{dd}$ ” and the drain of NMOS to “GND”, we can connect the source of PMOS to signal “A” and the drain of NMOS to signal “0 V clear”, so:

$$\begin{cases} C = 1 : B = \text{clear}_0 \\ C = 0 : B = A \end{cases}$$

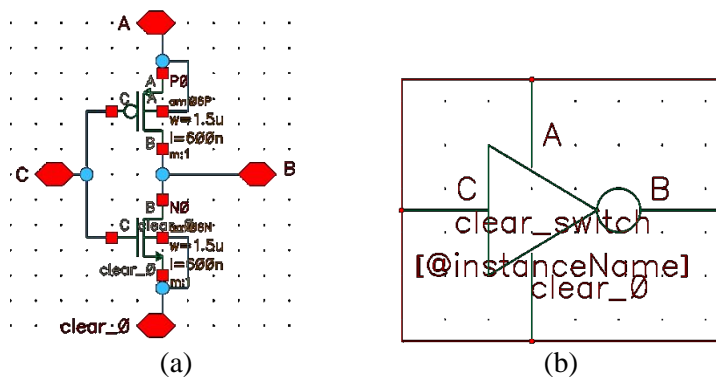


Figure 7-15. A switch with clear function: (a) schematic; (b) symbol.

### 7.4.2.3 Digital voltage buffer

The buffer is used to modify the TTL signals with less falling and rising edge. A typical buffer is connected by two inverters in series. The widths to length ratio of NMOS and PMOS for two inverters are different. The second inverter has larger width to further decrease the rising and falling time.  $V_1$  is the output after first inverter (out1), and the  $V_{out}$  is the final output of buffer.

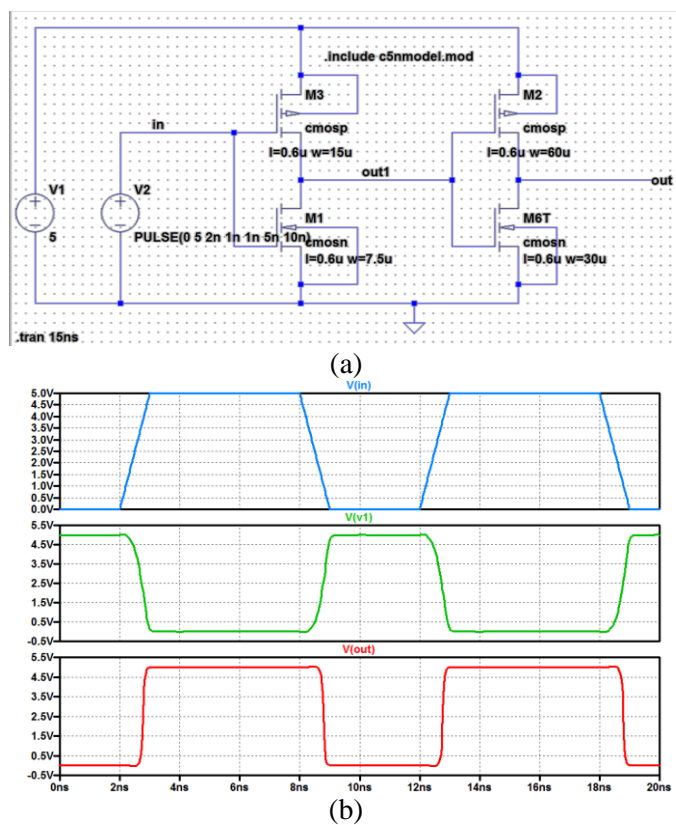


Figure 7-16. Schematic simulation of a buffer.

In the schematic simulation, the rising and falling of input signal have rising and falling of 1 ns. The first inverter changes the voltage during rising and falling, and the second inverter enlarges the propagation delay around 0.8 ns after rising and falling. Therefore, the rising and falling time of the signal after buffer decrease to ~ 0.2 ns.

#### 7.4.2.4 Transmission switch

A transmission switch works as a real switch in both digital and analog circuits. One NMOS or one PMOS can be used to connect source and drain depends on the gate voltage; with two of them connected in parallel, the transmission switch can control the on and off between two signals on sources and drains. Once the gate voltage of NMOS is “1” and the gate voltage of PMOS is “0”, the source and drain signal will be connected and same, regardless of the propagation delay and internal capacitance in small signal model of CMOS:

$$\begin{cases} C = 1: B = A \\ C = 0: B \neq A \end{cases}$$

Eq. 7-21

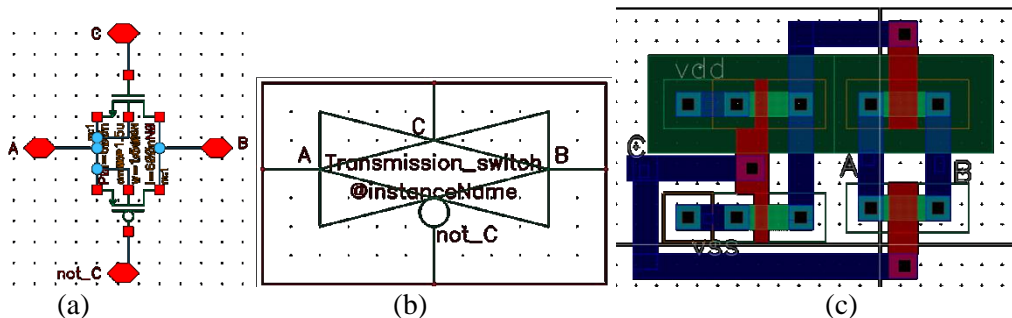


Figure 7-17. Structure of transmission switch: (a) schematic; (b) symbol; (c) layout.

#### 7.4.2.5 Logic units

The logic units provide basic logic executive operations for digital signals. The logic unit schematic structure can either be dynamic or static. The dynamic logic gates include clock signal to activate each unit, while the static gates do not involve clock signals. The operational frequency of the microchip inspection will be around 1 kHz, because of the electrochemical

properties of the planar membranes. Therefore, our simulation of the logic gates will be around kHz; in another word, the time sequences will be in milliseconds range.

### (1) Logic AND gate (2-input)

AND gate operates the logic calculation of  $C = A \cap B$ .

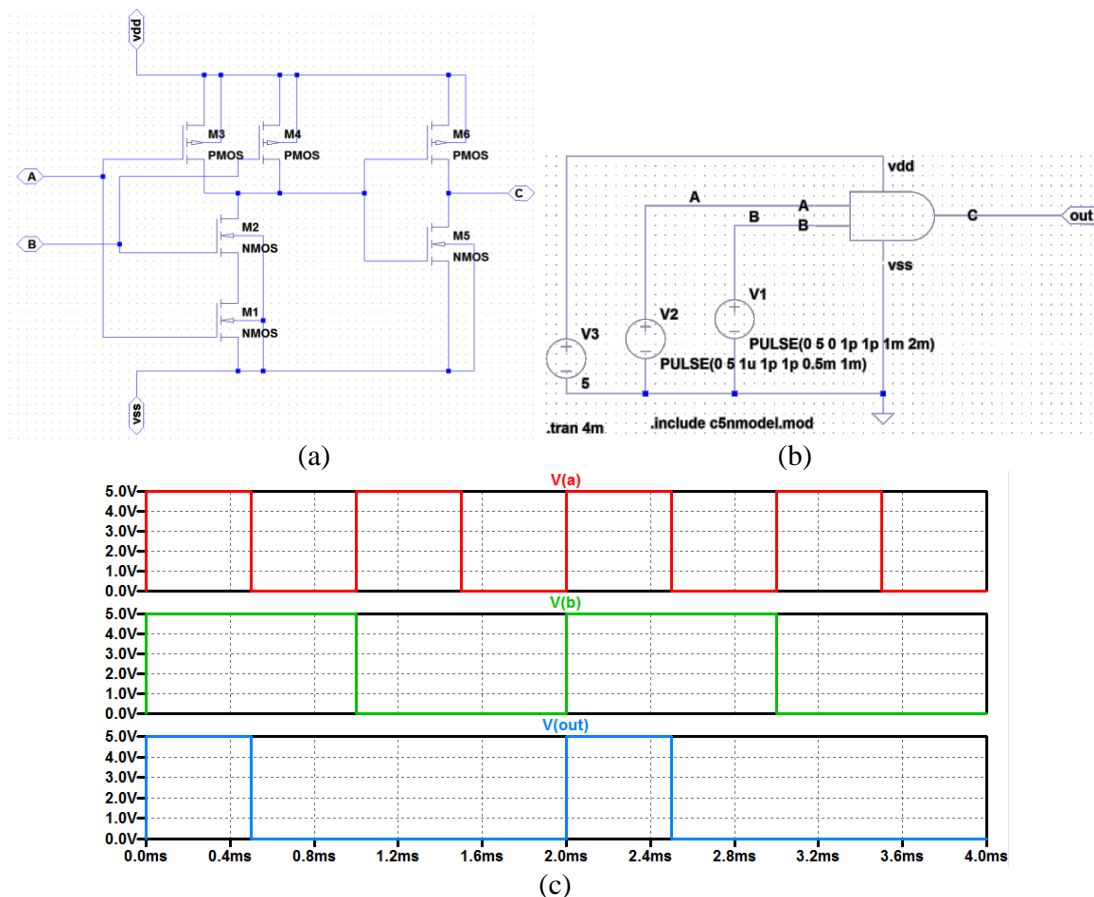


Figure 7-18. Schematic simulation of AND gate with 2 inputs: (a) schematic; (b) test circuit; (c) simulation results.

Besides the static AND gate, I also have dynamic AND gates simulated in Cadence. The dynamic gates are triggered by clock signal “clk”.

### (2) Dynamic logics

In the static CMOS design, a fan-in with N inputs need both NMOS and PMOS for each input signal. The layout of PMOS occupies a much larger area than NMOS, so the accumulations of PMOS will result in a large area of final layout. With the design of dynamic logics, a clock

signal “clk” is introduced to CMOS logic to pre-charge the NMOS and PMOS to reduce the required quantity of PMOS. The operation of dynamic CMOS logic is separated into two stages: pre-charge and evaluation.

In every dynamic logic unit, when clk is “0”, the output is pre-charged to  $v_{dd}$  by the PMOS. During this time, the NMOS with input clk is off, so that the pull-down path is disabled. When clk is “1”, the pre-charge PMOS is off, and the evaluation transistor NMOS is turned on. The output is discharged based on the input signals in the pull-down logic. For example, a dynamic AND gate is changed to:

$$out = \overline{clk} + clk \cdot (A \cdot B)$$

Eq. 7-22

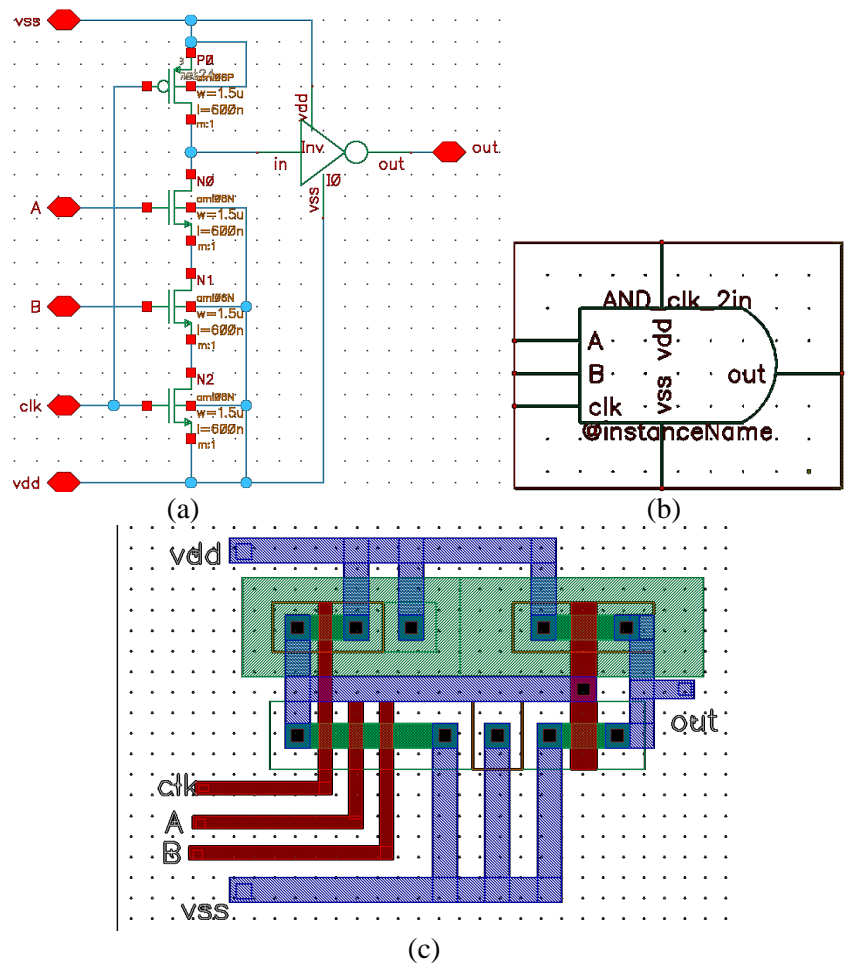


Figure 7-19. Structure of dynamic AND gate: (a) schematic; (b) symbol; (c) layout.

Dynamic gates have faster response time because the activation signal is “clk”, which will be used to activate other logic gates at the same time. The same step will improve the delay caused by propagation delay and other capacitance between CMOS and wires. In the layout simulation in Cadence, the dynamic AND gate uses a setup of rising and falling of 0.25 ns.

### (3) Logic AND gate (3-input)

AND gate with three inputs operates the logic calculation of  $OUT = A \cap B \cap C$ .

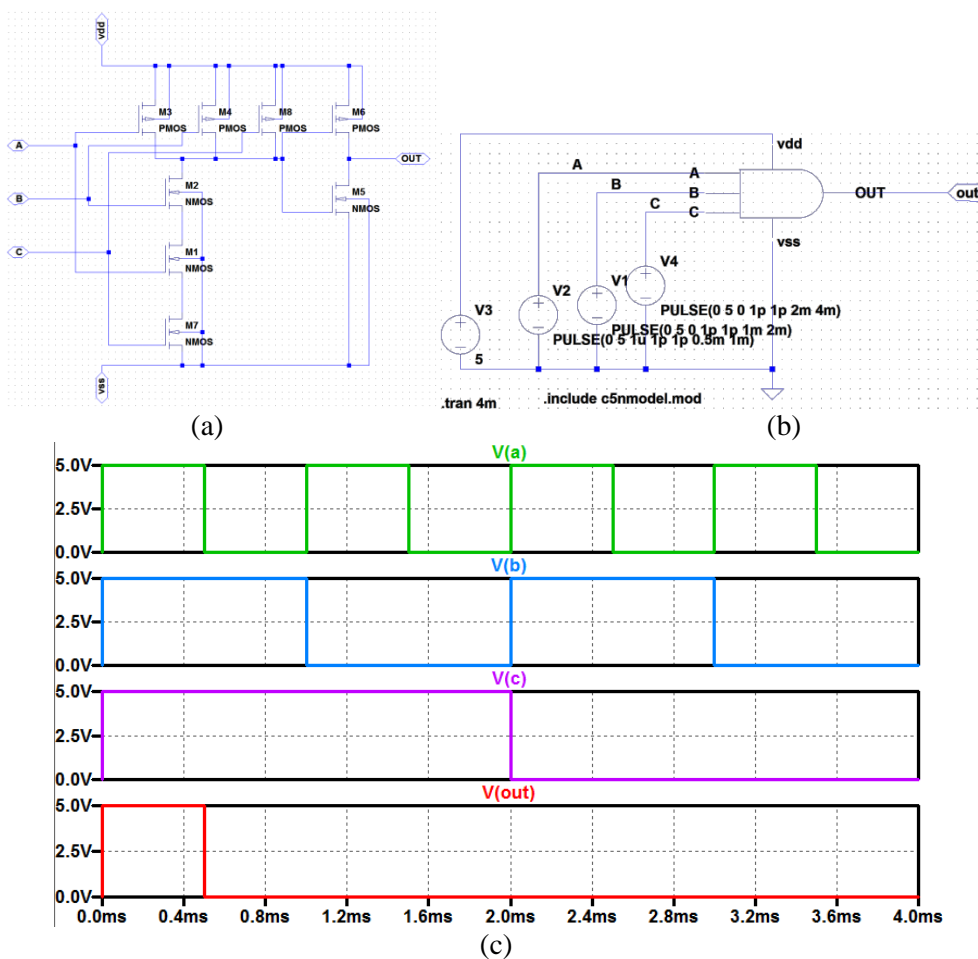


Figure 7-20. Schematic simulation of AND gate with 3 inputs: (a) schematic; (b) test circuit; (c) simulation results.

Similarly with the triggering of clock in dynamic AND gate with two inputs, we can build the dynamic AND gate layout with three inputs.

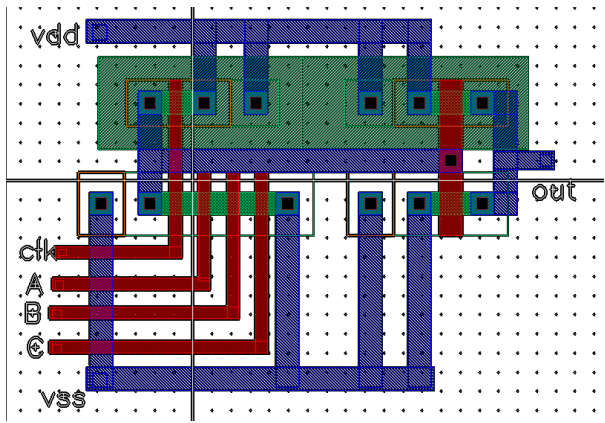


Figure 7-21. Layout of dynamic AND gate with 3 inputs.

**(4) Logic OR gate**

OR gate operates the logic calculation of  $C = A + B$ .

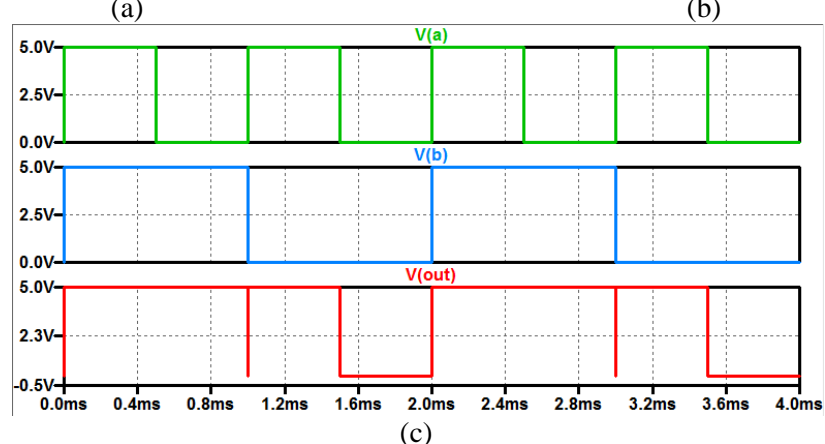
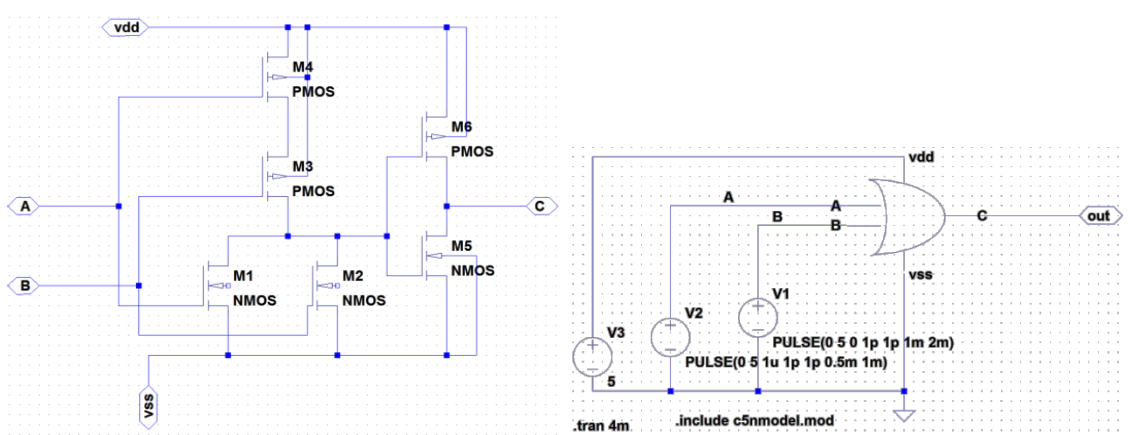


Figure 7-22. Schematic simulation of OR gate with 2 input. (a) schematic; (b) test circuit; (c) simulation results.

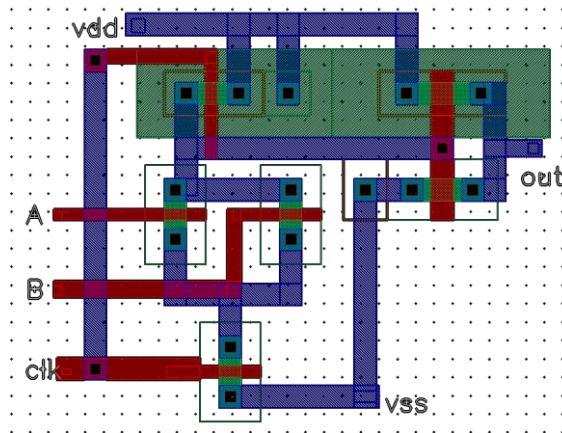


Figure 7-23. Layout of dynamic OR gate with 2 inputs.

### (5) Logic NAND gate

NAND gate operates the logic calculation of  $C = \overline{A \cap B}$ .

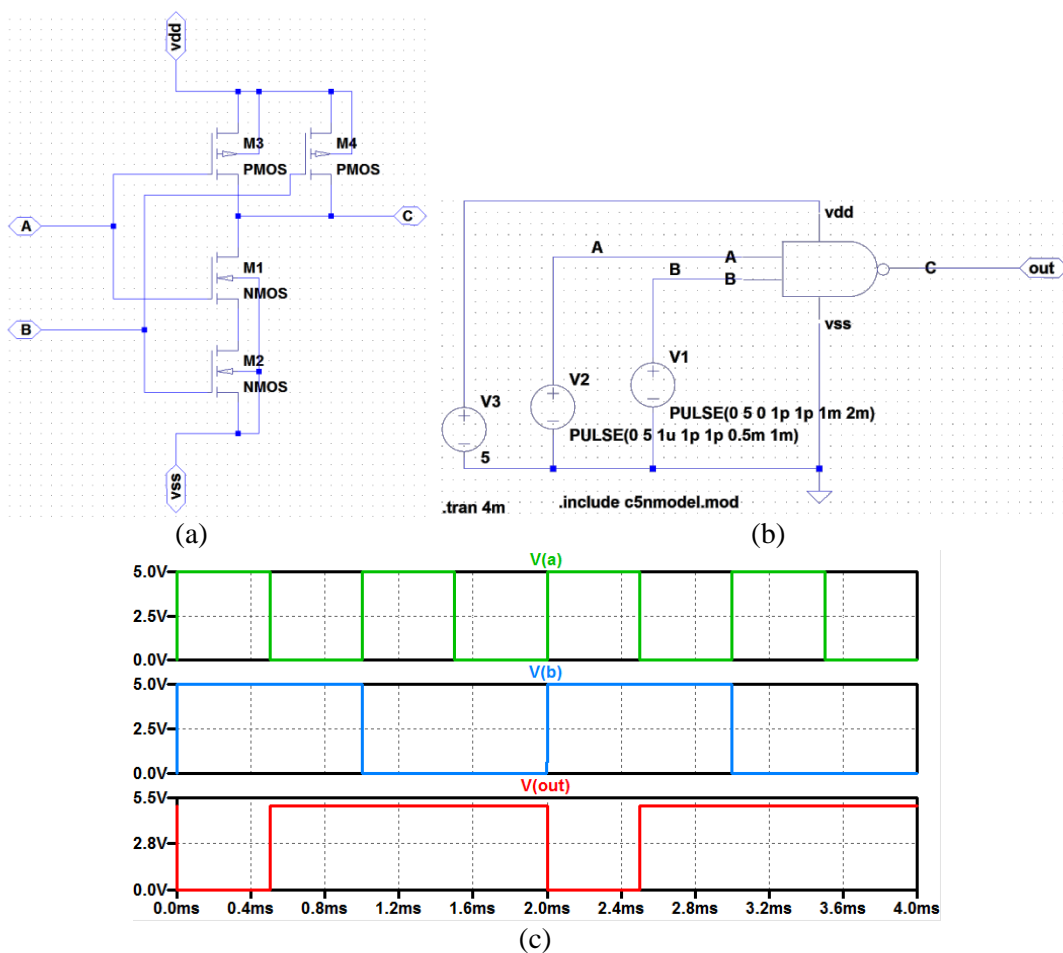


Figure 7-24. Schematic simulation of NAND gate with 2 input. (a) schematic; (b) test circuit; (c) simulation results.



NAND gate provides an logic operation of NAND. The truth table is:

in_a	in_b	out
0	0	1
0	1	1
1	0	1
1	1	0

The NAND gate contains two NMOS and two PMOS.  $out = \overline{in_a \cap in_b}$ .

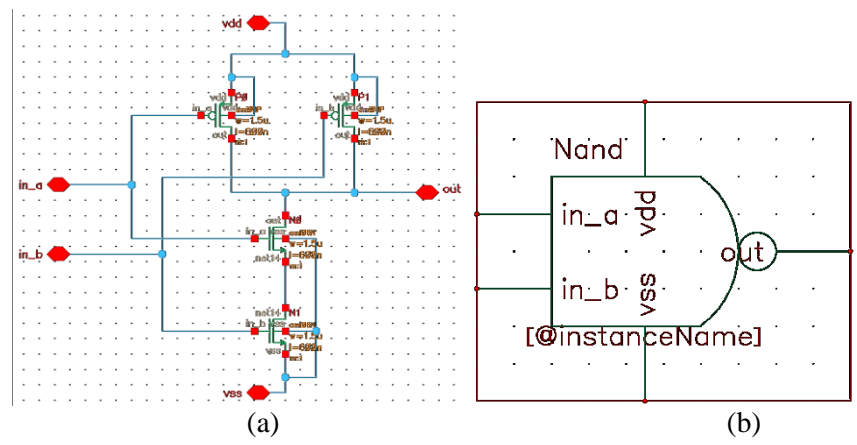


Figure 7-25. Schematic structure of static NAND gate in Cadence. (a) Schematic; (b) symbol.

To test the NAND gate, the input signals will test all the situations in the truth table. This NAND gate will be used in MHz range in the future, so the input signal frequency is around 1~100 MHz.

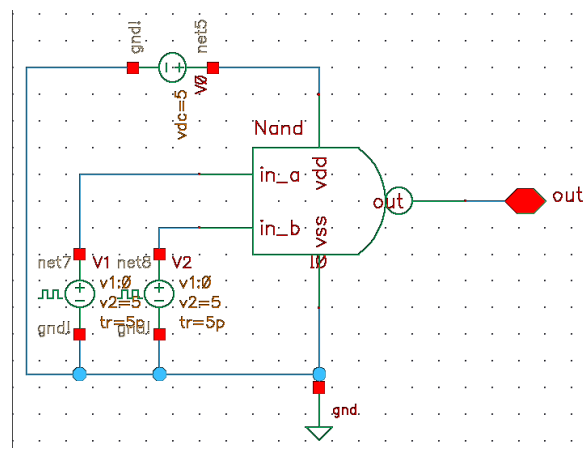


Figure 7-26. Schematic simulation structure of static NAND gate.

Signal “in\_a” is a square wave with period T of 100 ns, delay time of 25 ns, rising and falling time of 5 ps, pulse width of 50 ns; signal “in\_b” is another square pulse voltage source with period T of 200 ns, delay time of 25 ns, rising and falling time of 5 ps, and pulse width of 100 ns. Then, I use analog environment in Cadence Virtuoso to run the simulation of this static NAND gate test circuit.

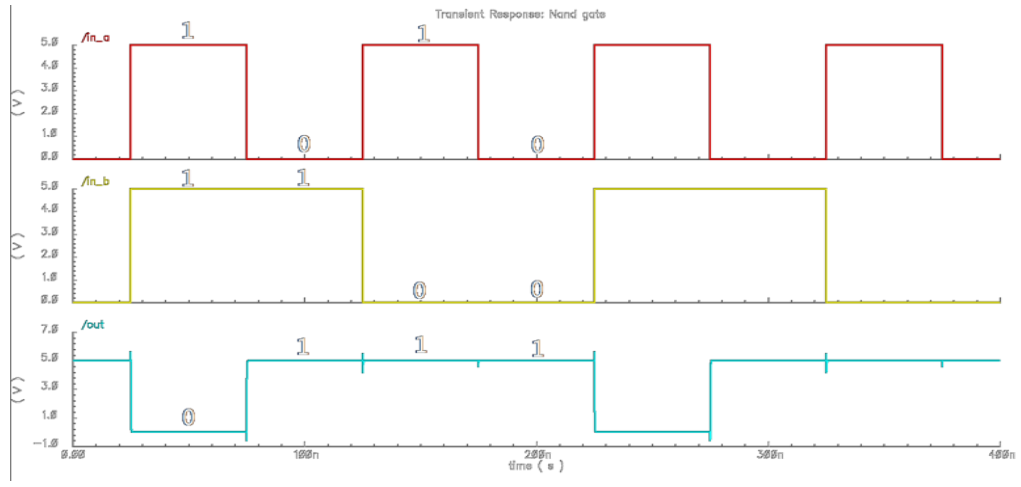
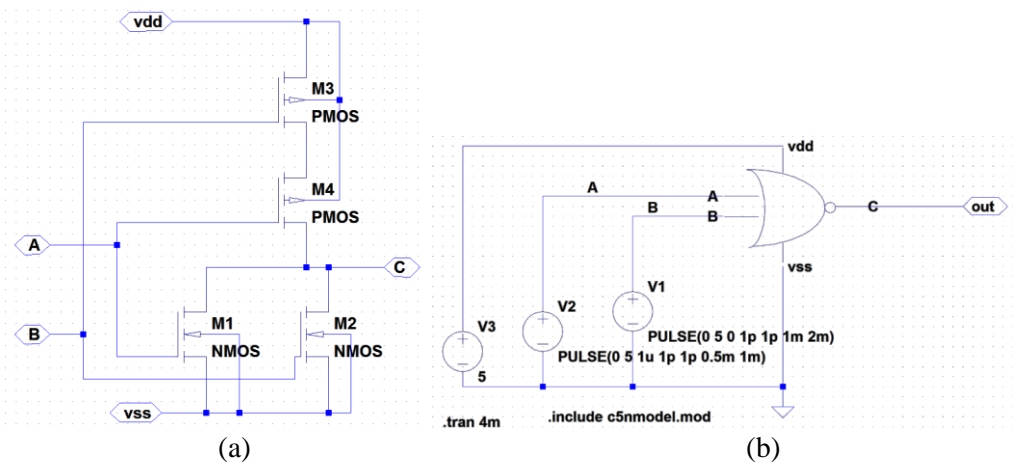


Figure 7-27. Test results of transient response of a static NAND gate.

**(6) Logic NOR gate**

NOR gate operates the logic calculation of  $C = \overline{A + B}$ .



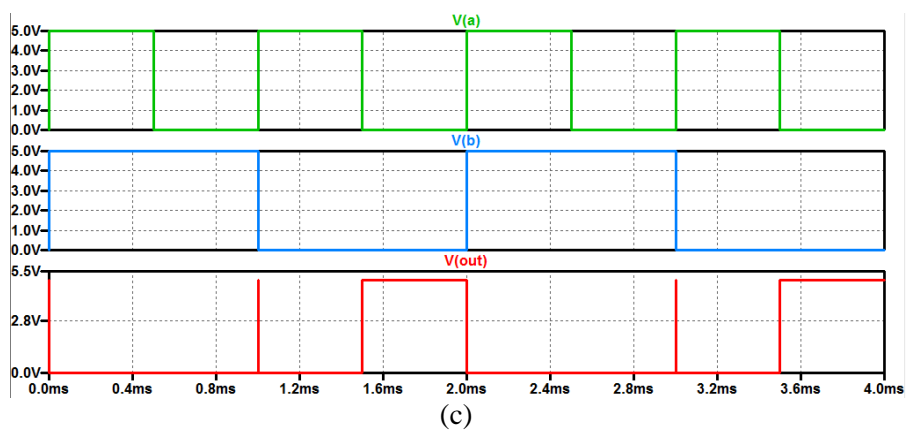


Figure 7-28. Schematic simulation of NOR gate with 2 input. (a) schematic; (b) test circuit; (c) simulation results.

NOR gate provides an logic operation of NOR. The truth table is:

in_a	in_b	Out
0	0	1
0	1	0
1	0	0
1	1	0

The NOR gate contained two NMOS and two PMOS.  $out = \overline{in_a + in_b}$

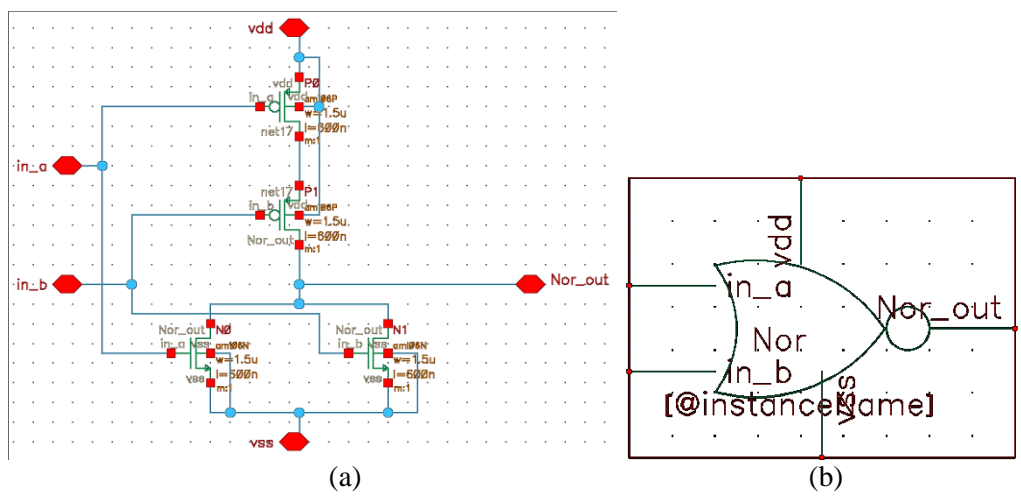


Figure 7-29. Schematic structure of static NOR gate in Cadence. (a) Schematic; (b) symbol.

To test the NOR gate, the input signal are tested all the situations in the truth table. This NOR gate will be used in MHz range in the future, so the input signal is around 1~100 MHz.

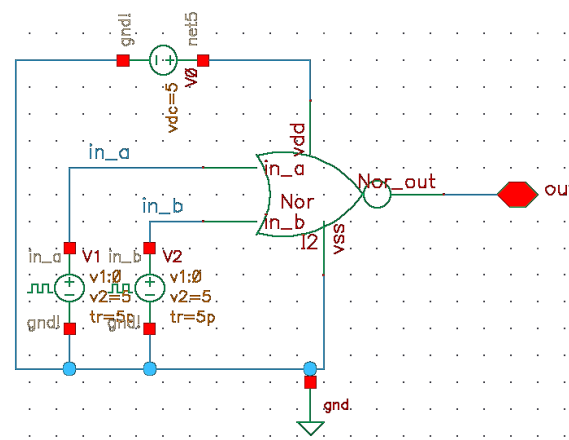


Figure 7-30. Schematic simulation structure of static NOR gate.

Signal “in\_a” is a square wave with period  $T$  of 100 ns, delay time of 25 ns, rising and falling time of 5 ps, pulse width of 50 ns; signal “in\_b” is another square pulse voltage source with period  $T$  of 200 ns, delay time of 25 ns, rising and falling time of 5 ps, and pulse width of 100 ns. Then, I use analog environment to run the simulation of this static NOR gate test circuit.

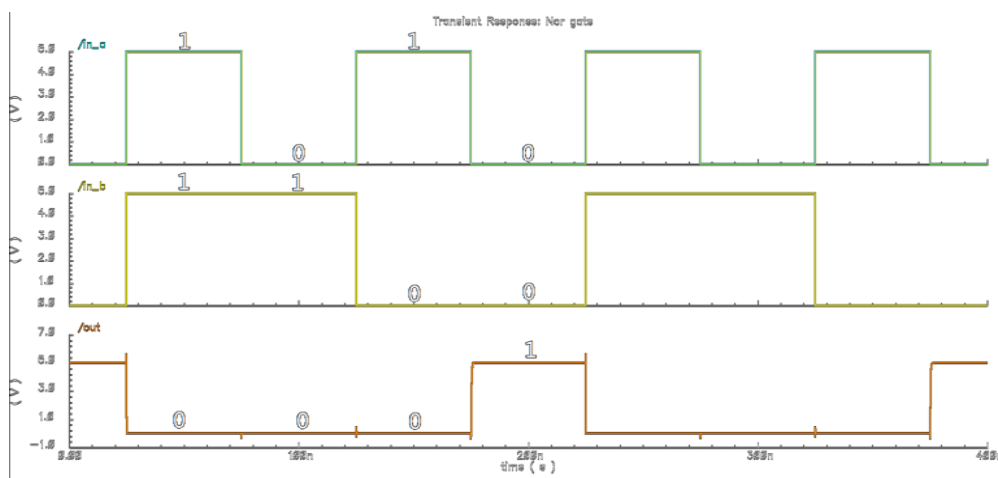


Figure 7-31. Test results of transient response of a static NOR gate.

### (7) Logic XOR gate

XOR gate operates the logic calculation of  $C = A \oplus B = \bar{A} \cdot B + A \cdot \bar{B}$ . If  $A$  and  $B$  are same,  $C$  will return “0”; otherwise, if  $A$  and  $B$  are different,  $C$  will return “1”.

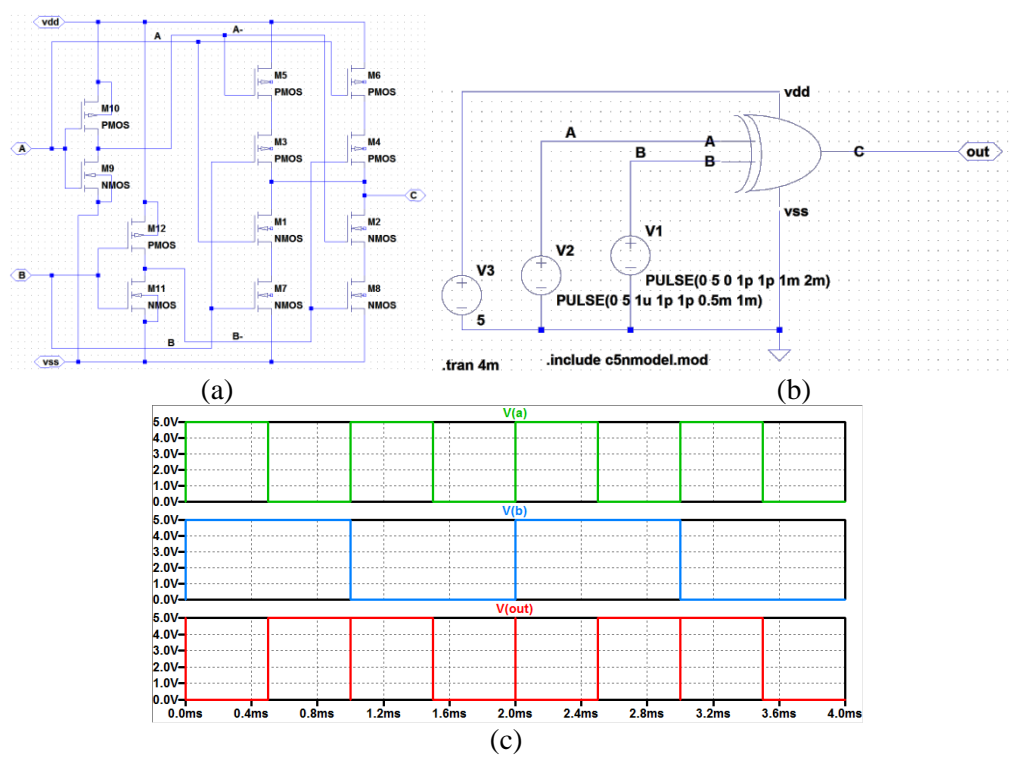


Figure 7-32. Schematic simulation of XOR gate with 2 input. (a) schematic; (b) test circuit; (c) simulation results.

XOR gate provides a logic operation of XOR. The truth table is:

a	b	out
0	0	0
0	1	1
1	0	1
1	1	0

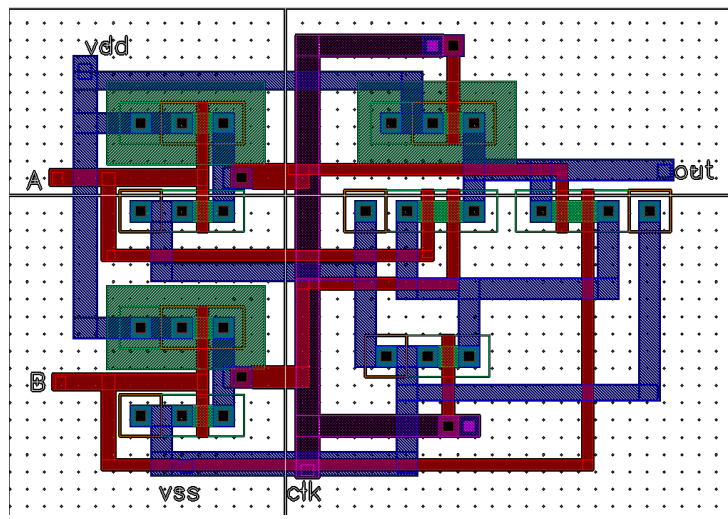
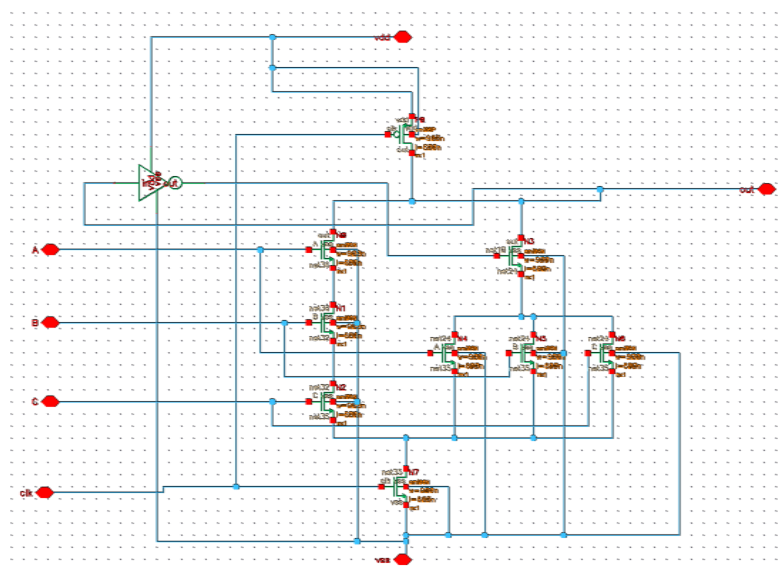
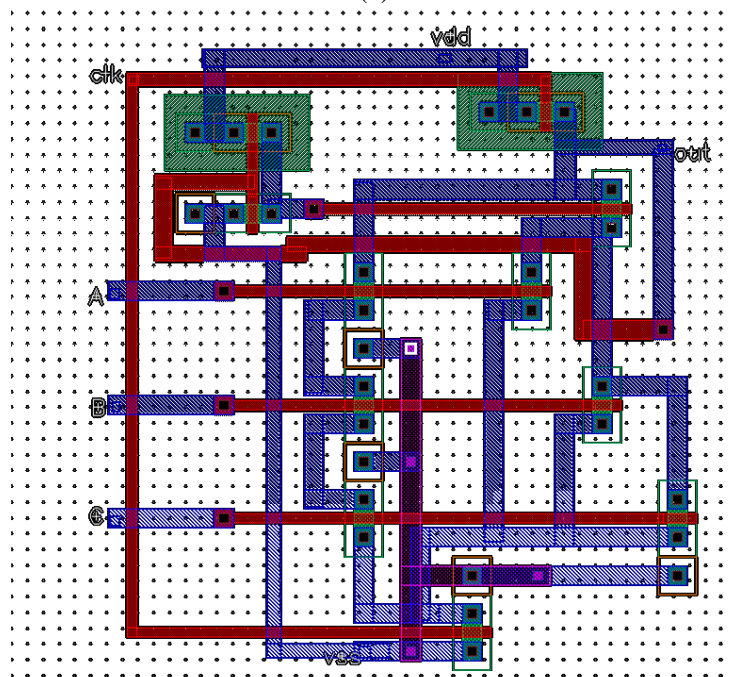


Figure 7-33. Layout of dynamic 2-input XOR gate.



(a)



(b)

Figure 7-34. 3-input dynamic XOR gate: (a) schematic; (b) layout.

**(8) Logic XNOR gate**

XOR gate operates the logic calculation of  $C = \overline{A \oplus B} = A \cdot B + \overline{A} \cdot \overline{B}$ . If A and B are different, C will return “0”; otherwise, if A and B are same, C will return “1”.

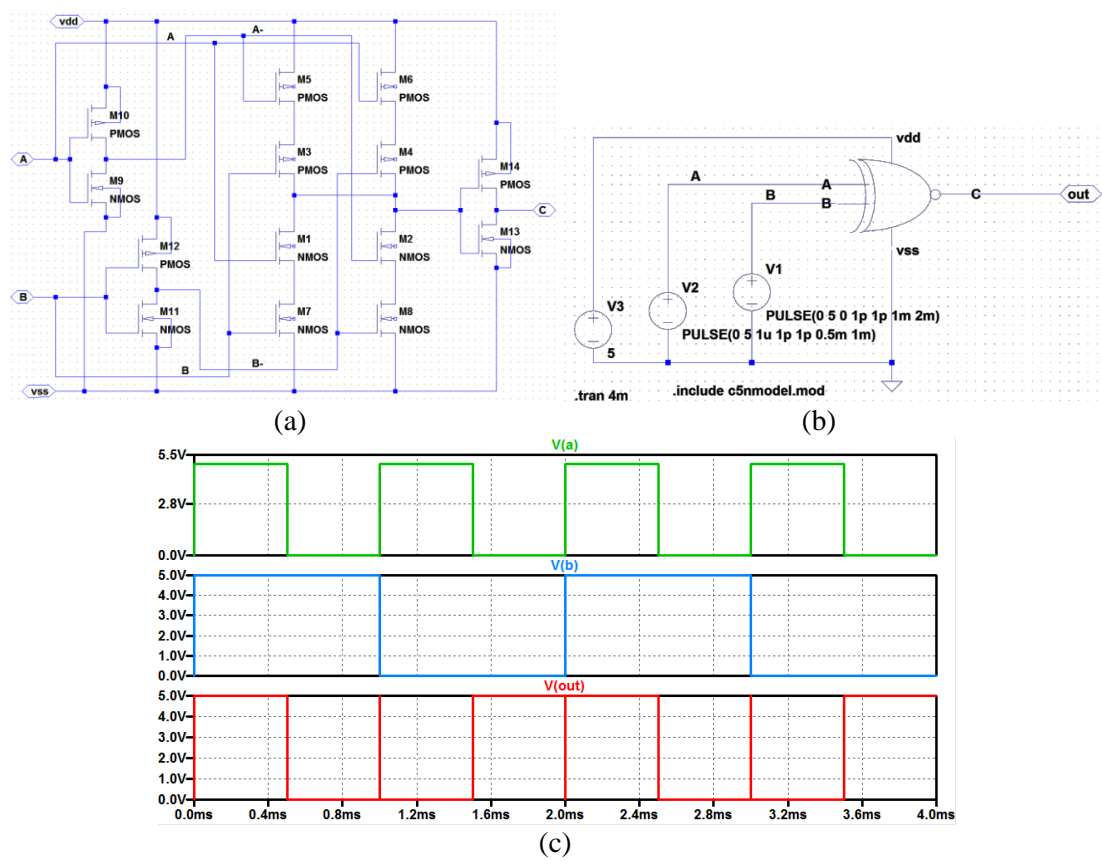


Figure 7-35. Schematic simulation of XNOR gate with 2 input. (a) schematic; (b) test circuit; (c) simulation results.

### 7.4.2.6 DQ register

#### (1) Simulation in Cadence

DQ register can be used to record digital information, such as the light reaction unit's X and Y coordinates information, so systems can write to or read out all the bits simultaneously. The master-slave register with positive edge triggered is broadly used with multiplexers.

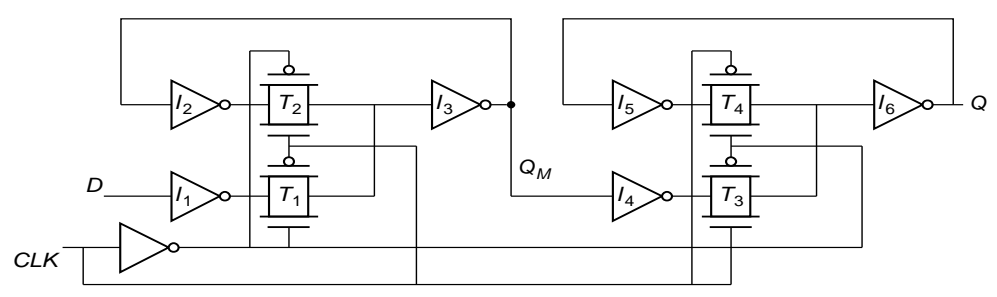


Figure 7-36. Schematic design of positive edge triggered master-slave register [365].

Sometimes, I need a DQ register with reset function, which can set the Q to 0, even though the reset function is not a dynamic clear function. An optional buffer is added before Q, in order to further reshape the output signal.

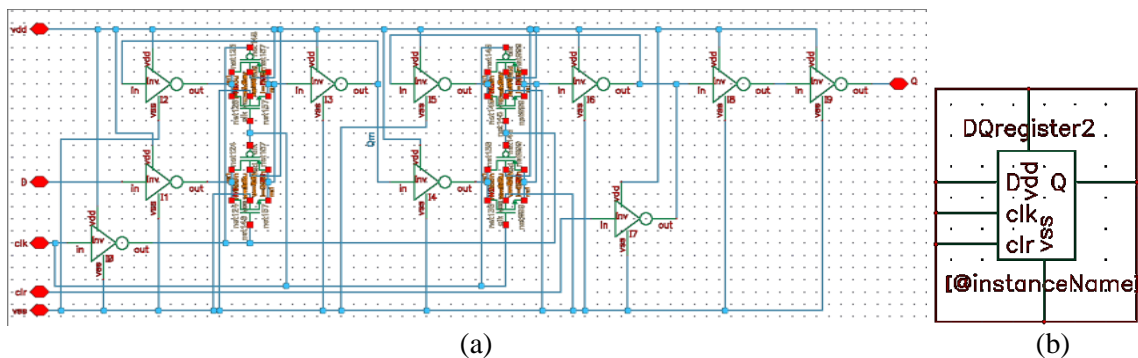


Figure 7-37. Schematic design of positive edge triggered master-slave register with reset function.

Then, I simulate this register with dynamic D signal and clock input. The DQ registers can be used to store the integrated microchips' working status, and collect data from sensors and input this signal to other processor units. The working status of each microchip can be determined by comparing the electric frequency response of the target microchip and a standard data through a comparator.

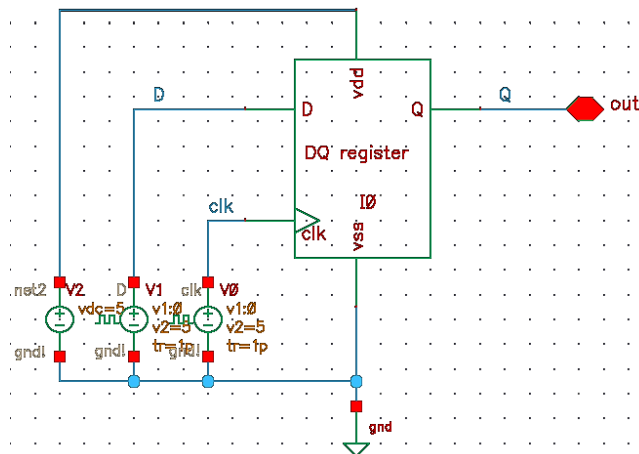


Figure 7-38. Schematic simulation structure of positive edge triggered DQ register.

The total time is set as 150 ns, clock period T of 8 ns, input D is a pulse voltage with period T of 50 ns, and delay of 1 ns.



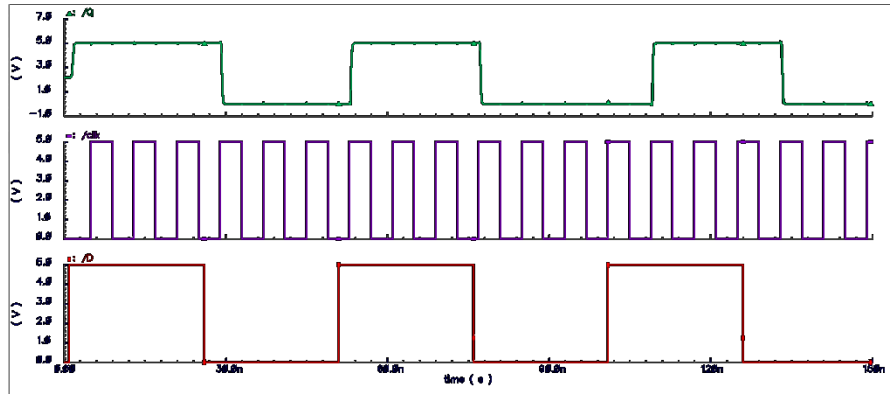


Figure 7-39. Test results of transient response of DQ register.

The result shows that the Q is activated to equal to D when the clock signal “clk” rises.

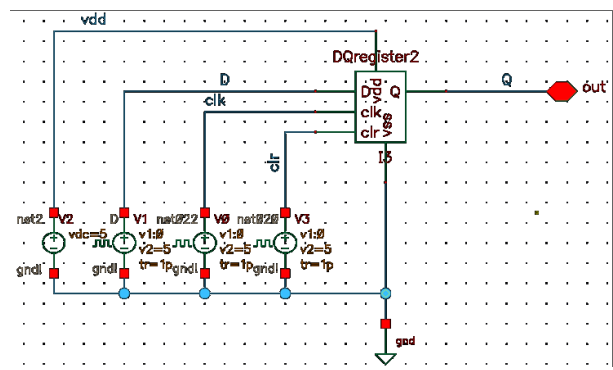


Figure 7-40. Schematic simulation circuit of DQ register with reset function “clr”.

The clock is set as period T of 10 ns, signal input D = 25 ns, and 50 ns in the form of square wave. The clear signal is sent to the input of DQ register with 120 ns delay to test the reset function on output Q.

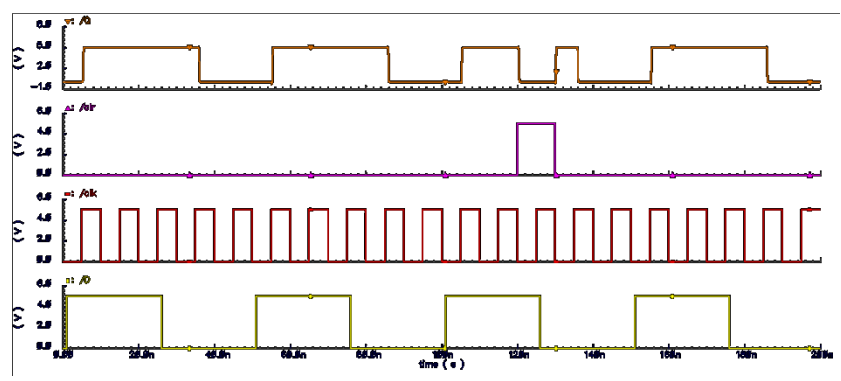


Figure 7-41. Schematic simulation of DQ register with reset function.

When the clear signal is on, the output Q is reset to 0, even though the clock is on for recording the data input D.

## (2) Simulation in LTspice

Similar to Cadence, LTspice can perform a simulation of the schematics with easier transistor sizes modification, as well as power electronics simulation. The DQ register is also simulated in LTspice at micro seconds range. The input signal is set as a large duty cycle pulse, and the clock is set as a higher frequency pulse with 2  $\mu$ s period.

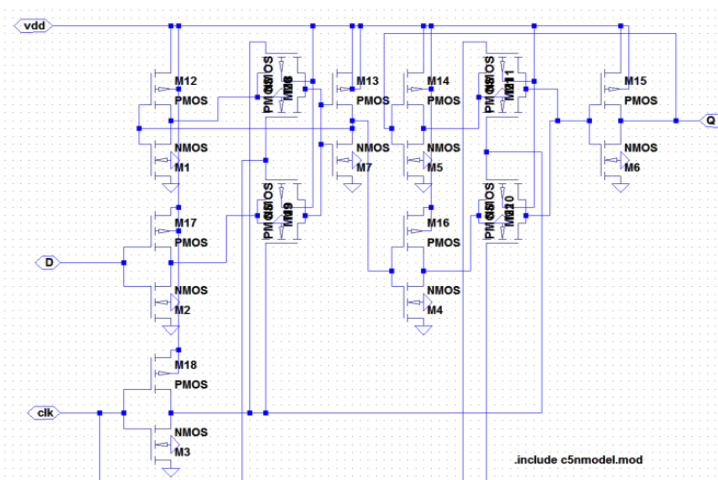


Figure 7-42. Schematic designs of DQ register for creating symbols in LTspice.

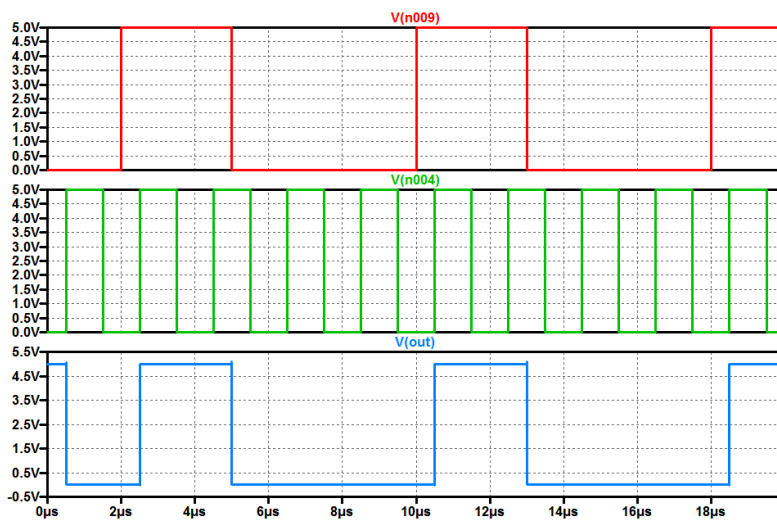


Figure 7-43. Schematic simulation results of the created DQ register in LTspice.

The results indicate an edge-triggered DQ register when clock is “1”.

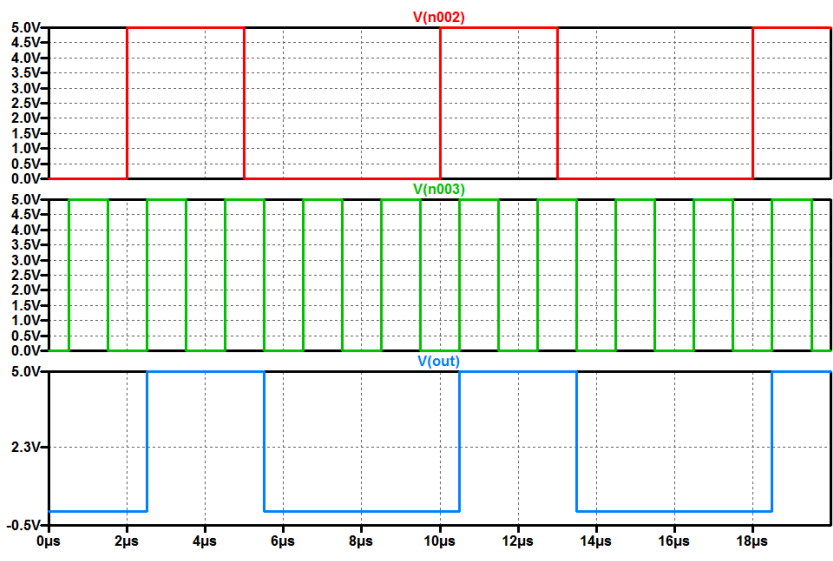


Figure 7-44. Schematic simulation results of edge-triggered DQ register symbol in LTspice.

An edge triggered DQ register with rising edge and falling edge trigger is useful in recording input data. The output copies the input data D when the clock edge is effective, either rising or falling in clock signal clk.

Sometimes we only need the register to record the data on the clock rising edge, such as counters and comparators, or dynamic logic units. Therefore, I also simulate the following schematic design of rising-edge-triggered DQ register.

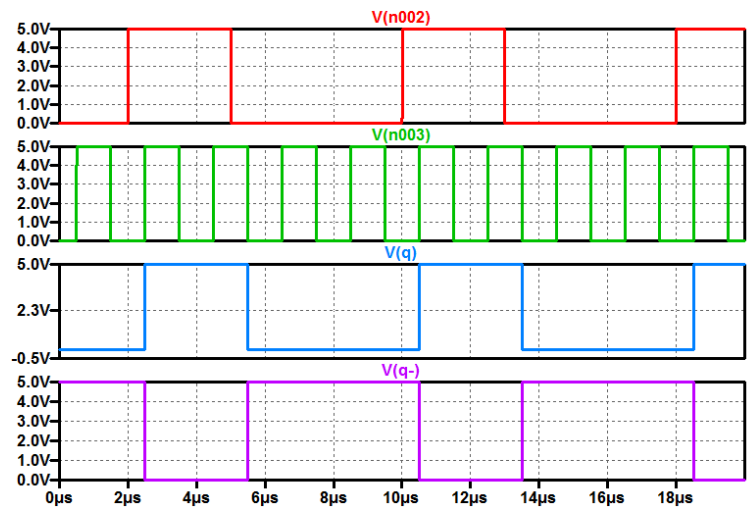


Figure 7-45. Schematic simulation results of rising-edge-triggered DQ register symbol in LTspice.

### 7.4.2.7 Decoder

#### (1) 2-4 decoder

Each unit will be encoded in binary numbers in each row and column. Hence, I need decoder for each output. 2-4 decoder translated 2-bit binary code into 4 output signals.

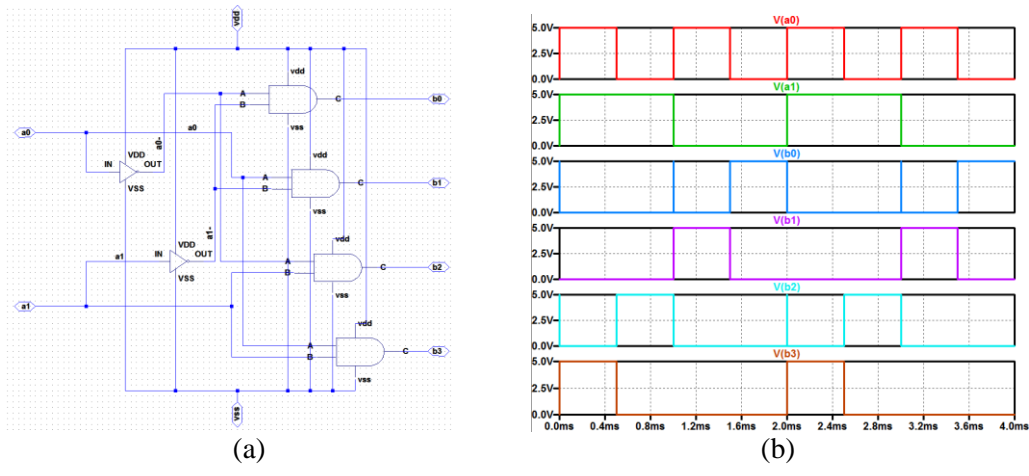


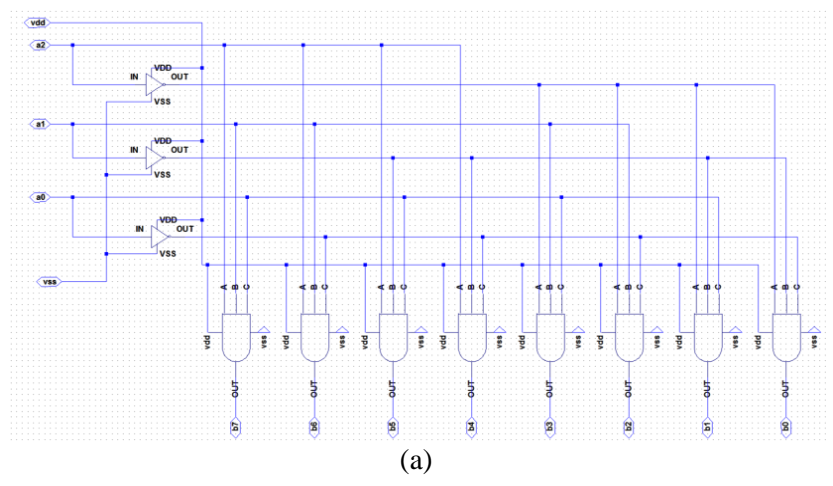
Figure 7-46. Schematic simulation of 2-4 binary decoder. (a) schematic; (b) simulation results.

The 2-4 decoder uses 2-bit (a1, a0) to select output b0~b3. The truth table is:

a1	a0	b0	b1	b2	b3
0	0	1	0	0	0
0	1	0	1	0	0
1	0	0	0	1	0
1	1	0	0	0	1

#### (2) 3-8 decoder

3-8 decoder translates 3-bit binary code into 8 output signals.



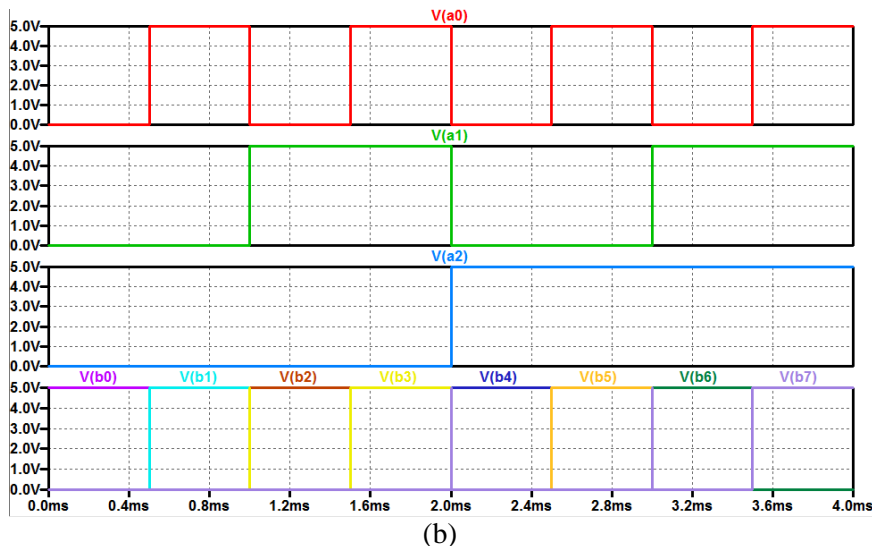


Figure 7-47. Schematic simulation of 3-8 binary decoder. (a) schematic; (b) simulation results.

The 3-8 decoder used 3-bit ( $a_2$ ,  $a_1$ ,  $a_0$ ) to select output  $b_0$ ~ $b_7$ . The truth table was:

$a_2$	$a_1$	$a_0$	$b_0$	$b_1$	$b_2$	$b_3$	$b_4$	$b_5$	$b_6$	$b_7$
0	0	0	1	0	0	0	0	0	0	0
0	0	1	0	1	0	0	0	0	0	0
0	1	0	0	0	1	0	0	0	0	0
0	1	1	0	0	0	1	0	0	0	0
1	0	0	0	0	0	0	1	0	0	0
1	0	1	0	0	0	0	0	1	0	0
1	1	0	0	0	0	0	0	0	1	0
1	1	1	0	0	0	0	0	0	0	1

If more bits are needed, similar to the 2-4 decoder and 3-8 decoder, a larger decoder can be built.

## 7.5 Ion channel monitoring

The ion channels with either alamethicin or BR transfers ions or protons through membranes. The small current generated through electrodes needs to be detected to monitoring the working status of ion channels.

### 7.5.1 ADC

CMOS ADC and DAC are always coming together in a mixed-mode VLSI. Delta-sigma ADC is broadly used in general analog to digital applications. The structure and diagram of ADC

varies depends on different applications, including input signal range, SNR, and clock frequency ranges, etc [366-368]. The principles of  $\Delta$ - $\Sigma$  ADC is demonstrated as an integrator with certain threshold, the generated pulses can be further counted by digital binary counter to binary numbers.

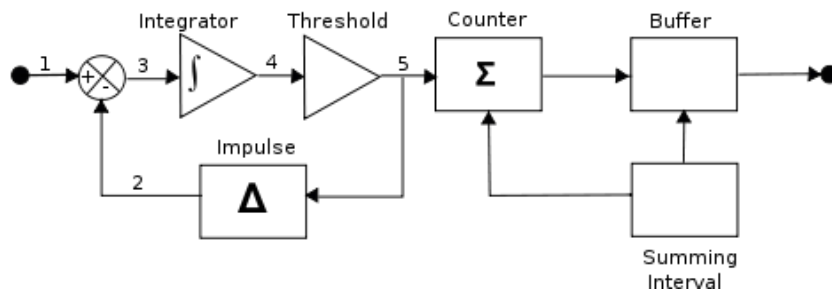


Figure 7-48. Block diagram of Delta-Sigma ADC.

The basic idea for this kind of ADC is changing the input voltage into time or frequency, and using the time differences variables as intermediate signals before the digital output [369, 370]. By counting the intermediate signal pulses, we can use the binary digital quantity to represent the analog input.

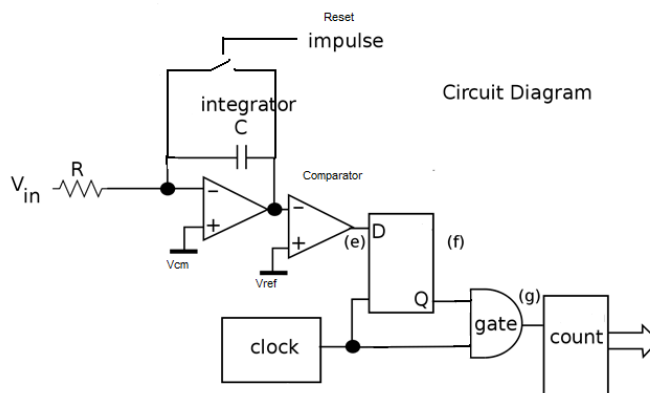


Figure 7-49. Circuit diagram of ADC.

Reference voltage is assigned to specific purpose in ADC. Similar to DAC, a least significant bit (LSB) is defined by two reference voltages.

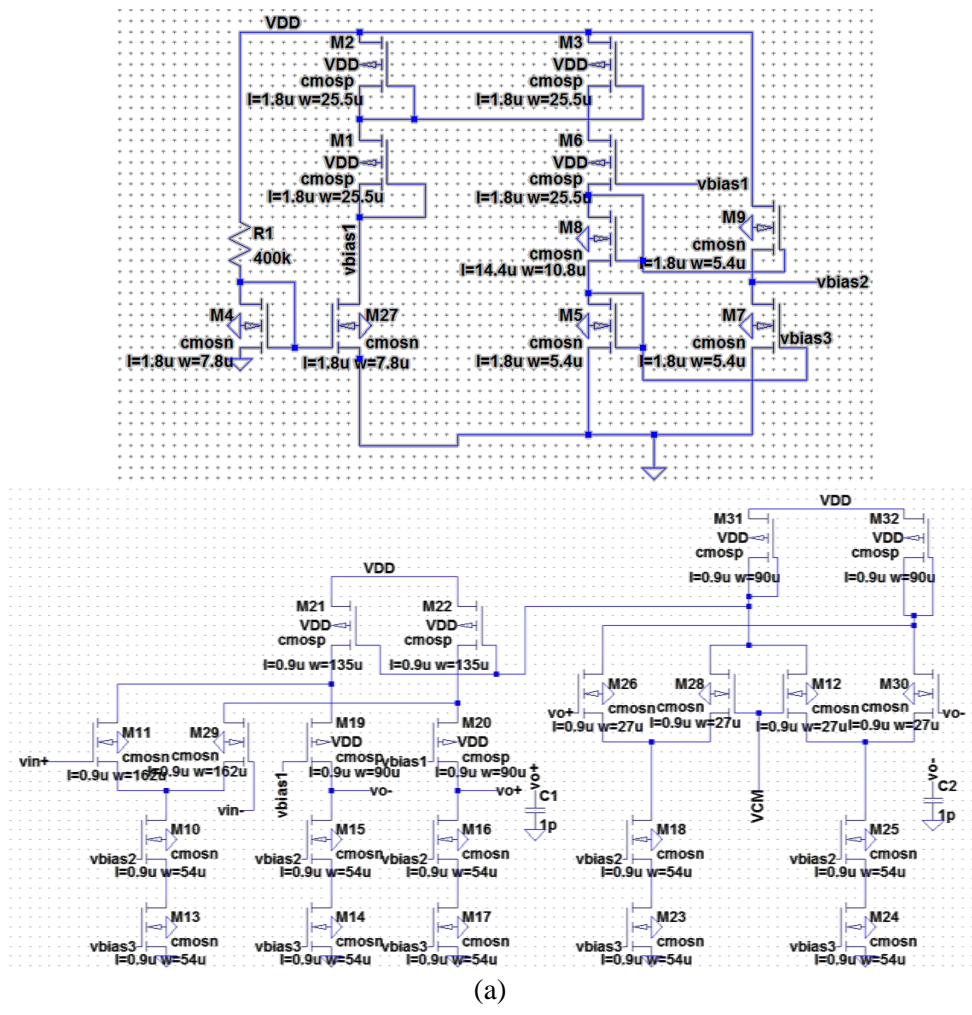
$$1 \text{ LSB} = \frac{V_{\text{ref}+} - V_{\text{ref}-}}{2^n} = V_{\text{LSB}}$$

The input voltage will be converted and normalized to digital binary output code. Even the ideal ADC, quantization noise will always be added to input signals.

### 7.5.2 OTA

#### 7.5.2.1 Full differential OTA

The operational trans-conductance amplifier (OTA) is an amplifier whose differential input voltage produces an output current [364]. Thus, it is a voltage controlled current source (VCCS). There is usually an additional input for a current to control the amplifier's trans-conductance. The OTA is similar to a standard operational amplifier in that it has a high impedance differential input stage and that it might be used with negative feedback.



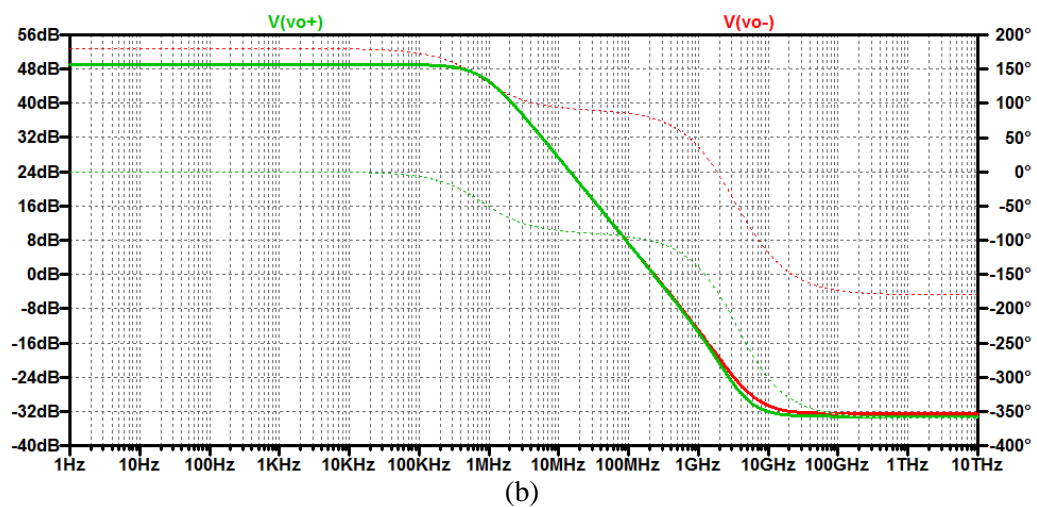


Figure 7-50. (a) A wide-range low noise full differential OTA; (b) Bode plot of full differential OTA.

### 7.5.2.2 5-transistor OTA and comparator

#### (1) 5-transistor OTA

The 5-transistor impedance amplifier takes the cascade current mirror to increase the current copied from  $I_{bias}$ .

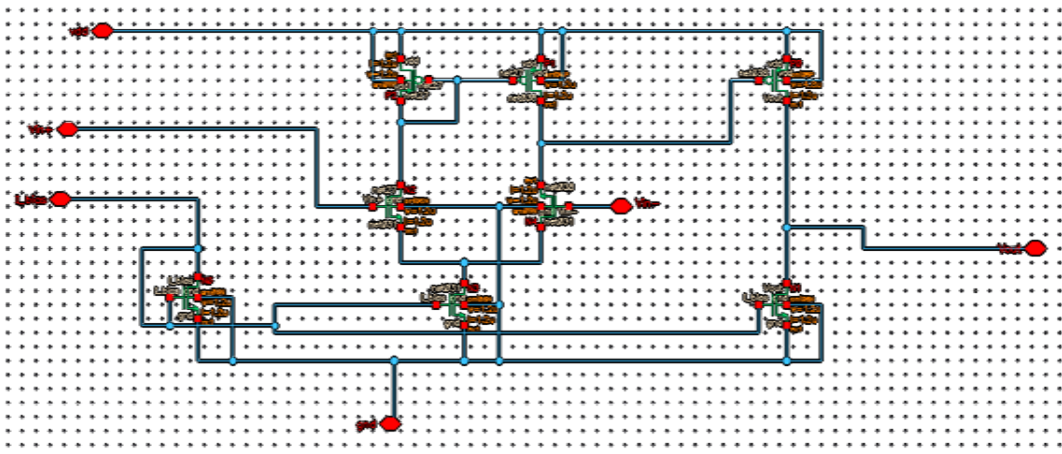


Figure 7-51. Schematic design of 5-transistor OTA.

The input current  $I_{dc}$  is set as 10 nA.



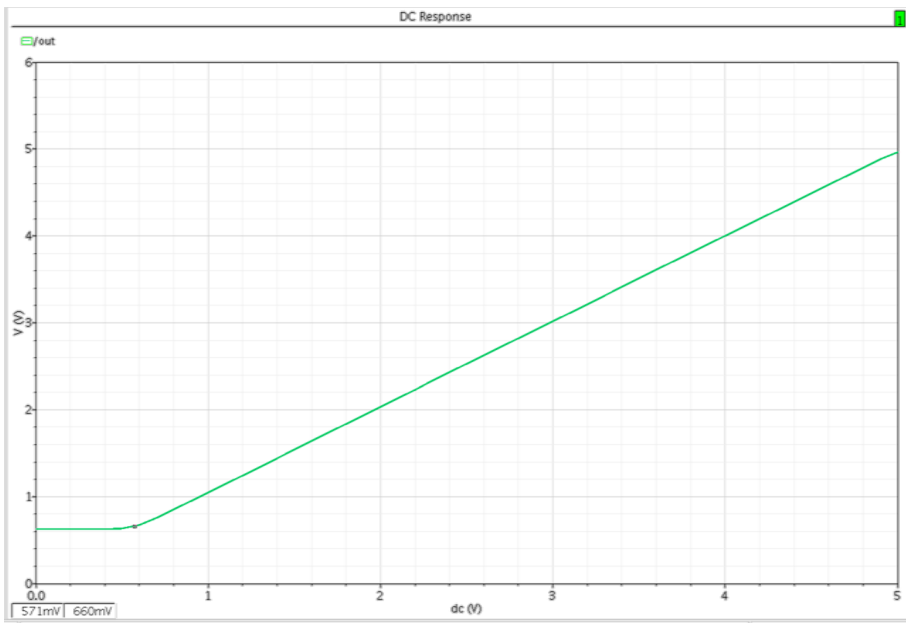


Figure 7-52. Schematic simulation results of 5-transistor OTA.

**(2) Test for comparator**

The comparator is used to compare a input signal to a standard signal. In ADC design, I set a threshold as resolution, where the input signal is compared. The output can generate “1” if the input is larger than the threshold. With a series of comparators, the ADC can generate pulses as the input for binary counters.

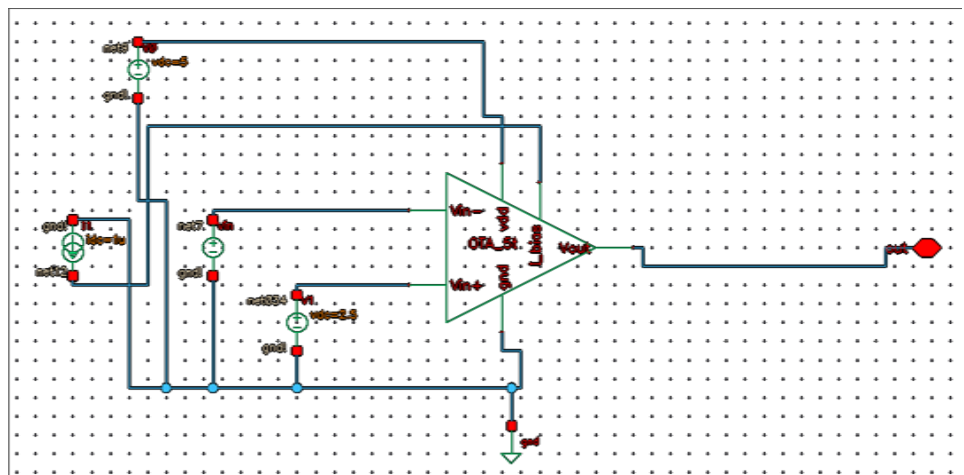


Figure 7-53. Schematic simulation of comparator formed by 5-transistor OTA.

In the schematic simulation, I set the reference voltage as 2.5 V, the DC response of 0~5 V created an output shown below. If the voltage is larger than 2.5 V, the output becomes 5 V; if the voltage is smaller than 2.5 V, the output becomes 0 V.

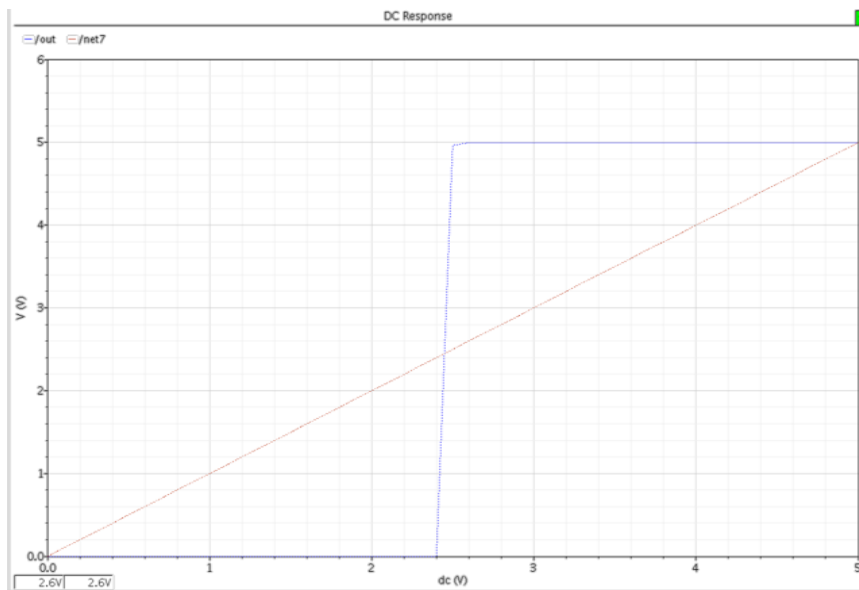


Figure 7-54. Schematic simulation DC response results of comparator formed by 5-transistor OTA.

I use the comparator with external capacitor and resistor to form an integrator circuit, with  $C = 1 \text{ nF}$ , and  $R = 1 \text{ M}\Omega$ . The simulation results are shown below.

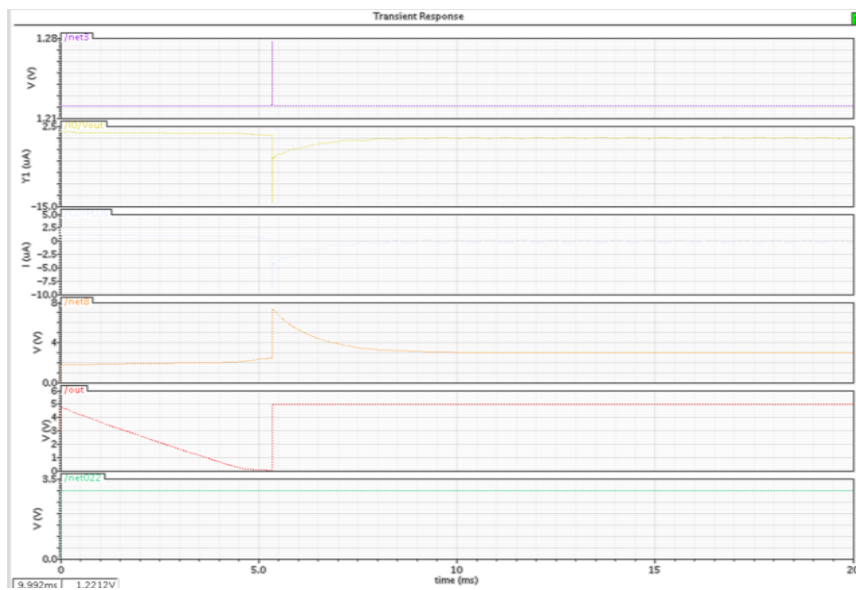


Figure 7-55. Schematic simulation results of integrator formed by 5-transistor OTA.

The output is set from 0 to 5 ms, the voltage drops linearly, and the current is set as constant to  $V/R$ . I set the input as 3 V first for simulation.

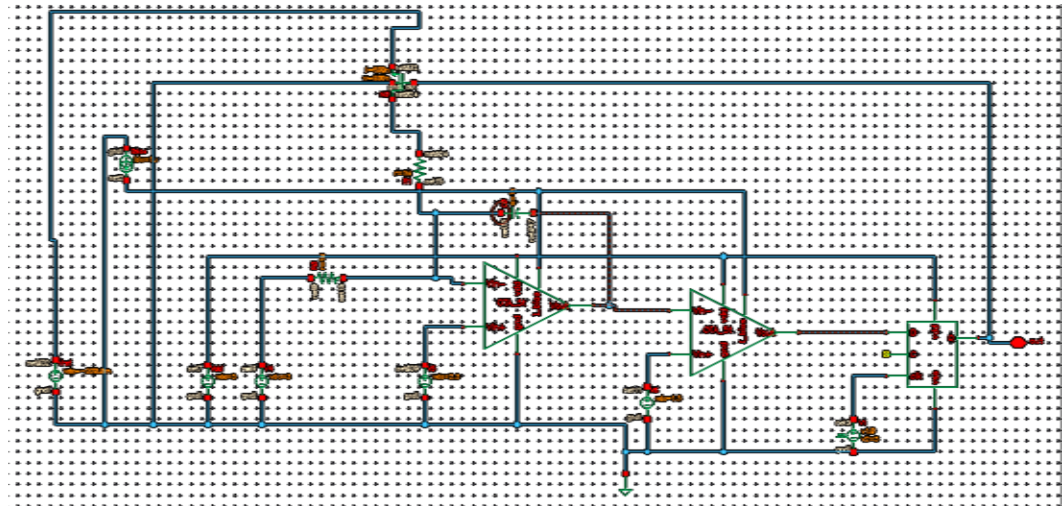


Figure 7-56. Schematic simulation of one bit ADC formed by 5-transistor OTA with input of 3 V.

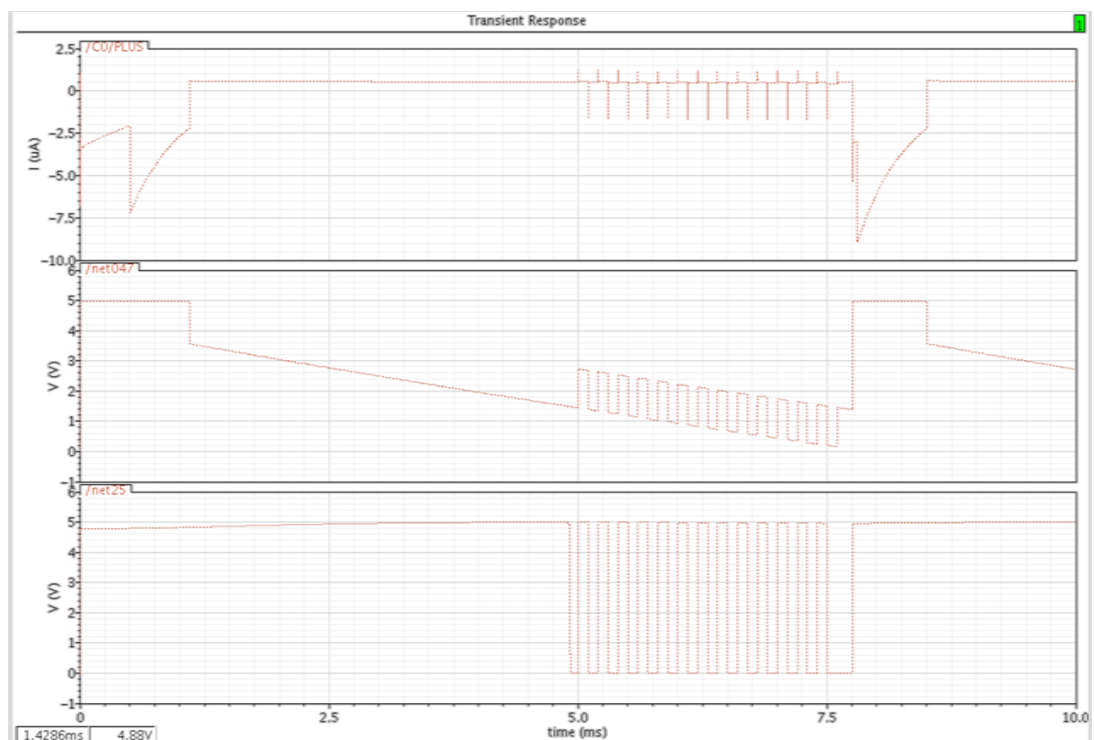


Figure 7-57. Schematic simulation results transient response of one bit ADC formed by 5-transistor OTA; the input voltage was 3 V.

The results indicate that there are 13 glitches after the D flip-flop. Then, I set the input as 2.6 V for second simulation.

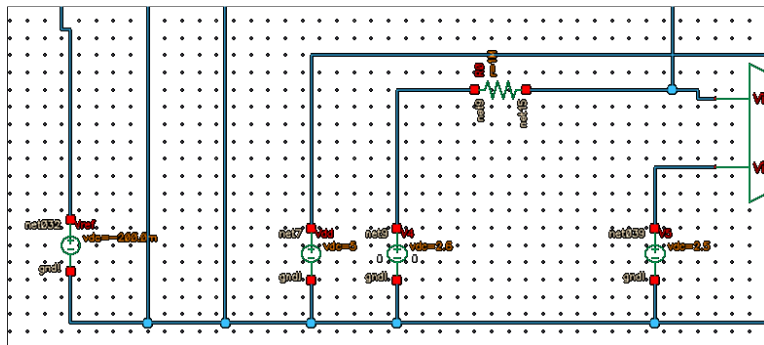


Figure 7-58. Schematic simulation of one bit ADC formed by 5-transistor OTA with input of 2.6 V. (The figure only demonstrated the input voltage).

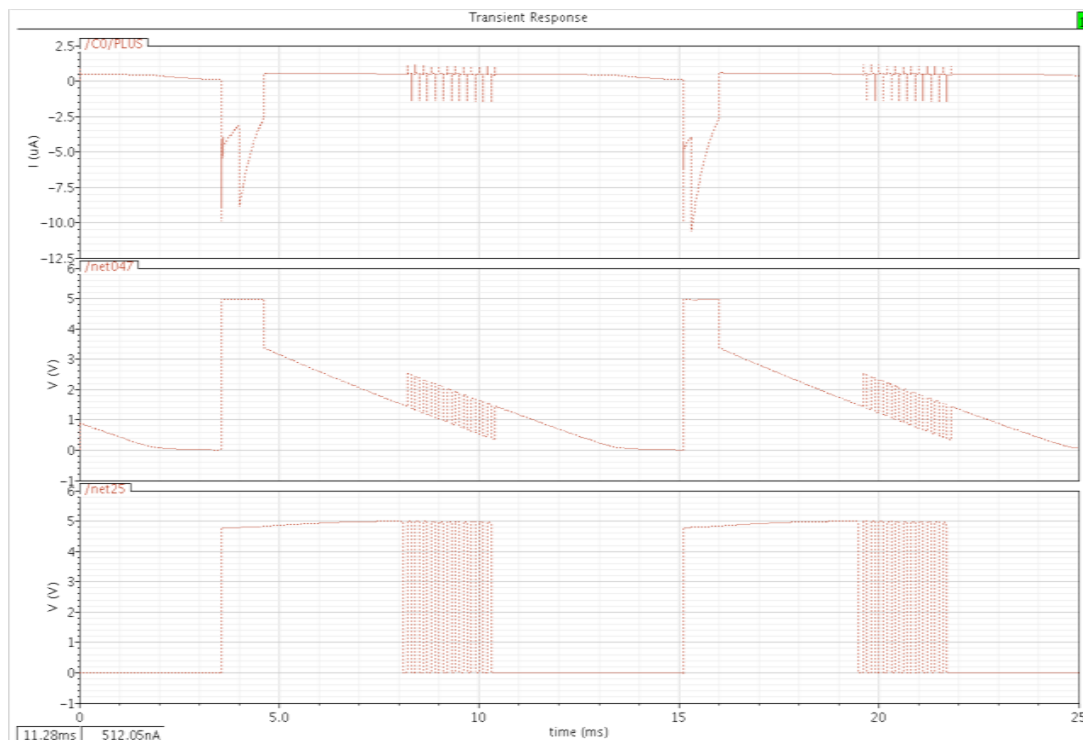


Figure 7-59. Schematic simulation results transient response of one bit ADC formed by 5-transistor OTA; the input voltage was 2.6 V.

The results show that it has 11 glitches. Comparing the input of 3V, there are 13 glitches, and I set the threshold  $V_{ref}$  as -200 mV, so the simulation results are correct.

**7.5.2.3 9-transistor OTA and integrator**

**(1) 9-transistor OTA**

The 9-transistor impedance amplifier has wide range [371].  $V_+$  will be equal to  $V_-$  while  $V_{out} < \frac{1}{2}V_{dd}$ . The first integrator takes different time to finish integrator for  $V_{in}$ , and  $V_{cm}$  is 2.5V for 9 transistor OTA. The first task is testing the different configurations of 9-transistor OTA.

The first diagram is a balanced CMOS OTA shown below.

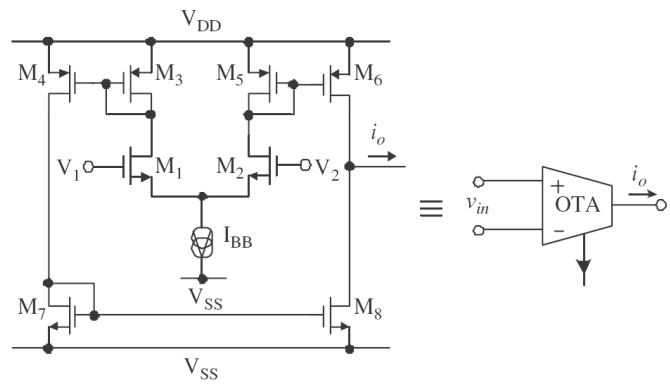


Figure 7-60. Diagram of balanced CMOS OTA.

The balanced CMOS OTA has coupled MOS pairs and current mirrors.  $V_{in}$  is the differential input voltage with

$$V_{in} = V_1 - V_2$$

M1 and M2 has to be perfectly matched and the current mirror will have unity current gain [371].

Then, the current output  $i_o = i_2 - i_1$ .

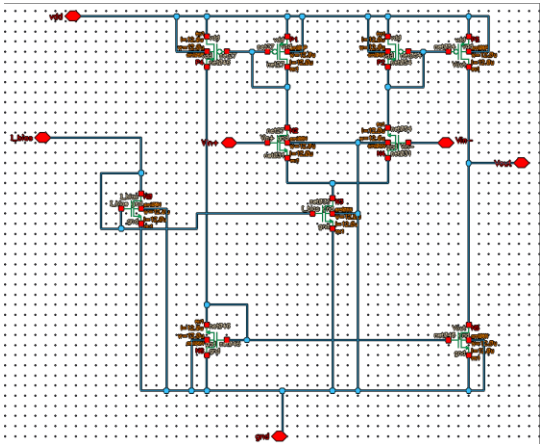


Figure 7-61. Schematic design of 9-transistor OTA (configuration 1).

In the schematic simulation circuit, another PMOS is added before the  $V_b$  for offset correction purpose.

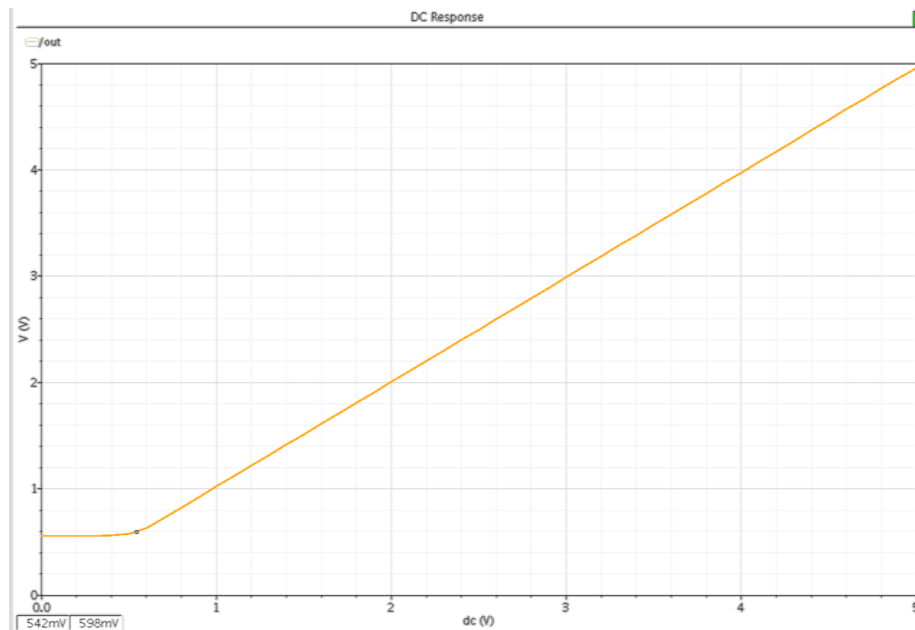


Figure 7-62. Schematic simulation results of 9-transistor OTA (configuration 1).

The schematic of 9-transistor OTA has different options; I use the second configuration of 9-transistor OTA schematic design.

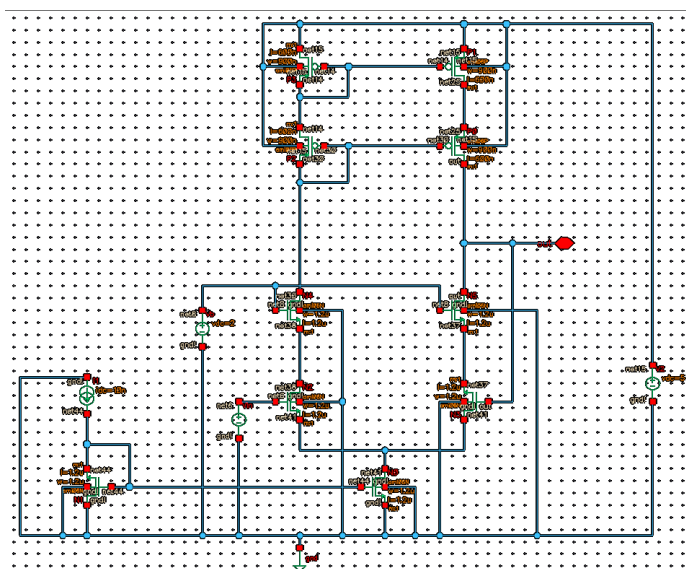


Figure 7-63. Schematic simulation of 9-transistor OTA (configuration 2).

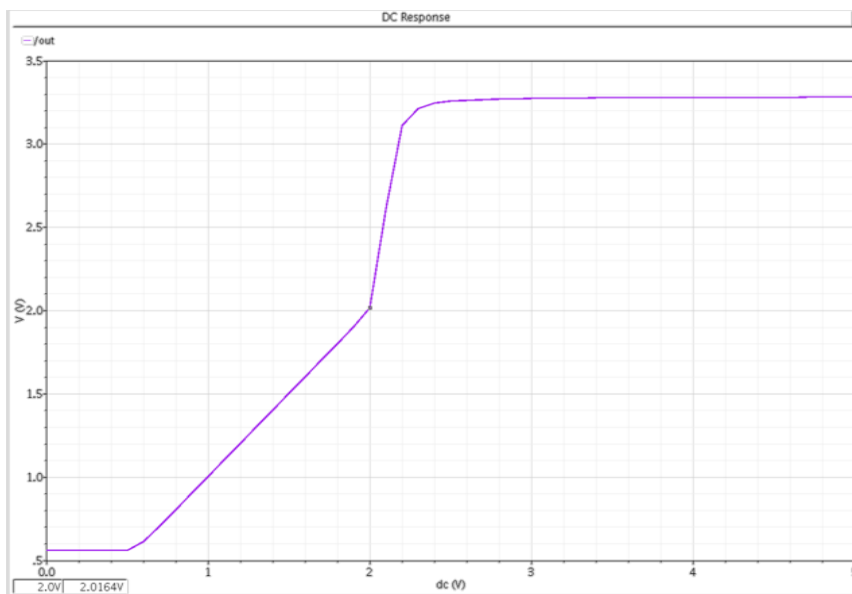


Figure 7-64. Schematic simulation results of 9-transistor OTA (configuration 2).

I set the  $V_b$  as 2 V. In the third configuration of 9-transistor OTA,  $V_{bias}$  is set and the PMOS sizes are doubled, so both the range and the offset are balanced.

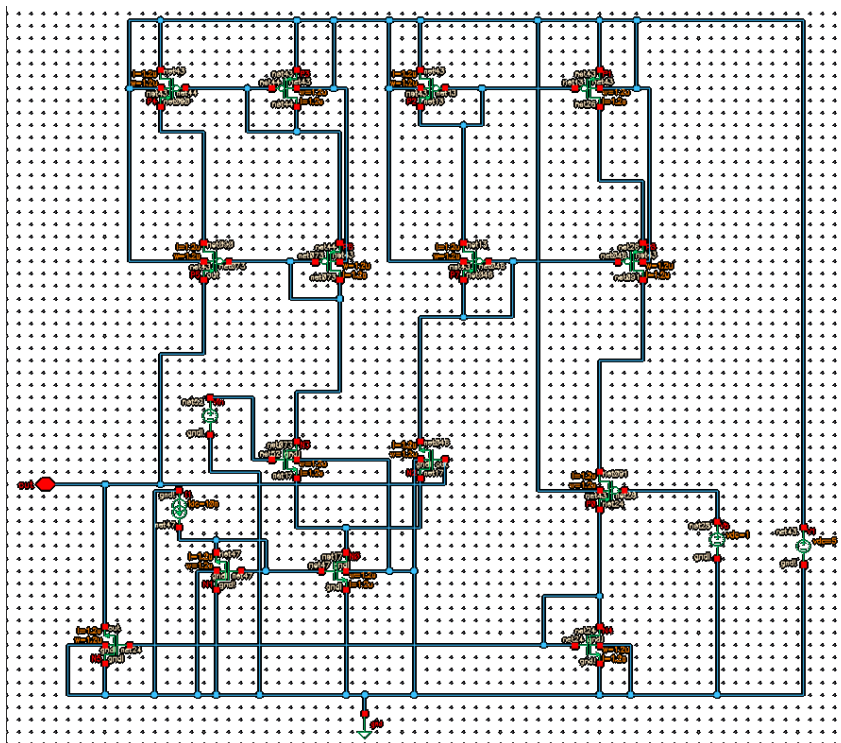


Figure 7-65. Schematic simulation of 9-transistor OTA (configuration 3).

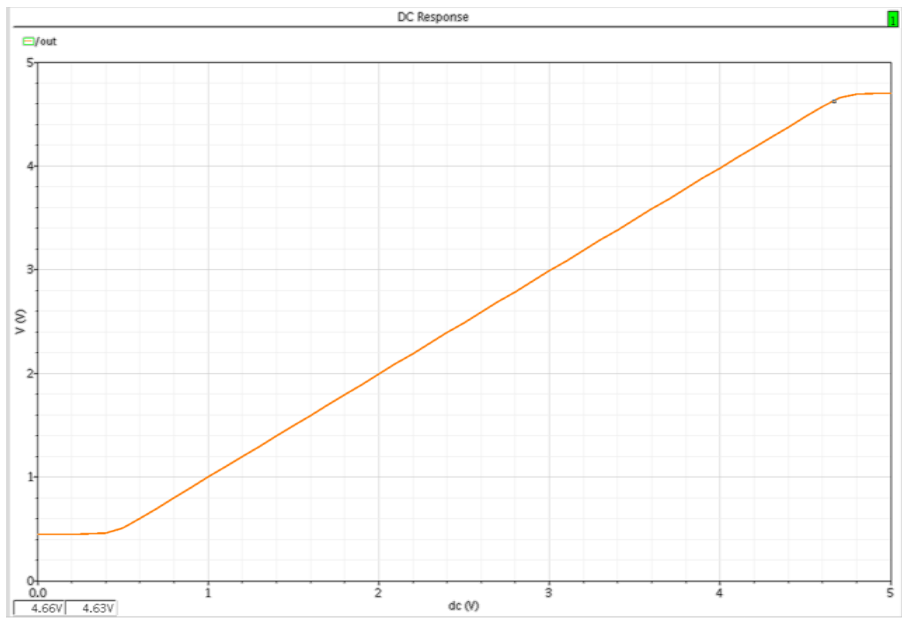


Figure 7-66. Schematic simulation results of 9-transistor OTA (configuration 3).

According to the simulation results, the offset of this configuration is about 0.01 V.

## (2) Integrator

Similar to the schematic simulation of comparator, I simulate integrator by OTA.

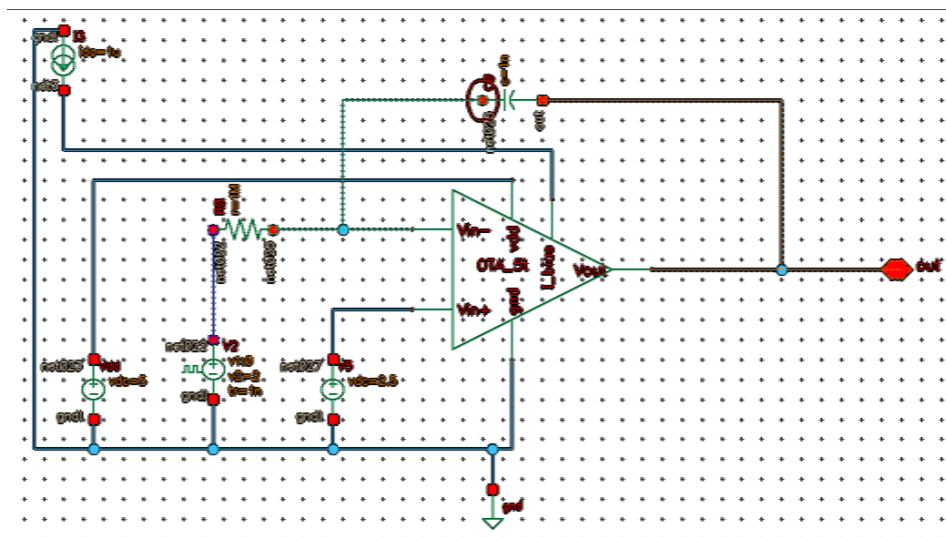


Figure 7-67. Schematic simulation of integrator.

The capacitance is set as 1 nF, and the external resistor is set as 1 M $\Omega$ . The simulation results are shown by transient response of output and input.



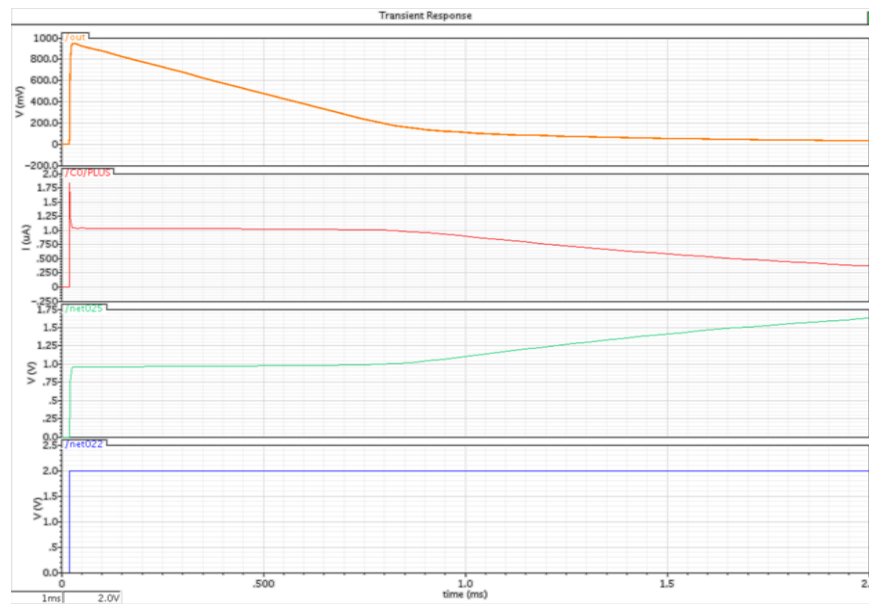


Figure 7-68. Schematic simulation results of integrator formed by 9-transistor OTA.

### (3) Comparator

Similar to the simulation of comparator by 5-transistor OTA, I simulate the comparator by 9-transistor OTA [372].

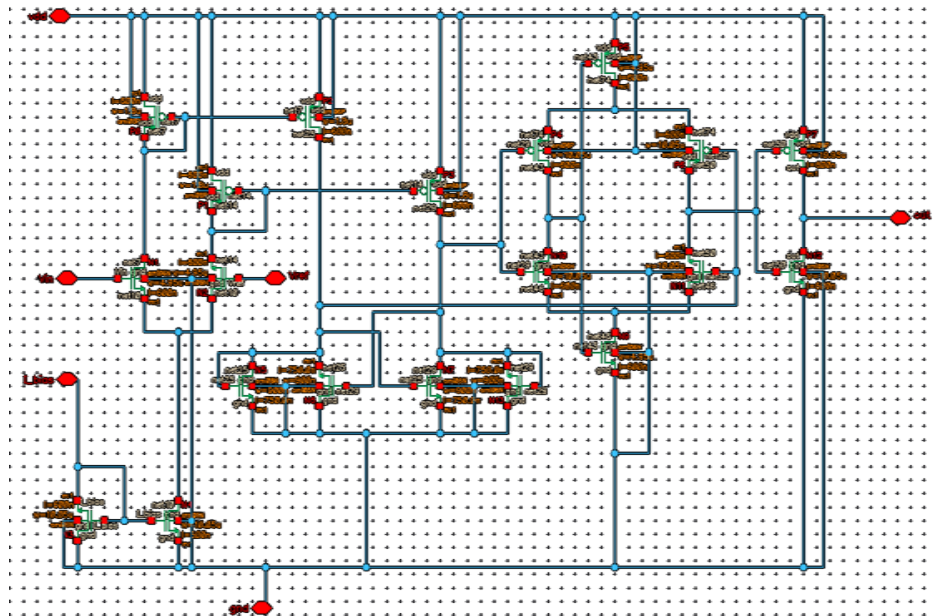


Figure 7-69. Schematic design of comparator constructed based on 9-transistor OTA.

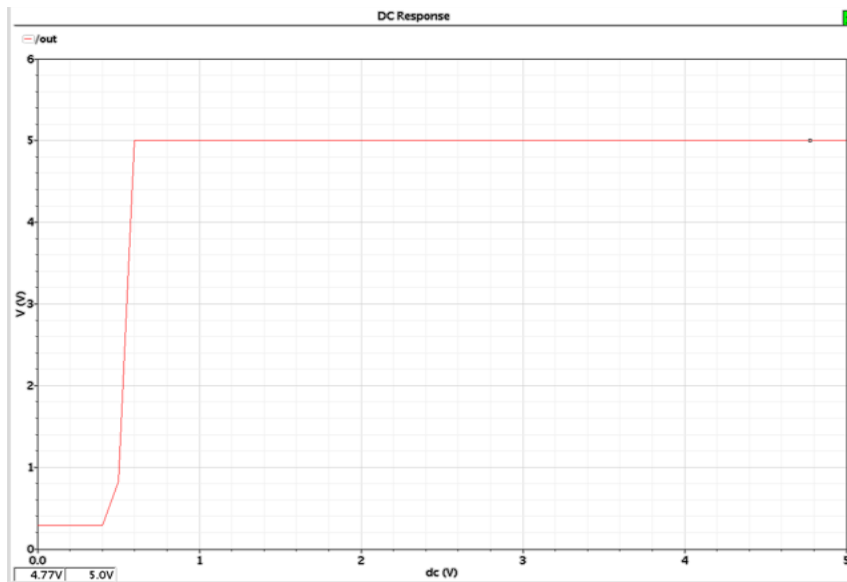


Figure 7-70. Schematic simulation results of comparator constructed based on 9-transistor OTA.

The simulation result of this comparator has sharper edge compared to the 5-transistor comparator.

### 7.5.3 ADC schematic simulation

The whole circuit for this ADC is configured as schematic structure shown below.

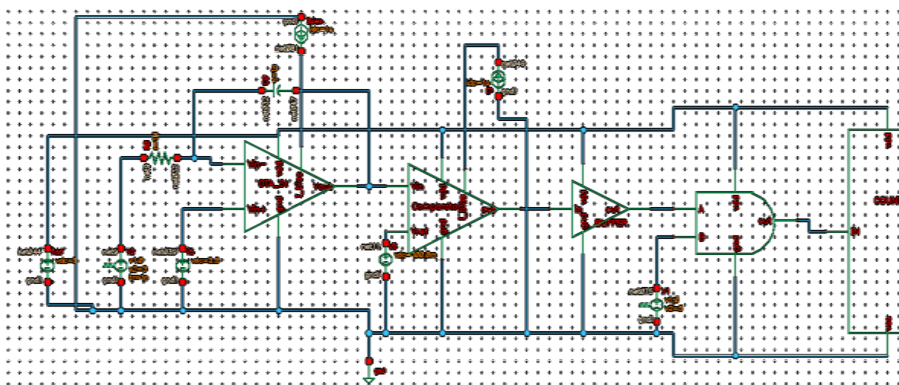


Figure 7-71. Schematic simulation design of ADC.

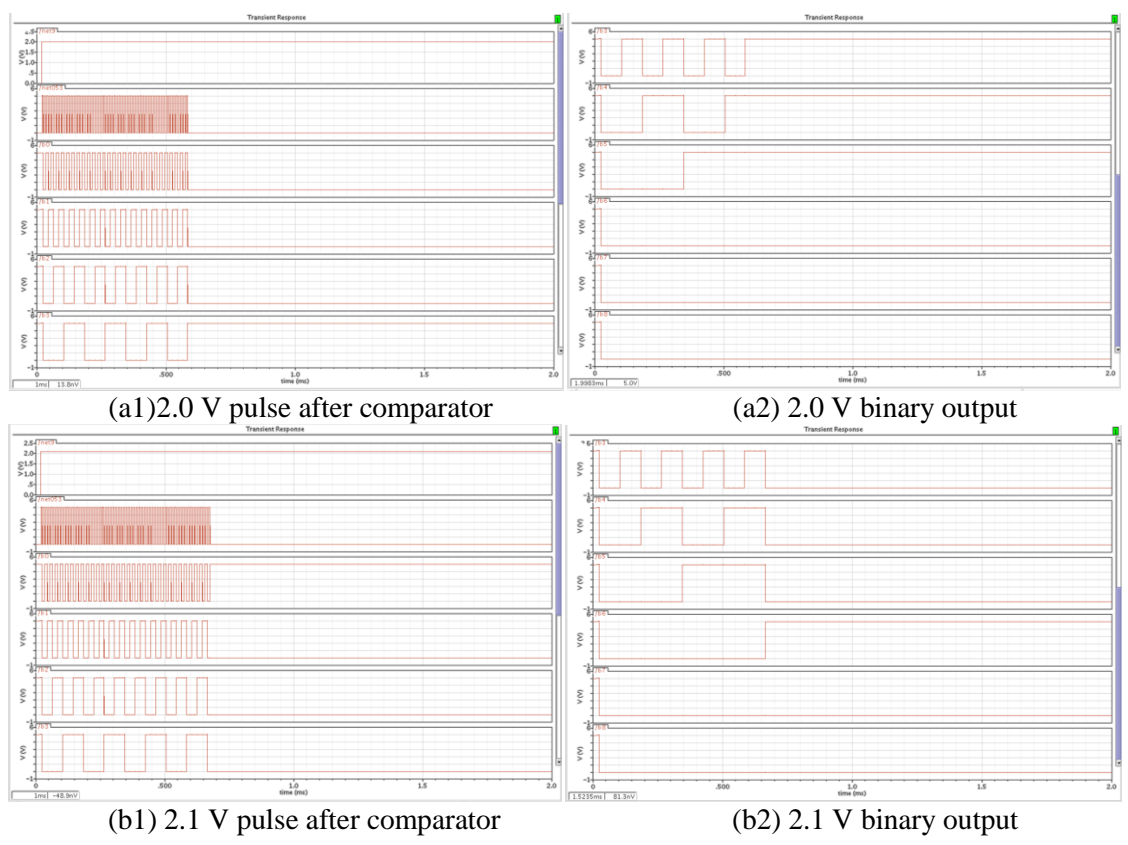
The comparator's output is connected to a buffer followed by a logic gate, which will translate the time into pulse train. Then, counter is used to get the digital binary code for input voltage.

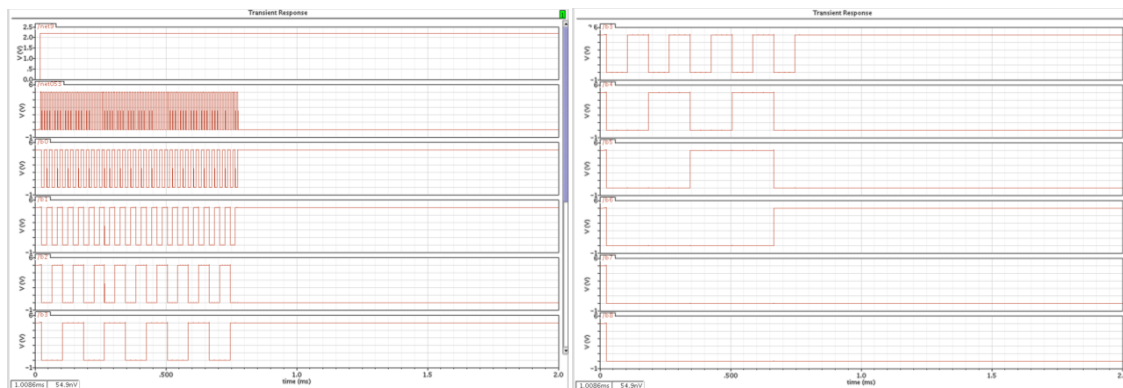
This schematic design can translate the analog voltage into digital numbers. The comparator is used to change the frequency into digital pulses, and the pulses are counted through a binary counter.

The buffer located after the comparator is not mandatory. However, the presence of this buffer can help the ADC to have a higher accuracy and resolution.

After a voltage translation is completed, a reset signal is able to be sent to a clear switch, which can discharge the capacitance of the integrator, so the data in register will be cleared and ready for the next cycle of analog to digital translation.

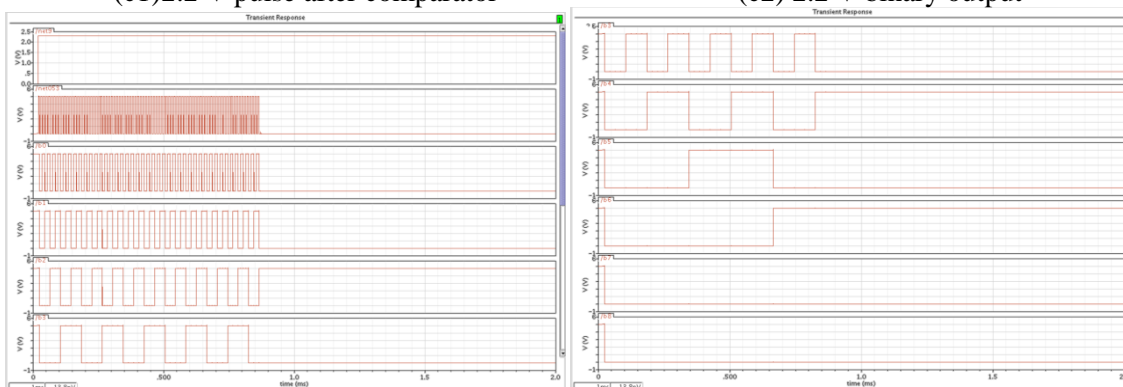
The simulation of this whole circuit is carried by voltage of 2.0 V to 3.0 V with a step of 0.1 V.





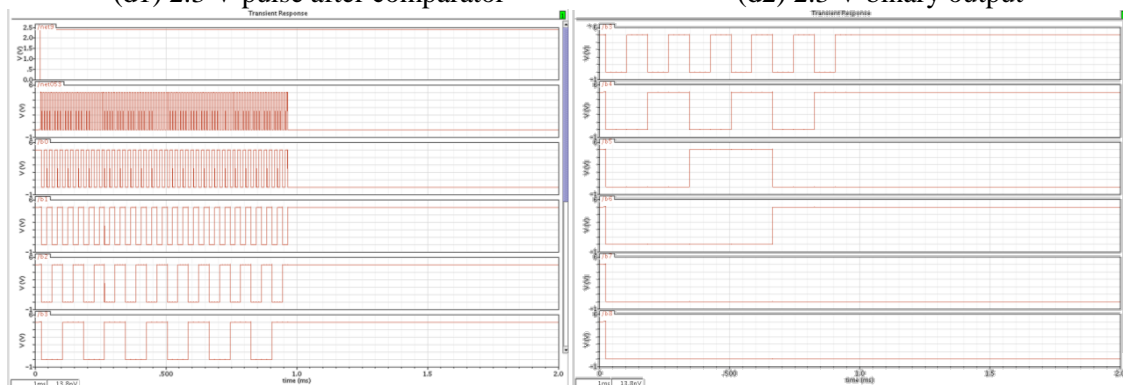
(c1) 2.2 V pulse after comparator

(c2) 2.2 V binary output



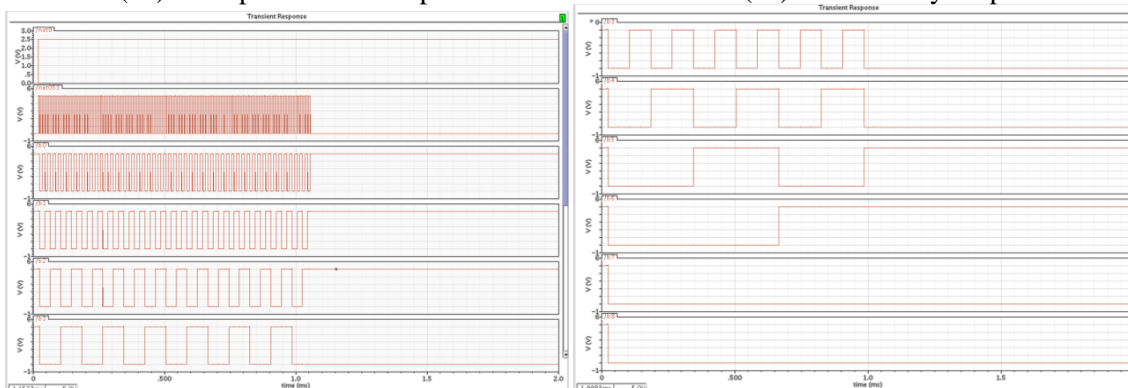
(d1) 2.3 V pulse after comparator

(d2) 2.3 V binary output



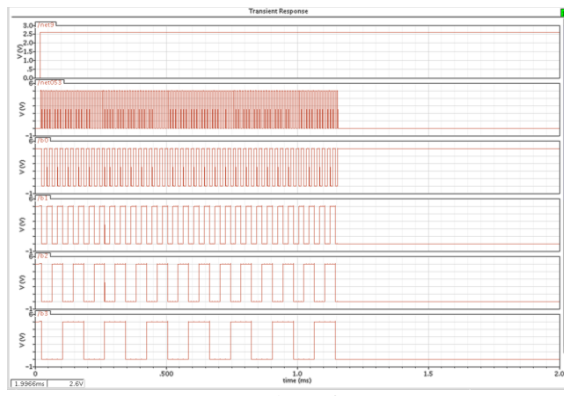
(e1) 2.4 V pulse after comparator

(e2) 2.4 V binary output

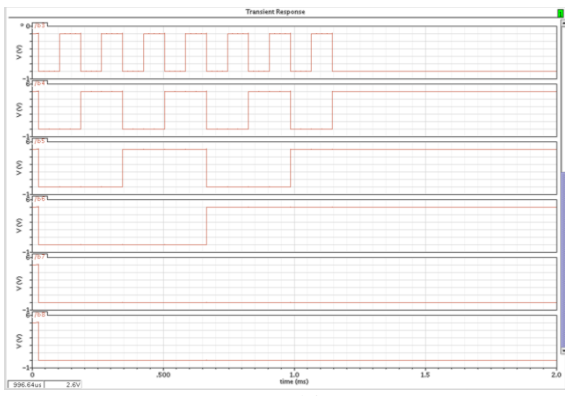


(f1) 2.5 V pulse after comparator

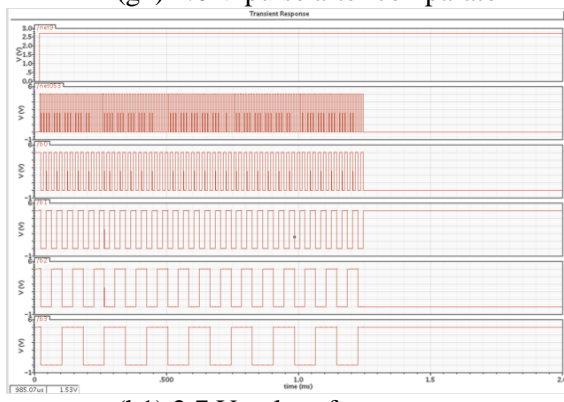
(f2) 2.5 V binary output



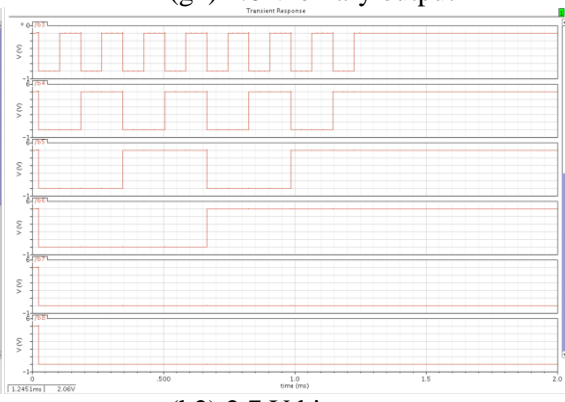
(g1) 2.6 V pulse after comparator



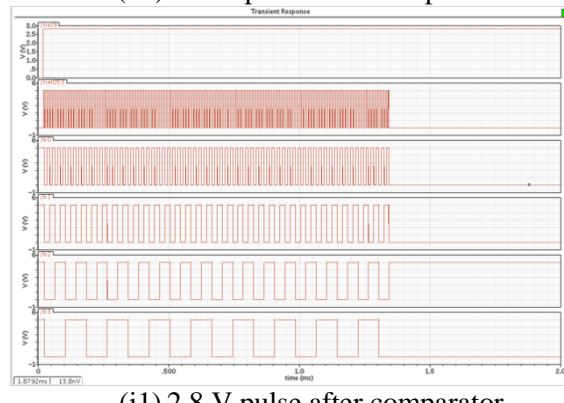
(g2) 2.6 V binary output



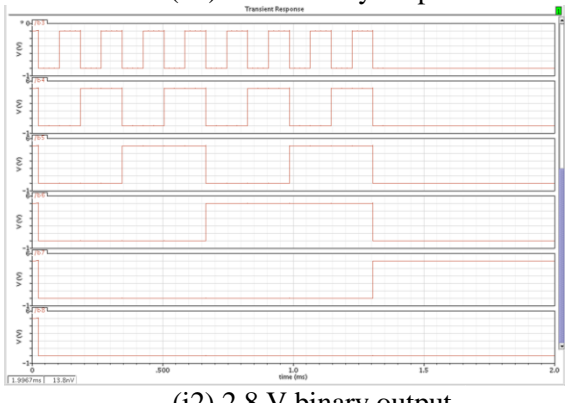
(h1) 2.7 V pulse after comparator



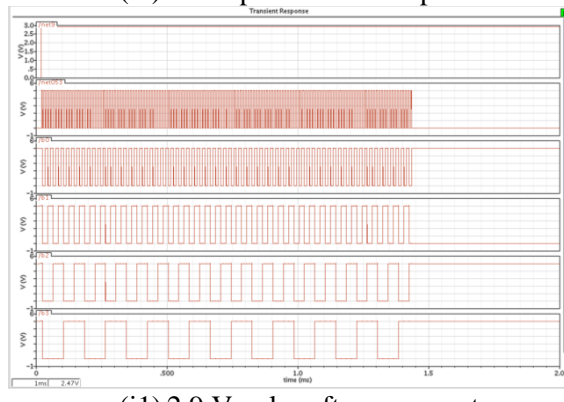
(h2) 2.7 V binary output



(i1) 2.8 V pulse after comparator



(i2) 2.8 V binary output



(j1) 2.9 V pulse after comparator



(j2) 2.9 V binary output

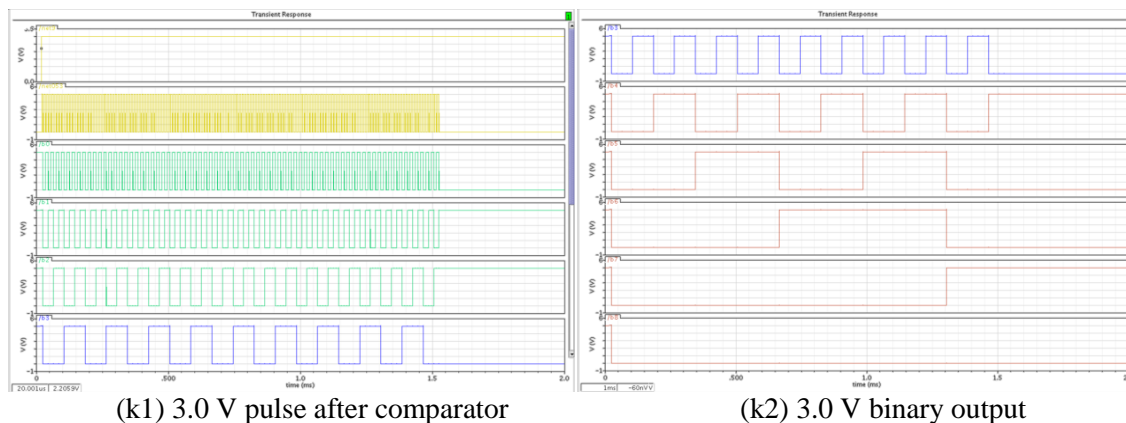


Figure 7-72. Schematic simulation results of ADC with testing input voltage from 2.0 V to 3.0 V.

According to the ADC simulation results, the resolution of this ADC is 0.01V. Application specific integrated circuit (ASIC) design of this high resolution low speed ADC is preferred in analyzing a large array of capacitive sensors.

#### 7.5.4 ADC Layout

The layout of ADC can be used to further simulation and fabrication of CMOS microchip. Since the resistors and capacitors are hard to be integrated into microchip, we can use external resistors and capacitors after mounting or testing of the CMOS chip.

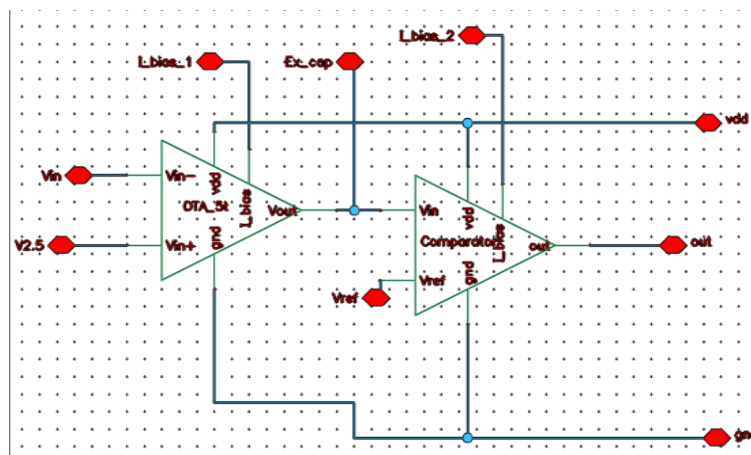


Figure 7-73. Schematic symbol design of comparator and OTA.

The correlated layout structure would be same as the schematic design. The external resistors and capacitors can be connected to CMOS chip on PCB, since the integral of resistors and



capacitors will occupy a large area in CMOS chip. Besides, replacing the resistor or capacitors will be much easier if those were mounted on PCB.

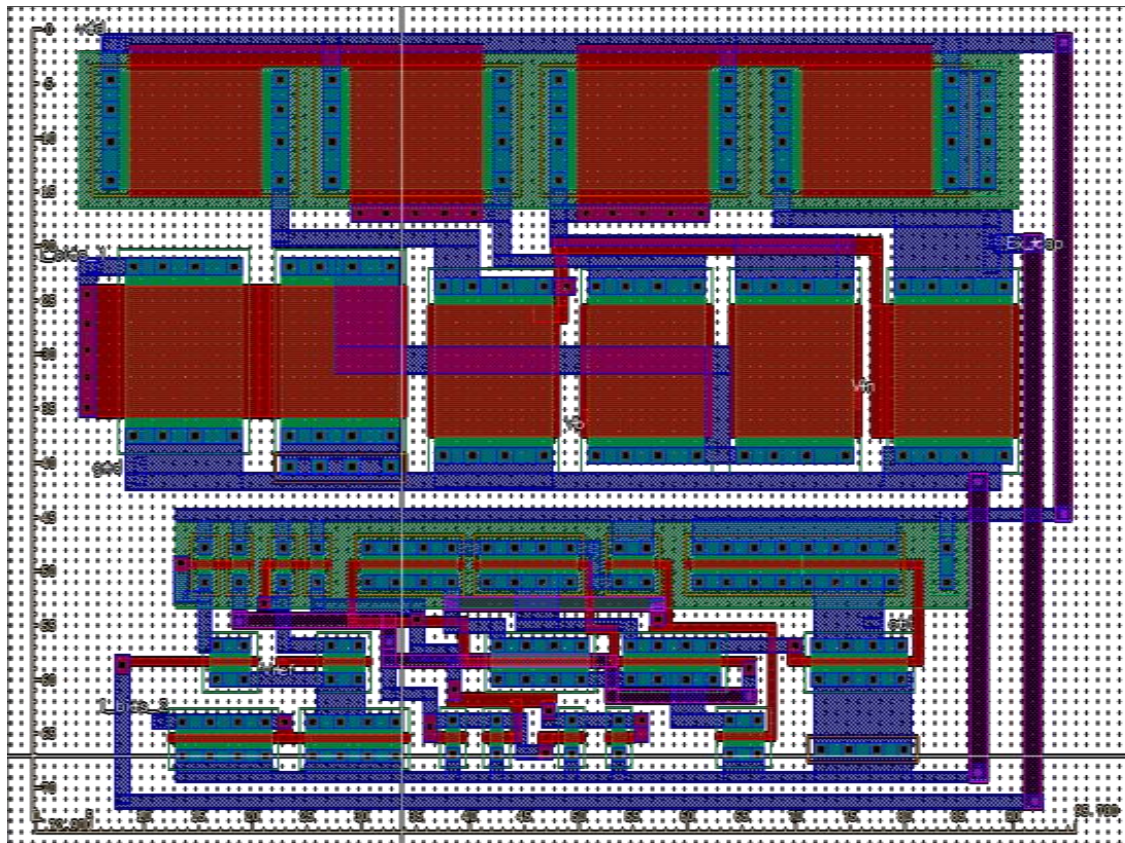


Figure 7-74. Layout design of comparator and OTA.

The layout of ADC core components is arranged within a  $95 \mu\text{m} \times 72 \mu\text{m}$  area. The large OTA occupies more than half of the chip, since the NMOS and PMOS in OTA needs large polysilicon width and length. Besides, the PMOS requires a larger N-well to support the PMOS transistor, even though I already try to reduce the used PMOS quantities.

## 7.6 Future work: microchip fabrication and test

A logic unit that deal with the operation and working status monitoring of the artificial photosynthesis system makes the system become a intelligent and semi-automatic platform without living cells.

The future work of this section is further finishing the schematic and layout simulation, and fabricates a microchip for system test. The CMOS chip should be designed for this microchip identification and ion channel inspection only. The load capacitance and resistance depended on the soldering of the wires on fluidic microchip and gold electrode plated on silicon and glass described in biomembrane study.

## 7.7 PCB demonstration board

The fabrication of microchip through MOSIS ® requires proposals and long term testing, so I designed analog circuit for current amplification on PCB.

### 7.7.1 Light reaction units integration

The sandwich-shape light reaction devices are assembled and connected on PCB board. The wires on PCB can form open electrodes for impedance inspection and ion channel monitoring. Two sets of pre-arranged LED can be used to identify the rows and columns of the light reaction units.

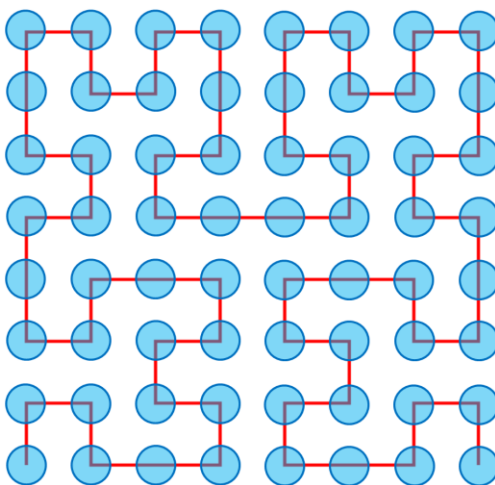


Figure 7-75. Schematic of Hilbert curve with 64 (8×8) units.

The interconnection of light reaction units was another issue. Linear connection can cause discontinuity if any of the units was malfunctioning or broken. Therefore, I used the path of Hilbert curve to connect the units. Every 4 ( $4^1$ ) units' connection method can be duplicated into



16 ( $4^2$ ) units' connection, and further into 64 ( $4^3$ ) units, etc. If any unit in this Hilbert curve line was broken, the connection tube can be directly connected to the next device, because the two nearby units have the distance within  $\sqrt{2}$  times of the unit distance.

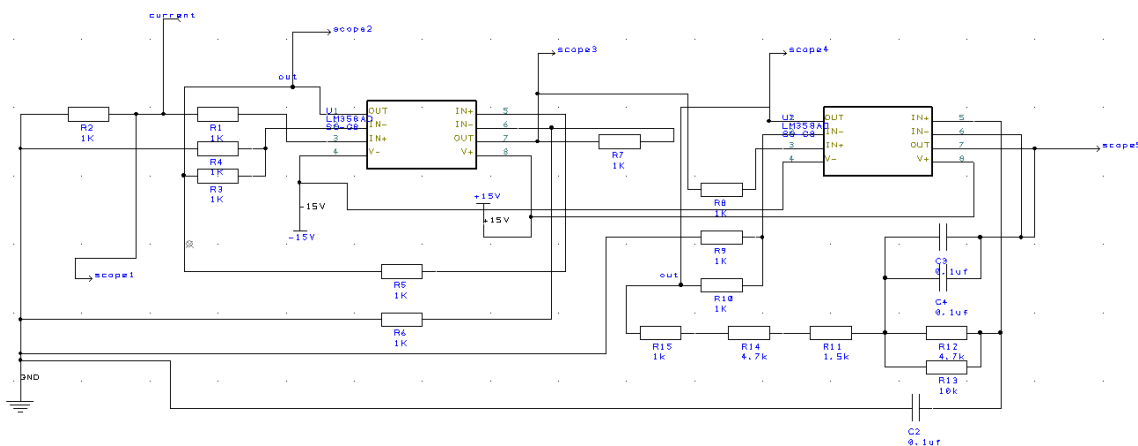


Figure 7-76. Schematic of low current amplifier for inspecting ion channels.

The ion channel generates small current among the membrane. An amplifier with higher sensitivity can monitor the ion channels or even single channel; however, on a PCB with analog IC, I used multiple levels LM358AD to reach low current amplification.

### 7.7.2 Dark reaction units integration

The dark reaction units contain fluidic channels with porous PDMS on it. We drilled holes on PCB to fit the porous PDMS cubes.

The solutions from integrated light reaction units can directly directed into the fluidic channel in this dark reaction units section. The solution contains ATP from light reaction units can be directed into the dark reaction channels with CO<sub>2</sub> absorption ability.

### 7.7.3 PCB layout and fabrication

The whole board was designed on a 6×10 inch two layer PCB.

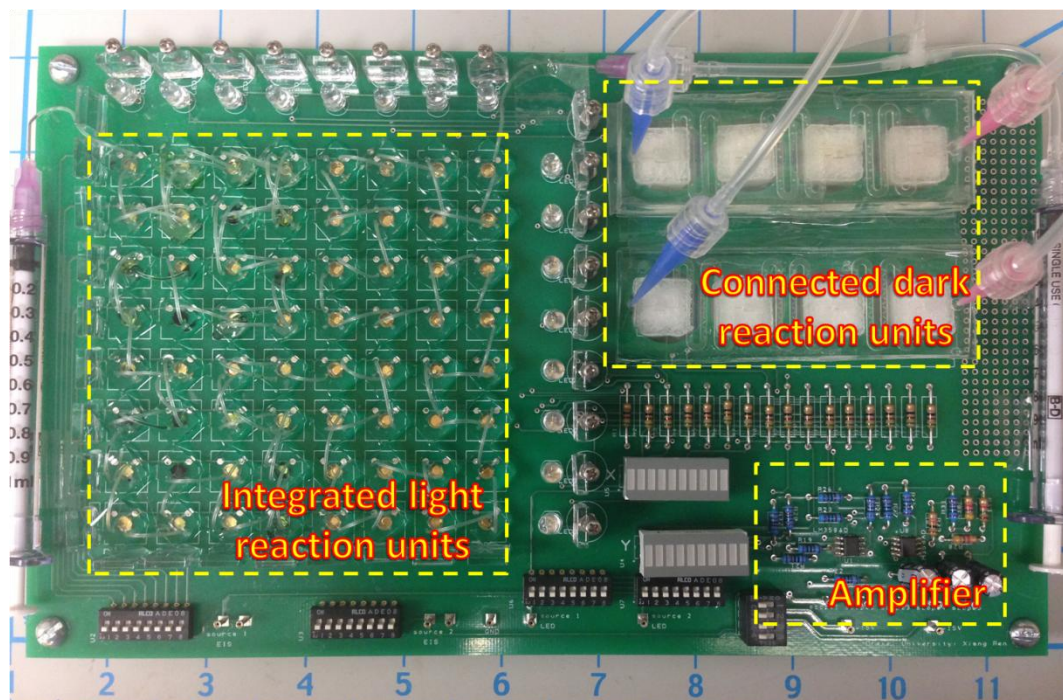


Figure 7-77. Image of the integrated PCB with both light reaction units and dark reaction units.

The whole PCB was arranged as impedance spectroscopy, current amplifier, and dark reaction units. An array of through-hole pads was arranged on the side of PCB for adding more external IC with jump wires.

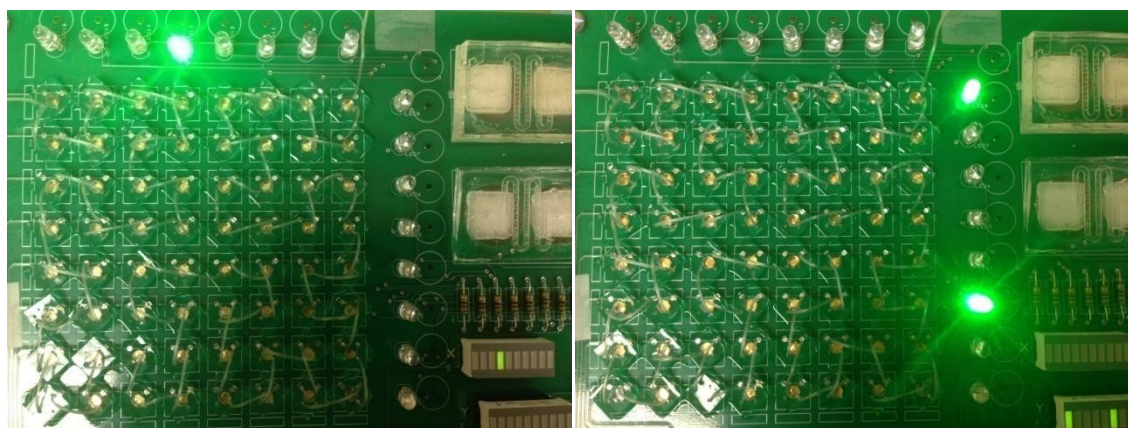


Figure 7-78. Integrated light reaction units identification.

## 7.8 Contributions

I designed and simulated the VLSI of light reaction unit's identification and shift the current signals to digital output through high resolution low speed ADC. The integration allows the artificial intelligence to be implanted on the artificial photosynthesis system.

The PCB demonstration test board with analog amplifier provides a vivid platform of integrated artificial photosynthesis system with both light reaction units and dark reaction units. The light reaction units were connected by the path of Hilbert curve, which can benefit the diagnosis of defected units during EIS monitoring.

## Chapter 8. SUMMARY

### 8.1 Project summary

This research project had four major aims that involves many majors and research fields, and required a broad knowledge in physics, chemistry, biology, and more specifically, MEMS, EIS, membrane science, biochemistry, basic botany, image processing, and mixed-mode VLSI; at the same time, this research involved both the theoretical analysis simulations and experiments. Some existing technologies, such as 3D printing and pH value fast detection on chip, were partially further developed in this research. The cell-free artificial photosynthesis system was a vivid integration and combination of all these knowledge and technologies.

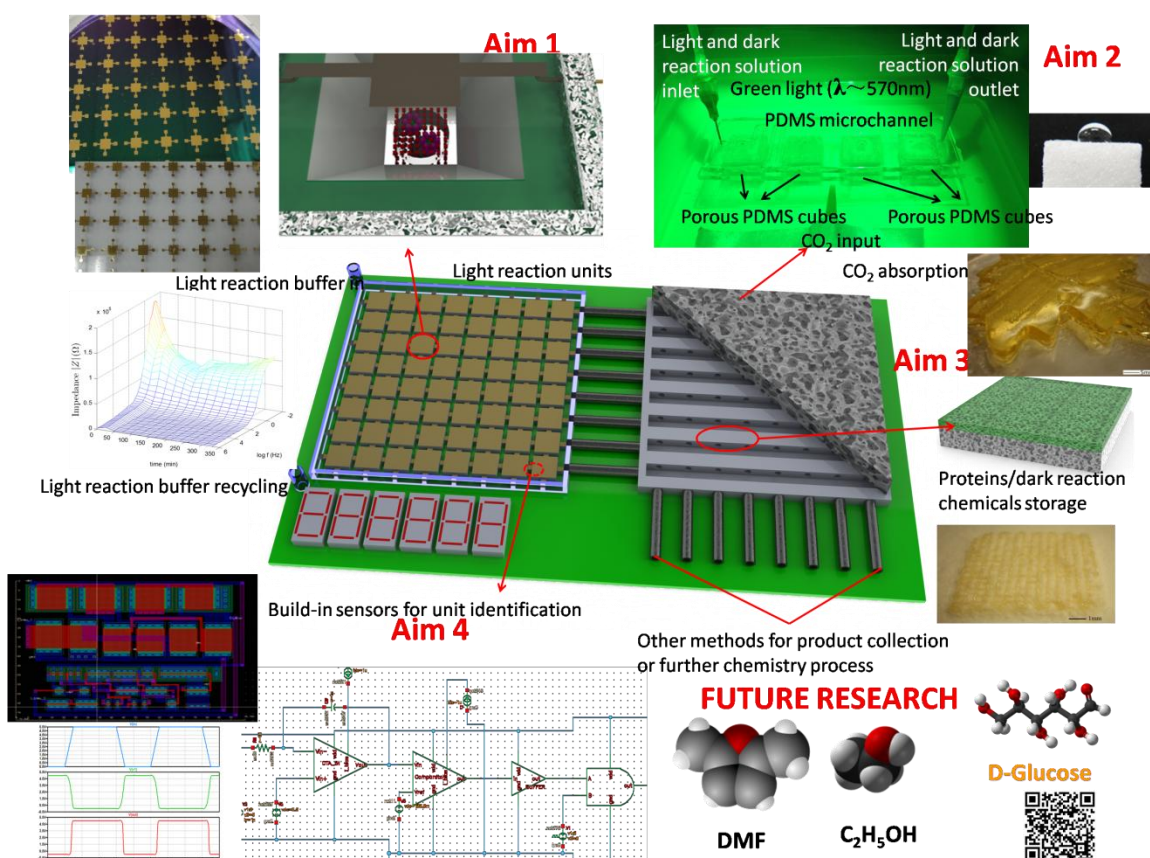


Figure 8-1. Illustration of cell-free artificial photosynthesis system.

#### (1) Aim 1: Light reaction unit (Chapter 2, 3)

Light reaction was realized in a microfluidic platform that consists of two fluid chambers separated by a planar membrane with embedded proteins that convert light energy into ATP. The membrane stability was studied on microchip for long-term study.

**(2) Aim 2: CO<sub>2</sub> absorption (Chapter 4, 5)**

Dark reaction was realized in another microfluidic platform with porous PDMS that can transport CO<sub>2</sub> from the air to the liquid chamber. The glucose was successfully synthesized in the microfluidic channels with CO<sub>2</sub> absorbed and green light energy.

**(3) Aim 3: Glucose synthesis storage (Chapter 6)**

Glucose synthesis and storage unit was developed by mimicking sponge mesophyll found in a leaf (dicotyledons leaf). Chitosan porous structures with interconnected pores will be used for this purpose and they will be fabricated by lyophilization after molding-casting or 3D printing.

**(4) Aim 4: Interconnection and integration (Chapter 7)**

Interconnection and integration of the above-mentioned three key components was investigated to generate a complete cell-free artificial platform for effective energy harvesting. Seamless interconnection of the three components is necessary for harvesting light energy and transforming the energy to organic compounds. Proper mixed-mode VLSI was designed and simulated in SPICE. Ion channel inspection was also designed by a delta-sigma ADC that designed for this application.

## **8.2 Future prospect**

Lab-on-chip with capacitive biosensing using EIS technologies will be broadly used in cell-free biological system, since the EIS is well established technique with adjustable sinusoidal current or voltage signals. ASIC combining with microfluidic structure can support intelligent analysis without the presence of cell during biochemistry reactions or processes.

The current microfluidic technology can achieve most of the physical and chemical requirements of biological reactions. For example, PDMS can build soft transparent environment

for microfluidics; indium tin oxide (ITO) coated on glass can work as transparent electrode during applications of EIS; PDMS-to-PCB bonding can realize the integration between ASIC and microfluidic systems. However, many challenging problems still remains, such as cleaning procedures form sensors in biological applications. After integrating ASIC with microfluidics, the cleaning of microfluidic systems, recalibration or offset cancelling of the ASIC might not be suitable for other biochemical reactions.

In the future, the ASIC technologies may improves the applications for intelligent operations for cell-free biochemical reactions environment. The intelligent or “smart” system can exist and operate individually without the controlling of living cells. History taught us that many unpredictable technologies can bring human society with both benefits and disasters. As Albert Einstein commented on quantum mechanics, “new science and technologies are just as new-born babies, no one knows it will become benefit or evil”. Quantum mechanics brings us new clean energy, as nuclear electricity power; on the other hand, quantum mechanics established the science theoretical principles of nuclear bomb. Even though a smart system without living cells can perform “thinking”, “operating”, or even “reproduction” may cause un-foreseen results, the development of intelligent systems will still be studied and improved.



## REFERENCES

1. Zhou, H., T. Fan, and D. Zhang, *An insight into artificial leaves for sustainable energy inspired by natural photosynthesis*. ChemCatChem, 2011. **3**(3): p. 513-528.
2. Hammarström, L. and S. Hammes-Schiffer, *Artificial photosynthesis and solar fuels*. Accounts of chemical research, 2009. **42**(12): p. 1859-1860.
3. Schou, L., et al., *The Path of Carbon in Photosynthesis, XI The Role of Glycolic Acid*. Physiologia Plantarum, 1950. **3**(4): p. 487-495.
4. Bassham, J.A., et al., *The Path of Carbon in Photosynthesis. XXI. The Cyclic Regeneration of Carbon Dioxide Acceptor I*. Journal of the American Chemical Society, 1954. **76**(7): p. 1760-1770.
5. Nelson, D.L., A.L. Lehninger, and M.M. Cox, *Lehninger principles of biochemistry*. 2008: Macmillan.
6. Buchanan, B.B., W. Gruissem, and R.L. Jones, *Biochemistry & molecular biology of plants*. Vol. 40. 2000: American Society of Plant Physiologists Rockville.
7. Schooley, J., *Introduction to Botany*. 1997, Albany, New York: Delmar Publishers.
8. Mullineaux, C.W., *The thylakoid membranes of cyanobacteria: structure, dynamics and function*. Functional Plant Biology, 1999. **26**(7): p. 671-677.
9. Varfolomeev, S.D., E.N. Efremenko, and L.P. Krylova, *Biofuels*. Russian Chemical Reviews, 2010. **79**(6): p. 491-509.
10. Meyer, H.-P., *Sustainability and biotechnology*. Organic Process Research & Development, 2010. **15**(1): p. 180-188.
11. Roy, S.C., et al., *Toward solar fuels: photocatalytic conversion of carbon dioxide to hydrocarbons*. Acs Nano, 2010. **4**(3): p. 1259-1278.
12. Von Blottnitz, H. and M.A. Curran, *A review of assessments conducted on bio-ethanol as a transportation fuel from a net energy, greenhouse gas, and environmental life cycle perspective*. Journal of cleaner production, 2007. **15**(7): p. 607-619.
13. Chisti, Y., *Biodiesel from microalgae beats bioethanol*. Trends in biotechnology, 2008. **26**(3): p. 126-131.
14. Kunjapur, A.M. and R.B. Eldridge, *Photobioreactor design for commercial biofuel production from microalgae*. Industrial & engineering chemistry research, 2010. **49**(8): p. 3516-3526.
15. Harun, R., M.K. Danquah, and G.M. Forde, *Microalgal biomass as a fermentation feedstock for bioethanol production*. Journal of Chemical Technology and Biotechnology, 2010. **85**(2): p. 199-203.
16. Demirbas, A., *Use of algae as biofuel sources*. Energy conversion and management, 2010. **51**(12): p. 2738-2749.
17. Oostergetel, G.T., H. van Amerongen, and E.J. Boekema, *The chlorosome: a prototype for efficient light harvesting in photosynthesis*. Photosynthesis research, 2010. **104**(2-3): p. 245-255.
18. González - López, C., et al., *Development of a process for efficient use of CO<sub>2</sub> from flue gases in the production of photosynthetic microorganisms*. Biotechnology and bioengineering, 2012. **109**(7): p. 1637-1650.
19. Chen, M. and R.E. Blankenship, *Expanding the solar spectrum used by photosynthesis*. Trends in plant science, 2011. **16**(8): p. 427-431.
20. Rosenbaum, M., Z. He, and L.T. Angenent, *Light energy to bioelectricity: photosynthetic microbial fuel cells*. Current Opinion in Biotechnology, 2010. **21**(3): p. 259-264.
21. Logan, B.E., et al., *Microbial fuel cells: methodology and technology*. Environmental science & technology, 2006. **40**(17): p. 5181-5192.
22. Tavano, C.L. and T.J. Donohue, *Development of the bacterial photosynthetic apparatus*. Current opinion in microbiology, 2006. **9**(6): p. 625-631.
23. Rittmann, B.E., *Opportunities for renewable bioenergy using microorganisms*. Biotechnology and bioengineering, 2008. **100**(2): p. 203-212.
24. Román-Leshkov, Y., et al., *Production of dimethylfuran for liquid fuels from biomass-derived carbohydrates*. Nature, 2007. **447**(7147): p. 982-985.
25. Chidambaram, M. and A.T. Bell, *A two-step approach for the catalytic conversion of glucose to 2, 5-dimethylfuran in ionic liquids*. Green Chemistry, 2010. **12**(7): p. 1253-1262.
26. Zhong, S., et al., *Combustion and emissions of 2, 5-dimethylfuran in a direct-injection spark-ignition engine*. Energy & Fuels, 2010. **24**(5): p. 2891-2899.

27. Tian, G., et al., *Laminar burning velocities of 2, 5-dimethylfuran compared with ethanol and gasoline*. Energy & Fuels, 2010. **24**(7): p. 3898-3905.
28. Wendell, D., J. Todd, and C. Montemagno, *Artificial photosynthesis in ranaspumin-2 based foam*. Nano letters, 2010. **10**(9): p. 3231-3236.
29. SeokáLee, J., et al., *Artificial photosynthesis on a chip: microfluidic cofactor regeneration and photoenzymatic synthesis under visible light*. Lab on a Chip, 2011. **11**(14): p. 2309-2311.
30. Meunier, C.F., et al., *Biofuel cells based on the immobilization of photosynthetically active bioentities*. ChemCatChem, 2011. **3**(3): p. 476-488.
31. Service, R.F., *Turning Over a New Leaf*. Science, 2011. **334**(6058): p. 925-927.
32. Barber, J. and P.D. Tran, *From natural to artificial photosynthesis*. Journal of The Royal Society Interface, 2013. **10**(81): p. 20120984.
33. Huber, V., S. Sengupta, and F. Würthner, *Structure–Property Relationships for Self-Assembled Zinc Chlorin Light-Harvesting Dye Aggregates*. Chemistry – A European Journal, 2008. **14**(26): p. 7791-7807.
34. Gust, D., T.A. Moore, and A.L. Moore, *Solar Fuels via Artificial Photosynthesis*. Accounts of Chemical Research, 2009. **42**(12): p. 1890-1898.
35. Razeghifard, M.R., et al., *Spectroscopic Studies of Photosystem II in Chlorophyll d-Containing *Acaryochloris marina**. Biochemistry, 2005. **44**(33): p. 11178-11187.
36. Amao, Y., Y. Maki, and Y. Fuchino, *Photoinduced Hydrogen Production with Artificial Photosynthesis System Based on Carotenoid– Chlorophyll Conjugated Micelles*. The Journal of Physical Chemistry C, 2009. **113**(38): p. 16811-16815.
37. Imahori, H., Y. Mori, and Y. Matano, *Nanostructured artificial photosynthesis*. Journal of Photochemistry and Photobiology C: Photochemistry Reviews, 2003. **4**(1): p. 51-83.
38. Tachibana, Y., L. Vayssieres, and J.R. Durrant, *Artificial photosynthesis for solar water-splitting*. Nature Photonics, 2012. **6**(8): p. 511-518.
39. Bard, A.J. and M.A. Fox, *Artificial Photosynthesis: Solar Splitting of Water to Hydrogen and Oxygen*. Accounts of Chemical Research, 1995. **28**(3): p. 141-145.
40. Andreiadis, E.S., et al., *Artificial Photosynthesis: From Molecular Catalysts for Light - driven Water Splitting to Photoelectrochemical Cells*. Photochemistry and photobiology, 2011. **87**(5): p. 946-964.
41. de la Garza, L., et al., *Enzyme-based photoelectrochemical biofuel cell*. The Journal of Physical Chemistry B, 2003. **107**(37): p. 10252-10260.
42. Calzaferri, G., *Artificial photosynthesis*. Topics in Catalysis, 2010. **53**(3-4): p. 130-140.
43. Bishop, M.B. and C.B. Bishop, *Photosynthesis and carbon dioxide fixation*. Journal of Chemical Education, 1987. **64**(4): p. 302.
44. Benniston, A.C. and A. Harriman, *Artificial photosynthesis*. Materials Today, 2008. **11**(12): p. 26-34.
45. Gust, D., T.A. Moore, and A.L. Moore, *Mimicking Photosynthetic Solar Energy Transduction*. Accounts of Chemical Research, 2000. **34**(1): p. 40-48.
46. Youngblood, W.J., et al., *Photoassisted overall water splitting in a visible light-absorbing dye-sensitized photoelectrochemical cell*. Journal of the American Chemical Society, 2009. **131**(3): p. 926-927.
47. Magnuson, A., et al., *Biomimetic and microbial approaches to solar fuel generation*. Accounts of chemical research, 2009. **42**(12): p. 1899-1909.
48. Xu, Y., et al., *Synthesis and Characterization of Dinuclear Ruthenium Complexes Covalently Linked to RuII Tris - bipyridine: An Approach to Mimics of the Donor Side of Photosystem II*. Chemistry-A European Journal, 2005. **11**(24): p. 7305-7314.
49. Borgström, M., et al., *Light induced manganese oxidation and long-lived charge separation in a Mn2II, II-RuII (bpy) 3-acceptor triad*. Journal of the American Chemical Society, 2005. **127**(49): p. 17504-17515.
50. Hambourger, M., et al., *[FeFe]-hydrogenase-catalyzed H2 production in a photoelectrochemical biofuel cell*. Journal of the American Chemical Society, 2008. **130**(6): p. 2015-2022.
51. Yang, C.-C., et al., *Artificial photosynthesis over crystalline TiO2-based catalysts: fact or fiction?* Journal of the American Chemical Society, 2010. **132**(24): p. 8398-8406.
52. Qu, Y., et al., *Rational design and synthesis of freestanding photoelectric nanodevices as highly efficient photocatalysts*. Nano letters, 2010. **10**(5): p. 1941-1949.
53. Kodis, G., et al., *Synthesis and photochemistry of a carotene–porphyrin–fullerene model photosynthetic reaction center*. Journal of physical organic chemistry, 2004. **17**(9): p. 724-734.



54. Yadav, R.K., et al., *A photocatalyst–enzyme coupled artificial photosynthesis system for solar energy in production of formic acid from CO<sub>2</sub>*. *Journal of the American Chemical Society*, 2012. **134**(28): p. 11455-11461.
55. Whipple, D.T. and P.J. Kenis, *Prospects of CO<sub>2</sub> utilization via direct heterogeneous electrochemical reduction*. *The Journal of Physical Chemistry Letters*, 2010. **1**(24): p. 3451-3458.
56. Varghese, O.K., et al., *High-rate solar photocatalytic conversion of CO<sub>2</sub> and water vapor to hydrocarbon fuels*. *Nano letters*, 2009. **9**(2): p. 731-737.
57. AlOtaibi, B., et al., *Wafer-Level Artificial Photosynthesis for CO<sub>2</sub> Reduction into CH<sub>4</sub> and CO using GaN Nanowires*. *ACS Catalysis*, 2015.
58. Hoffmann, M.R., J.A. Moss, and M.M. Baum, *Artificial photosynthesis: semiconductor photocatalytic fixation of CO<sub>2</sub> to afford higher organic compounds*. *Dalton Transactions*, 2011. **40**(19): p. 5151-5158.
59. Jayashree, R.S., et al., *Microfluidic hydrogen fuel cell with a liquid electrolyte*. *Langmuir*, 2007. **23**(13): p. 6871-6874.
60. Strik, D.P., et al., *Microbial solar cells: applying photosynthetic and electrochemically active organisms*. *Trends in biotechnology*, 2011. **29**(1): p. 41-49.
61. Burow, L.C., et al., *Hydrogen production in photosynthetic microbial mats in the Elkhorn Slough estuary, Monterey Bay*. *The ISME journal*, 2012. **6**(4): p. 863-874.
62. Jinkerson, R.E., V. Subramanian, and M.C. Posewitz, *Improving biofuel production in phototrophic microorganisms with systems biology*. *Biofuels*, 2011. **2**(2): p. 125-144.
63. Janssen, M., et al., *Enclosed outdoor photobioreactors: light regime, photosynthetic efficiency, scale - up, and future prospects*. *Biotechnology and Bioengineering*, 2003. **81**(2): p. 193-210.
64. Dau, H. and I. Zaharieva, *Principles, efficiency, and blueprint character of solar-energy conversion in photosynthetic water oxidation*. *Accounts of chemical research*, 2009. **42**(12): p. 1861-1870.
65. Mackenzie, C.D., et al., *Ranaspumin-2: structure and function of a surfactant protein from the foam nests of a tropical frog*. *Biophysical journal*, 2009. **96**(12): p. 4984-4992.
66. Pitard, B., et al., *ATP synthesis by the FOF1 ATP synthase from thermophilic Bacillus PS3 reconstituted into liposomes with bacteriorhodopsin*. *European Journal of Biochemistry*, 1996. **235**(3): p. 769-778.
67. Steinberg-Yfrach, G., et al., *Light-driven production of ATP catalysed by FOF1-ATP synthase in an artificial photosynthetic membrane*. *Nature*, 1998. **392**(6675): p. 479-482.
68. Choi, H.-J. and C.D. Montemagno, *Biosynthesis within a bubble architecture*. *Nanotechnology*, 2006. **17**(9): p. 2198.
69. Choi, H.-J., J. Germain, and C.D. Montemagno, *Effects of different reconstitution procedures on membrane protein activities in proteopolymersomes*. *Nanotechnology*, 2006. **17**(8): p. 1825.
70. Meier, W., C. Nardin, and M. Winterhalter, *Reconstitution of channel proteins in (polymerized) ABA triblock copolymer membranes*. *Angewandte Chemie International Edition*, 2000. **39**(24): p. 4599-4602.
71. Choi, H.-J., E. Brooks, and C.D. Montemagno, *Synthesis and characterization of nanoscale biomimetic polymer vesicles and polymer membranes for bioelectronic applications*. *Nanotechnology*, 2005. **16**(5): p. S143.
72. Ho, D., et al., *Hybrid protein-polymer biomimetic membranes*. *Nanotechnology*, *IEEE Transactions on*, 2004. **3**(2): p. 256-263.
73. Sauer, R.O. and D.J. Mead, *Dipole moments of linear and cyclic polymethylpolysiloxanes*. *Journal of the American Chemical Society*, 1946. **68**(9): p. 1794-1797.
74. Meyer, T.J., *Chemical approaches to artificial photosynthesis*. *Accounts of Chemical Research*, 1989. **22**(5): p. 163-170.
75. Choi, H.-J. and C.D. Montemagno, *Artificial organelle: ATP synthesis from cellular mimetic polymersomes*. *Nano letters*, 2005. **5**(12): p. 2538-2542.
76. Kannappan, B. and J.E. Gready, *Redefinition of Rubisco carboxylase reaction reveals origin of water for hydration and new roles for active-site residues*. *Journal of the American Chemical Society*, 2008. **130**(45): p. 15063-15080.
77. Rakovich, A., et al., *Resonance energy transfer improves the biological function of bacteriorhodopsin within a hybrid material built from purple membranes and semiconductor quantum dots*. *Nano letters*, 2010. **10**(7): p. 2640-2648.
78. Kühlbrandt, W., *Bacteriorhodopsin—the movie*. *Nature*, 2000. **406**(6796): p. 569-570.

79. von Ballmoos, C., A. Wiedenmann, and P. Dimroth, *Essentials for ATP synthesis by F1F0 ATP synthases*. Annual review of biochemistry, 2009. **78**: p. 649-672.
80. Hou, H.-H., et al., *Rapid glucose concentration detection utilizing disposable integrated microfluidic chip*. Microfluidics and nanofluidics, 2011. **11**(4): p. 479-487.
81. Ren, X., et al., *Design, Fabrication, and Characterization of Archaeal Tetraether Free-Standing Planar Membranes in a PDMS- and PCB-Based Fluidic Platform*. ACS Applied Materials & Interfaces, 2014. **6**(15): p. 12618-12628.
82. Malmstadt, N., et al., *Automated formation of lipid-bilayer membranes in a microfluidic device*. Nano letters, 2006. **6**(9): p. 1961-1965.
83. Kongsuphol, P., K.B. Fang, and Z. Ding, *Lipid bilayer technologies in ion channel recordings and their potential in drug screening assay*. Sensors and Actuators B: Chemical, 2013. **185**: p. 530-542.
84. Nardin, C., et al., *Polymerized ABA triblock copolymer vesicles*. Langmuir, 2000. **16**(3): p. 1035-1041.
85. Schmidt, C., M. Mayer, and H. Vogel, *A Chip - Based Biosensor for the Functional Analysis of Single Ion Channels*. Angewandte Chemie International Edition, 2000. **39**(17): p. 3137-3140.
86. Cheng, Y., et al., *Single ion channel sensitivity in suspended bilayers on micromachined supports*. Langmuir, 2001. **17**(4): p. 1240-1242.
87. Tien, H.T. and A.L. Ottova, *The lipid bilayer concept and its experimental realization: from soap bubbles, kitchen sink, to bilayer lipid membranes*. Journal of membrane science, 2001. **189**(1): p. 83-117.
88. Römer, W. and C. Steinem, *Impedance analysis and single-channel recordings on nano-black lipid membranes based on porous alumina*. Biophysical journal, 2004. **86**(2): p. 955-965.
89. Han, X., et al., *Nanopore Arrays for Stable and Functional Free - Standing Lipid Bilayers*. Advanced Materials, 2007. **19**(24): p. 4466-4470.
90. Studer, A.T., L. X., *Stable Planar Lipid Bilayers in Nanopores*. European Cells and Materials, 2007. **14**(Suppl. 3): p. 33.
91. Moffitt, M., K. Khougaz, and A. Eisenberg, *Micellization of ionic block copolymers*. Accounts of chemical research, 1996. **29**(2): p. 95-102.
92. Nardin, C. and W. Meier, *Hybrid materials from amphiphilic block copolymers and membrane proteins*. Reviews in Molecular Biotechnology, 2002. **90**(1): p. 17-26.
93. Chong, P.L.-G., *Archaeobacterial bipolar tetraether lipids: physico-chemical and membrane properties*. Chemistry and physics of lipids, 2010. **163**(3): p. 253-265.
94. Chang, E. and S. Lo, *Extraction and purification of tetraether lipids from Sulfolobus acidocaldarius*. Protocols for Archaeobacterial Research, 1991. **2**: p. 1-2.3.
95. Jacquemet, A., et al., *Archaeal tetraether bipolar lipids: Structures, functions and applications*. Biochimie, 2009. **91**(6): p. 711-717.
96. Lo, S.-L. and E. Chang, *Purification and characterization of a liposomal-forming tetraether lipid fraction*. Biochemical and biophysical research communications, 1990. **167**(1): p. 238-243.
97. Sugai, A., et al., *The structure of the core polyol of the ether lipids from Sulfolobus acidocaldarius*. Lipids, 1995. **30**(4): p. 339-344.
98. Jeworrek, C., et al., *Structure and phase behavior of archaeal lipid monolayers*. Langmuir, 2011. **27**(21): p. 13113-13121.
99. Bagatolli, L., et al., *Two-Photon Fluorescence Microscopy Studies of Bipolar Tetraether Giant Liposomes from Thermoacidophilic Archaeobacteria* *Sulfolobus acidocaldarius*. Biophysical journal, 2000. **79**(1): p. 416-425.
100. Chong, P.L.-G., et al., *Structure and conformation of bipolar tetraether lipid membranes derived from thermoacidophilic archaeon Sulfolobus acidocaldarius as revealed by small-angle X-ray scattering and high-pressure FT-IR spectroscopy*. The Journal of Physical Chemistry B, 2003. **107**(33): p. 8694-8700.
101. Chong, P.L.-G., et al., *On physical properties of tetraether lipid membranes: effects of cyclopentane rings*. Archaea, 2012. **2012**.
102. Gliozzi, A., A. Relini, and P.L.-G. Chong, *Structure and permeability properties of biomimetic membranes of bolaform archaeal tetraether lipids*. Journal of membrane science, 2002. **206**(1): p. 131-147.
103. Sprott, G.D., G.B. Patel, and L. Krishnan, *Archaeobacterial ether lipid liposomes as vaccine adjuvants*. Methods in enzymology, 2003. **373**: p. 155-172.

104. Zhai, Y., et al., *Physical properties of archaeal tetraether lipid membranes as revealed by differential scanning and pressure perturbation calorimetry, molecular acoustics, and neutron reflectometry: effects of pressure and cell growth temperature*. Langmuir, 2012. **28**(11): p. 5211-5217.
105. Garra, J., et al., *Dry etching of polydimethylsiloxane for microfluidic systems*. Journal of Vacuum Science & Technology A, 2002. **20**(3): p. 975-982.
106. McDonald, J.C. and G.M. Whitesides, *Poly (dimethylsiloxane) as a material for fabricating microfluidic devices*. Accounts of chemical research, 2002. **35**(7): p. 491-499.
107. Sodunke, T.R., et al., *Micropatterns of Matrigel for three-dimensional epithelial cultures*. Biomaterials, 2007. **28**(27): p. 4006-4016.
108. Walther, F., et al., *Stability of the hydrophilic behavior of oxygen plasma activated SU-8*. Journal of Micromechanics and Microengineering, 2007. **17**(3): p. 524.
109. Cai, D. and A. Neyer, *Polysiloxane based flexible electrical-optical-circuits-board*. Microelectronic Engineering, 2010. **87**(11): p. 2268-2274.
110. Welch, D. and J.B. Christen, *Seamless integration of CMOS and microfluidics using flip chip bonding*. Journal of Micromechanics and Microengineering, 2013. **23**(3): p. 035009.
111. Jang, L.-S., C.-C. Wu, and C.-F. Liu, *Fabrication of microfluidic devices for packaging CMOS MEMS impedance sensors*. Microfluidics and nanofluidics, 2009. **7**(6): p. 869-875.
112. Kim, K., S.W. Park, and S.S. Yang, *The optimization of PDMS-PMMA bonding process using silane primer*. BioChip Journal, 2010. **4**(2): p. 148-154.
113. Sunkara, V., et al., *Simple room temperature bonding of thermoplastics and poly (dimethylsiloxane)*. Lab on a Chip, 2011. **11**(5): p. 962-965.
114. Vlachopoulou, M., et al., *A low temperature surface modification assisted method for bonding plastic substrates*. Journal of Micromechanics and Microengineering, 2009. **19**(1): p. 015007.
115. Lei, S., et al., *AFM characterization of gramicidin-A in tethered lipid membrane on silicon surface*. Chemical physics letters, 2006. **429**(1): p. 244-249.
116. Abdelghani, A., et al., *Supported lipid membrane on semiconductor electrode*. Materials chemistry and physics, 2001. **70**(2): p. 187-190.
117. Nardin, C., M. Winterhalter, and W. Meier, *Giant free-standing ABA triblock copolymer membranes*. Langmuir, 2000. **16**(20): p. 7708-7712.
118. Krommenhoek, E., et al., *Monitoring of yeast cell concentration using a micromachined impedance sensor*. Sensors and Actuators B: Chemical, 2006. **115**(1): p. 384-389.
119. O'Rourke, M., et al., *Electrochemical impedance spectroscopy—a simple method for the characterization of polymer inclusion membranes containing Aliquat 336*. Membranes, 2011. **1**(2): p. 132-148.
120. Steinem, C., et al., *Impedance analysis of supported lipid bilayer membranes: a scrutiny of different preparation techniques*. Biochimica et Biophysica Acta (BBA)-Biomembranes, 1996. **1279**(2): p. 169-180.
121. Gritsch, S., et al., *Impedance spectroscopy of porin and gramicidin pores reconstituted into supported lipid bilayers on indium-tin-oxide electrodes*. Langmuir, 1998. **14**(11): p. 3118-3125.
122. Naumann, R., et al., *Proton transport through a peptide-tethered bilayer lipid membrane by the H<sup>+</sup>-ATP synthase from chloroplasts measured by impedance spectroscopy*. Biosensors and Bioelectronics, 2002. **17**(1): p. 25-34.
123. Becucci, L., et al., *Electrochemical impedance spectroscopy and fluorescence lifetime imaging of lipid mixtures self-assembled on mercury*. Soft Matter, 2010. **6**(12): p. 2733-2741.
124. Faiß, S., et al., *Formation of irreversibly bound annexin A1 protein domains on POPC/POPS solid supported membranes*. Biochimica et Biophysica Acta (BBA)-Biomembranes, 2008. **1778**(7): p. 1601-1610.
125. Kastl, K., et al., *Partially reversible adsorption of annexin A1 on POPC/POPS bilayers investigated by QCM measurements, SFM, and DMC simulations*. ChemBioChem, 2006. **7**(1): p. 106-115.
126. Lundgren, A., et al., *Resonance-mode electrochemical impedance measurements of silicon dioxide supported lipid bilayer formation and ion channel mediated charge transport*. Analytical chemistry, 2011. **83**(20): p. 7800-7806.
127. Morigaki, K. and K. Tawa, *Vesicle fusion studied by surface plasmon resonance and surface plasmon fluorescence spectroscopy*. Biophysical journal, 2006. **91**(4): p. 1380-1387.
128. Lin, J., et al., *Electrically addressable, biologically relevant surface-supported bilayers*. Langmuir, 2010. **26**(14): p. 12054-12059.

129. Gambacorta, A., A. Gliozzi, and M. De Rosa, *Archaeal lipids and their biotechnological applications*. World Journal of Microbiology and Biotechnology, 1995. **11**(1): p. 115-131.
130. Patel, G.B. and G.D. Sprott, *Archaeobacterial ether lipid liposomes (archaeosomes) as novel vaccine and drug delivery systems*. Critical reviews in biotechnology, 1999. **19**(4): p. 317-357.
131. Schiraldi, C., M. Giuliano, and M. De Rosa, *Perspectives on biotechnological applications of archaea*. Archaea, 2002. **1**(2): p. 75-86.
132. Benvegna, T., L. Lemiègre, and S. Cammas - Marion, *Archaeal lipids: innovative materials for biotechnological applications*. European Journal of Organic Chemistry, 2008. **2008**(28): p. 4725-4744.
133. Danson, M.J., D.W. Hough, and G.G. Lunt, *The archaeobacteria: biochemistry and biotechnology*. 1992: Portland Press London.
134. Langworthy, T.A. and J.L. Pond, *Membranes and lipids of thermophiles*. Thermophiles: General, Molecular, and Applied Microbiology, 1986: p. 107-134.
135. Freisleben, H.-J., et al., *Toxicity and biodistribution of liposomes of the main phospholipid from the archaeobacterium Thermoplasma acidophilum in mice*. Journal of Liposome Research, 1995. **5**(1): p. 215-223.
136. Patel, G.B., et al., *Safety of intranasally administered archaeal lipid mucosal vaccine adjuvant and delivery (AMVAD) vaccine in mice*. International journal of toxicology, 2008. **27**(4): p. 329-339.
137. Kaufman, Y., et al., *Towards Supported Bolaamphiphile Membranes for Water Filtration: Roles of Lipid and Substrate*. Journal of Membrane Science, 2014.
138. Bally, M., et al., *Liposome and lipid bilayer arrays towards biosensing applications*. Small, 2010. **6**(22): p. 2481-2497.
139. Melikyan, G., et al., *Electromechanical stability of planar lipid membranes from bipolar lipids of the thermoacidophilic archaebacterium *Sulfolobus acidocaldarius**. Biochimica et Biophysica Acta (BBA)-Biomembranes, 1991. **1068**(2): p. 245-248.
140. Chong, P.L.-G., *Physical properties of membranes composed of tetraether archaeal lipids?* In: Thermophiles: Biology and Technology at High Temperatures, 2007: p. 73.
141. Fittabile, L., et al., *Organization of monolayer-formed membranes made from archaeal ether lipids. thin solid films*, 1996. **284**: p. 735-738.
142. Gliozzi, A., et al., *Asymmetric black membranes formed by one monolayer of bipolar lipids at the air/water interface*. Biochimica et Biophysica Acta (BBA)-Biomembranes, 1994. **1189**(1): p. 96-100.
143. Gliozzi, A., et al., *Monolayer black membranes from bipolar lipids of archaeobacteria and their temperature-induced structural changes*. The Journal of membrane biology, 1983. **75**(1): p. 45-56.
144. Gliozzi, A., et al., *Artificial black membranes from bipolar lipids of thermophilic archaeobacteria*. Biophysical journal, 1982. **37**(2): p. 563-566.
145. Gufler, P.C., et al., *Highly robust lipid membranes on crystalline S-layer supports investigated by electrochemical impedance spectroscopy*. Biochimica et Biophysica Acta (BBA)-Biomembranes, 2004. **1661**(2): p. 154-165.
146. Stern, J., et al., *Black lipid membranes of tetraether lipids from *Thermoplasma acidophilum**. Biochimica et Biophysica Acta (BBA)-Lipids and Lipid Metabolism, 1992. **1128**(2): p. 227-236.
147. Ziaie, B., et al., *Hard and soft micromachining for BioMEMS: review of techniques and examples of applications in microfluidics and drug delivery*. Advanced Drug Delivery Reviews, 2004. **56**(2): p. 145-172.
148. West, J., et al., *Micro total analysis systems: latest achievements*. Analytical chemistry, 2008. **80**(12): p. 4403-4419.
149. Whitesides, G.M., *The origins and the future of microfluidics*. Nature, 2006. **442**(7101): p. 368-373.
150. Rosen, Y. and P. Gurman, *MEMS and microfluidics for diagnostics devices*. Current pharmaceutical biotechnology, 2010. **11**(4): p. 366-375.
151. Gong, X. and W. Wen, *Polydimethylsiloxane-based conducting composites and their applications in microfluidic chip fabrication*. Biomicrofluidics, 2009. **3**(1): p. 012007.
152. Rossing, T. and N.H. Fletcher, *Principles of vibration and sound*. 2012: Springer Science & Business Media.
153. Laschi, S. and M. Mascini, *Planar electrochemical sensors for biomedical applications*. Medical engineering & physics, 2006. **28**(10): p. 934-943.
154. Li, S.-S. and C.-M. Cheng, *Analogy among microfluidics, micromechanics, and microelectronics*. Lab on a Chip, 2013. **13**(19): p. 3782-3788.
155. Liu, K.-K., et al., *Microfluidic systems for biosensing*. Sensors, 2010. **10**(7): p. 6623-6661.

156. Haeberle, S. and R. Zengerle, *Microfluidic platforms for lab-on-a-chip applications*. Lab on a Chip, 2007. **7**(9): p. 1094-1110.
157. Rolfe, P., *Medical and biological measurement with micro-and nanosensors*. Optoelectronics, Instrumentation and Data Processing, 2010. **46**(4): p. 324-328.
158. Zeng, J., *Non-Linear Electrohydrodynamics in Microfluidic Devices*. International journal of molecular sciences, 2011. **12**(3): p. 1633-1649.
159. Lin, C.-C., J.-L. Hsu, and G.-B. Lee, *Sample preconcentration in microfluidic devices*. Microfluidics and nanofluidics, 2011. **10**(3): p. 481-511.
160. Löfdahl, L. and M. Gad-el-Hak, *MEMS-based pressure and shear stress sensors for turbulent flows*. Measurement Science and Technology, 1999. **10**(8): p. 665.
161. Yoo, J.-S., et al., *Real-time impedance measurements during electrochemical experiments and their application to aniline oxidation*. Analytical chemistry, 2003. **75**(14): p. 3294-3300.
162. Chen, J., J. Li, and Y. Sun, *Microfluidic approaches for cancer cell detection, characterization, and separation*. Lab on a Chip, 2012. **12**(10): p. 1753-1767.
163. Silvestri, S. and E. Schena, *Micromachined flow sensors in biomedical applications*. Micromachines, 2012. **3**(2): p. 225-243.
164. Cheung, K.C. and P. Renaud, *BioMEMS for medicine: On-chip cell characterization and implantable microelectrodes*. Solid-state electronics, 2006. **50**(4): p. 551-557.
165. Ghafar-Zadeh, E., M. Sawan, and D. Therriault, *A microfluidic packaging technique for lab-on-chip applications*. IEEE Transactions on Advanced Packaging, 2009. **32**(2): p. 410-416.
166. Dittami, G.M., et al., *A multilayer MEMS platform for single-cell electric impedance spectroscopy and electrochemical analysis*. Microelectromechanical Systems, Journal of, 2008. **17**(4): p. 850-862.
167. Takahashi, K., et al., *Surface stress sensor using MEMS-based Fabry-Perot interferometer for label-free biosensing*. Sensors and Actuators B: Chemical, 2013. **188**: p. 393-399.
168. Ghafar-Zadeh, E., M. Sawan, and D. Therriault, *Novel direct-write CMOS-based laboratory-on-chip: Design, assembly and experimental results*. Sensors and Actuators A: Physical, 2007. **134**(1): p. 27-36.
169. Collins, J. and A.P. Lee, *Microfluidic flow transducer based on the measurement of electrical admittance*. Lab on a Chip, 2004. **4**(1): p. 7-10.
170. Abdur Rahman, A.R., D.T. Price, and S. Bhansali, *Effect of electrode geometry on the impedance evaluation of tissue and cell culture*. Sensors and Actuators B: Chemical, 2007. **127**(1): p. 89-96.
171. Lee, C.H., et al., *Importance of proton conductivity measurement in polymer electrolyte membrane for fuel cell application*. Industrial & engineering chemistry research, 2005. **44**(20): p. 7617-7626.
172. Prakash, S.B. and P. Abshire, *On-chip capacitance sensing for cell monitoring applications*. Sensors Journal, IEEE, 2007. **7**(3): p. 440-447.
173. Guiducci, C., et al., *Microelectrodes on a silicon chip for label-free capacitive DNA sensing*. Sensors Journal, IEEE, 2006. **6**(5): p. 1084-1093.
174. Manesse, M., et al., *Electrochemical impedance spectroscopy and surface plasmon resonance studies of DNA hybridization on gold/SiO<sub>x</sub> interfaces*. Analyst, 2008. **133**(8): p. 1097-1103.
175. Zou, Z., et al., *Functionalized nano interdigitated electrodes arrays on polymer with integrated microfluidics for direct bio-affinity sensing using impedimetric measurement*. Sensors and Actuators A: Physical, 2007. **136**(2): p. 518-526.
176. Boehm, D.A., P.A. Gottlieb, and S.Z. Hua, *On-chip microfluidic biosensor for bacterial detection and identification*. Sensors and Actuators B: Chemical, 2007. **126**(2): p. 508-514.
177. Suehiro, J., et al., *Selective detection of viable bacteria using dielectrophoretic impedance measurement method*. Journal of Electrostatics, 2003. **57**(2): p. 157-168.
178. Graham, A.H., et al., *Commercialisation of CMOS integrated circuit technology in multi-electrode arrays for neuroscience and cell-based biosensors*. Sensors, 2011. **11**(5): p. 4943-4971.
179. Li, J., et al., *Inlaid Multi - Walled Carbon Nanotube Nanoelectrode Arrays for Electroanalysis*. Electroanalysis, 2005. **17**(1): p. 15-27.
180. Escobedo, C., *On-chip nanohole array based sensing: a review*. Lab on a Chip, 2013. **13**(13): p. 2445-2463.
181. Ebbesen, T.W., et al., *Extraordinary optical transmission through sub-wavelength hole arrays*. Nature, 1998. **391**(6668): p. 667-669.
182. Ji, J., et al., *High-throughput nanohole array based system to monitor multiple binding events in real time*. Analytical chemistry, 2008. **80**(7): p. 2491-2498.

183. Masson, J.-F., M.-P. Murray-Méthot, and L.S. Live, *Nanohole arrays in chemical analysis: manufacturing methods and applications*. Analyst, 2010. **135**(7): p. 1483-1489.
184. Chou, S.Y., P.R. Krauss, and P.J. Renstrom, *Imprint of sub - 25 nm vias and trenches in polymers*. Applied physics letters, 1995. **67**(21): p. 3114-3116.
185. Chou, S.Y., P.R. Krauss, and P.J. Renstrom, *25-nanometer resolution*. Science 272, 1996: p. 85-87.
186. Henzie, J., M.H. Lee, and T.W. Odom, *Multiscale patterning of plasmonic metamaterials*. Nature nanotechnology, 2007. **2**(9): p. 549-554.
187. Blodgett, K.B., *Films built by depositing successive monomolecular layers on a solid surface*. Journal of the American Chemical Society, 1935. **57**(6): p. 1007-1022.
188. Kim, B.M., D.J. Graves, and J.A. Quinn, *Analyzing gas mixtures with a dual-membrane counterdiffusion cell*. Journal of Membrane Science, 1980. **6**: p. 247-258.
189. Ahmad, A.L., et al., *Preparation and gas transport properties of dual - layer polysulfone membranes for high pressure CO2 removal from natural gas*. Journal of Applied Polymer Science, 2014.
190. Hisamoto, H., et al., *Chemicofunctional membrane for integrated chemical processes on a microchip*. Analytical chemistry, 2003. **75**(2): p. 350-354.
191. Jiang, H., et al., *A novel dual-membrane reactor for continuous heterogeneous oxidation catalysis*. Industrial & Engineering Chemistry Research, 2011. **50**(18): p. 10458-10464.
192. Wang, S., K. Hawboldt, and M. Abedinzadegan Abdi, *Novel dual-membrane gas-liquid contactors: Modelling and concept analysis*. Industrial & engineering chemistry research, 2006. **45**(23): p. 7882-7891.
193. Vladikova, D., et al., *Impedance spectroscopy studies of dual membrane fuel cell*. Electrochimica Acta, 2011. **56**(23): p. 7955-7962.
194. Bernabini, C., D. Holmes, and H. Morgan, *Micro-impedance cytometry for detection and analysis of micron-sized particles and bacteria*. Lab on a Chip, 2011. **11**(3): p. 407-412.
195. Bernabini, C., et al., *ON-CHIP IMPEDANCE SPECTROSCOPY OF pH-RESPONSIVE POLYELECTROLYTE MICROCAPSULES*.
196. Sheybani, R. and E. Meng, *High-efficiency MEMS electrochemical actuators and electrochemical impedance spectroscopy characterization*. Microelectromechanical Systems, Journal of, 2012. **21**(5): p. 1197-1208.
197. Seidel, H. *The mechanism of anisotropic silicon etching and its relevance for micromachinings*. in *Research and Development. Technical-Scientific Publications (1956-1987): Retrospective View and Prospects. Jubilee Edition on the Occasion of the 75th Anniversary of Dipl.-Engr. Dr.-Engr. EH Ludwig Boelkow*. 1987.
198. Lee, H.W., et al., *Silver (Ag) as a novel masking material in glass etching for microfluidics applications*. Microsystem technologies, 2013. **19**(2): p. 253-259.
199. Kim, Y., et al., *Direct inkjet printing of micro-scale silver electrodes on polydimethylsiloxane (PDMS) microchip*. Journal of Micromechanics and Microengineering, 2014. **24**(11): p. 115010.
200. van der PAUYV, L., *A method of measuring specific resistivity and Hall effect of discs of arbitrary shape*. Philips Res. Rep., 1958. **13**: p. 1-9.
201. Perloff, D.S., *Four - Point Probe Correction Factors for Use in Measuring Large Diameter Doped Semiconductor Wafers*. Journal of The Electrochemical Society, 1976. **123**(11): p. 1745-1750.
202. McDonald, J.C., et al., *Prototyping of microfluidic devices in poly (dimethylsiloxane) using solid-object printing*. Analytical chemistry, 2002. **74**(7): p. 1537-1545.
203. Duffy, D.C., et al., *Rapid prototyping of microfluidic systems in poly (dimethylsiloxane)*. Analytical chemistry, 1998. **70**(23): p. 4974-4984.
204. Anderson, J.R., et al., *Fabrication of topologically complex three-dimensional microfluidic systems in PDMS by rapid prototyping*. Analytical chemistry, 2000. **72**(14): p. 3158-3164.
205. Anderson, J.R., et al., *Fabrication of microfluidic systems in poly (dimethylsiloxane)*. Electrophoresis, 2000. **21**(1): p. 27-40.
206. Yuan, X.-Z.R., et al., *Electrochemical impedance spectroscopy in PEM fuel cells: fundamentals and applications*. 2009: Springer Science & Business Media.
207. Leitgeb, B., et al., *The history of alamethicin: a review of the most extensively studied peptaibol*. Chemistry & biodiversity, 2007. **4**(6): p. 1027-1051.
208. Woolley, G.A. and B. Wallace, *Model ion channels: gramicidin and alamethicin*. The Journal of membrane biology, 1992. **129**(2): p. 109-136.

209. Gordon, L. and D. Haydon, *Kinetics and stability of alamethicin conducting channels in lipid bilayers*. Biochimica et Biophysica Acta (BBA)-Biomembranes, 1976. **436**(3): p. 541-556.
210. Tieleman, D.P., M.S. Sansom, and H.J. Berendsen, *Alamethicin helices in a bilayer and in solution: molecular dynamics simulations*. Biophysical journal, 1999. **76**(1): p. 40-49.
211. Tieleman, D.P., B. Hess, and M.S. Sansom, *Analysis and evaluation of channel models: simulations of alamethicin*. Biophysical journal, 2002. **83**(5): p. 2393-2407.
212. Tieleman, D., H. Berendsen, and M. Sansom, *Voltage-dependent insertion of alamethicin at phospholipid/water and octane/water interfaces*. Biophysical journal, 2001. **80**(1): p. 331-346.
213. Keller, S.L., et al., *Probability of alamethicin conductance states varies with nonlamellar tendency of bilayer phospholipids*. Biophysical journal, 1993. **65**(1): p. 23.
214. Boheim, G., *Statistical analysis of alamethicin channels in black lipid membranes*. The Journal of membrane biology, 1974. **19**(1): p. 277-303.
215. You, S., et al., *Engineering stabilized ion channels: covalent dimers of alamethicin*. Biochemistry, 1996. **35**(20): p. 6225-6232.
216. Lee, D.C., A.A. Durrani, and D. Chapman, *A difference infrared spectroscopic study of gramicidin A, alamethicin and bacteriorhodopsin in perdeuterated dimyristoylphosphatidylcholine*. Biochimica et Biophysica Acta (BBA)-Biomembranes, 1984. **769**(1): p. 49-56.
217. Vodyanoy, I., J. Hall, and T. Balasubramanian, *Alamethicin-induced current-voltage curve asymmetry in lipid bilayers*. Biophysical journal, 1983. **42**(1): p. 71.
218. Lu, H., et al., *Glucose Synthesis in a Protein-Based Artificial Photosynthesis System*. Applied biochemistry and biotechnology, 2015. **177**(1): p. 105-117.
219. Wang, J., et al., *Air Bubble Bursting Effect of Lotus Leaf<sup>†</sup>*. Langmuir, 2009. **25**(24): p. 14129-14134.
220. Ren, X., et al. *Creating a Gas-Liquid Interface in a Microchannel Using Porous Polydimethylsiloxane (PDMS)*. in *Hilton Head Workshop 2014: A Solid-State Sensors, Actuators and Microsystems Workshop*. 2014. Hilton Head Island, South Carolina, USA.
221. Ren, X., et al., *Microfabricated Platform for Integrating Photosynthetic Biomembrane and in-situ Monitoring via Impedance Spectroscopy*, in *MicroTAS 2014 18th International Conference on Miniaturized Systems for Chemistry and Life Sciences*. 2014: San Antonio, Texas, USA. p. 2158-2160.
222. El-Ali, J., P.K. Sorger, and K.F. Jensen, *Cells on chips*. Nature, 2006. **442**(7101): p. 403-411.
223. Pedraza, E., et al., *Synthesis of macroporous poly (dimethylsiloxane) scaffolds for tissue engineering applications*. Journal of Biomaterials Science, Polymer Edition, 2013. **24**(9): p. 1041-1056.
224. Kang, Y.B.A., et al., *Layered long-term co-culture of hepatocytes and endothelial cells on a transwell membrane: toward engineering the liver sinusoid*. Biofabrication, 2013. **5**(4): p. 045008.
225. Sreenivasan, R., et al., *Ultra-thin, gas permeable free-standing and composite membranes for microfluidic lung assist devices*. Biomaterials, 2011. **32**(16): p. 3883-3889.
226. Huh, D., et al., *Microengineered physiological biomimicry: organs-on-chips*. Lab on a chip, 2012. **12**(12): p. 2156-2164.
227. Dittrich, P.S. and A. Manz, *Lab-on-a-chip: microfluidics in drug discovery*. Nature Reviews Drug Discovery, 2006. **5**(3): p. 210-218.
228. Ren, X., et al. *Fabrication of Chitosan Porous Structure and Applications on Artificial Photosynthesis Device*. in *ASME 2013 International Manufacturing Science and Engineering Conference collocated with the 41st North American Manufacturing Research Conference*. 2013. American Society of Mechanical Engineers.
229. Ren, X., Y. Kim, and J. Zhou, *Design and Fabrication of Chitosan for Application of Artificial Photosynthesis*. Journal of Mechanics Engineering & Automation, 2013. **3**(12): p. 739-746.
230. de Jong, J., et al., *Porous microfluidic devices—fabrication and applications*. Chemical engineering & technology, 2007. **30**(3): p. 309-315.
231. Yuen, P.K., et al., *Three-dimensional interconnected microporous poly (dimethylsiloxane) microfluidic devices*. Lab on a Chip, 2011. **11**(8): p. 1541-1544.
232. Bogdanov, I., et al., *Two-phase flow through fractured porous media*. Physical Review E, 2003. **68**(2): p. 026703.
233. Cha, K.J. and D.S. Kim, *A portable pressure pump for microfluidic lab-on-a-chip systems using a porous polydimethylsiloxane (PDMS) sponge*. Biomedical microdevices, 2011. **13**(5): p. 877-883.
234. Vericella, J.J., et al., *Encapsulated liquid sorbents for carbon dioxide capture*. Nature communications, 2015. **6**.

235. Abbaspourrad, A., et al., *Microfluidic Fabrication of Stable Gas-Filled Microcapsules for Acoustic Contrast Enhancement*. *Langmuir*, 2013. **29**(40): p. 12352-12357.
236. Li, W., et al., *Microfluidic study of fast gas-liquid reactions*. *Journal of the American Chemical Society*, 2012. **134**(6): p. 3127-3132.
237. Femmer, T., et al., *Efficient gas-liquid contact using microfluidic membrane devices with staggered herringbone mixers*. *Lab on a Chip*, 2015. **15**(15): p. 3132-3137.
238. Yue, J., E.V. Rebrov, and J.C. Schouten, *Gas-liquid-liquid three-phase flow pattern and pressure drop in a microfluidic chip: similarities with gas-liquid/liquid-liquid flows*. *Lab on a Chip*, 2014. **14**(9): p. 1632-1649.
239. Wang, K., et al., *Generating gas/liquid/liquid three-phase microdispersed systems in double T-junctions microfluidic device*. *Microfluidics and Nanofluidics*, 2010. **8**(6): p. 813-821.
240. Shim, S., et al., *Dissolution without disappearing: multicomponent gas exchange for CO<sub>2</sub> bubbles in a microfluidic channel*. *Lab on a Chip*, 2014. **14**(14): p. 2428-2436.
241. Park, J.I., et al., *A microfluidic approach to chemically driven assembly of colloidal particles at gas-liquid interfaces*. *Angewandte Chemie*, 2009. **121**(29): p. 5404-5408.
242. Jiang, K., et al., *Microfluidic generation of uniform water droplets using gas as the continuous phase*. *Journal of colloid and interface science*, 2015. **448**: p. 275-279.
243. Mäki, A.-J., et al., *Modeling carbon dioxide transport in PDMS-based microfluidic cell culture devices*. *Chemical Engineering Science*, 2015. **137**: p. 515-524.
244. Atencia, J. and D.J. Beebe, *Controlled microfluidic interfaces*. *Nature*, 2005. **437**(7059): p. 648-655.
245. Handa-Corrigan, A., A. Emery, and R. Spier, *Effect of gas-liquid interfaces on the growth of suspended mammalian cells: mechanisms of cell damage by bubbles*. *Enzyme and microbial technology*, 1989. **11**(4): p. 230-235.
246. Mansourizadeh, A. and A.F. Ismail, *Hollow fiber gas-liquid membrane contactors for acid gas capture: a review*. *Journal of hazardous materials*, 2009. **171**(1): p. 38-53.
247. Tremblay, P., et al., *Gas permeability, diffusivity and solubility of nitrogen, helium, methane, carbon dioxide and formaldehyde in dense polymeric membranes using a new on-line permeation apparatus*. *Journal of membrane science*, 2006. **282**(1): p. 245-256.
248. Ichiyanagi, M., et al., *Evaluation methodology of gas permeable characterization in a polymer-based microfluidic device by confocal fluorescence imaging*. *Journal of Micromechanics and Microengineering*, 2012. **22**(6): p. 065023.
249. Tang, S.K. and G.M. Whitesides, *Basic microfluidic and soft lithographic techniques*. *Optofluidics: Fundamentals, Devices and Applications*, McGraw-Hill Professional, 2009: p. 7-31.
250. De Bo, I., et al., *Investigation of the permeability and selectivity of gases and volatile organic compounds for polydimethylsiloxane membranes*. *Journal of membrane science*, 2003. **215**(1): p. 303-319.
251. Ziółkowska, K., R. Kwapiszewski, and Z. Brzózka, *Microfluidic devices as tools for mimicking the in vivo environment*. *New Journal of Chemistry*, 2011. **35**(5): p. 979-990.
252. Zhao, J., et al., *Preparation of Microporous Silicone Rubber Membrane with Tunable Pore Size via Solvent Evaporation-Induced Phase Separation*. *ACS applied materials & interfaces*, 2013. **5**(6): p. 2040-2046.
253. Danckwerts, P. and A. Kennedy, *The kinetics of absorption of carbon dioxide into neutral and alkaline solutions*. *Chemical Engineering Science*, 1958. **8**(3): p. 201-215.
254. Danckwerts, P., A. Kennedy, and D. Roberts, *Kinetics of CO<sub>2</sub> absorption in alkaline solutions—II: Absorption in a packed column and tests of surface-renewal models*. *Chemical Engineering Science*, 1963. **18**(2): p. 63-72.
255. Abbasi, M., J. Evans, and I. Abramson, *Diffusion of gases in porous solids: Monte Carlo simulations in the Knudsen and ordinary diffusion regimes*. *AIChE journal*, 1983. **29**(4): p. 617-624.
256. Cracknell, R.F., et al., *Modeling fluid behavior in well-characterized porous materials*. *Accounts of chemical research*, 1995. **28**(7): p. 281-288.
257. Tabeling, P., *Introduction to microfluidics*. 2010: Oxford University Press.
258. Folch, A., *Introduction to BioMEMS*. 2012: CRC Press.
259. Stroock, A.D., et al., *Chaotic mixer for microchannels*. *Science*, 2002. **295**(5555): p. 647-651.
260. Lee, C.-T. and C.-C. Lee, *A capillary-driven micromixer: idea and fabrication*. *Journal of Micromechanics and Microengineering*, 2012. **22**(10): p. 105034.



261. Lee, C.-Y., et al., *Microfluidic mixing: a review*. International journal of molecular sciences, 2011. **12**(5): p. 3263-3287.
262. Ahmed, D., et al., *A fast microfluidic mixer based on acoustically driven sidewall-trapped microbubbles*. Microfluidics and Nanofluidics, 2009. **7**(5): p. 727-731.
263. Tan, J.N. and A. Neild, *Microfluidic mixing in a Y-junction open channel*. AIP Advances, 2012. **2**(3): p. 032160.
264. Losey, M.W., et al., *Design and fabrication of microfluidic devices for multiphase mixing and reaction*. Microelectromechanical Systems, Journal of, 2002. **11**(6): p. 709-717.
265. Park, C.P. and D.-P. Kim, *Dual-channel microreactor for gas-liquid syntheses*. Journal of the American Chemical Society, 2010. **132**(29): p. 10102-10106.
266. Zhang, Y., et al., *An all-in-one microfluidic device for parallel DNA extraction and gene analysis*. Biomedical microdevices, 2010. **12**(6): p. 1043-1049.
267. Rangwala, H.A., *Absorption of carbon dioxide into aqueous solutions using hollow fiber membrane contactors*. Journal of Membrane Science, 1996. **112**(2): p. 229-240.
268. Merkel, T., et al., *Gas sorption, diffusion, and permeation in poly (dimethylsiloxane)*. Journal of Polymer Science Part B: Polymer Physics, 2000. **38**(3): p. 415-434.
269. Ren, X., et al., *Modeling of Pneumatic Valve Dispenser for Printing Viscous Biomaterials in Additive Manufacturing*. Rapid Prototyping Journal, 2014. **20**(6): p. null.
270. Lee, C.J., J.H. Jung, and T.S. Seo, *3D Porous sol-gel matrix incorporated microdevice for effective large volume cell sample pretreatment*. Analytical chemistry, 2012. **84**(11): p. 4928-4934.
271. Madhally, S.V. and H.W. Matthew, *Porous chitosan scaffolds for tissue engineering*. Biomaterials, 1999. **20**(12): p. 1133-1142.
272. Chenite, A., et al., *Novel injectable neutral solutions of chitosan form biodegradable gels in situ*. Biomaterials, 2000. **21**(21): p. 2155-2161.
273. Gan, Q. and T. Wang, *Chitosan nanoparticle as protein delivery carrier—systematic examination of fabrication conditions for efficient loading and release*. Colloids and Surfaces B: Biointerfaces, 2007. **59**(1): p. 24-34.
274. Ravi Kumar, M.N., *A review of chitin and chitosan applications*. Reactive and functional polymers, 2000. **46**(1): p. 1-27.
275. Portero, A., et al., *Development of chitosan sponges for buccal administration of insulin*. Carbohydrate Polymers, 2007. **68**(4): p. 617-625.
276. Clasen, C., T. Wilhelms, and W.-M. Kulicke, *Formation and characterization of chitosan membranes*. Biomacromolecules, 2006. **7**(11): p. 3210-3222.
277. Mao, J.S., Y.J. Yin, and K. De Yao, *The properties of chitosan-gelatin membranes and scaffolds modified with hyaluronic acid by different methods*. Biomaterials, 2003. **24**(9): p. 1621-1629.
278. Wen, P., et al., *Fabrication of chitosan scaffolds with tunable porous orientation structure for tissue engineering*. Journal of Biomaterials Science, Polymer Edition, 2011. **22**(1-3): p. 19-40.
279. Peter, M., et al., *Preparation and characterization of chitosan-gelatin/nanohydroxyapatite composite scaffolds for tissue engineering applications*. Carbohydrate Polymers, 2010. **80**(3): p. 687-694.
280. Jiankang, H., et al., *Fabrication and characterization of chitosan/gelatin porous scaffolds with predefined internal microstructures*. Polymer, 2007. **48**(15): p. 4578-4588.
281. Yang, B., et al., *Preparation and characterization of a novel chitosan scaffold*. Carbohydrate polymers, 2010. **80**(3): p. 860-865.
282. Ko, Y.G., et al., *Preparation of chitosan scaffolds with a hierarchical porous structure*. Journal of Biomedical Materials Research Part B: Applied Biomaterials, 2010. **93**(2): p. 341-350.
283. Denkbaşı, E.B. and M. Odabaşı, *Chitosan microspheres and sponges: Preparation and characterization*. Journal of applied polymer science, 2000. **76**(11): p. 1637-1643.
284. Foda, N.H., H.M. El-laithy, and M.I. Tadros, *Implantable biodegradable sponges: effect of interpolymer complex formation of chitosan with gelatin on the release behavior of tramadol hydrochloride*. Drug development and industrial pharmacy, 2007. **33**(1): p. 7-17.
285. Ren, X., et al. *Micro and Nano Design and Fabrication of a Novel Artificial Photosynthesis Device*. in ASME 2012 International Manufacturing Science and Engineering Conference collocated with the 40th North American Manufacturing Research Conference and in participation with the International Conference on Tribology Materials and Processing. 2012. American Society of Mechanical Engineers.
286. Di Martino, A., M. Sittlinger, and M.V. Risbud, *Chitosan: a versatile biopolymer for orthopaedic tissue-engineering*. Biomaterials, 2005. **26**(30): p. 5983-5990.

287. Huang, Y., et al., *In vitro characterization of chitosan–gelatin scaffolds for tissue engineering*. Biomaterials, 2005. **26**(36): p. 7616-7627.
288. Yeh, C.-H., P.-W. Lin, and Y.-C. Lin, *Chitosan microfiber fabrication using a microfluidic chip and its application to cell cultures*. Microfluidics and Nanofluidics, 2010. **8**(1): p. 115-121.
289. Park, I., et al., *Low temperature, low pressure nanoimprinting of chitosan as a biomaterial for bionanotechnology applications*. Applied Physics Letters, 2007. **90**(9): p. 093902.
290. Jiang, T., et al., *Surface functionalization of titanium with chitosan/gelatin via electrophoretic deposition: characterization and cell behavior*. Biomacromolecules, 2010. **11**(5): p. 1254-1260.
291. Peter, M., et al., *Novel biodegradable chitosan–gelatin/nano-bioactive glass ceramic composite scaffolds for alveolar bone tissue engineering*. Chemical Engineering Journal, 2010. **158**(2): p. 353-361.
292. Geng, L., et al., *Direct writing of chitosan scaffolds using a robotic system*. Rapid Prototyping Journal, 2005. **11**(2): p. 90-97.
293. Ang, T., et al., *Fabrication of 3D chitosan–hydroxyapatite scaffolds using a robotic dispensing system*. Materials Science and Engineering: C, 2002. **20**(1): p. 35-42.
294. Shen, K. and Q. Hu, *Layered chitosan conduits with controllable inner diameters*. Materials Letters, 2011. **65**(10): p. 1503-1505.
295. Yang, Y., et al., *Nerve conduits based on immobilization of nerve growth factor onto modified chitosan by using genipin as a crosslinking agent*. European Journal of Pharmaceutics and Biopharmaceutics, 2011. **79**(3): p. 519-525.
296. Yang, C.-H., K.-S. Huang, and J.-Y. Chang, *Manufacturing monodisperse chitosan microparticles containing ampicillin using a microchannel chip*. Biomedical microdevices, 2007. **9**(2): p. 253-259.
297. Cooney, M.J., et al., *Design of chitosan gel pore structure: towards enzyme catalyzed flow-through electrodes*. Journal of Materials Chemistry, 2008. **18**(6): p. 667-674.
298. Cheng, J.C. and A.P. Pisano, *Photolithographic process for integration of the biopolymer chitosan into micro/nanostructures*. Microelectromechanical Systems, Journal of, 2008. **17**(2): p. 402-409.
299. Dykstra, P., et al., *An optical MEMS sensor utilizing a chitosan film for catechol detection*. Sensors and Actuators B: Chemical, 2009. **138**(1): p. 64-70.
300. Liu, Y., et al., *Chitosan to electroaddress biological components in lab-on-a-chip devices*. Carbohydrate Polymers, 2011. **84**(2): p. 704-708.
301. Wu, L.Q., et al., *Biomimetic pattern transfer*. Advanced Functional Materials, 2005. **15**(2): p. 189-195.
302. Yi, H., et al., *Biofabrication with chitosan*. Biomacromolecules, 2005. **6**(6): p. 2881-2894.
303. Fan, W., et al., *Formation mechanism of monodisperse, low molecular weight chitosan nanoparticles by ionic gelation technique*. Colloids and Surfaces B: Biointerfaces, 2012. **90**: p. 21-27.
304. Huang, Z.-H., et al., *Electrochemistry assisted reacting deposition of hydroxyapatite in porous chitosan scaffolds*. Materials Letters, 2008. **62**(19): p. 3376-3378.
305. Koev, S., et al., *Chitosan: an integrative biomaterial for lab-on-a-chip devices*. Lab on a Chip, 2010. **10**(22): p. 3026-3042.
306. Tangsadthakun, C., et al., *The influence of molecular weight of chitosan on the physical and biological properties of collagen/chitosan scaffolds*. Journal of Biomaterials Science, Polymer Edition, 2007. **18**(2): p. 147-163.
307. Desbrieres, J., *Viscosity of semiflexible chitosan solutions: influence of concentration, temperature, and role of intermolecular interactions*. Biomacromolecules, 2002. **3**(2): p. 342-349.
308. Geng, X., O.-H. Kwon, and J. Jang, *Electrospinning of chitosan dissolved in concentrated acetic acid solution*. Biomaterials, 2005. **26**(27): p. 5427-5432.
309. Hoffmann, B., et al., *Glutaraldehyde and oxidised dextran as crosslinker reagents for chitosan-based scaffolds for cartilage tissue engineering*. Journal of Materials Science: Materials in Medicine, 2009. **20**(7): p. 1495-1503.
310. Monteiro, O.A. and C. Airoidi, *Some studies of crosslinking chitosan–glutaraldehyde interaction in a homogeneous system*. International Journal of Biological Macromolecules, 1999. **26**(2): p. 119-128.
311. Cumpston, B.H., et al., *Two-photon polymerization initiators for three-dimensional optical data storage and microfabrication*. Nature, 1999. **398**(6722): p. 51-54.
312. Serbin, J., et al., *Femtosecond laser-induced two-photon polymerization of inorganic organic hybrid materials for applications in photonics*. Optics letters, 2003. **28**(5): p. 301-303.
313. Lantada, A.D. and P.L. Morgado, *Rapid prototyping for biomedical engineering: current capabilities and challenges*. Annual review of biomedical engineering, 2012. **14**: p. 73-96.

314. Kim, G.H. and J.G. Son, *3D polycaprolactone (PCL) scaffold with hierarchical structure fabricated by piezoelectric transducer (PZT)-assisted biplotter*. Applied Physics A, 2009. **94**(4): p. 781-785.
315. Chang, R., J. Nam, and W. Sun, *Effects of dispensing pressure and nozzle diameter on cell survival from solid freeform fabrication-based direct cell writing*. Tissue Engineering Part A, 2008. **14**(1): p. 41-48.
316. Khalil, S. and W. Sun, *Bioprinting endothelial cells with alginate for 3D tissue constructs*. Journal of biomechanical engineering, 2009. **131**(11): p. 111002.
317. Chiu, W. and S. Tan, *Multiple material objects: from CAD representation to data format for rapid prototyping*. Computer-Aided Design, 2000. **32**(12): p. 707-717.
318. Visconti, R.P., et al., *Towards organ printing: engineering an intra-organ branched vascular tree*. Expert opinion on biological therapy, 2010. **10**(3): p. 409-420.
319. Lu, L., et al., *A novel sucrose porogen-based solid freeform fabrication system for bone scaffold manufacturing*. Rapid Prototyping Journal, 2010. **16**(5): p. 365-376.
320. Khalil, S., J. Nam, and W. Sun, *Multi-nozzle deposition for construction of 3D biopolymer tissue scaffolds*. Rapid Prototyping Journal, 2005. **11**(1): p. 9-17.
321. Shor, L., et al., *Fabrication of three-dimensional polycaprolactone/hydroxyapatite tissue scaffolds and osteoblast-scaffold interactions in vitro*. Biomaterials, 2007. **28**(35): p. 5291-5297.
322. Lee, H. and G. Kim, *Cryogenically fabricated three-dimensional chitosan scaffolds with pore size-controlled structures for biomedical applications*. Carbohydrate Polymers, 2011. **85**(4): p. 817-823.
323. Snyder, J., et al., *Bioprinting cell-laden matrigel for radioprotection study of liver by pro-drug conversion in a dual-tissue microfluidic chip*. Biofabrication, 2011. **3**(3): p. 034112.
324. Van Vlierberghe, S., P. Dubruel, and E. Schacht, *Biopolymer-based hydrogels as scaffolds for tissue engineering applications: a review*. Biomacromolecules, 2011. **12**(5): p. 1387-1408.
325. Zhang, Y., et al., *Calcium phosphate-chitosan composite scaffolds for bone tissue engineering*. Tissue Engineering, 2003. **9**(2): p. 337-345.
326. Sun, J., et al., *Performance characterization of drop-on-demand micro-dispensing system with multi-nozzles*. Microsystem technologies, 2010. **16**(12): p. 2087-2097.
327. Cohen, D.L., et al., *Direct freeform fabrication of seeded hydrogels in arbitrary geometries*. Tissue engineering, 2006. **12**(5): p. 1325-1335.
328. Shin, K.-H., et al., *A method for the design and fabrication of heterogeneous objects*. Materials & Design, 2003. **24**(5): p. 339-353.
329. Hockaday, L., et al., *Rapid 3D printing of anatomically accurate and mechanically heterogeneous aortic valve hydrogel scaffolds*. Biofabrication, 2012. **4**(3): p. 035005.
330. Duan, B., et al., *3D bioprinting of heterogeneous aortic valve conduits with alginate/gelatin hydrogels*. Journal of Biomedical Materials Research Part A, 2013. **101**(5): p. 1255-1264.
331. Kalpakjian, S. and S.R. Schmid, *Manufacturing processes for engineering materials*. 2010: Pearson education.
332. Pelofsky, A.H., *Surface Tension-Viscosity Relation for Liquids*. Journal of Chemical and Engineering Data, 1966. **11**(3): p. 394-397.
333. Schonhorn, H., *Surface Tension-Viscosity Relationship for Liquids*. Journal of Chemical and Engineering Data, 1967. **12**(4): p. 524-525.
334. Mironov, V., et al., *Designer 'blueprint' for vascular trees: morphology evolution of vascular tissue constructs*. Virtual and Physical Prototyping, 2009. **4**(2): p. 63-74.
335. Currie, I.G., *Fundamental mechanics of fluids*. 2012: CRC Press.
336. Ghafar-Zadeh, E., et al., *CMOS capacitive sensors for lab-on-chip applications*. 2010: Springer.
337. Nge, T.T., et al., *Microstructure and mechanical properties of bacterial cellulose/chitosan porous scaffold*. Cellulose, 2010. **17**(2): p. 349-363.
338. Shen, F., et al., *A study on the fabrication of porous chitosan/gelatin network scaffold for tissue engineering*. Polymer international, 2000. **49**(12): p. 1596-1599.
339. Wu, A., et al., *Modular integration of electronics and microfluidic systems using flexible printed circuit boards*. Lab on a Chip, 2010. **10**(4): p. 519-521.
340. Lee, W.-C., et al., *An integrated microfluidic system using magnetic beads for virus detection*. Diagnostic microbiology and infectious disease, 2008. **60**(1): p. 51-58.
341. Han, A., et al., *An approach to multilayer microfluidic systems with integrated electrical, optical, and mechanical functionality*. Sensors Journal, IEEE, 2005. **5**(1): p. 82-89.

342. Takao, H. and M. Ishida, *Microfluidic integrated circuits for signal processing using analogous relationship between pneumatic microvalve and MOSFET*. *Microelectromechanical Systems, Journal of*, 2003. **12**(4): p. 497-505.
343. Wu, H., et al., *Fabrication of complex three-dimensional microchannel systems in PDMS*. *Journal of the American Chemical Society*, 2003. **125**(2): p. 554-559.
344. Wang, C.-H. and G.-B. Lee, *Automatic bio-sampling chips integrated with micro-pumps and micro-valves for disease detection*. *Biosensors and Bioelectronics*, 2005. **21**(3): p. 419-425.
345. Mohan, R., et al., *Design considerations for elastomeric normally closed microfluidic valves*. *Sensors and Actuators B: Chemical*, 2011. **160**(1): p. 1216-1223.
346. Wang, L., et al., *Polydimethylsiloxane-integratable micropressure sensor for microfluidic chips*. *Biomicrofluidics*, 2009. **3**(3): p. 034105.
347. Chen, A. and T. Pan, *Three-dimensional fit-to-flow microfluidic assembly*. *Biomicrofluidics*, 2011. **5**(4): p. 046505.
348. Argentiere, S., et al., *Smart microfluidics: The role of stimuli-responsive polymers in microfluidic devices*. 2012: INTECH Open Access Publisher.
349. Land, K.J., et al., *Low cost fabrication and assembly process for re-usable 3D polydimethylsiloxane (PDMS) microfluidic networks*. *Biomicrofluidics*, 2011. **5**(3): p. 036502.
350. Cai, Z., et al. *Measurement of enzyme activity using a plug-based electrochemical microdevice*. in *Sensors, 2012 IEEE*. 2012. IEEE.
351. Ghafar-Zadeh, E. and M. Sawan, *A core-CBCM sigma delta capacitive sensor array dedicated to lab-on-chip applications*. *Sensors and Actuators A: Physical*, 2008. **144**(2): p. 304-313.
352. Ghafar-Zadeh, E., M. Sawan, and D. Therriault, *A 0.18- $\mu$ m CMOS capacitive sensor Lab-on-Chip*. *Sensors and Actuators A: Physical*, 2008. **141**(2): p. 454-462.
353. Ghafar-Zadeh, E. and M. Sawan, *A hybrid microfluidic/CMOS capacitive sensor dedicated to lab-on-chip applications*. *Biomedical Circuits and Systems, IEEE Transactions on*, 2007. **1**(4): p. 270-277.
354. Luque, A., et al., *Integrable silicon microfluidic valve with pneumatic actuation*. *Sensors and Actuators A: Physical*, 2005. **118**(1): p. 144-151.
355. Malik, A., et al., *Modeling and analysis of a phase change material thermohydraulic membrane microactuator*. *Microelectromechanical Systems, Journal of*, 2013. **22**(1): p. 186-194.
356. Satyanarayana, S., D.T. McCormick, and A. Majumdar, *Parylene micro membrane capacitive sensor array for chemical and biological sensing*. *Sensors and Actuators B: Chemical*, 2006. **115**(1): p. 494-502.
357. Elbuken, C., et al., *Detection of microdroplet size and speed using capacitive sensors*. *Sensors and Actuators A: Physical*, 2011. **171**(2): p. 55-62.
358. Perdignes, F., et al., *Capacitive depression sensor for microfluidic pneumatic networks*. *Sensors and Actuators A: Physical*, 2012. **173**(1): p. 75-80.
359. Wei, J., et al., *Design, fabrication and characterization of a femto-farad capacitive sensor for picoliter liquid monitoring*. *Sensors and Actuators A: Physical*, 2010. **162**(2): p. 406-417.
360. Kim, D.-S., et al., *An extended gate FET-based biosensor integrated with a Si microfluidic channel for detection of protein complexes*. *Sensors and Actuators B: Chemical*, 2006. **117**(2): p. 488-494.
361. Velten, T., et al., *Packaging of bio-MEMS: strategies, technologies, and applications*. *Advanced Packaging, IEEE Transactions on*, 2005. **28**(4): p. 533-546.
362. Erickson, D. and D. Li, *Integrated microfluidic devices*. *Analytica Chimica Acta*, 2004. **507**(1): p. 11-26.
363. Erickson, D., *Towards numerical prototyping of labs-on-chip: modeling for integrated microfluidic devices*. *Microfluidics and Nanofluidics*, 2005. **1**(4): p. 301-318.
364. Soltan, A. and A.M. Soliman, *A CMOS differential difference operational mirrored amplifier*. *AEU-International Journal of Electronics and Communications*, 2009. **63**(9): p. 793-800.
365. Nikolic, J.M.R.A.C.B., *Digital Integrated Circuits, A Design Perspective*. 2 ed. Prentice Hall Electronics and VLSI Series, ed. C.G. Sodini. 2003, Upper Saddle River, New Jersey: Pearson Education International.
366. Tang, A., F. Yuan, and E. Law. *CMOS current-mode active transformer sigma-delta modulators*. in *Circuits and Systems, 2008. MWSCAS 2008. 51st Midwest Symposium on*. 2008. IEEE.
367. Marelli, D., K. Mahata, and M. Fu, *Linear LMS compensation for timing mismatch in time-interleaved ADCs*. *Circuits and Systems I: Regular Papers, IEEE Transactions on*, 2009. **56**(11): p. 2476-2486.

368. Hoyos, S. and B.M. Sadler, *Ultra-wideband analog-to-digital conversion via signal expansion*. Vehicular Technology, IEEE Transactions on, 2005. **54**(5): p. 1609-1622.
369. Taillefer, C.S. and G.W. Roberts, *Delta-Sigma A/D conversion via time-mode signal processing*. Circuits and Systems I: Regular Papers, IEEE Transactions on, 2009. **56**(9): p. 1908-1920.
370. Miller, D.L., et al., *Superconducting sigma-delta analog-to-digital converters*. Applied superconductivity, 1999. **6**(10): p. 657-661.
371. Kaewdang, K. and W. Surakamponorn, *On the realization of electronically current-tunable CMOS OTA*. AEU-International Journal of Electronics and Communications, 2007. **61**(5): p. 300-306.
372. Jamshidi-Roudbari, A., P.-C. Kuo, and M.K. Hatalis, *A flash analog to digital converter on stainless steel foil substrate*. Solid-State Electronics, 2010. **54**(4): p. 410-416.



## Appendix I: Technical terms and abbreviations

### 1. Abbreviations:

3-PGA: 3-phosphoglycerate  
ABS: acrylonitrile butadiene styrene  
AC: alternating current  
ADC: analog to digital converter  
ADP: adenosine diphosphate  
AM: additive manufacturing  
AP: artificial photosynthesis  
APTES: (3-aminopropyl)triethoxysilane  
ASCII: American standard code for information interchange  
ASIC: application specific integrated circuit  
ATP: adenosine triphosphate  
ATPase: ATP synthase  
BLM: black lipid membrane  
BR: bacteriorhodopsin  
BOE: buffered oxide etching/etchant  
BSA: bovine serum albumin  
BTB: bromothymol blue  
CA: chronoamperometry/chronocoulometry  
CAD: computer-aided design  
CBB: Calvin Benson Bassham cycle  
CCD: charge-coupled device  
CEM: cation exchange membrane  
CMOS: complementary metal-oxide-semiconductor  
CNC: computer numerical control  
CV: cyclic voltammetry  
DAC: digital to analog converter  
DC: direct current  
DI: deionised water  
DMF: 2,5-dimethylfuran  
DNA: deoxyribonucleic acid  
DTT: dithiothreitol  
DPPC: dipalmitoyl-sn-glycero-3-phosphocholine  
DQ: diazoquinones  
DWFP: direct-write fabrication process  
EDTA: ethylene-diaminetetra-acetic acid  
EFD: engineered fluid dispensing  
EIS: electrochemical impedance spectroscopy

ER: endoplasmic reticulum  
F1,6BPase: fructose-1,6-bisphosphatase  
FDM: fused deposition modeling  
FESEM: field emission scanning electron microscope  
FITC: fluorescein isothiocyanate  
FoF1: F oligomycin and F1  
G3P: glyceraldehydes-3-phosphate  
G6Pase: glucose-6-phosphatase  
GAPDH: glyceraldehydes-3-phosphate dehydrogenase  
GDGT: glycerol dialkylglycerol tetraether  
GDH: glutamate dehydrogenase  
GDNT: glycerol dialkylcalditol tetraether  
GND: ground  
HPTS: 8-hydroxyprone-1,3,6-trisulphonic acid  
IC: integrated circuit  
INV: inverter  
IPA: isopropanol  
ITO: indium tin oxide  
LCD: liquid crystal display  
LED: light emission diode  
LOC: lab on a chip  
LSB: least significant bit  
MEMS: micro-electro-mechanical system  
MFC: microbial fuel cells  
MOPS: 3-(N-morpholino) propanesulfonic acid  
MOSFET: metal-oxide-semiconductor field effect transistors  
MPL: main tetraether phospholipid  
NADH: nicotinamide adenine dinucleotide hydrogen  
NADP<sup>+</sup>: nicotinamide adenine dinucleotide phosphate +  
NADPH: nicotinamide adenine dinucleotide phosphate hydrogen  
NHS: N-hydroxysuccinimide  
NMOS: N-type metal-oxide-semiconductor field effect transistors  
OD: optical density  
OEC: oxygen evolving complex  
OmpF: outer membrane protein F  
OTA: operational transconductance amplifier  
PAC: photoactive compound  
PCB: printed circuit board  
PCL: polycarprolactone  
PDMS: poly(dimethylsiloxane)  
PEG: polyethylene glycol



PEIS: potentio electrochemical impedance spectroscopy  
PEtOz: poly(ethyloxazoline)  
PGI: phosphoglucose isomerase  
PGK: phosphoglycerate kinase  
Pi: inorganic phosphate,  $\text{HPO}_3\text{O}^{2-}$   
PI: polyisoprene  
PLFE: polar lipid fraction E  
PM: purple membrane  
PMOS: P-type metal-oxide-semiconductor field effect transistors  
PMOXA: poly(2-methyloxazoline)  
POPC: 1-palmitoyl-2-oleoyl-sn-glycero-3-phosphocholine  
POPS: 1-palmitoyl-2-oleoyl-sn-glycero-3-phosphoserine  
PR: photoresist  
PSI: photosystem I  
PSII: photosystem II  
PU: polyurethane  
PWM: pulse-width modulation  
QD: quantum dot  
Reg: register  
RGB: red-green-blue map  
RNA: ribonucleic acid  
RP: rapid prototyping  
Rsn-2: ranaspumin-2  
RuBisCO: ribulose-1,5-bisphosphate carboxylase/oxygenase  
RuBP: ribulose-1,5-bisphosphate  
SNR: signal to noise ratio  
SPICE: simulation program with integrated circuit emphasis  
STL: stereolithography  
T20: tween-20  
TCA: trichloroacetic acid  
TEOA: triethanolamine  
TFOCS: tridecafluoro-1,1,2,2-tetrahydrooctyl-1-trichlorosilane  
TPI: triose phosphate isomerase  
Tris: tris(hydroxymethyl) aminomethane  
TTL: transistor-transistor logic  
ULSI: ultra large scale integration  
UV: ultraviolet  
 $\mu$ TAS: miniaturized total chemical analysis systems  
VCCS: voltage controlled current source  
VLSI: very-large-scale integration

## 2. Chemical elements and compounds

Ca: calcium  
CO: carbon monoxide  
CO<sub>2</sub>: carbon dioxide  
Cr<sub>2</sub>O<sub>3</sub>: chromium oxide  
Cu: copper  
CH<sub>2</sub>O: formaldehyde  
CH<sub>3</sub>COOH: acetic acid  
CH<sub>4</sub>: methane  
CHCl<sub>3</sub>: chloroform  
CdSe: cadmium selenium  
CaCl<sub>2</sub>: calcium chloride  
C<sub>60</sub>: fullerene  
Ag: silver  
Au: gold  
ArF: argon fluoride  
Al: aluminum  
H<sup>+</sup>: hydrogen ion / proton  
H<sub>2</sub>: hydrogen  
H<sub>2</sub>O<sub>2</sub>: hydrogen peroxide  
H<sub>2</sub>SO<sub>4</sub>: sulfuric acid  
HCl: hydrogen chloride  
HCOOH: formic acid  
GaN: gallium nitride  
Fe: iron  
N<sub>2</sub>: nitrogen  
Na<sub>2</sub>SO<sub>4</sub>: sodium sulfate  
MgCl<sub>2</sub>: magnesium chloride  
MgSO<sub>4</sub>: magnesium sulfate  
Mn: manganese  
KHCO<sub>3</sub>: potassium bicarbonate  
KOH: potassium hydroxide  
IrO<sub>2</sub>: iridium oxide  
K<sub>2</sub>SO<sub>4</sub>: potassium sulfate  
KCl: potassium chloride  
KH<sub>2</sub>PO<sub>4</sub>: monopotassium phosphate  
He: helium  
NaHCO<sub>3</sub>: sodium bicarbonate  
NaOH: sodium hydroxide  
Ne: neon  
NH<sub>3</sub>: ammonium

$\text{NH}_4^+$ : ammonium ion

Ni: nickel

$\text{O}_2$ : oxygen

Pt: platinum

Rh: rhodium

Ru: ruthenium

$\text{TiO}_2$ : titanium dioxide

## Appendix II: Matlab codes

### 1. Nyquist and Bode plot



data5.m

```
% data5.m
% copyright @ Xiang Ren
% Drexel University Dept.Mechanical Engineering and Mechanics
% xr27@drexel.edu
function data5(x,y,z) % impedance
figure(1)
plot(y,z,'b','linewidth',2) %this one is the true value from EIS
grid on % this one exist when "plot true value" is activated
xlabel('Re(Z)','FontName','Times New Roman','FontSize',15)
ylabel('Im(Z)','FontName','Times New Roman','FontSize',15)
% axis([-0.1e5,4.1e5,0,8.5e4]);% axis used for double membrane d3_5
figure(2)
loglog(x,sqrt(y.^2+z.^2),'*')
xlabel('f (Hz)','FontName','Times New Roman','FontSize',15);
h1=ylabel('Impedance log$$\left|Z\right| (\Omega)$$','FontName'...
, 'Times New Roman','FontSize',15,'FontWeight','bold'); %intro latex
command
set(h1,'Interpreter','latex');
grid on
% axis([1e-2,1e6,1e2,1e7]);
figure(3)
plot(log10(x),180/pi.*atan(z./y),'*')
xlabel('log f (Hz)','FontName','Times New Roman','FontSize',15);
% ylabel('phase angle')
h2=ylabel('Phase angle $$\angle\varphi (\text{\circ})$$','FontName'...
, 'Times New Roman','FontSize',15,'FontWeight','bold');
set(h2,'Interpreter','latex');
grid on
% axis([-2,6,-90,10]);
end
```



run22.m

```
% run22.m
%stability, d61, PLFE 39 degree C warm water bath
close all
clear
clc

tic
load('d61_1.mat')% PLFE
load('d61_2.mat')
%begin with data 1 cycle 1
data5(d61_1(1:48,1),d61_1(1:48,2),d61_1(1:48,3))
figure(1)
hold on
```

```

figure(2)
hold on
figure(3)
hold on
%*****
figure(4)
plot(tr,Ml.*2,'*k','markersize',5)
hold on
errorbar(tr,Ml.*2,Mlstd.*0.8,'ok','markersize',5)
% grid on
p1=polyfit(tr,Ml.*2,3);% fit stability curve
cc1=polyval(p1,tr);
plot(tr,cc1,'k','linewidth',2)
axis([0,3000,0,1e5])
xlabel('time (min)','FontSize',12)
ylabel({'PLFE','Impedance','|Z| (\Omega)'},'FontSize',12)
set(gca,'FontSize',12);
%=====
figure(5)
f=d61_1(1:48,1); % uniform frequency swipe, 1MHz to 10mHz
a=zeros(48,162);
for j=1:81
    a(:,j)=d61_1(1+48*(j-1):48+48*(j-1),4);
    a(:,j+81)=d61_2(1+48*(j-1):48+48*(j-1),4);
end
mesh(tr,log10(f),a.*2)
xlabel('time (min)','FontSize',15)
ylabel('log f (Hz)','FontSize',15)
% zlabel('Impedance Z(Ohm)')
h1=zlabel('Impedance  $Z$  |Z| (\Omega)', 'FontName'...'
    , 'Times New Roman', 'FontSize',15, 'FontWeight', 'bold'); %intro latex
command
set(h1,'Interpreter','latex');
set(gca,'XDir','reverse')
axis([0,3000,-2,6,0,7e4])
set(gca,'FontSize',15);
%=====
toc

```

## 2. pH measurement: image extraction from video



CO2exp1.m

```

% CO2 experiment vedio, .mov ->avi
mov=aviread('sampl.avi'); % read the video
fnum=size(mov,2); % remember the video's slice, mov is 1*temp
for i=1:fnum
    strtemp=strcat('d:\dropbox\2013.3.7 photosynthesis\8.15 CO2 absorb\12.13 CO2
experiment\sampl\',int2str(i),'.','jpg');
    % save each slice into "jpg" figure
    imwrite(mov(i).cdata,strtemp); %imwrite(mov(i).cdata,mov(i).colormap,strtemp);
    %no color map for this avi
end

```

### 3. pH measurement: Function: change image file to matrix



pic2mat.m

```
% picture to matrix; load picture from photo files
%% ***** Parameters *****
% Input:
%   path: the photo files storage place
%   length: total picture files quantity
% Output:
%   p_color: RGB color info: xxx*xxx*3 unit8 cell
%   p_gray: gray color matrix: xxx*xxx cell
%   n: normalization number, in order to change "length" normalize to ~100
% ===== END parameters =====
function [p_color,p_gray,n]=pic2mat(path,length)
n=ceil(length/100); %upper boundary as cutting
k=floor(length/n); %lower boundary as cell length
p_color=cell(1,k); % pic, color
% pic{1,10} is 1920x1080x3 unit8
p_gray=cell(1,k); % picc, gray
% picc{1,10} is 1920x1080 unit8
string=path;
for i=1:k, % large still.mov, La01.jpg~La90.jpg
    filename=strcat(string,'La',int2str(i*n),'.jpg');
% path=D:\Dropbox\2015.1.7 CO2 pH on-chip\7.15 exp-code\La0\
    im=imread(filename);
    imm=rgb2gray(im);
    p_color{i}=im; % every rgb become pic{1~80} %imshow(pic0{1,10}) can
view color image
    p_gray{i}=imm; % use imshow(picc0{1,10}) can view the gray image
end
end
```



pic2mat00sta.m

```
function [p_color,p_gray,n]=pic2mat00sta(path,length)
n=ceil(length/100); %upper boundary as cutting
k=floor(length/n); %lower boundary as cell length
p_color=cell(1,k); % pic, color
% pic{1,10} is 1920x1080x3 unit8
p_gray=cell(1,k); % picc, gray
% picc{1,10} is 1920x1080 unit8
string=path;
for i=1:k, % .mov, im1.jpg~imXX.jpg
    filename=strcat(string,'img',int2str(i*n),'.jpg');
% path=D:\Dropbox\2015.1.7 CO2 pH on-chip\7.15 exp-code\La0\
    im=imread(filename);
    imm=rgb2gray(im);
    p_color{i}=im; % every rgb become pic{1~80} %imshow(pic0{1,10}) can
view color image
    p_gray{i}=imm; % use imshow(picc0{1,10}) can view the gray image
end
% imshow(picc0{1,10}(900:1920,1:1080)) % cut partial of image
end
```

#### 4. pH measurement: Dynamic flow and static flow pH variation



dynamic\_prC\_run20.m

```

% static read
close all
clear
clc

tic
% file:
% \2016.2.1 CO2 experiment\2.3 paryleneC dynamic1 20ul-min 4s
delta_t20=4; % each frame 4 sec;
%% *****
[picc20,picc20,n20]=pic2mat('D:\Dropbox\2016.2.1 CO2 experiment\2.3 paryleneC
dynamic1 20ul-min 4s\',376);
%% *****
% -----set standard-----from stantard image-----
std_pH % run std_pH.m
%% analysis pixels
% -----check channel-----
figure(3)
warning off
subplot(2,1,1)
imshow(picc20{1,1}(550:1400,500:3000));
subplot(2,1,2)
imshow(picc20{1,94}(550:1400,500:3000));
title('20\muL/min')
% Warning: The initial magnification of the image is set to 'fit' in a docked
figure.
picc20_chn_frame=cell(1,94);% define channel parameter picc0 channel frame
pixels
avg_ch20=zeros(1,94);
for i=1:94
    picc20_chn_frame{1,i}=picc20{1,i}(550:1400,500:3000);
    avg_ch20(i)=mean(picc20_chn_frame{1,i}(picc20_chn_frame{1,i}<150));
end
% -----time series-----
% define time series
t20=0:n20*delta_t20:n20*93*delta_t20;
% plot frame intensity to time
figure(4)
title('20\muL/min channel frame vs. time')
hold on
plot(t20,avg_ch20,'+')
grid on

%% *****
%% evaluate pH value
% volume = flow rate * time;
% calculate pH: pH=-log[H+];
% accumulate fluid gray img.
y1=interp1(avg,pH_ex_cc,avg_ch20);

figure(5)
plot(t20,y1,'*')
xlabel('time (s)','FontSize',12)
ylabel('pH','FontSize',12)
set(gca,'FontSize',12);

```

```

grid on

figure(6)
for i=1:90
    imshow(pic20{1,i}(550:1400,500:3000,1:3))
    text(50,600,['t=',num2str(t20(i)),'s'],'fontsize',40);
    text(50,700,['pH=',num2str(y1(i))],'fontsize',40);
    pause(0.1)
    M(i)=getframe;
end
movie2avi(M,'dynamic_prc_20.avi','FPS',5) % output video

%% evaluate pH value
format long
% present data, pH and pCO2 vs. concentrations
load('CO2table.mat');
pCO2=CO2table(:,1); %pressure CO2
pH=CO2table(:,2); %pH
CO2=CO2table(:,3); %CO2 concentration
H2CO3=CO2table(:,4); %H2CO3 concentration
HCO3=CO2table(:,5); %HCO3- concentration
CO3=CO2table(:,6); %CO3^2- concentration

figure(7)
%plot pH vs. carbon concentration
total_c=CO2+H2CO3+HCO3+CO3;
lg_c=log10(total_c);
plot(pH,lg_c,'d')
hold on
title('standard pH vs. carbon concentration','FontSize',12)
xlabel('standard pH value','FontSize',12)
ylabel('log carbon concentration (mol/L)','FontSize',12)
pH_fit=polyfit(pH,lg_c,1);% fit curve == linear
pH_cc=polyval(pH_fit,pH);
plot(pH,pH_cc,'k','linewidth',2)
grid on
set(gca,'FontSize',12);
format short
%% evaluate carbon concentration based on pH value
y2=interp1(pH,pH_cc,y1);
% y1=interp1(avg2,pH_ex_cc2,avg_ch2);
figure(8)
plot(t20,y2,'*')
xlabel('time (s)','FontSize',12)
ylabel('log carbon concentration (mol/L)','FontSize',12)
grid on
set(gca,'FontSize',12);
%% dynamic; use total amount:
% flow rate 20 uL/min
figure(9)
% total amount Carbon vs. time
% time still t20
% calculate accumulated carbon amount: accumC
% unit: uL/min * s * mol/L
flow_rate=20; % uL/min
volume_t=flow_rate*t20/60; % uL
% concentration in figure(11), y2 mol/L
accumC=y2.*volume_t;
plot(t20,accumC)
%%
figure(10)
[AX,H1,H2] = plotyy(t20,y1,t20,y2,'plot');
set(AX(1),'XColor','k','YColor','k');

```



```

set (AX(2), 'XColor', 'k', 'YColor', 'k');
HH1=get (AX(1), 'Ylabel');
set (HH1, 'String', 'pH', 'FontSize', 12);
set (HH1, 'color', 'k');
HH2=get (AX(2), 'Ylabel');
set (HH2, 'String', 'log carbon concentration (mol/L)', 'FontSize', 12);
set (HH2, 'color', 'k');
set (H1, 'LineStyle', '*');
set (H1, 'color', 'k');
set (H2, 'LineStyle', '+');
set (H2, 'color', 'k');
xlabel('time (s)', 'FontSize', 12);
%% *****
Stable_pH=mean(y1(24:90));
fprintf('the stable pH is %d', Stable_pH)
% mean(y1(24:90))
toc

```



std\_pH.m

```

% -----set standard-----from standart image-----
% used before running for specific flow rate
s4=imread('D:\Dropbox\2016.2.1 CO2 experiment\img\ph4_7_10HD.jpg');
s6=imread('D:\Dropbox\2016.2.1 CO2 experiment\img\ph6_7_7.6HD.jpg');
s4c4=s4(240:350,180:200,1:3);
s4c7=s4(240:350,400:430,1:3);
s4c10=s4(240:350,600:630,1:3);
s6c6=s6(230:370,150:200,1:3);
s6c7=s6(240:360,400:430,1:3);
s6c76=s6(240:350,580:650,1:3);
s4g=rgb2gray(s4);
s6g=rgb2gray(s6);
%gray
s4g4=s4g(240:350,180:200);
s4g7=s4g(240:350,400:430);
s4g10=s4g(240:350,600:630);
s6g6=s6g(230:370,150:200);
s6g7=s6g(240:360,400:430);
s6g76=s6g(240:350,580:650);
figure(1)
subplot(2,3,1)
imshow(s4c4);
%check average value % white:255, black:0;
% mean(mean(s4g4))
% mean(s4g4(s4g4<mean(mean(s4g4)))) % rule out bright numbers
title('ph=4');
subplot(2,3,2)
imshow(s4c7);
% mean(s4g7(s4g7<mean(mean(s4g7))))
title('ph=7');
subplot(2,3,3)
imshow(s4c10);
title('ph=10');

subplot(2,3,4)
imshow(s6c6);
title('ph=6');

```

```

subplot(2,3,5)
imshow(s6c7);
title('ph=7');
% mean(s6g7(s6g7<mean(mean(s6g7))))
subplot(2,3,6)
imshow(s6c76);
title('ph=7.6');
% calculate average value number into vector avg(1~6)
avg(1)=mean(mean(s4g4));
avg(2)=mean(mean(s4g7));
avg(3)=mean(mean(s4g10));
avg(4)=mean(mean(s6g6));
avg(5)=mean(mean(s6g7));
avg(6)=mean(mean(s6g76));
% plot pH value vs. avg number
figure(2)
pH_ex_std=[4,7,10,6,7,7.6];
plot(avg,pH_ex_std,'*','markersize',10,'linewidth',2)
hold on
xlabel('gray image 0~255','FontSize',15);
ylabel('pH','FontSize',15);
set(gca,'FontSize',15);
grid on
% fitting this pH - intensity curve
% pH external image fit
pH_ex_fit=polyfit(avg,pH_ex_std,1);% fit curve === linear
pH_ex_cc=polyval(pH_ex_fit,avg);
plot(avg,pH_ex_cc,'k','linewidth',2)

```

## 5. Glucose synthesis OD value correlation



runcalibration.m

```

% % calibration curve
% OD reading value to glucose concentration
close all
clear
clc
load('OD2glucose.mat')
glucose=OD2glucose(:,1); % glucose concentration ug/min
ODvalue=OD2glucose(:,2); % plate reader, @ 540nm
figure(1)
plot(glucose,ODvalue,'*')
hold on
title('glucose concentration vs. OD value @ 540nm')
xlabel('glucose concentration (\mug/min)')
ylabel('OD value @ 540nm')
fit=polyfit(glucose,ODvalue,1);% fit curve === linear
fit_cc=polyval(fit,glucose);
plot(glucose,fit_cc,'k','linewidth',2)
grid on
figure(2)
plot(ODvalue,glucose,'*')
hold on
ylabel('glucose concentration (\mug/min)')
xlabel('OD value @ 540nm')

```

```

fit=polyfit(ODvalue,glucose,1);% fit curve === linear
fit_cc=polyval(fit,ODvalue);
plot(ODvalue,fit_cc,'k','linewidth',2)
grid on
y1=mean([0.249 0.257])-0.054;
y1c=interp1(ODvalue,fit_cc,y1);
% 0hour static OD
y2=mean([0.068 0.062])-0.054;
y2c=interp1(ODvalue,fit_cc,y2);
% 4hour glucose
% 3hour dynamic OD
y3=mean([0.368 0.338])-0.043;
y3c=interp1(ODvalue,fit_cc,y3);

```

## 6. Cyclic voltammetry (CV) and chronoamperometry/chronocoulometry (CA)



Icount.m

```

% start counting
% input:
%     current_o    % original data
%     I_step       % define step
% output:
%     I_current    % current series
%     quantity_I   % counted quantity numbers
% quantity of current in step domain
function [I_current,quantity_I]=Icount(I_step,current_o)
% I_step=10; % step: 10mA
I_current=I_step:I_step:ceil(max(current_o)); % x axis use current step
n=length(I_current);% quantity of current domains
% define current matrix: current original
% current_o=d6_5_01(:,11);
quantity_I=zeros(1,n);
k=length(current_o); %the size of current data matrix
m=length(I_current); % the size of x axis
for i=1:k % repeat k times to scan the current original data
    for j=1:m % repeat with j; m times, for the length of x axis
        if (current_o(i)>(I_step*(j-1))) && (current_o(i)<I_step*j) % check
each data; i;
            quantity_I(j)=quantity_I(j)+1; % counts add one;
        end
    end
end
% end counting
end

```

### Appendix III: Significance threshold of the correlation coefficient

$\alpha$ n-2	0.05	0.01	$\alpha$ n-2	0.05	0.01
1	0.997	1.000	21	0.413	0.526
2	0.950	0.990	22	0.404	0.515
3	0.878	0.959	23	0.396	0.505
4	0.811	0.917	24	0.388	0.496
5	0.754	0.847	25	0.381	0.487
6	0.707	0.834	26	0.374	0.478
7	0.666	0.798	27	0.367	0.470
8	0.632	0.765	28	0.361	0.463
9	0.602	0.735	29	0.355	0.456
10	0.576	0.708	30	0.349	0.449
11	0.553	0.684	35	0.325	0.418
12	0.532	0.661	40	0.304	0.393
13	0.514	0.641	45	0.288	0.372
14	0.497	0.623	50	0.273	0.354
15	0.482	0.606	60	0.250	0.325
16	0.468	0.590	70	0.232	0.302
17	0.456	0.575	80	0.217	0.283
18	0.444	0.561	90	0.205	0.267
19	0.433	0.549	100	0.195	0.254
20	0.423	0.537	200	0.138	0.181

### Appendix IV: Copyright clearance and reuse permission

	Article list	© Copyright	License Number
1	Ren, X., et al. (2014). "Modeling of Pneumatic Valve Dispenser for Printing Viscous Biomaterials in Additive Manufacturing." <i>Rapid Prototyping Journal</i> 20(6): 434-443.	Emerald Group Publishing	3742070682176
2	Ren, X., et al. (2014). "Design, Fabrication, and Characterization of Archaeal Tetraether Free-Standing Planar Membranes in a PDMS- and PCB-Based Fluidic Platform." <i>ACS applied materials &amp; interfaces</i> 6(15): 12618-12628.	ACS Publications	License Granted
3	Román-Leshkov, Y., et al., Production of dimethylfuran for liquid fuels from biomass-derived carbohydrates. <i>Nature</i> , 2007. 447(7147): p. 982-985.	Nature Publishing Group	3811671408331
4	Andreiadis, E. S., et al. (2011). "Artificial Photosynthesis: From Molecular Catalysts for Light-driven Water Splitting to Photoelectrochemical Cells." <i>Photochemistry and photobiology</i> 87(5): 946-964.	John Wiley And Sons	3742000875950
5	Gust, D., et al. (2009). "Solar Fuels via Artificial Photosynthesis." <i>Accounts of Chemical Research</i> 42(12): 1890-1898.	ACS Publications	License Granted
6	Borgström, M., et al. (2005). "Light induced manganese oxidation and long-lived charge separation in a Mn <sup>2+</sup> , II-Ru <sup>II</sup> (bpy) 3-acceptor triad." <i>Journal of the American Chemical Society</i> 127(49): 17504-17515.	ACS Publications	License Granted
7	Hambourger, M., et al. (2008). "[FeFe]-hydrogenase-catalyzed H <sub>2</sub> production in a photoelectrochemical biofuel cell." <i>Journal of the American Chemical Society</i> 130(6): 2015-2022.	ACS Publications	License Granted
8	Tachibana, Y., et al. (2012). "Artificial photosynthesis for solar water-splitting." <i>Nature Photonics</i> 6(8): 511-518.	Nature Publishing Group	3742020827587
9	Kodis, G., et al. (2004). "Synthesis and photochemistry of a carotene–porphyrin–fullerene model photosynthetic reaction center." <i>Journal of physical organic chemistry</i> 17(9): 724-734.	John Wiley And Sons	3742020991630
10	Yadav, R. K., et al. (2012). "A photocatalyst–enzyme coupled artificial photosynthesis system for solar energy in production of formic acid from CO <sub>2</sub> ." <i>Journal of the American Chemical Society</i> 134(28): 11455-11461.	ACS Publications	License Granted
11	Varghese, O. K., et al. (2009). "High-rate solar photocatalytic conversion of CO <sub>2</sub> and water vapor to hydrocarbon fuels." <i>Nano letters</i> 9(2): 731-737.	ACS Publications	License Granted

<b>12</b>	Roy, S. C., et al. (2010). "Toward solar fuels: photocatalytic conversion of carbon dioxide to hydrocarbons." <i>ACS Nano</i> 4(3): 1259-1278.	ACS Publications	License Granted
<b>13</b>	AlOtaibi, B., et al. (2015). "Wafer-Level Artificial Photosynthesis for CO <sub>2</sub> Reduction into CH <sub>4</sub> and CO using GaN Nanowires." <i>ACS Catalysis</i> .	ACS Publications	License Granted
<b>14</b>	Logan, B. E., et al. (2006). "Microbial fuel cells: methodology and technology." <i>Environmental science &amp; technology</i> 40(17): 5181-5192.	ACS Publications	License Granted
<b>15</b>	Janssen, M., et al. (2003). "Enclosed outdoor photobioreactors: light regime, photosynthetic efficiency, scale-up, and future prospects." <i>Biotechnology and Bioengineering</i> 81(2): 193-210.	John Wiley And Sons	3742050318470
<b>16</b>	Dau, H. and I. Zaharieva (2009). "Principles, efficiency, and blueprint character of solar-energy conversion in photosynthetic water oxidation." <i>Accounts of Chemical Research</i> 42(12): 1861-1870.	ACS Publications	License Granted
<b>17</b>	Magnuson, A., et al. (2009). "Biomimetic and microbial approaches to solar fuel generation." <i>Accounts of Chemical Research</i> 42(12): 1899-1909.	ACS Publications	License Granted
<b>18</b>	SeokáLee, J., et al. (2011). "Artificial photosynthesis on a chip: microfluidic cofactor regeneration and photoenzymatic synthesis under visible light." <i>Lab on a chip</i> 11(14): 2309-2311.	Royal Society Of Chemistry	3742050979176
<b>19</b>	Wendell, D., et al. (2010). "Artificial photosynthesis in ranaspumin-2 based foam." <i>Nano letters</i> 10(9): 3231-3236.	ACS Publications	License Granted
<b>20</b>	Kühlbrandt, W. (2000). "Bacteriorhodopsin—the movie." <i>Nature</i> 406(6796): 569-570.	Nature Publishing Group	3742070009347
<b>21</b>	von Ballmoos, C., et al. (2009). "Essentials for ATP synthesis by F <sub>1</sub> F <sub>0</sub> ATP synthases." <i>Annual review of biochemistry</i> 78: 649-672.	Annual Reviews	Permission Not Required

## Vita

Xiang Ren

### EDUCATION

**Doctor of Philosophy**, Dept. Mechanical Engineering & Mechanics

*Drexel University*, Philadelphia, PA, U.S

Thesis: **Cell-Free Artificial Photosynthesis System**

Advisor: Prof. Jack G. Zhou; Co-advisor: Prof. Moses Noh

**Master of Science in Engineering**, Dept. Electrical & Computer Engineering

*Johns Hopkins University*, Baltimore, MD, U.S

Thesis: **Design and fabrication of a micro-robot**

Advisor: Prof. Andreas G. Andreou

**Bachelor of Science**, Electronic Information Science and Technology

*University of Electronic Science and Technology of China*, P.R.China

Thesis: **Chaos theory and applications in secured communication**

Advisor: Prof. Shao-Yi Wu, Dr. Chuanji Fu

### PUBLICATIONS

1. Xiang Ren, Qingwei Zhang, Ho-lung Li, Jack Zhou, **Micro and Nano Design and Fabrication of a Novel Artificial Photosynthesis Device**, ASME 2012 International Manufacturing Science and Engineering Conference, Notre Dame, Indiana, MSEC2012-7394
2. Xiang Ren, Miao Yu, Xiaohang Zhou, Qingwei Zhang, Jack Zhou, **Fabrication of Chitosan Porous Structure and Applications on Artificial Photosynthesis Device**, ASME 2013 International Manufacturing Science and Engineering Conference, Madison, Wisconsin, Vol.2, MSEC 2013-1109
3. Xiang Ren, Qingwei Zhang, Kewei Liu, Ho-lung Li, Jack Zhou, **Modeling of Pneumatic Valve Dispenser for Printing Viscous Biomaterials in Additive Manufacturing**, *Rapid Prototyping Journal*, 2014, 20(6), pp.434-443
4. Xiang Ren, Yoontae Kim, Jack Zhou, **Design and Fabrication of Chitosan for Applications of Artificial Photosynthesis**, *Journal of Mechanics Engineering and Automation*, 2013, 3(12), pp.739-746
5. Xiang Ren, Miao Yu, Hongseok (Moses) Noh, Jack G. Zhou, **Creating a Gas-Liquid Interface in a Microchannel Using Porous Polydimethylsiloxane (PDMS)**, Hilton Head Workshop 2014, Hilton Head Island, South Carolina, pp.215-218
6. Yoontae Kim, Xiang Ren, Hongseok (Moses) Noh, **Direct Printing of Silver Nano-Particles Based Ink on Polydimethylsiloxane (PDMS) for MEMS Devices**, Hilton Head Workshop 2014, Hilton Head Island, South Carolina, pp.191-194
7. Xiang Ren, Kewei Liu, Qingwei Zhang, Hongseok (Moses) Noh, E.Caglan Kumbur, Wenqiao Yuan, Jack G. Zhou, Parkson Lee-Gau Chong, **Design, Fabrication and Characterization of Archaeal Tetraether Free-Standing Planar Membranes in a PDMS- and PCB-Based Fluidic Platform**, *ACS Applied Materials & Interfaces*, 2014, 6(15), pp.12618-12628
8. Xiang Ren, Xin Yang, Jack G. Zhou, Moses Noh, **Microfabricated Platform for Integrating Photosynthetic Biomembrane and in-situ Monitoring via Impedance Spectroscopy**, MicroTAS 2014 18th International Conference on Miniaturized Systems for Chemistry and Life Sciences, San Antonio, Texas, pp.2158-2160
9. Yoontae Kim, Xiang Ren, Jin Won Kim, Hongseok (Moses) Noh, **Direct Inkjet Printing of Silver Microelectrodes on Polydimethylsiloxane (PDMS)**, *Journal of Micromechanics and Microengineering*, (2014) Vol.24, Iss.11, pp. 115010
10. Xiang Ren, Jack G. Zhou, Moses Noh, **Fabrication of Porous Polydimethylsiloxane (PDMS) Thin Film for Gas-liquid Interface**, MicroTAS 2015 19th International Conference on Miniaturized Systems for Chemistry and Life Sciences, Gyeongju, Korea, pp.1404-1406

